

AFRL-AFOSR-VA-TR-2022-0089

Analysis and Modeling of Turbulence-Flame Interactions in Premixed Reacting Flows

Hamlington, Peter
REGENTS OF THE UNIVERSITY OF COLORADO
3100 MARINE ST 572 UCB
BOULDER, CO,
US

01/23/2022
Final Technical Report

DISTRIBUTION A: Distribution approved for public release.

Air Force Research Laboratory
Air Force Office of Scientific Research
Arlington, Virginia 22203
Air Force Materiel Command

REPORT DOCUMENTATION PAGE

PLEASE DO NOT RETURN YOUR FORM TO THE ABOVE ORGANIZATION.

1. REPORT DATE	2. REPORT TYPE	3. DATES COVERED	
20220123	Final	START DATE 20170201	END DATE 20210731

4. TITLE AND SUBTITLE
Analysis and Modeling of Turbulence-Flame Interactions in Premixed Reacting Flows

5a. CONTRACT NUMBER	5b. GRANT NUMBER	5c. PROGRAM ELEMENT NUMBER
	FA9550-17-1-0144	61102F
5d. PROJECT NUMBER	**5e. TASK NUMBER**	**5f. WORK UNIT NUMBER**

6. AUTHOR(S)
Peter Hamlington

7. PERFORMING ORGANIZATION NAME(S) AND ADDRESS(ES)
REGENTS OF THE UNIVERSITY OF COLORADO
3100 MARINE ST 572 UCB
BOULDER, CO
US

8. PERFORMING ORGANIZATION REPORT NUMBER

9. SPONSORING/MONITORING AGENCY NAME(S) AND ADDRESS(ES)	10. SPONSOR/MONITOR'S ACRONYM(S)	11. SPONSOR/MONITOR'S REPORT NUMBER(S)
Air Force Office of Scientific Research 875 N. Randolph St. Room 3112 Arlington, VA 22203	AFRL/AFOSR RTA1	AFRL-AFOSR-VA-TR-2022-0089

12. DISTRIBUTION/AVAILABILITY STATEMENT
A Distribution Unlimited: PB Public Release

13. SUPPLEMENTARY NOTES

14. ABSTRACT
In this research effort, the coupled interactions between turbulence and premixed flames were explored from a fundamental physical standpoint using both scale-dependent and Lagrangian analysis approaches. Improved understanding of these interactions is critical for developing new subgrid-scale (SGS) models that can capture energy transfer between disparate turbulent and flame scales in large eddy simulations (LES) of both fundamental and applied combustion problems. The scale-dependent analyses have included both Fourier and physical-space approaches in order to determine how chemical energy release from premixed flames is distributed to turbulent scales of motion both larger and smaller than the flame width. Moreover, the nonlinearly coupled dynamics of turbulent fluid motion and chemical species evolution have been examined using a Lagrangian analysis approach, with a particular emphasis on determining how chemical species evolution differs in turbulent settings as compared to the laminar and perfectly-stirred conditions for which most chemical kinetic mechanisms are developed. We have also examined the properties of turbulence from a Lagrangian perspective, including turbulent dispersion and enstrophy evolution along fluid particle pathlines. Finally, modern data-driven optimization and machine learning techniques were used to develop improved simulations of complex engineering flows, particularly through the use of approximate Bayesian computation (ABC).
The three primary objectives of this research project were:

15. SUBJECT TERMS

16. SECURITY CLASSIFICATION OF:			17. LIMITATION OF ABSTRACT	18. NUMBER OF PAGES
a. REPORT U	b. ABSTRACT U	c. THIS PAGE U	UU	204

19a. NAME OF RESPONSIBLE PERSON	19b. PHONE NUMBER *(Include area code)*
CHIPING LI	426-8574

Analysis and Modeling of Turbulence-Flame Interactions in Premixed Reacting Flows

AFOSR Project FA9550-17-1-0144
Final Report

PI: Prof. Peter E. Hamlington, *University of Colorado, Boulder*

1 Overview

In this research effort, the coupled interactions between turbulence and premixed flames were explored from a fundamental physical standpoint using both scale-dependent and Lagrangian analysis approaches. Improved understanding of these interactions is critical for developing new subgrid-scale (SGS) models that can capture energy transfer between disparate turbulent and flame scales in large eddy simulations (LES) of both fundamental and applied combustion problems. The scale-dependent analyses have included both Fourier and physical-space approaches in order to determine how chemical energy release from premixed flames is distributed to turbulent scales of motion both larger and smaller than the flame width. Moreover, the nonlinearly coupled dynamics of turbulent fluid motion and chemical species evolution have been examined using a Lagrangian analysis approach, with a particular emphasis on determining how chemical species evolution differs in turbulent settings as compared to the laminar and perfectly-stirred conditions for which most chemical kinetic mechanisms are developed. We have also examined the properties of turbulence from a Lagrangian perspective, including turbulent dispersion and enstrophy evolution along fluid particle pathlines. Finally, modern data-driven optimization and machine learning techniques were used to develop improved simulations of complex engineering flows, particularly through the use of approximate Bayesian computation (ABC).

The three primary objectives of this research project were:

1. Quantitatively characterize multi-scale interactions between turbulence and flames in premixed reacting flows for a range of different conditions (e.g., various Damköhler and Karlovitz numbers).

2. Using Lagrangian analyses, explore variations in the fundamental, nonlinearly coupled physics governing chemical species and turbulence evolution through premixed flamelets.

3. Using data-driven and machine learning techniques, develop improved techniques for simulations of turbulent engineering flows.

Ultimately, this project addressed both the fundamental understanding of turbulence-flame interactions in premixed combustion, as well as physical modeling in numerical simulations of both fundamental and applied flow problems. In the following, we briefly summarize progress made on each of these tasks during the project, and attach publications that describe project results.

2 Characterization of Multi-Scale Interactions in Premixed Combustion

- Scaling and collapse of conditional velocity structure functions in turbulent premixed flames
  Published in the *Proceedings of the Combustion Institute*
  A new scale-sensitive physical-space conditional analysis has been used to examine the scaling and collapse of velocity structure functions in turbulent premixed flames. The conditioning is based on local instantaneous temperatures in the premixed flame, and structure function scaling and collapse are examined using Kolmogorov-type dimensional arguments and scaling relations. Both longitudinal and lateral structure functions are computed using the local flame normal and tangent as reference directions. The analysis is based on data from direct numerical simulations of unconfined statistically-planar flames at three different intensities of turbulence in the premixed reactants. The analysis shows that as the turbulence intensity increases and for locations near the unburnt reactants, conditional structure functions approach the $r^{N/3}$ inertial range scaling predicted by Kolmogorov, where N is the structure function order. Using conditionally-calculated scaling variables, we have further shown that structure functions throughout the flame increasingly collapse as the turbulence intensity increases, with a more complete collapse observed for longitudinal structure functions and for small r within the analytic (or dissipative) range. These results suggest that, at sufficiently high intensities, Kolmogorov-type scaling laws and dimensional arguments may

retain some validity in premixed flames, provided that scaling variables are computed on a conditional basis for different temperatures.

- A scaling law for the required transition zone depth in hybrid LES-DNS
  Published in the *Journal of Turbulence*
  There is a substantial need to better understand multi-physics interactions in realistic laboratory experiments, yet it is currently unfeasible to perform direct numerical simulations (DNS) of most such problems. As a result, reduced-order models such as those used to represent unclosed subgrid-scale stresses in large-eddy simulations (LES) and advanced numerical techniques, including adaptive mesh refinement and nested grid structures, are required for the study of multi-physics interactions in practical situations. In particular, it is now possible to model many real-world flows with LES fidelity, and to selectively refine the computational mesh in a small region of the domain to resolve multi-physics interactions with DNS fidelity. However, rules and guidance for the valid implementation of this multi- fidelity 'hybrid LES-DNS' approach have yet to be fully formulated. Within the embedded DNS region, multi-physics interactions will be influenced by (*i*) macroscale features (e.g., large-scale shear gradients or body forces that produce turbulence), (*ii*) LES-regulated mesoscale features (e.g. advecting turbulent eddies), and (*iii*) microscale features that are subgrid-scale to the LES (e.g., layers of fast-reacting intermediate chemical species). In this study, we address the second of these effects, which poses particular challenges due to the transfer and overlapping nature of advecting mesoscale eddies between the purely LES (i.e., macroscale) and purely DNS (i.e., microscale) regions. By combining dimensional analysis and computational results, we formulate a scaling law for the required depth of the transition zone surrounding the embedded DNS region within hybrid LES-DNS computations of realistic turbulent flows.

- Structure and dynamics of highly turbulent premixed combustion
  Published in *Progress in Energy and Combustion Science*
  Turbulent premixed combustion involves simultaneous and mutually interacting fluid, chemical, and transport phenomena spanning a wide range of spatial and temporal scales. Many practical combustion devices – such as gas turbine combustors, afterburners, and ramjets – operate with turbulent flows that contain length and time scales smaller than those associated with premixed flame propagation. In this paper we reviewed current knowledge and understanding of premixed flames at such "highly turbulent" conditions, including the effects of turbulence on the flame and of the flame on turbulence. At these conditions, turbulent fluid motions can have a leading-order effect on the flame thermochemical structure, scalar gradients, and the resultant scalar dynamics. At the same time, the turbulent flow itself is affected by heat release from the flame, resulting in differences compared to classical non-reacting turbulence and to turbulence in flames at lower intensities. We addressed the following overarching questions in this review: (*a*) What are highly turbulent premixed flames, how do we characterize them, and what are some of their macroscale behaviors? (*b*) How are the flame thermochemical states, scalar gradients, diffusion, and other aspects of the flame structure affected by intense turbulence? (*c*) How are the structure and dynamics of the turbulence affected by the presence of the flame in terms of fluxes, spectra, kinetic energy, and other relevant quantities? This third question, in particular, directly touches on much of the research performed during the course of this project. We also provide a summary of critical knowledge gaps and an outlook for future research directions.

3 Lagrangian Analysis of Turbulent Premixed Reacting Flows

- Lagrangian analysis of high-speed turbulent premixed reacting flows: Thermochemical trajectories in hydrogen–air flames
  Published in *Combustion and Flame*
  A Lagrangian analysis approach is used to examine the effects of high-speed turbulence on thermochemical trajectories in unconfined, stoichiometric hydrogen–air (H_2–air) premixed flames. Two different intensities of turbulence in the unburnt reactants are considered, giving premixed flames with Karlovitz numbers of roughly 150 and 450. These two cases are modeled using direct numerical simulations (DNS) with both multi- and single-step H_2–air reaction kinetics. In each of the four resulting simulations, trajectories of fluid parcels are calculated using a high-order Runge–Kutta method, and time series of temperature and chemical composition within each parcel are recorded. The resulting thermochemical trajectories are used to examine the evolution of thermodynamic quantities and chemical composition, as well as

measure fluid parcel residence times and path lengths during different phases of the combustion process. Fuel mass fraction and temperature within fluid parcels are shown to be frequently non-monotonic along fluid trajectories in both single- and multi-step H_2–air simulations, and the prevalence of non-monotonic trajectories increases with increasing turbulence intensity. Using results from single-step simulations, it is shown that this non-monotonicity can be caused solely by molecular transport processes resulting from large gradients in temperature and species concentrations created by turbulent advection. As a related consequence of advection, fluid parcel residence times are found to be smaller than in a laminar flame and the ratio of turbulent to laminar residence times decreases from roughly 0.8 to 0.6 as the turbulence intensity increases. By contrast, fluid parcel path lengths in the present high-speed turbulent flames are found to be substantially greater than laminar path lengths, resulting in fluid parcels that travel 4 and 7 times further than in a laminar flame for the two different turbulence intensities considered here.

- Detonation initiation by compressible turbulence thermodynamic fluctuations
  Published in *Combustion and Flame*
  Theory and computations have established that thermodynamic gradients created by hot spots in reactive gas mixtures can lead to spontaneous detonation initiation. However, the current laminar theory of the temperature-gradient mechanism for detonation initiation is restricted to idealized physical configurations. Thus, it only predicts conditions for the onset of detonations in quiescent gases, where an isolated hot spot is formed on a timescale shorter than the chemical and acoustic timescales of the gas. In this work, we extend the laminar temperature-gradient mechanism into a statistical model for predicting the detonability of an autoignitive gas experiencing compressible isotropic turbulence fluctuations. Compressible turbulence forms non-monotonic temperature fields with tightly-spaced local minima and maxima that evolve over a range of timescales, including those much larger than chemical and acoustic timescales. We examine the utility of the adapted statistical model through direct numerical simulations of compressible isotropic turbulence in premixed hydrogen-air reactants for a range of conditions. We find strong, but not conclusive, evidence that the model can predict the degree of detonability in an autoignitive gas due to turbulence-induced thermodynamic gradients.

- Particle pair dispersion and eddy diffusivity in a high-speed premixed flame
  Published in the *Proceedings of the Combustion Institute*
  Turbulent mixing is a physical process of fundamental importance in high-speed premixed flames. This mixing results in enhanced transport of temperature and chemical scalars, leading to potentially large changes in flame structure and dynamics. To understand turbulent mixing in non-reacting flows, a number of classical theories have been proposed to describe the scaling and statistics of dispersing fluid particle pairs, including predictions of the effective, or turbulent, eddy diffusivity. In this study we have examined the validity of these classical theories through the study of fluid particle pair dispersion and eddy diffusivity in highly turbulent premixed methane-air flames at a Karlovitz number of approximately 140. Using data from a DNS and a higher-order Lagrangian tracking algorithm, particle pair centroids are seeded at different initial temperatures and separations, and then integrated forward in time. We show that scaling relations and results developed for pair dispersion in non-reacting flows remain relevant in this high-intensity premixed flame, and we identify the impacts of heat release on dispersion and eddy diffusivity.

- Lagrangian analysis of enstrophy dynamics in a highly turbulent premixed flame
  Published in *Physics of Fluids*
  A Lagrangian analysis approach is used to examine the effects of heat release on the dynamics of the enstrophy during highly turbulent premixed combustion. The analysis is performed using data from a direct numerical simulation of a statistically planar premixed methane–air flame at a Karlovitz number of 100. Through cumulative, conditional, and correlation analyses, we show, consistent with prior studies, that vortex stretching and baroclinic torque both increase enstrophy at these highly turbulent conditions, while viscous transport and dilatation both lead to enstrophy destruction. However, although vortex stretching and viscous transport are individually an order of magnitude greater than all other terms in the enstrophy budget, the cumulative and combined effect of these two terms along Lagrangian trajectories is roughly only twice as large as the combined cumulative effect of dilatation and baroclinic torque. Moreover, trajectories that exhibit an increase in enstrophy through the flame are found to frequently have cumulative contributions from budget terms outside a single standard deviation of the mean contribution, indicating that enstrophy production at such highly turbulent conditions is associated with relatively infrequent but

large values of dynamical terms. Lagged correlations further reveal a small but measurable contribution of baroclinic torque in enstrophy production, but these increases are overwhelmed, on average, by concurrent decreases in enstrophy due to viscous transport and dilatation. Taken together, these results provide further understanding of enstrophy dynamics in highly turbulent premixed flames.

- WENO interpolation for Lagrangian particles in highly compressible flow regimes
  Published in *Journal of Computational Physics*
  Lagrangian particles can be used either to analyze different complex flows, as massless tracers, or to model multiphase flows, as particles with mass. As particles can have arbitrary positions within the computational domain, interpolation of different flow quantities from the Eulerian grid is essential. Low-order centered interpolation schemes generally do not provide a sufficient level of accuracy for many flow configurations of interest. Thus, typically, high-order centered interpolation schemes are utilized. The current study demonstrates that for highly compressible non-reacting and reacting flow regimes, in which discontinuities in the flow field, e.g., shock waves arise, centered interpolation schemes tend to smear the shock and high order schemes also produce numerical oscillations. It is shown that this problem can be remedied by using Weighted- Essentially-Non-Oscillatory (WENO) interpolation schemes. Extensive numerical tests are performed in order to demonstrate this, comparing the performance of WENO-3 and WENO-5 interpolation schemes with a variety of centered interpolation schemes. The first test case involves specially designed steady state two-dimensional vortex flows. For a smooth flow, WENO schemes provide comparable accuracy to other high-order centered schemes. For flow fields with discontinuities, WENO-3 and WENO-5 interpolation schemes can decrease the interpolation error by more than two and three orders of magnitude, respectively, in comparison with centered schemes. Solution accuracy is further studied with a normal shock wave test. It is demonstrated that centered schemes tend to smear the shock, whereas, WENO schemes capture it in a much sharper manner. Moreover, high-order centered schemes tend to oscillate in the vicinity of the discontinuity leading to non- physical results, such as negative absolute pressure values. The same trends are retained for an unsteady three-dimensional spherical blast wave, where the shock is smeared across several grid cells, which is typical for shock-capturing flow solvers. Finally, the benefits of WENO schemes for the Lagrangian-particle tracking analysis of highly compressible reactive flows are explored by comparing various Lagrangian particle trajectories and joint probability density functions (PDFs) for a two-dimensional cellular detonation. The results indicate that high-order centered schemes lead to unphysical results, whereas WENO schemes can provide high-order interpolation that is free of severe numerical oscillations and non-physical artifacts, which is critical for the proper analysis of the flow.

4 Physics-Based and Data-Driven LES Model Development

- Parameter estimation for complex thermal-fluid flows using approximate Bayesian computation
  Published in *Physical Review Fluids*
  Approximate Bayesian computation (ABC) is a data-driven technique that uses many low-cost numerical simulations to estimate unknown physical or model parameters (e.g., boundary conditions and material properties), as well as their uncertainties, given reference data from real-world experiments or higher-fidelity numerical simulations. In this study, ABC is used to estimate unknown parameters in complex thermal-fluid flows, and the technique is demonstrated on a periodically forced high-temperature jet and a steadily forced helium-air plume. In the first case, computational reference data are used to assess the accuracy of ABC when estimating the frequency, amplitude, and mean of the periodic velocity forcing at the jet inlet. These tests show that ABC provides accurate and reasonably certain estimates of inflow parameters even when the model simulations imperfectly represent the physics underlying the reference data. These tests also show that measurements far from the inlet can be used to perform the estimation, and that temperature measurements can be used to infer velocity inflow parameters. For the second case, ABC is used to estimate the inlet Richardson number and its uncertainty given experimental measurements of the Strouhal number within the plume. Once again, the approach is able to accurately estimate unknown parameters with relatively low uncertainty. As a result, ABC is shown to be a versatile technique for estimating unknown physical parameters when knowledge of a real-world system is limited or incomplete.

- Flow parameter estimation using laser absorption spectroscopy and approximate Bayesian computation
  Published in *Experiments in Fluids*

Given spatially sparse or lower dimensional experimental measurements, approximate Bayesian computation (ABC) and numerical simulations can be used to estimate unknown characteristics of complex multi-physics engineering systems. Here, we describe the ABC approach and use it to estimate the speed of high-temperature gases exiting an industrially relevant catalytic burner, as well as to estimate the completeness of combustion within the burner. Using vertical profiles of absorption-weighted average temperature from laser absorption spectroscopy (LAS) at three different burner operating conditions, we combine ABC and large eddy simulations (LES) to generate posterior distributions of inflow speeds and heat addition characteristics above the burner. We show that the ABC method correctly estimates trends in the inflow speed for different conditions, and we find that there is a strong likelihood of incomplete combustion for higher equivalence ratios. We evaluate the predictive capability of the approach using an observing system experiment, indicating that the ABC method, when combined with LES, is able to accurately predict LAS measurements. We thus demonstrate that ABC is an effective tool for obtaining additional insights from available experimental measurements, thereby improving understanding of real-world engineering systems.

- Parameter Estimation for Reynolds-Averaged Navier–Stokes Models Using Approximate Bayesian Computation
  Published in *AIAA Journal*
  Approximate Bayesian computation (ABC) is used to estimate unknown parameter values, as well as their uncertainties, in Reynolds-averaged Navier–Stokes (RANS) simulations of turbulent flows. The ABC method approximates posterior distributions of model parameters, but does not require the direct computation, or estimation, of a likelihood function. This method thus enables relatively simple and flexible parameter estimation for complex models and a wide range of reference data. This paper describes the ABC approach, including the use of a calibration step, adaptive proposal, and Markov chain Monte Carlo (MCMC) technique to accelerate the parameter estimation, resulting in an ABC approach with improved MCMC, denoted ABC-IMCMC. As a test of the classic ABC rejection algorithm and ABC-IMCMC, parameters are estimated in a nonequilibrium RANS model using reference data from direct numerical simulations of periodically sheared homogeneous turbulence. The use of ABC-IMCMC is then demonstrated to estimate parameters in the Menter shear-stress-transport (SST) model using experimental reference data for an axisymmetric transonic bump. This paper shows that the accuracy of the SST model for this test case can be improved using ABC-IMCMC, indicating that ABC-IMCMC is a promising method for the calibration of RANS models using a wide range of reference data.

5 Research Products

The following list summarizes the research products related to this project, including journal publications, conference papers, and conference presentations. Invited lectures related to this project are also listed.

Peer-Reviewed Journal Publications:

1. J. D. Christopher, O. A. Doronina, D. Petrykowski, T. R. S. Hayden, C. Lapointe, N. T. Wimer, I. Grooms, G. B. Rieker, and P. E. Hamlington. Flow Parameter Estimation Using Laser Absorption Spectroscopy and Approximate Bayesian Computation. Experiments in Fluids, 62:43, 2021.
2. R. Darragh, C. A. Z. Towery, M. A. Meehan, and P. E. Hamlington. Lagrangian Analysis of Enstrophy Dynamics in a Highly Turbulent Premixed Flame. Physics of Fluids, 33:055120, 2021.
3. R. Darragh, C. A. Z. Towery, A. Y. Poludnenko, and P. E. Hamlington. Particle Pair Dispersion and Eddy Diffusivity in a High-Speed Premixed Flame. Proceedings of the Combustion Institute, 38:2845–2852, 2021.
4. O. Doronina, S. Murman, and P. E. Hamlington. Parameter Estimation for RANS Models Using Approximate Bayesian Computation. AIAA Journal, 59(11):4703–4718, 2021.
5. A. M. Steinberg, P. E. Hamlington, and X. Zhao. Structure and Dynamics of Highly Turbulent Premixed Flames. Progress in Energy and Combustion Science, 85:100900, 2021.
6. Y. Kozak, S. S. Dammati, L. G. Bravo, P. E. Hamlington, and A. Y. Poludnenko. WENO interpolation for Lagrangian particles in highly compressible flow regimes. Journal of Computational Physics, 402:109054, 2020.

7. C. A. Z. Towery, A. Y. Poludnenko, and P. E. Hamlington. Detonation initiation by compressible turbulence thermodynamic fluctuations. Combustion and Flame, 213:172–183, 2020.
8. C. A. Z. Towery, S. Walters, S. M. Guzik, X. Gao, and P. E. Hamlington. A Scaling Law for the Required Transition Zone Depth in Hybrid LES-DNS of Turbulent Premixed Flames. Journal of Turbulence, 21(12):722–734, 2020.
9. S. H. R. Whitman, C. A. Z. Towery, A. Y. Poludnenko, and P. E. Hamlington. Scaling and collapse of conditional velocity structure functions in turbulent premixed flames. Proceedings of the Combustion Institute, 37(2):2527–2535, 2019.
10. J. D. Christopher, C. Lapointe, N. T. Wimer, T. R. S. Hayden, I. Grooms, G. B. Rieker, and P. E. Hamlington. Parameter estimation for complex thermal-fluid flows using approximate Bayesian computation. Physical Review Fluids, 3:104602, 2018.
11. P. E. Hamlington, R. Darragh, C. A. Briner, C. A. Z. Towery, and A. Y. Poludnenko. Lagrangian analysis of high-speed turbulent premixed reacting flows: thermochemical trajectories in hydrogen-air flames. Combustion and Flame, 186:193–207, 2017.

Conference Proceedings:

12. Y. Kozak, S. S. Dammati, L. Bravo, P. Hamlington, and A. Poludnenko. Novel Lagrangian-Particle Tracking Method for Highly Compressible, Turbulent, Reacting Flows. AIAA Paper, AIAA-2019-1642, 2019.
13. B. Schmidt, C. Towery, P. Hamlington, and J. Sutton. Evaluation of Wavelet-Based Optical Flow Velocimetry from OH Scalar Fields in Reacting Turbulent Flows. AIAA Paper, AIAA-2019-0270, 2019.
14. P. E. Hamlington, R. Darragh, C. A. Z. Towery, and A. Y. Poludnenko. Retrospective Lagrangian analysis of turbulence-chemistry interactions in highly turbulent premixed flames. Proceedings of the 11th U.S. National Meeting on Combustion, 2019.
15. C. Towery, B. Schmidt, J. Sutton, and P. Hamlington. Benchmark Direct Numerical Simulations with Lagrangian Tracers for Evaluating Combustion Diagnostics Algorithms. AIAA Paper, AIAA-2019-0836, 2019.
16. C. Towery, P. Hamlington, X. Zhao, C. Xu, T. Lu, and A. Poludnenko. Lagrangian Chemical Explosive Mode Analysis of Highly Turbulent Premixed Flames. AIAA Paper, AIAA-2019-1643, 2019.
17. C. A. Z. Towery, J. Urzay, A. Y. Poludnenko, and P. E. Hamlington. The cross-scale flux of kinetic energy by baropycnal work in premixed reacting flows. Proceedings of the 2019 Western States Section of the Combustion Institute Fall Technical Meeting, 2019.
18. R. Darragh, C. A. Z. Towery, A. Y. Poludnenko, and P. E. Hamlington. Lagrangian Analysis of Enstrophy in Turbulent Premixed Flames. Proceedings of the 2017 Western States Section of the Combustion Institute Fall Technical Meeting, Paper ID: 29TF-0085, 2017.

Conference Presentations (abstract only):

19. O.Doronina, S. Murman, and P. E. Hamlington (2019) Approximate Bayesian Computation for Parameter Estimation in RANS Turbulence Models. 72nd Annual meeting, Division of Fluid Dynamics, American Physical Society, Seattle, WA, 23-26 November 2019.
20. R. Darragh, C. Towery, and P. E. Hamlington (2019) Particle Pair Dispersion in a Turbulent Premixed Flame. 72nd Annual meeting, Division of Fluid Dynamics, American Physical Society, Seattle, WA, 23-26 November 2019.
21. C. A. Z. Towery, A. Y. Poludnenko, and P. E. Hamlington (2019) Initiation of Spontaneous Detonation in Highly Compressible Turbulence. 17th International Conference on Numerical Combustion, SIAM, 6-8 May 2019, Aachen, Germany.
22. C. A. Z. Towery, A. Y. Poludnenko, and P. E. Hamlington (2018) Spontaneous Detonation Initiation by Temperature Gradients in Compressible Isotropic Turbulence. 71st Annual meeting, Division of Fluid Dynamics, American Physical Society, Atlanta, GA, 18-20 November 2018.
23. P. E. Hamlington, C. A. Z. Towery, and A. Y. Poludnenko (2018) Analysis of Highly-Turbulent Premixed Flames Using a Retrospective Lagrangian Analysis. 71st Annual meeting, Division of Fluid Dynamics, American Physical Society, Atlanta, GA, 18-20 November 2018.
24. Y. Kozak, S. S. Dammati, L. O'Neill, P. E. Hamlington, and A. Y. Poludnenko (2018) Novel method for Lagrangian-particle analysis of highly compressible reacting turbulence. 71st Annual meeting, Division of Fluid Dynamics, American Physical Society, Atlanta, GA, 18-20 November 2018.

25. S. S. Dammati, Y. Kozak, L. O'Neill, P. E. Hamlington, and A. Y. Poludnenko (2018) Lagrangian Analysis of the Thermochemical Trajectories in High-Speed, Turbulent, Premixed Methane-Air and Jet-Fuel-Air Flames. 71st Annual meeting, Division of Fluid Dynamics, American Physical Society, Atlanta, GA, 18-20 November 2018.
26. C. Towery, P. Hamlington, and A. Poludnenko (2018) Modes of Combustion in Highly Compressible Turbulent Premixed Reacting Flows. 16th Premixed Turbulent Flame Workshop, July 28, 2018, Dublin, Ireland.
27. A. M. Steinberg and P. E. Hamlington (2018) Structure and Dynamics of Highly Turbulent Premixed Flames. Joint Session of the 14th International Workshop on Measurement and Computation of Turbulent Flames and the 16th Premixed Turbulent Flame Workshop, July 27, 2018, Dublin, Ireland.
28. C. A. Z. Towery, A. Y. Poludnenko, and P. E. Hamlington (2018) Direct Numerical Simulations of High Intensity Turbulent Combustion and Fire. World Congress of Computational Mechanics, July 23-27, 2018, New York, NY.
29. R. Darragh, C. Towery, A. Poludnenko, and P. Hamlington (2017) Lagrangian Enstrophy Dynamics in Highly Turbulent Premixed Flames. 70th Annual meeting, Division of Fluid Dynamics, American Physical Society, Denver, CO, 19-21 November 2017.
30. S. H. R. Whitman, C. A. Z. Towery, A. Y. Poludnenko, and P. E. Hamlington (2017) A Structure Function Analysis of Intermittency and Universality in Turbulent Premixed Flames. 70th Annual meeting, Division of Fluid Dynamics, American Physical Society, Denver, CO, 19-21 November 2017.
31. C. Towery, R. Darragh, A. Poludnenko, and P. Hamlington (2017) Direct numerical simulations of premixed autoignition in compressible uniformly-sheared turbulence. 70th Annual meeting, Division of Fluid Dynamics, American Physical Society, Denver, CO, 19-21 November 2017.
32. P. Hamlington (2017) Structure Functions and Intermittency in Turbulent Premixed Reacting Flows. Frontiers in Turbulence KRS 70 at the Denver Symposium, 17-18 November, 2017, Denver. CO.

Invited Seminars:

33. "Progress and Challenges in High-Fidelity Numerical Simulations of Combustion and Fire." Department of Mechanical and Aerospace Engineering Seminar, University of California, San Diego, CA, October 28, 2019.
34. "Progress and Challenges in High-Fidelity Numerical Simulations of Combustion and Fire." Oregon State University, Corvallis, OR, October 26, 2018.
35. "High-Fidelity Numerical Simulations of Combustion and Fire: A Hot Topic in a Warming World." Department of Mechanical Engineering, University of Colorado, Boulder, CO, October 19, 2018.
36. "Insights Obtained from Direct Numerical Simulations of Highly Turbulent Combustion." Pennsylvania State University, State College, PA, October 11, 2018.
37. "Direct Numerical Simulations of Combustion and Fire." University of Wyoming, Laramie, WY, October 4, 2018.
38. "From Turbines to Trees: Direct Numerical Simulations of Combustion and Fire." National Renewable Energy Laboratory, Golden, CO, July 9, 2018.
39. "Structure and Dynamics of Highly Turbulent Premixed Combustion." Department of Aerospace Engineering, Texas A&M University, College Station, TX, March 26, 2018.
40. "Structure and Dynamics of Highly Turbulent Premixed Combustion." Mechanical and Aerospace Engineering Seminar, Arizona State University, Tempe, AZ, October 13, 2017.

Available online at www.sciencedirect.com

ScienceDirect

Proceedings of the Combustion Institute 37 (2019) 2527–2535

Proceedings of the Combustion Institute

www.elsevier.com/locate/proci

Scaling and collapse of conditional velocity structure functions in turbulent premixed flames

Samuel H.R. Whitman [a], Colin A.Z. Towery [a], Alexei Y. Poludnenko [b], Peter E. Hamlington [a,*]

[a] Department of Mechanical Engineering, University of Colorado, Boulder, CO, USA
[b] Department of Aerospace Engineering, Texas A&M University, College Station, TX, USA

Received 1 December 2017; accepted 2 July 2018
Available online 9 August 2018

Abstract

A new scale-sensitive physical-space conditional analysis is outlined and used to examine the scaling and collapse of velocity structure functions in turbulent premixed flames. The conditioning is based on local instantaneous temperatures in the premixed flame, and structure function scaling and collapse are examined using Kolmogorov-type dimensional arguments and scaling relations. Both longitudinal and lateral structure functions are computed using the local flame normal and tangent as reference directions. The analysis is based on data from direct numerical simulations of unconfined statistically-planar flames at three different intensities of turbulence in the premixed reactants. The analysis shows that as the turbulence intensity increases and for locations near the unburnt reactants, conditional structure functions approach the $r^{N/3}$ inertial range scaling predicted by Kolmogorov, where N is the structure function order. Using conditionally-calculated scaling variables, it is further shown that structure functions throughout the flame increasingly collapse as the turbulence intensity increases, with a more complete collapse observed for longitudinal structure functions and for small r within the analytic (or dissipative) range. These results suggest that, at sufficiently high intensities, Kolmogorov-type scaling laws and dimensional arguments may retain some validity in premixed flames, provided that scaling variables are computed on a conditional basis for different temperatures.
© 2018 The Combustion Institute. Published by Elsevier Inc. All rights reserved.

Keywords: Premixed; Turbulence; Scaling

1. Introduction

Over the past several years, substantial research has been devoted to the effects of premixed flames on turbulence at different spatial scales. Of particular interest has been the problem of determining how turbulence at different scales varies within premixed flames, especially at high turbulence intensities (corresponding to high Karlovitz numbers). Such variations are important for developing a more complete physical understanding of turbulence-flame interactions and premixed flame structure under highly turbulent conditions, as well

* Corresponding author.
E-mail address: peh@colorado.edu (P.E. Hamlington).

https://doi.org/10.1016/j.proci.2018.07.010
1540-7489 © 2018 The Combustion Institute. Published by Elsevier Inc. All rights reserved.

as for improving the accuracy of subgrid-scale models used in large eddy simulations of practical turbulent combustion problems. In the present study, we contribute to this body of knowledge by examining the scaling and collapse of velocity structure functions conditioned on temperature, with a particular focus on whether Kolmogorov-type scaling relations remain valid for turbulence affected by premixed flames.

Prior work studying premixed flame effects on turbulent scales of motion has spanned a wide range of approaches, each of which are intended to provide scale-sensitive information at different spatial locations within or near premixed flames. Furukawa et al. [1] were perhaps the first to examine this problem by computing turbulence kinetic energy spectra either side of a premixed flame, conditioning the analysis on either burnt products or unburnt reactants. More recently, this problem has been addressed using spatial correlation functions in slot flames [2], and Fourier spectral [3], differential filtering [4], and wavelet [5] analyses in statistically planar flames. Taken together, these studies provide a consistent picture of turbulent small scale motions that are suppressed by increased viscous dissipation and dilatation associated with the flame, and large scales that are enhanced by dilatation and, to a lesser extent, kinetic energy backscatter by nonlinear advective processes from small to large scales. Related studies focused on non-premixed combustion by Knaus and Pantano [6] and O'Brien et al. [7] have provided largely consistent results with those from premixed combustion.

In this paper, we build upon these prior studies by using velocity structure functions [8–11] conditioned on temperature to examine variations in turbulent scales of motion at different locations within premixed flames, and for different turbulence intensities. Physical space approaches such as the analysis implemented here (in addition to previous correlation function [2], differential filtering [4,7], and wavelet [5] approaches) are attractive because they provide scale-dependent information, while at the same time allowing control over the physical space location. In the present study, velocity structure functions are defined as moments of the absolute value of two-point velocity differences, given in Cartesian coordinates as [8,11,12]

$$S_{ij}^{N}(r) = \langle |u_i(\boldsymbol{x} + r\boldsymbol{e}_j, t) - u_i(\boldsymbol{x}, t)|^N \rangle \,, \tag{1}$$

where u_i is the velocity, r is the separation distance, $\boldsymbol{e}_j$ is the unit vector indicating the direction of the separation in the two-point velocity difference, and N is the order of the structure function. The use of the absolute value in Eq. (1) differs from the classical definition from Kolmogorov [13], but this formulation, called the "generalized structure function" [8], is now commonly examined because it permits fractional values of N [11]. The average $\langle \cdot \rangle$ in Eq. (1) is generically an ensemble average, but may also be replaced by appropriate spatial or temporal averages. Structure functions in reacting flows were first proposed as a useful diagnostic by Kuznetsov and Sabel'nikov [14], and the present study is the first to explore their characteristics in premixed flames.

Theoretical predictions for structure function scaling in non-reacting flows extend back to Kolmogorov [13], who tied the scaling of longitudinal structure functions (i.e., structure functions for which the velocities considered are parallel to the separation vector $\boldsymbol{e}_j$) in homogeneous isotropic turbulence to the energy cascade and the transfer of energy from large to small scales. Using dimensional arguments in the inertial range of scales, Kolmogorov's theory predicts that $S_{ij}^{N}(r) \sim \varepsilon^{N/3} r^{N/3}$, where ε is the mean dissipation rate of kinetic energy. However, the so-called Kolmogorov-Richardson cascade, a good approximation for non-reacting turbulence at high Reynolds numbers [12], may not hold in the same strict sense for the case of turbulent premixed flames, where assumptions of homogeneity and isotropy can be poor [1,15,16] and the flame may provide an additional source of energy input that disrupts the net down-scale cascade of kinetic energy, leading instead to net backscatter of energy [3,4]. There is thus substantial reason to suspect that the Kolmogorov scaling hypotheses may not hold in premixed turbulent flames, and the present study is focused on characterizing the accuracy of these classical scaling relations for different scales of motion, different turbulence intensities, and different locations within premixed flames.

In the following, we use data from direct numerical simulations (DNS) of statistically planar turbulent premixed flames at three different turbulence intensities to compute velocity structure functions conditioned on temperature. By conditioning on temperature, structure functions can be effectively explored within different regions of the premixed flame. We then show that normalization by conditionally-calculated viscosity and dissipation rates yields an approach to the Kolmogorov scaling $S_{ij}^{N}(r) \sim \varepsilon^{N/3} r^{N/3}$ as the turbulence intensity increases.

2. Numerical simulations

The numerical simulations analyzed here were performed using Athena-RFX [17], which solves the fully compressible, reactive-flow equations. These equations are solved for turbulent premixed flames in unconfined domains and at atmospheric conditions, where single step Arrhenius reaction kinetics are used to model source terms in the species equations. The single-step kinetics have been designed to represent combustion of a stoichiometric H_2-air mixture [18], and the single-step model is outlined in detail in Towery et al. [3]. Viscosity,

Table 1
Physical and reaction parameters for cases I1, I2 and I3.

T_r	293 K	Initial temperature
p_r	101.3 kPa	Initial pressure
ρ_r	0.873 kg/m^3	Initial density
γ	1.17	Adiabatic index
M	21 kg/kmol	Molecular weight
T_p	2135 K	Post-flame temperature
ρ_p	0.12 kg/m^3	Post-flame density
B	6.85×10^9 m^3/(kg s)	Pre-exponential factor
Q	$46.37RT_r$	Activation energy
q	$43.28RT_r/M$	Chemical energy release
ν_r	1.89×10^{-5} m^2/s	Initial kinematic viscosity
α_r	1.77×10^{-4} m^2/s	Initial thermal diffusivity
D_r	1.77×10^{-4} m^2/s	Initial mass diffusivity
n	0.7	Temperature exponent
δ_L	3.2×10^{-4} m	Laminar thermal width
S_L	3.02 m/s	Laminar flame speed

μ, bulk viscosity, μ_B, mass diffusivity, ζ, and thermal conductivity, k, have power-law dependencies on temperature given by

$$\mu = \mu_B = \rho_r \nu_r (T/T_r)^n , \tag{2}$$

$$\zeta = \rho_r D_r (T/T_r)^n , \tag{3}$$

$$k = \rho_r \alpha_r c_p (T/T_r)^n , \tag{4}$$

where $c_p = \gamma R/M(\gamma - 1)$ is the specific heat capacity at constant pressure and coefficient values are given in Table 1. The density decreases by a factor of roughly 7.3 from the unburnt reactants to burnt products, and μ, μ_B, ζ, and k all correspondingly increase by factors of roughly 4. Schmidt and Prandtl numbers are 0.2 and the Lewis number is unity in the reactants. Thermodynamic quantities are related to each other using the ideal gas equation of state. The resulting laminar flame speed is $S_L = 3.02$ m/s and the laminar flame thermal width based on the maximum temperature gradient is $\delta_L = 3.2 \times 10^{-4}$ m. Additional properties and parameters used in the DNS are provided in Table 1.

The three simulations performed model different intensities of turbulence in the reactants, denoted I1, I2 and I3, as shown in the regime diagram in Fig. 1. Turbulence is sustained in the simulations using large-scale forcing, as described in [17]. The data for case I1 was previously analyzed in Fourier spectral space by Towery et al. [3] and using differential filtering by O'Brien et al. [4]. Recently, the data for I2 has been analyzed using wavelets by Kim et al. [5]. Case I3, which has the highest intensity turbulence examined here, is analyzed for the first time in the present study.

Parameters for each simulation are shown in Table 2, where Damköhler (Da) and Karlovitz (Ka) numbers are defined as [20]

$$\mathrm{Da} \equiv \frac{\tau_{ed}}{\tau_c} = \left(\frac{\ell}{\delta_L}\right)\left(\frac{U_\ell}{S_L}\right)^{-1} , \tag{5}$$

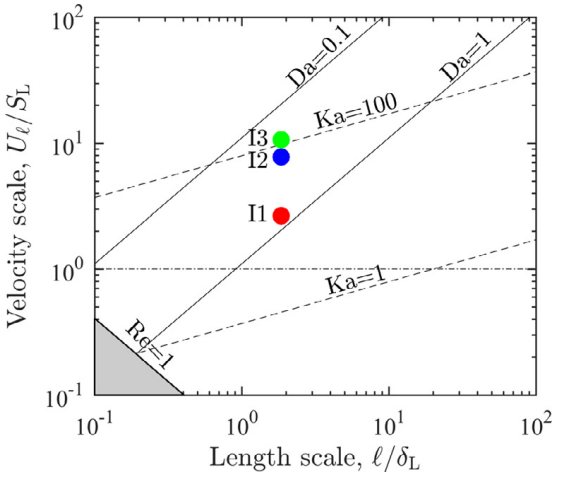


Fig. 1. Combustion regime diagram [19] showing the location of each DNS case.

Table 2
Turbulence intensity, $I_t = (U_\ell/S_L)$, Karlovitz, Damköhler, and Taylor scale Reynolds numbers numbers for all simulations. All parameters are computed based on properties in the unburnt reactants.

Simulation	I_t (U_ℓ/S_L)	Ka	Da	Re_λ
I1	2.5	20.3	0.77	100
I2	7.3	71.9	0.25	170
I3	9.9	166	0.19	200

$$\mathrm{Ka} \equiv \frac{\tau_c}{\tau_K} = \left(\frac{S_L \delta_L}{\nu_r}\right)^{1/2}\left(\frac{\ell}{\delta_L}\right)^{-1/2}\left(\frac{U_\ell}{S_L}\right)^{3/2} . \tag{6}$$

Here $\tau_c \equiv \delta_L/S_L$ is the chemical time scale, and $\tau_{ed} \equiv \ell/U_\ell$ and $\tau_K \equiv (\nu_r/\varepsilon_r)^{1/2}$ are the eddy turnover and Kolmogorov timescales in the unburnt reactants, where ℓ is the turbulence integral length scale, U_ℓ is the integral scale velocity, and ν_r and ε_r are the viscosity and dissipation rate, respectively, in the reactants. Taylor scale Reynolds numbers, $\mathrm{Re}_\lambda = U_\ell \lambda/\nu_r$, are also shown in Table 2 and span values from 100 to 200 for I1 to I3, where the Taylor scale λ is estimated using the classical relation for homogeneous isotropic turbulence, namely $\varepsilon_r = 15\nu_r u'^2_{rms}/\lambda^2$. It should be noted that the values of Re_λ considered in the present study are relatively low, resulting in a very small or no inertial range of scales. As such, the present study is primarily focused on whether an *approach* to Kolmogorov scaling is observed as Re_λ increases from 100 to 200. Exploring larger values of Re_λ (up to 10^3 or greater) is a critical direction for future research, but the computational cost of such simulations is currently prohibitive.

The simulations model statistically-planar premixed flames with periodic boundary conditions in spanwise directions and open boundaries normal to the direction of flame propagation. The domain width was set to $L = 8\delta_L$, resulting in a width of

$L = 2.59 \times 10^{-3}$ m. The length of the domain was $32L$ for I1 and $16L$ for I2 and I3 in order to allow sufficient space for the flame to freely propagate in the domain. The simulations used grids of size $512^2 \times 16384$ for I1 and $512^2 \times 8192$ for I2 and I3. In the cold reactants this results in resolutions of $\eta/\Delta x = 2$ for I1, $\eta/\Delta x = 1$ for I2, and $\eta/\Delta x = 0.8$ for I3, where Δx is the grid cell size and $\eta = (\nu_r^3/\varepsilon_r)^{1/4}$ is the Kolmogorov lengthscale in the reactants. Due to the increase in kinematic viscosity with temperature T and the subsequent increase in η, there are more than 10 grid cells per η in the hot products for all cases, providing ample resolution for the structure function analysis. Temporally, turbulence was allowed to develop for roughly two τ_{ed} prior to ignition. Following ignition, flame speed and thickness were monitored and statistics taken once a statistically steady state was reached.

3. Conditional structure functions

3.1. Description of conditional analysis

In order to compute structure functions in the spatially-inhomogeneous flame region, we modify Eq. (1) to include conditional averaging based on the local instantaneous temperature T, namely

$$S_{ij}^N(r;T) = \langle |u_i(\boldsymbol{x} + r\boldsymbol{e}_j, t) - u_i(\boldsymbol{x}, t)|^N \mid T(\boldsymbol{x}, t)\rangle \tag{7}$$

where, for the statistically planar cases studied here, $\langle\cdot\rangle$ is a space-time average. In this formulation, the temperature acts as a surrogate for the spatial location $\boldsymbol{x}$, thereby accounting, in part, for the inhomogeneity of the flame. To ensure convergence of statistics, conditional averages are computed for 40 temperature 'bins' between 400 K and 2000 K. In flames where the Lewis number is not unity, the conditioning on T can be replaced by an appropriate progress variable based, for example, on the fuel mass fraction.

Four different types of conditional structure functions are analyzed here up to third order (i.e., $N = 3$). Only low-order structure functions are examined since higher-order structure functions are known to substantially depart from classical Kolmogorov scaling laws due to internal intermittency, even in non-reacting turbulence [9,21]. Anomalous (i.e., non-Kolmogorov) scaling of low-order structure functions has also been observed in non-reacting flows [8,11,22], particularly at low Reynolds numbers, although such departures from classical Kolmogorov scaling laws are generally smaller than for higher order moments. At each location and time, the temperature gradient provides a definition of the flame surface normal $\boldsymbol{n}$ given by $\boldsymbol{n} = \nabla T/(\nabla T \cdot \nabla T)^{1/2}$. Bearing in mind that scaling theories developed by Kolmogorov are primarily valid for longitudinal structure functions for which velocities are in the same direction as the separation vector, we then define the flame normal velocity as $u_n \equiv \boldsymbol{u}\cdot\boldsymbol{n}$. Also using the flame tangent direction $\boldsymbol{t} = \boldsymbol{I} \times \boldsymbol{n}$ (where $\boldsymbol{I} = [1, 1, 1]$) and the tangent velocity $u_t \equiv \boldsymbol{u}\cdot\boldsymbol{t}$, we can thus define longitudinal structure functions

$$S_{nn}^N(r;T) = \langle |u_n(\boldsymbol{x} + r\boldsymbol{n}, t) - u_n(\boldsymbol{x}, t)|^N \mid T(\boldsymbol{x}, t)\rangle , \tag{8}$$

$$S_{tt}^N(r;T) = \langle |u_t(\boldsymbol{x} + r\boldsymbol{t}, t) - u_t(\boldsymbol{x}, t)|^N \mid T(\boldsymbol{x}, t)\rangle , \tag{9}$$

and lateral structure functions

$$S_{nt}^N(r;T) = \langle |u_n(\boldsymbol{x} + r\boldsymbol{t}, t) - u_n(\boldsymbol{x}, t)|^N \mid T(\boldsymbol{x}, t)\rangle , \tag{10}$$

$$S_{tn}^N(r;T) = \langle |u_t(\boldsymbol{x} + r\boldsymbol{n}, t) - u_t(\boldsymbol{x}, t)|^N \mid T(\boldsymbol{x}, t)\rangle . \tag{11}$$

The lateral structure functions are included since they are expected to be more sensitive to anisotropy [23–25], although the Kolmogorov scaling relations primarily apply to longitudinal structure functions (particularly at lower Reynolds numbers [26]). It should also be noted that the velocities u_n and u_t at $\boldsymbol{x} + r\boldsymbol{n}$ and $\boldsymbol{x} + r\boldsymbol{t}$ are always computed using $\boldsymbol{n}$ and $\boldsymbol{t}$ at $\boldsymbol{x}$. The use of $\boldsymbol{n}$ and $\boldsymbol{t}$ at $\boldsymbol{x}$ to define u_n and u_t is required in order to ensure invariance of the definitions of the longitudinal and lateral structure functions as r increases. To calculate u_n and u_t at separations $r\boldsymbol{n}$ and $r\boldsymbol{t}$, which may fall between grid points, Akima spline interpolation [27,28] is used over a 4^3 stencil surrounding the exact locations $\boldsymbol{x} + r\boldsymbol{n}$ and $\boldsymbol{x} + r\boldsymbol{t}$.

There are two caveats of the present analysis worth noting. First, density weighted averages are not employed here and, indeed, were checked and found not to have a substantial impact on either the unnormalized structure functions or the collapse of the structure functions. This insensitivity is likely due to the conditioning on temperature in the present analysis, which effectively restricts the range of densities within a given temperature bin (due to the close correspondence between density and temperature via the ideal gas law in the unconfined domains examined here). This is not to say that density weighting is irrelevant; simply that it does not appear to have a significant impact on the present results or the conclusions provided herein.

Second, the separation vectors $r\boldsymbol{n}$ and $r\boldsymbol{t}$ are likely to probe regions of the flame where $T(\boldsymbol{x} + r\boldsymbol{n})$ and $T(\boldsymbol{x} + r\boldsymbol{t})$ differ from $T(\boldsymbol{x})$, particularly for large r. However, this is an unavoidable consequence of the 'uncertainty principle' applied to the task at hand [5]. That is, as the degree of physical space locality increases, the degree of scale space locality decreases. Thus, for an extremely certain physical space location, only small scales can be accurately probed. Conversely, as larger scales are probed, physical space locality decreases. Regardless of the approach (including wavelet analyses [5],

where this issue was first described in the present context), all prior studies of scale variations in premixed flames have suffered from the uncertainty principle. The advantage of the present approach is not that it subverts this principle, but rather that it provides results that can be directly compared with Kolmogorov scaling relations.

Finally, it should be noted that there are many different ways to construct and compute structure functions in premixed flames. For example, conditionally-averaged mean velocities can be subtracted prior to structure function calculation, the conditioning can be performed on the average of the temperatures at (or between) $\boldsymbol{x}$ and $\boldsymbol{x}+\boldsymbol{r}$, or the analysis can be restricted to only isosurfaces of temperature (related to the pair dispersion work in Chaudhuri [29]), with the distance between two points computed based on the arc-length along the surface. There may also be different approaches to density weighting that yield a more complete collapse of the structure functions at different flame locations and for different intensities. Given all of these alternatives, the present analysis should be considered just one of many possible structure function approaches, each providing different physical insights. The primary focus of the present analysis is thus to determine whether Kolmogorov scaling and collapse can be recovered using a relatively straightforward conditional structure function formulation.

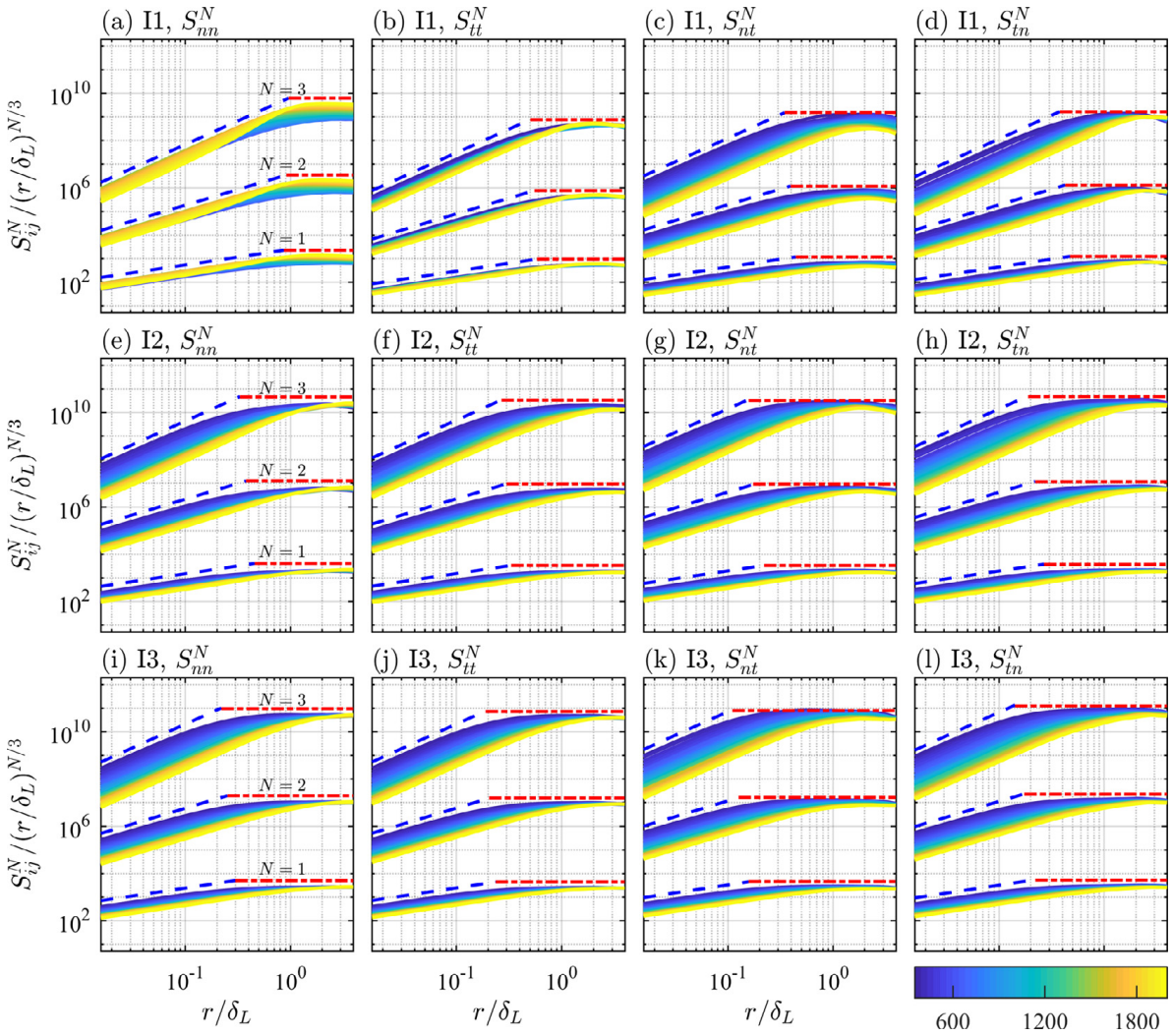


Fig. 2. Unnormalized compensated conditional structure functions $S^N_{ij}/(r/\delta_L)^{N/3}$ for each intensity, structure function type, and moment N. The analytic scaling r^N is shown by blue dashed lines and the Kolmogorov scaling $r^{N/3}$ is shown by red dash-dot lines. The first two columns show flame normal, S^N_{nn}, and flame tangential, S^N_{tt}, longitudinal structure functions, respectively. The third and fourth columns show the lateral structure functions S^N_{nt} and S^N_{tn}. (For interpretation of the references to color in this figure legend, the reader is referred to the web version of this article.)

3.2. Conditional structure function results

Figure 2 shows the scaling of the unnormalized conditional structure functions defined in Eqs. (8)–(11) as a function of temperature for all three intensities. The structure functions shown in Fig. 2 are compensated by $r^{N/3}$, such that horizontal lines are associated with Kolmogorov-type inertial range scaling. The longitudinal structure functions in the first two columns show an initial $\sim r^N$ analytic scaling before approaching Kolmogorov-type scaling $\sim r^{N/3}$ for sufficiently large r. The analytic scaling relation is obtained from the leading-order term in the Taylor expansion of the structure function for small r and is typically associated with the viscous dissipation range [30]. For the two higher intensity cases (i.e., I2 and I3), Fig. 2 shows that the roll-off to the Kolmogorov scaling generally occurs for smaller r near the reactants. Near the products for higher T, the viscosity increases substantially, resulting in an extended dissipation range and an adherence to the analytic scaling over a wider range of r.

Except for the lowest intensity case (i.e., I1), structure function values are greatest at locations near the reactants. The different temperature trends for S^N_{nn} in the I1 case are due to the thinness of the flame, the importance of dilatation and baroclinic torque in the dynamics, and the relatively close correspondence of this turbulent flame to a laminar flame; this was checked by computing S^N_{nn} for the laminar flame, resulting in a similar dependence on T.

Comparing the three different intensities in Fig. 2, there is an increasing approach to Kolmogorov scaling at large r as the intensity increases. There is also little noticeable effect of structure function type (i.e., longitudinal, S^N_{nn} and S^N_{tt}, and lateral, S^N_{nt} and S^N_{tn}) on the scaling. In nearly all cases, there is an initial $\sim r^N$ analytic scaling followed by a roll-off approaching $\sim r^{N/3}$ Kolmogorov-type scaling that occurs for increasingly large r through the flame. A more complete correspondence to the Kolmogorov inertial range scaling requires much higher Reynolds numbers (with Re_λ approaching 10^3 or greater), which is beyond current computational capabilities for simulations of turbulent premixed flames.

4. Conditional structure function collapse

4.1. Conditional scaling variables

The Kolmogorov inertial range scaling $S^N_{ij} \sim \varepsilon^{N/3} r^{N/3}$ is fundamentally based on the hypotheses that ε, ν, and r are uniquely responsible for the scaling of turbulence quantities in the universal equilibrium range, and that only ε and r are needed within the inertial range [13]. In prior non-reacting flow studies [11,22,31], structure function collapse has been examined by showing $S^N_{ij}/(\varepsilon\eta)^{N/3}$ versus r/η. However, in premixed flames both ε and η depend on temperature, and we seek here to determine whether the unnormalized structure functions in Fig. 2 can be collapsed onto a single curve for each intensity using temperature-dependent values of ε and ν.

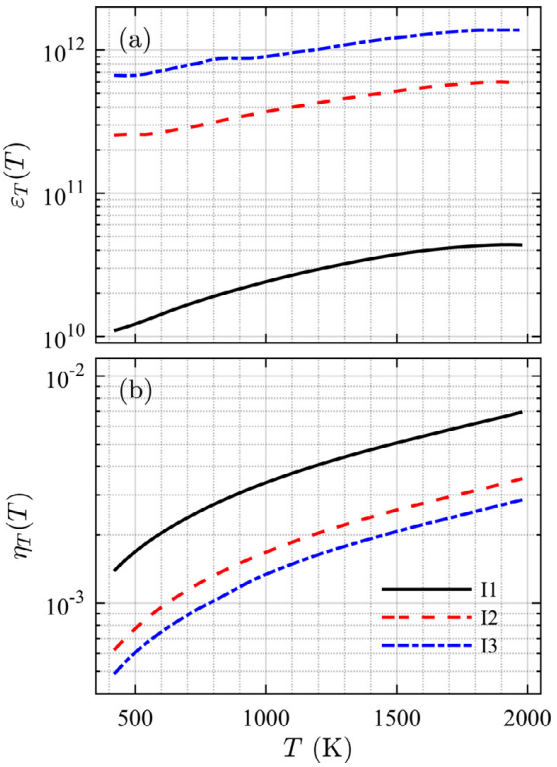


Fig. 3. Conditional mean values of fluctuating dissipation rate $\varepsilon_T(T)$ and Kolmogorov length scale $\eta_T(T)$ for all intensities.

First, from the thermochemical model used to perform the DNS, the local viscosity ν at each point in the flow is a function of temperature and density given by

$$\nu = \frac{\rho_r \nu_r}{\rho}\left(\frac{T}{T_r}\right)^{0.7}, \tag{12}$$

where the reactant properties are given in Table 1. The fluctuating strain rate necessary to compute the dissipation rate is computed by first subtracting the conditional mean of the total strain, namely

$$S_{ij} = \frac{1}{2}\left(\frac{\partial u_i}{\partial x_j} + \frac{\partial u_j}{\partial x_i}\right), \quad S'_{ij} = S_{ij} - \langle S_{ij}|T\rangle, \tag{13}$$

which can then be used along with ν to compute a spatially varying turbulent dissipation as $\xi = 2\nu S'_{ij} S'_{ij}$. It should be noted that ν and ξ are spatially and temporally varying quantities, leading to potential ambiguity in the definition of appropriate scaling variables, particularly in inhomogeneous and temperature-dependent flows such as those examined here. Many different approaches to

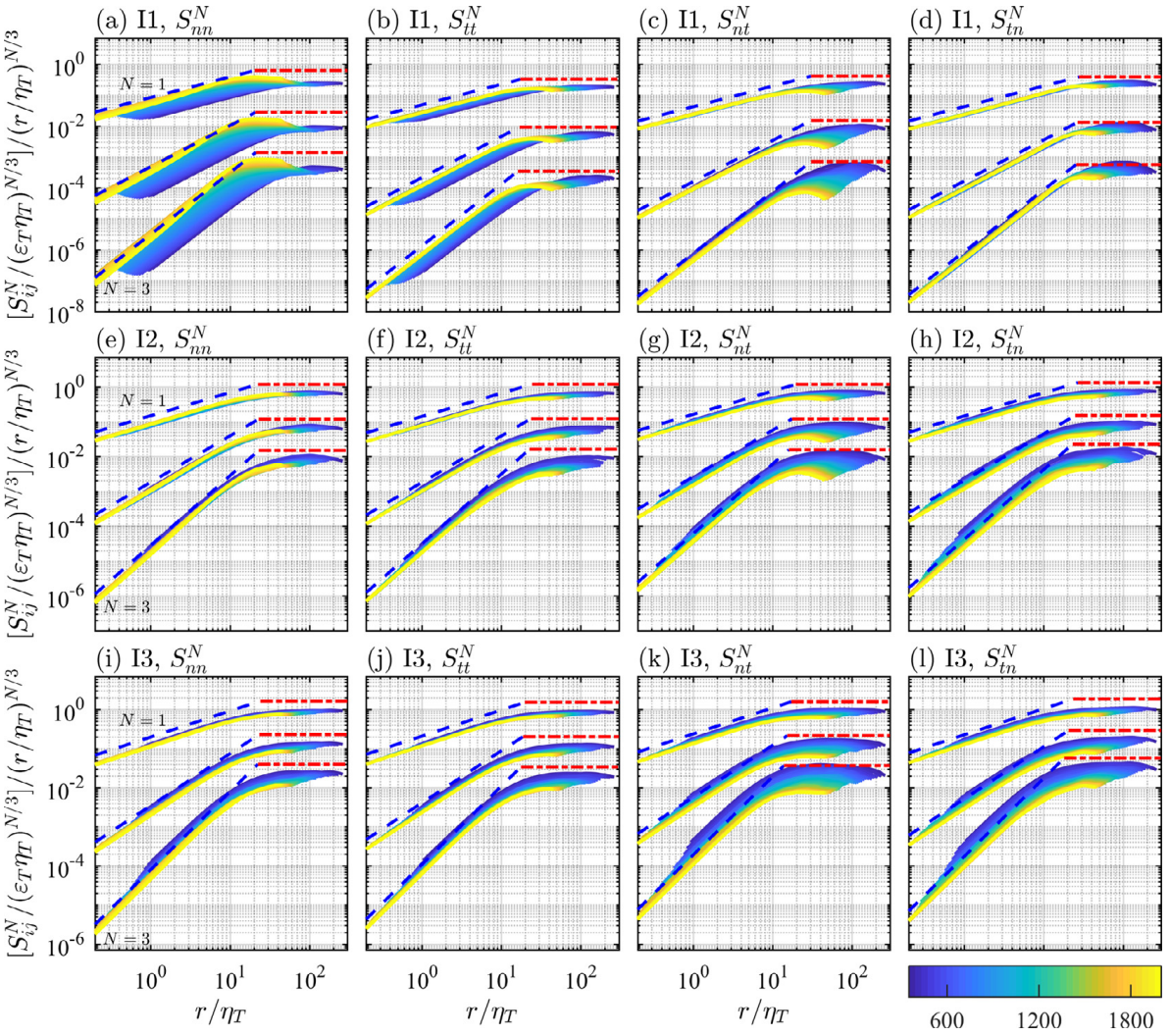


Fig. 4. Compensated conditional structure functions normalized by conditional dissipation $\varepsilon_T(T)$ and conditional Kolmogorov length scale $\eta_T(T)$. The analytic scaling r^N is shown by blue dashed lines and the Kolmogorov scaling $r^{N/3}$ is shown by red dash-dot lines. Each column represents a different combination of separation vector with structure function type, as described in the caption of Fig. 2. (For interpretation of the references to color in this figure legend, the reader is referred to the web version of this article.)

constructing such variables are possible, and here the conditional mean values of ν and ξ are computed in order to obtain single conditional values of the viscosity and dissipation at each T, defined as $\varepsilon_T = \langle \xi \mid T \rangle$ and $\nu_T = \langle \nu \mid T \rangle$. These conditional values are then used to define the conditional Kolmogorov length, $\eta_T = (\nu_T^3/\varepsilon_T)^{1/4}$.

Figure 3 shows the conditional mean values for each intensity, where both ε_T and η_T are smooth functions of T. While the simplified chemical model used here mandates a monotonic increase in ν_T with T, similar effects have also been observed for multi-step kinetic mechanisms [32].

4.2. Normalized structure function results

In order to determine whether the Kolmogorov-type scaling variables ε_T and η_T can be used to collapse the structure functions at each intensity, Fig. 4 shows normalized compensated structure functions $[S^N_{ij}/(\varepsilon_T\eta_T)^{N/3}]/(r/\eta_T)^{N/3}$. In the I2 and I3 cases, the two longitudinal structure functions S^N_{nn} and S^N_{tt} roughly collapse for all temperatures in the flame, particularly for small values of r within the analytic (or dissipation) range. For larger r there is some divergence of the structure functions with increasing power N, which may be due to inertial range intermittency, which varies through the flame [33,34]. Such deviations from Kolmogorov-type scaling have also been widely observed in non-reacting turbulence [9], particularly for low Reynolds numbers and higher-order moments. For S^N_{nt} and S^N_{tn} in Fig. 4 there is only partial collapse, consistent with the recent study by Iyer et al. [26] showing that the Kolmogorov scaling hypotheses may only apply to lateral structure functions in

the limit of very large Reynolds number. Compared to I2 and I3, the collapse is quite poor for the lower turbulence intensity I1, where dilatational effects of heat release are felt comparatively strongly. This is supported by the observation that the flame normal longitudinal structure function S^N_{nn}, which is most directly tied to dilatation, experiences the least collapse.

These results indicate that at sufficiently high turbulence intensities (i.e., high Ka), Kolmogorov scaling may be recovered, while at lower turbulence intensities the recovery, if possible, requires further corrections. These results are consistent with the prediction from Bilger [35] that dilatation from heat release becomes dynamically insignificant when the Kolmogorov time scale $(\nu/\varepsilon)^{1/2}$ becomes much smaller than the characteristic chemical timescale τ_c. For the cases considered here, this condition is satisfied progressively less as the intensity decreases (i.e., from I3 to I1) and as the temperature increases (i.e., from reactants to products).

Beyond such timescale arguments, the degree of the collapse for each intensity shown in Fig. 4 also has dynamical significance. As the turbulence intensity increases, the effects of baroclinic torque and dilatation on the dynamics of the turbulence are known to become less significant [36], and the primary effect of heat release thus occurs via changes in viscosity. The scaling variables ε_T and η_T primarily account for these viscosity changes, and do not directly address other heat release effects such as baroclinic torque and dilatation. As a result, normalization by these scaling variables leads to a more complete collapse as the intensity increases and the dynamics are less affected by these other heat release effects.

The collapse shown in Fig. 4 is also generally more complete for small r within the dissipation range, again consistent with the dominant variation in the dynamics coming from changes in viscosity. The relatively complete collapse of the structure functions within the analytic (or dissipative) range is consistent with prior work by Schumacher et al. [30], where it was shown that analytic range scaling and collapse can be achieved at surprisingly low Reynolds numbers (as small as $Re_\lambda = 24$).

5. Conclusions and future work

We have used a conditional velocity structure function analysis to probe the effects of premixed flames on turbulence at different scales. The conditioning was based on the local instantaneous temperature within the flame, and the analysis was based on data from DNS of three different turbulence intensities. Unnormalized conditional structure functions revealed a roll-off approaching the $r^{N/3}$ inertial range scaling from Kolmogorov for sufficiently large r; this roll-off was found to occur at increasingly larger r as the temperature increased. Longitudinal conditional structure functions normalized using conditionally-computed scaling variables were found to approximately collapse, particularly at high intensities. By contrast, the collapse was poor for the low intensity case, supporting earlier work [6,35] noting the importance of dilatational and baroclinic torque effects on the dynamics for weak turbulence. For the two higher intensity cases, the collapse of the structure functions was relatively complete for small r within the analytic (or dissipative) scale range, indicating that the primary heat release effect on the turbulence for these conditions is due to changes in temperature-dependent viscosity.

The results of this study motivate further research in several different directions. First and foremost, simulations with larger values of Re_λ and a larger inertial range should be examined to gain a better understanding of the extent of Kolmogorov-type scaling at large r. As noted in Section 3.1, there are also many different ways in which the structure function analysis can be formulated, and each such approach has the potential to provide new and unique physical insights. Finally, a more complete collapse of the structure functions may be achieved by including other quantities, such as the density, dilatation, or gradients of the temperature, in the scaling analysis. It may also be necessary to distinguish between solenoidal and dilatational dissipation rates in the scaling relations for higher turbulence intensities where the turbulent Mach number is greater.

Future work may also include implementation of tensorial structure functions [37,38] to more specifically look at the effects of anisotropy through structure functions, and the investigation of intermittency corrections to improve the analysis for higher powers N. The latter is especially important as intermittency effects are expected to have strong dynamical significance in reacting flows [39]. The analysis should also be extended to data from DNS with more complex finite-rate chemistry and transport. The effects of such increases in fidelity are expected to be of importance especially at lower turbulence intensities where the heat release profile has a significant effect on structure functions.

Acknowledgments

Insightful discussions with Drs. Javier Urzay, James Brasseur, and Yuan Xuan, as well as Paulo Paes, are gratefully acknowledged. SHRW, CAZT and PEH were supported, in part, by AFOSR award FA9550-17-1-0144 and by DoD HPCMP under a Frontier project award. AYP was supported in part by AFOSR award F4FGA05260G001. Computing resources were provided by DoD HPCMP under a Frontier project award.

References

[1] J. Furukawa, Y. Noguchi, T. Hirano, F.A. Williams, *J. Fluid Mech.* 462 (2002) 209–243.
[2] H. Kolla, E.R. Hawkes, A.R. Kerstein, N. Swaminathan, J.H. Chen, *J. Fluid Mech.* 754 (2014) 456–487.
[3] C.A.Z. Towery, A.Y. Poludnenko, J. Urzay, J. O'brien, M. Ihme, P.E. Hamlington, *Phys. Rev. E* 93 (5) (2016).
[4] J. O'Brien, C.A.Z. Towery, P.E. Hamlington, M. Ihme, A.Y. Poludnenko, J. Urzay, *Proc. Combust. Inst.* 36 (2) (2017) 1967–1975.
[5] J. Kim, M. Bassenne, C.A.Z. Towery, P.E. Hamlington, A.Y. Poludnenko, J. Urzay, *J. Fluid Mech.* 848 (2018) 78–116.
[6] R. Knaus, C. Pantano, *J. Fluid Mech.* 626 (2009) 67–109.
[7] J. O'Brien, J. Urzay, M. Ihme, P. Moin, A. Saghafian, *J. Fluid Mech.* 743 (2014) 554–584.
[8] N. Cao, S. Chen, K.R. Sreenivasan, *Phys. Rev. Lett.* 77 (1996) 3799–3802.
[9] K.R. Sreenivasan, R.A. Antonia, *Annu. Rev. Fluid Mech.* 29 (1997) 435–472.
[10] B.R. Pearson, R.A. Antonia, *J. Fluid Mech.* 444 (2001) 343–382.
[11] S.Y. Chen, B. Dhruva, S. Kurien, K.R. Sreenivasan, M.A. Taylor, *J. Fluid Mech.* 533 (2005) 183–192.
[12] U. Frisch, *Turbulence: The Legacy of A.N. Kolmogorov*, Cambridge University Press, 1995.
[13] A.N. Kolmogorov, in: Dokl. Akad. Nauk SSSR, 30, 1941, pp. 299–303.
[14] V.R. Kuznetsov, V.A. Sabel'nikov, *Turbulence and Combustion*, Hemisphere Publishing, New York, NY (United States);, 1990.
[15] A.N. Lipatnikov, J. Chomiak, *Prog. Energy Combust. Sci.* 36 (1) (2010) 1–102.
[16] V. Robin, A. Mura, M. Champion, *J. Fluid Mech.* 689 (2011) 149–182.
[17] A.Y. Poludnenko, E.S. Oran, *Combust. Flame* 157 (5) (2010) 995–1011.
[18] V.N. Gamezo, T. Ogawa, E.S. Oran, *Combust. Flame* 155 (1) (2008) 302–315.
[19] N. Peters, *Turbulent Combustion*, Cambridge University Press, 2000.
[20] A.Y. Poludnenko, *Phys. Fluids* 27 (1) (2015) 014106.
[21] A.N. Kolmogorov, *J. Fluid Mech.* 13 (1962) 82–85.
[22] R.A. Antonia, L. Djenidi, L. Danaila, S.L. Tang, *Phys. Fluids* 020715 (2017).
[23] I. Arad, B. Dhruva, S. Kurien, V.S. L'vov, I. Procaccia, K.R. Sreenivasan, *Phys. Rev. Lett.* 81 (24) (1998) 5330.
[24] S. Kurien, V.S. L'vov, I. Procaccia, K.R. Sreenivasan, *Phys. Rev. E* 61 (1) (2000) 407.
[25] S. Kurien, K.R. Sreenivasan, in: New Trends in Turbulence, Springer, 2001, pp. 53–111.
[26] K.P. Iyer, K.R. Sreenivasan, P.K. Yeung, *Phys. Rev. E* 021101(R) (2017).
[27] R.A. Darragh, C.A.Z. Towery, P.E. Hamlington, A.Y. Poludnenko, in: Fourty-Seventh AIAA Fluid Dynamics Conference, 2017, p. 3466.
[28] P.E. Hamlington, R. Darragh, C.A. Briner, C.A. Towery, B.D. Taylor, A.Y. Poludnenko, *Combust. Flame* 186 (2017) 193–207.
[29] S. Chaudhuri, *Phys. Rev. E* 91 (2015) 021001(R).
[30] J. Schumacher, K.R. Sreenivasan, V. Yakhot, *New J. Phys.* 9 (2007) 89.
[31] R.A. Antonia, B.R. Pearson, T. Zhou, *Phys. Fluids* 12 (2000) 3000.
[32] S. Lapointe, B. Savard, G. Blanquart, *Combust. Flame* 162 (9) (2015) 3341–3355.
[33] P.E. Hamlington, A.Y. Poludnenko, E.S. Oran, *Phys. Fluids* 24 (7) (2012) 075111.
[34] S. Chaudhuri, H. Kolla, H.L. Dave, E.R. Hawkes, J.H. Chen, C.K. Law, *Combust. Flame* 184 (2017) 273–285.
[35] R.W. Bilger, *Flow Turbul. Combust.* 72 (2–4) (2004) 93–114.
[36] P.E. Hamlington, A.Y. Poludnenko, E.S. Oran, *Phys. Fluids* 23 (12) (2011) 125111.
[37] S. Kurien, K.R. Sreenivasan, *Phys. Rev. E* 62 (2) (2000) 2206.
[38] L. Biferale, I. Procaccia, *Phys. Rep.* 414 (2) (2005) 43–164.
[39] K.R. Sreenivasan, *Flow Turbul. Combust.* 72 (2–4) (2004) 115–131.



Journal of Turbulence

ISSN: (Print) (Online) Journal homepage: https://www.tandfonline.com/loi/tjot20

A scaling law for the required transition zone depth in hybrid LES-DNS

C. A. Z. Towery , S. Walters , S. M. Guzik , X. Gao & P. E. Hamlington

To cite this article: C. A. Z. Towery , S. Walters , S. M. Guzik , X. Gao & P. E. Hamlington (2020) A scaling law for the required transition zone depth in hybrid LES-DNS, Journal of Turbulence, 21:12, 722-734, DOI: 10.1080/14685248.2020.1849711

To link to this article: https://doi.org/10.1080/14685248.2020.1849711

Published online: 20 Nov 2020.

Submit your article to this journal

Article views: 18

View related articles

View Crossmark data

Full Terms & Conditions of access and use can be found at
https://www.tandfonline.com/action/journalInformation?journalCode=tjot20

JOURNAL OF TURBULENCE
2020, VOL. 21, NO. 12, 722–734
https://doi.org/10.1080/14685248.2020.1849711

Taylor & Francis
Taylor & Francis Group

Check for updates

A scaling law for the required transition zone depth in hybrid LES-DNS

C. A. Z. Towery [a], S. Walters[b], S. M. Guzik[b], X. Gao[b] and P. E. Hamlington[a]

[a]Paul M. Rady Department of Mechanical Engineering, University of Colorado, Boulder, CO, USA;
[b]Department of Mechanical Engineering, Colorado State University, Fort Collins, CO, USA

ABSTRACT

There is a substantial need to better understand multi-physics interactions in realistic laboratory experiments, yet it is currently unfeasible to perform direct numerical simulations (DNS) of most such problems. As a result, reduced-order models such as those used to represent unclosed subgrid-scale stresses in large-eddy simulations (LES) and advanced numerical techniques, including adaptive mesh refinement and nested grid structures, are required for the study of multi-physics interactions in practical situations. In particular, it is now possible to model many real-world flows with LES fidelity, and to selectively refine the computational mesh in a small region of the domain to resolve multi-physics interactions with DNS fidelity. However, rules and guidance for the valid implementation of this multi-fidelity 'hybrid LES-DNS' approach have yet to be fully formulated. Within the embedded DNS region, multi-physics interactions will be influenced by (*i*) macroscale features (e.g. large-scale shear gradients or body forces that produce turbulence), (*ii*) LES-regulated mesoscale features (e.g. advecting turbulent eddies), and (*iii*) microscale features that are subgrid-scale to the LES (e.g. layers of fast-reacting intermediate chemical species). In this study, we address the second of these effects, which poses particular challenges due to the transfer and overlapping nature of advecting mesoscale eddies between the purely LES (i.e. macroscale) and purely DNS (i.e. microscale) regions. By combining dimensional analysis and computational results, we formulate a scaling law for the required depth of the transition zone surrounding the embedded DNS region within hybrid LES-DNS computations of realistic turbulent flows.

ARTICLE HISTORY
Received 22 May 2020
Accepted 30 October 2020

KEYWORDS
Direct numerical simulation; large eddy simulation; adaptive mesh refinement; turbulence cascade

1. Introduction

The computational resources required to perform well-resolved direct numerical simulations (DNS) of laboratory-scale experiments at high Reynolds numbers, Re, are not likely to arrive within the next decade, and yet there is a need to better understand the effects of real flow geometries and operating conditions on various detailed nonlinear multi-physics interactions, including particle-turbulence interactions in atmospheric and industrial processes [1,2], magnetic confinement effects on plasma turbulence [3], and

CONTACT C. A. Z. Towery colin.towery@colorado.edu Paul M. Rady Department of Mechanical Engineering, University of Colorado, Boulder, CO 80309, USA

© 2020 Informa UK Limited, trading as Taylor & Francis Group

turbulence-chemistry interactions in reacting flows [4,5]. These interactions can become leading-order dynamical processes governing the evolution of a flow over a wide range of conditions, resulting in connections between large-scale coherent flow structures and small-scale incoherent fluctuations that must be modeled in both large-eddy simulations (LES) and unsteady Reynolds-averaged Navier-Stokes simulations (URANS).

For example, kinetic energy transfer in premixed turbulent reacting flows may occur dominantly from small to large scales as a result of both transient and statistically-stationary chemical heat release, contrary to the net transfer of energy from large to small scales required by essentially all stable subgrid-scale (SGS) models [6,7]. Similarly, turbulence can generate intermittent and strong thermochemical fluctuations that induce the formation of detonations [5,8]. However, nearly all DNS studies of multi-physics interactions in combustion and other contexts use simplified, and usually periodic, box-like configurations that remove all influence of flow geometry, which has a leading-order effect on the local flow structure (see, for instance, [9]). Therefore, it is necessary to place future studies of multi-physics interactions within the proper context of realistic experimental flow geometries.

An intriguing possibility is to embed a DNS subdomain within a much coarser LES domain that "drives" the DNS with initial and boundary conditions that closely match experimental configurations. In this approach, the DNS would be fully coupled to the surrounding LES, allowing for a natural flow of information between the host LES and the embedded DNS. Such a numerical method, which might be termed *hybrid LES-DNS* or *embedded DNS*, has not previously been explicitly studied in the literature. However, the more general use of static grid nesting or stretching for the purposes of finely resolving an interior subdomain while coarsely resolving exterior boundary conditions, whether conducted within a DNS, LES, or URANS simulation, is a well-established technique (e.g. [10]). Similarly, there has been some effort to derive dynamic turbulence models that automatically adapt to the local resolution of unstructured meshes to correctly provide URANS, LES, or DNS dynamics, as appropriate for the grid resolution and flow properties [11].

An explicit hybrid LES-DNS approach using structured grids has, however, yet to be validated for use in studying any type of multi-physics interaction. Moreover, an improved understanding of all mechanisms appropriate for information transfer across interfaces needs to be established and a set of mesh design rules needs to be formulated in order to eliminate known issues in hybrid modeling strategies, such as the well-documented modeled stress depletion problem [12] in hybrid RANS-LES and detached-eddy simulations (DES), wherein a high-degree of grid refinement causes a large drop in the RANS-level modeled Reynolds stress without a simultaneous increase in LES-resolved viscous stresses to compensate. The resultant 'stress depletion' can cause premature boundary-layer separation in regions of adverse pressure gradient. Similar problems may also occur in a hybrid LES-DNS, where a sudden increase in resolution would cause a loss of modeled SGS stress without an immediate increase in DNS-resolved viscous stress.

More specifically, whether the highly-refined DNS region of the computational mesh is fixed in space and time or adapts to follow a user-defined quantity of interest through the domain (e.g. in an adaptive mesh approach [13–16]), critical numerical information relevant to the evolution of the flow will inevitably span across, pass into and out of, or be resolved only within this region. Such information includes, for instance: (*i*) mean or

macroscale shear gradients (i.e. turbulence-production scales) that span across the embedded DNS; (*ii*) *mesoscale* flow structures (e.g. turbulent eddies formed by the inertial-range turbulence cascade) that must transition from being dissipated by the SGS model in the LES region to cascading down to the physical dissipation scales resolved by the DNS region; and (*iii*) *microscale* turbulence structures (i.e. sub-LES inertial-range and dissipation-range eddies), high-frequency acoustic waves, and coupled physical phenomena (e.g. thin chemical radical layers within a turbulent flame) that can be resolved by the embedded DNS, but not the host LES.

In this paper, we restrict our focus to the challenge of accurately transitioning the evolution of the turbulence cascade from the host LES domain, where an SGS model dissipates turbulence fluctuations at the LES-resolved mesoscales, into the embedded DNS region, where the viscous-dissipation-range microscales must be populated and a new equilibrium reached between turbulence production and viscous dissipation. Eddies at this range of scales are of particular importance since they provide a bridge between macroscale flow features captured only by the outer LES domain and microscale physics captured only in the inner embedded DNS domain. Mesoscale eddies can, in principle, be transitioned from the LES to DNS regions by means of a *transition zone*, but the extent (or 'depth') of this zone requires new mesh design heuristics that depend on the inter-scale turbulence cascade process and the resolution difference between the LES and DNS grids. The depth of this zone plays a critical role in 'matching' the physics between the LES and DNS regions; we require, in particular, that all small-scale motions not present in the LES region should be fully repopulated in the DNS region. In other words, the transition zone should be sufficiently large to allow the 'filling in' of the scale-space gap between the LES and DNS mesh resolutions.

The primary objective of the present study is to develop a scaling law in terms of only bulk-flow, integral-scale turbulence, and grid properties that describes the transition zone depth, L_{tz}, necessary for the mesoscale turbulence cascade active in the LES region to extend through the full range of microscales in the DNS region. We require, in particular, that $\tau_{\mathrm{adv}}/\tau_{\mathrm{eq}} > 1$, where τ_{eq} is the necessary equilibration time, $\tau_{\mathrm{adv}} = L_{\mathrm{tz}}/U_n$ is the bulk advection time of a turbulent eddy in the transition zone, and U_n is the bulk-flow velocity within the transition zone. Here and throughout this paper, L_{tz} and U_n are both defined to be normal to the LES-DNS interface.

To develop this scaling law, here we perform a series of simulations modeling the refill of small-scale energy content after truncation of the kinetic energy spectrum in non-reacting homogeneous isotropic turbulence (HIT). This approach is fundamentally motivated by the hypothesis that initial guidelines for L_{tz} can be based on simulations that measure the equilibration time of HIT subjected to a suddenly refined grid resolution. In particular, we measure how long it takes the low-pass-filtered (i.e. LES resolution) turbulence kinetic energy spectrum of a uniform-grid DNS of HIT to recover from a scale truncation operation. From these measurements, a scaling law for τ_{eq} can be formulated based on the filter width, Δ_{LES}, and finest grid size, Δ_{DNS}, as well as the governing parameters of the turbulence kinetic energy cascade. Once acquired, this scaling law can be applied to develop the minimum transition-zone-depth requirement, which is expressed generically for a mesoscale eddy advecting at speed U_n as

$$L_{\mathrm{tz}} > \tau_{\mathrm{eq}} U_n. \tag{1}$$

By combining dimensional analysis and computational results, we formulate a scaling relation for L_{tz} such that the turbulence cascade has equilibrated with the DNS-resolved scales, thereby allowing multi-physics interactions at microscales to be fully captured by a hybrid LES-DNS.

It should be noted that the temporal response of the energy cascade to perturbations has been examined previously, although using different approaches than the spectral truncation employed here. Cardesa et al. [17] examined the time taken for an increase in the energy flux at one scale to travel to surrounding scales. These authors found that the time required for the energy cascade to reach equilibrium after such a perturbation scaled with the wavenumber of the perturbation as $k^{-2/3}$, where k is the wavenumber magnitude. The same two-thirds scaling was proposed by Lumley [18] to describe the transfer of energy between scales in a turbulent cascade, and additional support for this result has been provided by Pope [19] and Wan et al. [20]. Alternatively, an SGS dissipation time scale can be derived for LES using a simple eddy viscosity model [21], such that the time scale is directly proportional to the inverse of the mean resolved-scale strain rate. Further assuming a Kolmogorov kinetic energy spectrum that scales as $k^{-5/3}$ in the inertial range, it can be shown that the dissipation time scales as $\Delta_{\text{LES}}^{2/3}$, consistent with the previous findings that the time scale associated with the turbulence cascade is proportional to $k^{-2/3}$ [22].

Each of these previous temporal scaling relations rely on the assumption of a fully-developed statistically-stationary turbulence cascade. By contrast, here we instead seek a temporal scaling associated with the non-stationary response of the cascade to a sudden increase in scale bandwidth. Nevertheless, we will show that a similar scaling relation is obtained for the equilibration time τ_{eq} after filter truncation of a real (i.e. finite Re) HIT kinetic energy spectrum at scale Δ_{LES} (i.e. we will show that $\tau_{\text{eq}} \sim \Delta_{\text{LES}}^{2/3}$).

In the following, the dimensional analysis of the filtered HIT equilibration time will be described first, followed by the details of the numerical methods for performing the necessary HIT simulations and the quantitative definition for τ_{eq} of the filtered HIT spectrum. Results of the simulations and dimensional analysis will then be presented.

2. Methods

Given the fundamental condition for the required transition zone depth in Equation (1), we first seek a scaling law for the truncated-spectrum equilibration time, τ_{eq}, in terms of turbulence properties and characteristics of the simulations. Using a combination of dimensional analysis and physical intuition, we first develop a general expression for τ_{eq} that introduces new unknown functions and coefficients. We then constrain these functions and coefficients using a series of filtered simulations of HIT. The derivation of the general scaling law is provided in the next section and details of the simulations are provided in Section 2.2. The specific definitions of τ_{eq} used here are then described in Section 2.3.

2.1. Dimensional analysis of filtered HIT spectral equilibration

In general, the equilibration time of an LES-truncated turbulence cascade to a finer DNS grid may depend on any or all of the governing parameters of the turbulence kinetic energy (TKE) dynamics within the DNS grid. In the specific case of low-pass-filtered HIT, τ_{eq} can only depend on the filter scale, Δ_{LES}, grid scale, Δ_{DNS}, domain size, L, integral length

scale, $\ell = \frac{\pi}{2} u_\ell^{-2} \int_0^\infty k^{-1} \widehat{E}(k)\, \mathrm{d}k$, Kolmogorov length scale, η, Kolmogorov time scale, τ_K, and turbulence Mach number, Ma_t, where $u_\ell^2 = \frac{2}{3} \int_0^\infty \widehat{E}(k)\, \mathrm{d}k$ is the integral velocity scale and $\widehat{E}(k)$ is the kinetic energy spectrum. While turbulence dynamics are commonly also related to the kinematic viscosity, ν, viscous dissipation rate, ε, and Reynolds number, Re_ℓ, these parameters are implicitly included in η, τ_K, and ℓ, noting that $\eta = (\nu^3/\varepsilon)^{1/4}$, $\tau_K = (\nu/\varepsilon)^{1/2}$, and $\ell/\eta \sim \mathrm{Re}_\ell^{3/4}$. Additionally, $\mathrm{Ma}_t \ll 1$ for most laboratory experiments, and so we ignore this dependency within this study.

This leaves seven dimensional parameters with two dimensions (i.e. length and time), and thus five distinct non-dimensional parameters can be arranged into a functional relationship as

$$\frac{\tau_{\mathrm{eq}}}{\tau_K} = f\left(\frac{L}{\ell}, \frac{\ell}{\eta}, \frac{\Delta_{\mathrm{LES}}}{\eta}, \frac{\eta}{\Delta_{\mathrm{DNS}}}\right), \tag{2}$$

where $f(\cdots)$ is an unknown function of its dimensionless arguments. However, in the limit that the DNS region is fully resolved such that $\eta/\Delta_{\mathrm{DNS}} > 1$ (or, conversely, as $\Delta_{\mathrm{DNS}} \to 0$), we would expect $\tau_{\mathrm{eq}}/\tau_K$ to approach a constant value when holding all other quantities fixed. Consequently, $\eta/\Delta_{\mathrm{DNS}}$ can be dropped from the right-hand side (RHS) of Equation (2). Similarly, the integral scale ℓ must, by definition, be smaller than the computational domain scale L, no matter the flow configuration, and we do not expect any dependence of $\tau_{\mathrm{eq}}/\tau_K$ on L/ℓ for $L/\ell \gg 1$ since the turbulent cascade is assumed to start at the integral scale ℓ, which is associated with the turbulence production mechanism. For realistic shear-driven flows such as jets, wakes, mixing layers, or boundary layers, it is computationally necessary that $L/\ell \gg 1$ if the entire flow structure is to be simulated correctly without influence from the boundary conditions. As a result, L/ℓ can also be dropped from the RHS of Equation (2).

It should be noted that it is equally valid to include either $\Delta_{\mathrm{LES}}/\eta$ or $\Delta_{\mathrm{LES}}/\ell$ in Equation (2); indeed, the latter is most appropriate for characterizing the energy cascade time associated with the range of scales resolved by an LES. Here, however, we instead include $\Delta_{\mathrm{LES}}/\eta$ in Equation (2) due to the present focus on the time taken, τ_{eq}, for scales between Δ_{LES} and η to 'refill' after an abrupt spectral truncation at Δ_{LES}. Given this definition of τ_{eq}, which is specifically connected to energy dynamics in the range of scales unresolved by an LES, the scale separation between Δ_{LES} and η is of primary significance. For similar reasons, we use τ_K instead of the integral time scale $\tau_\ell = \ell/u_\ell$ to normalize τ_{eq} on the left-hand side of Equation (2).

Based on these considerations, we propose that the functional relationship from Equation (2) should consist of the product of unknown functions of ℓ/η and $\Delta_{\mathrm{LES}}/\eta$ as

$$\frac{\tau_{\mathrm{eq}}}{\tau_K} = f_1\left(\frac{\ell}{\eta}\right) f_2\left(\frac{\Delta_{\mathrm{LES}}}{\eta}\right). \tag{3}$$

Within the self-similar range for $\ell \gg \Delta_{\mathrm{LES}} \gg \eta$, which corresponds to large Re_ℓ, we expect τ_{eq} to become independent of ℓ/η and to depend on $\Delta_{\mathrm{LES}}/\eta$ via a self-similar power-law scaling [23], giving

$$\frac{\tau_{\mathrm{eq}}}{\tau_K} = C\left(\frac{\Delta_{\mathrm{LES}}}{\eta}\right)^a, \tag{4}$$

where C and a are both constants. If we instead use integral-scale quantities for the normalization of τ_{eq}, we can rewrite Equation (4) as

$$\frac{\tau_{\text{eq}}}{\tau_\ell} = \left(\frac{\tau_{\text{eq}}}{\tau_K}\right)\left(\frac{\tau_K}{\tau_\ell}\right) = CD^{-1/3}\left(\frac{\ell}{\eta}\right)^{a-2/3}\left(\frac{\Delta_{\text{LES}}}{\ell}\right)^{a}, \tag{5}$$

where $D = \varepsilon\ell/u_\ell^3$ is the non-dimensional dissipation rate, which is a non-constant variable coefficient for small values of ℓ/η, but asymptotes to $D \approx 0.46$ for $\ell/\eta \gg 1$ in a fully-developed and self-similar equilibrium cascade [24]. It will be seen that $a = 2/3$ and, as a result, $\tau_{\text{eq}}/\tau_\ell$ becomes independent of ℓ/η and the constant C is multiplied by an additional factor of roughly 1.3. For values of Δ_{LES} outside the self-similar range and for smaller values of ℓ/η, these simple scaling relations are no longer valid and the more general relation in Equation (3) must be used instead.

The exponent a in Equation (4) can be inferred from previous scaling studies [17–20] and common LES models [21] in the limits $\ell/\eta \gg 1$ and $\Delta_{\text{LES}}/\eta \gg 1$. In particular, these studies suggest that τ_{eq} should take the general form $\tau_{\text{eq}} \sim {\Delta_{\text{LES}}}^{2/3}$ (i.e. $a = 2/3$), with no dependence on ℓ/η in these limits. This result is also supported by several other related approaches, including: (*i*) Kolmogorov scaling arguments assuming that τ_{eq} depends only on the scale Δ_{LES} and ε; (*ii*) Equilibrium energy cascade arguments assuming that $\tau_{\text{eq}} \sim \Delta_{\text{LES}}/u_{\text{LES}}$, where u_{LES} is obtained from the constancy of the scale-local dissipation rate $\varepsilon_\lambda \sim u_\lambda^3/\lambda$ at each scale λ throughout the cascade; (*iii*) The definition of the eddy turnover time $\tau_{\text{eddy}}^{-2} = \int_0^{2\pi/\Delta_{\text{LES}}} k^2\widehat{E}(k)\,\mathrm{d}k$ from Kraichnan [22], where the Kolmogorov inertial range spectrum is used for $\widehat{E}(k)$.

We will show in the following that the present simulations also yield $\tau_{\text{eq}} \sim \Delta_{\text{LES}}^{2/3}$ for large values of Δ_{LES}/η, and that $f_1(\ell/\eta) \approx 1$. However, we will provide a functional form for $f_2(\Delta_{\text{LES}}/\eta)$ that accounts for small Δ_{LES}/η. This form is based on the simulation data and is thus empirical, although $f_2(\Delta_{\text{LES}}/\eta)$ may be obtainable analytically from the definition of τ_{eddy} provided by Kraichnan [22], assuming an empirical form for $\widehat{E}(k)$ at small scales. Given ongoing ambiguity regarding the appropriate form of the empirical relation for $\widehat{E}(k)$ (e.g. [25]), we do not attempt this derivation here, and simply note it is a direction for future research.

2.2. Filtered HIT simulations

The compressible Navier-Stokes equations for a calorically-perfect ideal gas are solved numerically by the fully-unsplit corner transport upwind scheme with piecewise-parabolic spatial reconstruction and the HLLC Riemann solver [26,27] implemented in a multi-physics-capable DNS finite-volume code with overall second-order accuracy [28]. The simulations solve the fully compressible governing equations for conservation of mass, momentum, and energy given by

$$\frac{\partial\rho}{\partial t} + \frac{\partial(\rho u_j)}{\partial x_j} = 0, \tag{6}$$

$$\frac{\partial(\rho u_i)}{\partial t} + \frac{\partial}{\partial x_j}\left[\rho u_i u_j + p\delta_{ij} - \mu\left(\frac{\partial u_i}{\partial x_j} + \frac{\partial u_j}{\partial x_i}\right) - \frac{2}{3}\mu_{\text{B}}\frac{\partial u_k}{\partial x_k}\delta_{ij}\right] = \mathcal{F}_i, \tag{7}$$

$$\frac{\partial(\rho E)}{\partial t}+\frac{\partial}{\partial x_j}\left[\rho E u_j+p u_j-\kappa\frac{\partial T}{\partial x_j}-\mu u_i\left(\frac{\partial u_i}{\partial x_j}+\frac{\partial u_j}{\partial x_i}\right)-\frac{2}{3}u_j\mu_{\mathrm{B}}\frac{\partial u_k}{\partial x_k}\right]=u_i\mathcal{F}_i, \quad (8)$$

where ρ is the density, u_i is the velocity, p is the pressure, μ is the dynamic viscosity, μ_{B} is the dynamic bulk viscosity, E is the specific total energy, κ is the heat conduction coefficient, T is the temperature, and $\mathcal{F}_i$ is a volumetric body forcing term. We close the system of governing equations using an ideal gas equation of state $p=\rho R_u T/W$, where R_u is the universal gas constant and W is the mixture molecular weight, and we use temperature-dependent relations for the transport coefficients. Since the present simulations do not include reactions and have a relatively low turbulent Mach number, the simulations are approximately isothermal and the temperature does not change significantly from its initial value of 300 K. As a result, all transport coefficients are also approximately constant.

The physical setup for each simulation consists of a triply-periodic cubic domain with equal sides of length L and a uniform mesh discretization of N_x cells per side (giving N_x^3 total computational cells in each simulation). The simulations are initialized with uniform density and pressure and a random velocity field with a prescribed solenoidal, isotropic kinetic energy spectrum. Turbulence is sustained through a deterministic force, denoted $\mathcal{F}_i$ in the governing equations above, that is computed as a large-scale, isotropic perturbation momentum field with the kinetic energy addition scaled to provide a constant rate of energy injection discretely after each timestep, as in [29]. The kinetic energy addition is spectrally sharp, with energy injected into the second and third wavenumber modes only, resulting in statistically-stationary HIT with an average integral length scale of $L/\ell\approx 9.1$.

After initialization, the turbulent flow field in each simulation is allowed to fully develop over ten integral-scale eddy-turnover times, τ_ℓ. After $10\tau_\ell$, an isotropic, spectrally-sharp, low-pass filter is applied to each of the flow field variables for each test case at the prescribed filter width, Δ_{LES}, thereby truncating the kinetic energy spectrum. The simulations are then allowed to run for a further $6\tau_\ell$ while isotropic kinetic energy spectra are output 16 times per τ_ℓ. The convergence of these spectra to the corresponding equilibrium spectrum is used to define the equilibration time τ_{eq}, as described in the next section. The forcing $\mathcal{F}_i$ is maintained at the same intensity for the duration of the simulations, both before and after truncating the kinetic energy spectrum using low-pass filtering.

As summarized in Table 1, DNS were performed for each of nine different cases to span a range of four different values of $\Delta_{\mathrm{LES}}/\eta$ and three different values of ℓ/η. Eight independent simulations with different randomized initial conditions were performed for each of

Table 1. Summary of filtered HIT simulations performed in the present study, showing the number of grid cells per side of the cubic simulation domain (N_x) and values for the non-dimensional parameters relevant to Equations (3)–(5).

N_x	Re_ℓ	ℓ/η	$\Delta_{\mathrm{LES}}/\eta$	$\ell/\Delta_{\mathrm{LES}}$
128	40	14.1	4	3.52
			8	1.76
256	110	28.2	4	7.04
			8	3.52
			16	1.76
512	280	56.3	4	14.1
			8	7.04
			16	3.52
			32	1.76

the nine cases to allow for ensemble averaging of the instantaneous kinetic energy spectra, as described in the next section, resulting in a total of 72 individual simulations. At equilibrium, the simulations span three values of Re_ℓ from 40 to 280. All simulations were performed at the same turbulence Mach number, $\mathrm{Ma}_t = 0.1$, and Kolmogorov-grid size ratio, $\eta/\Delta_{\mathrm{DNS}} = 1.0$. Additionally, the integral-domain size ratio, $L/\ell \approx 9.1$, is approximately constant across all simulations by virtue of the chosen forcing mechanism. The initial temperature and pressure in the domain were 300 K and 1 atm with molecular weight $W = 24.62$ such that the density was 1 kg/m^3.

2.3. Equilibration time definition

The equilibration time, τ_{eq}, is generally defined as the time required for the ensemble-averaged isotropic kinetic energy spectrum to reach a long-time equilibrium spectrum, to within a certain error tolerance, after each simulation has been low-pass filtered. For this purpose, the time at which the low-pass filtering occurs is defined as $t = 0$, and the ensemble-averaged isotropic kinetic energy spectrum is given as a function of time for each test case as

$$\widehat{E}(k,t) = \frac{\Delta k}{8}\sum_{n=1}^{8}\sum_{\Omega_k}\frac{1}{2}\widehat{\mathbf{u}}_n^*(\mathbf{k},t)\cdot\widehat{\mathbf{u}}_n(\mathbf{k},t), \quad \Omega_k = \{\mathbf{k} : k \le |\mathbf{k}| < k + \Delta k\}, \tag{9}$$

where $\widehat{\mathbf{u}}_n(\mathbf{k},t)$ is the Fourier transform of the velocity field of the nth simulation in each ensemble, $(\cdot)^*$ denotes a complex conjugate, $\mathbf{k}$ is the wavenumber vector, $k \equiv |\mathbf{k}|$ is the wavenumber magnitude, and $\Delta k = 2\pi/L$. Furthermore, the isotropic spectrum is dependent on the discrete wavenumber magnitude, $k \in \{0, \Delta k, 2\Delta k, \ldots, N_x\Delta k/2\}$, due to the summation of each kinetic energy spectrum within spherical shells of thickness Δk in the three-dimensional Fourier space. As noted in the previous section, each ensemble average is comprised of eight independent simulations for each of the nine test cases summarized in Table 1.

Two different metrics are used to measure the relative error between $\widehat{E}(k,t)$ and the temporal average of $\widehat{E}(k,t)$ over the last $0.25\tau_\ell$ of each simulation, which we define as the equilibrium spectrum $\widehat{E}_{\mathrm{eq}}(k)$. The first error metric is the L_1-norm given by

$$\epsilon_1(t) = \frac{1}{N_k}\sum_k \frac{|\widehat{E}(k,t) - \widehat{E}_{\mathrm{eq}}(k)|}{\widehat{E}_{\mathrm{eq}}(k)}, \tag{10}$$

where N_k is the total number of discrete wavenumber modes in the spectra. This metric provides a straightforward error measure that gives equal weight to the relative error in the kinetic energy spectrum at all wavenumber modes. The second error metric is the L_2-norm of the error between equally-scaled spectra, given by

$$\epsilon_2(t) = \left[\sum_k \left(\frac{\widehat{E}(k,t)}{\sum_k \widehat{E}(k,t)} - \frac{\widehat{E}_{\mathrm{eq}}(k)}{\sum_k \widehat{E}_{\mathrm{eq}}(k)}\right)^2\right]^{1/2}. \tag{11}$$

This metric provides an error measure that emphasizes differences in spectral shape and disregards the difference in total kinetic energy. In both cases, we define τ_{eq} as the time

required for the error to drop beneath some critical value ϵ_{crit} (i.e. the time required for $\epsilon_i \leq \epsilon_{\text{crit}}$). In the following, we present results using both error metrics in order to assess the sensitivity of the dimensional analysis, if any, to the specific definition of τ_{eq}.

3. Results and discussion

Examples of the temporal evolution of the ensemble-averaged isotropic kinetic energy spectrum and the L_2 error norm, $\epsilon_2(t)$, after low-pass filter truncation for the test cases where $\Delta_{\text{LES}}/\eta = 8$ are provided in Figure 1. The mesoscale kinetic energy (i.e. $0.01 > k\eta > 0.06$) inflates beyond the equilibrium spectrum during the time that the spectrum at the microscales (i.e. $k\eta > 0.1$) increases to equilibrium energy levels. This energy build-up is due to the interruption of the scale-to-scale cascade of kinetic energy by the low-pass filtering event, and approximates how a material volume of LES-resolved turbulent eddies would respond when swept from the LES region of the domain, where the SGS model is dissipating mesoscale kinetic energy, into a DNS-resolved transition zone without an active SGS model. As a consequence, the turbulence cascade process transfers the excess mesoscale energy into the microscales faster than viscous dissipation can remove the energy in these scales, and the microscales subsequently exceed the energy of the equilibrium spectrum for a brief time. This transient process of microscale over-inflation is the cause of the non-monotonic evolution of ϵ_2 in time, shown in the right panel of Figure 1.

We note that the mesoscale build-up at earlier times does not overly influence the error (right panel of Figure 1), since far more wavenumber modes exist in the viscous region and each mode is given equal weight in the error norms. Although it is possible to define an absolute error metric biased towards the more energetic wavenumber modes, the purpose of the present study is to assess the time required for the turbulence cascade to extend down and "fill in" the sub-LES scales within the embedded DNS region, rather than to assess the time required for complete equilibration of the entire spectral energy cascade, since a statistically-stationary cascade is only theorized to exist for stationary and homogeneous

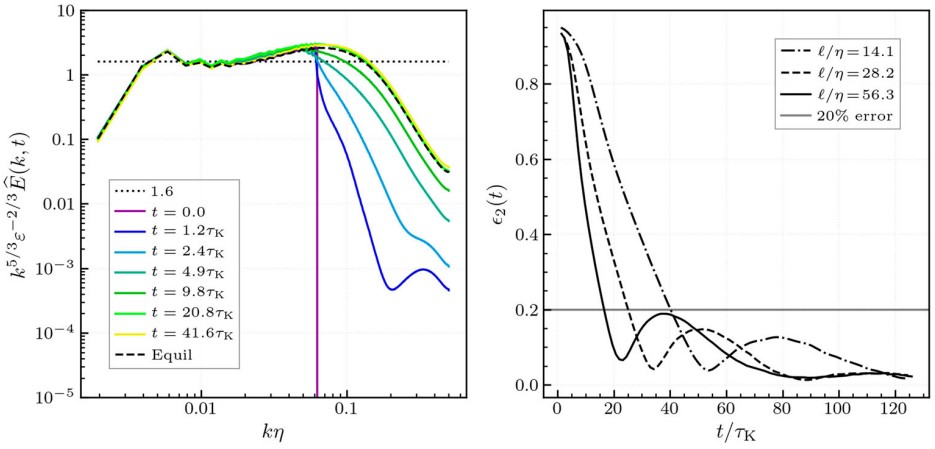


Figure 1. Ensemble-averaged isotropic kinetic energy spectra, $\widehat{E}(k,t)$ for the case $\ell/\eta = 56.3$ and $\Delta_{\text{LES}}/\eta = 8$ (left), and the time history of L_2 error, $\epsilon_2(t)$, for all three cases where $\Delta_{\text{LES}}/\eta = 8$.

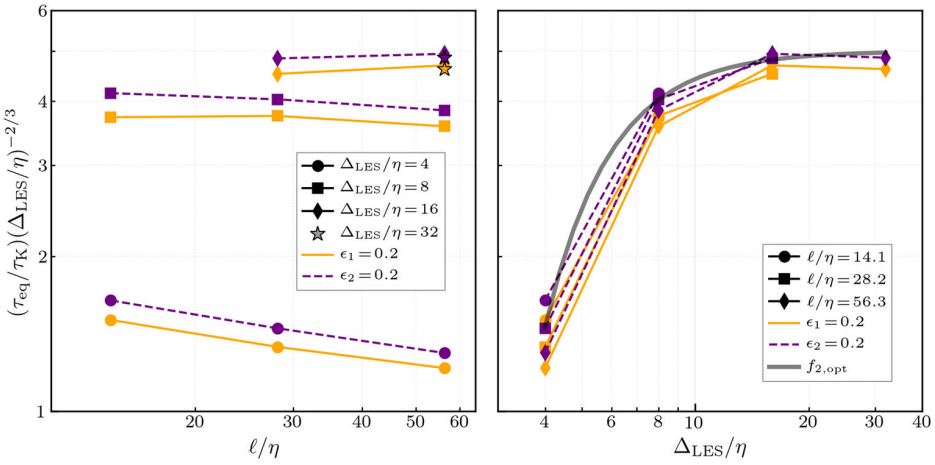


Figure 2. Scaling plots of τ_{eq}/τ_K versus ℓ/η (left), and Δ_{LES}/η (right) compensated by $(\Delta_{LES}/\eta)^{-2/3}$. The solid gray line in the right panel corresponds to the least-squares-optimal curve fit of Equation (12) to the data for $\epsilon_2 = 0.2$, denoted $f_{2,opt}$, where $C = 5.00$, $\alpha = 39.4$, and $\beta = 2.50$.

turbulence configurations such as HIT [19], and will certainly not exist within a region of interacting multi-physics such as a turbulent flame [6].

Figure 2 shows a test of the self-similar-range scaling of τ_{eq}/τ_K with Δ_{LES}/η for $\epsilon_{crit} = 0.2$, where τ_{eq}/τ_K is compensated by a factor of $(\Delta_{LES}/\eta)^{-2/3}$. It was found that values of ϵ_{crit} less than 0.2 yielded statistically non-converged τ_{eq} curves, due to insufficient sample sizes for the ensemble average of the spectra at those error tolerances (i.e. at error levels where the error norms are non-monotonic). However, when $\epsilon_{crit} = 0.2$, τ_{eq}/τ_K varied smoothly and was insensitive to the choice of error metric. The results in the left panel of Figure 2 suggest that τ_{eq}/τ_K does indeed scale as $(\Delta_{LES}/\eta)^{2/3}$, corresponding to $a = 2/3$ in Equation (4), since the curves are essentially horizontal for both sufficiently large values of Δ_{LES}/η and all values of ℓ/η.

The right panel of Figure 2 demonstrates that there is a strong non-similar dependence of τ_{eq}/τ_K on small values of Δ_{LES}/η, while τ_{eq}/τ_K appears to saturate to a constant value for $\Delta_{LES}/\eta > 10$. This suggests that the more general functional relation for f_2 in Equation (3) only approaches the asymptotic scaling in Equation (4) for the largest values of Δ_{LES}/η examined here. In order to compensate for the small Δ_{LES}/η dependence of f_2, we can fit an exponential roll-off to the data for $\epsilon_2 = 0.2$ of the general form $f_2(x) = Cx^{2/3}\exp(-\alpha x^{-\beta})$ such that

$$\frac{\tau_{eq}}{\tau_K} = C\left(\frac{\Delta_{LES}}{\eta}\right)^{2/3}\exp\left[-\alpha\left(\frac{\Delta_{LES}}{\eta}\right)^{-\beta}\right], \tag{12}$$

where α, and β are both strictly positive free coefficients such that $f_2(0) = 0$ and $f_2(x \to \infty) = Cx^{2/3}$, and C is the same leading coefficient as in Equation (4).

Using least-squares optimization, we find a curve-fit for the $\epsilon_2 = 0.2$ data points, denoted as $f_{2,opt}$, corresponding to $C = 5.00$, $\alpha = 39.4$, and $\beta = 2.50$, and we show the resulting curve in the right panel of Figure 2. We further test the quality of the fit $f_{2,opt}$ in Figure 3, which shows the residual deviation of τ_{eq}/τ_K from Equation (12) when using the

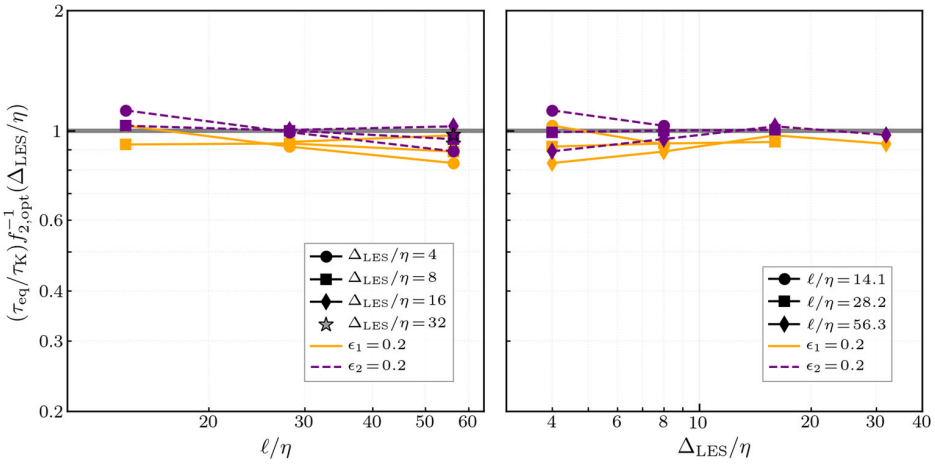


Figure 3. Scaling plots of τ_{eq}/τ_K versus ℓ/η (left), and Δ_{LES}/η (right) compensated by Equation (12), corresponding to $f_{2,opt}$ for parameters $C = 5.00$, $\alpha = 39.4$, and $\beta = 2.50$.

fitted parameters. It should be noted that we have assumed that $f_1(\ell/\eta) = 1$ for the range of ℓ/η examined here, but the left panel of Figure 2 does indicate that there may be some remaining dependence of τ_{eq}/τ_K on ℓ/η; larger ensemble sizes and additional simulations are required to more precisely determine the functional form of f_1 from Equation (4) over a broader range of values.

Finally, by combining Equation (1) with (12), using $\tau_K = (\ell\eta^2/Du_\ell^3)^{1/3}$ and $\eta = \ell D^{1/4}\mathrm{Re}_\ell^{-3/4}$, and then setting $D = 0.46$, we can derive the requirement for the minimum transition-zone depth based solely on integral-scale parameters directly obtainable from LES or experimental measurements, namely

$$\frac{L_{tz}}{\Delta_{LES}} \gtrsim 6.5\left(\frac{U_n}{u_\ell}\right)\left(\frac{\ell}{\Delta_{LES}}\right)^{1/3}\exp\left[-24\mathrm{Re}_\ell^{-15/8}\left(\frac{\ell}{\Delta_{LES}}\right)^{5/2}\right], \tag{13}$$

where the exponential roll-off becomes significant at either small Re_ℓ (e.g. $\mathrm{Re}_\ell < 500$ when $\ell/\Delta_{LES} = 10$) or large ℓ/Δ_{LES} (e.g. $\ell/\Delta_{LES} > 100$ when $\mathrm{Re}_\ell = 10^4$). For a given set of integral-scale characteristics and simulation mesh parameters, this relation can be used *a priori* to set the transition-zone depth in a hybrid LES-DNS approach.

4. Conclusions

In this study, we have addressed the problem of accurately capturing the advective sweep of LES-resolved turbulent eddies, mediated by a truncated turbulence cascade, from a host LES to an embedded DNS region in a hybrid LES-DNS, where the previously truncated turbulence cascade must equilibrate with the increased scale bandwidth of the DNS grid. Using dimensional analysis and a suite of computational simulations, we have formulated an empirical scaling law for the minimum necessary depth of the transition zone between LES and DNS regions; the resulting scaling law, given by Equation (13), represents the primary and most significant result of the present study. In a valid implementation of the

hybrid LES-DNS approach, this scaling relation should guarantee that the transition zone is sufficiently large to allow the turbulent cascade process to reach equilibrium with the small scales of the DNS mesh, thereby 'filling in' the scale-space bandwidth gap between the LES and DNS grid resolutions.

However, there are many technical challenges that must still be overcome before true hybrid LES-DNS computations of complex multi-physics configurations are realized, including how to address the transition of microscale phenomena, such as acoustic or chemical dynamics, as they propagate from the DNS to LES regions of the domain. Nevertheless, the present analysis does provide confidence that these simulations can be used to effectively bridge the enormous scale ranges found in practical laboratory flows.

Disclosure statement

No potential conflict of interest was reported by the author(s).

Funding

This work was supported by Air Force Office of Scientific Research under awards FA9550-18-1-0057 and FA9550-17-1-0144, Dr. Chiping Li, program manager.

ORCID

C. A. Z. Towery http://orcid.org/0000-0002-1090-7939

References

[1] Shaw RA. Particle-turbulence interactions in atmospheric clouds. Annu Rev Fluid Mech. 2003;35(1):183–227.
[2] Elghobashi S. On predicting particle-laden turbulent flows. Appl Sci Res. 1994;52(4):309–329.
[3] Conway GD. Turbulence measurements in fusion plasmas. Plasma Phys Control Fusion. 2008 Nov;50(12):124026.
[4] Urzay J. Supersonic combustion in air-breathing propulsion systems for hypersonic flight. Annu Rev Fluid Mech. 2018;50:593–627.
[5] Poludnenko AY, Chambers J, Ahmed K, et al. A unified mechanism for unconfined deflagration-to-detonation transition in terrestrial chemical systems and type Ia supernovae. Science. 2019;366(6465).
[6] Towery CAZ, Poludnenko AY, Urzay J, et al. Spectral kinetic energy transfer in turbulent premixed reacting flows. Phys Rev E. 2016;93(5):053115.
[7] O'Brien J, Towery CAZ, Hamlington PE, et al. The cross-scale physical-space transfer of kinetic energy in turbulent premixed flames. Proc Combust Inst. 2017;36(2):1967–1975.
[8] Towery CA, Poludnenko AY, Hamlington PE. Detonation initiation by compressible turbulence thermodynamic fluctuations. Combust Flame. 2020;213:172–183.
[9] Magnotti G, Barlow RS. Effects of high shear on the structure and thickness of turbulent premixed methane/air flames stabilized on a bluff-body burner. Combust Flame. 2015;162(1):100–114.
[10] Sullivan PP, McWilliams JC, Moeng CH. A grid nesting method for large-eddy simulation of planetary boundary-layer flows. Boundary Layer Meteorol. 1996;80(1-2):167–202.
[11] Perot JB, Gadebusch J. A self-adapting turbulence model for flow simulation at any mesh resolution. Physics of Fluids. 2007;19(11):115105.
[12] Spalart PR, Deck S, Shur ML, et al. A new version of detached-eddy simulation, resistant to ambiguous grid densities. Theor Comput Fluid Dyn. 2006;20(3):181–195.

[13] Bell JB, Day MS, Grcar JF, et al. Numerical simulation of a laboratory-scale turbulent slot flame. Proc Combust Inst. 2007;31(1):1299–1307.
[14] Day MS, Tachibana S, Bell JB. A combined computational and experimental characterization of lean premixed turbulent low swirl laboratory flames: I. Methane flames. Combust Flame. 2012;159(1):275–290.
[15] Gao X, Groth CPT. A parallel adaptive mesh refinement algorithm for predicting turbulent non-premixed combusting flows. Int J Comut Fluid Dyn. 2006;20(5):349–357.
[16] Gao X, Groth CPT. A parallel solution-adaptive method for three-dimensional turbulent non-premixed combusting flows. J Comput Phys. 2010;229:3250–3275.
[17] Cardesa JI, Vela-Martín A, Dong S, et al. The temporal evolution of the energy flux across scales in homogeneous turbulence. Phys Fluids. 2015;27(11):111702.
[18] Lumley JL. Some comments on turbulence. Phys Fluids A. 1992;4(2):203–211.
[19] Pope SB. Turbulent flows. Cambridge University Press; 2000, Cambridge, UK.
[20] Wan M, Xiao Z, Meneveau C, et al. Dissipation-energy flux correlations as evidence for the lagrangian energy cascade in turbulence. Phys Fluids. 2010;22(6):061702.
[21] Sagaut P. Large eddy simulation for incompressible flows: an introduction. Springer-Verlag; 2006, Heidelberg, DE.
[22] Kraichnan RH. Inertial-range transfer in two- and three-dimensional turbulence. J Fluid Mech. 1971;47(3):525–535.
[23] Barenblatt GI. Scaling, self-similarity, and intermediate asymptotics: dimensional analysis and intermediate asymptotics. Cambridge University Press; 1996.
[24] Jagannathan S, Donzis DA. Reynolds and mach number scaling in solenoidally-forced compressible turbulence using high-resolution direct numerical simulations. J Fluid Mech. 2016;789:669–707.
[25] Martinez DO, Chen S, Doolen GD, et al. Energy spectrum in the dissipation range of fluid turbulence. J Plasma Phys. 1997;57(1):195–201.
[26] Colella P. Multidimensional upwind methods for hyperbolic conservation-laws. J Comput Phys. 1990;87:171–200.
[27] Gardiner TA, Stone JM. An unsplit Godunov method for ideal MHD via constrained transport in three dimensions. J Comput Phys. 2008;227:4123–4141.
[28] Stone JM, Gardiner TA, Teuben P, et al. Athena: a new code for astrophysical MHD. Astrophys J Suppl Ser. 2008;178(1):137–177.
[29] Petersen MR, Livescu D. Forcing for statistically stationary compressible isotropic turbulence. Phys Fluids. 2010;22(11):116101.

Progress in Energy and Combustion Science 85 (2021) 100900

Contents lists available at ScienceDirect

Progress in Energy and Combustion Science

journal homepage: www.elsevier.com/locate/pecs

Structure and dynamics of highly turbulent premixed combustion

Adam M. Steinberg [a,*], Peter E. Hamlington [b], Xinyu Zhao [c]

[a] Daniel Guggenheim School of Aerospace Engineering, Georgia Institute of Technology, Atlanta, GA, 30332, USA
[b] Paul M. Rady Department of Mechanical Engineering, University of Colorado, Boulder, CO, 80309, USA
[c] Department of Mechanical Engineering, University of Connecticut, Storrs, CT, 06269, USA

ARTICLE INFO

Article history:
Received 16 June 2020
Accepted 12 December 2020

Keywords:
Turbulent combustion
Premixed flames
Turbulence-flame interaction
Direct numerical simulations
Laser diagnostics

ABSTRACT

Turbulent premixed combustion involves simultaneous and mutually interacting fluid, chemical, and transport phenomena spanning a wide range of spatial and temporal scales. Many practical combustion devices – such as gas turbine combustors, afterburners, and ramjets – operate with turbulent flows that contain length and time scales smaller than those associated with premixed flame propagation. This paper reviews current knowledge and understanding of premixed flames at such "highly turbulent" conditions, including the effects of turbulence on the flame and of the flame on turbulence. At these conditions, turbulent fluid motions can have a leading-order effect on the flame thermochemical structure, scalar gradients, and the resultant scalar dynamics. At the same time, the turbulent flow itself is affected by heat release from the flame, resulting in differences compared to classical non-reacting turbulence and to turbulence in flames at lower intensities. We therefore aim to address the following overarching questions: (a) What are highly turbulent premixed flames, how do we characterize them, and what are some of their macroscale behaviors? (b) How are the flame thermochemical states, scalar gradients, diffusion, and other aspects of the flame structure affected by intense turbulence? (c) How are the structure and dynamics of the turbulence affected by the presence of the flame in terms of fluxes, spectra, kinetic energy, and other relevant quantities? We also provide a summary of critical knowledge gaps and an outlook for future research directions.

© 2020 The Author(s). Published by Elsevier Ltd.
This is an open access article under the CC BY-NC-ND license
(http://creativecommons.org/licenses/by-nc-nd/4.0/)

Contents

1. Introduction . . . 2
2. Preliminary comments and global characteristics . . . 3
  2.1. Governing equations . . . 4
  2.2. Laminar premixed flames . . . 4
    2.2.1. Deflagrations and auto-ignition . . . 4
    2.2.2. Laminar premixed deflagrations . . . 4
  2.3. Configurations and other practical considerations . . . 6
  2.4. Turbulent flame characterization . . . 8
    2.4.1. Characteristic scales and dimensionless parameters . . . 8
    2.4.2. Expected parameters for highly turbulent flames . . . 10
    2.4.3. Comments on regimes . . . 11
  2.5. Turbulent flame speed . . . 13
  2.6. Summary . . . 15
3. Thermochemical structure and dynamics . . . 15

* Corresponding author.
E-mail addresses: adam.steinberg@gatech.edu (A.M. Steinberg), peh@colorado.edu (P.E. Hamlington), xinyu.zhao@uconn.edu (X. Zhao).

https://doi.org/10.1016/j.pecs.2020.100900
0360-1285/© 2020 The Author(s). Published by Elsevier Ltd. This is an open access article under the CC BY-NC-ND license
(http://creativecommons.org/licenses/by-nc-nd/4.0/)

3.1. Flame structure in physical space . . . 15
3.2. Flame structure in thermochemical space . . . 17
3.2.1. Non-unity Lewis number effects . . . 17
3.2.2. Scalar distributions in thermochemical space . . . 19
3.3. Chemical reactions in the enlarged thermochemical space . . . 20
3.3.1. Chemical pathways . . . 20
3.3.2. Reaction rates . . . 22
3.3.3. Decorrelated fuel consumption and heat release rates . . . 23
3.4. Local combustion mode and its diagnostics . . . 23
3.4.1. Budget analysis . . . 23
3.4.2. Computational singular perturbation . . . 24
3.4.3. Chemical explosive model analysis . . . 24
3.5. Summary . . . 25
4. Turbulence structure and dynamics . . . 26
4.1. Turbulence kinetic energy, stresses, and fluxes . . . 26
4.1.1. Turbulence kinetic energy . . . 26
4.1.2. Turbulent stresses . . . 29
4.1.3. Turbulent scalar fluxes . . . 29
4.2. Vorticity, strain rate, and scalar gradients . . . 30
4.2.1. Scalar gradients . . . 30
4.2.2. Vorticity and strain rate . . . 33
4.2.3. Coherent structures . . . 36
4.3. Spectral and multi-scale characteristics . . . 37
4.3.1. Spectral and multi-scale structure . . . 39
4.3.2. Spectral and multi-scale dynamics . . . 40
4.4. Summary . . . 42
5. Outlook . . . 42
Declaration of Competing Interest . . . 43
Acknowledgements . . . 43
References . . . 44
Further reading . . . 48

1. Introduction

Nearly all practical applications of combustion occur in turbulent flows, generally by design. Turbulent combustion involves non-linear multi-scale interactions between chemistry, transport, and fluid motions that have leading order effects on the flame and flow behavior. For premixed turbulent combustion, turbulent fluid motions lead to an increase in the surface area of reactive scalars that is associated with an increase in the turbulent burning rate. Turbulence also creates large gradients in thermodynamic and chemical quantities, resulting in substantially greater thermochemical complexity than in laminar flames (e.g., broader thermochemical phase spaces and highly varied thermochemical trajectories along Lagrangian fluid pathlines). Moreover, the fluid dynamic strain rate and vorticity directly affect the dynamics of reactive thermochemical scalar gradients, thus impacting, for example, the local flame orientation, thickness, and iso-surface propagation speed. Thermochemical gradients generated by combustion chemistry also influence the turbulence, both by altering transport properties and through thermal expansion (e.g., flow divergence, density gradients, etc.).

Although numerous studies, including several detailed reviews [1–10], have addressed turbulent premixed combustion occurring at relatively modest turbulence intensities, comparatively little research has addressed fundamental turbulence-flame interactions at the highly turbulent conditions relevant to many practical devices and situations, such as lean premixed gas turbine combustors, afterburners, ramjets, and other occurrences of fast subsonic flames [11]. Indeed, a surge of studies on highly turbulent premixed flames emerged around 2015. The purpose of this paper is to review the current state of knowledge regarding the structure and dynamics of highly-turbulent premixed flames, including both the effects of turbulence on the flame and the flame on turbulence.

The dynamical system describing turbulent combustion is outlined mathematically in Section 2. For now, it is sufficient to note that this system is nonlinear due to various physical effects represented in the governing equations, including advection, chemical sources, pressure-velocity coupling, and temperature-dependent molecular transport processes. Of note is the advective nonlinearity in the Navier-Stokes equations describing conservation of momentum. In turbulent flows, this nonlinearity dominates over the (linear) effects of viscous diffusion of momentum. The integral-scale Reynolds number, Re_ℓ, which characterizes the relative magnitudes of the advective nonlinearity and viscous diffusion, is thus typically very large in turbulent flows.

As a result of the dominant nonlinearity in high Re_ℓ turbulent flows, large spatial and temporal variations in flow properties are created over a wide range of length and time scales. This multi-scale spatio-temporal complexity leads to the formation of turbulent fluctuations at increasingly small scales as Re_ℓ increases, resulting in the creation of large spatial gradients in velocity and other quantities (e.g., temperature and chemical species concentrations). These large gradients, in turn, lead to rapid molecular transport of thermochemical scalars (e.g., temperature and chemical species concentrations), as compared to variations due to chemical reactions alone.

It is this mixing property of turbulence that makes it particularly attractive for many combustion systems. For non-premixed combustion, turbulence accelerates the rate-limiting process of fuel and oxidizer mixing. For premixed combustion—in which reaction rates are not limited by the rate of fuel and oxidizer mixing—turbulence increases the rate at which energy and species are mixed between the products and reactants, ultimately leading to

Nomenclature

Dimensionless Parameters

$\mathrm{Da}_{\ell,\delta}$	Damköhler number
$\mathrm{Ka}_{\delta,\mathrm{K}}$	Karlovitz number
Le	Lewis number
Re_ℓ	Integral scale Reynolds number

Greek

α	Thermal diffusivity
$\boldsymbol{\omega}$	Vorticity vector
χ_j	Scalar gradient
δ_L^0	Unstretched laminar flame thermal thickness
δ_r^0	Unstretched laminar flame reaction zone thickness
δ_t	Scalar field thickness
$\dot{\omega}_\beta$	Chemical source term
κ	Thermal conductivity
λ_e	Eigenvalue of eigenmode of chemical Jacobian
λ_K	Kolmogorov length scale
μ	Dynamic viscosity
μ_B	Bulk viscosity
ν	Kinematic viscosity
Ω	Enstrophy
ϕ	Equivalence ratio
ψ	Generic scalar
ρ	Fluid density
τ_δ	Characteristic laminar flame propagation time scale
τ_i	Induction time
τ_K	Kolmogorov time scale
τ_r	Characteristic laminar flame reaction zone time scale
τ_{ij}	Viscous stress tensor
ε	Mean kinetic energy dissipation rate
φ_s	Contribution of diffusion to evolution of CEM
φ_ω	Contribution of reaction to evolution of CEM

Mathematical Operators

$(\cdot)'$	Fluctuation about ensemble average
ϵ_{ijk}	Cyclic permutation tensor
$\bar{(\cdot)}$	Ensemble average
$\tilde{(\cdot)}$	Favre average
$(\cdot)''$	Fluctuation about Favre average

Roman

$\boldsymbol{a}_\mathrm{e}$	Right chemical eigenvector
$\boldsymbol{b}_\mathrm{e}$	Left chemical eigenvector
e	Eigenvector of rate-of-strain tensor
$\boldsymbol{J}_\omega$	Chemical Jacobian
$\boldsymbol{k}$	Wavevector for spectral analysis
$\boldsymbol{n}$	Scalar isosurface normal vector
$\boldsymbol{r}$	Scale separation for structure function analysis
$\boldsymbol{u}$	Fluid velocity
$\dot{m}_\mathrm{r}$	Reactant mass flow rate
ℓ	Integral length scale
$\mathcal{D}$	Molecular transport coefficient
$\mathcal{D}_\mathrm{T}$	Turbulent diffusivity
$\mathcal{F}$	Body force
$\mathcal{T}$	Integral time scale
A_T	Turbulent flame surface area
$A_{\tilde{c}=0.5}$	Mean flame brush area
a_{ij}	Anisotropy tensor
c	Reaction progress variable
c_K	Scaling factor relating λ_K, ℓ, and Re_ℓ
c_s	Scaling factor relating s_L^0, $\tilde{\alpha}$ and δ_L^0
e_0	Total energy
I	Dependency of Karlovitz and Damköhler numbers on flow conditions and geometry
I_0	Flame speed stretch factor
II	Dependency of Karlovitz and Damköhler numbers on thermochemical parameters
k	Turbulence kinetic energy
L	Induction length
n_s	Number of chemical species
p	Pressure
P_{ij}	Plane parallel to scalar isosurface
s	Non-chemical source terms in CEM analysis
s_L^0	Unstretched laminar flame speed
s_D	Displacement speed
$s_{\mathrm{T,GC}}$	Global consumption speed of turbulent flame
S_{ij}	Rate-of-strain tensor
T	Temperature
u_ℓ	Integral velocity scale
u_K	Kolmogorov velocity scale
Y	Mass fraction

an increased reaction rate compared to laminar flames. We note that "mixing" in this context refers to combined advective and diffusive processes; non-linear advective stirring increases the magnitude and spatial extent of scalar and velocity gradients, which then lead to rapid molecular diffusion. Together, the statistical effect of advective turbulent stirring and enhanced molecular diffusion is often referred to as "turbulent diffusion".

However, turbulence also complicates the design, analysis, and operation of combustion systems. The broad range of length and time scales at play in turbulent combustion—from the large integral scales to the Kolmogorov and chemical scales—precludes direct numerical simulations (DNS) of practical devices in engineering contexts; models must therefore be employed. For example, in the context of large eddy simulations (LES), models are required to describe the influence of unresolved subfilter scale (SFS) phenomena on resolved scale behaviors. In highly turbulent flames, much of the turbulence-induced thermochemical complexity and the flame-induced turbulence dynamics exist in the subfilter scales and must be modeled. In order to create physics-based models, it therefore is critical to understand the various interactions between the flame and turbulence that can occur at highly turbulent conditions.

In this review, we address the following overarching questions:

1. What are highly turbulent flames, how are they characterized, and what are some of their macro-scale behaviors?
2. How are the thermochemical structure and dynamics of the flame modified by the presence of intense turbulence?
3. How are turbulence structure and dynamics modified by premixed flames at highly turbulent conditions?

The first items are addressed primarily in Section 2, while the second and third questions are addressed in Sections 3 and 4, respectively. An outlook for future research directions is provided in Section 5.

2. Preliminary comments and global characteristics

We will often discuss the effects of turbulence on premixed flames by differentiating the turbulent flame "structure" and "dynamics" from that which would occur under laminar flow conditions. The expected impact of turbulence on the flame is typically described through various dimensionless parameters constructed using characteristic length, time, and/or velocity-scales, which may be visualized through regime diagrams. We therefore begin this

review with a brief discussion of laminar flame structure, dimensionless parameters, regime diagrams, and the locations of some engineering-relevant devices in the regime diagrams. We also include a brief discussion of experimental and DNS configurations commonly used to study highly turbulent combustion, as well as the turbulent flame speeds observed in these configurations. Several practical and theoretical challenges are highlighted, and some best practices are recommended.

2.1. Governing equations

In general terms, turbulent combustion is characterized by highly irregular fluid motions that are coupled with reactive scalar dynamics, both of which vary in space and time in a complicated manner. The fluid density (ρ), velocity vector (u_i), total energy (e_0, sum of thermal, chemical, and kinetic energy), and species mass fractions[1] (Y_β, where $\beta = 1, \ldots, n_s$ for n_s total chemical species), evolve according to the system of equations

$$\frac{\mathrm{D}\rho}{\mathrm{D}t} = -\rho \frac{\partial u_k}{\partial x_k}, \tag{1}$$

$$\frac{\mathrm{D}u_i}{\mathrm{D}t} = -\frac{1}{\rho}\frac{\partial p}{\partial x_i} + \frac{1}{\rho}\frac{\partial \tau_{ij}}{\partial x_j} + \mathcal{F}_i, \tag{2}$$

$$\frac{\mathrm{D}e_0}{\mathrm{D}t} = -\frac{1}{\rho}\frac{\partial (u_j p)}{\partial x_j} + \frac{1}{\rho}\frac{\partial}{\partial x_j}\left(\kappa \frac{\partial T}{\partial x_j}\right) + \frac{1}{\rho}\frac{\partial (u_i \tau_{ij})}{\partial x_j} + u_i \mathcal{F}_i, \tag{3}$$

$$\frac{\mathrm{D}Y_\beta}{\mathrm{D}t} = \frac{1}{\rho}\frac{\partial}{\partial x_k}\left(\rho \mathcal{D}_\beta \frac{\partial Y_\beta}{\partial x_k}\right) + \dot{\omega}_\beta, \tag{4}$$

where summation over Greek indices in Eq. (4) is not implied. Here, $\mathrm{D}/\mathrm{D}t \equiv \partial/\partial t + u_j \partial/\partial x_j$ is the material, or Lagrangian, derivative that represents advection following a fluid element. Other quantities in these equations are the pressure (p), temperature (T), volumetric (or body) force ($\mathcal{F}_i$), thermal conductivity (κ), and molecular transport coefficient for Y_β ($\mathcal{D}_\beta$). We have assumed gradient diffusion, ignoring Soret and Dufour effects. Radiant energy transfer is also neglected in Eq. (3). The Newtonian viscous stress tensor τ_{ij} is expressed as

$$\tau_{ij} = 2\mu S_{ij} - \frac{2}{3}\delta_{ij}\mu_\mathrm{B} S_{kk}, \tag{5}$$

where μ and μ_B are the dynamic viscosity and bulk viscosity, respectively, and

$$S_{ij} = \frac{1}{2}\left(\frac{\partial u_i}{\partial x_j} + \frac{\partial u_j}{\partial x_i}\right), \tag{6}$$

is the rate-of-strain tensor. Sources of Y_β (i.e., due to chemical reactions) are represented by $\dot{\omega}_\beta$ and may take on positive or negative values. All of the transport coefficients (i.e., κ, $\mathcal{D}_\beta$, μ, and μ_B) appearing in the above equations depend on the local temperature and fluid composition, and are not constant in reacting flows. A full description of the system dynamics therefore requires auxiliary relations to represent the chemical reactions, transport coefficients, and the thermodynamic equation of state. From a Lagrangian point of view, Eqs. (1)–(4) state that the change in thermodynamic, flow, and chemical properties following a fluid element at location $\boldsymbol{x}$ at time t is a result of the balance between diffusive (molecular transport) effects and various source terms.

For chemical species, the source term is generally local, depending only on the local composition and temperature-dependent reaction rate coefficient. By contrast, diffusion processes are nonlocal, being driven by gradients (e.g., $\chi_j \equiv \partial Y/\partial x_j$) that couple adjacent dissimilar fluid states. In laminar flames, the competition between advection, reaction, and molecular diffusion ultimately determines the structure and evolution of the scalar field. This also holds true in turbulent flames, but with turbulent advection leading to a broader range of scalar gradients than are found in laminar flames (thereby affecting the diffusion process) and, consequently, a wider range of thermochemical states (affecting the reaction process).

2.2. Laminar premixed flames

2.2.1. Deflagrations and auto-ignition

Turbulent flames may exhibit local behaviors ranging from being similar to laminar premixed deflagrations—in which energy and species diffusion are necessary to sustain the reactions—to being similar to autoignition[2]. While laminar deflagrations are most common, as will be discussed in Section 3, turbulence may create local gas mixtures that should be viewed as auto-igniting fronts [13–16]. Hence, this distinction will become important for discussions in Section 3, although devices that rely on autoignition as the major combustion mode (e.g. some sequential gas turbine combustors [17]) are not the main focus of this review.

To illustrate these combustion modes, consider a one-dimensional (1D) linear domain with a steady laminar flame in the observer reference frame. Hence, the speed of the gas upstream of the flame is the "laminar flame speed", denoted s_L^0 (the superscript '0' indicates that the flame is 'unstretched'). In cases where the ignition delay time (or induction time, τ_i) of the reactant mixture is long compared to the residence time of the unburnt mixture in the system (i.e., L/s_L^0, where L is the characteristic induction length), reactions are sustained by diffusion of energy and species from the products to the reactants (a deflagration). The laminar flame speed is then an intrinsic property of the reactant mixture that can be solved through an eigenvalue problem [18] and is independent of the ignition delay time.

For reactant mixtures in which the ignition delay is short compared to the residence time of the gas in the domain, the reactants will auto-ignite in the absence of any external source and without the need for diffusion from the products. The flame then stabilizes after an induction length $L = s_\mathrm{L}^0 \tau_\mathrm{i}$. Whereas τ_i is a unique function of the reactant state, in this context, the "laminar flame speed" depends both on the reactants and the "desired" induction length; it is not a unique function of the mixture. These two limiting cases are demonstrated in Fig. 1, which shows the laminar flame speed (i.e., the reactant gas speed for a stationary flame) as a function of induction length for various atmospheric pressure H_2/air flames at different reactant temperatures.

2.2.2. Laminar premixed deflagrations

We now turn briefly to laminar premixed deflagrations in order to define some quantities and concepts needed for the subsequent discussion. Fig. 2 shows computed profiles of various quantities through laminar unstretched deflagrations with different fuels at a constant pressure of $p = 1$ atm and a reactant temperature of $T_\mathrm{r} = 500$ K[3]. The fuel consumption and heat release rates are

[1] Eq. (4) can also be written in terms of species mole fractions. Indeed, it can be viewed as a general equation for any reactive scalar with gradient diffusion, given an appropriate diffusion coefficient. For clarity, we will largely treat chemical scalars in terms of mass fractions in this paper.

[2] Detonation waves occur when the combustion wave travels at a supersonic speed. Although this mode of combustion can occur in many engineering and natural contexts, the focus of the present review is on subsonic, non-detonative, combustion.

[3] All laminar flame calculations in this work are done in PREMIX [19] using the HyChem approach [20–22] with multi-component and Soret diffusion.

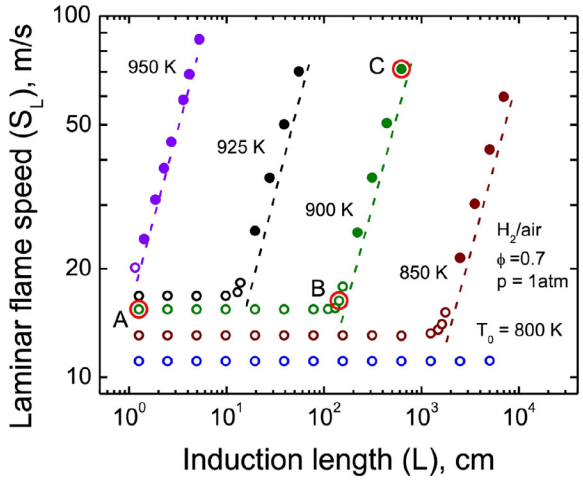


Fig. 1. Unstretched laminar flame speed (s_L^0) as a function of the induction length (L) . Reprinted from [12] with permission of Elsevier.

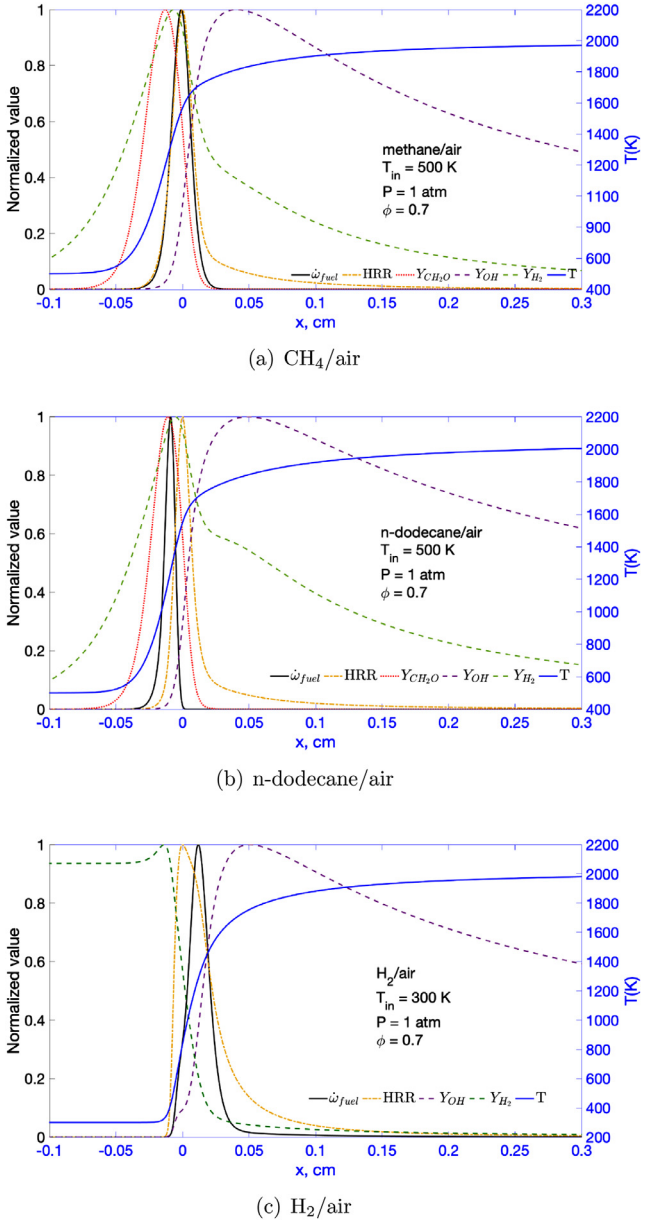
shown, along with mass fractions of a few key species. Temperature is used to demarcate different regions of the laminar flame, and also to serve as a reasonable measure of the progress variable c (see Refs. [23,24] for other methods of defining c). The origin of the physical space coordinates is at the peak heat release rate for each flame.

For the methane/air flame shown in Fig. 2(a), the exothermic reactions are confined to a relatively compact region at high temperature ($T \gtrsim 1200$ K) termed the "reaction zone". Upstream of this is a similarly compact region over which the reactants begin to breakdown, forming CH_2O, H_2, and other species. Species and energy diffuse further upstream in a relatively inert "preheat zone" that is dominated by molecular transport processes. Ultimately, however, the species profiles at all locations reflect the simultaneous effects of reaction, diffusion, and laminar convection, even as the relative balance of these effects varies throughout the flame.

The fuel consumption and heat release rates are co-located for the lean methane/air flame due to the relatively high temperatures required for methane-to-methyl initiation reactions. However, this relationship is compromised for the n-dodecane/air and hydrogen/air flames shown in Figs. 2(b)-(c). For the n-dodecane/air flame, fuel consumption precedes the heat release zone due to endothermic fuel pyrolysis. Such fuel cracking is expected for all heavy hydrocarbons [20,21,25]. For the hydrogen/air flame, the heat release zone overlaps with the fuel consumption region, although the peak of heat release precedes that of the fuel consumption. Heat release and fuel consumption both occur near the leading edge of the flame. Hence, a largely inert preheat zone and thin chemically-active reaction zone do not occur for these laminar flames (though the exothermic reactions are confined to a relatively thin region in the n-dodecane flame).

Important scales in these flames include a length characterizing the overall thermal thickness, $\delta_L^0 \equiv \left(T_p - T_r\right)\max(|\nabla T|)^{-1}$, and a thickness characterizing the region of rapid exothermic reactions δ_r^0. The interpretation of δ_L^0 in terms of scalar field dynamics will be discussed in Section 3.1. In the hydrocarbon/air flames, $\delta_r^0 = \mathcal{O}(10^{-1})\delta_L^0$. However, δ_r^0 is larger relative to δ_L^0 in the H_2 flame. Characteristic flame time-scales are defined by dividing these length-scales by the laminar flame speed, viz. $\tau_\delta = \delta_L^0/s_L^0$ and $\tau_r = \delta_r^0/s_L^0 = \mathcal{O}(10^{-1})\tau_\delta$. Hence, the range of length- and time-scales associated with an unstretched laminar premixed flame typically spans about one order of magnitude.

The unstretched laminar flame speed s_L^0 is a critical quantity for understanding turbulent premixed flames, as it is traditionally em-



(a) CH_4/air

(b) n-dodecane/air

(c) H_2/air

Fig. 2. One-dimensional unstretched laminar flames in physical space for lean methane/air, n-dodecane/air and hydrogen/air flames at atmospheric pressure. All profiles are normalized by their respective peak values.

ployed to define normalization chemical time scales for turbulent flames, both locally and globally. As previously mentioned, the unstretched laminar flame speed of a deflagration is a unique function of the reactant state, including composition, temperature, and pressure. The laminar flame speed is conventionally derived from 1D unstretched laminar flames where the least ambiguity is introduced in its definition/computation [26].

Fig. 3 shows the laminar flame speed of n-dodecane as a function of temperature (from $T = 500$ K to 1100 K in 100 K intervals), equivalence ratios (from $\phi = 0.6$ to 1 in 0.05 intervals), and pressures (from $p = 28$ bar to 32 bar in 0.5 bar intervals). As predicted by combustion theory [27], the laminar flame speed has a weak negative correlation with pressure, as well as a weak dependence on equivalence ratio in the fuel-lean (i.e., $\phi < 1$) region. Temperature has a leading-order effect on the laminar flame speed; s_L^0 increases by approximately seven-fold as the reactant temperature is raised from 500 K to 1100 K. It is important to recognize this

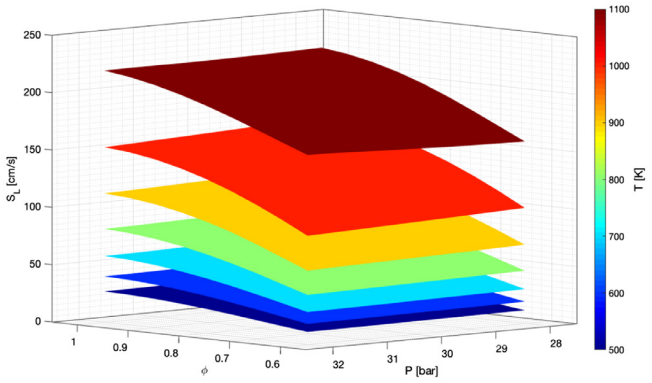


Fig. 3. Unstretched laminar flame speed s_L^0 obtained at different temperatures T, equivalence ratios ϕ, and pressures p for an n-dodecane/air mixture.

dependence, because local variations of the equivalence ratio and temperature are expected in highly turbulent flames, as discussed in Sec. 3.2.1. The temperature range in Fig. 3 is chosen to demonstrate the strong temperature dependence of laminar flame speed. However, it should be recognized that it is challenging to measure laminar flame speeds with preheat temperatures above 700 K, especially for heavy hydrocarbon fuels, due to fuel decomposition during the fuel heating and delivery process.

It is worth briefly mentioning that this discussion of laminar flame speed treats the deflagration as a coherent wave moving at speed s_L^0. However, due to gas acceleration normal to the flame and the corresponding decrease in density, different locations in the flame must move at different speeds in order to maintain a stationary flame. This leads to the definition of the displacement speed of a scalar isosurface (i.e., the surface of constant scalar value Y_β^*), defined as

$$s_D|_{Y_\beta^*} = \frac{1}{|\nabla Y_\beta|}\frac{DY_\beta}{Dt}\bigg|_{Y_\beta^*}, \tag{7}$$

where DY_β/Dt is given by Eq. (4). Hence, the displacement speed can be viewed as a field quantity that obeys a transport equation and obtains different values throughout both laminar and turbulent flames. This also highlights that, unlike the "laminar flame speed", the displacement speed is not a single value for a given reactant mixture. Indeed, for a steady laminar flame, the displacement speed varies between the gas speeds in the reactants and products in order to maintain a steady flame structure; care must be taken when evaluating the displacement speed to ensure that precise scalar isovalues are tracked.

The instantaneous and local thermochemical state of the reacting system can be expressed as the vector quantity $[T(\boldsymbol{x},t), \rho(\boldsymbol{x},t), \boldsymbol{Y}(\boldsymbol{x},t)]^\intercal \in \mathbb{R}^{n_s+2}$, where n_s is the number of species. In a steady, unstretched laminar flame with a known reactant thermochemical state the thermochemical state at any point can be uniquely indexed to the progress variable; the thermochemical state is a surjective function with c that is an (n_s+2)-dimensional curve in state space. Of course, Eqs. (4) and (7) show that the scalar field dynamics are controlled not only by the reaction rate, which depends on the local thermochemical state, but also by diffusive processes that depend on scalar gradients that couple dissimilar fluid states. However, in a laminar premixed deflagration, the scalar gradients are also uniquely mapped by c. Hence, the dynamics of the scalar fields depend only on c.

The idea that the thermochemical and spatial structure of a 1D laminar premixed flame can be uniquely mapped to the progress variable has been very influential in the theory and modeling of turbulent premixed flames. In particular, laminar flamelet theory posits that, in cases where flame structures are thinner than the turbulence scales distorting the flame (or, equivalently, the flame time scales are shorter than turbulence time scales), the internal flame structure remains nearly constant while it moves in the flow [2,28]. Hence, in such situations, the thermochemical structure and dynamics of a 3D turbulent flame can be mapped onto the structure of an ensemble of 1D laminar flame solutions based on a small number of parameters. This idea underlies a large number of reaction rate modeling strategies, such as flamelet prolongation of intrinsic low dimensional manifolds [29], flamelet generated manifolds [30], flame surface density methods [31], and level set (e.g., G-equation) methods [32].

Our focus here is on the structure and dynamics of turbulent premixed combustion at conditions where flame structures are thicker, potentially by a considerable amount, than some of the turbulent scales of motion. This includes both the local thermochemical structure of the scalar fields and their gradients, along with the structure and dynamics of the underlying turbulence that interacts with the thermochemical scalars. We note that the aim is not to evaluate the validity of different modelling paradigms that may be applied to turbulent flames, but rather to review current understanding of the physics and chemistry in these systems.

2.3. Configurations and other practical considerations

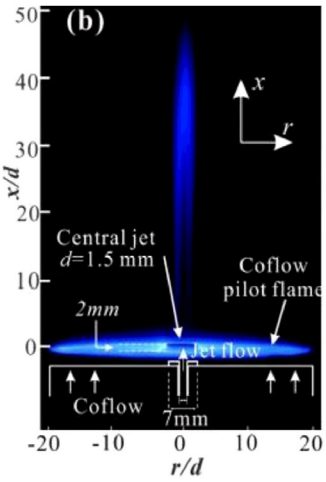
Before discussing the parameters and characteristics of highly-turbulent flames, it is helpful to briefly review some of the attributes of configurations—both experimental and computational—that are used to study them. As the focus of this paper is on the underlying structure and dynamics of flames and turbulence, we exclude from consideration configurations that contain highly turbulent flames but have been used to study other aspects of combustion. For example, we do not consider studies or configurations focused on thermoacoustic instabilities or blow-out. Detailed reviews of these topics are provided elsewhere [33–35].

Experimental configurations that have been used to investigate turbulent flame structure and dynamics include rod-stabilized bluff-body flames [36–39], swirl flames (both low-swirl and high-swirl) [40–43], jet flames [44–50], Bunsen flames [51–59], expanding flame kernels [60–63], and propagating flames in tubes [64]. With few exceptions [64], these flames have been either unconfined by mechanical boundaries (i.e., combustion chambers), or the experiments ended before the flame interacted with the walls. This lack of confinement provides optical access for laser diagnostics without the complication of windows, but adds other complications that will be discussed below.

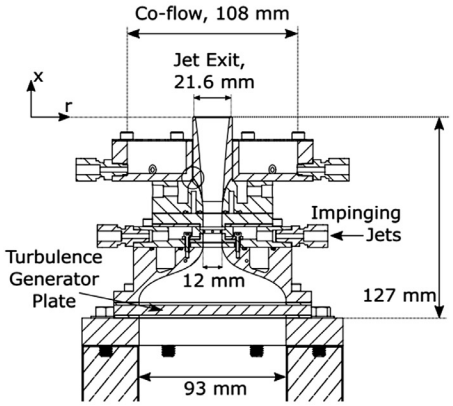
A common feature of jet and Bunsen flames[4] is that, in the absence of an open flame tip, the flame envelopes the reactants. Hence, the mass flow rate of reactants burnt by the flame is known, which allows calculation of the global consumption speed of the turbulent flame. In contrast, reactants may bypass the flame in bluff-body and swirl-flame configurations. A potential advantage of the latter flames is that they all involve a recirculation zone that helps anchor the flames, whereas jet and Bunsen flames require pilots in order to stabilize the flame base at highly turbulent conditions.

However, unconfined flames, whether piloted or not, add complications under highly turbulent conditions. To illustrate this, we consider the Lund University piloted jet (LUPJ) burner [47–50] and the Michigan Hi-Pilot Bunsen burner [56–58]. Schematics of these

[4] Both jet and Bunsen flames involve a jet of reactants issuing from a nozzle. The difference between the two is that the turbulence that interacts with the flame in the jet configuration arises due to shear between the jet fluid and surroundings, whereas the turbulence that is meant to interact with a Bunsen flame is generated upstream of the reactants exiting the nozzle.



(a) II_{Ka}



(b) II_{Da}

Fig. 4. Example piloted flame configurations. Reprinted from Refs. [47] and [56] with permission of Elsevier.

burners are shown in Fig. 4. Both burners involve central jets issuing into large co-flows containing the products of the pilot flames. The pilots are meant to both stabilize the flame and isolate the reactants from the surrounding ambient air. In order to achieve high Karlovitz numbers, the jets are often operated fuel lean, whereas the pilots are operated at richer conditions to enhance stability.

Recently, the thermochemical structures of the LUPJ and Hi-Pilot burners have been assessed through DNS and Raman scattering measurements, respectively [59,65]. At conditions where the the jet and pilot were at different equivalence ratios, rapid turbulence-induced mixing of the pilot and jet fluids drastically altered the composition of the reaction zones compared to what would occur purely from combustion of the reactants. For example, Fig. 5 shows the probability density function (PDF) of the measured atom-based equivalence ratio conditioned on fluid being in the primary reaction zone of the flame (taken to be $0.7 \leq c \leq 0.8$) [59]. The jet fluid was at $\phi = 0.65$ and the pilot was at $\phi = 0.90$. Fig. 6 shows similar PDFs of the local equivalence ratio and conditionally-averaged heat release rates at different heights above the LUPJ burner from the DNS [65]. These figures clearly demonstrate that the reaction zone composition was not that of the jet, but a mixture of jet and pilot fluid. No evidence of local extinction was found in either the DNS or experiments, demonstrating that these flames are simultaneously mixing in surrounding fluid while burning; such flames are better classified as "stratified" than premixed.

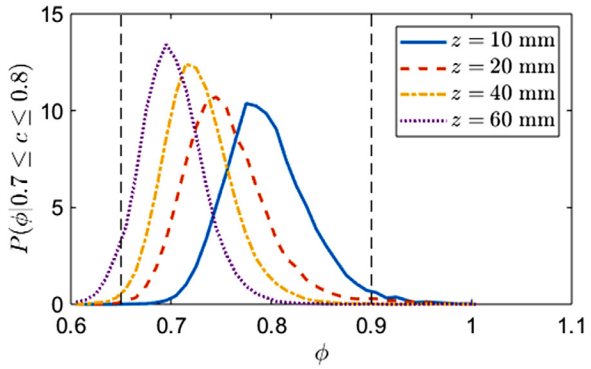


Fig. 5. PDFs of the local measured equivalence ratio in the reaction zone (taken as $0.7 \leq c \leq 0.8$) at various axial locations above the exit of the Hi-Pilot burner. The premixed reactants are at $\phi = 0.65$ and the pilot flame has $\phi = 0.90$. Reprinted from Ref. [59] with permission of Elsevier.

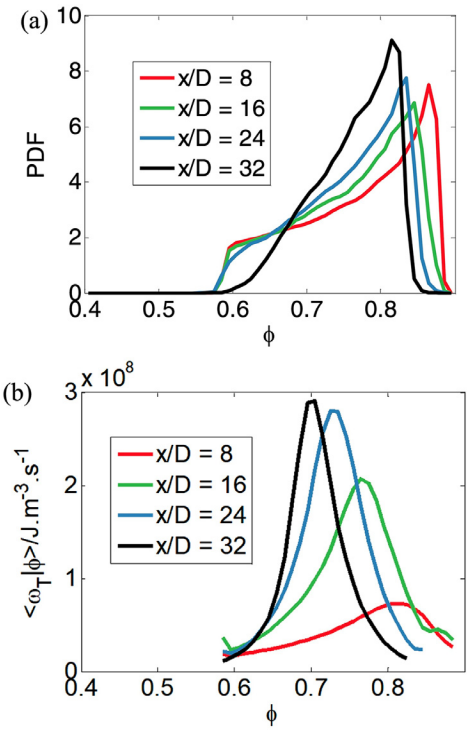


Fig. 6. (a) PDFs of the equivalence ratio and (b) heat release rate conditionally averaged on the equivalence ratio at different heights above the LUPJ burner from DNS. Reprinted from Ref. [65] with permission of Elsevier.

It is therefore apparent that configurations that do not isolate the flame of interest from the ambient environment, or that isolate it using a thermochemically mismatched pilot, present challenges for analysis. That is, the effective composition that is burning in these flames is not entirely determined by the intended reactant flow. Instead, these flames are stratified by mixing of the surrounding fluid into the flame structure.

A major implication of this observation is that the chemical scales used to characterize the flames, place them on regime diagrams, normalize the turbulent burning velocity, etc. (see Sections 2.4 and 2.5), may not actually be characteristic of the chemistry occurring in the flame. Caution therefore must be applied when interpreting such results and comparing results across configurations. It is recommended that future configurations used to study highly turbulent flames be either isolated from the ambi-

ent environment or have large co-flow pilots that are thermochemically matched to the reactants.

Contrary to the experimental configurations, the most popular computational configurations for DNS include the freely propagating planar flame (e.g., [66–71]) and expanding flame kernels (e.g., [72–76]), with the rare exception of piloted jet flames [77–79] and Bunsen flames [80]. The choice of configuration is mostly limited by the target range of dynamic scales (i.e., Re_ℓ), computational cost, complexities of boundary conditions, and robustness in numerical implementations. Direct comparisons with experiments have begun to emerge in recent years [81]. However, most DNS remain as theoretical tools to study the underlying governing physics or to extract *a priori* information for SFS modeling in LES or closure models for Reynolds averaged Navier Stokes (RANS) simulations.

With an estimated integral length-scale of approximately one-eighth the constraining dimension of the computational domain [82], the attainable integral length-scales of current DNS studies are still quite limited compared to laboratory-scale experiments; most DNS studies of highly turbulent flames have a computational domain of $\mathcal{O}(1-10\ \mathrm{mm})$. This also implies that the impact of large-scale motion, such as that seen in experimental investigations [56], is challenging to capture using DNS.

The most common remedy to create the desirable turbulence statistics in DNS include various schemes of numerical forcing or spectral nudging [66,67,83], which introduces modeling elements into DNS. Numerical forcing has also been employed to maintain statistically steady-state turbulence (i.e., to compensate the decay of turbulence due to dissipation), although subtleties require extra caution whenever flames exist [84]. In addition to forcing, another category of treatment feeds the inlet of the computational domain with auxiliary homogeneous isotropic turbulence superimposed on a mean velocity field, leveraging Taylor's hypothesis [85]. The mean velocity field is often adjusted, based on the turbulent burning rate, to maintain a statistically stationary flame in space.

Recently, DNS has progressed beyond single-step global chemical models, with more studies employing reduced or skeletal chemical kinetic models, leveraging recent developments in compact kinetic models [20–22]. Carefully calibrated chemical kinetic models can account for the response to strain and curvature, as well as differential diffusion, more realistically. Consequently, fuel-specific differential diffusion or pyrolysis effects can be studied [66,69,86]. Moreover, in the regime of highly turbulent premixed flames, the competition between elementary reactions becomes more prominent [87], which can lead to local or global limit conditions such as extinction [76]. It should be noted that DNS with global chemical kinetic models has the distinct advantage of readily enabling parametric studies, which can be particularly suitable to investigate problems involving scaling [71]. However, this review focuses mostly on studies with more detailed descriptions of chemistry, since the impact of turbulence on chemistry is of particular interest here.

2.4. Turbulent flame characterization

One goal of understanding the physics and chemistry of turbulent flames is the ability to predict *a priori* what flame structures will occur based on a few characteristic parameters, as this can inform proper model selection. Indeed, considerable research effort has been devoted to correlating characteristic dimensionless parameters with observed flame structures [8,11]. Traditionally, the focus has been on whether certain scalar fields are observed to be "broadened" relative to a laminar counterpart, the correlation of different scalars relative to laminar flames, or the correlation of scalars and scalar gradients (see Section 3 for a detailed discussion). This section reviews some of the basic principles used to characterize turbulent flames, highlights challenges with this characterization, discusses recent attempts to classify turbulent flames into regimes, and presents some suggestions for future regime classifications. Open questions from this Section (and Section 2.5) motivate the discussion of flame thermochemistry and turbulence dynamics in Sections 3 and 4.

2.4.1. Characteristic scales and dimensionless parameters

Turbulent fluid motions are characterized by a wide range of scales, from the larger integral scales (i.e., length-scale ℓ, time-scale $\mathcal{T}$, and velocity-scale u_ℓ) where kinetic energy input occurs, to the Kolmogorov microscales (i.e., length-, time-, and velocity-scales λ_K, τ_K, and u_K, respectively) where kinetic energy is dissipated into heat by viscous processes. The integral length- and time-scales for a particular quantity are defined based on the integral under the autocorrelation function for that quantity in either space or time, with $u_\ell \equiv \ell\mathcal{T}^{-1}$. Physically, these scales indicate the spatial and temporal extents required for turbulent fluctuations to become de-correlated, or de-coherent. There are different integral scales for different flow properties and spatial autocorrelation directions, as well as for different locations in the flow. However, for the purposes of characterizing turbulence/flame interactions, the integral length-scale is often represented by some large-scale geometric feature of the system, such as a nozzle diameter, shear layer width, or DNS domain size. The integral velocity-scale is often approximated as $u_\ell \approx \left(u_i' u_i'\right)^{1/2}$, where $(\cdot)'$ represents a fluctuation about an appropriately defined mean.[5]

The Kolmogorov scales are defined based on dimensional arguments in constant density turbulence as

$$\lambda_\mathrm{K} = \left(\frac{\nu^3}{\varepsilon}\right)^{1/4},\ \tau_\mathrm{K} = \left(\frac{\nu}{\varepsilon}\right)^{1/2},\ u_\mathrm{K} = (\nu\varepsilon)^{1/4} \tag{8}$$

where ν and ε are the local values of the kinematic viscosity and mean kinetic energy dissipation rate, respectively. It should be noted that the Kolmogorov scales are defined statistically. This presents challenges in turbulent flames, wherein the local temperature at a point (and hence viscosity) can fluctuate widely as the flame structure moves across the point. As such, the Kolmogorov scales computed from mean properties at a point may not be representative of the turbulence with which the flame interacts at any instant in time (see, e.g., [67,84,88]). Physically, the Kolmogorov length-scale is proportional to the scale at which the effects of viscous diffusion and turbulent straining on the evolution of the velocity field balance. When characterizing a particular experiment or simulation, turbulence is often described at a user-selected location in the reactants where $\nu = \nu_\mathrm{r}$ is a constant.

The integral and Kolmogorov length-scales are related by $\ell/\lambda_\mathrm{K} = c_\mathrm{K}\mathrm{Re}_\ell^{3/4}$ where $\mathrm{Re}_\ell = u_\ell\ell/\nu$ is the integral-scale Reynolds number and c_K, is an $\mathcal{O}(1)$ constant. Hence, for high Reynolds number turbulence (i.e., $\mathrm{Re}_\ell \ggg 1$), there is a large range of scales in the flow. In contrast, a laminar flame involves steep gradients over a relatively small range of scales, corresponding to one order of magnitude between the characteristic length-scale of rapid exothermic reactions (δ_r^0) and the overall thermal structure of the flame (i.e., $\delta_\mathrm{L}^0 = \mathcal{O}(10\delta_\mathrm{r}^0)$) in hydrocarbon/air flames.

Common practice is to construct dimensionless groups characterizing turbulence/flame interactions based on (a) the ratio of the integral velocity-scale to laminar flame speed u_ℓ/s_L^0; (b) the ratio of the integral length-scale to flame thermal thickness ℓ/δ_L^0; (c) the ratio of flame time-scale to Kolmogorov time-scale,[6] which defines

[5] We will interpret the mean as an ensemble mean taken over a large number of realizations of nominally identical simulations/experiments, even if spatial or temporal means are employed in practice.

[6] The definition of Karlovitz number based on τ_K and Damköhler number based on $\mathcal{T}$ is historical. One could equally define $\mathrm{Da}_{\mathrm{K},\delta} = \mathrm{Ka}_{\delta,\mathrm{K}}{}^{-1}$ and $\mathrm{Ka}_{\delta,\ell} = \mathrm{Da}_{\ell,\delta}{}^{-1}$.

a Karlovitz number $\mathrm{Ka}_{\delta,\mathrm{K}} = \tau_\delta/\tau_\mathrm{K}$; and (d) the ratio of the integral time-scale to flame time-scale, which defines a Damköhler number $\mathrm{Da}_{\ell,\delta} = \mathcal{T}/\tau_\delta$. Based on dimensional arguments, $s_\mathrm{L}^0 = c_\mathrm{s}\bar{\alpha}/\delta_\mathrm{L}^0$, where c_s is a scaling factor and $\bar{\alpha}$ is an appropriate thermal diffusivity. Hence, the resulting dimensionless groups can be written as

$$\mathrm{Ka}_{\delta,\mathrm{K}} = \left(\frac{\delta_\mathrm{L}^0}{\lambda_\mathrm{K}}\right)^2 \frac{\nu_\mathrm{r}}{\bar{\alpha}c_\mathrm{s}}, \tag{9}$$

$$\mathrm{Da}_{\ell,\delta} = \left(\frac{\ell}{\delta_\mathrm{L}^0}\right)^2 \frac{\bar{\alpha}c_\mathrm{s}}{\nu_\mathrm{r}}\mathrm{Re}_\ell^{-1}, \tag{10}$$

$$\mathrm{Re}_\ell = c_\mathrm{K}^{-4}\mathrm{Ka}_{\delta,\mathrm{K}}{}^2\mathrm{Da}_{\ell,\delta}{}^2. \tag{11}$$

We note that $\bar{\alpha}$ can be manually selected for a given flame such that $c_\mathrm{s} = 1$ [58,89]. Peters [89] recommends that it should correspond to the diffusivity in the "inner reaction layer" for atmospheric methane/air flames, at a temperature between 1600-2000 K. Alternatively, one may define $\bar{\alpha}$ at the mean temperature between the reactants and products, at the peak of the heat release rate, or at some other point. We therefore choose to explicitly leave c_s as a variable in these equations.

As is common practice, we have chosen to characterize the turbulence in the reactants. Hence, Re_ℓ is measured based on u_ℓ, ℓ, and $\nu = \nu_\mathrm{r}$ in the unburnt reactants. The group $\nu_\mathrm{r}(\bar{\alpha}c_\mathrm{s})^{-1} = \nu_\mathrm{r}\left(s_\mathrm{L}^0\delta_\mathrm{L}^0\right)^{-1}$ is often taken to be unity. That is, the kinematic viscosity in the reactants is taken to be equal to the characteristic thermal diffusivity, which may be determined at the peak of the heat release rate. However, laminar flame calculations indicate that $\nu_\mathrm{r}\left(s_\mathrm{L}^0\delta_\mathrm{L}^0\right)^{-1}$ is between 0.1 and 0.2 for hydrocarbon/air flames.

Furthermore, c_K is often taken to be unity, whereas many measurements show that $c_\mathrm{K} \approx 0.5$ and, hence, $c_\mathrm{K}^{-4} \approx 16$ [90–93]. Nevertheless, Karlovitz and Damköhler numbers based on Eqs. (9) and (10) are often reported with unity factors. Moreover, due to the difficulty in measuring λ_K, experiments may use Eq. (11) to estimate the Karlovitz number, again with a unity factor. While we do not advocate that $c_\mathrm{K} \approx 0.5$ is a fundamental result that should be used universally moving forward, the resultant order-of-magnitude ambiguity mandates that caution be taken where comparing turbulence conditions across different studies and that the method of computing $\mathrm{Ka}_{\delta,\mathrm{K}}$ be clearly reported. Recommendations on the latter are provided below.

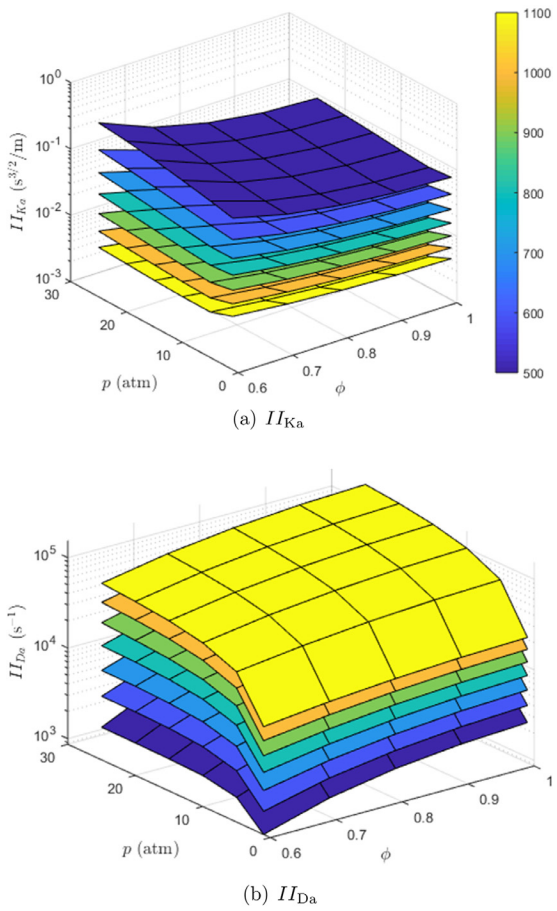
It is useful to describe how the Karlovitz and Damköhler numbers vary with the physical operating parameters of a combustor. To this end, these dimensionless groups can be re-written as

$$\mathrm{Ka}_{\delta,\mathrm{K}} = c_\mathrm{K}^2 \overbrace{\left(\frac{u_\ell^{3/2}}{\ell^{1/2}}\right)}^{I_\mathrm{Ka}} \overbrace{\left(\frac{\delta_\mathrm{L}^0}{s_\mathrm{L}^0}\frac{1}{\nu_\mathrm{r}^{1/2}}\right)}^{II_\mathrm{Ka}}, \tag{12}$$

$$\mathrm{Da}_{\ell,\delta} = \underbrace{\left(\frac{\ell}{u_\ell}\right)}_{I_\mathrm{Da}} \underbrace{\left(\frac{s_\mathrm{L}^0}{\delta_\mathrm{L}^0}\right)}_{II_\mathrm{Da}}. \tag{13}$$

The I-quantities represent terms that depend on the flow conditions and geometry (e.g., the bulk velocity, turbulence generation, and scale) of the system. These terms can be varied independently of the II-quantities, which depend on the thermodynamic state and chemical composition (e.g., the reactant pressure, temperature, and composition) in a complex manner.

Fig. 7 shows how II_Ka and II_Da vary with pressure, reactant temperature, and equivalence ratio for n-dodecane/air flames. High Karlovitz numbers are associated with lower reactant temperatures, lower equivalence ratios, and higher pressure, with the largest sensitivity to preheat temperature. Unsurprisingly given the definitions of II_Ka and II_Da, high Damköhler numbers follow a generally opposite trend, being associated with higher temperatures and higher equivalence ratios. However, II_Da also increases with pressure due to the lack of dependence on kinematic viscosity, as compared to II_Ka.



(a) II_Ka

(b) II_Da

Fig. 7. Variation of II_Ka and II_Da from Eqs. (12) and (13), respectively, with pressure, equivalence ratio, and preheat temperature (indicated by different colors, with the colorbar in (a) giving T in units of K) in unstretched laminar n-dodecane/air flames.

This analysis demonstrates a natural mitigation of extremely high Karlovitz numbers and low Damköhler numbers in terrestrial systems of engineering relevance. That is, adiabatic compression is associated with simultaneous increases in both pressure and temperature. Fig. 8 shows how II_Ka and II_Da vary with isentropic compression up to 25 atm for a fixed equivalence ratio n-dodecane/air flame. The Karlovitz and Damköhler number responses are dominated by the temperature dependence, decreasing and increasing, respectively, as the temperature and pressure increase.

It should be noted that, under the assumption that $\nu_\mathrm{r} \approx s_\mathrm{L}^0\delta_\mathrm{L}^0$, knowledge of any two of the aforementioned dimensionless parameters (i.e., u_ℓ/s_L^0, ℓ/δ_L^0, $\mathrm{Ka}_{\delta,\mathrm{K}}$, $\mathrm{Da}_{\ell,\delta}$, or Re_ℓ) uniquely defines all other parameters. Furthermore, under this condition and with $c_\mathrm{K} = 1$, Eq. (12) can be written in the popular form

$$\mathrm{Ka}_{\delta,\mathrm{K}} = \left(\frac{u_\ell}{s_\mathrm{L}^0}\right)^{3/2}\left(\frac{\delta_\mathrm{L}^0}{\ell}\right)^{1/2}. \tag{14}$$

It is interesting to note that Eqs. (12) and (14) differ by a factor of $c_\mathrm{K}^2(s_\mathrm{L}^0\delta_\mathrm{L}^0/\nu_\mathrm{r})^{1/2}$, which has an $\mathcal{O}(1)$ value. Hence, through a convenient cancellation of factors, Karlovitz numbers calculated by these two equations will be approximately equal. However, this may differ by a factor of $\mathcal{O}(10)$ compared to calculations based on Eq. (9), depending on how λ_K is calculated and whether $\nu_\mathrm{r}/(\bar{\alpha}c_\mathrm{s})$ is taken

Table 1
Properties used for calculation of engine conditions. All calculations used n-dodecane fuel and 10 mm $\leq \ell \leq$ 20 mm. All parameters are based on approximate typical operation, e.g. portions of the inflow condition range specified in Ref. [102].

	p (bar)	T_r (K)	ϕ	u_ℓ (m/s)
Gas turbine combustor	$10 \leq p \leq 20$	$500 \leq T_r \leq 700$	$0.7 \leq \phi \leq 0.8$	$5 \leq u_\ell \leq 15$
Afterburner	$2 \leq p \leq 4$	$900 \leq T_r \leq 1100$	$0.7 \leq \phi \leq 0.8$	$10 \leq u_\ell \leq 40$
Ramjet	$1 \leq p \leq 5$	$500 \leq T_r \leq 900$	0.7	$20 \leq u_\ell \leq 60$

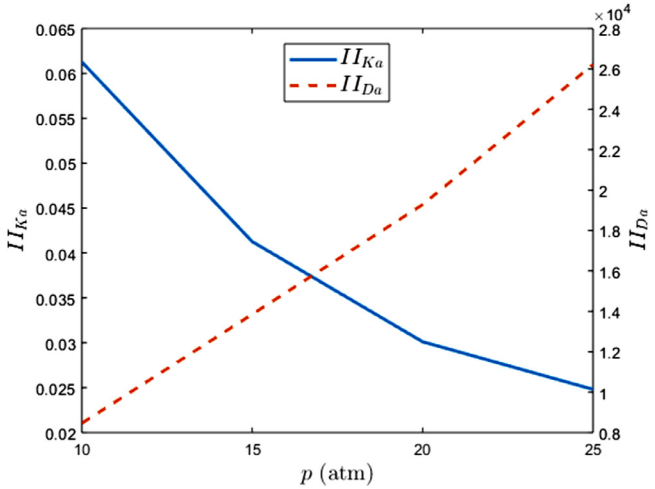


Fig. 8. Variation of II_{Ka} and II_{Da} during isentropic compression for an n-dodecane/air flame at $\phi = 0.8$.

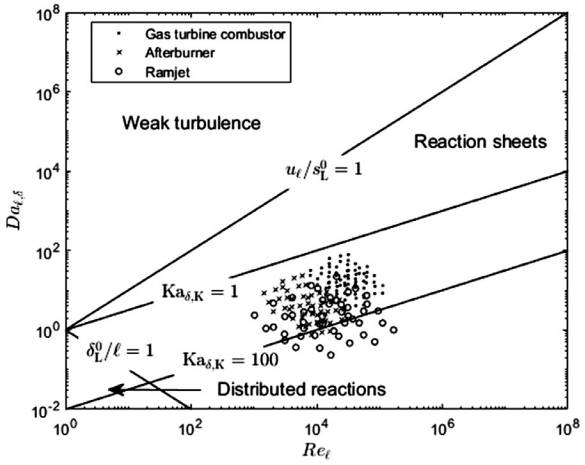
to be unity. *For consistency, it is thus recommended that Eq. (14) be used when reporting Karlovitz numbers.*

Finally, we note that turbulent flames are generally characterized at a single point, often in the unburnt reactants at the exit of a nozzle or inlet of a DNS domain. However, practical flames exhibit widely varying turbulence properties with position. Furthermore, local flame structures may not correlate directly with local turbulence due to the finite interaction time and advection parallel to the flame surface [78,79,94]. These issues are discussed more in Section 2.4.2.

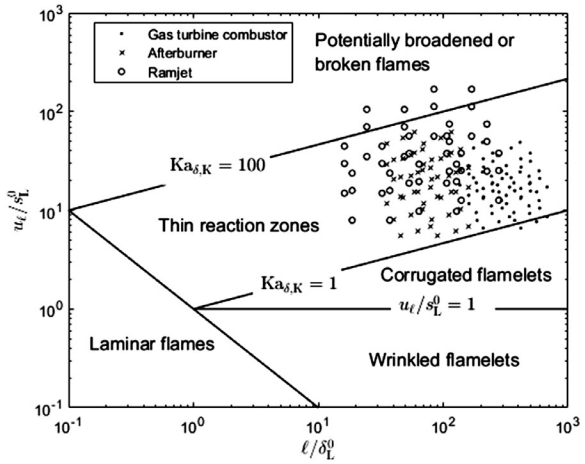
2.4.2. Expected parameters for highly turbulent flames

Theoretical expectations regarding the parameter space at which different flame structures occur are graphically expressed using regime diagrams. The two most popular regime diagrams are those proposed by Williams [95] and by Borghi [96], which was later modified by Peters [2]; for compactness, we will refer to the former as the "Williams" diagram and the latter as the "Borghi/Peters" diagram. The former uses Re_ℓ and $\mathrm{Da}_{\ell,\delta}$ as abscissa and ordinate measures, respectively. The latter uses ℓ/δ_L^0 and u_ℓ/s_L^0. As mentioned above, in the case of premixed combustion and assuming $c_K = \nu_r(\overline{\alpha} c_s)^{-1} = 1$, any two dimensionless groups establish the other groups; the two diagrams are conceptually equivalent in this case, though different regime labels are traditionally used[7].

The regime diagrams are shown in Fig. 9, with some significant lines and regime labels indicated. The points shown in Fig. 9 correspond to typical operating conditions of gas turbine main combustors, gas turbine afterburners, and ramjet engines, which are summarized in Table 1 and described in more detail below. Note that the Borghi/Peters diagram typically includes lines at constant values of $\mathrm{Ka}_{\delta,K}$, whereas the Williams diagram shows lines at



(a) Regime diagram of Williams [46]



(b) Regime diagram of Borghi [43] and Peters [2]

Fig. 9. Regime diagrams with estimated conditions for various engines.

constant λ_K/δ_L^0. However, under the assumptions above, $\mathrm{Ka}_{\delta,K} = \left(\lambda_K/\delta_L^0\right)^2$ (see Eq. (9)) and lines are labeled as constant $\mathrm{Ka}_{\delta,K}$ on both diagrams.

The line $\mathrm{Ka}_{\delta,K} = 1$ is known as the Klimov-Williams (K-W) condition [95,97,98], which represents $\lambda_K = \delta_L^0$ and $u_K = s_L^0$. Hence, at lower Karlovitz numbers, the Kolmogorov scale in the reactants is larger than the thermal thickness of the flame and the magnitude of the associated velocity fluctuations is smaller than the laminar flame speed. The flame is expected to retain the internal structure of a laminar flame, corresponding to thin "reaction sheets" or "flamelets", which is supported by numerous studies [8].

The main focus of this review is on turbulence intensities well above the K-W criterion, i.e. $\mathrm{Ka}_{\delta,K} \gg 1$, where the internal flame structure and turbulence mutually interact in complicated ways. Indeed, the parameter space beyond the K-W criterion is described

[7] The Williams diagram also describes non-premixed combustion.

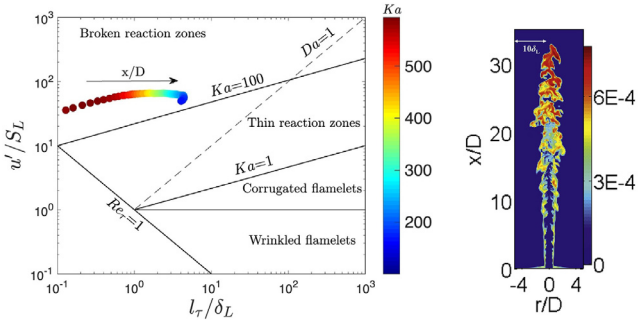
differently in the different regime diagrams. In the Borghi/Peters diagram, an additional line is drawn at $\mathrm{Ka}_{\delta,\mathrm{K}} = 100$, corresponding to $\lambda_\mathrm{K} = 0.1\delta_\mathrm{L}^0$; in methane/air flames this gives $\lambda_\mathrm{K} \approx \delta_\mathrm{r}^0$. That is, the Kolmogorov length-scale (in the reactants) is smaller than 1/10th the laminar flame thermal thickness, which is the approximate thickness of the exothermic reaction layer in laminar methane/air flames. Correspondingly, the Kolmogorov time-scale (in the reactants) becomes shorter than the characteristic reaction time-scale. This boundary has been proposed as the lower limit at which turbulence would modify the "reaction zone" structure of a methane/air flame. The region $1 \lesssim \mathrm{Ka}_{\delta,\mathrm{K}} \lesssim 100$ is proposed to have flames exhibiting broadening of the "preheat zone", but not the "reaction zone". Note that this boundary does not account for any affect of the flame on the turbulence (Section 4)

Williams [28] does not specify a label for the parameter space immediately beyond $\mathrm{Ka}_{\delta,K} > 1$, but does propose a regime of "distributed reactions" or "stirred reactors" at $\ell/\delta_\mathrm{L}^0 < 1$, corresponding to Damköhler's second hypothesis regarding small-scale turbulence [99]. We note that the intervening parameter space is sometimes labelled "flamelets in eddies", following a modification to the Williams diagram by Turns [100]. Furthermore, Williams [101] adds additional lines and labels corresponding to the "thin reaction zone" and "broken flamelet" regimes in the Borghi/Peters diagram.

Section 2.4.3 discusses limitations of—and recent proposed modifications to—regime diagrams and regime boundaries. Nevertheless, regardless of these limitations, it is instructive to demonstrate where some typical combustion systems—in which "highly turbulent" flames may be expected—operate in terms of the regime diagram. Hence, for illustrative purposes, we consider a gas turbine combustor, afterburner, and ramjet. In every case, the fuel is represented as n-dodecane. While other fuels could be considered (e.g., more realistic jet fuels, methane, hydrogen, etc.), we do not expect a qualitative change in the parameter space encompassed on the regime diagrams.[8] In the gas turbine combustor and ramjet, the fuel is mixed with fresh air; in the afterburner, fuel is mixed with appropriately diluted combustion products. Even though these devices would be partially premixed in reality, we represent them as perfectly premixed. We take 10 mm $\leq \ell \leq$ 20 mm to represent a characteristic integral scale in each device. The other properties used in these calculations are provided in Table 1 and are based on typical approximate operating parameters, e.g., Ref. [102].The specific operating points shown in Fig. 9 are taken from a uniform sampling of conditions over the range shown in the table. While other parameters could be selected, they are not expected to make qualitative changes to the results. We note that there is a minor discrepancy between the location of the engine points relative to the constant $\mathrm{Ka}_{\delta,\mathrm{K}}$ lines in Fig. 9(a) versus Fig. 9(b). This arises because Re_ℓ is calculated using ν_r, whereas the constant $\mathrm{Ka}_{\delta,\mathrm{K}}$ lines are calculated assuming that ν_r is equal to both the molecular and thermal diffusivity.

The majority of the conditions lie between $1 \leq \mathrm{Ka}_{\delta,\mathrm{K}} \leq 100$. No conditions approach the range $\mathrm{Ka}_{\delta,\mathrm{K}} > 1000$. All configurations have $\ell \gg \delta_\mathrm{L}^0$ and, therefore, do not approach the distributed reaction regime predicted by Williams. Such conditions would require very broad flames (e.g., low pressures or highly diluted preheated reactants) and/or small integral scales. Combustion of highly diluted premixed reactants is associated with moderate or intense low-oxygen dilution (MILD), flameless, or colorless combustion systems, which are reviewed elsewhere [103,104]. The focus here is largely on combustion in the parameter space around the points shown in Fig. 9, though we also include some studies at higher

[8] Hydrogen may shift the parameter space to lower Karlovitz numbers for the flows specified here, but may also accommodate higher flow speeds.



(a) Variation of local conditions with downstream position.

(b) Typical instantaneous CH_2O field.

Fig. 10. Results from DNS of a highly turbulent jet flame showing an inverse relationship between the local conditions and physical appearance of the flame. Reprinted from Refs. [94] and [79] with permission of Elsevier.

$\mathrm{Ka}_{\delta,\mathrm{K}}$ and lower ℓ/δ_L^0, which may be of interest to devices not considered in Fig 9.

2.4.3. Comments on regimes

Despite the placement of the various points on the regime diagrams, it is not clear that the parameters employed or the lines drawn are sufficient to fully characterize the mutual interactions between turbulence and flames for several reasons. This section discusses these issues and recent results, and provides some recommendations on the use of regimes and regime diagrams.

To begin, a comment is warranted regarding lines based on $\mathrm{Ka}_{\delta,\mathrm{K}}$ or λ_K. The Kolomogrov length-scale is obtained purely from dimensional arguments. However, measurements and simulations in constant density turbulent flows have shown that the actual observed smallest scales (denoted λ_ν due to their connection to the kinematic viscosity ν) are proportional to λ_K, but several times larger (values in the range of $\lambda_\nu \approx 5\lambda_\mathrm{K}$ are often reported) [90–93]. Such a difference would significantly impact the parameter space at which different regimes/behaviors are expected. For example, if the K-W condition is modified to be $\lambda_\nu \leq \delta_\mathrm{L}^0$ with $\lambda_\nu \approx 5\lambda_\mathrm{K}$, this would indicate that modification of the flame structure could be expected around $\mathrm{Ka}_{\delta,\mathrm{K}} \approx 25$. Furthermore, if $c_\mathrm{K} = 0.5$, this would be $\mathrm{Ka}_{\delta,\mathrm{K}} \approx 50$. If $\nu_\mathrm{r}\left(s_\mathrm{L}^0\delta_\mathrm{L}^0\right)^{-1} \approx 0.2$, this would instead correspond to $\mathrm{Ka}_{\delta,\mathrm{K}} \approx 5$ or 10. Similar to the K-W criterion, it can be argued that the effects of small scale turbulence on the reaction zone structure should occur at considerably higher Karlovitz numbers than $\mathrm{Ka}_{\delta,\mathrm{K}} = 100$ because $\lambda_\nu > \lambda_\mathrm{K}$. The purpose of this discussion is not to propose moving the K-W line to $\mathrm{Ka}_{\delta,\mathrm{K}} = 5$, 25, or some other number, but simply to highlight a potential order-of-magnitude disagreement between the physical reasoning behind some regime boundaries and the practical realization of the effects in experiments and simulations. One, therefore, should not be surprised when experimental or DNS results do not show transitions between regimes at the conditions predicted by the theoretical arguments underlying regime diagrams (or even within an order of magnitude).

In addition to this ambiguity, it is not clear that turbulence characterized at a single point (typically in the reactants) is sufficient to predict a combustion regime, for several reasons. Practical combustion devices exhibit considerable variation in both turbulence conditions and flame structures. For example, Fig. 10(a), shows how u_ℓ/s_L^0, ℓ/δ_L^0, and $\mathrm{Ka}_{\delta,\mathrm{K}}$ vary with downstream distance (x/D) in DNS of a highly turbulent jet flame in the LUPJ configuration [78,79,94]. The local values of $\mathrm{Ka}_{\delta,\mathrm{K}}$ decrease with downstream distance, which would indicate a decreased effect of small-

scale turbulence. However, the visual appearance of the scalar fields (see Fig. 10(b)) indicates the opposite, with increased corrugation and broadening of the CH_2O contours with downstream distance. The scalar fields observed in the DNS are consistent with experiments of the same configuration [47,48]. Hence, using a single value of dimensionless parameters to characterize a practical turbulent flame is insufficient and the local flame structure may not reflect the local characteristics of the turbulent flow.

It is worth noting that the apparent broadening of the CH_2O regions at downstream locations in Fig. 10(b) involves both the effects of local turbulence and the advection of turbulence-influenced CH_2O from further upstream (which has also been affected by the turbulence). Since the jet flow speed in these flames is much higher than the laminar flame speed, the turbulence and flame simultaneously advect a considerable distance downstream before turbulence in the reactants passes into the products. Near the flame base, the turbulence and flame have not interacted for long and the flame retains a laminar-like structure; towards the flame tip, the flame has "consumed" more turbulence. Hence, the flame structure observed at higher axial locations may be more consistent with the expected consequence (i.e., flame structure) arising from the turbulence/flame interactions than near the flame base. This is somewhat analogous to the temporal evolution of a laminar flame initial condition to the fully turbulent state during DNS of planar flames, which requires a certain number of flow-through times to establish the statistically steady flame structure.

Moreover, the traditional turbulence characterization does not account for the influence of the flame on the turbulence or the detailed distribution of kinetic energy amongst scales in turbulence (see Section 4 for a detailed discussion). Several researchers have introduced new parameters or modifications to regime diagrams to account for these effects. For example, Lapointe et al. [67] propose to use a "reaction zone" Karlovitz number—based on the Kolmogorov scale in the reaction zone and 1–2 orders of magnitude lower than $\mathrm{Ka}_{\delta,\mathrm{K}}$ due to the increased viscosity—to characterize whether turbulence will disrupt the inner flame structure. Aspden et al. [105] argue that, at sufficiently high Karlovitz numbers ($\mathrm{Ka}_{\delta,\mathrm{K}} \gg 100$), λ_K scale structures are too small compared to the thermochemical gradients to enhance mixing. Instead, a metric is proposed that is similar to a Karlovitz number, but uses the turbulence time-scale at δ_L^0.

Recent evidence, reviewed by Driscoll et al. [11], also has brought into question the conventional regime diagrams and boundaries. In particular, they indicate that experiments and DNS at $\mathrm{Ka}_{\delta,\mathrm{K}} \geq 1$ may or may not exhibit preheat zone broadening, depending on Re_ℓ. This is demonstrated in Fig. 11 from Skiba et al. [58], which shows that $\mathrm{Ka}_{\delta,\mathrm{K}} \geq 1$ is necessary but not sufficient for broadening of the preheat zone to occur. In the experimental data, the division between broadened preheat zones/thin reaction zones (BP-TR) and thin flamelets requires an effective "turbulent diffusivity" ($\mathcal{D}_\mathrm{T}$) of 180 times the characteristic molecular diffusivity ($\mathcal{D}^*$). Based on scaling arguments, Driscoll et al. [11] proposed that this corresponds to a boundary of $\mathrm{Re}_\ell \gtrsim 2800$ and that this value was necessary to observe preheat layer broadening (this value assumes unity scaling factors in all relationships). However, the DNS studies in Fig. 11 indicate broadened preheat zones for lower $\mathcal{D}_\mathrm{T}/\mathcal{D}^*$, but only at $\mathrm{Ka}_{\delta,\mathrm{K}} \gtrsim 60$. We note that "turbulent diffusivity" is a modeling concept that is meant to statistically reflect the increased molecular mixing rate generated by turbulence; it is not a physical process affecting the instantaneous dynamics of velocity or scalar according to Eqs. (1)–(4).

Broadened reactions are observed for DNS and some experiments, although other experiments do not observe broadened reactions at similar Karlovitz numbers. In particular, broadened reactions in Fig. 11 (black and blue stars) occur at smaller ℓ/δ_L^0 than the experimental BP-TR points at similar Karlovitz numbers (filled red squares). The majority of the black stars were obtained in the LUPJ burner with $\ell/\delta_\mathrm{L}^0 \lesssim 10$ [47], whereas the red dots were obtained in the Michigan Hi-Pilot burner with $\ell/\delta_\mathrm{L}^0 \gtrsim 10$ [58]. Indeed, broadened reactions occur for $\mathrm{Da}_{\ell,\delta} \lesssim 1$ and BP-TR occur for $\mathrm{Da}_{\ell,\delta} \gtrsim 1$, at least to $\mathrm{Ka}_{\delta,\mathrm{K}} \approx 550$ in the Hi-Pilot burner. We note that the DNS and experimental cases with broadened reactions were omitted from the regime diagram in Driscoll et al. [11], although the other data in Ref. [11] is identical to that of Skiba et al. [58].

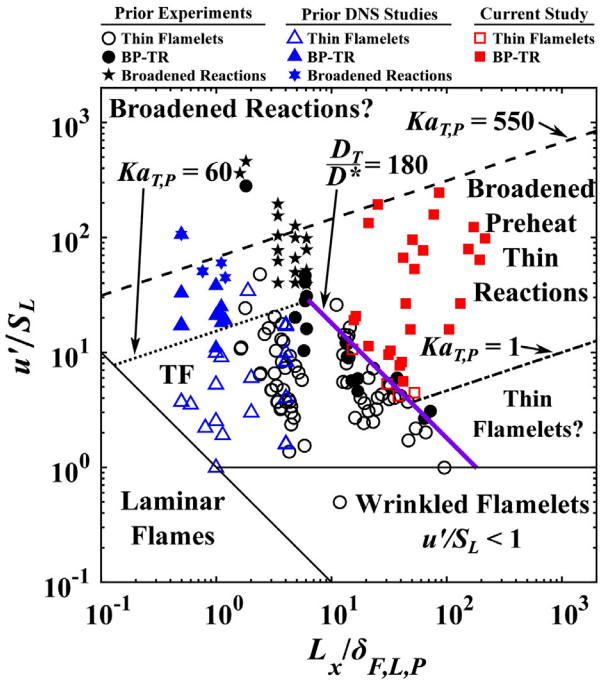


Fig. 11. Regime diagram compiled by Skiba et al. [58]. 'BP-TR' indicates that broadened preheat zones and thin reactions were observed. Reprinted from Ref. [58] with permission of Elsevier.

As a final comment, the terms "broadened preheat", "thin reaction", "broadened reaction", etc. in the Borghi/Peters diagram are somewhat limiting. These terms apply most readily to flames that posses a relatively broad and inert preheat zone, followed by a thin reaction zone. Fig. 2 demonstrates that this structure is most relevant to flames for relatively simple hydrocarbon fuels (e.g., CH_4); hydrogen flames possess an exothermic structure throughout, whereas large hydrocarbon flames possess an endothermic fuel pyrolysis zone coincident with the "preheat" zone. The Williams diagram avoids these issues by not prescribing labels to the parameter space between flame sheets and broadened reactions.

More broadly applicable labels could be applied to the various regions of the regime diagrams. As mentioned above and discussed in more detail in Sections 3 and 4, a laminar-like flame structure implies a correlation between different scalar values and between values of a scalar and its gradient. The boundary $\mathrm{Ka}_{\delta,\mathrm{K}} \gtrsim 1$ may more generally be conceived as the conditions at which turbulence in the reactants has scales that can disrupt the correlation of scalars that are distributed over lengths similar to $\mathcal{O}(\delta_\mathrm{L}^0)$, whether or not reactions are occurring. Similarly, $\mathrm{Ka}_{\delta,\mathrm{K}} \gtrsim 100$ may more accurately be considered the condition at which turbulence in the reactants has scales that could disrupt the correlation of scalars that are distributed over lengths similar to $\mathcal{O}(0.1\delta_\mathrm{L}^0)$.

In total, the observations described above highlight some of the limitations of regime diagrams, namely: (a) the scale-based arguments used to prescribe regime boundaries may have order-of-magnitude quantitative differences with the physical scales present

in turbulent flames; (b) they do not account for spatial inhomogeneity and the advection of flame structures; (c) they do not account for the influence of the flame on the turbulence; (d) regime labels that distinguish between preheat and reaction zones are restrictive in terms of fuels; and (e) additional length/velocity/time scales may be needed to predict regimes. Despite these limitations, regime diagrams provide a useful conceptual/academic aid for understanding and articulating the general influences of turbulence on flames as a function of conditions (it can be argued that this was their original intent). They can also provide conservative *a priori* guidance on appropriate/efficient modelling paradigms for closing reaction source terms for a given configuration/condition, although recent developments on adaptive modeling provide an alternative path (e.g., Ref. [106]). However, the utility of comparing the detailed regime transitions between different configurations is limited.

2.5. Turbulent flame speed

We close this introductory section with a brief review of the current understanding of the turbulent flame speed in highly turbulent flames. The turbulent flame speed is a convenient overall metric of a flame that captures the net effects of the complicated turbulence/flame interactions. Comparisons of turbulent flame speeds to theoretical expectations—e.g., based on a collection of thin propagating flame surfaces—can be used to assess theories and help identify open questions. Models for the turbulent flame speed can also be used to close the reaction rate source term, as reviewed by Lipatnikov and Chomiak [6].

Driscoll [8] presents a review of the turbulent flame speed, its definitions, ambiguities in these definitions, and measurements/simulations in the flamelet regime. Of particular relevance here is the global consumption speed

$$s_{T,GC} \equiv \frac{\bar{\dot{m}}_r}{\rho_r A_{\tilde{c}=0.5}}, \tag{15}$$

where $\bar{\dot{m}}_r$ is the mean mass flow rate of reactants consumed by the flame and $A_{\tilde{c}=0.5}$ is the area of the surface corresponding to a mean reaction progress variable of $\tilde{c} = 0.5$. This surface roughly represents the midpoint of the flame brush. Experimentally, envelope flames (e.g., jet and Bunsen flames) without local extinction allow direct calculation of $s_{T,GC}$ because $\bar{\dot{m}}_r$ and ρ_r are known, and $A_{\tilde{c}=0.5}$ can be reasonably measured. In DNS, $s_{T,GC}$ can be calculated directly from the simulated reaction rates and/or from reactant mass flow rates.

Under the assumption that a turbulent premixed flame consists of a collection of thin 1D propagating flame structures that are similar to stretched laminar deflagrations, we obtain

$$\bar{\dot{m}}_r = \rho_r s_{T,GC} A_{\tilde{c}=0.5} = \rho_r \bar{I}_0 s_L^0 \bar{A}_T, \tag{16}$$

where $\bar{A}_T$ is the mean area of a selected c isosurface and $\bar{I}_0$ is an $\mathcal{O}(1)$ factor that accounts for the effects of stretch of the flame speed. Hence,

$$\frac{s_{T,GC}}{s_L^0} = I_0 \frac{\bar{A}_T}{A_{\tilde{c}=0.5}}, \tag{17}$$

where we have taken $A_{\tilde{c}=0.5}$ to characterize the area of an "equivalent" laminar flame (i.e., one with the same area as the mean flame brush, which would be exactly true for statistically 1D flames).

It is common practice to plot $s_{T,GC}$ versus u_ℓ, both normalized by s_L^0. However, as discussed above, caution must be applied when considering the laminar flame properties attributed to highly turbulent combustion experiments due to the tendency to mix surrounding fluid into the reaction zone [59,65]. Unless this ambient fluid is thermo-chemically matched to the products of the reactants, the laminar flame speed of the reactants may not properly characterize the flame.

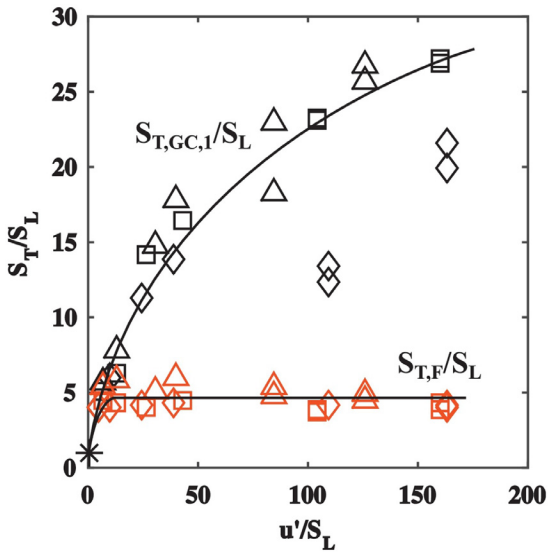


Fig. 12. Experimentally measured turbulent flame speed versus turbulence intensity. $S_{T,F}/S_L$ is equivalent to $\bar{A}_T/A_{\tilde{c}=0.5}$ in our notation. Reprinted from Ref. [56] with permission of Elsevier.

The data of Wabel et al. [56] were acquired in the Hi-Pilot Bunsen flame across a range of turbulence conditions (up to $u_\ell/s_L^0 \approx 150$), all with equal jet and pilot equivalence ratios of $\phi = 0.75$. Fig. 12 summarizes their findings, which also includes the results of Yuen and Gülder [52] for $u_\ell/s_L^0 \lesssim 25$. The mean progress variable field was estimated by binarizing instantaneous OH planar laser-induced fluorescence (PLIF) images and then taking the average. The turbulent flame surface area was estimated from the instantaneous PLIF images.

Values of $s_{T,GC}/s_L^0 > 25$ were observed. These increased continuously, but at a decreasing rate with increasing u_ℓ. The maximum in $s_{T,GC}$ from previous studies at lower turbulence intensities was not observed [107], which is attributed to the large co-flow of hot pilot fluid that prevented local flame extinction. In contrast to the continuously increasing $s_{T,GC}$, measured values of $\bar{A}_T/A_{\tilde{c}=0.5}$ (denoted $S_{T,F}/S_L$ in Fig. 12) increased for low u_ℓ but plateaued at $\bar{A}_T/A_{\tilde{c}=0.5} \approx 5$.

We note that comparing the measured $\bar{A}_T/A_{\tilde{c}=0.5}$ with $s_{T,GC}/s_L^0$ via Eq. (17) requires consideration of the stretch factor I_0. However, the $\phi = 0.75$ methane/air flame studied has a near-zero Markstein length, resulting in $I_0 \approx 1$ and indicating that the laminar flame speed should decrease slightly with increasing stretch rate due to turbulence [108]. Hence, flame stretch would increase the discrepancy between the measured turbulent flame speed and the consumption rate expected from the flame area and stretched laminar flame speed.

Imaging of CH_2O and OH using PLIF in these flames demonstrated broadened regions of CH_2O, but topologically thin and connected regions of exothermic reactions (identified from the overlap of CH_2O and OH). There was thus no evidence of broken or broadened reaction zones. Hence, these experiments provide evidence of increased reaction rates while maintaining a reaction zone spatial structure that qualitatively remains similar to that of a laminar flame. This is consistent with the observations of Osborne et al. [55], who experimentally showed increased local flame speeds in regions of thickened preheat zones and thin reaction zones.

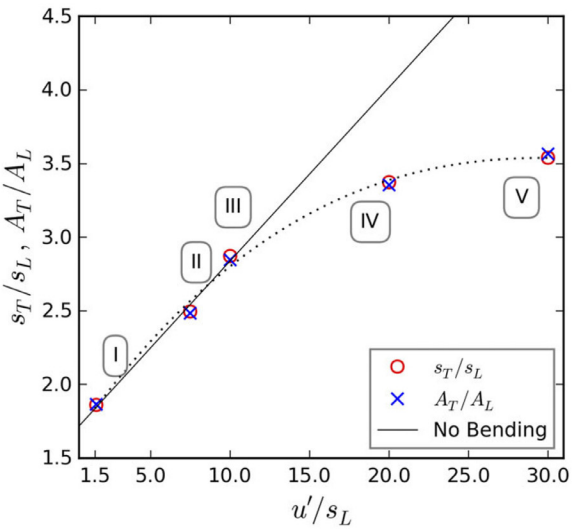
Other experimental evidence supports this general conclusion. For example, Wang et al. [50] reported $s_{T,GC}/s_L^0$ measurements in the LUPJ jet burner. If the area of the turbulent flame was calculated using the area of the CH_2O surface, their data corresponded very well with that of Wabel et al. [56]. However, the flames used in this study had mismatched pilot and jet equivalence ratios. There consequently may be some ambiguity in the proper s_L^0 normalization factor.

Another study by Sosa et al. [64] presented turbulent flame speeds in a planar flame propagating into a heated flow at a sufficient velocity for fluid compressibility to have an influence. Since the flame was stationary in the laboratory frame, the turbulent flame speed was determined directly from the velocity of the oncoming reactants. They reported $s_{T,GC}/s_L^0$ values above 60. While flame surface areas were not measured, it is expected that $\tilde{A}_T/A_{\tilde{c}=0.5}$ is considerably less than $s_{T,GC}/s_L^0$.

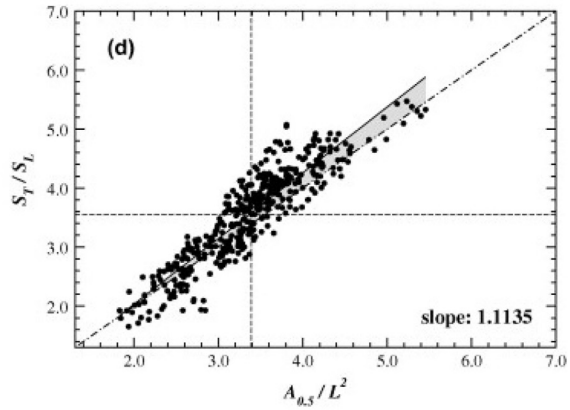
In contrast to the experiments, most DNS of flames in boxes of homogeneous isotropic turbulence find much lower $s_{T,GC}/s_L^0$ values than experiments at similar u_ℓ/s_L^0. Furthermore, the DNS studies often find that $s_{T,GC}/s_L^0$ is very similar to $\tilde{A}_T/A_{\tilde{c}=0.5}$ [71,109]. Typical results are shown in Fig. 13. It should be noted that the studies shown in Fig. 13 utilized single-step chemistry, which may be insufficient to describe the effects of stretch on the flame speed. Nevertheless, the simulations of Nivarti and Cant [71] utilized a $\phi = 1.0$ methane/air flame that should be relatively insensitive to stretch.

Regarding the higher values of $s_{T,GC}/s_L^0$ for a given $\tilde{A}_T/A_L$ measured in experiments, one potential explanation is that the experiments are over-measuring $s_{T,GC}$ or under-measuring $\tilde{A}_T$. The former is unlikely since the mass flow rate of reactants and reactant density can generally be well controlled in experiments. As long as there is not substantial local extinction—which is prevented by the large co-flow of hot products in most configurations—$\bar{\dot{m}}_r$ is known. The use of the $\tilde{c} = 0.5$ isosurface area to normalize the reactant flux in Eq. (16) is arbitrary and affects the reported values of $s_{T,GC}$. Given that the density of the unburnt reactants is used to compute the reactant volume flux, it may be more appropriate to use a $\tilde{c}$ isosurface towards the reactant side of the flame brush. However, in the jet and Bunsen flames studied, this would reduce the normalizing surface area and further increase the reported $s_{T,GC}$.

While it is likely that experiments are under-estimating $\tilde{A}_T$, this cannot account for the large discrepancy between $s_{T,GC}/s_L^0$ and $\tilde{A}_T/A_{\tilde{c}=0.5}$ (nor the much higher values of $s_{T,GC}/s_L^0$ in the experiments compared to the DNS). Such under-estimation arises primarily due to resolution limitations and the use of two-dimensional (2D) measurements to estimate 3D flame areas. These effects have been evaluated in several recent studies. For example, Wabel et al. [111] post-processed DNS data to mimic the experimental signal collection process. They found that the measurement process decreased the measured area, but the decrease was limited to about a 10-30% under-estimation over a reasonable range of experimental parameters. Similarly, Wang et al. [112] showed that 2D measurements tend to under-predict flame areas by about 30%. Wang et al. [50] post-processed their experimental data in the LUPJ burner using two different effective pixel sizes. While they did find some sensitivity of the measured flame area to the pixel size, this was insufficient to compensate for the difference between $s_{T,GC}/s_L^0$ and $\tilde{A}_T/A_{\tilde{c}=0.5}$. Skiba et al. [113] experimentally demonstrated that a six-fold decrease in resolution reduced the measured flame area by approximately 30%. Klein et al. [114] used DNS of H_2/air flames and showed some sensitivity of flame area calculated using scalar isosurfaces to that deduced by the generalized flame surface density, depending on the choice of scalar, progress variable level, and number of dimensions considered. Similar to the other studies, these sensitivities were insufficient to explain the discrepancy between the experimentally observed turbulent



(a) Normalized flame speed and flame area versus turbulence intensity. Reprinted from Ref. [86] with permission of AIP Publishing.



(b) Normalized flame speed versus flame area. Reprinted from Ref. [103] with permission of Elsevier.

Fig. 13. DNS results indicating correspondence between turbulent flame speed and flame area.

flame speed and flame area. Hence, while experiments may under-measure the flame area, this is insufficient to account for the differences between $s_{T,GC}/s_L^0$ and $\tilde{A}_T/A_{\tilde{c}=0.5}$.

The experiments therefore show an increase in the local flame propagation speed, such that a given amount of area consumes more reactants per unit time than would be expected in a laminar flame, which does not occur in the DNS. This allows the turbulent flame speed to increase by more than would be possible based on flame surface area. One potential explanation is that there is a large-scale (geometry dependent and/or high Reynolds number) effect that is not captured in the DNS. For example, flame merging has been shown to cause an increase in the local consumption rate [115–118], which would be more prevalent in jet and Bunsen flames (see Fig. 10a) and in flames with larger integral-scale corrugations than in most DNS configurations. Another potential explanation is based on enhanced mixing due to flame-scale turbulence. A recent study by Nivarti et al. [119] has investigated whether the $s_{T,GC}$ discrepancy can be attributed to the si-

multaneous action of increased turbulent diffusivity and flame area increase (i.e., if Damköhler's first and second hypothesis [99] are acting concurrently), which is similar to the arguments made by Osborne et al. [55]. Using a model spectrum, they showed that the increase in $s_{T,GC}/s_L$ relative to $A_T/A_{\tilde{c}=0.5}$ in experiments could be reconciled by an increase in the "turbulent diffusivity", essentially leading to a faster local flame speed. However, this does not reconcile the discrepancy between the experiments and DNS, as DNS should predict the local flame behavior if the chemistry and transport are sufficiently modelled. Thus, understanding the reasons for this discrepancy remains an area of active research and is discussed further in Section 3.

2.6. Summary

The main takeaways from the discussion in Section 2 are:

1. The idealized separation of laminar premixed deflagrations into inert preheat zones and chemically active reaction zones is only appropriate for a limited range of fuels (e.g., methane). Conceptualizations of turbulent flames that rely on this separation may face challenges for other fuels, such as hydrogen or large hydrocarbons.
2. Experimental configurations to study highly turbulent flames should isolate the region being investigated from the surroundings using either physical confinement or a co-flow that is thermochemically matched to the environment. Otherwise, rapid turbulence-induced mixing can stratify the reaction zones with fluid from the surroundings.
3. DNS can provide valuable insights into flame structure and dynamics at highly turbulent conditions, and modern calculations now routinely use multi-step reduced or skeletal chemical kinetic models. Caution must, however, be used when developing insights from such studies, since DNS still requires substantial simplifications as compared to experiments and often includes models for large-scale kinetic energy input.
4. Significant ambiguity can exist in the calculation of the dimensionless parameters used to characterize turbulent flames, depending on where certain parameters are measured and what assumptions are made. We recommend the use of Eqs. (13) and (14) to calculate $\mathrm{Da}_{\ell,\delta}$ and $\mathrm{Ka}_{\delta,\mathrm{K}}$, respectively.
5. There is a natural mitigation of extremely high Karlovitz numbers and low Damköhler numbers in terrestrial systems of engineering interest due to the linkage between system temperature and pressure.
6. While regime diagrams provide a useful academic and conceptual aid for understanding the effects of turbulence on flame structures, their utility for accurately predicting the flame structure in real flames based on a small number of characteristic parameters is questionable. Ambiguities arise due to the parameters used to define regime boundaries (particularly in flames with spatially varying turbulence and flame structures), the impact of the flame on the turbulence, the lack of inert preheat zones when burning many fuels, the smallest turbulence scales being much smaller than the smallest thermochemical scales, etc.
7. Despite significant progress in both experiments and DNS, phenomenological disagreements still exist in the relationship between turbulent flame speed and flame surface area that are not explained by experimental uncertainty.

3. Thermochemical structure and dynamics

The objective of this section is to report current information regarding the thermochemical structure and dynamics of highly turbulent premixed flames. Extending Eq. (4) for chemical scalars to a generic scalar ψ (which could also include, e.g., temperature or progress variable) yields

$$\frac{\mathrm{D}\psi}{\mathrm{D}t} = \frac{1}{\rho}\frac{\partial}{\partial x_k}\left(\rho D\frac{\partial \psi}{\partial x_k}\right) + \dot{\omega}\,. \tag{18}$$

Hence, the Lagrangian evolution of ψ is dictated by both the scalar gradient $\chi_k = \partial\psi/\partial x_k$ and the corresponding source term. For chemical scalars, the source term is generally a local quantity, whereas the gradients are inherently non-local.

The major focus of this section is on characterizing the local thermochemical state and associated source terms during highly turbulent premixed combustion. Although we discuss the spatial structure of the flame—and, hence, the scalar gradients and molecular transport—where appropriate, scalar gradient dynamics are closely linked to turbulence dynamics. As such, much of the discussion regarding scalar gradient dynamics in turbulent flames is deferred to Section 4.2.

From the perspective of the thermochemical state space, the attainable states in a highly turbulent premixed flame are more varied than in a laminar flame, due to the larger range of scalar gradients and associated time scales. To investigate their effects, in Section 3.1 we first describe the structure of highly turbulent premixed flames from the perspective of their characteristics in physical space. The thermochemical states observed in highly turbulent premixed flames, and the associated reaction rates, are subsequently described in Section 3.2. Given the impacts of turbulence on thermochemical states in highly turbulent flames, we discuss potential deviations from the chemical pathways observed in laminar flames in Section 3.3. Chemical pathways are closely related to local combustion modes, and we discuss the classification and quantification of these modes in Section 3.4. A brief summary is provided in Section 3.5.

3.1. Flame structure in physical space

In studies that focus on high Karlovitz number premixed flames, the flame structure is frequently probed and described; Fig. 1 in Ref. [120] provides a comprehensive summary of these studies and their corresponding Karlovitz numbers. Both computational and experimental studies [53,55,56,66,67,78,86,105,113,121–127] have compared turbulent premixed flames at high $\mathrm{Ka}_{\delta,\mathrm{K}}$ to corresponding laminar flames in physical space, with the primary goal of assessing whether "flame broadening" is observed under highly turbulent conditions. This topic is comprehensively reviewed in Ref. [11] and, hence, is not discussed in detail here.

A challenge when considering turbulent flame spatial structure is that phenomenological observations of thinning or broadening are often qualitative and depend on the definitions of "preheat" and "reaction" zones. Such definitions are often not unified across studies, as is evident by the various isolines or radical layers employed in Refs. [56,67,127].

To avoid complications arising from such different definitions, the physical structure of flames can be re-cast into a consideration of scalar field dynamics. In particular, for a scalar that characterizes the location of the flame (e.g., the temperature), a scalar field with dimensions of length can be defined based on the local scalar gradient magnitude $\chi \equiv (\chi_k\chi_k)^{1/2}$ as [128,129]

$$\delta_\mathrm{t} = \frac{(\Delta\psi)_\mathrm{ref}}{\chi}\,, \tag{19}$$

where $(\Delta\psi)_\mathrm{ref}$ denotes a reference change in ψ (e.g., the difference in product and reactant temperatures when $\psi = T$). In the case of an unstretched laminar flame where $\psi = T$ and χ is evaluated at the location of the maximum gradient, $\delta_\mathrm{t} = \delta_\mathrm{L}^0$. A primary advantage of the scalar gradient approach to understanding flame structure is that ψ and δ_t are both field quantities that have exact,

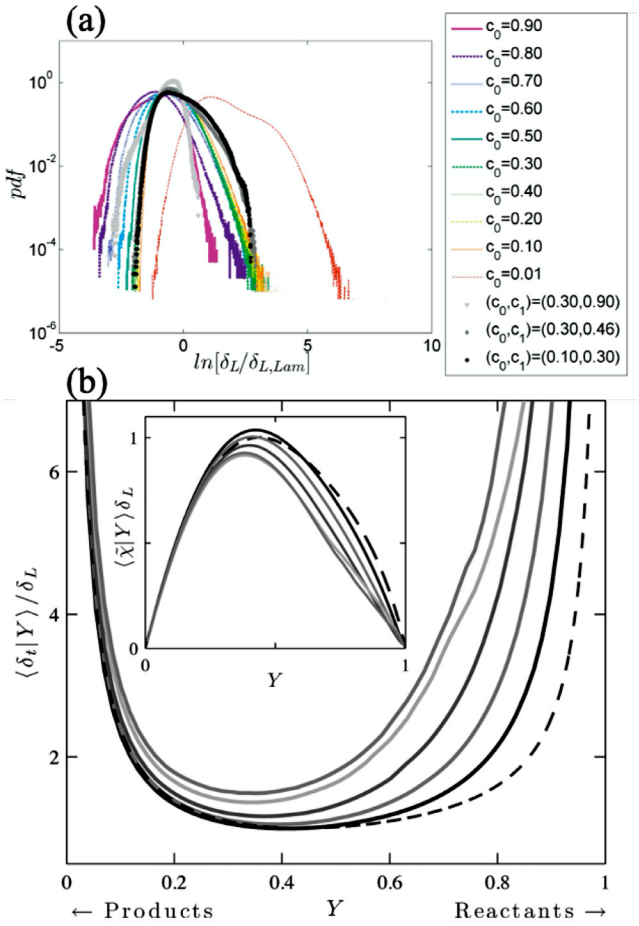


Fig. 14. Statistics of the local flame thickness δ_t from DNS. (a) Reprinted from Ref. [129] with permission of Elsevier; (b) Reprinted from Ref. [128] with permission of AIP Publishing.

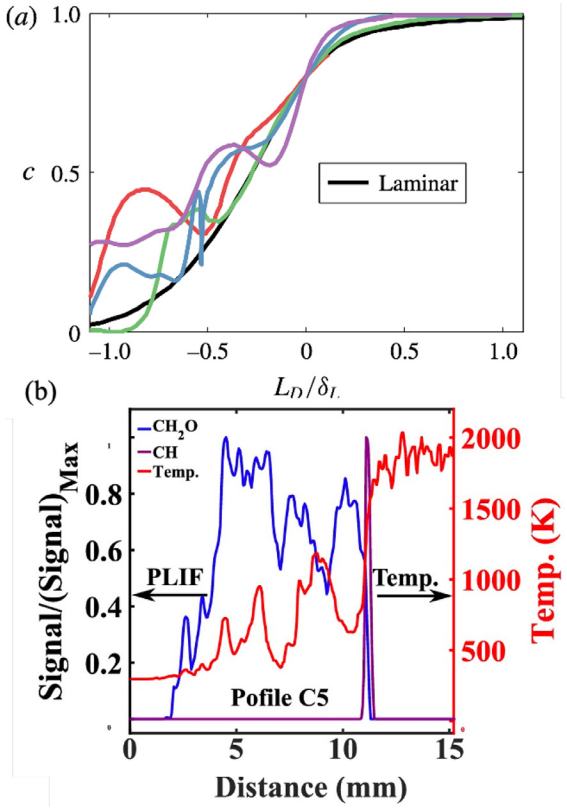


Fig. 15. Instantaneous temperature profiles across the flame brushes obtained (a) from DNS of the LUPJ burner, reprinted from Ref. [78] with permission Cambridge University Press; (b) experimental measurements of instantaneous temperature, CH_2O-PLIF and CH-PLIF signals across the flame brush for the Hi-Pilot burner, reprinted from Ref. [130] with permission of Elsevier.

physics-based governing equations. Such equations directly reveal the dynamics of the fields – both globally and locally – even for highly turbulent conditions where the concept of a quasi-laminar coherent flamelet may be lost (see Section 4.2.1).

Fig. 14 shows examples of probability density functions and conditional statistics of δ_t evaluated at different locations in highly turbulent premixed flames, as characterized by a progress variable, $\psi = c$, or reactant mass fraction, $\psi = Y$. These results show that a wide range of δ_t—both thinner and thicker than the corresponding laminar flame—can occur at any position within the flame for highly turbulent conditions. As the turbulence intensity increases, the fluid dynamic strain rate locally increases thermochemical gradients and decreases the width of high-gradient structures, resulting in broad regions of reduced gradients; that is, the dynamics lead to small regions of intense scalar gradients with intervening broad regions of low gradients. Hence, the overall flame width increases while strong gradients—higher than those found in laminar flames—are concentrated. This behavior is demonstrated in Fig. 15 from both experiments and DNS [78,130], and is likely due to a combination of two related effects. In particular, for the larger Reynolds numbers found in many highly turbulent configurations, internal intermittency, which is associated with the concentration of velocity gradients into an increasingly small volume of the flow, becomes more pronounced. At the same time, the turbulent velocity field itself has an increasingly dominant effect on the scalar dynamics, and the scalar field begins to reflect the intermittent properties of the turbulence. Although disentangling the relative contributions of these effects on the scalar intermittency remains a subject of active research, both are responsible in some measure for the increasing concentration of strong scalar gradients noted above. Internal intermittency in the context of turbulence structure and dynamics is discussed in more detail in Sections 4.2.3 and 4.3.

Another factor complicating the structure of a turbulent flame is the potential for reactions occurring throughout the flame, (i.e., the lack of chemically inert preheat zones). As demonstrated by the profiles of the unstrained laminar flames in Fig. 2, an inert region of diffusive mixing generally does not occur upstream of highly exothermic reactions when considering detailed elementary chemical reactions. For example, significant endothermic fuel cracking reactions (due to pyrolysis) occur in the preheat zone for dodecane/air flames. Exothermic reactions can also take place throughout hydrogen/air flames, in a region that is broader than the fuel consumption region due to differential diffusion.

Strong turbulence can further complicate the concept of a preheat zone if flames locally extinguish. In such situations, turbulent advection can rapidly stir hot products into the preheat zone, from which enthalpy and species subsequently diffuse. One manifestation of this is the presence of product “pockets” that are separated from reactants by extinguishing flame surfaces (i.e., isosurfaces with zero or negative displacement speed). Such pockets were observed in all DNS of n-dodecane/air flames at Karlovitz numbers from 100 to 10,000 [66], as visualized by the blue regions in Fig. 16(b). The presence of pockets complicates the physical space structure of the flame, as well as the thermochemical structure and reaction rates (see Section 3.3.2). We also note that reactant pockets can be formed in the products, as visualized by the red regions in Fig. 16(b).

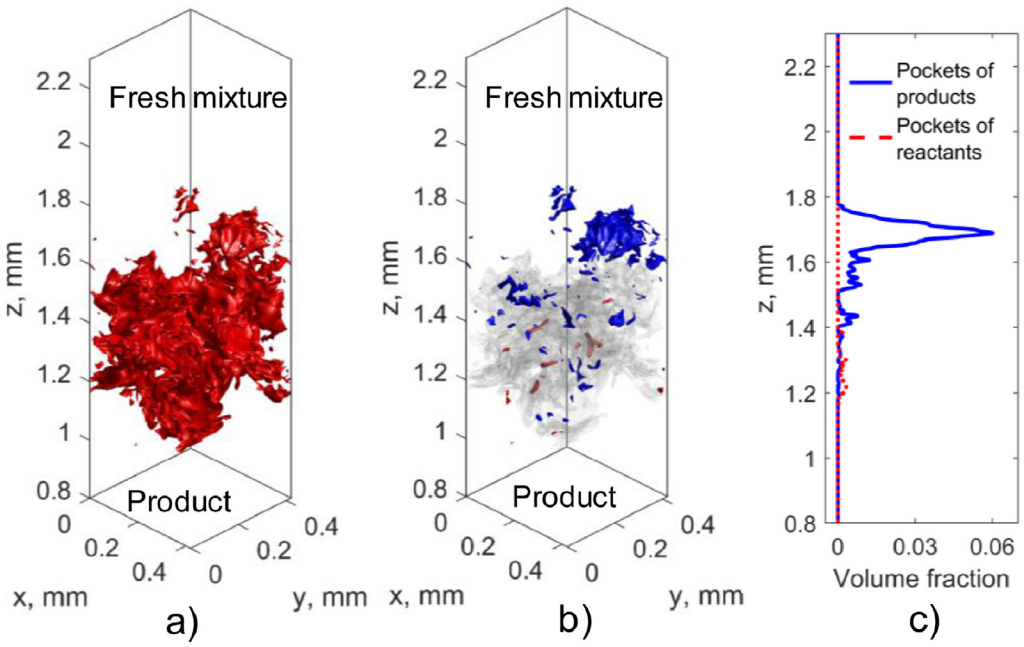


Fig. 16. (a) 3D isosurfaces identified by zero crossing of the maximum positive eigenvalue of the chemical Jacobian, (b) the reactant (red) and product (blue) pockets, for $Ka_{\delta,K}$=1000, and (c) volume fractions of the two types of pockets in the streamwise direction. The grey isosurface in panel (b) indicates the continuous main reaction front. Reprinted from Ref. [66] with permission of Elsevier. (For interpretation of the references to color in this figure legend, the reader is referred to the web version of this article.)

As mentioned in Section 2.4.3, the distinction between the preheat zones and reaction zones becomes unhelpful for highly turbulent flames, particularly when considering fuels other than methane. Terminologies such as "volumes of reacting fluids" or "volumes of packed flame filaments" may be more appropriate [70,121]. Consequently, traditional experimental and computational diagnostics and models can be insufficient and/or inappropriate in describing the flame structures under these challenging conditions where clear interfaces between fresh mixture and products cease to exist. We will further elaborate on this point in Sections 3.2 and 3.3.1.

3.2. Flame structure in thermochemical space

The ability of turbulence to alter the spatial distribution of scalars in physical space is associated with changes in scalar gradients. This, in turn, alters the rate of molecular transport processes responsible for scalar mixing, ultimately resulting in changes to scalar source terms (i.e., chemical reaction rates). This section reviews changes in the thermochemical states observed in highly turbulent premixed flames.

3.2.1. Non-unity Lewis number effects

Molecular transport is the fundamental process that mixes scalars at the molecular level, which is necessary for chemical reactions. Turbulent advection alters the gradients that drive this process, but any differences in transport properties between different scalars remain. Nevertheless, there is a phenomenological understanding that differences in transport properties become less significant, in a practical sense, as turbulence intensity increases. Physically, this should be interpreted as the creation of a state that appears to have uniform transport properties in some statistical sense (i.e., in an average or filtered field), due to rapid spatio-temporal variations in the magnitude and orientation of scalar gradients. Therefore, statistically, differences between diffusion coefficients for various species and heat are expected to become less significant under highly turbulent conditions. With such an expectation, effects due to varying Lewis number ($\mathrm{Le} = \alpha/\mathcal{D}$) are frequently examined and discussed in the literature on highly turbulent premixed flames [67,69,83,86,122,131,132].

Before we discuss the relevant findings, we wish to clarify some terminology commonly employed to describe molecular and thermal transport; namely, preferential diffusion, differential diffusion, and Lewis number effects. Preferential diffusion is conventionally employed to indicate different molecular diffusivities for different species (i.e., $\mathcal{D}_A \neq \mathcal{D}_B$) in a multi-component chemical system [5]. Similarly, the term "non-unity Lewis number effect" conventionally indicates that the molecular diffusivity of species A is different from the thermal diffusivity of the local gas mixture (i.e., $\mathcal{D}_A \neq \alpha$). For a multi-component reacting mixture, the global Lewis number is often defined based on the deficient species in the fresh mixture [5], although an individual Lewis number can be defined for each species. Consequently, the term "non-unity Lewis number effect" alone can be ambiguous and more clarification is usually needed to elucidate its exact meaning. Differential diffusion, similar to "non-unity Lewis number effects", is also used liberally in the literature; it has been used as a synonym to "preferential diffusion" [133,134] or "non-constant non-unity Lewis number effects" [67,83,122,132].

To avoid ambiguity, we recommend explicit specification of the transport models where possible, so that readers can have a precise understanding of the meaning. During discussion, more specific descriptions are suggested, such as "differential species diffusion" or "differential diffusion between species and heat", or consistently reserving "non-unity Lewis number effect" for the description of differential heat and species transport.

Physically, a multi-component chemical system always has non-constant non-unity Lewis number (i.e., $\mathcal{D}_A \neq \mathcal{D}_B \neq \alpha$). Hence, the issues mentioned above are mostly observed in computational studies. However, physical systems can "appear" or "behave" as if the Lewis number were unity or no differential diffusion existed, to the extent observable by the experiment. Recognizing physical conditions that lead to such observations is beneficial for modeling studies.

Although non-unity Lewis number effects are expected to decrease in importance with increasing turbulence intensity, they

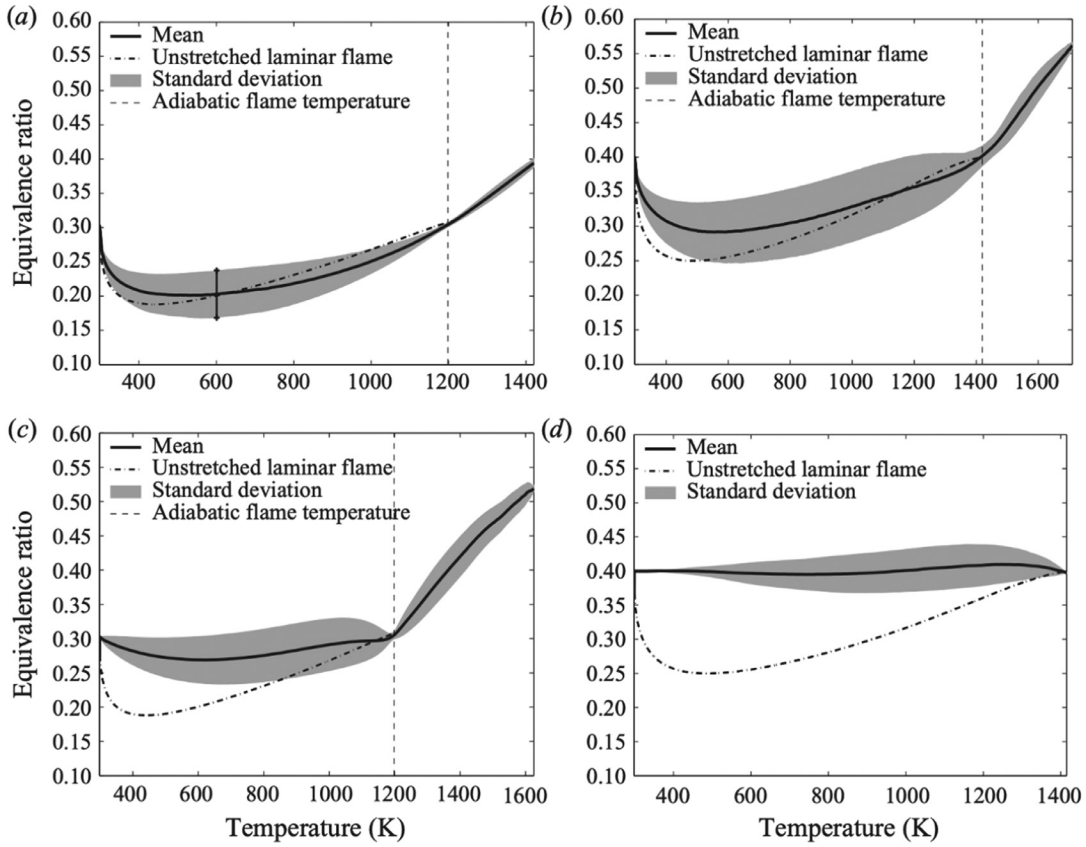


Fig. 17. Conditional mean (solid line) and standard deviation (shaded area) of local equivalence ratio as a function of temperature for: (a) $\phi_0 = 0.31$ and $Ka_{\delta,K} = 10$; (b) $\phi_0 = 0.4$ and $Ka_{\delta,K} = 10$; (c) $\phi_0 = 0.31$ and $Ka_{\delta,K} = 1.6 \times 10^3$; and (d) $\phi_0 = 0.4$ and $Ka_{\delta,K} = 1.6 \times 10^3$. The dashed line indicates the corresponding unstrained laminar flame solutions. The vertical dashed line denotes the adiabatic flame temperature at ϕ_0. Reprinted from Ref. [69] with permission of Cambridge University Press.

can remain significant even at quite high turbulence intensities [69,83,86,131,135]. Aspden et al. [69] reported the distribution of local (atom-based) equivalence ratios versus temperature through DNS of hydrogen/air flames from $Ka_{\delta,K} = 10$ to 1.6×10^3 with inlet equivalence ratios of $\phi_0 = 0.31$ and 0.40 (see Fig. 17). Similar variations in mean equivalence ratio versus temperature were observed between the $Ka_{\delta,K} = 10$ turbulent flames and corresponding laminar flames for both inlet equivalence ratios, indicating the continued importance of differential diffusion. Additionally, the $Ka_{\delta,K} = 10$ flames exhibited locations with mean equivalence ratios greater than ϕ_0 and temperatures above the adiabatic flame temperature as a result of differential diffusion. At $Ka_{\delta,K} = 1.6 \times 10^3$, both flames have different mean equivalence ratio profiles that remain close to ϕ_0, indicating a statistically decreased significance of differential diffusion. Nevertheless, the standard deviation around the mean remains significant compared to the $Ka_{\delta,K} = 10$ cases, particularly at $\phi_0 = 0.31$. Interestingly, the $\phi > \phi_0$ branch beyond the adiabatic flame temperature was only observed for $\phi_0 = 0.31$ at $Ka_{\delta,K} = 1.6 \times 10^3$.

Barlow et al. [135] measured C/H, C/O and C/N ratios for the Cambridge bluff-body stabilized burner with both streams comprised of methane/air mixtures at $\phi = 0.75$ (Case SwB1). The Reynolds numbers for the inner and outer jets were 5,960 and 11,500, respectively. They observed varying atomic ratios across the turbulent premixed flame as shown in Fig. 18, which suggests the role of differential species diffusion in these turbulent premixed flames. The same trends of atomic ratios were observed in an LES/PDF study [136], where mixture-averaged molecular transport was invoked to account for molecular transport on the resolved grid only. However, the subgrid differential diffusion remains unaccounted for in this study, which could contribute to the reported discrepancy between experiments and computation.

Non-unity Lewis number effects have also been delineated by comparing simulations conducted with different molecular transport models [67,83,122,127,132]. For example, Lapointe et al. [67] conducted 3D DNS of forced turbulent planar n-heptane/air flames. The Karlovitz number based on the unburnt gases up to 1050 were studied, which corresponds to 237 when defined based on the properties in the reaction zone. For each Karlovitz number, two transport models were compared, namely a unity Lewis number model and a non-unity Lewis number model that was obtained from an unstrained laminar premixed flame simulation using full transport.

The different transport models showed differences in the peak temperature corresponding to the maximum fuel consumption rate. However, such differences decreased with increasing Karlovitz number, indicating a weakened role of Lewis number effects. Lapointe et al. [67] observed higher levels of local extinction with non-unity Lewis number transport, which is expected because the response to strain and curvature can be significantly impacted by transport properties [5], thereby modifying the local extinction behavior. The scalars were more scattered in state space with the non-unity Lewis number model. However, the mean mass fractions of C_2H_4 (and other scalars) versus temperature agreed better with laminar solutions obtained using unity Lewis number, as opposed to those obtained with non-unity Lewis number. This supports the phenomenological observation of decreased effects of differential diffusion on the mean state when turbulence is intense.

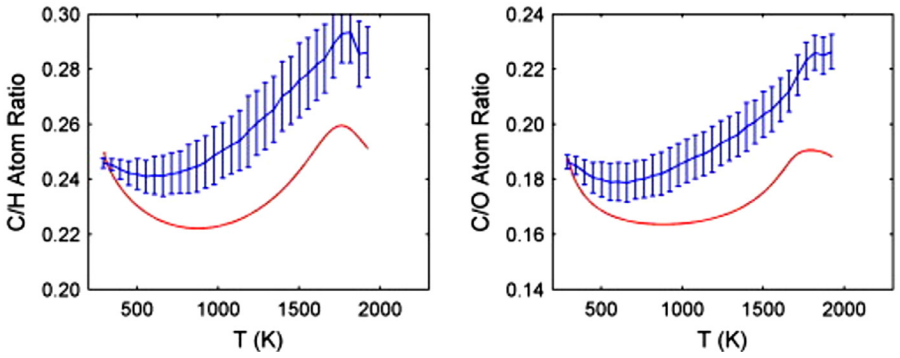


Fig. 18. Comparison of measured results for selected atomic ratios at $z = 10$ mm above the bluff body surface in the turbulent flame plotted versus temperature (blue) and compared with calculated results for an unstrained laminar flame at $\phi = 0.75$ (red). Reprinted from Ref. [135] with permission of Elsevier. (For interpretation of the references to color in this figure legend, the reader is referred to the web version of this article.)

Hence, the aforementioned studies point to a reduced influence of non-unity Lewis numbers on the mean thermochemical state with increased turbulence intensity. Nevertheless, differential diffusion can significantly influence the mean state at highly turbulent conditions, and also influences the distribution of states around the mean. We note that non-unity Lewis number effects have predominantly been studied in canonical configurations with relatively simple fuels. The impact of differential diffusion may change with composition/thermal stratification and with more complicated fuels.

3.2.2. Scalar distributions in thermochemical space

Ultimately, the combination of molecular diffusion with turbulence-induced scalar gradients and chemical reactions results in more varied thermochemical states compared to laminar flames. Scatter plots or joint PDFs of two or three thermochemical variables are frequently employed to examine the extent to which turbulence impacts the flame in thermochemical space. The conditional means of key thermochemical variables in turbulent flames are subsequently compared with profiles extracted from corresponding laminar flames. Comparison between conditional statistics in turbulent flames with laminar solutions have been comprehensively discussed in Section 3.1 of Ref. [11]. Hence, we only present some typical results that are useful for motivating/understanding the subsequent discussion of reaction rates and chemical pathways.

Fig. 19 shows scatter plots of the mass fractions of HO_2, OH, and CH_3 obtained from a 3D simulation of a premixed Jet-A/air flame kernel subjected to intense turbulence [87]. The scatter plots are colored by a temperature-based progress variable in the range between 0.84 and 0.92, representing the transition from the preheat to the reaction zone. Compared to the corresponding laminar solution, which is essentially a 1D manifold, the OH-CH_3-HO_2 mass fraction space for the turbulent flame is larger and 3D. In particular, CH_3 penetrates into the reaction zone in the turbulent flames, while there is zero CH_3 beyond $c = 0.84$ in the corresponding laminar flame. Reactions such as $CH_3 + OH = CH_2^* + HO_2$ are expected to have faster reaction rates with CH_3 exposed to higher temperatures, which can potentially impact the global burning rate and chemical pathway.

The thermochemical space also has been explored in the experiments and DNS of the LUPJ burner over the range $Ka_{\delta,K} = \mathcal{O}(10) - \mathcal{O}(1,000)$ [47,78]. In the experiments, OH and CH_2O were measured by PLIF, and temperature was measured by Rayleigh scattering. Substantial amounts of OH were observed in the low-temperature regions of the flame (i.e., $T < 1200$ K), which is absent in the corresponding laminar flame. The temperature-conditioned mean OH mass fractions gradually deviated from the laminar flame

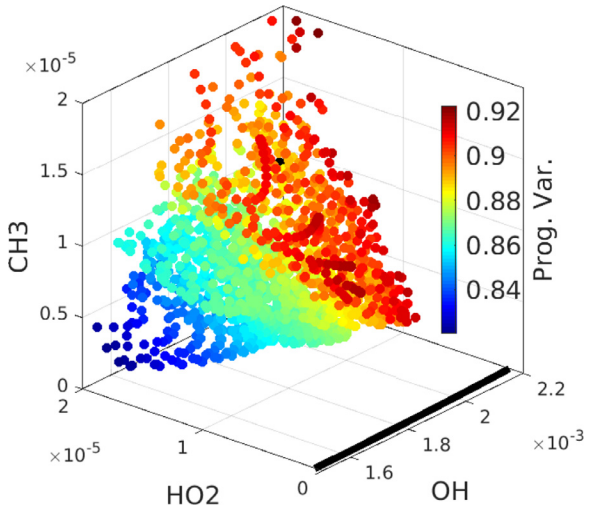


Fig. 19. Scatter plot in the OH-CH_3-HO_2 mass fraction space in a 3D turbulent premixed flame, colored by progress variable. The solid (black) line corresponds to the laminar flame solution. Reprinted from Ref. [87] with permission of Elsevier.

as $Ka_{\delta,K}$ was increased. Scatter plots of a few important species from both the experiments and DNS are shown in Fig. 20. The DNS showed good qualitative agreement with the experiments, although there were notable differences in the shape of the scatter plots. For example, the simulations show more samples at low concentrations of HCO and at high concentrations of CH_2O and OH. The experimental results are generally more scattered in the plots due to noise in the measurements. Clearly, this degree of scatter deviates significantly from the profiles that would occur in laminar flames. Such wide variations in species-species and species-temperature correlations are ubiquitous in highly turbulent flames. Despite the wide variation in thermochemical states, conditional mean profiles generally resemble those of laminar flames at "appropriate" conditions (i.e., with a particular strain-rate and transport model) [79,132], although a large standard deviation around the conditional mean is always observed.

The wide variation of thermochemical states can challenge the assumptions of existing turbulent combustion closures, including both flamelet-like and non-flamelet-like models. For example, the LUPJ burner has been used for *a priori* and *a posteriori* assessment of a flamelet model [137], a thickened-flame approach [138], and a transported PDF approach [139]. Five different flamelet tabulation methods (i.e., "chem-tables") are compared [137], including one obtained using the conditional statistics from DNS, two obtained from counterflow stratified premixed 1D flames with and without differential diffusion, one from freely propagating premixed

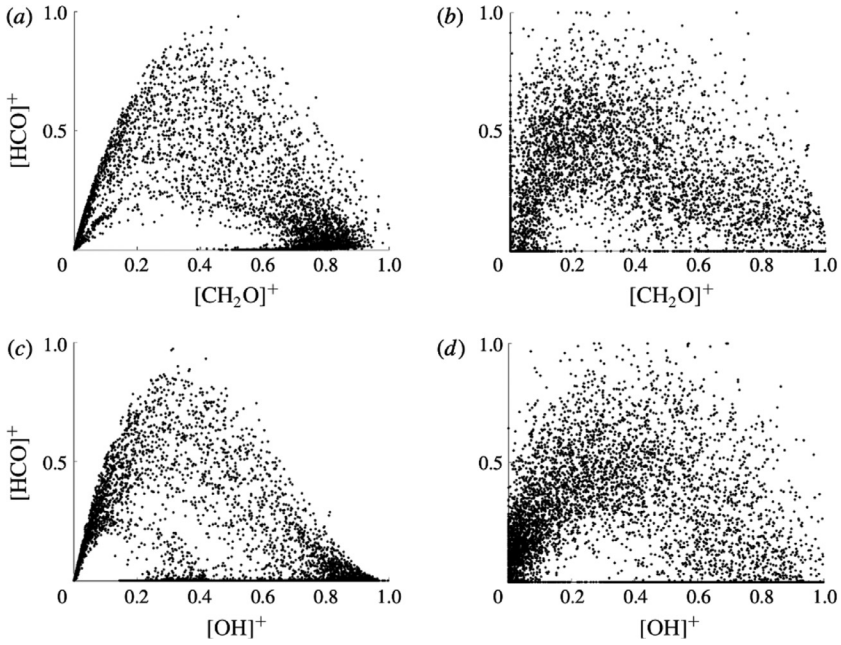


Fig. 20. Normalised scatter plots of (a,b) [HCO] versus [CH_2O] and (c,d) [HCO] versus [OH], where [X] denotes the concentration of species X. The left-hand plots show the species concentrations from the DNS and the right-hand plots show the species PLIF signals of the experiment. Reprinted from Ref. [78] with permission of Cambridge University Press.

1D flames, and one from zero-dimensional autoigniting plug-flow reactors. All of the flamelet tables capture the mean and root-mean-squared fluctuation profiles of the flow and major species well, with more discrepancies observed in predicting CH_2O. However, the flamelet table based on counterflow stratified premixed 1D flames with differential diffusion shows better agreement with DNS upstream near the inlet, while the flamelet table based on auto-igniting plug flow predicts CH_2O and the instantaneous flame structure the best further downstream. That is, the flamelet tables need to be adjusted in order to capture the local flame structure.

Similarly, the thickened flame model also needs to be adapted to account for the local variation of thermochemical states when constructing the thickening factor. Compared to the traditional approach, where the thickening factor is estimated based on unstrained laminar flames at corresponding boundary conditions, the thickening factor in Ref. [138] accounts for variations in the local hydrodynamic strain and adjusts the reference flame thickness based on the heat release rate layer thickness, subject to different strains. Similar adjustments have also been implemented in the context of transported PDF methods with a power-law based mixing frequency model [139]. One additional model constant is multiplied in the expression for thermal thickness of an unstrained laminar flame in the proposed power-law scaling function, compared to an earlier version of the power law model; the new mixing model yields better agreement with DNS in predicting scalar mixing rates. Based on these three studies, all three traditional models are applicable to the high Karlovitz number LUPJ jet flame. However, the wide distribution of thermochemical states arising from strong turbulence-chemistry interactions requires modifications (e.g., estimates of the reference flame thickness) in all three models. A future challenge lies in how to obtain the knowledge of thermochemical states and model their diversity *a priori*, when no DNS or experimental insights are available.

3.3. Chemical reactions in the enlarged thermochemical space

Responding to the enlarged thermochemical space in turbulent flames, local reaction rates are also more varied than in laminar flames. Indeed, the exponential relationship between reaction rate and temperature means that relatively small temperature variations can result in large reaction rate variations. In the following section, we review the impact of thermochemical states on combustion chemistry.

3.3.1. Chemical pathways

One of the major questions concerning highly turbulent combustion is whether turbulence alters the chemical pathway of a given reactant mixture [65,87,126,140–144]. Here "chemical pathway" indicates a network of key elementary reactions, which could be the complete collection of elementary reactions for specific reactive mixtures at certain specific initial conditions, or a certain subset thereof. For example, when heat release rates are targeted, the relevant chemical pathway is tightly connected to fuel oxidation processes. For hydrocarbon fuels, the oxidation pathway is equivalent to tracking the major carbon flow.

Understanding such chemical pathways under highly turbulent conditions has practical implications for the optimization/reduction of chemical kinetic models. With hundreds or thousands of model parameters, chemical kinetic models (detailed or global) require experimental or theoretical measurements to anchor the optimization of model parameters. The experiments are mostly canonical, including data from flow reactors, laminar flame speed experiments, rapid compression machines, or shock tubes. For example, the GRI-Mech mechanisms are optimized based on a collection of reliable experiments that relate to natural gas combustion, including NO formation and re-burn [145]. Turbulent conditions are rarely included in the experimental data sets that support the development of kinetic models. Therefore, it is of primary interest to understand whether optimizations based on non-turbulent data are sufficient to describe turbulent flames.

We note that many chemical pathway studies are constrained by the fact that a particular chemical mechanism was used to conduct the analysis; if a certain chemical pathway is missing from the particular chemical mechanism, such studies are not designed to identify these. Meanwhile, conclusive comparisons between dif-

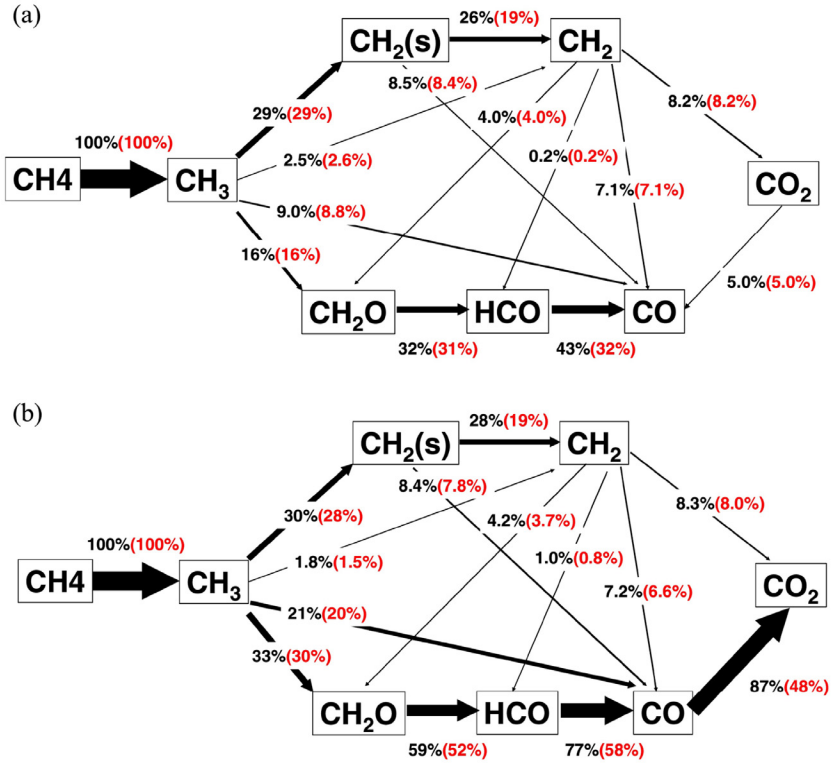


Fig. 21. The main C1 reaction path for carbon flow at two downstream locations of a piloted jet flame: (a) $x/D = 8$; (b) $x/D = 32$. The numbers in red are based on unity Lewis number laminar flames at the corresponding mean strain rate and temperature. The thickness of the arrows is weighted with the fraction of the carbon flow. Reproduced from Ref. [65] with permission of Elsevier. (For interpretation of the references to color in this figure legend, the reader is referred to the web version of this article.)

ferent chemical mechanisms that have different reactions are also difficult, because of the above-mentioned optimization of chemical kinetic models. Therefore, caution must be taken regarding statements that the same reactions are at play when comparing two chemical mechanisms with different lineages.

The chemical pathways reproduced in Fig. 21 track the carbon flow resulting from relevant chemical reactions in the DNS of the LUPJ burner [65]. The numbers and thickness of the arrows indicate the fraction of carbon flow through each route, and the values obtained from the turbulent flame (black) are compared to those obtained from corresponding laminar flames (red). Similar dominant paths are observed between laminar and turbulent flames; the black and red numbers are, for the most part, similar. The relative rates of the different reactions change with position; e.g., the CO-CO_2 conversion is shifted downstream due to the accumulation of CO further downstream and longer residence times required for this process.

A few recent DNS studies at high Karlovitz numbers have discussed the impact of turbulence on reaction pathways through analyses of reaction fluxes [65,140,142,143]. Dasgupta et al. [140] analyzed a recent series of DNS of lean hydrogen-air flames at different Karlovitz numbers [86] by analyzing integrated reaction fluxes along local flame normal directions. They also examined methane/air flames [142] and n-dodecane/air flames [143] using corresponding DNS datasets [121,123]. For all three flames, the conclusions remain that the fractional contribution from each reaction to the overall heat release is not significantly altered by turbulence. Therefore, they conclude that kinetic models that are optimized using laminar targets are adequate for describing chemistry in turbulent flows.

Recognizing the uncertainties that exist in the elemental rate parameters, Zhao et al. [87] systematically examined the possible change of chemical pathways through sensitivity analysis using 620 2D DNS of flame kernels in decaying isotropic turbulence. Global first-order and second-order sensitivity analyses [146] of target quantities, such as heat release rates and CO mass fraction, were performed. They found that the top ten reactions that contributed to the overall heat release rate stay comparable between laminar and turbulent conditions, although more reactions are sensitive in the turbulent flame. In particular, the chain branching reaction H+O_2=OH+O and the oxidation reaction CO+OH=CO_2+H are consistently predicted to be the most significant reactions impacting heat release rates.

Based on quantified uncertainties in the reaction rates, this study also provides a ranked list of important reactions for further study/refinement based on their impact factor, defined as the product of the sensitivity coefficient and the uncertainty factor for each reaction. The sixteen most impactful reactions are shown in Fig. 22. Although H+O_2=OH+O is the most sensitive reaction, CH_3 + OH = CH_2^* + H_2O is the most impactful reaction since it is less studied experimentally compared to H+O_2=OH+O and has a larger uncertainty factor. Such a ranked list can provide guidance in setting priorities for obtaining more precise experimental/theoretical data of chemical reaction rates.

When pollutant formation is the primary concern (e.g., soot [87] or NOx [144]), the reaction rates of key species (e.g., C_2H_2, N_2O, and NO_2) are often employed as the quantities of interest; reactions leading to production and consumption of these targeted species are considered components of the chemical pathways. Karimkashi et al. [144] examined chemical pathways for NO production in turbulent premixed methane/air flames using 2D DNS of freely propagating planar flames for increasing turbulence intensities and with a reduced mechanism based on GRI-Mech 3.0 [145]. They reported a negative net contribution of the prompt NO pathway under highly turbulent conditions, leading to a reduction of NO compared to the expected prompt NO production under

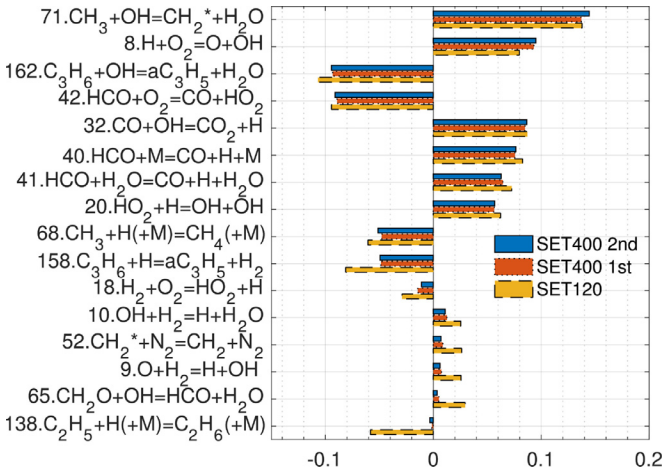


Fig. 22. Ranked composite impact factors obtained using (from left to right): SET400 with second order regression (blue solid); SET400 with first-order regression (red dotted); and SET120 with first-order regression (yellow dashed) for Case2ms. The impact factor is defined as the product of sensitivity coefficient and uncertainty factor. A negative impact factor results from a negative sensitivity coefficient, which indicates that the heat release rate decreases with increasing reaction rate constant. Reprinted from Ref. [87] with permission of Elsevier. (For interpretation of the references to color in this figure legend, the reader is referred to the web version of this article.)

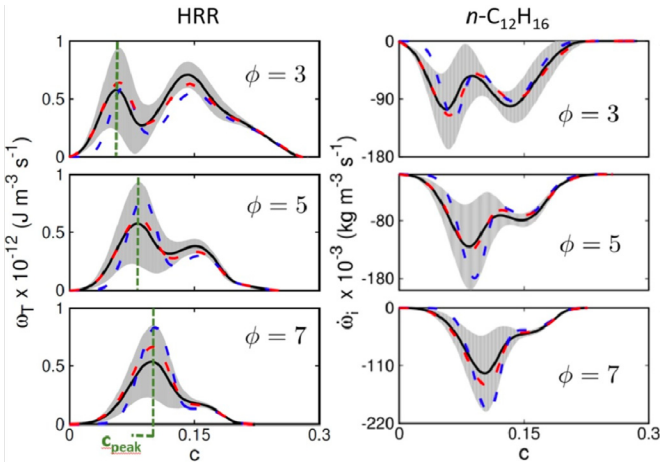


Fig. 23. Turbulent flame structure in progress variable space from [132]. Left: heat release rates. Right: reaction rates of n-$C_{12}H_{16}$. Black solid lines: conditional means. Gray-shaded areas: plus/minus one conditional standard deviation. Blue dashed lines: laminar flames with non-unity Le. Red dashed line: laminar flames with unity Le. The location in c space of the first peak in HRR, denoted c_{peak}, is shown by green dashed lines. Reprinted from Ref. [132] with permission from Elsevier. (For interpretation of the references to color in this figure legend, the reader is referred to the web version of this article.)

low turbulence intensity and laminar conditions. The negative contribution was attributed to turbulent transport of the unburnt intermediate species, such as CH_3 and CH_2, to the high-temperature reaction zone.

Zhao et al. [87] studied the sensitivity of the integrated mass of C_2H_2 to gas-phase reactions, as C_2H_2 is on the critical path to soot formation. They observed that the top ranked reactions contributing to the production of C_2H_2 are very similar between turbulent and laminar conditions. Interestingly, they also reported accumulated CH_3 radicals in the reaction zone under turbulent conditions, which is absent in the laminar counterpart.

A common conclusion from all of the above studies with different fuels and methods is that, although the same underlying reactions are at play, the relative importance of these reactions can be altered under highly turbulent conditions. This conclusion also indicates that calibration of chemical kinetic models should take into account the effects of the turbulence-enlarged thermochemical state space.

3.3.2. Reaction rates

As seen in the previous section, relevant reactions for high-temperature heat release are similar between laminar and turbulent flames. Consequently, certain similarities in thermochemical state space are expected even when turbulence is intense, at least in the statistical sense. Driscoll et al. [11] review evidence and discuss this statistical similarity in detail. Here, a few examples are introduced to provide a perspective on this topic. In addition, we highlight a few physical scenarios at which this laminar/turbulent similarity does not hold (e.g., product/reactant mixing at extinction locations).

Different influences of turbulence on reaction rate have been reported, depending on the fuel. For example, Aspden et al. [69,86] reported strong variations in the local hydrogen consumption rates for a series of hydrogen/air flames, which resulted in an overall increase in the mean consumption rate compared to freely propagating 3D laminar flames. Here, 3D freely propagating premixed laminar flames are employed as reference flames to include effects of thermodiffusive instabilities that are not captured by idealized flat laminar premixed flames with low Lewis number [147]. Lapointe et al. [67] also observed strong variations in local fuel consumption rate for n-heptane/air flames, although the mean fuel consumption rates were lower than the laminar counterpart. Sankaran et al. [80] examined the mean reaction rate of CH_4, CO and OH at several downstream locations of a turbulent premixed methane/air Bunsen flame in the thin reaction zone regime. The mean reaction rates, conditioned on progress variable, were bounded by solutions obtained from an unstrained laminar flame and a strained laminar flame with a strain rate matching that of the mean tangential strain in the turbulent flame. More recently, Savard et al. [132] examined the conditional mean reaction rates of three rich n-dodecane/air premixed flames ($\phi = 3$, 5, and 7) at a constant pressure of 60 atm, matching the Karlovitz number from the Engine Combustion Network Spray A condition. The heat release rate and reaction rates of n-$C_{12}H_{26}$, $C_{12}H_{15}O_2$, CH_2O and C_2H_2 were compared against laminar flame solutions using unity and non-unity Lewis number solutions. As shown in Fig. 23, there is a broad spread of reaction rates around the corresponding laminar solutions. The mean reaction rates in progress variable space match more closely with the unity Lewis number laminar solutions than the non-unity Lewis number solutions.

Most studies of reaction rates in highly turbulent flames have shown that conditional means resemble those of laminar flames at “appropriate” conditions (i.e., with a particular strain-rate and transport model), although a large standard deviation around the conditional mean is always observed. However, such a resemblance may be compromised by mixing of hot radical-rich products with the reactants directly, for example through the pocket flames shown by Fig. 16 in Section 3.1. When these pockets fail to ignite the surrounding fresh mixture, the enthalpy and species in the pocket flame gradually mix with the surrounding fresh mixture. Such mixing can be highly consequential for large hydrocarbons because, in laminar flames, endothermic fuel cracking processes are segregated from oxidation reactions (see Fig. 2). If the fresh reactants mix with the products without reacting, the subsequent reaction rates can be enhanced. This was demonstrated by Smolke et al. [148] using calculations from a series of isobaric and adiabatic pyrolytic reactors with initial temperatures at 1100 K, 1200 K and 1300 K. They found that the laminar flame speed and the extinction strain rates were increased when the reactants em-

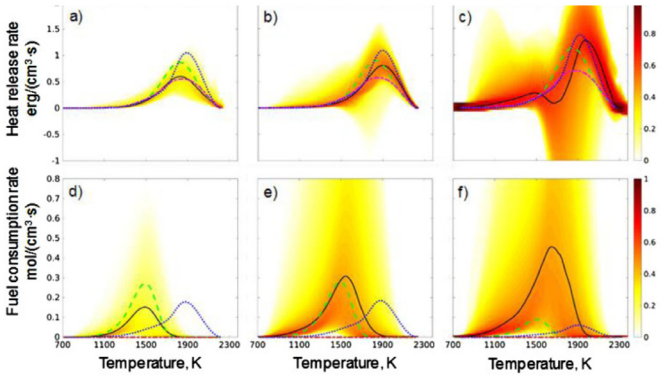


Fig. 24. Joint PDFs (contour) and conditional mean (black solid lines) of heat release rate (a–c) and fuel consumption rate (d–f) versus temperature, for $Ka_{\delta,K}$ = 100 (a, d), 1000 (b, e), and 10000 (c, f), in comparison with solutions from zero-dimensional auto-ignition (red dash-dotted-dash lines), perfectly stirred reactors (blue dotted lines), and 1D freely propagating premixed flames (green dashed lines). Color of each pixel indicates the logarithmic number of computational cells within the pixel normalized by the maximum value. In panel (f), the fuel consumption rate is scaled by 1/4. Reprinted from Ref. [66] with permission of Elsevier. (For interpretation of the references to color in this figure legend, the reader is referred to the web version of this article.)

ployed in these calculations were obtained from the partially "reformed" products in the pyrolytic reactors.

3.3.3. Decorrelated fuel consumption and heat release rates

Whether the fuel decomposition rate is correlated (or decorrelated) with heat release rate in the same manner as in a corresponding laminar flame is a potentially useful metric for assessing the influence of turbulence on chemistry. As shown in Fig. 2, the location of fuel consumption relative to heat release rate in laminar flames depends on the fuel/air mixture. Indeed, despite being the most investigated fuel, methane is rather an exception in terms of the co-location of fuel consumption and heat release. Unsurprisingly, the enlarged thermochemical space induced by strong turbulence can alter these relationships in a fuel-dependent manner.

Aspden et al. [69,86,131] reported an increasing de-correlation between fuel consumption and heat release rates with increasing Karlovitz numbers in H_2/air flames. They suggested that differential diffusion of the highly mobile hydrogen atom, in conjunction with turbulent advection and molecular mixing, contribute to the observed de-correlation.

Xu et al. [66] observed a de-correlation between fuel consumption and heat release rates for a series of DNS of n-dodecane/air flames at 30 bar. As shown in Fig. 24, the fuel consumption rate peaks around 1500 K and the heat release rate peaks around 1900 K at a relatively modest Karlovitz number of 100. Similar de-correlations have been reported in a few other heavy-hydrocarbon based DNS studies [67,123], and have also been observed in corresponding unstrained laminar flames (e.g., as shown in Fig. 2), as an expected consequence of fuel cracking [148]. However, the fuel consumption peak is brought closer to the heat release peak in temperature space with increasing Karlovitz numbers (i.e., Fig. 24(b) and (c) for $Ka_{\delta,K}$ = 1,000 and 10,000, respectively). That is, the de-correlation of fuel consumption and heat release rates found in laminar n-dodecane/air flames is statistically reduced in intense turbulence due to the rapid turbulence-induced mixing. Fuel consumption rates are much larger than in corresponding laminar flames at $Ka_{\delta,K}$ = 10,000, because the endothermic fuel cracking process is exposed to temperatures up to 1800 K.

Although the limit of a perfectly stirred reactor (PSR) is employed in Fig. 24, PSR-like behaviors are rarely observed in the reviewed literature, except under the extreme conditions around Karlovitz numbers of 10,000 as shown in Fig. 24. As reflected in Fig. 9(a), conditions relevant to practical combustors reside outside the "distributed reactions" regime. The irrelevance of the PSR limit is partly due to the fact that practical devices are designed to avoid detrimental limit conditions. As observed in the previous sections, transition to extinction, autoignition and compressible regimes occur more frequently with increasing turbulence intensity. Such limit phenomena might be precursors to global flame extinction or the onset of combustion instability [33], which are undesirable in practical combustors.

For methane/air flames, the normally co-located fuel consumption and heat release rates in a laminar flame can become de-correlated due to hydrodynamic effects. As noted by Wabel et al. [111], heat release rates in the LUPJ burner do not completely coincide with methane consumption. Their study post-processed DNS of two high Karlovitz number flames to assess experimentally accessible heat release rate markers, accounting for experimental factors. They reported the existence of a spatially distributed low-intensity heat release zone that makes up approximately 30% of the total heat release rate, due to slow oxidation of CO that is convected downstream to CO_2 due to insufficient residence time upstream. We note that this distributed heat release region is fundamentally different than that hypothesized to occur due to rapid turbulent stirring in the main heat release zone of a methane/air flame. The low-intensity heat release zone cannot be detected by common flame markers, because these markers are designed to detect key chemical reactions in the process of transitioning from hydrocarbon fuels to CO, instead of CO oxidation.

Wang et al. [65] also reported "two-stage" combustion in DNS of stratified flames. They found that the temperature-conditioned mean reaction rate of the recombination reaction CO + OH = CO_2 + H is lower than in a laminar flame in the upstream regions with low residence time. Further downstream, the conditional mean of the reaction rate becomes comparable to, or higher than, corresponding laminar flames, indicating that CO is not completely oxidized upstream and significant CO oxidation occurs further downstream. As a result of the low residence time upstream, fuel fragments such as CO and H_2 are not allowed sufficient time to be converted to CO_2 or H_2O. Consequently, they are convected downstream and fully oxidized at the flame tip.

3.4. Local combustion mode and its diagnostics

To understand the dynamics of flame propagation in highly turbulent premixed flames, diagnosis of the local combustion mode is vitally important [15,134,149,150]. Here, we aim to distinguish between the different modes of premixed combustion described in Section 2.2.1, as opposed to whether local flame segments are premixed, non-premixed, or partially premixed. Knowledge of whether a local mixture is a diffusion-enabled premixed deflagration or a chemistry-driven auto-ignition front is critical for developing physics-based combustion models. For a chemistry-driven auto-ignition front, its propagation is more sensitive to the local composition and details of finite-rate chemistry, compared to a conventional deflagration wave.

3.4.1. Budget analysis

Quantitative diagnostics of the local combustion mode are related to the balance between advection, diffusion, and reaction, as these are the three driving processes for chemical scalar dynamics. Transport budget analysis of advection, diffusion, and reaction has been widely adopted to differentiate various local dynamics [13,70,149,151]. The quantity of interest in these studies is usually a scalar, such as mass fraction of a species or progress variable, or the scalar gradient. The analysis is conventionally conducted in physical space. For example, through transport budget

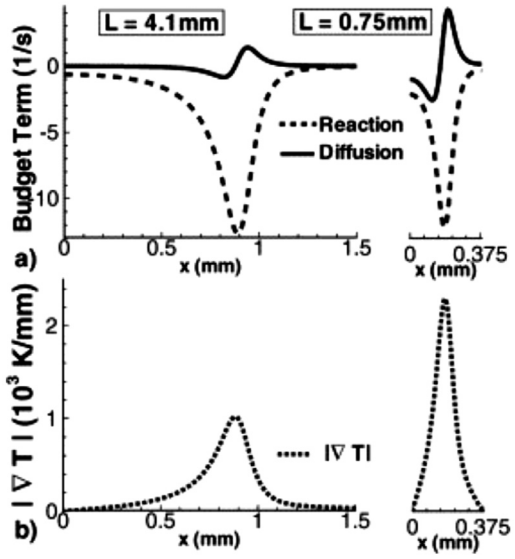


Fig. 25. Reprinted from Fig. 4 in Ref. [13] with permission of Elsevier. Transport budget analysis of Y_{H_2} for two one-dimensional hydrogen/air flames propagating into inhomogeneous temperatures. The L=4.1 mm case represents an auto-ignition front while the L=0.75 mm case represents a premixed front. Dashed line: reaction. Solid line: diffusion. Dotted line: temperature gradient.

analysis, Krisman et al. [152] demonstrated that advection is balanced by reactions under autoignitive conditions, while diffusion is balanced by reactions for deflagration waves.

However, this form of budget analysis can be ambiguous under certain complicated conditions (e.g., turbulent stratified flames). Other quantities, such as the scalar dissipation rates or temperature gradients, need to be considered to clearly identify the mode. For example, Fig. 25 shows two different scenarios in a thermally stratified H_2/air flame where two one-dimensional hydrogen/air flames propagate into inhomogeneous temperature fields whose fluctuations are characterized by different wavelength L [13]; at $L = 4.1$ mm (large wavelength limit), reactions are much larger than diffusion, whereas reactions and diffusion are more balanced at $L = 0.75$ mm (small wavelength limit). However, there is no clear distinction between combustion modes and additional information (e.g., based on the temperature gradient in Fig. 25(b)), is required to more clearly identify the auto-igniting (lower gradient at L=4.1 mm) and deflagration (higher gradient at L=0.75 mm) fronts. Hence, although transport budget analysis can provide helpful insights for differentiating auto-ignition and deflagration fronts, its effectiveness is often configuration-dependent, and the comparison between diffusion, advection and reaction sources is rather qualitative.

3.4.2. Computational singular perturbation

A more quantitative method to quantify the contributions of chemistry and diffusion to scalar evolution employs the computational singular perturbation (CSP) method [153,154]. A vector of modes can be defined for a nonlinear time-dependent ordinary differential equation (ODE) system. For a combustion system involving detailed chemistry, each element of the vector of modes is a linear combination of reaction rates for each species. The CSP method provides a refinement procedure to decouple the fast and slow modes, and subsequently identifies exhausted fast processes that can be algebraically related to other processes. It has been primarily applied in the analysis and reduction of stiff nonlinear ODE systems, to identify quasi-steady-state species, to eliminate unimportant species, and to remove stiffness.

For dynamic systems involving diffusion and advection, the CSP refinement procedure is extended to treat partial differential equations. For example, Valorani et al. [155] employed CSP to study the dynamic balances between chemistry, diffusion, and advection in a methane/air flame-vortex interaction simulation. The time scales of the local chemistry are represented by time scales of the fast and slow CSP modes, and the roles of diffusion, convection, and chemistry are compared in each CSP mode. They found that the cold reactant zone is driven by diffusion, where active chemical time scales are much slower than those of diffusion and convection. In the flame region, the driving time scales are those from chemical reactions, and the thermochemical manifold has a large dimension. Finally, downstream of the flame, the dynamics are locally controlled by slow transport processes and slow chemical kinetics.

In addition to understanding the flame structure, an importance index can be defined using the CSP concept to measure the relative importance of transport (convection and diffusion) and temperature [14]. The importance index was applied to the regions ahead of the reaction fronts in a series of HCCI-type syngas/air flames and successfully differentiated deflagration from auto-ignition. To further avoid the tolerance-based selection of individual chemical time scales, Valorani et al. [156] formulated a tangential stretching rate (TSR) method for reactive-diffusive systems, in which the relative importance of transport and chemistry were compared in the direction of the most energy-containing mode.

3.4.3. Chemical explosive model analysis

Chemical explosive mode analysis (CEMA), which is closely related to CSP, provides another approach to describing the local combustion mode and has been widely adopted in the analysis of turbulent reactive flows and other limiting phenomena in combustion, e.g., Refs. [66,158–161].

CEMA is performed through the eigen-decomposition of the chemical Jacobian ($\boldsymbol{J}_{\boldsymbol{\omega}} \equiv \partial\dot{\boldsymbol{\omega}}/\partial\boldsymbol{\psi}$), as shown by

$$\frac{\mathrm{D}\dot{\boldsymbol{\omega}}}{\mathrm{D}t} = \frac{\partial\dot{\boldsymbol{\omega}}}{\partial\boldsymbol{\psi}}\frac{\mathrm{D}\boldsymbol{\psi}}{\mathrm{D}t} = \boldsymbol{J}_{\boldsymbol{\omega}}(\dot{\boldsymbol{\omega}} + \boldsymbol{s}). \tag{20}$$

Here $\boldsymbol{\psi}$ is comprised of all species concentrations and temperature, and $\dot{\boldsymbol{\omega}}$ and $\boldsymbol{s}$ are two vectors containing the chemical and non-chemical (i.e., diffusion) source terms for all components of $\boldsymbol{\psi}$, respectively. A chemical mode is defined as an eigenmode of the chemical Jacobian $\boldsymbol{J}_{\boldsymbol{\omega}}$. Each chemical mode is associated with an eigenvalue (λ_e) and a corresponding pair of left ($\boldsymbol{b}_e$) and right ($\boldsymbol{a}_e$) eigenvectors. A chemical mode is further classified as a chemical *explosive* mode (CEM) if the real part of the associated eigenvalue, $\mathrm{Re}(\lambda_e)$, is positive [157]. The existence of a CEM indicates that the reaction rates of the mixture tend to grow exponentially along the direction of the eigenvector associated with the CEM, if the mixture is isolated in a lossless environment where all non-chemical sources are negligible; the existence of a CEM indicates that the mixture could undergo thermal runaway. However, the thermal runaway does not necessarily occur, particularly when other non-chemical effects, such as diffusion, are strong. To avoid ambiguity, the largest $\mathrm{Re}(\lambda_e)$ generally is taken to visualize the CEMs of the mixture.

Additional procedures have been developed in the past five years [12,66] to introduce transport effects into CEMA-based methods. The objective is to distinguish different local combustion modes by measuring the contributions of diffusion (φ_s) and reaction (φ_ω) on the evolution of a (purley chemical) CEM. Both φ_s and φ_ω are defined based on the projection of the diffusion ($\boldsymbol{s}$) and reaction ($\dot{\boldsymbol{\omega}}$) source terms to the left eigenvector $\boldsymbol{b}_e$ associated with CEM, respectively, namely

$$\varphi_s \equiv \boldsymbol{b}_{\boldsymbol{e}} \cdot \boldsymbol{s}, \quad \varphi_\omega \equiv \boldsymbol{b}_{\boldsymbol{e}} \cdot \dot{\boldsymbol{\omega}}. \tag{21}$$

Comparison of φ_s and φ_ω systematically quantifies the competition between molecular diffusion and chemical reactions. Note

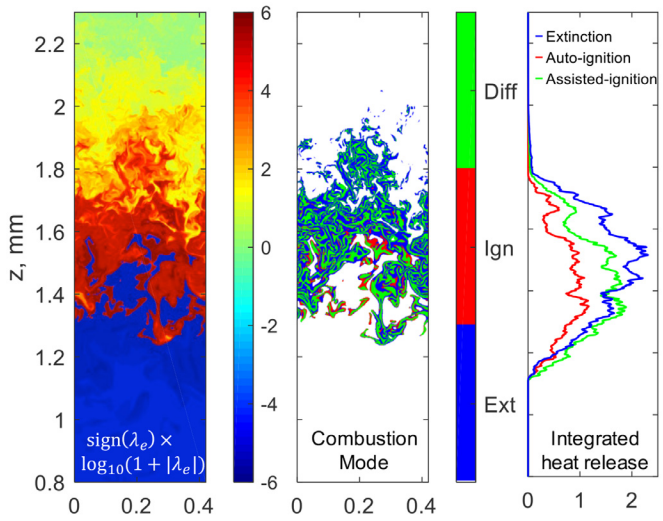


Fig. 26. Distributions of the chemical explosive mode eigenvalue, local combustion modes, and integrated HRR per unit-length in the streamwise direction attributable to the different combustion modes. Colors in eigenvalue fields indicate the value of $\text{sign}(\lambda_e) \times \log 10(1 + |\lambda_e|, 1/\text{s})$. Colors on the combustion mode fields represent the assisted-ignition (green, Diff), auto-ignition (red, Ign), and extinction modes (blue, Ext), respectively. The product zone ($\lambda_e < 0$) and the fresh reactant zone ($T < 1000$ K) are truncated in the mode plots (the middle panel). Reproduced by permission of the Combustion Institute.

that φ_ω is strictly positive. When $\varphi_s > \varphi_\omega$, energy and radicals are transported in a manner that moves the mixture towards thermal runaway, at a faster rate than chemistry drives the mixture. This is termed (diffusion) "assisted ignition" in the CEMA literature. When $-\varphi_\omega < \varphi_s < \varphi_\omega$, chemical kinetics dominate the local scalar dynamics compared to transport, which is termed "auto-ignition" in the literature. Finally, $\varphi_s < -\varphi_\omega$ indicates that heat and radical loss through diffusion adjust the mixture away from ignition faster than the chemistry moves it towards ignition; this is termed "extinction". The ratio φ_s/φ_ω then indicates the local combustion mode.

As an example, Fig. 26 shows CEMA of the combustion mode in the central plane of an upward-propagating n-dodecane/air planar jet flame at 30 atm and $\text{Ka}_{\delta,\text{K}} = 1{,}000$ [66]. The real part of the eigenvalue associated with the CEM is shown in the left panel, where the zero-crossing (i.e., the interface between positive and negative, or visually between red and blue in Fig. 26) indicates the location of ignition fronts. The local combustion modes (i.e., φ_s/φ_ω) are identified within the explosive region of the flame, as shown in the middle panel. The two diffusion-dominant modes (i.e., "extinction" mode and "assisted-ignition" mode) are frequently observed in the pre-ignition region of the turbulent flame brush, indicating a strong influence from diffusion on the ignition propensity in these flames. The integrated heat release rates, conditional on each local combustion mode and axial position, are shown in the right panel in Fig. 26. All three modes contribute significantly to the integrated heat release rate across the broad flame brush, demonstrating the intense competition between diffusion and reaction throughout this highly turbulent premixed flame.

We note that having significant heat release rate in regions identified as "extinction" is not paradoxical, given the definition of "extinction" used in this analysis. In fact, similar confusion might arise when relating the local "auto-ignition" mode with the conventional concept of "auto-ignition" in a mixture. The local "auto-ignition mode" and conventional "auto-ignition" share common characteristics in the sense that thermal runaway is a dominating factor compared to diffusion. Similarly, the "extinction mode" from CEMA describes a local and instantaneous condition where diffusion moves heat and radicals away from the ignition direction. Depending on the dynamics of the flame, the local extinction mode may or may not lead to extinction of the chemical reactions. The concepts of local extinction and local auto-ignition in turbulent flames are not unique to CEMA-based local mode analysis. In fact, local extinction/auto-ignition has been constantly delineated in turbulent combustion literature using scatter plots and budget analysis (e.g., Fig. 25). CEMA-based local mode analysis only offers a specific mathematical definition.

An experimental approach for identifying CEMs (and heat release rate) has recently been proposed [162] and assessed using DNS of the LUPJ burner [163]. Raman/Rayleigh/OH PLIF measurements were simulated, providing information on the major species, temperature, and OH concentration. Promising agreement with computational predictions was shown in measuring the location of zero-crossing of the eigenvalues of the chemical Jacobian (i.e., the location of the ignition fronts) for both laminar and turbulent flames. This introduces the possibility of performing CEMA of local combustion modes in flames that are not accessible to DNS.

3.5. Summary

As a summary, the burning rates of flames are determined by reaction and transport (including both macroscopic transport through turbulence and microscopic transport through molecular diffusion) of the mixture. The competition between the processes intensifies with increasing turbulence intensity, and the resulting local combustion modes/states diversify in these highly turbulent flames. A few takeaway points are summarized below:

1. In physical space, highly turbulent premixed flames can be locally thinned or thickened. Preheat zones are shown to be reactive, enabled by pyrolysis reactions, differential diffusion, local extinction, and intense turbulent advection.
2. Non-unity Lewis number effects persist in these highly turbulent premixed flames, and are particularly noticeable in local flame dynamics, such as local heat release rates [69,86] and responses to stretch [76], etc. Consequently, the choice of molecular transport models can have a significant impact, at least on local flame dynamics.
3. Reaction rates are more varied in highly turbulent flames compared to their laminar counterparts, for example as demonstrated in Refs. [67,69,86,132], due to the enlarged thermochemical state space created by turbulence-chemistry interactions. Chemical pathways remain similar between different conditions, although more reactions are consequential to a significant level for turbulent flames. Due to the optimization process used to develop chemical kinetic models, the task of identifying missing chemical pathways in reduced chemical mechanisms remains challenging.
4. Fuel consumption and heat release rates are not closely correlated in highly turbulent premixed flames, as a result of fuel pyrolysis [66,67,123], differential diffusion [69,86,131], local extinction [66], and turbulent advection [65,111]. Caution should be taken when employing fuel consumption rates as a surrogate for heat release rate, either experimentally or computationally.
5. For high Karlovitz number turbulent premixed flames, local flame characteristics are diversified and adjusted to local turbulence and chemistry conditions. Such adjustments can manifest in terms of local flame thickness, flame surface density, and frequency of local limit conditions, etc. Consequently, many state-of-the-art turbulent combustion models can still provide reasonable predictions of flames in this regime, although prior knowledge of local conditions and the ability to adjust to these conditions are required to attain sufficient accuracy.

4. Turbulence structure and dynamics

The discussion in Section 3 focused on the impact of turbulence on flame structure and dynamics, primarily through the modification of scalar gradients controlling diffusion and, consequently, the complexity of the thermochemical state space and reaction rates. However, chemical reactions also influence the turbulent flow, both by altering fluid transport properties and by coupling thermal and mechanical energies. This section reviews current knowledge regarding the impact of combustion on turbulence structure and dynamics in highly turbulent premixed flames. In the following, we outline both *kinematic* and *dynamic* properties of turbulence. Kinematic properties pertain to *how* the flow is structured and moves, including both single and multi-point statistics of velocity (e.g., turbulence kinetic energy) and velocity gradient (e.g., vorticity and strain rate) quantities. Spectra and scale-dependent turbulence characteristics can also be considered kinematic properties. The *dynamics* of turbulence provide an explanation for *why* the flow behaves as it does, in particular revealing the physical mechanisms by which the flame affects the turbulent flow. For example, dynamics encompasses the study of terms found in the turbulence kinetic energy transport equation, in either physical or spectral space, as well as the study of the coupled evolution of the vorticity and strain rate, including alignments between the vorticity and strain rate eigenvectors. We also discuss the status and outlook for universal theories of turbulence during highly turbulent premixed combustion, with a particular focus on the applicability of classical theories developed for non-reacting turbulence.

It should be noted that we focus here specifically on the properties of turbulence for highly turbulent premixed combustion. It has been established that there are substantial effects of the flame on turbulence at lower intensities, and an exhaustive review of knowledge in this area has been provided by Lipatnikov & Chomiak [9]. By contrast, we are just now beginning to understand the properties of turbulence at high intensities, and how these properties vary as the turbulence intensity (or Karlovitz number) increases. It should also be noted that, in the following discussion, we devote substantial attention to the properties of non-reacting (i.e., constant density and constant viscosity) turbulence. It will be seen from this review that properties of non-reacting turbulence are of more than simply academic interest since, in many respects, the characteristics of turbulence for highly turbulent combustion are similar to those found in non-reacting flows.

4.1. Turbulence kinetic energy, stresses, and fluxes

For any high-Re_ℓ turbulent flow, there is substantial spatial and temporal complexity, and fluid mixing is enhanced compared to laminar flows. This complexity can be quantified using second-order, single-point statistics, including the turbulence kinetic energy, turbulent stresses, and turbulent fluxes of various scalar quantities, such as the temperature and reactant mass fraction. In the following, we summarize the current understanding of these statistics in highly turbulent premixed reacting flows. It should be noted that these quantities, including their dynamics, are also frequently studied using multi-scale and spectral analyses; we will discuss these characteristics in Section 4.3.

4.1.1. Turbulence kinetic energy

The intensity of turbulence is often quantified using the turbulence kinetic energy $k \equiv (1/2)\overline{u_i' u_i'}$, where $u_i' = u_i - \overline{u}_i$ and $\overline{(\cdot)}$ is an appropriately defined average (e.g., an ensemble average). In many studies of premixed combustion, the ensemble averaged k is replaced instead by the Favre-averaged definition of turbulence kinetic energy, $\widetilde{k} \equiv (1/2)\widetilde{u_i'' u_i''}$, where $u_i'' = u_i - \widetilde{u}_i$ and $\widetilde{\psi} = \overline{\rho\psi}/\overline{\rho}$ denotes a Favre-average of a generic variable ψ. Favre averages are often used to simplify the analysis of governing equations in compressible and reacting flows, due to the considerable temporal and spatial variations in density found in such flows. In some cases, the turbulence intensity is quantified using a single component of u_i'', for example the root mean square intensity $\widetilde{(u_1'')^2}^{1/2}$.

The transport equation for $\widetilde{k}$ is obtained from the trace of the transport equation for the single-point momentum flux $\widetilde{u_i'' u_j''}$ as [164]

$$\frac{\partial}{\partial t}\left(\overline{\rho}\widetilde{k}\right) + \frac{\partial}{\partial x_k}\left(\overline{\rho}\widetilde{u}_k\widetilde{k}\right) = -\overline{\rho}\left(\widetilde{u_k'' u_i''}\right)\frac{\partial \widetilde{u}_i}{\partial x_k} - \overline{u_i''\frac{\partial p}{\partial x_i}} + \frac{\partial}{\partial x_k}\left[\overline{u_i''\tau_{ik}} - \frac{\overline{\rho}}{2}\left(\widetilde{u_k'' u_i'' u_i''}\right)\right] - \overline{\tau_{ik}\frac{\partial u_i''}{\partial x_k}}. \tag{22}$$

The first term on the right-hand side represents kinetic energy production by Favre-averaged velocity gradients, the second term represents the velocity-pressure gradient interaction, the third term represents viscous and turbulent transport, and the last term represents viscous dissipation. Although the production and dissipation terms are roughly equal in magnitude across a wide range of flows, the balance of the various terms Eq. (22) can nevertheless vary substantially, particularly in premixed reacting flows where the velocity-pressure gradient term can be significant. This term can be rewritten as

$$\overline{u_i''\frac{\partial p}{\partial x_i}} = \frac{\partial}{\partial x_k}\left(\overline{u_k'' p}\right) - \overline{p\frac{\partial u_k''}{\partial x_k}}, \tag{23}$$

where the second term on the right-hand side represents pressure-dilatation effects, which are present only in compressible flows where $\partial u_k''/\partial x_k \neq 0$. The first term on the right in Eq. (23) is present even in incompressible non-reacting flows and represents pressure transport; this term is often combined with the viscous and turbulent transport terms in Eq. (22).

A number of studies have examined the properties of the turbulence kinetic energy during premixed combustion spanning a wide range of turbulence intensities, including conditions characterized by high $\mathrm{Ka}_{\delta,\mathrm{K}}$. Using DNS of statistically planar flames, Chakraborty et al. [166] and Wang & Abraham [165] showed that $\widetilde{k}$ decreases monotonically across the flame brush at high $\mathrm{Ka}_{\delta,\mathrm{K}}$, where $\mathrm{Ka}_{\delta,\mathrm{K}} = 0.54$ and 13 in Ref. [166] and 1.1–49 in Ref. [165]. For example, Fig. 27 shows the decrease in $\widetilde{k}$ as a function of the planar averaged progress variable [165]. This decrease was found by both Chakraborty et al. [166] and Wang & Abraham [165] to be due to the dominance of viscous dissipation and viscous transport as the kinematic viscosity increases across the flame. Wang & Abraham [165] used a scaling analysis to further show that both viscous transport and dissipation vary as the square of $\mathrm{Ka}_{\delta,\mathrm{K}}$, with the production and pressure-dilatation terms having weaker scalings with $\mathrm{Ka}_{\delta,\mathrm{K}}$. For lower values of $\mathrm{Ka}_{\delta,\mathrm{K}}$, pressure-velocity coupling terms, including the pressure-dilatation, were found to be more significant in the overall dynamics, but the magnitudes of these terms weakened relative to the production and dissipation terms as $\mathrm{Ka}_{\delta,\mathrm{K}}$ increased. It is important to note, however, that there is no mean shear in these statistically planar flames that would lead to the production of turbulence kinetic energy via the first term on the right side of Eq. (22). These results are also statistical, and it is still possible to have locally and instantaneously large values of the pressure-dilatation, even if the average effect is small.

Mean shear is present in jet flames, for example the planar premixed hydrogen-air jet studied using DNS by MacArt et al. [164,167] and Lee et al. [168]. In these jet configurations, the stress components $\widetilde{u_\alpha'' u_\alpha''}$ (summation over repeated Greek indices is not implied) were each shown to decrease across the flame as a whole, consistent with results for the planar configuration studied

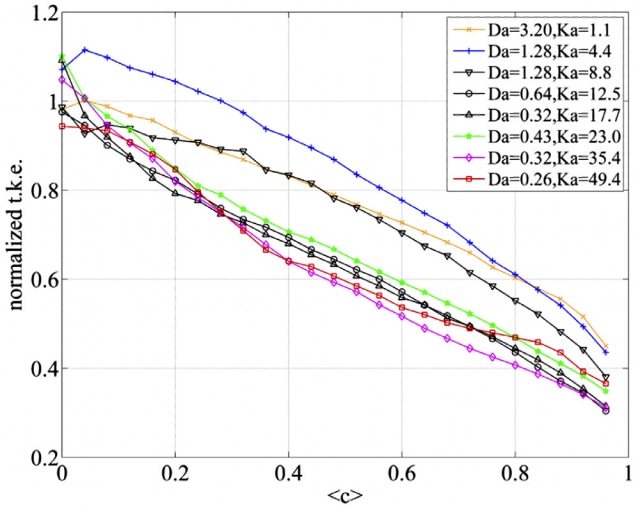


Fig. 27. Favre-averaged turbulence kinetic energy $\widetilde{k}$ as a function of planar-averaged reaction progress variable for different $\mathrm{Ka}_{\delta,\mathrm{K}}$ and $\mathrm{Da}_{\ell,\delta}$ in a statistically planar lean methane-air premixed flame studied using DNS. Reprinted from Ref. [165] with permission of AIP Publishing.

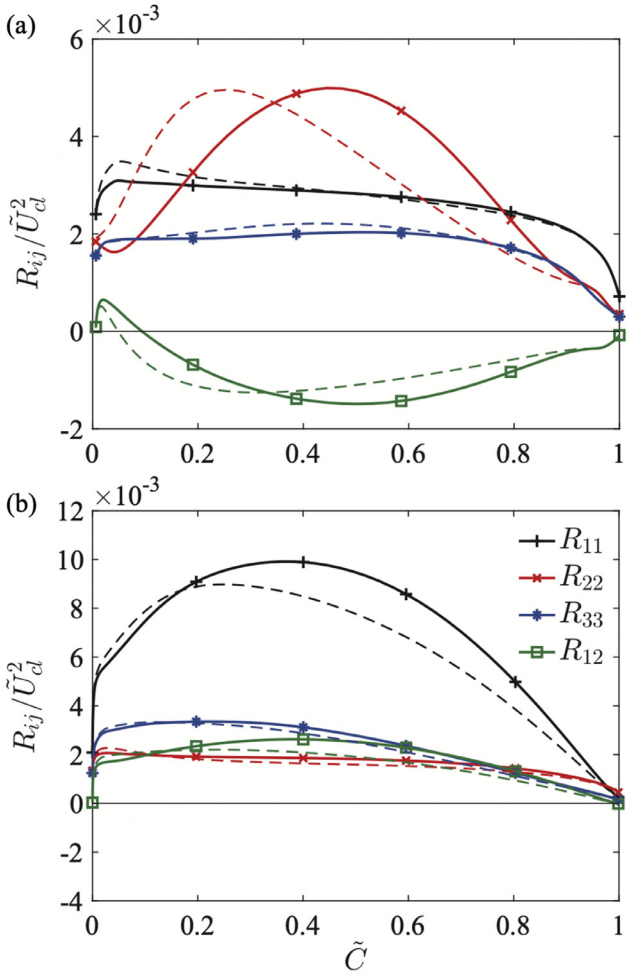


Fig. 28. Turbulent stresses $\widetilde{u_i''u_j''}$ (solid lines) and $\overline{u_i'u_j'}$ (dashed lines) as a function Favre-averaged reaction progress variable for a planar premixed hydrogen-air jet flame at (a) low and (b) high $\mathrm{Ka}_{\delta,\mathrm{K}}$ (corresponding to in-flame Karlovitz numbers of 3.7 and 54, respectively). The ij component of the stress tensor is labeled as R_{ij}. Reprinted from Ref. [168] with permission of Elsevier.

by Wang & Abraham [165]. However, there also was an increase in $\widetilde{u_\alpha''u_\alpha''}$ and, hence, $\widetilde{k}$ for intermediate values of the Favre-averaged progress variable $\widetilde{c}$ (see Fig. 28). This increase, which was present for both low and high values of $\mathrm{Ka}_{\delta,\mathrm{K}}$ (corresponding to in-flame Karlovitz numbers of 3.7 and 54, respectively), had different dynamical origins in each case, as shown in Fig. 29 [164]. In particular, for low $\mathrm{Ka}_{\delta,\mathrm{K}}$, each term in the transport equation for $\widetilde{k}$ was substantially non-zero, except for the turbulence and viscous transport terms, and the velocity-pressure gradient term was found to be dominant in the overall dynamics. However, for high $\mathrm{Ka}_{\delta,\mathrm{K}}$, the velocity-pressure gradient term was found to be negligible, with the dominant balance occurring between the production and viscous dissipation terms. This is the same balance observed in many non-reacting jet flows, where the mean shear results in large kinetic energy production that is primarily balanced by dissipation.

Consistent with the premixed jet cases examined by MacArt et al. [164,167] and Lee et al. [168], the DNS study of a stratified premixed methane-air jet flame by Wang et al. [65] also shows that the turbulent velocity u' is largest for intermediate values of the Favre-averaged progress variable $\widetilde{c}$, with the peak shifting to larger values of $\widetilde{c}$ with greater downstream distance (see Fig. 30). At all downstream locations, the final value of u' for $\widetilde{c} \to 1$ is smaller than the initial value for $\widetilde{c} \to 0$, and this disparity increases in magnitude with greater downstream distance. Although kinetic energy transport terms were not explicitly calculated in this study, it can again be inferred based on the results from MacArt et al. [164] that the increase in turbulence intensity for intermediate values of $\widetilde{c}$ corresponds to a dominance of shear-influenced production for intermediate values. It should be noted that Galeazzo et al. [169] show radial profiles of the axial velocity variance, which is connected to the turbulence kinetic energy, for the same high $\mathrm{Ka}_{\delta,\mathrm{K}}$ stratified premixed jet flame as that studied by Wang et al. [65]. The variance in this study peaks off the centerline of the jet, and results from LES with tabulated flamelets are shown to agree closely with corresponding DNS results for the same flow [65]. A similar peak in the variance was also observed experimentally by Coriton et al. [170] for a partially premixed dimethyl ether/air jet flame.

Taken together, these studies indicate that the turbulence intensity, reflected in the value of the turbulence kinetic energy, $\widetilde{k}$, generally decreases across premixed planar and jet flames at high $\mathrm{Ka}_{\delta,\mathrm{K}}$ conditions, due primarily to the increase in viscous dissipation resulting from heat release and the corresponding increase in viscosity. In flows with strong mean shear, such as jets, dissipation is balanced primarily by production due to mean velocity gradients. A similar importance of mean shear has been observed for the propagation of flames in channels [171] and boundary layers [172]. Although velocity-pressure gradient effects can be dominant for low $\mathrm{Ka}_{\delta,\mathrm{K}}$, this effect contributes increasingly weakly to the overall dynamics, as compared to production and dissipation, with increasing $\mathrm{Ka}_{\delta,\mathrm{K}}$. As such, the dynamics of the turbulence kinetic energy increasingly approach that of a corresponding non-reacting flow as $\mathrm{Ka}_{\delta,\mathrm{K}}$ increases, although locally and instantaneously large magnitudes of heat release effects such as the pressure-dilatation correlation may still be present. This is particularly true for higher turbulence intensities where the internal intermittency (discussed more in subsequent sections) is greater, leading to potentially large values of gradient quantities relative to their means.

In contrast to these results for premixed planar and jet flames, in highly turbulent Bunsen flames relatively little change has been observed in the turbulence kinetic energy across the flame. In particular, despite the tendency for the turbulence kinetic energy to generally decrease across premixed planar and jet flames, Wabel et al. [173] did not observe a decrease in the turbulence kinetic energy across the preheat layer of a highly turbulent premixed pi-

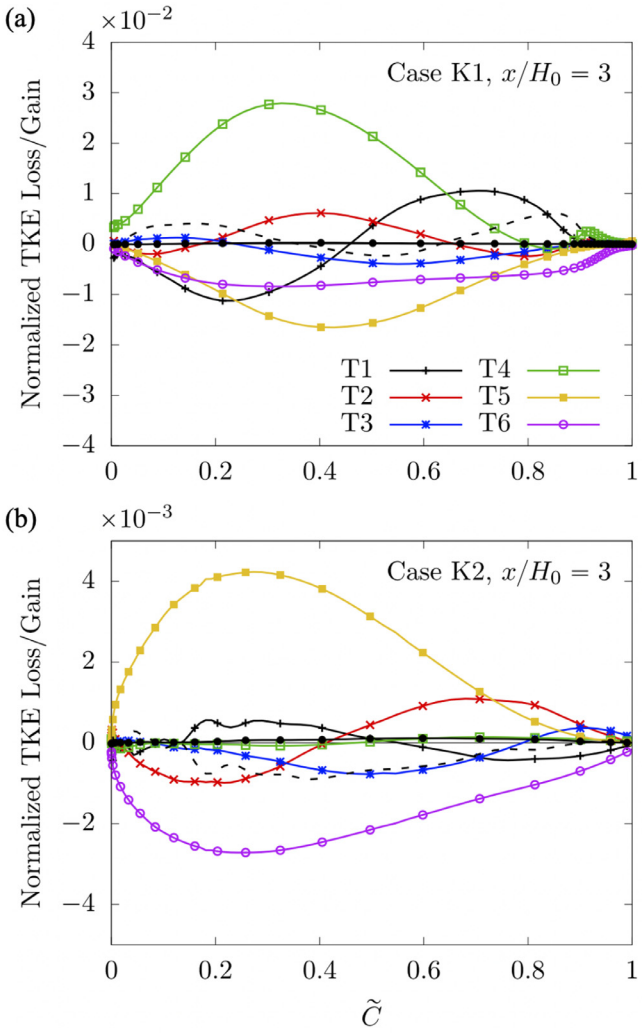


Fig. 29. Terms in the transport equation for the turbulence kinetic energy $\tilde{k}$ as a function Favre-averaged reaction progress variable for a planar premixed hydrogen-air jet flame at (a) low and (b) high $Ka_{\delta,K}$ (corresponding to in-flame Karlovitz numbers of 3.7 and 54, respectively). The terms shown are the mean convective transport (T1), turbulent transport (T2), viscous transport (T3), velocity-pressure gradient correlation (T4), production by the mean shear (T5), and viscous dissipation (T6). Black dashed lines in each panel indicate the residual. Reprinted from Ref. [164] with permission of Elsevier.

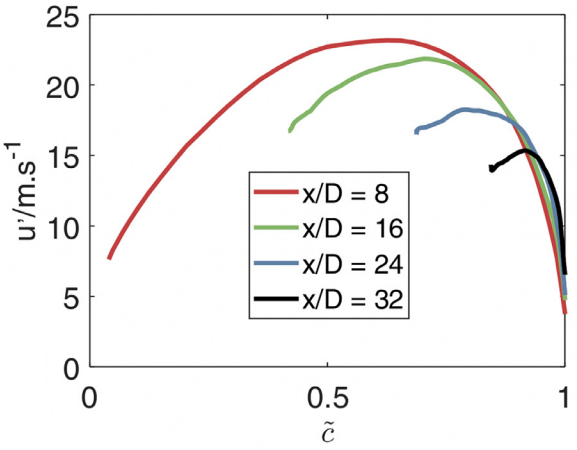


Fig. 30. Turbulent velocity u' as a function of the Favre-averaged reaction progress variable at different downstream distances, x/D, for DNS of a stratified premixed methane-air jet flame. Reprinted from Ref. [65] with permission of Elsevier.

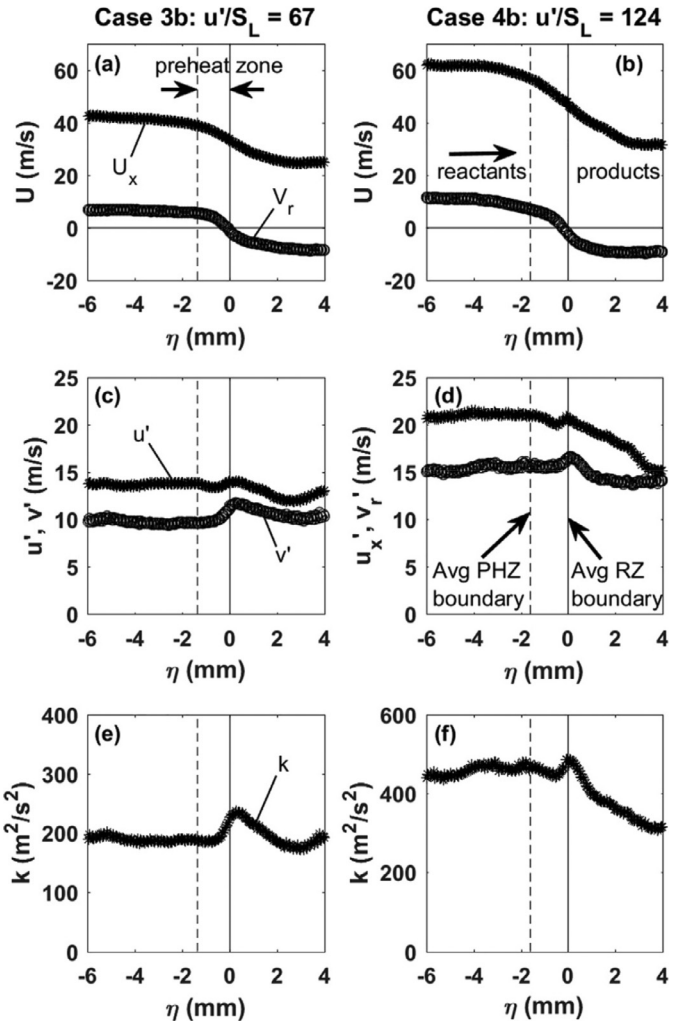


Fig. 31. Turbulence statistics conditioned on distance from the reaction zone, η, showing the conditional mean velocity (a,b), conditional RMS velocity fluctuations (c,d), and the conditional turbulence kinetic energy k (e,f) for a highly turbulent premixed Bunsen flame. Preheat and reaction zone (PHZ and RZ, respectively) boundaries are indicated by dashed and solid vertical lines, respectively. Reprinted from Ref. [173] with permission of Elsevier.

loted Bunsen flame (see Fig. 31). This difference may be due to the higher free-stream turbulence levels in this case, although an increase in the integral scale was observed through the flame, suggesting that energy was shifted to larger scales, even if the overall kinetic energy was largely unaffected.

There is also evidence for a dependence on the fuel type in the kinetic energy dynamics. In particular, Paxton et al. [174] examined fuel effects on the turbulence kinetic energy and shear stress for premixed jet flames at high intensities, finding that these quantities decrease more rapidly along the jet centerline for methane-air mixtures than for mixtures with larger hydrocarbon fuels. Moreover, the fuel dependence was found to become more pronounced as the Reynolds number increased. This study additionally showed that the effects of heat release can be partially accounted for in the scaling of the shear layer thickness when using a density-based momentum diameter, and that there is a fuel dependence of the shear layer structure. The underlying physical reasons for this fuel dependence, including the role played by changes in the diffusive transport of chemical species for different fuels, remains an important area for further research.

Finally, it should be noted that the comparison of ensemble- and Favre-averaged quantities in Fig. 28 from Lee et al. [168] in-

dicates that the difference between these two types of averages becomes less pronounced as $\mathrm{Ka}_{\delta,\mathrm{K}}$ increases. Thus, not only are the kinetic energy dynamics increasingly similar to non-reacting flows as $\mathrm{Ka}_{\delta,\mathrm{K}}$ increases, but density weighting also becomes less significant such that $\widetilde{u_i''u_j''} \rightarrow \overline{u_i'u_j'}$ as $\mathrm{Ka}_{\delta,\mathrm{K}}$ increases.

4.1.2. Turbulent stresses

The turbulent transport, or "flux", of a generic quantity ψ can be quantified using the single-point, second-order statistic $\overline{u_i'\psi'}$ (in terms of an ensemble or other appropriately defined average) or as $\widetilde{u_i''\psi''}$ (in terms of a Favre average). For example, $\widetilde{u_i''u_j''}$ are turbulent fluxes of velocity u_j in the ith direction (this quantity is often referred to as the "turbulent stress"), and $\widetilde{u_i''Y_\beta''}$ are turbulent fluxes in the ith direction of the Y_β mass fraction. These fluxes also appear as unclosed terms in the ensemble- or Favre-averaged governing equations for reacting flows. For example, from the Navier-Stokes equation in Eq. (2), the transport equation for the Favre-averaged velocity $\widetilde{u}_i$ is given by

$$\frac{\partial}{\partial t}(\overline{\rho}\widetilde{u}_i) + \frac{\partial}{\partial x_j}\left(\overline{\rho}\widetilde{u}_i\widetilde{u}_j\right) = -\frac{\partial \overline{p}}{\partial x_i} + \frac{\partial \overline{\tau}_{ij}}{\partial x_j} - \frac{\partial}{\partial x_j}\left(\overline{\rho}\widetilde{u_i''u_j''}\right), \tag{24}$$

where the last term on the right-hand side is the unclosed turbulent stress. A similar unclosed term appears in the transport equation for $\widetilde{Y}_j$.

Given the physical and modeling importance of turbulent stresses, substantial focus has been placed on quantifying their properties in different flows. Fig. 28 shows four components of the stress tensor $\widetilde{u_i''u_j''}$ for a premixed methane-air jet flame for both low and high $\mathrm{Ka}_{\delta,\mathrm{K}}$ [164,168]. As noted in the previous section, the on-diagonal components of this tensor increase for intermediate values of $\widetilde{c}$ and decrease overall across the flame, but Fig. 28 further shows that the shear stress component $\widetilde{u_1''u_2''}$ changes sign from being predominantly negative for low $\mathrm{Ka}_{\delta,\mathrm{K}}$ to predominantly positive for high $\mathrm{Ka}_{\delta,\mathrm{K}}$. Lee et al. [168] show that this change is due to differences in the velocity-pressure gradient effect through the flame. In particular, by decomposing this term into contributions from the fluctuating and mean pressure, Lee et al. [168] show that the fluctuating pressure component dominates at high $\mathrm{Ka}_{\delta,\mathrm{K}}$ and acts to isotropize the turbulence, whereas the mean pressure component dominates for low $\mathrm{Ka}_{\delta,\mathrm{K}}$ where dilatation by the flame is significant relative to turbulence-induced fluctuations in the flow.

There are two primary implications of this result. The first is that the turbulence is expected to be more anisotropic due to effects from the flame at low $\mathrm{Ka}_{\delta,\mathrm{K}}$. This is a result that has been demonstrated in a number of reacting flow studies using a variety of metrics. In Section 4.2 we will comment on the generation of turbulence anisotropy in the context of vorticity characteristics, and a similar increase in the anisotropy within the flame was first observed for a premixed Bunsen flame by Steinberg et al. [175]. More recently, MacArt et al. [164] have shown using the Favre-averaged anisotropy tensor $\widetilde{a}_{ij} = \widetilde{u_i''u_j''}/\widetilde{k} - 2\delta_{ij}/3$ that the turbulent stress tensor is anisotropic. Through an analysis of barycentric maps of $\widetilde{a}_{ij}$, MacArt et al. [164] show that turbulence is anisotropic within the flame for both low and high $\mathrm{Ka}_{\delta,\mathrm{K}}$, but after the flame, only the high $\mathrm{Ka}_{\delta,\mathrm{K}}$ case returns to an isotropic state. The tendency towards isotropy for high $\mathrm{Ka}_{\delta,\mathrm{K}}$ noted by MacArt et al. [164], was also demonstrated from an analysis of small-scale (i.e., SFS) stresses by Klein et al. [176] for a statistically planar hydrogen-air premixed flame. For lower $\mathrm{Ka}_{\delta,\mathrm{K}}$, increased anisotropy was again observed, which was once more attributed to the effects of dilatation by the flame.

The second primary implication of the change in stress behavior between low and high $\mathrm{Ka}_{\delta,\mathrm{K}}$ conditions is related to the applicability of the Boussinesq, or gradient transport, hypothesis that is the basis of many closure models for LES and RANS simulations. In the context of Favre-averaged quantities, this hypothesis states that $\widetilde{u_i''\psi''} \propto -\partial\widetilde{\psi}/\partial x_i$. That is, the turbulent flux of an arbitrary quantity ψ in the ith direction occurs along the direction of decreasing $\widetilde{\psi}$ (given by the gradient). Through an examination of the alignments of velocity (i.e., turbulent stress) and scalar fluxes, MacArt et al. [164] showed that, at high $\mathrm{Ka}_{\delta,\mathrm{K}}$, the gradient transport hypothesis is approximately valid (or, at least, no less valid than in a corresponding non-reacting turbulent jet flow). Conversely, for low $\mathrm{Ka}_{\delta,\mathrm{K}}$, the turbulent scalar flux and turbulent stresses are substantially misaligned with the mean gradients, indicating counter-gradient transport and invalidating the Boussinesq hypothesis. This is reflected in conditional statistics of the turbulent shear stress, which reverses sign between the low and high $\mathrm{Ka}_{\delta,\mathrm{K}}$ cases [164,167,168] (see also Fig. 28).

It is emphasized that, although the Boussinesq hypothesis is approximately valid in premixed jet flames at high $\mathrm{Ka}_{\delta,\mathrm{K}}$, it should not be assumed that this hypothesis is valid across all high $\mathrm{Ka}_{\delta,\mathrm{K}}$ premixed reacting flows. The more appropriate understanding of this result is that the Boussinesq hypothesis becomes *as valid* in these high $\mathrm{Ka}_{\delta,\mathrm{K}}$ flows as it is in the corresponding non-reacting flows. However, there are many non-reacting flows (e.g., rapidly strained flows or flows with high geometric curvatures) that also do not conform to the Boussinesq hypothesis [177]. It is unlikely that the addition of reactions to such flows would improve this agreement, particularly given the reduced applicability of the Boussinesq hypothesis observed in low $\mathrm{Ka}_{\delta,\mathrm{K}}$ premixed jet flames.

4.1.3. Turbulent scalar fluxes

As noted previously, the turbulent flux of a scalar quantity ψ, written as either $\overline{u_i'\psi'}$ or $\widetilde{u_i''\psi''}$ for ensemble and Favre averages, respectively, provides a quantitative measure of the strength of turbulent transport of ψ in the ith direction. In studies of turbulent premixed combustion across a range of turbulence intensities, it has been common, in particular, to study the turbulent transport of species mass fractions, Y_β, and the combustion progress variable, c. In addition to providing fundamental insights into the strength and direction of turbulent mixing, these fluxes also appear as unclosed terms in scalar model equations for RANS and LES (in the latter case, the average used to compute the scalar fluxes is replaced by an appropriate low-pass filter).

Due to their relevance to both RANS and LES, much of the research on scalar fluxes for highly turbulent conditions has, to date, focused primarily on the appropriate way in which to model these quantities, with a particular emphasis on determining the validity of the gradient transport, or Boussinesq, hypothesis for different flows and conditions. In general, the gradient transport hypothesis has been found to provide poor predictions for scalar fluxes in premixed flames at low $\mathrm{Ka}_{\delta,\mathrm{K}}$ (see, e.g., Refs. [178,179]), but the agreement improves as $\mathrm{Ka}_{\delta,\mathrm{K}}$ increases. Klein et al. [176] examined SFS scalar fluxes (for species mass fraction scalars) in statistically planar hydrogen-air premixed flames across a range of both low and high $\mathrm{Ka}_{\delta,\mathrm{K}}$ (spanning Karlovitz numbers from 0.75 to 126), finding counter-gradient transport across all $\mathrm{Ka}_{\delta,\mathrm{K}}$, although the correspondence with the gradient transport hypothesis increased as $\mathrm{Ka}_{\delta,\mathrm{K}}$ increased. It should be noted that Ranjan et al. [179] observed substantial counter-gradient transport even at high initial $\mathrm{Ka}_{\delta,\mathrm{K}}$, although for a statistically planar premixed flame interacting with decaying isotropic turbulence, where the local $\mathrm{Ka}_{\delta,\mathrm{K}}$ decreases in time as the turbulence decays.

MacArt et al. [164] showed that conditionally averaged cross-stream fluxes of the water mass fraction were generally positive for low $\mathrm{Ka}_{\delta,\mathrm{K}}$ and negative for high $\mathrm{Ka}_{\delta,\mathrm{K}}$, with the former corresponding to counter-gradient transport. Through an analysis of the transport equation for the flux $\widetilde{u_i''Y_\beta''}$, it was shown that this change

in behavior was due to the changing behavior of the mean scalar gradient and mean velocity gradient production terms as $Ka_{\delta,K}$ increased. MacArt et al. [164] additionally examined the variance of the scalar mass fraction, observing that the dynamics of $\widetilde{Y''^2_{H_2O}}$ are dominated by heat release from the flame at low $Ka_{\delta,K}$, while the primary balance is between the production by the mean scalar gradient and dissipation at high $Ka_{\delta,K}$, in correspondence with non-reacting scalar variance dynamics.

Ultimately, although the properties of turbulent scalar fluxes do, in general, approach those of non-reacting passive scalar fluxes as $Ka_{\delta,K}$ increases, the gradient transport hypothesis remains of dubious validity at high $Ka_{\delta,K}$ and across all regions of a premixed flame. As such, further study of the dynamics of these fluxes, such as that performed by MacArt et al. [164], remains an important direction of research, particularly across different flows and spanning a wider range of conditions. The improved understanding resulting from such studies may result in the more widespread use in RANS and LES approaches of differential second-order moment closures that do not rely on algebraic gradient transport hypotheses.

4.2. Vorticity, strain rate, and scalar gradients

Velocity gradient quantities, and the vorticity and strain rate in particular, have received substantial focus in studies of both reacting and non-reacting turbulent flows. There are many reasons for this focus, including:

1. Due to the linear wavenumber weighting associated with gradients in spectral space, velocity gradient quantities more directly represent small-scale properties than velocities alone;
2. In many flows, vorticity and strain rate magnitude fields are punctuated by coherent and spatially localized structures (e.g., vortex "tubes" and "sheets") that provide potential building blocks of turbulence;
3. Statistics, and PDFs in particular, of the vorticity and strain rate reveal the internal intermittency associated with high Reynolds number turbulent flows;
4. The formation of small-scale fluid motions by nonlinear processes can be directly examined, in isolation from purely convective changes, through the vortex stretching term that appears in the vorticity transport equation;
5. The effects of chemical heat release on turbulence can be directly studied by examining dilatation and baroclinic torque terms in the vorticity transport equation;
6. The vorticity and strain rate have direct impacts on the dynamics of scalar gradients, which is particularly significant in reacting flows due to the connection between scalar gradients and flame structure (as was also discussed in Section 3).

Although each of these reasons provide motivation for the study of velocity gradients in premixed reacting flows, the last reason, in particular, allows the explicit study of interactions between turbulence and flame structure in highly turbulent premixed combustion. The local scalar gradient χ_i can be used to express a local flame normal direction as $n_i = \chi_i/\chi$, where χ is the scalar gradient magnitude, and the local flame width, δ_t can be expressed in terms of χ using Eq. (19). Given this connection between vorticity, strain rate, and scalar gradients, we begin this section with a discussion of the properties and dynamics of scalar gradients in highly turbulent premixed flames.

4.2.1. Scalar gradients

The gradients of thermochemical scalars are important for understanding the local, instantaneous structure of premixed flames, the influence of turbulence on the flame structure and dynamics, and the origins of thermochemical complexity under highly turbulent conditions. Thermochemical scalar gradients are also fundamental to understanding the scalar dissipation rate, which must be modeled in many RANS and LES approaches to simulating premixed combustion. These gradients have consequently been extensively studied over a range of premixed flame conditions, including high turbulence intensities.

The orientation of n_i in highly turbulent premixed combustion has been explored in several studies, including those by Kim & Pitsch [180], Chakraborty et al. [181–183], Hartung et al. [184], and Hamlington et al. [128]. However, most such studies have focused primarily on the orientation of n_i with respect to the eigenvectors of the fluid dynamic strain rate tensor, S_{ij}, and relatively few have examined distributions of n_i or their connection to wrinkling. The alignments of n_i with the strain rate eigenvectors, as well as their physical significance, will be discussed in more detail below, but it is worth noting that distributions of observed orientations of n_i have been found to become more broad as the turbulence intensity increases [128]. For premixed flames in the presence of isotropic turbulence, in particular, the flame orientation becomes increasingly isotropic as the intensity increases [128], indicating that the flame increasingly reflects properties of the underlying turbulence.

The characteristics of δ_t have also been explored in a number of studies of highly turbulent premixed combustion. Kamal et al. [185] examined the scalar dissipation rate, which is related to the inverse of δ_t, in swirling bluff body stabilized premixed flames over a range of turbulence intensities, including high intensities. It was found that diffusive scalar structures become more broadly distributed as the turbulence intensity increases. This results, in particular, in higher probabilities of thin diffusive regions at low turbulence intensity, and broader distributions of diffusive widths at higher turbulence intensity; this range of widths was also discussed in Section 3.1. Similarly, Kamal et al. [186] examined temperature gradients and associated scalar dissipation rates in bluff-body stabilized stratified turbulent premixed methane-air flames, finding that gradients were reduced compared to the corresponding laminar flow, indicating a thickening of the flame (i.e., an increase in δ_t) compared to corresponding laminar strained and unstrained flames). Magnotti & Barlow [187] examined progress variable gradients and dissipation rates in a high-shear premixed methane-air bluff-body stabilized flame, revealing a decrease in gradient magnitudes through the flame and a corresponding increase in the flame thickness. For a fuel-lean flame this broadening was observed in the preheat zone only, but for a fuel rich flame the broadening was observed in both the preheat and reaction zones.

Numerical studies have largely confirmed these experimental results. Kim & Pitsch [180], Sankaran et al. [80,188], Chakraborty et al. [189], and Hamlington et al. [128] all found that δ_t was greater than the corresponding local laminar flame width in the preheat zone of premixed flames, as compared to the reaction zone, and that these values increased in all regions of the flame as the turbulence intensity increased. This is indicative of local flame broadening by turbulence, although the continued correspondence between the turbulent and laminar reaction zone widths, even for high turbulence intensities, was unexpected. This resilience of the reaction zone to strong turbulence has been explained [128,182] by the reduction of vorticity and strain rate magnitudes by dilatation and the increase in viscous dissipation associated with heat release by the flame, as will be demonstrated in more detail in the next section. Distributions of the local flame width were also examined by Chaudhuri et al. [129] and Hamlington et al. [190], showing that a wide range of flame widths, both thinner and broader than the corresponding laminar flame, are found in highly turbulent conditions (see also Fig. 14).

The dynamics of n_i and δ_t are fundamentally governed by the dynamics of χ_i, which evolves according to the transport equation

$$\frac{\mathrm{D}\chi_i}{\mathrm{D}t} = -\chi_j S_{ij} - \frac{1}{2}\epsilon_{ijk}\chi_j\omega_k + \frac{\partial}{\partial x_i}\left(\frac{\mathrm{D}\psi}{\mathrm{D}t}\right), \tag{25}$$

where $\mathrm{D}\psi/\mathrm{D}t$ appearing in the last term is obtained from Eq. (18). There are thus direct interaction terms between χ_i, the fluid dynamic strain rate S_{ij} given in Eq. (6), and the vorticity $\omega_i = \epsilon_{ijk}\partial u_k/\partial x_j$, where ϵ_{ijk} is the cyclic permutation tensor. The presence of the cross product of χ_i and ω_i means that the vorticity will act to rotate the flame surface normal, which is aligned with χ_i, in a direction that is orthogonal to ω_i. This explicit vorticity interaction term is, however, not present in the transport equation for χ, which is most directly connected to the flame width δ_t, namely

$$\frac{\mathrm{D}\chi}{\mathrm{D}t} = -\frac{\chi_i\chi_j}{\chi}S_{ij} + \frac{\chi_i}{\chi}\frac{\partial}{\partial x_i}\left(\frac{\mathrm{D}\psi}{\mathrm{D}t}\right). \tag{26}$$

The vorticity ω_i does not explicitly appear in the above equation, indicating that only S_{ij} is responsible for direct changes in the scalar gradient magnitude. From these transport equations, we can then derive transport equations for n_i and δ_t as

$$\frac{\mathrm{D}n_i}{\mathrm{D}t} = P_{ij}S_{jk}n_k - \frac{1}{2}\epsilon_{ijk}n_j\omega_k - \frac{1}{\chi}P_{ij}\frac{\partial}{\partial x_j}\left(\frac{\mathrm{D}\psi}{\mathrm{D}t}\right), \tag{27}$$

$$\frac{1}{\delta_\mathrm{t}^2}\frac{\mathrm{D}\delta_\mathrm{t}}{\mathrm{D}t} = \chi n_i S_{ij} n_j - n_i\frac{\partial}{\partial x_i}\left(\frac{\mathrm{D}\psi}{\mathrm{D}t}\right). \tag{28}$$

where $P_{ij} \equiv (n_i n_j - \delta_{ij})$ corresponds to the plane parallel to the isosurface of ψ, or the plane for which n_i is the normal direction. The first terms on the right-hand sides of both of these equations account for the effect of the strain rate S_{ij} on n_i and δ_t. The last terms in each equation are also similar, but the effects of vorticity only explicitly appear in Eq. (27) for the evolution of n_i. This means that, in a conceptual field that is purely rotational and unstrained, the vorticity would cause changes to the direction of the flame surface normal without changing the flame width. Moreover, the presence of the cross product of the flame surface normal and the vorticity means that the vorticity vector will act to rotate the flame surface normal orthogonally to the direction of ω_i. Both S_{ij} and ω_i are properties of the turbulent flow in which the flame burns, and the interaction terms on the right-hand side of Eq. (25) represent the dominant terms leading to changes in n_i.

Prior studies of scalar gradient dynamics have shown that the dominant effects of turbulence on δ_t and χ are represented by the strain rate interaction terms found on the right-hand sides of Eqs. (26) and (28) [80,128,182,183,188]. In order to understand the sign and magnitude of this term for different conditions, it has been common to rewrite it in terms of the magnitude, eigenvalues, and eigenvectors of the strain rate S_{ij} as

$$n_i S_{ij} n_j = S\left(\lambda_1|\boldsymbol{e}_1\cdot\boldsymbol{n}|^2 + \lambda_2|\boldsymbol{e}_2\cdot\boldsymbol{n}|^2 + \lambda_3|\boldsymbol{e}_3\cdot\boldsymbol{n}|^2\right), \tag{29}$$

where $S = (S_{ij}S_{ji})^{1/2}$ is the strain rate magnitude, λ_i are the eigenvalues of S_{ij}/S, with $\lambda_1 \geq \lambda_2 \geq \lambda_3$, and $\boldsymbol{e}_i$ are the corresponding eigenvectors. For $\lambda_1 > 0$ and $\lambda_3 < 0$, the most negative and positive eigenvalues are often referred to as the "compressional" and "extensional" eigenvalues, respectively. One effect of strain on a flame is to increase δ_t when n_i is more closely aligned with $\boldsymbol{e}_1$, and to decrease δ_t when n_i is more closely aligned with $\boldsymbol{e}_3$. That is, the sign of this turbulence interaction term is completely determined by the relative magnitudes of the eigenvalues and the alignments of the local flame normal orientation with the strain rate eigenvectors.

In non-reacting turbulent flows where ψ is a passive scalar, the dominant alignment is between $\boldsymbol{n}$ and $\boldsymbol{e}_3$ [191–193], which would correspond to an increase in scalar gradient magnitude χ via Eq. (25) and to a decrease in the flame width δ_t due to the effects of fluid straining. By contrast, in non-premixed reacting flows, Boratav et al. [193,194] found preferential alignment between the scalar gradient and most extensional strain rate eigenvector $\boldsymbol{e}_1$, indicating the destruction of the scalar gradient magnitude.

A number of studies of lower $\mathrm{Ka}_{\delta,\mathrm{K}}$ flows (outside of the highly turbulent regime that is the focus here, e.g., Refs. [184,195]) have shown that there is preferential alignment between the scalar gradient and $\boldsymbol{e}_1$ in premixed reacting flows, contrary to results found in non-reacting turbulence. However, Chakraborty et al. [181] found that, in low $\mathrm{Da}_{\ell,\delta}$ statistically planar premixed flames (corresponding to $\mathrm{Ka}_{\delta,\mathrm{K}} = 11$) the scalar gradient is dominantly aligned with $\boldsymbol{e}_3$. This, in turn, indicates production of the scalar gradient magnitude and local thinning of the flame at these conditions. Consistent with prior studies, Chakraborty et al. [181] also found that, in high $\mathrm{Da}_{\ell,\delta}$ flames (with $\mathrm{Ka}_{\delta,\mathrm{K}} = 0.3$), the scalar gradient is aligned with $\boldsymbol{e}_1$, indicating reduction of the gradient magnitude and local flame broadening. It was noted, however, that even for the low $\mathrm{Da}_{\ell,\delta}$ premixed flame, significant regions of alignment with $\boldsymbol{e}_1$ were observed in regions with high local heat release.

Comparing with the high $\mathrm{Da}_{\ell,\delta}$ results of Swaminathan & Grout [195], which showed preferential alignment between $\boldsymbol{e}_1$ and scalar gradient, Kim & Pitsch [180] similarly noted that the alignment with $\boldsymbol{e}_3$ increases as $\mathrm{Ka}_{\delta,\mathrm{K}}$ increases, although this alignment weakens for intermediate values of the progress variable within the flame brush (see Fig. 32). These trends were further confirmed through a series of simulations with increasing $\mathrm{Ka}_{\delta,\mathrm{K}}$ by Hamlington et al. [128], where it was shown that there is increasingly dominant alignment between n_i and $\boldsymbol{e}_3$ as $\mathrm{Ka}_{\delta,\mathrm{K}}$ increases from 3.9 to 174.

Several studies have further examined the variation in alignments between the scalar gradient and strain rate eigenvectors at different locations within highly turbulent premixed flames. This is typically accomplished using conditional statistics based on a local progress variable value. Both Kim & Pitsch [180] and Hamlington et al. [128] found that, over a range of different intensities, the alignment of $\boldsymbol{n}$ with $\boldsymbol{e}_1$ was most pronounced near locations of dominant heat release, approximately corresponding to the reaction zone. For both smaller and larger progress variable values, by contrast, preferential alignment was observed with $\boldsymbol{e}_3$.

Supporting the conclusions from these earlier numerical studies, Coriton & Frank [196] experimentally examined the effects of heat release on the eigenvalues and eigenvectors of S_{ij} for a premixed methane-air Bunsen flame. The flame normal was found to preferentially align with $\boldsymbol{e}_1$ close to the products, whereas alignment with $\boldsymbol{e}_3$ was observed in the preheat zone (see Fig. 33). In examining a high-intensity counter-flow premixed flame, Hampp & Lindstedt [197] similarly observed preferential alignment of the flame front normal with $\boldsymbol{e}_1$, as well as reduced vorticity magnitude for larger Da. These results are, correspondingly, consistent with a change in sign of the interaction term $n_i S_{ij} n_j$ through the flame for sufficiently weak turbulence intensities; when $\mathrm{Ka}_{\delta,\mathrm{K}}$ is large enough (e.g., over 100), this term was found to be negative for all locations in a statistically planar premixed flame, on average, indicating a reduction in δ_t [128].

It should be noted, however, that these results obtained for statistically planar and jet premixed flames are not universal, and variations have been observed, particularly at low turbulence intensities. For example, Steinberg et al. [175] experimentally examined the alignment of the flame normal with the strain rate eigenvectors in a premixed methane-air slot Bunsen burner at low turbulence intensities. It was found that the flame normal and $\boldsymbol{e}_1$ were predominantly misaligned, and that this mis-alignment increased as turbulence structures approached the flame. Similarly, Zhou & Frank [198] experimentally examined the effects of heat re-

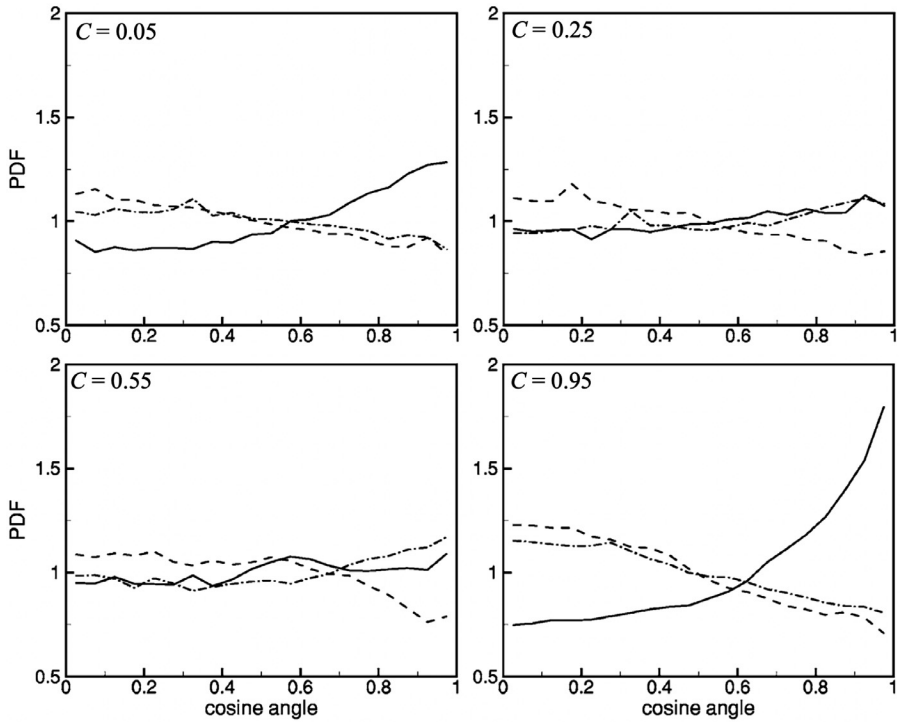


Fig. 32. Alignment between $\boldsymbol{n}$ and the eigenvectors of the strain rate tensor at four different values of the reaction progress variable for a statistically planar premixed flame. Dash-dot lines show alignment with $\boldsymbol{e}_1$, dashed lines show alignment with $\boldsymbol{e}_2$, and solid lines show alignment with $\boldsymbol{e}_3$. Cosine angles close to 1 indicate better alignment, while those close to 0 indicate orthogonality. Reprinted from Ref. [180] with permission of AIP Publishing.

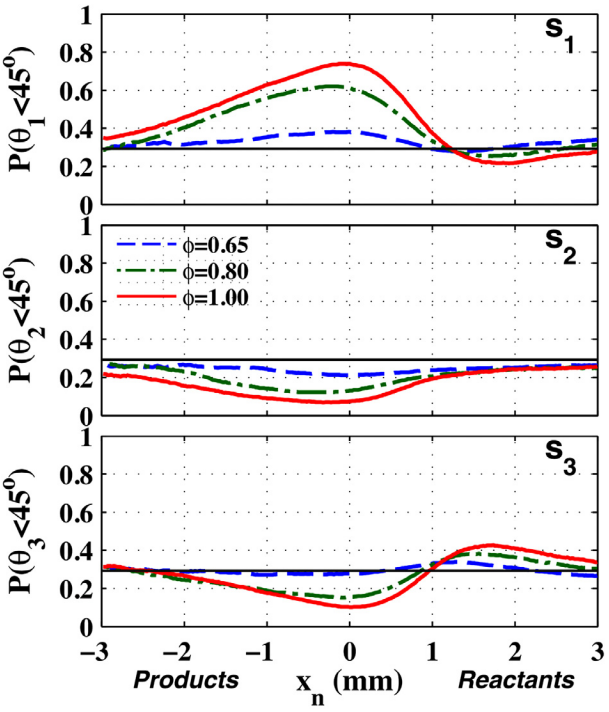


Fig. 33. Flame-normal conditional probabilities as a function of the flame-normal coordinate, x_n for a premixed Bunsen flame. Reprinted from Ref. [196] with permission of Elsevier.

lease on strain rate eigenvectors in a counterflow flame at low turbulence intensities. They found that there is preferential alignment between $\boldsymbol{e}_3$ and $\boldsymbol{n}$ due to the effects of the bulk strain rate. Once again, dilatation from heat release promotes alignment between $\boldsymbol{e}_1$ and $\boldsymbol{n}$, although this alignment was not found to be dominant for this configuration.

With respect to other factors affecting scalar gradient alignment, Kim & Pitsch [180] examined the effects of flame curvature on alignment between the scalar gradient and strain rate eigenvectors, finding that larger negative curvatures were associated with increased alignment between the scalar gradient and $\boldsymbol{e}_1$. In general, alignment between the scalar gradient and $\boldsymbol{e}_1$ was attributed to the importance of dilatation effects on the scalar dynamics. Chakraborty et al. [182,183] also examined the effects of Lewis number (Le) and flow curvature on scalar gradient alignment. In Ref. [182], it was found for a range of high $\mathrm{Ka}_{\delta,\mathrm{K}}$ premixed flames (spanning roughly $\mathrm{Ka}_{\delta,\mathrm{K}} = 10 - 34$) that the alignment between the scalar gradient and $\boldsymbol{e}_1$ increases as Le decreases, indicating increased prevalence of flame broadening by turbulent straining.

Beginning with Kim & Pitsch [180] and Chakraborty et al. [181], several authors have made a distinction between flame-induced and fluid dynamic strain rates. The production term, $n_i S_{ij} n_j$, is equivalent to a flame normal strain rate, and accounts for the straining of the flame surface along its normal direction, leading to either flame broadening or thinning. By contrast, the tangential strain rate $(n_i n_j - \delta_{ij})S_{ij}$ acting along the flame surface is generally assumed to be representative of changes in the flame surface area. The study of highly turbulent premixed jet flames by Wang et al. [112] showed that the magnitude of the production term is small near the jet exit due to preferential alignment of $\boldsymbol{n}$ with $\boldsymbol{e}_1$, but that this term becomes larger and positive due to the preferential alignment of $\boldsymbol{n}$ with $\boldsymbol{e}_3$ further downstream (see Fig. 34). Similar alignment results have been observed in many other studies spanning a range of turbulence intensities (e.g., [196,199]).

In summary, in statistically planar and jet premixed flames at sufficiently low turbulence intensities, there is increased alignment between $\boldsymbol{n}$ and $\boldsymbol{e}_1$ in the reaction zone, corresponding to an increase in the local flame width δ_t by the fluid dynamic strain rate

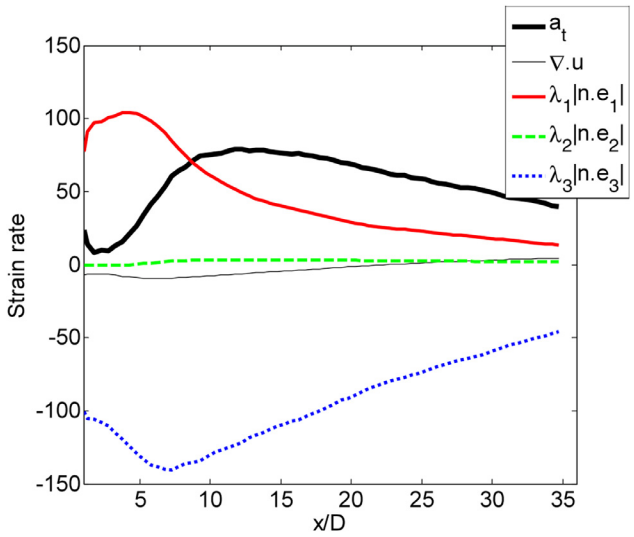


Fig. 34. Average values of the scalar gradient magnitude production (a_t), the dilatation $\nabla \cdot \boldsymbol{u}$, and the components of the production due to the alignment of $\boldsymbol{n}$ with different strain rate eigenvectors $\boldsymbol{e}_i$ for the high Karlovitz premixed jet flame studied using DNS by Wang et al. [112]. Reprinted from Ref. [112] with permission from AIP.

S_{ij}. However, as the turbulence intensity increases, this alignment is lost and there is an increasingly dominant alignment between the scalar gradient (or $\boldsymbol{n}$) and $\boldsymbol{e}_3$, consistent with the dynamics of a passive conserved scalar in non-reacting turbulence. The resulting creation of large scalar gradients is of leading-order importance for understanding many aspects of the thermochemical complexity noted in Section 3. In particular, the creation of large gradients, associated with the strain rate interaction term, leads to the increasing dominance of molecular transport processes in the thermochemical dynamics. Moreover, since turbulence increases the magnitudes of both negative and positive gradients, resulting in both negative and positive values of transport fluxes, substantial non-monotonicity is found along thermochemical trajectories as the turbulence intensity increases [70]. It is cautioned, however, that these conclusions must be examined further in practical configurations where, for example, there are mean pressure gradients, as discussed in the next section.

4.2.2. Vorticity and strain rate

Given their central importance in the characterization and understanding of turbulence-flame interactions, the vorticity and strain rate are perhaps the most widely studied properties of turbulence in research on highly-turbulent premixed combustion. The dynamics of ω_i are governed by the transport equation

$$\frac{\mathrm{D}\omega_i}{\mathrm{D}t} = \omega_j S_{ij} - \omega_i S_{kk} + \frac{1}{\rho^2}\epsilon_{ijk}\frac{\partial \rho}{\partial x_j}\frac{\partial p}{\partial x_k} + \epsilon_{ijk}\frac{\partial}{\partial x_j}\left(\frac{1}{\rho}\frac{\partial \tau_{kl}}{\partial x_l}\right), \quad (30)$$

where the first term on the right represents nonlinear vortex stretching associated with the fluid dynamic strain rate S_{ij}, the second term represents dilatation associated with compressibility (where $S_{kk} \neq 0$ in reacting flows), the third term is the baroclinic torque, and the last term represents the effects of viscous transport. The corresponding transport equation for the enstrophy, $\Omega = (1/2)\omega_i\omega_i$, is obtained from Eq. (30) as

$$\frac{\mathrm{D}\Omega}{\mathrm{D}t} = \omega_i\omega_j S_{ij} - 2\Omega S_{kk} + \frac{\omega_i}{\rho^2}\epsilon_{ijk}\frac{\partial \rho}{\partial x_j}\frac{\partial p}{\partial x_k} + \omega_i\epsilon_{ijk}\frac{\partial}{\partial x_j}\left(\frac{1}{\rho}\frac{\partial \tau_{kl}}{\partial x_l}\right). \quad (31)$$

Both of these transport equations include vortex-stretching terms that account for the interaction between the vorticity and the strain rate. These terms are associated with the nonlinear cascade process and the generation of small-scale features in turbulent flows. Transport equations can also be obtained for S_{ij} and its magnitude, explicitly revealing the nonlinear coupling between the dynamics of the vorticity and strain rate [200,201].

In the above transport equations, there are three important reacting flow effects that are not present in constant density, constant viscosity flows. Namely, dilatation dynamically affects the magnitude of the vorticity and enstrophy, while also changing the form of the viscous stress tensor. Second, transport properties, particularly the viscosity, are strong functions of the local thermodynamic state. For example, Sutherland's law for the viscosity of an ideal gas yields a nearly linear increase in viscosity with temperature for typical combustion temperatures [202]. Hence, the influence of viscous dissipation increases from the reactants to products. Finally, the combined action of density and pressure gradients influences the turbulence evolution, as expressed through the baroclinic torque terms. The baroclinic torque is generally thought to contribute to "flame-generated" turbulence and is only substantially non-zero where gradients of density and pressure are both large and misaligned.

In non-reacting, incompressible turbulent flows with constant transport properties, only the first (i.e., vortex stretching) and last (i.e., viscous transport) terms in the above transport equations are non-zero. The vortex stretching term, in particular, has received considerable attention due to its role in the production and destruction of vorticity. As with studies of scalar gradient dynamics, it has been common over the past three decades to examine this term via the alignments between the vorticity and the three eigenvectors of the strain rate tensor. In particular, it can be shown that the vortex stretching term appearing in Eq. (31) can be written as

$$\omega_i S_{ij} \omega_j = S\left(\lambda_1 |\boldsymbol{e}_1 \cdot \boldsymbol{\omega}|^2 + \lambda_2 |\boldsymbol{e}_2 \cdot \boldsymbol{\omega}|^2 + \lambda_3 |\boldsymbol{e}_3 \cdot \boldsymbol{\omega}|^2\right). \quad (32)$$

In non-reacting homogeneous isotropic turbulence, the result of the vortex stretching process is to preferentially align vorticity with the eigenvector of the strain rate corresponding to the intermediate eigenvalue, or $\boldsymbol{e}_2$ [192]. There is preferential misalignment with the eigenvector corresponding to the most negative eigenvalue, $\boldsymbol{e}_3$, and relatively weak alignment with the most positive eigenvector, $\boldsymbol{e}_1$. The alignment with $\boldsymbol{e}_2$ has been shown to result from the nonlinear coupling between the vorticity and strain rate [203,204], although preferential alignment with the most extensional eigenvector of the background or large-scale strain rate has also been identified [205,206].

In a premixed jet flame, Coriton & Frank [201] found that the presence of combustion increased the magnitude of the vortex stretching term and the associated alignment of the vorticity with $\boldsymbol{e}_2$ due to the increased spatial correspondence between large magnitudes of vorticity and strain rate. Ultimately, this change was found to be due to the effects of the increased shear in the reacting jet flame, as compared to a corresponding non-reacting jet, and the consequent formation of overlapping "sheets" of large vorticity and strain rate magnitudes.

Using numerical simulations, Hamlington et al. [128] examined the properties and interactions of the vorticity, strain rate, and scalar gradient in statistically planar premixed flames for a range of turbulence intensities, including high intensities (spanning Karlovitz numbers between 3.9 and 174). It was found that dilatation and baroclinic torque were significant with respect to vortex stretching for low intensities, but that these two effects became less significant at higher intensities. Moreover, the flame generated anisotropy in the orientations of ω_i and the strain rate eigenvectors at low intensities, but this anisotropy was lost for higher intensities. The alignments between ω_i, n_i, and the strain rate eigenvectors were similar to those found in non-reacting flows for high

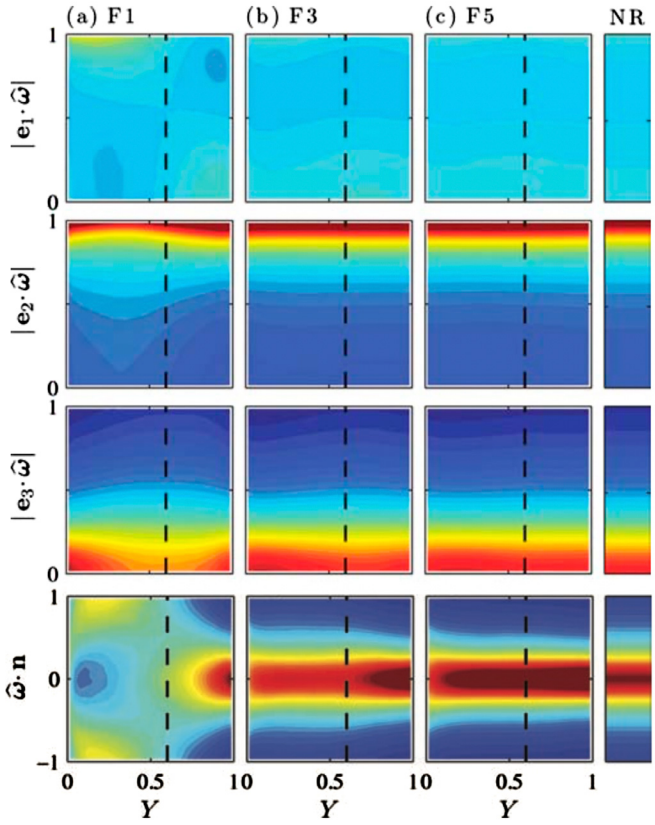


Fig. 35. Alignments between the strain rate eigenvectors $\boldsymbol{e}_i$, the vorticity direction vector $\widehat{\omega}_i = \omega_i/\omega$, and the flame normal vector $n_i = \chi_i/\chi$ conditioned on the local instantaneous value of the reactant mass fraction Y for a statistically planar premixed flame at increasing turbulence intensity (left to right), with corresponding non-reacting results shown in the last column. The colorbar goes from 0 (blue) to 1 (red), with larger values indicating better alignment. Vertical dashed black lines indicate the approximate separation between preheat ($Y > 0.6$) and reaction ($Y < 0.6$) zones in the flame. Modified from Ref. [128] with permission of AIP Publishing.

intensities (that is, ω_i was misaligned with n_i and preferentially aligned with $\boldsymbol{e}_2$), but for low intensities there was increased alignment between ω_i and $\boldsymbol{e}_1$, as well as increased alignment between ω_i and n_i (see Fig. 35).

Many of these results were attributed to the influence of dilatation due to fluid expansion by the flame on the coupled dynamics of ω_i, S_{ij}, and n_i, although this study did not include explicit temperature-dependent viscous transport or dissipation terms in the governing equations solved by the simulations. However, the decreasing magnitude of the baroclinic torque and dilatation terms relative to the vortex stretching and viscous dissipation terms has been confirmed in a number of other studies of statistically planar premixed flames with homogeneous isotropic turbulence in the reactants, including those by Bobbitt et al. [207], Ranjan et al. [179], and Papapastolou et al. [208].

In particular, using DNS of statistically planar premixed flames, including temperature-dependent viscosity, Bobbitt et al. [207] showed that, at high $\mathrm{Ka}_{\delta,\mathrm{K}}$ (this study spanned Karlovitz numbers between 70 and 750), the primary balance in the vorticity transport equation was between viscous dissipation and the vortex stretching term. Contrary to low $\mathrm{Ka}_{\delta,\mathrm{K}}$ conditions where dilatation plays a significant role in the dynamics, generally resulting in vorticity suppression, at high $\mathrm{Ka}_{\delta,\mathrm{K}}$ the vorticity magnitude continues to decrease, but due almost exclusively to the increase in kinematic viscosity across the flame. Indeed, as $\mathrm{Ka}_{\delta,\mathrm{K}}$ increases, Bobbitt et al. [207] showed that the normalized change in vorticity magnitude became insignificant, when the normalization was performed using local values of the kinematic viscosity and dissipation to construct the Kolmogorov scales. Consequently, vorticity magnitude decreased across the flame, but the dependence on density ratio (connected to dilatation), became weaker as $\mathrm{Ka}_{\delta,\mathrm{K}}$ increased (see, for example, Fig. 36). As $\mathrm{Ka}_{\delta,\mathrm{K}}$ increases, baroclinic torque, vortex stretching, and viscous dissipation all increase in magnitude, but the scaling of the baroclinic torque with $\mathrm{Ka}_{\delta,\mathrm{K}}$ is weaker than for the other two effects, resulting in the dominance of the vortex stretching and dissipation terms at high $\mathrm{Ka}_{\delta,\mathrm{K}}$ (see Fig. 37).

Papapastolou et al. [208] examined the enstrophy transport equation in statistically planar hydrogen-air premixed flames spanning three different values of $\mathrm{Ka}_{\delta,\mathrm{K}}$ (i.e., 0.75, 14, and 126), finding that baroclinic torque has an increasingly minor contribution to the overall dynamics as $\mathrm{Ka}_{\delta,\mathrm{K}}$ increases. In this study, Papapastolou et al. [208] further conditioned the analysis on the local flow topol-

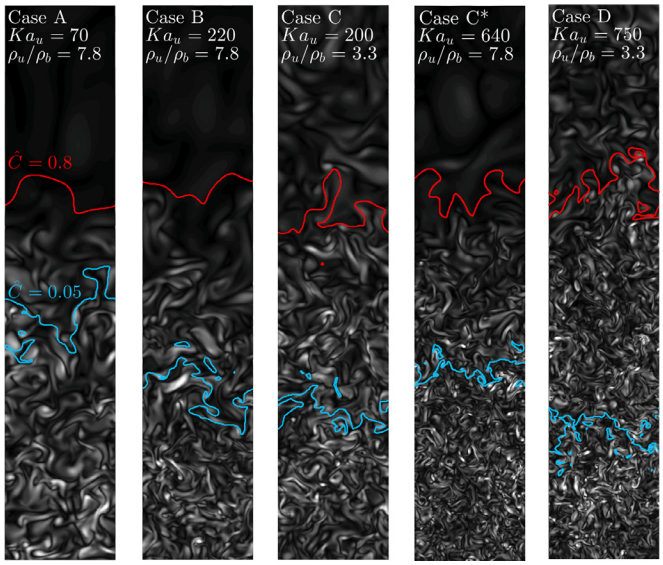


Fig. 36. Fields of the vorticity magnitude $|\boldsymbol{\omega}|$ from DNS of a statistically planar n-heptane and air premixed flame. The unburnt Karlovitz number and density ratio for each case are labeled at the top of the panels. Reprinted from Ref. [207] with permission of AIP Publishing.

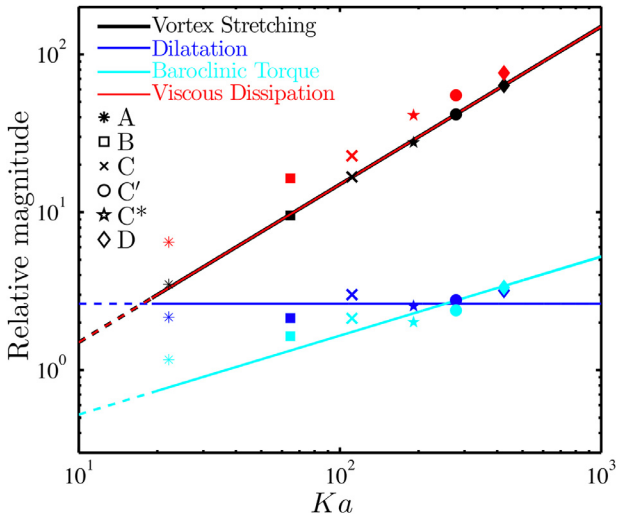


Fig. 37. Scaling of the vortex stretching, dilatation, baroclinic torque, and viscous dissipation terms as a function of $\mathrm{Ka}_{\delta,\mathrm{K}}$ in the dynamics of the enstrophy. Data are obtained from DNS of statistically planar n-heptane and air premixed flames. Reprinted from Ref. [207] with permission of AIP Publishing.

ogy, based on the three invariants of the velocity gradient tensor $\partial u_i/\partial x_j$, showing that topologies corresponding to positive dilatation have an increasingly weak impact on the dynamics as $Ka_{\delta,K}$ increases. A related topologically conditioned analysis of a statistically planar premixed flame yielded similar results [209].

Through an analysis of vorticity alignment for the same statistically planar premixed flame configuration as that studied by Bobbitt et al. [207], Bobbitt & Blanquart [210] have further shown that turbulence anisotropy generated by the flame becomes less pronounced as $Ka_{\delta,K}$ increases. The alignments between ω_i and the eigenvectors of S_{ij} are similar to those found in non-reacting homogeneous isotropic turbulence at high $Ka_{\delta,K}$. For low $Ka_{\delta,K}$, the vorticity alignment and corresponding vortex stretching term are altered, and the effect of the flame on the vortex stretching term was identified as the primary source of the vorticity anisotropy. Wang et al. [112] similarly found using DNS of a highly turbulent methane-air premixed jet flame that the alignments between ω_i and the eigenvectors of S_{ij} were similar to those found in non-reacting flows (i.e., preferential alignment between ω_i and $\boldsymbol{e}_2$). Moreover, ω_i was preferentially aligned with the most extensional strain rate of the mean flow, and was preferentially misaligned (or orthogonal) to the local flame normal n_i. The former result is similar to that obtained for sheared non-reacting flows, and the latter result is consistent with results for statistically planar flames [128]. Zhao et al. [211] also observed a misalignment between ω_i and n_i for a near-wall quenched premixed flame.

Despite the overall demonstration in these prior studies of the decreasing significance of baroclinic torque and flame generated anisotropy as the turbulence intensity increases, substantial generation of vorticity and anisotropy by baroclinic torque can occur locally and for short periods of time, even at high turbulence intensities. Significantly, Poludnenko [212] showed that, even for highly turbulent conditions, statistically planar premixed flames can self-accelerate and undergo substantial vorticity generation by baroclinic torque during periods of high system pressures (see Fig. 38). Moreover, this turbulence generation was found to be strongly anisotropic, with the bulk of the baroclinic torque production occurring transverse to the direction of the mean flow.

Substantial changes to the dynamics of the vorticity and strain rate have also been observed for non-unity Lewis numbers, Le. Using DNS of statistically planar premixed flames spanning Karlovitz numbers from 0.54 to 19.5, Chakraborty et al. [213,214] found that the vorticity magnitude decreases across statistically planar premixed flames and that the vorticity vector is predominantly aligned with $\boldsymbol{e}_2$ at higher $Ka_{\delta,K}$, in agreement with results from studies examining premixed flames for unity (or close to unity) Le. Interestingly, however, alignment with $\boldsymbol{e}_1$ increases in the region of peak heat release within the flame. In particular, for lower $Ka_{\delta,K}$ with unity Le and for all $Ka_{\delta,K}$ with Le < 1, there is increased, although unstable, alignment with $\boldsymbol{e}_1$. For small $Ka_{\delta,K}$ and Le, increased alignment was observed with $\boldsymbol{e}_3$. These changes with Le and $Ka_{\delta,K}$ were found to be the result of changes in the influence of dilatation in the flame relative to the effects of vortex stretching. In two related studies, Chakraborty et al. [215] and Dopazo et al. [216] also showed that there is increased vorticity magnitude generated within the flame as Le decreases (see Fig. 39), and that this is accompanied by increased vorticity anisotropy. These changes were attributed to the increasing influence of dilatation and baroclinic torque as Le decreases for all $Ka_{\delta,K}$.

A number of other studies, spanning a range of conditions and configurations, have also contributed to, and largely confirmed, our understanding of vorticity-strain rate dynamics and properties during highly turbulent premixed combustion in statistically planar and jet flames. Nilsson et al. [199] examined statistically planar flames spanning a range of very high $Ka_{\delta,K}$ from 65 to 3,350, showing that the flow-induced strain rate becomes increasingly larger

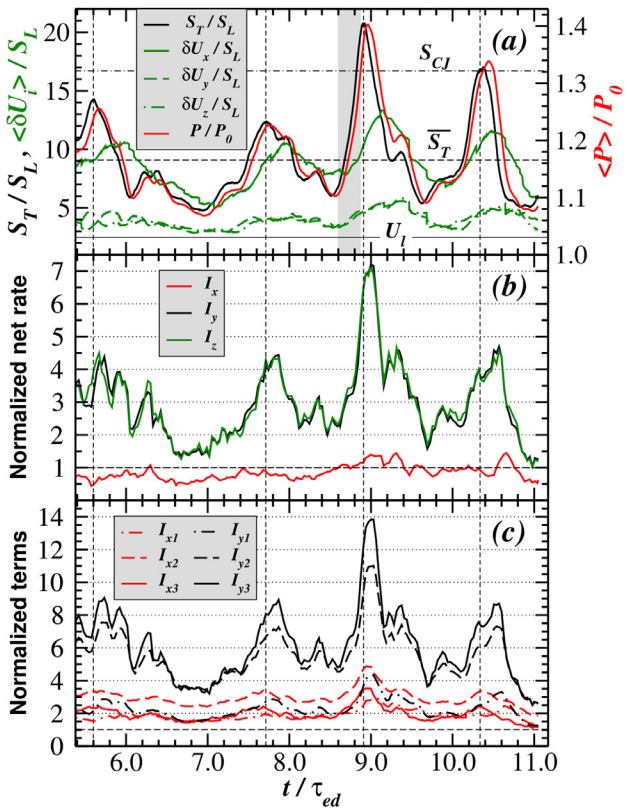


Fig. 38. Flame speeds, turbulent velocity fluctuations, and average pressure (a), normalized total vorticity production rates, I_i, in different directions i (b), and normalized vortex stretching I_{i1}, dilatation I_{i2}, and baroclinic torque, I_{i3} terms in direction i (c) as functions of time for a highly turbulent statistically planar premixed flame. Reprinted from Ref. [212] with permission of AIP.

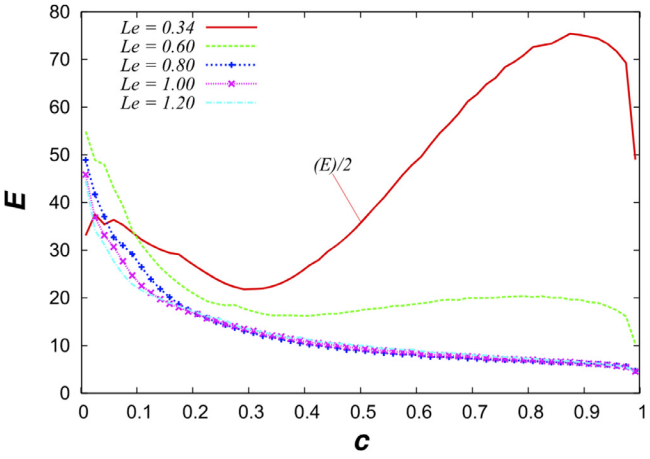


Fig. 39. Mean enstrophy Ω (denoted 'E' here) conditioned on the local progress variable for different Lewis numbers, Le, from DNS of statistically planar premixed flames. Reprinted from Ref. [216] with permission of AIP.

than the strain rate associated with fluid expansion (i.e., dilatation) by the flame as $Ka_{\delta,K}$ increases. The scalar gradient is correspondingly aligned with $\boldsymbol{e}_3$, as in passive scalar evolution in many non-reacting flows. It was also shown that, across the flame, the vorticity magnitude decreases and the characteristic size of intense vortical structures increases.

Ahmed et al. [217] have performed a multiscale analysis of wall bounded turbulent premixed flames, using a bandpass filtering approach to examine the contribution of variously sized eddies on the vorticity and strain rate fields. It was found, in particular,

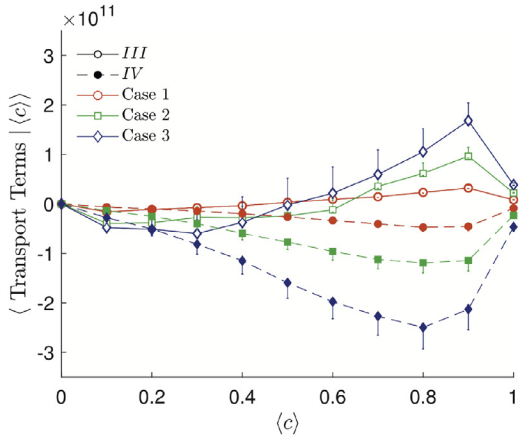


Fig. 40. Mean baroclinic torque (*III*) and viscous transport (*IV*) conditioned on the mean progress variable in a turbulent premixed swirl flame, where Cases 1–3 correspond to Karlovitz numbers of 20, 35, and 50, respectively. Reprinted from Ref. [220] with permission of Elsevier.

that flame-wall interactions alter vortex stretching by reducing the contribution of non-local strain rates and increasing the effect of small-scale turbulence. It remains unclear, however, to what extent these effects are also present in non-reacting flows, where substantial variations in the flow and vortex stretching process can also occur in the near-wall region.

It should be noted that much of the current understanding of vorticity dynamics and vorticity-strain properties in highly turbulent premixed combustion is based on studies of statistically planar and jet flames. However, recent studies of more realistic configurations have shown that in instances where there are mean pressure gradients imposed on the flow, such as those found in converging channels [218] and in high-swirl combustors [219,220], the baroclinic torque term can become the dominant effect in the overall dynamics, resulting in substantial flame-generated vorticity. Geikie & Ahmed [218] have shown that the baroclinic torque is increasingly dominant in the dynamics as the magnitude of the pressure gradient increases. Kazbekov et al. [219,220] observed a similar dominance of the barocinic torque term, even for high turbulence intensities, in a swirl combustor close to the burnt product gases (see the results for $Ka_{\delta,K} = 20$, 35, and 50 in Fig. 40). Lai et al. [221] also found an increase in the effect of the baroclinic torque in the near-wall region of a quenched high-intensity turbulent premixed flame.

Compared to studies of the vorticity, and vorticity-strain rate interactions in particular, studies of the strain rate field itself have been somewhat more limited. Coriton & Frank [222] examined the strain rate fields and intermittency in turbulent partially-premixed jet flames, and Hampp et al. [223] examined strain rate and vorticity conditioned to different isosurfaces in a lean premixed opposed jet configuration at low Da, showing that there is an increase in tangential strain rate due to dilatation. Steinberg et al. [200] examined the transport of the principal components of the strain rate in a premixed jet flame, including measurements of the strain-strain and vorticity interaction terms in the dynamics. These terms were found to be weaker in regions with significant heat release, due to the effects of pressure and density gradients.

To summarize our current understanding of vorticity and strain rate characteristics for highly turbulent premixed combustion, the properties and dynamics of the vorticity and strain rate at high $Ka_{\delta,K}$ generally correspond to non-reacting results, for Le close to unity, outside of periods of large system pressure increases, and for flows without a mean pressure gradient. Consequently, studies of statistically planar and jet flame configurations with Lewis numbers close to unity have generally found that the effects of dilatation and baroclinic torque become less pronounced at higher $Ka_{\delta,K}$, and that the orientation of the vorticity and strain rate eigenvectors (including their relative alignments and anisotropy) are also less affected by the flame. However, recent studies of statistically planar flames with large pressure oscillations [212], non-unity Lewis numbers [213,214], as well as studies of more realistic geometries with non-zero mean pressure gradients [218–220], indicate that the correspondence between turbulence in non-reacting flows and high-$Ka_{\delta,K}$ premixed combustion requires continued study.

It is also important to note that many of the statistically planar cases discussed here involve some type of forcing to sustain turbulence in the region of the flame, resulting in a statistically stationary DNS that is amenable to longer term statistical analysis. As in DNS studies of non-reacting turbulence that date back over three decades [224], this forcing is typically implemented as a body force in the Navier-Stokes equations and is designed to introduce energy primarily at the largest scales of the flow, even when the forcing is also applied within the region of the flame. Both broadband [127,207,210] and spectrally truncated [225] linear forcing schemes, as well as stochastic methods [69,110,128,212] that introduce velocity perturbations at large scales, have been used to study turbulent premixed combustion at higher Karlovitz numbers than are typically achievable experimentally. In each of these cases, the forcing is applied both before, within, and downstream of the flame, mimicking energy input by larger-scale flow phenomena that are independent of the flame itself. To avoid interactions between the forcing and the flame, others have pre-computed 3D volumes of homogeneous isotropic turbulence which are then fed into the domain [208], or have forced only the region immediately upstream of the flame [199]. In each case, however, the intent is to create a statistically stationary turbulent flame that allows for more straightforward statistical analyses than the temporally decaying cases studied by, for example, Nishiki et al. [226] and Chakraborty et al. [166,213,214].

Despite the variety of forcing methods for statistically planar cases, however, observations regarding the vorticity, strain rate, and scalar gradient dynamics are consistent amongst all studies, even those where the forcing is sustained in the flame region and those where the turbulence is allowed to decay. Although some quantitative differences do exist, particularly when discussing the specific Karlovitz numbers at which different phenomena are observed, the general trends for low and high Karlovitz behaviors are consistent across different studies. This conclusion is also supported by Klein et al. [227], who compared premixed flame results from DNS using decaying turbulence, boundary forcing, and linear forcing, finding no notable advantages or disadvantages of any particular approach. It is nevertheless still important to specify when and how forcing is implemented in numerical simulations, since turbulence properties within and downstream of the flame do depend, at least in part, on the details of the forcing scheme.

4.2.3. Coherent structures

To this point, the discussion of vorticity and strain rate has focused on field quantities, rather than on coherent or isolated structures. In the past, a number of studies have explored the interactions between isolated, often 2D, vortices and flame sheets (see, e.g., Mueller et al. [228]). However, the dynamical significance of such structures has been called into question, even in non-reacting flows, given their apparent lack of impact on nonlinearity and inertial range dynamics [229].

Nevertheless, many illustrations of turbulence in both non-reacting and reacting flows continue to show isosurfaces of the vorticity magnitude to reveal characteristic tube-like structures, for example those shown in Fig. 41 for a statistically planar pre-

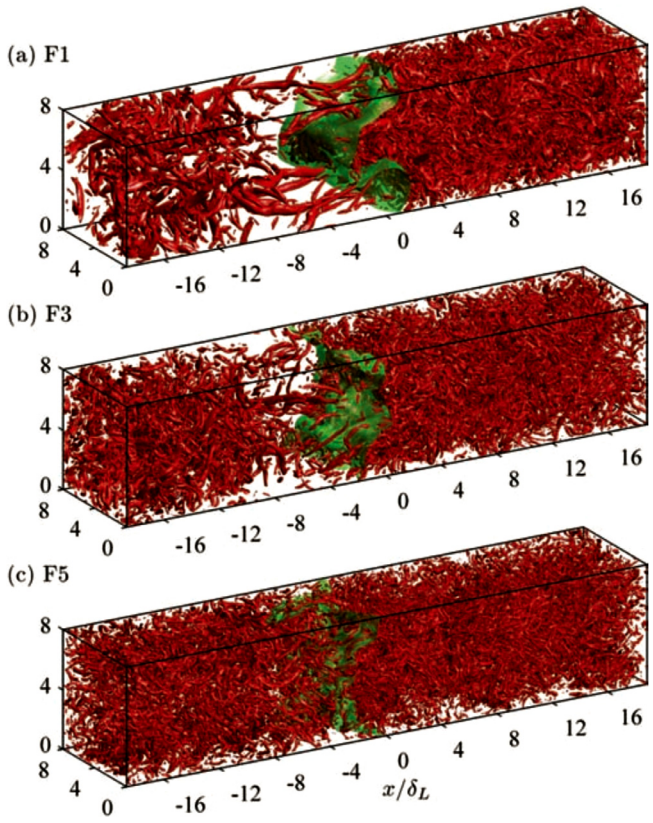


Fig. 41. Isosurfaces of large vorticity magnitude in simulations of statistically planar premixed flames with increasing turbulence intensity (corresponding to Karlovitz numbers of 3.9, 32, and 174 from top to bottom). Semi-transparent green isosurfaces correspond to the flame surface. Reprinted from Ref. [128] with permission of AIP.

mixed flame spanning a range of turbulence intensities [128]. Steinberg et al. [230–232] examined the coupled dynamics of the vorticity and strain rate, including the evolution of intense vorticity and strain rate structures, in a premixed Bunsen flame. Wang et al. [233] examined the structure of turbulent premixed methane-air jet flames over a wide range of turbulence intensities, including very large $Ka_{\delta,K}$, with a particular focus on the effects of turbulent eddies on preheat and reaction zone widths. Skiba et al. [113] have similarly examined the influence of large eddies on the wrinkling and broadening of flame fronts in highly turbulent premixed jet flames, finding that large eddies can in fact broaden the flame.

Beginning with the work of Tanahashi et al. [234], it has been known that intense turbulent vortical structures become less prevalent in premixed flames. Moreover, the orientation of intense vortices becomes increasingly anisotropic. However, this anisotropy is again lost as the turbulence intensity increases. Hamlington et al. [128] studied the alignment of intense vorticity within a statistically planar premixed flame and just downstream of the flame brush, showing that such intense vorticity is strongly aligned with the mean flame normal direction for low intensities. This alignment is much more pronounced than for the vorticity field as a whole (i.e., including less intense vorticity). Within the reaction zone of the flame, intense vorticity is preferentially aligned with the flame normal direction; this alignment is again more pronounced than for the vorticity field as a whole (i.e., not just intense vorticity).

There are additional questions about the representativeness of isolated 2D or quasi-2D structures in highly turbulent flows with substantial 3D complexity and nonlinear interactions between vortical structures spanning a wide range of scales. In particular, using the cinema stereoscopic particle image velocimetry (PIV) techniques described in Steinberg et al. [230,232], Steinberg & Driscoll [231] examined the effects of isolated vortices and vortex pairs on flame curvature and wrinkling, but found that such canonical configurations were present less than 10% of the time in the experimental data record. More often, much more complex 3D vortical structures interacted with the flame front. It was further found in this study that straining of the flame surface was caused by coherent strain rate structures, while vortical structures were primarily responsible for flame wrinkling. This result is consistent with the formulation of the governing equations for χ_i and χ in Eqs. (25) and (26), respectively, where the strain rate has impacts on both quantities, while the vorticity only has an explicit impact on χ_i and, hence, the local flame orientation n_i. Similar strain rate structures were also shown by Steinberg et al. [175] to be important for turbulence-flame interactions in premixed Bunsen flames (see Fig. 42).

Connected to the appearance of small-scale coherent structures is the highly intermittent spatial distribution of intense velocity gradients in high Reynolds number turbulent flows [235,236]. In particular, the dissipation rate field is comprised of many fine-scale features and is concentrated at small scales, resulting in much of the energy in a flow being dissipated within a very small fraction of the total flow volume [237,238]. As the Reynolds number increases, the fraction of the total volume in which most of the dissipation occurs decreases, corresponding to an increasingly wide distribution of dissipation rates relative to the mean dissipation rate.

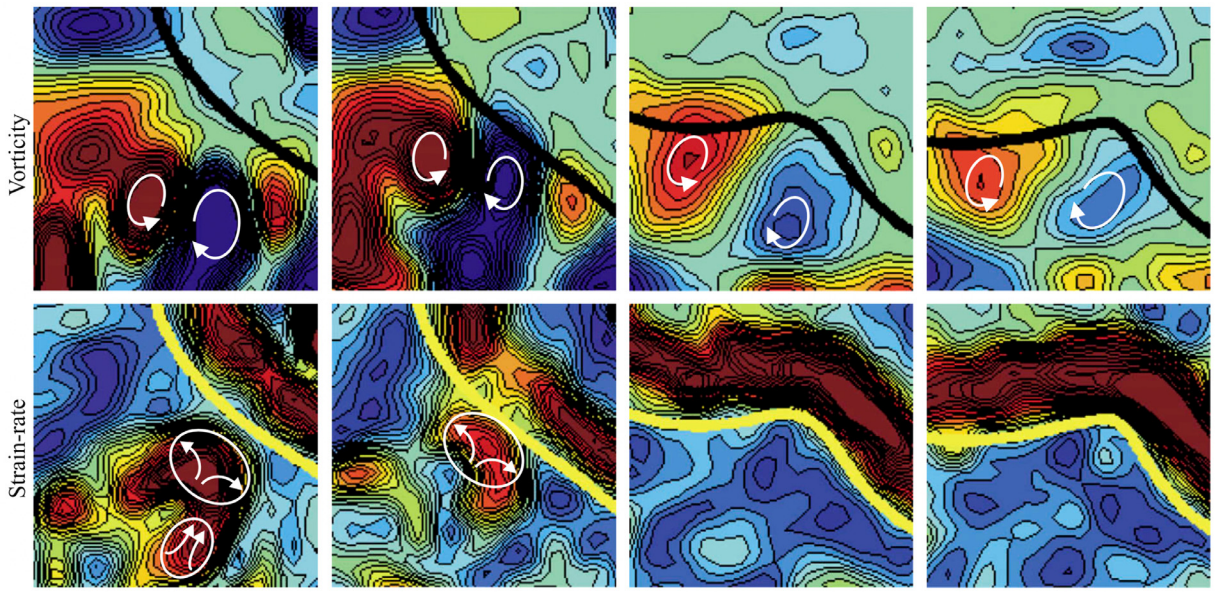
This intermittency was also noted in Section 3.1 in the context of scalar gradients and is evident in comparisons of vorticity and strain rate magnitude PDFs. Generally, the vorticity displays a wider range of values than the dissipation rate, but both are characterized by local instantaneous values that can be orders of magnitude larger than the mean values. These distributions reflect the spatial structure of the vorticity and dissipation rate values, which are small nearly everywhere in high Reynolds number flows, but are punctuated by extremely large values at widely spaced locations. It has been shown [190] that these behaviors remain generally valid in highly turbulent premixed flames, but there are variations in the degree of intermittency through the flame. Further study across a broader range of flame configurations is, however, still required.

4.3. Spectral and multi-scale characteristics

High Reynolds number turbulent flows are characterized by wide spatial and temporal scale ranges [229], and a number of approaches have been used to characterize the multi-scale structure and dynamics of turbulence. These approaches include spatial and temporal correlation functions, structure functions, and spectra (computed using either Fourier or other basis functions). In the following, we will primarily focus on velocity correlation and structure functions spanning different scale separations, denoted $\boldsymbol{r}$, and on Fourier spectra of the kinetic energy spanning different wavevectors $\boldsymbol{k}$.

Using these analyses, substantial research has been devoted over the last decade to addressing the following questions in premixed reacting flows spanning a range of turbulence intensities:

1. How is the multi-scale structure of turbulence affected by chemical heat release from premixed flames for different conditions (e.g., $Ka_{\delta,K}$) and at different locations (e.g., in the unburnt reactants or burnt products)?
2. Is there flame-generated turbulence and transfer of kinetic energy from small to large scales due to chemical heat release?



(a) Measured vortical and strain-rate structures in the canonical configuration at $t = 0$ ms.

(b) At $t = 0.9$ ms, the leading strain-rate structure interacted with the flame. The vortical structures had not yet interacted and the trailing strain-rate structure had been attenuated.

(c) At $t = 5.4$ ms, the vortical structures had interacted, wrinkling the flame. There was no longer any strain-rate exerted.

(d) At $t = 7.2$ ms, the flame wrinkle formed a cusp due to propagation.

Fig. 42. Intense vorticity (top row) and strain-rate (bottom row) structures interacting with a premixed flame. The flame is represented by the thick lines and the reactants are towards the bottom left of each panel. Reprinted from Ref. [231] with permission of Elsevier.

3. Are there universal aspects of multi-scale turbulence structure and dynamics that span different flame configurations and conditions?
4. Can classical theories of multi-scale turbulence structure and dynamics developed for non-reacting flows be applied to highly turbulent premixed flames?

The first question is motivated by the need to quantify the multi-scale structure of turbulence in a variety of contexts, and has spawned a number of studies of premixed flames using different multi-scale analysis approaches, as described in the next section. The second question is primarily motivated by the need to understand whether the flame disrupts the predominantly net forward (or down-scale) cascade of kinetic energy found in most non-reacting turbulent flows, or whether there is net up-scale transfer of energy. This information, in turn, dictates the dynamical effects that must be captured by SFS models for LES of highly turbulent premixed reacting flows. The third question is motivated by the observation that kinetic energy spectra in a variety of non-reacting flows (see, e.g., Refs. [82,239]) collapse to a single universal form. It is thus of interest to determine whether there are similar universal aspects of multi-scale turbulence structure and dynamics, either across different premixed reacting flows or across both non-reacting and reacting flows.

The final question is motivated by the success of the Richardson energy cascade concept and the Kolmogorov hypotheses [240] in describing multi-scale turbulence structure and dynamics in non-reacting flows. Briefly, the three Kolmogorov hypotheses are the following [82]: (*i*) Turbulence at sufficiently small scales is homogeneous, isotropic, and stationary, (*ii*) Turbulence statistics at sufficiently small scales are universal and depend only on the kinematic viscosity ν, the mean dissipation rate ε, and the scale (i.e., r in physical space or the wavenumber k in Fourier space), and (*iii*) Turbulence statistics in an intermediate range of scales smaller than the energy input scale and larger than the dissipation scale are universal and depend only on ε and the scale. These hypotheses are fundamentally based on the Richardson cascade model of energy transfer in turbulent flows [238], whereby energy input at large scales is assumed to be transferred non-dissipatively from larger to smaller scales until viscous dissipation becomes sufficiently strong to dissipate energy at small scales. The third hypothesis, in particular, establishes the existence of an 'inertial' range of scales where energy cascades non-dissipatively between scales.

Although the Kolmogorov hypotheses and Richardson cascade concept are substantial simplifications of the true physics governing real-world flows, both have proven remarkably successful at providing physical space and spectral scaling laws that are in close agreement with experimental and DNS data across a wide range of flows [82,239]. These scaling laws include the prediction of a $k^{-5/3}$ inertial range scaling of the kinetic energy spectrum, where $k = |\boldsymbol{k}|$ is the wavevector magnitude, and of an $r^{N/3}$ scaling of the Nth-order velocity structure function, where $r = |\boldsymbol{r}|$ is the magnitude of the spatial separation vector. These scaling laws, which are fundamentally based on the Kolmogorov hypotheses and Richardson cascade concept, are generally successful for small N in non-reacting (i.e., constant density and viscosity) turbulence [229], but are known to become inaccurate for larger N due to intermittency effects [238]. Departures from these classical scaling relations in highly turbulent reacting flows will be discussed in more detail in the context of spectral and multi-scale structure in Section 4.3.1.

In the following, we review recent research on spectral and multi-scale analyses of turbulence during highly turbulent premixed combustion. Early efforts to understand spectra and multi-scale structure in turbulent combustion were made by examining reactants and products separately (i.e., outside the flame) [241,242], and also by examining non-premixed flames [243]. Here we review more recent attempts to understand the spectral and multi-scale characteristics of turbulence across a range of conditions and flame locations during highly turbulent premixed combustion, with a particular focus on attempts to address the questions outlined above.

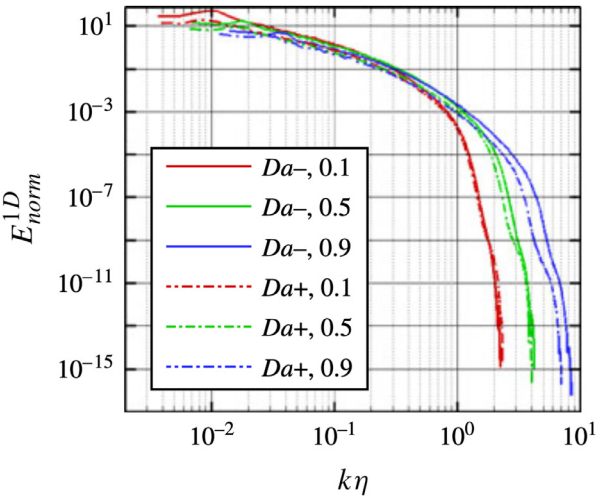


Fig. 43. Normalized one-dimensional kinetic energy spectra for low (Da−) and high (Da+) intensity temporally evolving premixed slot jet flame DNS. Results are shown for three locations in the flame, corresponding to Favre-averaged progress variables of $\widetilde{c} = 0.1$, 0.5, and 0.9. Reprinted from Ref. [84] with permission of Cambridge University Press.

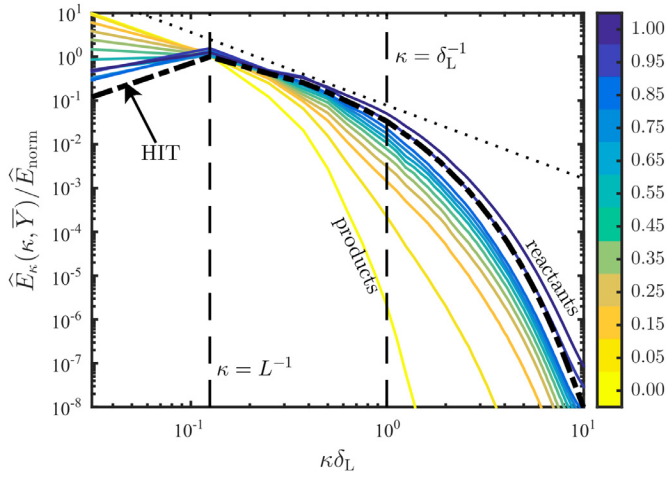


Fig. 44. Normalized 2D kinetic energy spectra conditioned on the planar averaged reactant mass fraction for a statistically planar premixed flame with a turbulence intensity of $u_\ell/S_{\rm L} = 2.5$. A corresponding spectrum for homogeneous isotropic turbulence (HIT; heavy black dash-dot line) and a $k^{-5/3}$ slope (dotted line) are also shown, where $k = |\boldsymbol{k}|$ is the wavevector magnitude. Reprinted from Ref. [88] with permission of the American Physical Society.

4.3.1. Spectral and multi-scale structure

A number of approaches have recently been used to understand spectral properties of turbulence in premixed flames, including both physical and Fourier space analyses. The governing equation for the two-point velocity correlation was examined in detail by Kolla et al. [84,85] for a temporally developing premixed shear layer at a range of turbulence intensities. In these studies, it was found that there is a spectral bump in the kinetic energy spectrum near the scale of the flame, and that this feature is due specifically to dilatation associated with the flame (see Fig. 43). Using conditional density-weighted kinetic energy and scalar spectra, Kolla et al. [84] further showed that turbulence spectra collapse to classical Kolmogorov predictions (i.e., the $k^{-5/3}$ inertial range scaling) only at intermediate scales far from the flame scale.

Using 2D kinetic energy spectra conditioned on the planar-averaged reactant mass fraction, Towery et al. [88] examined DNS of a lower intensity statistically planar premixed flame (with $\mathrm{Ka}_{\delta,\mathrm{K}} = 20$, but a turbulence intensity of only $u_\ell/S_{\rm L} = 2.5$) to show that turbulent small-scale motions are suppressed in the burnt combustion products (see Fig. 44). This result persists even for higher turbulence intensities, as was shown for a similar statistically planar premixed flame configuration using a conditional wavelet analysis by Kim et al. [244]. Due to the use of non-density weighted statistics, however, neither of these studies revealed a spectral bump near the scale of the flame, as was found in the studies by Kolla et al. [84,85].

It should be noted that each of these prior analyses were based on planar-averaged combustion progress variables, complicating the interpretation of the results in physical space. As a result of this difficulty, conditionally averaged structure functions have recently been used to study the multiscale structure of turbulence in highly turbulent premixed combustion. Velocity structure functions correspond to moments of velocity difference distributions for different separation distances; that is $\langle |u_i(\boldsymbol{x}+\boldsymbol{r}) - u_i(\boldsymbol{x})|^N \rangle$, where the average $\langle\cdot\rangle$ denotes either a conditional or unconditional, ensemble or Favre, average and N is the structure function order. Structure functions are closely related to the correlation functions studied by Kolla et al. [84,85], and research on non-reacting turbulence has shown that these structure functions have power-law r dependencies as predicted using scale similarity and dimensional arguments, but their exponent values indicate increasing non-Gaussianity and intermittency as the order increases [229].

Using DNS of statistically planar premixed flames, Whitman et al. [245] examined conditional velocity structure functions over turbulence intensities $u_\ell/S_{\rm L} \approx 2$–10 (corresponding to $\mathrm{Ka}_{\delta,\mathrm{K}} \approx 20$–170). The conditioning was based on the local flame temperature at the first of the two points used to compute each velocity difference, and both separation directions and velocity components were aligned either parallel or tangentially to the local flame normal. It was found that, for high $\mathrm{Ka}_{\delta,\mathrm{K}}$ conditions, the structure functions approached the $r^{N/3}$ scaling predicted using the Kolmogorov hypotheses for sufficiently large r, and that the curves at different locations in the flame could be collapsed using conditionally averaged values of the Kolomogorov scale and dissipation rate (see Fig. 45). At low $\mathrm{Ka}_{\delta,\mathrm{K}}$, the importance of heat release, most likely due to the increasing importance of dilatation and baroclinic torque in the dynamics, was found to prevent the collapse of the different curves. Interestingly, the collapse at higher $\mathrm{Ka}_{\delta,\mathrm{K}}$ observed by Whitman et al. [245] mirrors the earlier results from Bobbitt et al. [207], who showed that, when normalizing by local values of the kinematic viscosity and dissipation rate (i.e., using local Kolmogorov scales), the normalized vorticity magnitude was similar on either side of a highly turbulent premixed flame. The collapse in both cases reflects the purely kinematic effect of the flame on turbulence at highly turbulent conditions in statistically planar configurations; that is, heat release by the flame increases the fluid viscosity which, in turn, increases viscous dissipation and reduces the local Reynolds number.

Sabelnikov et al. [246,247] also performed conditional structure analyses of statistically planar premixed flames, although for lower turbulence intensities and using conditioning based on whether the two velocity locations were in the reactants, flame region, or products. Due to the low intensity of the cases examined, substantial differences in the structure function statistics were observed compared to non-reacting flows, with a substantial impact from dilatation by the flame. This dilatation also generated increased anisotropy in the flame. A related analysis by Brearley et al. [248] examined the same conditional structure functions for a more turbulent premixed flame, again finding substantial effects due to dilatation and the creation of anisotropy by the flame. Interestingly, this study showed that even structure functions computed

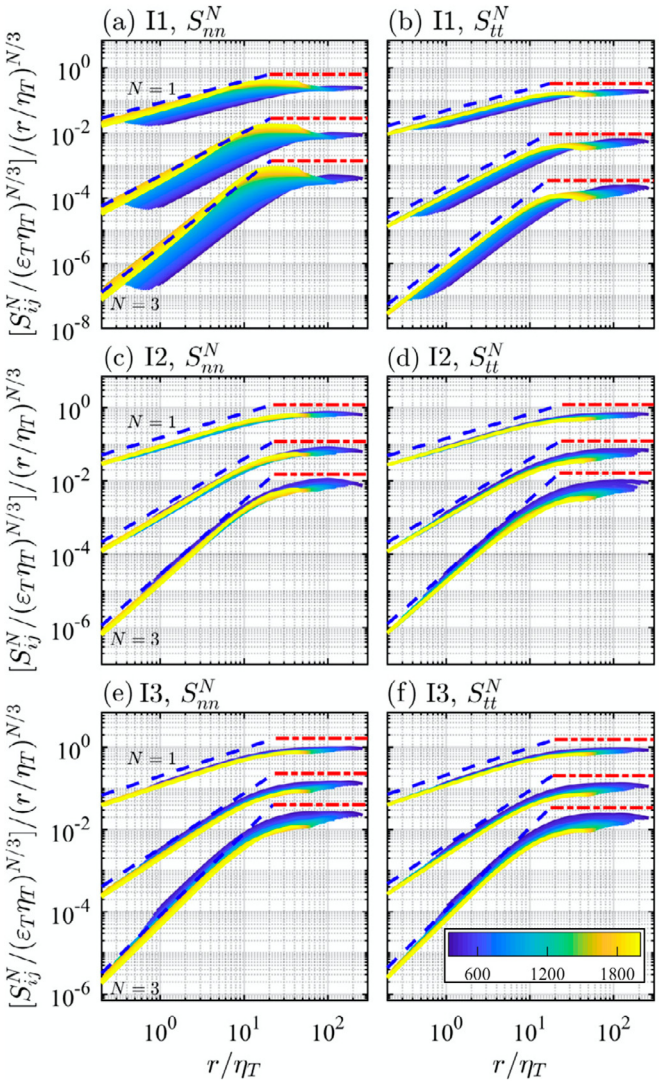


Fig. 45. Compensated conditional structure functions from order $N = 1$ to 3 normalized by the conditional dissipation rate and Kolmogorov length scale for statistically planar flames at three intensities: (a,b) $u_\ell/S_L = 2.5$, (c,d) $u_\ell/S_L = 7.3$, and (e,f) $u_\ell/S_L = 9.9$. Results are shown for longitudinal structure functions both (a,c,e) normal and (b,d,f) tangential to the flame. Blue curves correspond to conditioning on lower temperatures, and yellow curves correspond to higher temperatures. The analytic scaling r^N is shown by blue dashed lines and the Kolmogorov scaling $r^{N/3}$ is shown by red dash-dot lines. Reprinted from Ref. [245] with permission of Elsevier.

purely in the reactants just upstream of the flame differ from non-reacting results.

Ultimately, the multi-scale characterization of turbulence structure in premixed flames remains a subject of substantial ongoing research. It is unclear, in particular, to what extent the spatial variability associated with premixed flames has affected all results obtained to date. Each of the studies described here have sought to examine multi-scale structure at different locations within, or near, premixed flames, and various Fourier and spatial domain approaches have been used. However, as noted by Kim et al. [244], questions requiring both spatial and spectral localization are ill-posed due to the uncertainty principle applied to such analyses. That is, the degree of spatial localization decreases as the spectral localization increases, and vice versa. In this respect, the wavelet analysis used by Kim et al. [244] offers the best control over the respective spatial and spectral localizations, at the expense of substantially increased complexity compared to other approaches. Even using this and related approaches, however, the limitations of the uncertainty principle are fundamental and cannot be overcome.

Connected to the study of multi-scale structure, a renewed focus must be placed on understanding the effects of internal intermittency and on developing new phenomenological theories of turbulence at highly turbulent conditions. Even in non-reacting flows, the Kolmogorov hypotheses become increasingly inaccurate for higher-order quantities, such as velocity structure functions of order four or higher [238]. These deviations from Kolmogorov scaling laws are often called "anomalous" scaling, and are the result of internal intermittency at the intermediate range of scales. Such intermittency causes a break-down in the assumption of scale similarity within the inertial range, and corrections to the Kolmogorov scaling laws have been proposed by Kolmogorov and many others (see Ref. [229] for a review). Given these observations in non-reacting flows, it is difficult to disentangle the underlying reasons for the departures from classical scaling laws, for example for structure functions of order $N = 3$ and 4 in Fig. 45. These departures could be due simply to the increasing importance of intermittency effects as N increases, but during premixed combustion, particularly in the presence of non-unity Lewis numbers and mean pressure gradients, modifications of the Kolmogorov scaling laws may be necessary.

4.3.2. Spectral and multi-scale dynamics

Even after the spectral and multi-scale structure of turbulence has been quantified through the flame, there is the remaining matter of exactly which direction (i.e., up or down scale) combustion processes cause energy to move in a turbulent reacting flow. In the classical picture of turbulence developed by Richardson and Kolmogorov [240,250], energy input on large scales cascades non-dissipatively through the inertial range until it is eventually dissipated as heat by viscous processes at small scales. Despite this classical picture, however, it is still possible for energy to be transferred from small to large scales; that is, it is possible for there to be "backscatter" of energy. There are at least three possible sources of backscatter in turbulent combustion, as described in the following.

1. From the dynamics of the energy cascade in spectral-space, it can be shown that even though the *net* cascade is typically down-scale in 3D turbulent flows, nonlinear inertial processes are responsible for a measurable amount of up-scale energy transfer [251]. This up-scale transfer occurs even in non-reacting homogeneous isotropic turbulence and is typically examined through calculation and partitioning of triadic interactions [252–257] into positive (i.e., down-scale) and negative (i.e., up-scale) contributions. The existence of this up-scale energy transfer is well-known [82] and many efforts have been made to capture this physical backscatter in SFS models for LES [251,258–264]. In most cases, however, such SFS models have proven to be insufficiently dissipative due to inaccurate predictions of local, instantaneous backscatter, resulting in unstable simulations for most practical problems [264].
2. Heat release by combustion causes fluid expansion, which results in a suppression of small-scale turbulence [128]. Moreover, recent results indicate that while small scales are suppressed, there is a corresponding increase in the kinetic energy of large scales (or the mean flow). There are indications that much of this change occurs due to pressure-dilatation effects [249], although turbulent advective processes associated with the cascade process have also been shown to create net energy backscatter near the scale of the flame [88]. Another manifestation of combustion-related backscatter is a large-scale change in the flow due to a small-scale event. This can occur, for example, when there is a locally extreme temperature or

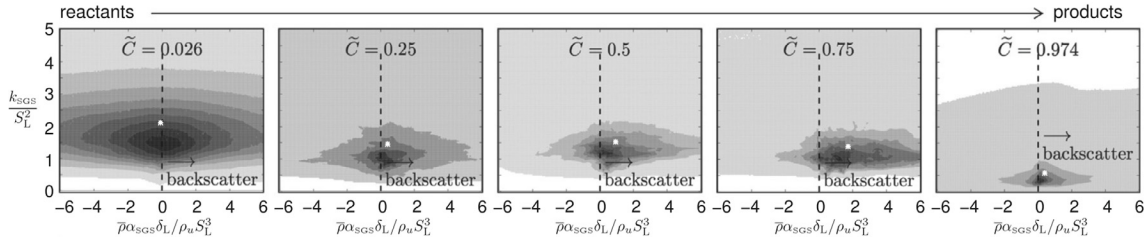


Fig. 46. Normalized joint probability density functions conditioned on the local Favre-filtered progress variable (left to right) for SFS (denoted subgrid scale, SGS, in the figure) kinetic energy k_{SFS} versus SFS production rate α_{SFS} in a statistically planar premixed flame at $u_\ell/S_L = 2.5$. Larger positive values of α_{SFS} are indicative of energy transfer from small to large scales (i.e., energy backscatter). Reprinted from Ref. [249] with permission of Elsevier.

pressure that causes, for example, auto-ignition [265] or deflagration to detonation transition (DDT) [266]. A recent study by Poludnenko [212] has also shown that certain flames exhibit a "pulsating behavior", resulting in pressure pulses emitted from the flame that affect distant locations. These events are typically initiated at very small scales but can have enormous consequences for the larger-scale behavior of the system.

3. In strictly 2D turbulent flows, which occur most frequently in geophysical contexts at very large scales (e.g., hurricanes and mesoscale eddies in the ocean), the nonlinear vortex stretching process that leads to the transfer of energy from large to small scales in most 3D flows is no longer active. As a result, it has been observed that in 2D turbulence, there is an inverse cascade of kinetic energy and a forward cascade of enstrophy, or vorticity magnitude [267]. From a physical standpoint, this means that small eddies in 2D turbulence coalesce to form larger eddies, by contrast to the break-up of large eddies into smaller eddies found in classical non-reacting 3D turbulence. This is a very particular type of energy backscatter that is likely to only be present in 2D simulations of turbulent combustion, or in certain special circumstances where anisotropy generated by the flame results in quasi-2D flow.

It should additionally be noted that both computations [268–270] and experiments [271,272] have revealed a "bump" in the kinetic energy spectrum near the transition between the inertial and dissipation ranges. Although not an example of backscatter in the traditional sense, this bump is associated with the build-up of kinetic energy at the bottom of the inertial range and results in a modest and localized increase in spectral kinetic energy at large wavenumbers, by contrast to the monotonically decreasing spectral kinetic energy associated with the classical cascade process. The resulting effect is termed the "bottleneck" and has been explained [273] as resulting from the relatively rapid decrease of spectral kinetic energy at small scales (i.e., in the dissipation range) and insufficiently broad inertial ranges. As a result, the energy collects at the bottom of the inertial range and creates a bump in the energy spectrum. When there is insufficient dissipation of energy in an LES or DNS of a turbulent flow, energy can also "pile-up" at small-scales and begin to pollute larger scale motions. This effect is, however, non-physical and could be termed the "numerical bottleneck."

The relative importance of each source of backscatter in the list above is still being understood in premixed combustion. Using differential filtering in physical space, O'Brien et al. [249,274] examined energy transfer between subfilter and resolved scales in the compressible, Favre-filtered Navier-Stokes equations using DNS of both diffusion [274] and premixed [249] flames. An analysis of DNS data for a statistically planar premixed flame at a turbulence intensity of $u_\ell/S_L = 2.5$ ($\mathrm{Ka}_{\delta,K} = 20$) showed that SFS backscatter occurs primarily in regions undergoing dilatation due to heat release (see Fig. 46). This net backscatter was found to be predominantly due to the correlation between the velocity and pressure-gradient in the region of highest heat release. Backscatter was also found to occur due to nonlinear advective effects, although this effect was generally weaker than that due to the velocity pressure-gradient dilatation. This result is largely consistent with the purely spatial domain analyses of the kinetic energy dynamics described in Section 4.1, and both Wang & Abraham [165] and MacArt et al. [164] have shown that, at low $\mathrm{Ka}_{\delta,K}$, the velocity pressure-gradient correlation term is dominant in the kinetic energy dynamics.

With respect to the inter-scale transfer of energy by nonlinear advective effects, Towery et al. [88] used a conditional Fourier spectral analysis to examine the exchange of energy between scales and the net direction of the cascade process in a statistically planar premixed flame at $\mathrm{Ka}_{\delta,K} = 20$. This analysis showed that, within the flame brush close to the burnt products, nonlinear advective processes preferentially transfer energy from small to large scales. This net backscatter of energy is contrary to the net forward cascade of energy found in non-reacting turbulence. In this study, the inverse energy cascade was found to extend from slightly smaller than the scale of the flame up to the turbulence integral scale. However, determining whether this inverse cascade remains scale-local to the flame, or always extends to the integral scale, was made difficult by the relatively small separation between ℓ and δ_L^0 in this study.

Finally, the conditional wavelet analysis of a higher intensity (where $\mathrm{Ka}_{\delta,K} = 72$) statistically planar premixed flame by Kim et al. [244] showed that, in the flow as a whole, the spectral dynamics were largely similar to that found in non-reacting incompressible turbulent flows, with net down-scale transfers of energy due to advective and pressure gradient effects. Once again, however, within the flame brush near the region of greatest heat release, both of these effects reverse direction, resulting in up-scale transfer of kinetic energy. The resulting net effect is relatively weak up-scale energy transfer (or at least substantially weakened down-scale transfer) for intermediate values of the progress variable.

Returning to the questions posed at the beginning of this section, tentative and preliminary answers are now available. Turbulent small scale motions are generally suppressed through premixed flames at high turbulence intensities, due primarily to the effects of increased viscous dissipation associated with chemical heat release. At lower turbulence intensities, there is evidence of flame-generated turbulence, up-scale net energy transfer, and backscatter, none of which are explicitly addressed by purely (or mostly) dissipative SFS models developed for LES of non-reacting turbulence. At highly turbulent conditions, it appears that the Kolmogorov hypotheses remain relevant, at least for statistically planar premixed flames, and that results for different flame locations, conditions, and configurations can be collapsed using locally defined Kolmogorov scales. Tentatively, there are thus indications that there *may* be universal aspects of spectral and multi-scale turbulence characteristics during highly turbulent premixed combustion.

It should be cautioned, however, that although these studies provide a consistent view of up-scale kinetic energy transfer by nonlinear advective and pressure-gradient effects in premixed flames at moderate values of $Ka_{\delta,K}$, each study was focused on DNS data of statistically planar premixed flames stochastically forced at large scales. Moreover, two of these studies (i.e., Refs. [88,249]) examined the same DNS data set. It is thus now important to perform similar analyses of spectral kinetic energy dynamics in a broader range of flows, particularly those involving mean shear, geometric complexity, and persistent pressure gradients. The effects of different forcing mechanisms—including the absence of forcing, as in DNS of premixed flames interacting with decaying turbulence—must also be examined in more detail to quantify the dependence of these results on the energy injection method. Stronger claims of universality, in particular, cannot be made until these studies have been undertaken. Kazbekov & Steinberg [275] have begun taking initial steps in this direction using experimental measurements of premixed swirl flames and physical space filtering, revealing mean up-scale energy transfer within the flame across scales in the range of the laminar flame thickness for moderate Karlovitz numbers.

4.4. Summary

Our understanding of the properties — both kinematic and dynamic — of turbulence during highly turbulent premixed combustion has advanced considerably over the past decade. From the studies and prior research summarized in this section, we now know, in particular, that:

1. *Turbulence characteristics are similar to those found in corresponding non-reacting flows for highly turbulent statistically planar and jet premixed flames.* This includes the dynamics of the turbulence kinetic energy and stresses, the coupled dynamics and properties of the vorticity and strain rate, and the applicability of the Kolmogorov hypotheses and Richardson cascade concept. The creation of anisotropy by the flame also weakens as the turbulence intensity increases for these flows.
2. *The primary effect of the flame on turbulence for highly turbulent statistically planar and jet premixed flames is kinematic in nature and results from the increase in temperature dependent viscosity due to chemical heat release.* This accounts for the collapse of vorticity and structure function results when normalizing statistics either side of a premixed flame using local (or conditioned) values of the kinematic viscosity and viscous dissipation rate.
3. *Turbulence characteristics can be substantially affected by the flame, beyond simply the kinematic viscous effect, even at highly turbulent conditions due to non-unity Lewis numbers, mean pressure-gradients, and pressure pulsations.* These conditions result in the continued importance, and even dominance, of dilatation, baroclinic torque, and velocity-pressure gradient effects as the turbulence intensity increases, weakening the similarity to corresponding non-reacting flows during highly turbulent premixed combustion.
4. *The gradient transport (or Boussinesq) hypothesis is as applicable for highly turbulent premixed statistically planar and jet flames as for corresponding non-reacting flows, but this hypothesis is unlikely to remain valid in more practically relevant flows.* In particular, non-unity Lewis numbers and mean pressure gradients are likely to create counter-gradient transport even at highly turbulent conditions, similar to results for lower turbulence intensities.
5. *There is a weakening of the forward kinetic energy cascade even in highly turbulent statistically planar premixed flames, and there is a net backscatter of energy for lower turbulence intensities.* As a result, even in reacting flows where there is no net backscatter of energy, the assumption of a filter cutoff for LES in the inertial range, as well as the assumption of uniform equilibrium down-scale transfer of energy, may become inaccurate.

It should be noted that the last two summary points relate to the manner in which turbulence is modeled, in either RANS or LES approaches, for highly turbulent conditions. Although no model has yet been developed to explicitly account for these insights, recent studies of highly turbulent statistically planar and jet flames have shown that many of the assumptions central to models for non-reacting flows (e.g., the gradient transport hypothesis and net down-scale energy transfer) are still relevant at highly turbulent conditions. However, the same may not be true for more complicated and physically realistic flows, such as swirl [219,220] and bluff body [218] configurations where there is known to be substantial turbulence production at small scales by baroclinic torque. Before non-reacting models can be confidently applied at highly turbulent conditions, additional work must be done to understand kinetic energy dynamics in these and other more realistic configurations.

5. Outlook

Through this paper, we hope to have provided a succinct summary of the current state-of-knowledge regarding the structure and dynamics of highly turbulent premixed flames. Summary points are included at the ends of Sections 2–4 and are not repeated here. Instead, we present a brief outlook; although we have substantially increased our knowledge of highly turbulent premixed combustion in a relatively short period of time, our current understanding does motivate several new areas of inquiry and study.

Fundamentally, the community needs to critically assess the validity and utility of defining combustion regimes in real configurations at highly turbulent conditions. At a minimum, consensus must be reached on a standardized method of characterizing flames in systems with widely varying turbulence properties, many of which simultaneously generate and attenuate turbulence over the flame brush. Furthermore, additional care must be taken in the design of experimental configurations to ensure that the rapid mixing between the targeted experiment and the surroundings—induced by intense turbulence—does not alter the thermochemistry in the flame brush. While both experiments and DNS have progressed considerably, there remain leading order discrepancies (e.g., between measured and simulated turbulent flame speed enhancement) that require reconciliation through improved understanding of both the combustion thermochemistry and turbulence dynamics.

From the perspective of advancing understanding of thermochemistry in highly turbulent flames, one approach is to quantify the multi-dimensional thermochemical space; e.g., its dimensionality, dynamic evolution, and impact on local and global flame characteristics, etc. The underlying physico-chemical conditions that create this high-dimensional space should also be understood and quantified. In particular, connecting the dynamics of turbulent flames to fundamental flame properties—such as laminar flame speed, extinction and ignition residence times in perfectly stirred reactors, and homogeneous auto-ignition—can be attempted. Experimentally, simultaneous multi-scalar and/or scalar-velocity measurements can facilitate such understanding, in particular under conditions that are computationally challenging for DNS. Theoretically, scaling analysis of the turbulent flame speed should be expanded to consider contributions from the local conditions, instead of relying on a single laminar flame speed to scale the entire thermochemistry.

With established physical understanding and quantitative description of thermochemistry, improvements in modeling can be attempted. One particular challenge in modeling highly turbulent premixed flames is that the rich small-scale flame structures and dynamics can potentially occur entirely at sub-filter scales. As most existing turbulent combustion models have certain intrinsic assumptions regarding the dimensionality of the thermochemical space, it is important to incorporate the latest understanding into modeling studies.

Two approaches have emerged going forward: one is to continue improving existing turbulent combustion models, leveraging new physical understanding, DNS data, and computational and experimental diagnostics. This approach has been constantly pursued and progressively perfected. The second approach is to develop adaptive modeling [276]. The adaptivity can manifest in terms of adaptive mesh resolutions around different flame features. For example, recent developments on combining adaptive mesh refinement [277] with local flame feature detection resolve premixed flame fronts such that local flame speed can be adequately captured. Embedding DNS into LES is another idea to ensure that multi-modal flame features can be captured without prohibitive computational cost. The adaptivity can also manifest as model adaptivity, such as in [106,277] where different turbulent combustion models are selected for different regions of a turbulent flame. For either approach, robust coupling and transition among different combustion models or different mesh resolutions remain outstanding challenges.

Chemical kinetic modelling is closely connected to turbulent combustion closure models. The recent development of lumped chemical kinetic models, such as HyChem [20,21], has set a good example in reducing the complexities of chemistry for real fuels. Further model reduction to 10–30 species is often required to enable DNS or LES. It is important to recognize the impact from abundant, and sometimes extreme, thermochemical states in highly turbulent flames when constructing reduced kinetic models; their verification and validation should be expanded to account for possible thermochemical states that are created in turbulent flames. Construction and reduction of chemical kinetic models is another area that benefits from a physical and quantitative understanding of the high-dimensional thermochemical state space.

In order to understand this state space under more practical conditions, characterization of large hydrocarbon fuels under pressurized conditions is necessary to reach conditions close to those in Table 1. Moreover, most existing studies focus on gaseous flames; interactions between highly turbulent reacting flows and sprays are comparatively less studied. Droplet motion, evaporation, and heat transfer introduce additional sinks/sources to alter local compositional space (i.e., temperature and species), and introduce additional time and length scales to the dynamics of combustion. An experimental framework targeting model validation, such as that reported in [278] for dilute acetone/ethanol sprays, should be initiated for a larger variety of fuels under highly turbulent conditions. Development of DNS in simulating spray flames should also receive more attention.

From the perspective of understanding turbulence structure and dynamics, the analyses of turbulence kinetic energy, stresses, and fluxes described in Section 4.1, as well as the spectral and multiscale analyses described in Section 4.3, must now be extended to more realistic flows and conditions that include non-unity Lewis numbers, mean pressure gradients, solid boundaries, and other practically relevant flow effects. Recent research has shown that our understanding of turbulence properties based on the study of only statistically planar and jet configurations is incomplete and not necessarily representative of more realistic configurations. However, progress has already been made towards understanding vorticity dynamics in such configurations [218–220], and similar studies must now be undertaken to more fully understand impacts on turbulence statistics and spectra.

The further study of these statistics and spectra will also provide insights into new model forms for numerical simulations of practical highly turbulent premixed combustion using RANS and LES approaches. Current studies have demonstrated the inadequacy of the gradient transport hypothesis and purely and uniformly dissipative SFS models, particularly for moderate and low turbulence intensities, and now further work must be carried out to formulate new models that are sensitive to local flow conditions (e.g., the local Karlovitz and Damköhler numbers) across a broader range of practical configurations.

The renewed study of internal intermittency as a function of configuration and local turbulence-flame conditions is also an important area of further research. From an operational standpoint, turbulence can lead to unexpectedly high probabilities of extreme events, such as local increases in pressure, temperature, and scalar gradients. Each of these events can lead to undesirable transient phenomena such as extinction, ignition, or deflagration to detonation transition of reactive mixtures at difficult-to-predict locations and times. The onset of these extreme events—which arise locally, often at small scales, with significant global consequences—is intrinsically connected to the intermittent character of turbulence.

In general, internal intermittency becomes more pronounced as the turbulence intensity increases, and increased probabilities of extreme gradients (e.g., in temperature or pressure) associated with highly turbulent conditions may result in global changes to system properties. Recent research, for example, has indicated that turbulence-induced fluctuations in thermodynamic quantities can lead to detonation formation in highly turbulent auto-igniting reactant mixtures [225], as well as in highly turbulent deflagrating systems [212,279]. The understanding of how such transitions can be predicted, particularly at highly turbulent conditions, remains an important direction for future study. Further study is also required to determine whether the fundamental assumptions encompassed by the Kolmogorov hypotheses, including the presence of a universal equilibrium range, remain valid in premixed reacting flows over a variety of conditions.

Finally, complexity and turbulent mixing have previously been characterized in non-reacting flows through the dispersion of fluid parcels or tracer quantities. This dispersion can be quantified in an Eulerian sense using fluxes, but can also be characterized through a Lagrangian approach that tracks the separation of two initially close fluid parcels in time [280]. In turbulent flows, these parcels move apart at a rate specified by the Lyapunov exponents, where positive exponents indicate a nonlinear unstable dynamical system characterized by an extreme sensitivity to initial conditions. The separation of these tracer parcels has been connected to turbulent diffusion, with studies showing more rapid separation of tracers in turbulent, as compared to laminar, flows (see Refs. [281,282] for reviews). Similar to the new insights obtained from Lagrangian analyses of thermochemical trajectories, Lagrangian analyses of turbulence properties and fluid particle dispersion may result in new models of turbulent transport during highly turbulent premixed combustion.

Declaration of Competing Interest

The authors declare that they have no known competing financial interests or personal relationships that could have appeared to influence the work reported in this paper.

Acknowledgements

The authors acknowledge the support of AFOSR grants FA9550-17-01-0011, FA9550-17-1-0144, FA9550-18-1-0173, and Project

Monitor Dr. Chiping Li. P. E. Hamlington acknowledges support from NSF award 1847111, as well as helpful discussions with Dr. Ryan Darragh, Dr. Colin Towery, Mr. Michael Meehan, and Mr. Samuel Whitman. X. Zhao acknowledges Mr. Ji-Woong Park and Mr. Peiyu Zhang for their helpful contribution in generating laminar flame databases.

References

[1] Pope S. Turbulent premixed flames. *Annu Rev Fluid Mech* 1987;**19**:237–70.
[2] Peters N. Laminar flamelet concepts in turbulent combustion. *Proc Combust Inst* 1988;**21**(1):1231–50.
[3] Bradley D. How fast can we burn? *Proc Combust Inst* 1992;**24**:247–62.
[4] Bray K. The challenge of turbulent combustion. *Proc Combust Inst* 1996;**26**(1):1–26. doi:10.1016/S0082-0784(96)80195-0.
[5] Law C, Sung C. Structure, aerodynamics, and geometry of premixed flamelets. *Prog Energy Combust Sci* 2000;**26**(4):459–505.
[6] Lipatnikov A, Chomiak J. Turbulent flame speed and thickness: phenomenology, evaluation, and application in multi-dimensional simulations. *Prog Energy Combust Sci* 2002;**28**:1–74.
[7] Bilger R, Pope S, Bray K, Driscoll J. Paradigms in turbulent combustion research. *Proc Combust Inst* 2005;**30**(1):21–42. doi:10.1016/j.proci.2004.08.273.
[8] Driscoll JF. Turbulent premixed combustion: flamelet structure and its effect on turbulent burning velocities. *Prog Energy Combust Sci* 2008;**34**(1):91–134.
[9] Lipatnikov A, Chomiak J. Effects of premixed flames on turbulence and turbulent scalar transport. *Prog Energy Combust Sci* 2010;**36**(1):1–102. doi:10.1016/j.pecs.2009.07.001.
[10] Lipatnikov A. *Fundamentals of premixed turbulent combustion*. CRC Press; 2012. ISBN 978-1-46-651024-1.
[11] Driscoll JF, Chen JH, Skiba AW, Carter CD, Hawkes ER, Wang H. Premixed flames subjected to extreme turbulence: some questions and recent answers. *Prog Energy Combust Sci* 2020;**76**:100802. doi:10.1016/j.pecs.2019.100802.
[12] Xu C, Park J-W, Yoo CS, Chen JH, Lu T. Identification of premixed flame propagation modes using chemical explosive mode analysis. *Proc Combust Inst* 2018a. doi:10.1016/j.proci.2018.07.069.
[13] Chen JH, Hawkes ER, Sankaran R, Mason SD, Im HG. Direct numerical simulation of ignition front propagation in a constant volume with temperature inhomogeneities: I. Fundamental analysis and diagnostics. *Combust Flame* 2006;**145**(1):128–44.
[14] Pal P, Valorani M, Arias PG, Im HG, Wooldridge MS, Ciottoli PP, et al. Computational characterization of ignition regimes in a syngas/air mixture with temperature fluctuations. *Proc Combust Inst* 2017;**36**(3):3705–16.
[15] Yoo CS, Lu T, Chen JH, Law CK. Direct numerical simulations of ignition of a lean n-heptane/air mixture with temperature inhomogeneities at constant volume: parametric study. *Combust Flame* 2011;**158**(9):1727–41.
[16] Martz JB, Lavoie GA, Im HG, Middleton RJ, Babajimopoulos A, Assanis DN. The propagation of a laminar reaction front during end-gas auto-ignition. *Combust Flame* 2012;**159**(6):2077–86.
[17] Schulz O, Noiray N. Autoignition flame dynamics in sequential combustors. *Combust Flame* 2018;**192**:86–100.
[18] Smooke DM, Miller JA, Kee RJ. Determination of adiabatic flame speeds by boundary value methods. *Combust Sci Technol* 1983;**34**(1-6):79–90.
[19] Kee RJ, Grcar JF, Smooke MD, Miller J, Meeks E. Premix: a Fortran program for modeling steady laminar one-dimensional premixed flames. *Report No. SAND85-8249*; 1985.
[20] Wang H, Xu R, Wang K, Bowman C, Davidson D, Hanson R, et al. A physics-based approach to modeling real-fuel combustion chemistry - I. Evidence from experiments, and thermodynamic, chemical kinetic and statistical considerations. *Combust Flame* 2018a;**193**:502–19.
[21] Xu R, Wang K, Banerjee S, Shao J, Parise T, Zhu Y, et al. A physics-based approach to modeling real-fuel combustion chemistry – II. Reaction kinetic models of jet and rocket fuels. *Combust Flame* 2018b;**193**:520–37.
[22] Wang H, You X, Joshi A, Davis S, Laskin FA. High-temperature combustion reaction model of H_2/CO/C_1-C_4 compounds. http://ignis.usc.edu/usc_mech_ii.htm; 2007. USC Mech Version II.
[23] Ihme M, Shunn L, Zhang J. Regularization of reaction progress variable for application to flamelet-based combustion models. *J Comput Phys* 2012;**231**:7715–21.
[24] Barlow RS, Magnotti G, Cutcher HC, Masri AR. On defining progress variable for Raman/Rayleigh experiments in partially-premixed methane flames. *Combust Flame* 2017;**179**(9):117–29.
[25] Ranzi E, Dente M, Goldaniga A, Bozzano G, Faravelli T. Lumping procedures in detailed kinetic modeling of gasification, pyrolysis, partial oxidation and combustion of hydrocarbon mixtures. *Prog Energy Combust Sci* 2001;**27**:99–139.
[26] Poinsot T, Veynante D. *Theoretical and numerical combustion*. 3rd ed. R.T. Edwards; 2012.
[27] Turns SR. *An introduction to combustion: concepts and applications*. 3rd ed. McGraw-Hill; 2012.
[28] Williams F. *Combustion theory*. 2nd ed. CRC Press; 1985.
[29] Gicquel O, Darabiha N, Thvenin D. Laminar premixed hydrogen/air counterflow flame simulations using flame prolongation of ILDM with differential diffusion. *Proc Combust Inst* 2000;**28**(2):1901–8. doi:10.1016/S0082-0784(00)80594-9.
[30] van Oijen J, de Goey L. Modelling of premixed laminar flames using flamelet–generated manifolds. *Combust Sci Technol* 2000;**161**(1):113–37.
[31] Hawkes E, Cant R. A flame surface density approach to large-eddy simulation of premixed turbulent combustion. *Proc Combust Inst* 2000;**28**(1):51–8. doi:10.1016/S0082-0784(00)80194-0.
[32] Pitsch H. A consistent level set formulation for large-eddy simulation of premixed turbulent combustion. *Combust Flame* 2005;**143**(4):587–98. doi:10.1016/j.combustflame.2005.08.031.
[33] Shanbhogue SJ, Husain S, Lieuwen T. Lean blowoff of bluff body stabilized flames: scaling and dynamics. *Prog Energy Combust Sci* 2009;**35**(1):98–120. doi:10.1016/j.pecs.2008.07.003.
[34] Huang Y, Yang V. Dynamics and stability of lean-premixed swirl-stabilized combustion. *Prog Energy Combust Sci* 2009;**35**(4):293–364. doi:10.1016/j.pecs.2009.01.002.
[35] O'Connor J, Acharya V, Lieuwen T. Transverse combustion instabilities: acoustic, fluid mechanic, and flame processes. *Prog Energy Combust Sci* 2015;**49**:1–39. doi:10.1016/j.pecs.2015.01.001.
[36] Kariuki J, Dowlut A, Yuan R, Balachandran R, Mastorakos E. Heat release imaging in turbulent premixed methane-air flames close to blow-off. *Proc Combust Inst* 2015;**35**(2):1443–50. doi:10.1016/j.proci.2014.05.144.
[37] Kariuki J, Dowlut A, Balachandran R, Mastorakos E. Heat release imaging in turbulent premixed ethylene-air flames near blow-off. *Flow Turb Combust* 2016;**96**(4):1039–51. doi:10.1007/s10494-016-9720-y.
[38] Roy Chowdhury B, Cetegen BM. Experimental study of the effects of free stream turbulence on characteristics and flame structure of bluff-body stabilized conical lean premixed flames. *Combust Flame* 2017;**178**:311–28. doi:10.1016/j.combustflame.2016.12.019.
[39] Chowdhury BR, Wagner JA, Cetegen BM. Experimental study of the effect of turbulence on the structure and dynamics of a bluff-body stabilized lean premixed flame. *Proc Combust Inst* 2017;**36**(2):1853–9.
[40] Gregor M, Seffrin F, Fuest F, Geyer D, Dreizler A. Multi-scalar measurements in a premixed swirl burner using ID Raman/Rayleigh scattering. *Proc Combust Inst* 2009;**32**(2):1739–46. doi:10.1016/j.proci.2008.06.133.
[41] Cheng R, Littlejohn D, Strakey P, Sidwell T. Laboratory investigations of a low-swirl injector with H_2 and CH_4 at gas turbine conditions. *Proc Combust Inst* 2009;**32 II**(2):3001–9. doi:10.1016/j.proci.2008.06.141.
[42] Nogenmyr K-J, Fureby C, Bai X, Petersson P, Collin R, Linne M. Large eddy simulation and laser diagnostic studies on a low swirl stratified premixed flame. *Combust Flame* 2009;**156**(1):25–36. doi:10.1016/j.combustflame.2008.06.014.
[43] Nogenmyr K-J, Petersson P, Bai X, Fureby C, Collin R, Lantz A, et al. Structure and stabilization mechanism of a stratified premixed low swirl flame. *Proc Combust Inst* 2011;**33**(1):1567–74. doi:10.1016/j.proci.2010.06.011.
[44] Dunn MJ, Masri AR, Bilger RW. A new piloted premixed jet burner to study strong finite-rate chemistry effects. *Combust Flame* 2007;**151**(1-2):46–60. doi:10.1016/j.combustflame.2007.05.010.
[45] Dunn MJ, Masri AR, Bilger RW, Barlow RS, Wang G-H. The compositional structure of highly turbulent piloted premixed flames issuing into a hot coflow. *Proc Combust Inst* 2009;**32**:1779–86. doi:10.1007/s10494-010-9280-5.
[46] Dunn MJ, Masri AR, Bilger RW, Barlow RS. Finite rate chemistry effects in highly sheared turbulent premixed flames. *Flow Turb Combust* 2010;**85**(3-4):621–48. doi:10.1007/s10494-010-9280-5.
[47] Zhou B, Brackmann C, Li Q, Wang Z, Petersson P, Li Z, et al. Distributed reactions in highly turbulent premixed methane/air flames. Part I. Flame structure characterization. *Combust Flame* 2015a;**162**(7):2937–53. doi:10.1016/j.combustflame.2014.12.021.
[48] Zhou B, Brackmann C, Li Z, Aldén M, Bai XS. Simultaneous multi-species and temperature visualization of premixed flames in the distributed reaction zone regime. *Proc Combust Inst* 2015b;**35**(2):1409–16. doi:10.1016/j.proci.2014.06.107.
[49] Rosell J, Bai X-S, Sjoholm J, Zhou B, Li Z, Wang Z, et al. Multi-species PLIF study of the structures of turbulent premixed methane/air jet flames in the flamelet and thin-reaction zones regimes. *Combust Flame* 2017;**182**:324–38. doi:10.1016/j.combustflame.2017.04.003.
[50] Wang X, Jin T, Luo KH. Response of heat release to equivalence ratio variations in high Karlovitz premixed H_2/air flames at 20 atm. *Int J Hydrog* 2019a;**44**(5):3195–207. doi:10.1016/j.ijhydene.2018.12.027.
[51] Yuen FT, Gülder Ö L. Premixed turbulent flame front structure investigation by Rayleigh scattering in the thin reaction zone regime. *Proc Combust Inst* 2009;**32**:1747–54. doi:10.1016/j.proci.2008.08.005.
[52] Yuen FTC, Gülder Ö L. Dynamics of lean-premixed turbulent combustion at high turbulence intensities. *Combust Sci Technol* 2010;**182**(4-6):544–58. doi:10.1080/00102200903463274.
[53] Yuen F, Gülder O. Turbulent premixed flame front dynamics and implications for limits of flamelet hypothesis. *Proc Combust Inst* 2013;**34**:1393–400.
[54] Tamadonfar P, Gülder Ö L. Experimental investigation of the inner structure of premixed turbulent methane/air flames in the thin reaction zones regime. *Combust Flame* 2015;**162**(1):115–28. doi:10.1016/j.combustflame.2014.07.001.
[55] Osborne JR, Ramji SA, Carter CD, Steinberg AM. Relationship between local reaction rate and flame structure in turbulent premixed flames from simultaneous 10 kHz TPIV, OH PLIF, and CH_2O PLIF. *Proc Combust Inst* 2017;**36**(2):1835–41. doi:10.1016/j.proci.2016.07.124.
[56] Wabel TM, Skiba AW, Driscoll JF. Turbulent burning velocity measurements: extended to extreme levels of turbulence. *Proc Combust Inst* 2017a;**36**(2):1801–8. doi:10.1016/j.proci.2016.08.013.
[57] Wabel TM, Skiba AW, Temme JE, Driscoll JF. Measurements to determine the regimes of premixed flames in extreme turbulence. *Proc Combust Inst* 2017b;**36**(2):1809–16. doi:10.1016/j.proci.2016.08.065.

[58] Skiba AW, Wabel TM, Carter CD, Hammack SD, Temme JE, Driscoll JF. Premixed flames subjected to extreme levels of turbulence Part I: flame structure and a new measured regime diagram. *Combust Flame* 2018a;**189**:407–32.
[59] Wabel TM, Barlow RS, Steinberg AM. Reaction zone stratification in piloted highly-turbulent fuel-lean premixed jets. *Combust Flame* 2019;**208**:327–9.
[60] Fries D, Ochs BA, Saha A, Ranjan D, Menon S. Flame speed characteristics of turbulent expanding flames in a rectangular channel. *Combust Flame* 2019;**199**:1–13.
[61] Ochs BA, Fries D, Ranjan D, Menon S. Turbulent flame speeds of premixed supersonic flame kernels. *Flow Turb Combust* 2018;**101**(3):927–51.
[62] Yang S, Saha A, Liang W, Wu F, Law CK. Extreme role of preferential diffusion in turbulent flame propagation. *Combust Flame* 2018a;**188**:498–504.
[63] Yang S, Saha A, Liu Z, Law CK. Role of Darrieus-Landau instability in propagation of expanding turbulent flames. *J Fluid Mech* 2018b;**850**:784–802. doi:10.1017/jfm.2018.426.
[64] Sosa J, Chambers J, Ahmed KA, Poludnenko A, Gamezo VN. Compressible turbulent flame speeds of highly turbulent standing flames. *Proc Combust Inst* 2019;**37**(3):3495–502. doi:10.1016/j.proci.2018.07.039.
[65] Wang H, Hawkes ER, Savard B, Chen JH. Direct numerical simulation of a high Ka CH4/air stratified premixed jet flame. *Combust Flame* 2018b;**193**:229–45. doi:10.1016/j.combustflame.2018.03.025.
[66] Xu C, Poludnenko AY, Zhao X, Wang H, Lu T. Structure of strongly turbulent premixed n-dodecane–air flames: Direct numerical simulations and chemical explosive mode analysis. *Combust Flame* 2019;**209**:27–40. doi:10.1016/j.combustflame.2019.07.027.
[67] Lapointe S, Savard B, Blanquart G. Differential diffusion effects, distributed burning, and local extinctions in high Karlovitz premixed flames. *Combust Flame* 2015;**162**(9):3341–55. doi:10.1016/j.combustflame.2015.06.001.
[68] Im HG. Direct numerical simulations for combustion science: past, present, and future. In: De S, Agarwal AK, Chaudhuri S, Sen S, editors. *Modeling and simulation of turbulent combustion*. Singapore: Springer Singapore; 2018. p. 99–132. doi:10.1007/978-981-10-7410-3_4.
[69] Aspden AJ, Day MS, Bell JB. Turbulence-flame interactions in lean premixed hydrogen: Transition to the distributed burning regime. *J Fluid Mech* 2011a;**680**:287–320. doi:10.1017/jfm.2011.164.
[70] Hamlington PE, Darragh R, Briner CA, Towery CA, Taylor BD, Poludnenko AY. Lagrangian analysis of high-speed turbulent premixed reacting flows: thermochemical trajectories in hydrogen–air flames. *Combust Flame* 2017;**186**:193–207. doi:10.1016/j.combustflame.2017.08.001.
[71] Nivarti GV, Cant RS. Scalar transport and the validity of Damköhler's hypotheses for flame propagation in intense turbulence. *Phys Fluids* 2017;**29**(8):085107.
[72] Klein M, Chakraborty N, Jenkins KW, Cant RS. Effects of initial radius on the propagation of premixed flame kernels in a turbulent environment. *Phys Fluids* 2006;**18**(5).
[73] Shalaby H, Thévenin D. Statistically significant results for the propagation of a turbulent flame kernel using direct numerical simulation. *Flow Turb Combust* 2010;**84**(3):357–67.
[74] Uranakara HA, Chaudhuri S, Dave HL, Arias PG, Im HG. A flame particle tracking analysis of turbulence-chemistry interaction in hydrogen-air premixed flames. *Combust Flame* 2016;**163**:220–40. doi:10.1016/j.combustflame.2015.09.033.
[75] Falkenstein T, Kang S, Cai L, Bode M, Pitsch H. DNS study of the global heat release rate during early flame kernel development under engine conditions. *Combust Flame* 2020;**213**:455–66. ArXiv:1908.07556. doi:10.1016/j.combustflame.2019.11.031.
[76] Krisman A, Meagher P, Zhao X, Park J-W, Lu T, Chen JH. A direct numerical simulation of jet a flame kernel quenching. *Combust Flame* 2020;**225**:349–63. doi:10.1016/j.combustflame.2020.11.003.
[77] Wang L, Jiang Y, Pan L, Xia Y, Qiu R. Lagrangian investigation and chemical explosive mode analysis of extinction and re-ignition in H2/CO/N2 syngas non-premixed flame. *Int J Hydrog* 2016a;**41**(8):4820–30. doi:10.1016/j.ijhydene.2016.01.043.
[78] Wang H, Hawkes ER, Chen JH, Zhou B, Li Z, Aldén M. Direct numerical simulations of a high Karlovitz number laboratory premixed jet flame – an analysis of flame stretch and flame thickening. *J Fluid Mech* 2017a;**815**:511–36. doi:10.1017/jfm.2017.53.
[79] Wang H, Hawkes ER, Chen JH. A direct numerical simulation study of flame structure and stabilization of an experimental high Ka CH_4/air premixed jet flame. *Combust Flame* 2017b;**180**:110–23. doi:10.1016/j.combustflame.2017.02.022.
[80] Sankaran R, Hawkes ER, Chen JH, Lu T, Law CK. Structure of a spatially developing turbulent lean methane–air Bunsen flame. *Proc Combust Inst* 2007;**31**(1):1291–8. doi:10.1016/j.proci.2006.08.025.
[81] Wang H, Hawkes ER, Zhou B, Chen JH, Li Z, Aldén M. A comparison between direct numerical simulation and experiment of the turbulent burning velocity-related statistics in a turbulent methane-air premixed jet flame at high Karlovitz number. *Proc Combust Inst* 2017c;**36**(2):2045–53. doi:10.1016/j.proci.2016.07.104.
[82] Pope SB. *Turbulent flows*. Cambridge University Press; 2000.
[83] Lapointe S, Blanquart G. Fuel and chemistry effects in high Karlovitz premixed turbulent flames. *Combust Flame* 2016;**167**:294–307. doi:10.1016/j.combustflame.2016.01.035.
[84] Kolla H, Hawkes ER, Kerstein AR, Swaminathan N, Chen JH. On velocity and reactive scalar spectra in turbulent premixed flames. *J Fluid Mech* 2014;**754**:456–87. doi:10.1017/jfm.2014.392.
[85] Kolla H, Zhao X-Y, Chen JH, Swaminathan N. Velocity and reactive scalar dissipation spectra in turbulent premixed flames. *Combust Sci Technol* 2016;**188**(9):1424–39. doi:10.1080/00102202.2016.1197211.
[86] Aspden AJ, Day MS, Bell JB. Turbulence-chemistry interaction in lean premixed hydrogen combustion. *Proc Combust Inst* 2015;**35**(2):1321–9. doi:10.1016/j.proci.2014.08.012.
[87] Zhao X, Tao Y, Wang H, Lu T. Sensitivities of direct numerical simulations to chemical kinetic uncertainties: spherical flame kernel evolution of a real jet fuel. *Combust Flame* 2019a;**209**:117–32.
[88] Towery CAZ, Poludnenko AY, Urzay J, O'Brien J, Ihme M, Hamlington PE. Spectral kinetic energy transfer in turbulent premixed reacting flows. *Phys Rev E* 2016;**93**(5):053115. doi:10.1103/PhysRevE.93.053115.
[89] Peters N. Length scales in laminar and turbulent flames. In: Oran E, Boris J, editors. *Numerical approaches to combustion modeling*, vol. 135. AIAA; 1991. p. 155–82.
[90] Jiménez J, Wray AA, Saffman PG, Rogallo RS. The structure of intense vorticity in isotropic turbulence. *J Fluid Mech* 1993;**265**:65–90.
[91] Buch KA, Dahm WJA. Experimental study of the fine-scale structure of conserved scalar mixing in turbulent shear flows. Part 1. Sc≫1. *J Fluid Mech* 1996;**317**:21–71. doi:10.1017/S0022112096000651.
[92] Buch KA, Dahm WJA. Experimental study of the fine-scale structure of conserved scalar mixing in turbulent shear flows. Part 2. Sc≫1. *J Fluid Mech* 1998;**364**:1–29. doi:10.1017/S0022112098008726.
[93] Ganapathisubramani B, Lakshminarasimhan K, Clemens NT. Investigation of three-dimensional structure of fine scales in a turbulent jet by using cinematographic stereoscopic particle image velocimetry. *J Fluid Mech* 2008;**598**:141–75. doi:10.1017/S0022112007009706.
[94] Han W, Wang H, Kuenne G, Hawkes ER, Chen JH, Janicka J, et al. Large eddy simulation/dynamic thickened flame modeling of a high Karlovitz number turbulent premixed jet flame. *Proc Combust Inst* 2019a;**37**(2):2555–63. doi:10.1016/j.proci.2018.06.228.
[95] Williams F. Criteria for existence of wrinkled laminar flame structure of premixed turbulent flames. *Combust Flame* 1976;**26**:269.
[96] Borghi R. Turbulent combustion modelling. *Prog Energy Combust Sci* 1988;**14**(4):245–92.
[97] Klimov AM. Laminar flame in a turbulent flow. *Prikladnoy Mekhaniki i Tekhnicheskoy Fiziki Zhurnal* 1963;**3**:49–58.
[98] Gökalp I. An evaluation of the Klimov-Williams criterion. *Combust Flame* 1987;**67**:111–19.
[99] Damköhler G. Der Einfluss der Turbulenz auf die Flammengeschwindigkeit in Gasgemischen. *Z Elektrochem* 1940;**11**:601–52.
[100] Turns SR. *An introduction to combustion: concepts and applications*. 1st ed. McGraw-Hill; 1995. ISBN 978-0-07-911812-7.
[101] Williams F. Progress in knowledge of flamelet structure and extinction. *Prog Energy Combust Sci* 2000;**26**(4):657–82.
[102] Ebrahimi HB. Overview of gas turbine augmentor design, operation, and combustion oscillation. In: 42nd AIAA/ASME/SAE/ASEE Joint propulsion conference & exhibit. Sacramento, California: American Institute of Aeronautics and Astronautics; 2006.
[103] Cavaliere A, de Joannon M. MILD combustion. *Prog Energy Combust Sci* 2004;**30**(4):329–66. doi:10.1016/j.pecs.2004.02.003.
[104] Perpignan AA, Rao AG, Roekaerts DJ. Flameless combustion and its potential towards gas turbines. *Prog Energy Combust Sci* 2018;**69**:28–62. doi:10.1016/j.pecs.2018.06.002.
[105] Aspden AJ, Day MS, Bell JB. Towards the distributed burning regime in turbulent premixed flames. *J Fluid Mech* 2019;**871**:1–21.
[106] Wu H, See YC, Wang Q, Ihme M. A Pareto-efficient combustion framework with submodel assignment for predicting complex flame configurations. *Combust Flame* 2015;**162**(11):4208–30.
[107] Filatyev SA, Driscoll JF, Carter CD, Donbar JM. Measured properties of turbulent premixed flames for model assessment, including burning velocities, stretch rates, and surface densities. *Combust Flame* 2005;**141**(1):1–21. doi:10.1016/j.combustflame.2004.07.010.
[108] Chen Z. On the extraction of laminar flame speed and Markstein length from outwardly propagating spherical flames. *Combust Flame* 2011;**158**(2):291–300.
[109] Poludnenko A, Gradiner TA, Oran ES. Spontaneous transition of turbulent flames to detonations in unconfined media. *Phys Rev Lett* 2011;**107**(5):054501.
[110] Poludnenko A, Oran E. The interaction of high-speed turbulence with flames: turbulent flame speed. *Combust Flame* 2011;**158**(2):301–26.
[111] Wabel TM, Zhang P, Zhao X, Wang H, Hawkes E, Steinberg AM. Assessment of chemical scalars for heat release rate measurement in highly turbulent premixed combustion including experimental factors. *Combust Flame* 2018a;**194**:485–506. doi:10.1016/j.combustflame.2018.04.016.
[112] Wang H, Hawkes ER, Chen JH. Turbulence-flame interactions in DNS of a laboratory high Karlovitz premixed turbulent jet flame. *Phys Fluids* 2016b;**28**(9):095107. doi:10.1063/1.4962501.
[113] Skiba AW, Carter CD, Hammack SD, Miller JD, Gord JR, Driscoll JF. The influence of large eddies on the structure of turbulent premixed flames characterized with stereo-PIV and multi-species PLIF at 20 kHz. *Proc Combust Inst* 2019;**37**(2):2477–84. doi:10.1016/j.proci.2018.07.122.
[114] Klein M, Herbert A, Kosaka H, Böhm B, Dreizler A, Chakraborty N, et al. Evaluation of flame area based on detailed chemistry DNS of premixed turbulent hydrogen-air flames in different regimes of combustion. *Flow Turb Combust* 2020;**104**:403–19.
[115] Chen C, Sohrab S. Upstream interactions between planar symmetric laminar methane premixed flames. *Combust Flame* 1995;**101**(3):360–70.

[116] Chen JH, Echekki T, Kollmann W. The mechanism of two-dimensional pocket formation in lean premixed methane-air flames with implications to turbulent combustion. *Combust Flame* 1999;**116**(1):15–48.

[117] Ranganath B, Echekki T. Effects of preferential and differential diffusion on the mutual annihilation of two premixed hydrogen–air flames. *Combust Theory Model* 2005;**9**(4):659–72.

[118] Osborne JR, Ramji SA, Carter CD, Peltier S, Hammack S, Lee T, et al. Simultaneous 10 kHz TPIV, OH PLIF, and CH2O PLIF measurements of turbulent flame structure and dynamics. *Exp Fluids* 2016;**57**:65.

[119] Nivarti GV, Cant RS, Hochgreb S. Reconciling turbulent burning velocity with flame surface area in small-scale turbulence. *J Fluid Mech* 2019;**858**:R1. doi:10.1017/jfm.2018.841.

[120] Bouaniche A, Jaouen N, Domingo P, Vervisch L. Vitiated high Karlovitz n-decane/air turbulent flames: scaling laws and micro-mixing modeling analysis. *Flow Turb Combust* 2019;**102**(1):235–52. doi:10.1007/s10494-018-9946-y.

[121] Aspden AJ, Day MS, Bell JB. Three-dimensional direct numerical simulation of turbulent lean premixed methane combustion with detailed kinetics. *Combust Flame* 2016;**166**:266–83. doi:10.1016/j.combustflame.2016.01.027.

[122] Savard B, Blanquart G. Effects of dissipation rate and diffusion rate of the progress variable on local fuel burning rate in premixed turbulent flames. *Combust Flame* 2017;**180**:77–87. doi:10.1016/j.combustflame.2017.02.025.

[123] Aspden AJ, Bell JB, Day MS, Egolfopoulos FN. Turbulence-flame interactions in lean premixed dodecane flames. *Proc Combust Inst* 2017;**36**(2):2005–16. doi:10.1016/j.proci.2016.07.068.

[124] Zhou B, Brackmann C, Wang Z, Li Z, Richter M, Aldén M, et al. Thin reaction zone and distributed reaction zone regimes in turbulent premixed methane/air flames: scalar distributions and correlations. *Combust Flame* 2017a;**175**:220–36. doi:10.1016/j.combustflame.2016.06.016.

[125] Zhou B, Costa M, Li Z, Aldén M, Bai XS. Characterization of the reaction zone structures in a laboratory combustor using optical diagnostics: from flame to flameless combustion. *Proc Combust Inst* 2017b;**36**(3):4305–12. doi:10.1016/j.proci.2016.06.182.

[126] Savard B, Lapointe S, Teodorczyk A. Numerical investigation of the effect of pressure on heat release rate in iso-octane premixed turbulent flames under conditions relevant to SI engines. *Proc Combust Inst* 2017;**36**(3):3543–9. doi:10.1016/j.proci.2016.07.056.

[127] Savard B, Bobbitt B, Blanquart G. Structure of a high Karlovitz n-C7H16 premixed turbulent flame. *Proc Combust Inst* 2015;**35**(2):1377–84. doi:10.1016/j.proci.2014.06.133.

[128] Hamlington PE, Poludnenko AY, Oran ES. Interactions between turbulence and flames in premixed reacting flows. *Phys Fluids* 2011;**23**(12):125111. doi:10.1063/1.3671736.

[129] Chaudhuri S, Kolla H, Dave HL, Hawkes ER, Chen JH, Law CK. Flame thickness and conditional scalar dissipation rate in a premixed temporal turbulent reacting jet. *Combust Flame* 2017;**184**:273–85. doi:10.1016/j.combustflame.2017.02.027.

[130] Skiba AW, Carter CD, Hammack SD, Lee T. A simplified approach to simultaneous multi-scalar imaging in turbulent flames. *Combust Flame* 2018b;**189**:207–11. doi:10.1016/j.combustflame.2017.10.035.

[131] Aspden AJ. A numerical study of diffusive effects in turbulent lean premixed hydrogen flames. *Proc Combust Inst* 2017;**36**(2):1997–2004. doi:10.1016/j.proci.2016.07.053.

[132] Savard B, Wang H, Wehrfritz A, Hawkes ER. Direct numerical simulations of rich premixed turbulent n-dodecane/air flames at diesel engine conditions. *Proc Combust Inst* 2019a;**37**(4):4655–62. doi:10.1016/j.proci.2018.08.022.

[133] Masri A. Partial premixing and stratification in turbulent flames. *Proc Combust Inst* 2015;**35**(2):1115–36.

[134] Yoo CS, Sankaran R, Chen JH. Three-dimensional direct numerical simulation of a turbulent lifted hydrogen jet flame in heated coflow: flame stabilization and structure. *J Fluid Mech* 2009;**640**:453–81.

[135] Barlow RS, Dunn MJ, Sweeney MS, Hochgreb S. Effects of preferential transport in turbulent bluff-body-stabilized lean premixed CH_4/air flames. *Combust Flame* 2012;**159**(8):2563–75.

[136] Turkeri H, Zhao X, Pope SB, Muradoglu M. Large eddy simulation/probability density function simulations of the cambridge turbulent stratified flame series. *Combust Flame* 2019;**199**:24–45.

[137] Galeazzo FCC, Savard B, Wang H, Hawkes ER, Chen JH, Krieger Filho GC. Performance assessment of flamelet models in flame-resolved LES of a high Karlovitz methane/air stratified premixed jet flame. *Proc Combust Inst* 2019a;**37**(2):2545–53.

[138] Han W, Wang H, Kuenne G, Hawkes ER, Chen JH, Janicka J, et al. Large eddy simulation/dynamic thickened flame modeling of a high Karlovitz number turbulent premixed jet flame. *Proc Combust Inst* 2019b;**37**(2):2555–2563.

[139] Zhang P, Xie T, Kolla H, Wang H, Hawkes ER, Chen JH, et al. A priori analysis of a power-law mixing model for transported PDF model based on high Karlovitz turbulent premixed DNS flames. *Proc Combust Inst* 2020.

[140] Dasgupta D, Sun W, Day M, Lieuwen T. Effect of turbulence–chemistry interactions on chemical pathways for turbulent hydrogen–air premixed flames. *Combust Flame* 2017a;**176**:191–201.

[141] Yang S, Ranjan R, Yang V, Sun W, Menon S. Sensitivity of predictions to chemical kinetics models in a temporally evolving turbulent non-premixed flame. *Combust Flame* 2017;**183**:224–41.

[142] Dasgupta D, Sun W, Day MS, Lieuwen TC. Turbulence effects on the chemical pathways for premixed methane/air flames. In: *55th AIAA Aerospace sciences meeting*. Grapevine, Texas: American Institute of Aeronautics and Astronautics; 2017b. p. 1–15. doi:10.2514/6.2017-1782.

[143] Dasgupta D, Sun W, Day M, Aspden AJ, Lieuwen T. Analysis of chemical pathways and flame structure for n-dodecane/air turbulent premixed flames. *Combust Flame* 2019;**207**:36–50.

[144] Karimkashi S, Bolla M, Wang H, Hawkes ER. A direct numerical simulation study of turbulence intensity effects on NOx formation in freely propagating premixed flames. In: *20th Australasian fluid mechanics conference*, December; 2016. p. 8–11.

[145] Frenklach M, Wang H, Rabinowitz MJ. Optimization and analysis of large chemical kinetic mechanisms using the solution mapping method—combustion of methane. *Prog Energy Combust Sci* 1992;**18**(1):47–73.

[146] Wang H. Chapter 14 - uncertainty quantification and minimization. In: Faravelli T, Manenti F, Ranzi E, editors. *Mathematical modelling of gas-phase complex reaction systems: pyrolysis and combustion*. Computer Aided Chemical Engineering, vol. 45. Elsevier; 2019. p. 723–62.

[147] Aspden A, Day M, Bell J. Characterization of low lewis number flames. *Proc Combust Inst* 2011b;**33**(1):1463–71. doi:10.1016/j.proci.2010.05.090.

[148] Smolke J, Carbone F, Egolfopoulos FN, Wang H. Effect of n-dodecane decomposition on its fundamental flame properties. *Combust Flame* 2018;**190**:65–73.

[149] Krisman A, Hawkes ER, Talei M, Bhagatwala A, Chen JH. Characterisation of two-stage ignition in diesel engine-relevant thermochemical conditions using direct numerical simulation. *Combust Flame* 2016;**172**:326–41.

[150] Konduri A, Gruber A, Xu C, Lu T, Krisman A, Bothien MR, et al. Direct numerical simulation of flame stabilization assisted by autoignition in a reheat gas turbine combustor. *Proc Combust Inst* 2019;**37**(2):2635–42.

[151] Gordon RL, Masri AR, Pope SB, Goldin GM. A numerical study of auto-ignition in turbulent lifted flames issuing into a vitiated co-flow. *Combust Theory Model* 2007;**11**(3):351–76.

[152] Krisman A, Hawkes ER, Chen JH. The structure and propagation of laminar flames under autoignitive conditions. *Combust Flame* 2018;**188**:399–411.

[153] Lam S. Using CSP to understand complex chemical kinetics. *Combust Sci Technol* 1993;**89**(5-6):375–404.

[154] Lam S, GOUSSIS D. The CSP method for simplifying kinetics. *Int J Chem Kinet* 1994;**26**:461486.

[155] Valorani M, Najm HN, Goussis DA. CSP analysis of a transient flame-vortex interaction. *Combust Flame* 2003;**134**(1-2):35–53.

[156] Valorani M, Ciottoli PP, Galassi RM. Tangential stretching rate (TSR) analysis of non premixed reactive flows. *Proc Combust Inst* 2017;**36**(1):1357–67.

[157] Lu T, Law CK, Yoo CS, Chen JH. Dynamic stiffness removal for direct numerical simulations. *Combust Flame* 2009;**156**(8):1542–51.

[158] Boivin P, Dauptain A, Jimnez C, Cuenot B. Simulation of a supersonic hydrogen–air autoignition-stabilized flame using reduced chemistry. *Combust Flame* 2012;**159**(4):1779–90.

[159] Fureby C, Nordin-Bates K, Petterson K, Bresson A, Sabelnikov V. A computational study of supersonic combustion in strut injector and hypermixer flow fields. *Proc Combust Inst* 2015;**35**(2):2127–35.

[160] Savard B, Hawkes ER, Aditya K, Wang H, Chen JH. Regimes of premixed turbulent spontaneous ignition and deflagration under gas-turbine reheat combustion conditions. *Combust Flame* 2019b;**208**:402–19.

[161] Mal Q, Vermorel O, Ravet F, Poinsot T. Direct numerical simulations and models for hot burnt gases jet ignition. *Combust Flame* 2021;**223**:407–22.

[162] Hartl S, Geyer D, Dreizler A, Magnotti G, Barlow RS, Hasse C. Regime identification from raman/rayleigh line measurements in partially premixed flames. *Combust Flame* 2018;**189**:126–41.

[163] Hartl S, Geyer D, Hasse C, Zhao X, Wang H, Barlow RS. Assessing an experimental approach for chemical explosive mode and heat release rate using DNS data. *Combust Flame* 2019;**209**:214–24.

[164] MacArt JF, Grenga T, Mueller ME. Effects of combustion heat release on velocity and scalar statistics in turbulent premixed jet flames at low and high Karlovitz numbers. *Combust Flame* 2018;**191**:468–85. doi:10.1016/j.combustflame.2018.01.022.

[165] Wang Z, Abraham J. Effects of Karlovitz number on turbulent kinetic energy transport in turbulent lean premixed methane/air flames. *Phys Fluids* 2017;**29**(8):085102. doi:10.1063/1.4995303.

[166] Chakraborty N, Katragadda M, Cant RS. Statistics and modelling of turbulent kinetic energy transport in different regimes of premixed combustion. *Flow Turb Combust* 2011;**87**(2-3):205–35. doi:10.1007/s10494-010-9312-1.

[167] MacArt JF, Grenga T, Mueller ME. Evolution of flame-conditioned velocity statistics in turbulent premixed jet flames at low and high Karlovitz numbers. *Proc Combust Inst* 2019;**37**(2):2503–10. doi:10.1016/j.proci.2018.08.030.

[168] Lee J, MacArt JF, Mueller ME. Heat release effects on the Reynolds stress budgets in turbulent premixed jet flames at low and high Karlovitz numbers. *Combust Flame* 2020;**216**:1–8. doi:10.1016/j.combustflame.2020.02.014.

[169] Galeazzo FCC, Savard B, Wang H, Hawkes ER, Chen JH, Krieger Filho GC. Performance assessment of flamelet models in flame-resolved LES of a high Karlovitz methane/air stratified premixed jet flame. *Proc Combust Inst* 2019b;**37**(2):2545–53. doi:10.1016/j.proci.2018.09.025.

[170] Coriton B, Im S-K, Gamba M, Frank JH. Flow field and scalar measurements in a series of turbulent partially-premixed dimethyl ether/air jet flames. *Combust Flame* 2017;**180**:40–52. doi:10.1016/j.combustflame.2017.02.014.

[171] Gruber A, Richardson ES, Aditya K, Chen JH. Direct numerical simulations of premixed and stratified flame propagation in turbulent channel flow. *Phys Rev Fluids* 2018;**3**(11):110507. doi:10.1103/PhysRevFluids.3.110507.

[172] Ahmed U, Pillai AL, Chakraborty N, Kurose R. Statistical behavior of turbulent kinetic energy transport in boundary layer flashback of

hydrogen-rich premixed combustion. *Phys Rev Fluids* 2019;**4**(10):103201. doi:10.1103/PhysRevFluids.4.103201.
[173] Wabel TM, Skiba AW, Driscoll JF. Evolution of turbulence through a broadened preheat zone in a premixed piloted Bunsen flame from conditionally-averaged velocity measurements. *Combust Flame* 2018b;**188**:13–27. doi:10.1016/j.combustflame.2017.09.013.
[174] Paxton L, Smolke J, Egolfopoulos FN. Effects of heat release and fuel type on highly turbulent premixed jet flames. *Proc Combust Inst* 2019;**37**(2):2565–72. doi:10.1016/j.proci.2018.08.041.
[175] Steinberg AM, Driscoll JF, Swaminathan N. Statistics and dynamics of turbulence–flame alignment in premixed combustion. *Combust Flame* 2012;**159**(8):2576–88. doi:10.1016/j.combustflame.2011.12.001.
[176] Klein M, Kasten C, Chakraborty N, Mukhadiyev N, Im HG. Turbulent scalar fluxes in H_2-air premixed flames at low and high Karlovitz numbers. *Combust Theory Model* 2018;**22**(6):1033–48. doi:10.1080/13647830.2018.1468034.
[177] Hamlington PE, Dahm WJA. Reynolds stress closure for nonequilibrium effects in turbulent flows. *Phys Fluids* 2008;**20**(11):115101. doi:10.1063/1.3006023.
[178] Lipatnikov A, Nishiki S, Hasegawa T. Closure relations for fluxes of flame surface density and scalar dissipation rate in turbulent premixed flames. *Fluids* 2019;**4**(1):43. doi:10.3390/fluids4010043.
[179] Ranjan R, Muralidharan B, Nagaoka Y, Menon S. Subgrid-scale modeling of reaction-diffusion and scalar transport in turbulent premixed flames. *Combust Sci Technol* 2016;**188**(9):1496–537. doi:10.1080/00102202.2016.1198336.
[180] Kim SH, Pitsch H. Scalar gradient and small-scale structure in turbulent premixed combustion. *Phys Fluids* 2007;**19**(11):115104. doi:10.1063/1.2784943.
[181] Chakraborty N, Swaminathan N. Influence of the Damköhler number on turbulence-scalar interaction in premixed flames. I. Physical insight. *Phys Fluids* 2007;**19**(4). doi:10.1063/1.2714070.
[182] Chakraborty N, Klein M, Swaminathan N. Effects of Lewis number on the reactive scalar gradient alignment with local strain rate in turbulent premixed flames. *Proc Combust Inst* 2009;**32 I**(1):1409–17. doi:10.1016/j.proci.2008.06.021.
[183] Chakraborty N, Rogerson JW, Swaminathan N. The scalar gradient alignment statistics of flame kernels and its modelling implications for turbulent premixed combustion. *Flow Turb Combust* 2010;**85**(1):25–55. doi:10.1007/s10494-010-9250-y.
[184] Hartung G, Hult J, Kaminski CF, Rogerson JW, Swaminathan N. Effect of heat release on turbulence and scalar-turbulence interaction in premixed combustion. *Phys Fluids* 2008;**20**(3):1–16. doi:10.1063/1.2896285.
[185] Mustafa Kamal M, Coriton B, Zhou R, Frank JH, Hochgreb S. Scalar dissipation rate and scales in swirling turbulent premixed flames. *Proc Combust Inst* 2017;**36**(2):1957–65. doi:10.1016/j.proci.2016.08.067.
[186] Kamal MM, Barlow RS, Hochgreb S. Conditional analysis of turbulent premixed and stratified flames on local equivalence ratio and progress of reaction. *Combust Flame* 2015;**162**(10):3896–913. doi:10.1016/j.combustflame.2015.07.026.
[187] Magnotti G, Barlow RS. Effects of high shear on the structure and thickness of turbulent premixed methane/air flames stabilized on a bluff-body burner. *Combust Flame* 2015;**162**(1):100–14. doi:10.1016/j.combustflame.2014.06.015.
[188] Sankaran R, Hawkes ER, Yoo CS, Chen JH. Response of flame thickness and propagation speed under intense turbulence in spatially developing lean premixed methane–air jet flames. *Combust Flame* 2015;**162**(9):3294–306. doi:10.1016/j.combustflame.2015.05.019.
[189] Chakraborty N, Cant RS. Effects of Lewis number on scalar transport in turbulent premixed flames. *Phys Fluids* 2009;**21**(3):1–11. doi:10.1063/1.3097007.
[190] Hamlington PE, Poludnenko AY, Oran ES. Intermittency in premixed turbulent reacting flows. *Phys Fluids* 2012;**24**(7):075111. doi:10.1063/1.4729615.
[191] Kerr RM. Higher-order derivative correlations and the alignment of small-scale structures in isotropic numerical turbulence. *J Fluid Mech* 1985;**153**:31–58. doi:10.1017/S0022112085001136.
[192] Ashurst WT, Kerstein AR, Kerr RM, Gibson CH. Alignment of vorticity and scalar gradient with strain rate in simulated Navier-Stokes turbulence. *Phys Fluids* 1987;**30**:2343.
[193] Nomura KK, Elghobashi SE. The structure of inhomogeneous turbulence in variable density nonpremixed flames. *Theor Comp Fluid Dyn* 1993;**5-5**(4-5):153–75. doi:10.1007/BF00271656.
[194] Boratav ON, Elghobashi SE, Zhong R. On the alignment of strain, vorticity and scalar gradient in turbulent, buoyant, nonpremixed flames. *Phys Fluids* 1998;**10**(9):2260–7. doi:10.1063/1.869747.
[195] Swaminathan N, Grout RW. Interaction of turbulence and scalar fields in premixed flames. *Phys Fluids* 2006;**18**(4). doi:10.1063/1.2186590.
[196] Coriton B, Frank JH. Impact of heat release on strain rate field in turbulent premixed Bunsen flames. *Proc Combust Inst* 2017;**36**(2):1885–92. doi:10.1016/j.proci.2016.07.006.
[197] Hampp F, Lindstedt R. Strain distribution on material surfaces during combustion regime transitions. *Proc Combust Inst* 2017;**36**(2):1911–18. doi:10.1016/j.proci.2016.07.018.
[198] Zhou B, Frank JH. Effects of heat release and imposed bulk strain on alignment of strain rate eigenvectors in turbulent premixed flames. *Combust Flame* 2019;**201**:290–300. doi:10.1016/j.combustflame.2018.12.016.
[199] Nilsson T, Carlsson H, Yu R, Bai X-S. Structures of turbulent premixed flames in the high Karlovitz number regime – DNS analysis. *Fuel* 2018;**216**:627–38. doi:10.1016/j.fuel.2017.12.046.
[200] Steinberg A, Coriton B, Frank J. Influence of combustion on principal strain-rate transport in turbulent premixed flames. *Proc Combust Inst* 2015;**35**(2):1287–94. doi:10.1016/j.proci.2014.06.089.
[201] Coriton B, Frank JH. Experimental study of vorticity-strain rate interaction in turbulent partially premixed jet flames using tomographic particle image velocimetry. *Phys Fluids* 2016;**28**(2):025109. doi:10.1063/1.4941528.
[202] Sutherland W. LII. The viscosity of gases and molecular force. *London Edinb Dublin PhilosMag J Sci* 1893;**36**(223):507–31. doi:10.1080/14786449308620508.
[203] Jimenez J. Kinematic alignment effects in turbulent flows.. *Phys Fluids A* 1992;**4 (4)**:652.
[204] Nomura KK, Post GK. The structure and dynamics of vorticity and rate of strain in incompressible homogeneous turbulence. *J Fluid Mech* 1998;**377**:65–97. doi:10.1017/S0022112098003024.
[205] Hamlington PE, Schumacher J, Dahm WJA. Local and nonlocal strain rate fields and vorticity alignment in turbulent flows. *Phys Rev E* 2008a;**77**(2):026303. doi:10.1103/PhysRevE.77.026303.
[206] Hamlington PE, Schumacher J, Dahm WJA. Direct assessment of vorticity alignment with local and nonlocal strain rates in turbulent flows. *Phys Fluids* 2008b;**20**(11):111703. doi:10.1063/1.3021055.
[207] Bobbitt B, Lapointe S, Blanquart G. Vorticity transformation in high Karlovitz number premixed flames. *Phys Fluids* 2016;**28**(1):015101. doi:10.1063/1.4937947.
[208] Papapostolou V, Wacks DH, Chakraborty N, Klein M, Im HG. Enstrophy transport conditional on local flow topologies in different regimes of premixed turbulent combustion. *Sci Rep* 2017;**7**(1):11545. doi:10.1038/s41598-017-11650-x.
[209] Wacks D, Chakraborty N. Flow topology and alignments of scalar gradients and vorticity in turbulent spray flames: a direct numerical simulation analysis. *Fuel* 2016;**184**:922–47. doi:10.1016/j.fuel.2016.04.061.
[210] Bobbitt B, Blanquart G. Vorticity isotropy in high Karlovitz number premixed flames. *Phys Fluids* 2016;**28**(10):105101. doi:10.1063/1.4962305.
[211] Zhao P, Wang L, Chakraborty N. Vectorial structure of the near-wall premixed flame. *Phys Rev Fluids* 2019b;**4**(6):063203. doi:10.1103/PhysRevFluids.4.063203.
[212] Poludnenko AY. Pulsating instability and self-acceleration of fast turbulent flames. *Phys Fluids* 2015;**27**(1):014106. doi:10.1063/1.4905298.
[213] Chakraborty N. Statistics of vorticity alignment with local strain rates in turbulent premixed flames. *Eur J Mech B-Fluids* 2014;**46**:201–20. doi:10.1016/j.euromechflu.2014.01.002.
[214] Chakraborty N, Wang L, Konstantinou I, Klein M. Vorticity statistics based on velocity and density-weighted velocity in premixed reactive turbulence. *J Turbul* 2017;**18**(9):825–53. doi:10.1080/14685248.2017.1334905.
[215] Chakraborty N, Konstantinou I, Lipatnikov A. Effects of Lewis number on vorticity and enstrophy transport in turbulent premixed flames. *Phys Fluids* 2016;**28**(1):015109. doi:10.1063/1.4939795.
[216] Dopazo C, Cifuentes L, Chakraborty N. Vorticity budgets in premixed combusting turbulent flows at different Lewis numbers. *Phys Fluids* 2017;**29**(4):045106. doi:10.1063/1.4981219.
[217] Ahmed U, Doan NAK, Lai J, Klein M, Chakraborty N, Swaminathan N. Multi-scale analysis of head-on quenching premixed turbulent flames. *Phys Fluids* 2018;**30**(10):105102. doi:10.1063/1.5047061.
[218] Geikie MK, Ahmed KA. Pressure-gradient tailoring effects on the turbulent flame-vortex dynamics of bluff-body premixed flames. *Combust Flame* 2018;**197**:227–42. doi:10.1016/j.combustflame.2018.08.001.
[219] Kazbekov A, Kumashiro K, Steinberg AM. Enstrophy transport in swirl combustion. *J Fluid Mech* 2019;**876**:715–32. doi:10.1017/jfm.2019.551.
[220] Kazbekov A, Steinberg AM. Flame- and flow-conditioned vorticity transport in premixed swirl combustion. *Proc Combust Inst* 2020a. doi:10.1016/j.proci.2020.06.211.
[221] Lai J, Chakraborty N, Lipatnikov A. Statistical behaviour of vorticity and enstrophy transport in head-on quenching of turbulent premixed flames. *Eur J Mech B/Fluids* 2017;**65**:384–97. doi:10.1016/j.euromechflu.2016.10.013.
[222] Coriton B, Frank JH. High-speed tomographic PIV measurements of strain rate intermittency and clustering in turbulent partially-premixed jet flames. *Proc Combust Inst* 2015;**35**(2):1243–50. doi:10.1016/j.proci.2014.06.045.
[223] Hampp F, Shariatmadar S, Lindstedt R. Quantification of low Damkhler number turbulent premixed flames. *Proc Combust Inst* 2019;**37**(2):2373–81. doi:10.1016/j.proci.2018.06.079.
[224] Eswaran V, Pope S. An examination of forcing in direct numerical simulations of turbulence. *Comput Fluids* 1988;**16**(3):257–78.
[225] Towery CA, Poludnenko AY, Hamlington PE. Detonation initiation by compressible turbulence thermodynamic fluctuations. *Combust Flame* 2020;**213**:172–83. doi:10.1016/j.combustflame.2019.11.025.
[226] Nishiki S, Hasegawa T, Borghi R, Himeno R. Modeling of flame-generated turbulence based on direct numerical simulation databases. *Proc Combust Inst* 2002;**29**(2):2017–22. doi:10.1016/S1540-7489(02)80246-2.
[227] Klein M., Chakraborty N., Ketterl S.. A comparison of strategies for direct numerical simulation of turbulence chemistry interaction in generic planar turbulent premixed flames. Flow Turb Combust 99(3-4). 10.1007/s10494-017-9843-9.
[228] Mueller C. Vorticity generation and attenuation as vortices convect through a premixed flame. *Combust Flame* 1998;**112**(3):342–6. doi:10.1016/S0010-2180(97)00122-3.
[229] Sreenivasan KR, Antonia RA. The phenomenology of small-scale turbulence. *Ann Rev Fluid Mech* 1997;**29**(1):435–72. doi:10.1146/annurev.fluid.29.1.435.
[230] Steinberg AM, Driscoll JF, Ceccio SL. Three-dimensional temporally resolved measurements of turbulence–flame interactions using orthogonal-plane cinema-stereoscopic PIV. *Exp Fluids* 2009;**47**(3):527–47. doi:10.1007/s00348-009-0677-7.

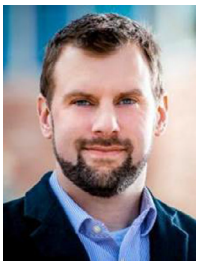
[231] Steinberg AM, Driscoll JF. Straining and wrinkling processes during turbulence–premixed flame interaction measured using temporally-resolved diagnostics. *Combust Flame* 2009;**156**(12):2285–306. doi:10.1016/j.combustflame.2009.06.024.
[232] Steinberg AM, Driscoll JF, Ceccio SL. Measurements of turbulent premixed flame dynamics using cinema stereoscopic PIV. *Exp Fluids* 2008;**44**(6):985–99. doi:10.1007/s00348-007-0458-0.
[233] Wang Z, Zhou B, Yu S, Brackmann C, Li Z, Richter M, et al. Structure and burning velocity of turbulent premixed methane/air jet flames in thin-reaction zone and distributed reaction zone regimes. *Proc Combust Inst* 2019b;**37**(2):2537–44. doi:10.1016/j.proci.2018.09.023.
[234] Tanahashi M, Fujimura M, Miyauchi T. Coherent fine-scale eddies in turbulent premixed flames. *Proc Combust Inst* 2000;**28**(1):529–35. doi:10.1016/S0082-0784(00)80252-0.
[235] Meneveau C, Sreenivasan KR. Simple multifractal cascade model for fully developed turbulence. *Phys Rev Lett* 1987;**59**(13):1424–7. doi:10.1103/PhysRevLett.59.1424.
[236] Sreenivasan KR. Fluid turbulence. *Rev Mod Phys* 1999;**71**(2):S383–95. doi:10.1103/revmodphys.71.s383.
[237] Meneveau C. Dual spectra and mixed energy cascade of turbulence in the wavelet representation. *Phys Rev Lett* 1991;**66**(11):1450.
[238] Frisch U. *Turbulence: the legacy of A.N. Kolmogorov*. Cambridge University Press; 1995.
[239] Dimotakis PE. The mixing transition in turbulent flows. *J Fluid Mech* 2000;**409**:69–98.
[240] Kolmogorov AN. The local structure of turbulence in incompressible viscous fluid for very large Reynolds numbers.. *Dokl Akad Nauk SSSR* 1941;**30**:299–303.
[241] Furukawa J, Harada E, Hirano T. Local reaction zone thickness of a high intensity turbulent premixed flame.. *Proc Combust Inst* 1990;**23**(1):789–94.
[242] Furukawa J, Noguchi Y, Hirano T, Williams FA. Anisotropic enhancement of turbulence in large-scale, low-intensity turbulent premixed propane–air flames. *J Fluid Mech* 2002;**462**:209–43. doi:10.1017/S0022112002008650.
[243] Knaus R, Pantano C. On the effect of heat release in turbulence spectra of non-premixed reacting shear layers. *J Fluid Mech* 2009;**626**:67–109.
[244] Kim J, Bassenne M, Towery CAZ, Hamlington PE, Poludnenko AY, Urzay J. Spatially localized multi-scale energy transfer in turbulent premixed combustion. *J Fluid Mech* 2018;**848**:78–116. doi:10.1017/jfm.2018.371.
[245] Whitman SH, Towery CA, Poludnenko AY, Hamlington PE. Scaling and collapse of conditional velocity structure functions in turbulent premixed flames. *Proc Combust Inst* 2019;**37**(2):2527–35. doi:10.1016/j.proci.2018.07.010.
[246] Sabelnikov VA, Lipatnikov AN, Nishiki S, Hasegawa T. Application of conditioned structure functions to exploring influence of premixed combustion on two-point turbulence statistics. *Proc Combust Inst* 2019a;**37**(2):2433–41. doi:10.1016/j.proci.2018.08.029.
[247] Sabelnikov VA, Lipatnikov AN, Nishiki S, Hasegawa T. Investigation of the influence of combustion-induced thermal expansion on two-point turbulence statistics using conditioned structure functions. *J Fluid Mech* 2019b;**867**:45–76. doi:10.1017/jfm.2019.128.
[248] Brearley P, Ahmed U, Chakraborty N, Lipatnikov A. Statistical behaviors of conditioned two-point second-order structure functions in turbulent premixed flames in different combustion regimes. *Phys Fluids* 2019;**31**(11):115109. doi:10.1063/1.5124143.
[249] O'Brien J, Towery CA, Hamlington PE, Ihme M, Poludnenko AY, Urzay J. The cross-scale physical-space transfer of kinetic energy in turbulent premixed flames. *Proc Combust Inst* 2017;**36**(2):1967–75. doi:10.1016/j.proci.2016.05.005.
[250] Davidson PA. *Turbulence: an introduction for scientists and engineers*. Oxford University Press; 2004.
[251] Piomelli U, Cabot WH, Moin P, Lee S. Subgridscale backscatter in turbulent and transitional flows. *Phys Fluids A* 1991;**3**:1766–71.
[252] Domaradzki JA, Rogallo RS. Local energy transfer and nonlocal interactions in homogeneous, isotropic turbulence. *Phys Fluids A* 1990;**2**:413.
[253] Waleffe F. The nature of triad interactions in homogeneous turbulence. *Phys Fluids A* 1992;**4**:350–63.
[254] Zhou Y. Degrees of locality of energy transfer in the inertial range. *Phys Fluids A* 1993;**5**:1092–4.
[255] Domaradzki JA, Liu W, Hartel C, Kleiser L. Energy transfer in numerically simulated wall-bounded turbulent flows. *Phys Fluids* 1994;**6**:1583.
[256] Brasseur JG, Wei C. Interscale dynamics and local isotropy in high Reynolds number turbulence within triadic interactions. *Phys Fluids* 1994;**6**(2):842–70. doi:10.1063/1.868322.
[257] Domaradzki JA, Carati D. An analysis of the energy transfer and the locality of nonlinear interactions in turbulence. *Phys Fluids* 2007;**19**:085112.
[258] Piomelli U. High Reynolds number calculations using the dynamic subgrid-scale stress model. *Phys Fluids A* 1993;**5**:1484–90.
[259] Germano M, Piomelli U, Moin P, Cabot WH. A dynamic subgridscale eddy viscosity model. *Phys Fluids A* 1991;**3**:1760–5.
[260] Moin P, Squires K, Cabot W, Lee S. A dynamic subgrid-scale model for compressible turbulence and scalar transport. *Phys Fluids A* 1991;**3**:2746–57.
[261] Carati D, Ghosal S, Moin P. On the representation of backscatter in dynamic localization models. *Phys Fluids* 1995;**7**:606–16.
[262] Schumann U. Stochastic backscatter of turbulence energy and scalar variance by random subgrid-scale fluxes. *Proc R Soc Lond A* 1995;**451**:293–318.
[263] Domaradzki JA, Saiki EM. Backscatter models for large-eddy simulations. *Theor Comp Fluid Dyn* 1997;**9**:75–83.
[264] Meneveau C, Katz J. Scale-invariance and turbulence models for large-eddy simulation. *Ann Rev Fluid Mech* 2000;**32**(1):1–32. doi:10.1146/annurev.fluid.32.1.1.
[265] Peters N. Multiscale combustion and turbulence. *Proc Comb Inst* 2009;**32**:1–25.
[266] Oran ES, Gamezo VN. Origins of the deflagration-to-detonation transition in gas-phase combustion. *Combust Flame* 2007;**148**:4–47.
[267] Boffetta G, Ecke RE. Two-dimensional turbulence. *Annu Rev Fluid Mech* 2012;**44**:427–51.
[268] Yeung PK, Zhou Y. Universality of the Kolmogorov constant in numerical simulations of turbulence. *Phys Rev E* 1997;**56**(2):1746–52. doi:10.1103/PhysRevE.56.1746.
[269] Gotoh T, Fukayama D, Nakano T. Velocity field statistics in homogeneous steady turbulence obtained using a high-resolution direct numerical simulation. *Phys Fluids* 2002;**14**(3):1065–81. doi:10.1063/1.1448296.
[270] Kaneda Y, Ishihara T, Yokokawa M, Itakura K, Uno A. Energy dissipation rate and energy spectrum in high resolution direct numerical simulations of turbulence in a periodic box. *Phys Fluids* 2003;**15**(2):L21–4. doi:10.1063/1.1539855.
[271] Saddoughi SG, Veeravalli SV. Local isotropy in turbulent boundary layers at high reynolds number.. *J Fluid Mech* 1994;**268**:333–72.
[272] She Z, Jackson E. On the universal form of energy spectra in fully developed turbulence. *Phys Fluids A* 1993;**5**(7):1526–8. doi:10.1063/1.858591.
[273] Verma MK, Donzis D. Energy transfer and bottleneck effect in turbulence. *J Phys A* 2007;**40**:4401–12.
[274] O'Brien J, Urzay J, Ihme M, Moin P, Saghafian A. Subgrid-scale backscatter in reacting and inert supersonic hydrogen-air turbulent mixing layers.. *J Fluid Mech* 2014;**743**:554–84.
[275] Kazbekov A, Steinberg AM. Experimental measurement of filtered kinetic energy dynamics in premixed swirl flames. In: AIAA Scitech 2020 Forum. Orlando, FL: American Institute of Aeronautics and Astronautics.
[276] Pope S. Small scales, many species and the manifold challenges of turbulent combustion. *Proc Combust Inst* 2013;**34**(1):1–31.
[277] Xu C, Ameen MM, Som S, Chen JH, Ren Z, Lu T. Dynamic adaptive combustion modeling of spray flames based on chemical explosive mode analysis. *Combust Flame* 2018c;**195**:30–9. Special Commemorative Issue: Professor Chung King (Ed) Law 70th Birthday
[278] Gounder JD, Kourmatzis A, Masri AR. Turbulent piloted dilute spray flames: flow fields and droplet dynamics. *Combust Flame* 2012;**159**(11):3372–97. doi:10.1016/j.combustflame.2012.07.014.
[279] Poludnenko AY, Chambers J, Ahmed K, Gamezo VN, Taylor BD. A unified mechanism for unconfined deflagration-to-detonation transition in terrestrial chemical systems and type la supernovae. *Science* 2019;**366**(6465):eaau7365. doi:10.1126/science.aau7365.
[280] Darragh R, Towery CA, Poludnenko AY, Hamlington PE. Particle pair dispersion and eddy diffusivity in a high-speed premixed flame. *Proc Combust Inst* 2020. doi:10.1016/j.proci.2020.06.056.
[281] Sawford B. Turbulent relative dispersion. *Ann Rev Fluid Mech* 2001;**33**:289–317.
[282] Salazar JP, Collins LR. Two-particle dispersion in isotropic turbulent flows. *Ann Rev Fluid Mech* 2009;**41**(1):405–32. doi:10.1146/annurev.fluid.40.111406.102224.

Further reading

Luo Z, Yoo CS, Richardson ES, Chen JH, Law CK, Lu T. Chemical explosive mode analysis for a turbulent lifted ethylene jet flame in highly-heated coflow. *Combust Flame* 2012;**159**(1):265–74.
HLAM S. Reduced chemistry-diffusion coupling. *Combust Sci Technol* 2007;**179**(4):767–86.



Adam M. Steinberg is an Associate Professor in the Daniel Guggenheim School of Aerospace Engineering at the Georgia Institute of Technology. His research develops and applies laser-based measurement techniques to unravel the behavior of turbulent reacting flows, with the aim of understanding both fundamental processes and practical combustion devices. He is an Associate Fellow of the American Institute for Aeronautics and Astronautics and an Associate Editor of Combustion and Flame.



Peter Hamlington is an Associate Professor and Vogel Faculty Fellow in the Paul M. Rady Department of Mechanical Engineering at the University of Colorado, Boulder. His research is focused on understanding fundamental flow physics in boh reacting and non-reacting turbulent flows, and on using the resulting insights for the development of physically accurate, computationally efficient models for large-scale simulations of real-world engineering systems. He is the recent recipient of the NSF CAREER Award.



Xinyu Zhao is an Assistant Professor in the Department of Mechanical Engineering at University of Connecticut. Her research aims at understanding complex turbulence-chemistry-radiation interactions in turbulent reacting flows through detailed simulations. She also actively works on developing physics-based combustion and radiation models for canonical and practical combustion systems. She is a recent recipient of the AFOSR Young Investigator Award and the Irvin Glassman Young Investigator Award.

Combustion and Flame 186 (2017) 193–207

Contents lists available at ScienceDirect

Combustion and Flame

journal homepage: www.elsevier.com/locate/combustflame

Lagrangian analysis of high-speed turbulent premixed reacting flows: Thermochemical trajectories in hydrogen–air flames

Peter E. Hamlington[a,*], Ryan Darragh[b], Clarissa A. Briner[c], Colin A.Z. Towery[a], Brian D. Taylor[d], Alexei Y. Poludnenko[e]

[a] Department of Mechanical Engineering, University of Colorado, Boulder, CO 80309, USA
[b] Department of Aerospace Engineering Sciences, University of Colorado, Boulder, CO 80309, USA
[c] Department of Physics, University of Colorado, Boulder, CO 80309, USA
[d] Air Force Research Laboratory, Eglin AFB, FL 32542, USA
[e] Department of Aerospace Engineering, Texas A&M University, College Station, TX 77843, USA

ARTICLE INFO

Article history:
Received 21 April 2017
Revised 28 May 2017
Accepted 4 August 2017

Keywords:
Turbulent combustion
Premixed flames
Numerical simulations

ABSTRACT

A Lagrangian analysis approach is used to examine the effects of high-speed turbulence on thermochemical trajectories in unconfined, stoichiometric hydrogen–air (H_2–air) premixed flames. Two different intensities of turbulence in the unburnt reactants are considered, giving premixed flames with Karlovitz numbers of roughly 150 and 450. These two cases are modeled using direct numerical simulations (DNS) with both multi- and single-step H_2–air reaction kinetics. In each of the four resulting simulations, trajectories of fluid parcels are calculated using a high-order Runge–Kutta method, and time series of temperature and chemical composition within each parcel are recorded. The resulting thermochemical trajectories are used to examine the evolution of thermodynamic quantities and chemical composition, as well as measure fluid parcel residence times and path lengths during different phases of the combustion process. Fuel mass fraction and temperature within fluid parcels are shown to be frequently non-monotonic along fluid trajectories in both single- and multi-step H_2–air simulations, and the prevalence of non-monotonic trajectories increases with increasing turbulence intensity. Using results from single-step simulations, it is shown that this non-monotonicity can be caused solely by molecular transport processes resulting from large gradients in temperature and species concentrations created by turbulent advection. As a related consequence of advection, fluid parcel residence times are found to be smaller than in a laminar flame and the ratio of turbulent to laminar residence times decreases from roughly 0.8 to 0.6 as the turbulence intensity increases. By contrast, fluid parcel path lengths in the present high-speed turbulent flames are found to be substantially greater than laminar path lengths, resulting in fluid parcels that travel 4 and 7 times further than in a laminar flame for the two different turbulence intensities considered here.

© 2017 The Combustion Institute. Published by Elsevier Inc. All rights reserved.

1. Introduction

Turbulent premixed combustion is a multi-scale, multi-physics problem involving coupled nonlinear interactions between turbulence and chemical reactions. For sufficiently high turbulence intensities, in particular, flame surfaces undergo substantial wrinkling and the internal structure of the flame, including the spatial region over which reactions occur, may become broadened relative to the structure of the corresponding laminar flame [1–4]. These changes, in turn, suggest a potentially large impact of turbulence on the evolution of thermodynamic (e.g., temperature and density) and chemical (e.g., species mass fractions) quantities in different regions of the flame. The focus of the present study is to understand these impacts using Lagrangian analyses of high-speed turbulent premixed reacting flows.

In general, the study of turbulence effects on thermodynamic and chemical (i.e., thermochemical) quantities in premixed reacting flows is made difficult by the concurrent, coupled, and often competing effects of turbulent advection, molecular transport, and chemical reactions. The latter two effects, in particular, affect the chemical composition and temperature of fluid parcels as they are advected by the turbulent flow. The difficulty in separating each of these effects has resulted in continued uncertainty regarding predictions of flame structure for different Damköhler (Da) and Karlovitz (Ka) numbers. Furthermore, significant changes in thermochemical properties of fluid parcels in highly turbulent

* Corresponding author.
E-mail address: peh@colorado.edu (P.E. Hamlington).

http://dx.doi.org/10.1016/j.combustflame.2017.08.001
0010-2180/© 2017 The Combustion Institute. Published by Elsevier Inc. All rights reserved.

settings can have important implications for the validity and accuracy of reaction kinetics mechanisms developed and calibrated for more idealized conditions, for example those of a laminar flame or a perfectly-stirred reactor. Conditional analyses based on location within the flame have become common for the study of turbulence-chemistry interactions (e.g., [3–10]) but, even though such approaches yield valuable insights, they cannot reveal the full thermochemical evolution of a fluid parcel. These approaches also do not typically permit an unambiguous separation of advective processes from molecular transport and reactions.

In order to obtain a more fine-grained picture of turbulence-chemistry coupling in premixed reacting flows, here we employ a Lagrangian approach to track changes in chemical species concentrations and thermodynamic variables as they occur in fluid parcels during premixed hydrogen (H_2) and air combustion. We define a fluid 'parcel' as an infinitesimal volume whose motion is completely determined by the flow velocity, and a 'trajectory' is the path followed by such a parcel. A 'thermochemical trajectory' gives the evolution of thermodynamic and chemical properties within the fluid parcel along its path. The Lagrangian flow description is an alternative, but equivalent, representation to the more commonly used Eulerian description of fluid flows. Lagrangian analyses of turbulence have been widely used for the study of both simple and complex non-reacting flows over the last several decades, including passive scalar mixing [11], homogeneous shear flow [12], stratified homogeneous turbulence [13], and convective turbulence [14] (see also reviews by Yeung [15] and Toschi and Bodenschatz [16]). Methods and numerical algorithms for calculating Lagrangian trajectories in turbulence have also been described and discussed at length by Yeung and Pope [17] and Yu et al. [18].

Lagrangian analyses have three primary benefits in the context of premixed flame studies: (i) changes in temperature and chemical composition within a fluid parcel can be directly tracked during the combustion process, (ii) residence times and path lengths of fluid parcels during different stages of combustion (e.g., in preheat and reaction zones) can be computed, and (iii) effects due to molecular transport and reactions can be isolated from those due to advection. In particular, since fluid parcels exactly follow the flow and there is no advection of fluid into or out of the parcels, any changes in the thermochemical state within these parcels *must* be solely due to molecular transport and reactions. It has also been noted that flamelet-based conditional analysis approaches are poorly defined in low Lewis number thermo-diffusively unstable flames [19], providing further motivation for a Lagrangian analysis approach.

As a result of these advantages, Lagrangian analyses have become increasingly common for the study of turbulent combustion over the last several years. Steinberg et al. [20] have calculated Lagrangian trajectories from experimental measurements of a premixed dimethyl-ether and air piloted jet flame in order to examine variations in vorticity and strain rate dynamics within fluid parcels undergoing combustion. In a related study by Osborne et al. [21], it was found that residence times of fluid parcels in the flame preheat zone were almost 40% smaller, on average, than corresponding laminar flame times, despite broadening of the preheat zone by turbulence. Using a Lagrangian analysis, Day et al. have performed joint experimental and computational studies of both lean methane [19] and lean hydrogen [22] turbulent premixed flames in low swirl burners (LSB). In Ref. [22], in particular, diffusive fuel fluxes were calculated along Lagrangian trajectories, and were shown to correlate with fuel consumption rate. Despite the relatively low turbulence intensities in the LSB and similarities between turbulent and laminar trajectories, Day et al. [19,22] also noted the complex nature of thermodynamic and chemical evolutions along Lagrangian trajectories, including the non-monotonic evolution of temperature within fluid parcels. More recently, Uranakara et al. [23] examined turbulence-induced extinction of spherical H_2–air flame kernels using a flame particle tracking algorithm (i.e., flame surfaces, rather than fluid parcels, were tracked using a Lagrangian approach). This study showed that turbulence wrinkles flame surfaces to create "pointed" structures where increased thermal conduction leads to local and, eventually, global extinction.

The present study builds upon these prior works by specifically examining the effects of high-speed turbulence on thermochemical trajectories in premixed H_2–air flames, where the intensity of the turbulence is characterized by the magnitude of turbulent velocity fluctuations in the unburnt reactants relative to the laminar flame speed. In such high-speed cases, turbulent advection has an increasingly dominant effect on premixed flame structure, and even greater complexity can be expected than in the studies by Day et al. [19,22]. Ultimately, our primary focus is to determine how and to what extent thermochemical trajectories vary as the turbulence intensity is increased. To this end, we seek to address the following questions: (i) How do the characteristics of thermochemical trajectories in high-speed premixed flames differ from those in laminar flames? (ii) How do these characteristics depend on turbulence intensity? (iii) What are the roles of advection, reaction, and diffusion in creating non-monotonic thermochemical trajectories? and (iv) How are fluid parcel residence times and path lengths affected by turbulence? An answer to the last question, in particular, will provide insight into the accuracy of chemical models developed for idealized conditions such as those of a laminar flame or a perfectly stirred reactor.

In order to address these questions, we examine data from direct numerical simulations (DNS) of stoichiometric H_2–air premixed flames at atmospheric conditions. Chemical kinetics are modeled using both multi- and single-step mechanisms, and large scale turbulence velocities considered are 16 and 32 times greater than the corresponding laminar flame speeds. The turbulence in these reacting flows is thus high-speed, and both flames correspond to the thin reaction zones regime of premixed combustion [1].

In the following, we provide details on the numerical simulations performed, followed by a description of the Lagrangian analysis. We then outline properties of thermochemical trajectories in H_2–air premixed flames for both multi- and single-step simulations and provide a summary and conclusions at the end.

2. Numerical simulations

The present DNS of stoichiometric H_2–air premixed turbulent flames is performed using the code `Athena-RFX` [2,24,25], which uses a fully unsplit corner transport upwind scheme with piecewise parabolic spatial reconstruction and an HLLC Riemann solver [26] to solve the fully compressible, reactive-flow Navier–Stokes equations. In the simulations, both multi- and single-step models are employed for the stoichiometric H_2–air reaction kinetics.

The multi-step reaction kinetics for H_2–air combustion are based on the 2014 San Diego mechanism [27], which includes 21 different reactions involving 8 reacting species: H, H_2, O, O_2, OH, H_2O, HO_2, H_2O_2, and the inert N_2. The equation of state is that of an ideal gas with various thermodynamic functions of pure chemical species computed using the NASA seven-coefficient format [28]. Molecular transport coefficients are calculated using mixture averaging. In particular, mixture-averaged conduction as well as diffusion coefficients for each species are computed as in the `TRANSPORT` library [29]. Viscosity coefficients are computed using the averaging formula of order six recommended by Ern and Giovangigli [30]. Pure species shear and bulk viscosities and binary diffusion coefficients are evaluated from standard kinetic theory expressions [31]. Thermal conduction coefficients of pure species

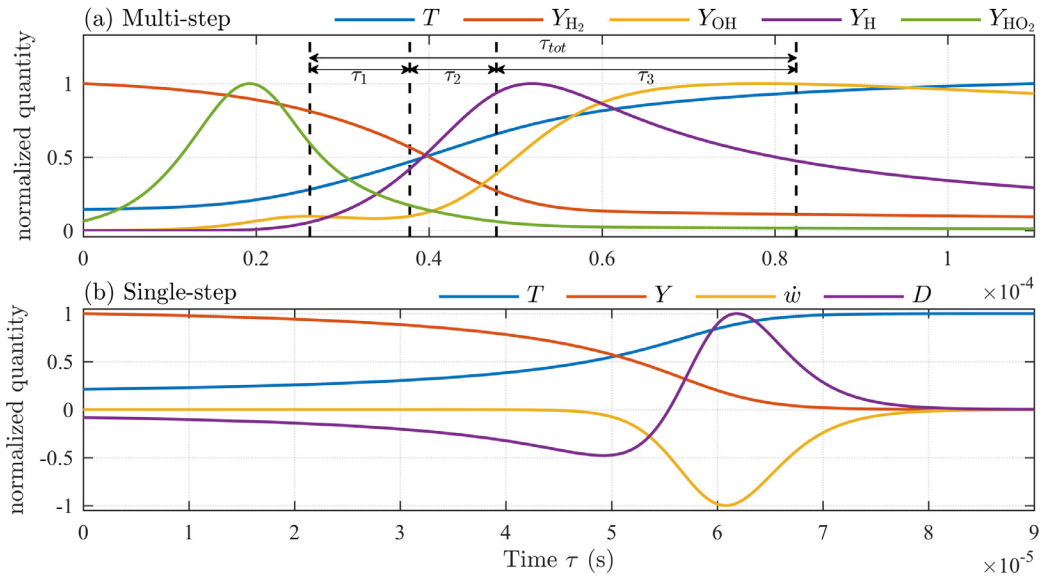


Fig. 1. Lagrangian thermochemical trajectories for fluid parcels undergoing combustion in laminar flames, corresponding to (a) multi-step and (b) single-step H_2–air chemical kinetics. For the multi-step case in panel (a), the laminar flame structure is calculated using CHEMKIN and evolutions of temperature T and mass fraction of H_2, OH, H, and HO_2 are shown. Residence times τ_1, τ_2, τ_3, and τ_{tot} are also shown for the multi-step case in panel (a) and are defined in Eq. (7). In panel (b) for the single-step case, the reaction rate $\dot{w}$ and total diffusive transport D from Eq. (1) are shown alongside T and the reactant mass fraction Y. All curves are normalized by the corresponding peak values in the laminar flame.

are evaluated using expressions given by Warnatz [32], giving a fuel Lewis number close to unity [33]. Figure 1(a) shows the laminar flame structure computed using CHEMKIN for this physical model as a function of time along a fluid parcel trajectory. The laminar flame speed is $S_L = 250$ cm/s and the laminar flame thermal width based on the maximum temperature gradient is $\delta_L = 0.034$ cm. The fuel temperature is 300 K and the adiabatic flame temperature is 2383 K.

Although the primary emphasis in this study is on results obtained from the higher-fidelity multi-step simulations, there are two primary motivations for also performing and analyzing single-step simulations: (i) comparison of the multi- and single-step results will indicate whether single-step mechanisms can qualitatively reproduce thermochemical trajectories observed for multi-step cases, and (ii) the dynamical reasons for changes in the thermochemical state within fluid parcels are more easily examined in the single-step case. The second point is of particular importance because, for a single-step reaction, the corresponding governing equation for the reactant mass fraction Y can be written in relatively simple non-conservative form as

$$\underbrace{\frac{\partial Y}{\partial t} + u_i \frac{\partial Y}{\partial x_i}}_{\mathrm{d}Y/\mathrm{d}t} = \dot{w} + \underbrace{\frac{1}{\rho}\frac{\partial}{\partial x_i}\left(\lambda \frac{\partial Y}{\partial x_i}\right)}_{D}, \tag{1}$$

where $Y = 1$ in the unburnt reactants and $Y = 0$ in the burnt products. In Eq. (1), u_i is the velocity vector, $\dot{w}$ is the reaction rate, ρ is the density, and λ is the mass diffusion transport coefficient. In this equation, the left hand side is denoted dY/dt in a Lagrangian framework and the entire diffusive term on the right-hand side is denoted D. Along fluid parcel trajectories, Y is a function of time only, and Eq. (1) shows that Y can only change as the result of reactions or diffusion. In the case of an irreversible reaction, $\dot{w}$ is strictly negative, and thus any complex changes in Y (such as increases in Y through the flame) *must* be due to diffusive effects. In particular, it will be shown in the following that the fuel mass fraction can vary non-monotonically along thermochemical trajectories in high-speed turbulent premixed flames modeled using single-step kinetics, and that increases in Y along the trajectories, therefore, are entirely due to D.

Table 1
Parameters used to define the single-step H_2–air chemical model [34].

T_r	293 K	Initial temperature
p_r	1.01×10^6 erg/cm^3	Initial pressure
ρ_r	8.73×10^{-4} g/cm^3	Initial density
γ	1.17	Adiabatic index
M	21 g/mol	Molecular weight
T_p	2135 K	Post-flame temperature
ρ_p	1.2×10^{-4} g/cm^3	Post-flame density
B	6.85×10^{12} cm^3/(g s)	Pre-exponential factor
Q	46.37 RT_r	Activation energy
q	43.28 RT_r/M	Chemical energy release
ν_r	0.189 cm^2/s	Initial kinematic viscosity
α_r	1.77 cm^2/s	Initial thermal diffusivity
D_r	1.77 cm^2/s	Initial mass diffusivity
n	0.7	Temperature exponent

In the single-step simulations, each of the transport coefficients has a power-law dependence on temperature T given by

$$\mu = \mu_B = \rho_r \nu_r (T/T_r)^n, \quad k = \rho_r \alpha_r c_p (T/T_r)^n, \quad \lambda = \rho_r D_r (T/T_r)^n, \tag{2}$$

where μ is the shear viscosity, μ_B is the bulk viscosity, k is the thermal conductivity, and λ is the mass diffusivity. Here n is a constant, ν_r, α_r, and D_r are the kinematic viscosity, thermal diffusivity, and mass diffusivity at the unburnt reactant conditions T_r and ρ_r, and $c_p = \gamma R/M(\gamma - 1)$ is the specific heat capacity at constant pressure. The Lewis number in the single-step cases, $\mathrm{Le} = \alpha_r/D_r$, is unity. The reaction rate, $\dot{w}$, is modeled using first-order, single-step Arrhenius kinetics as

$$\dot{w} = -\rho Y B \exp\left(-\frac{Q}{RT}\right), \tag{3}$$

where B is the pre-exponential factor and Q is the activation energy. The corresponding chemical energy release is denoted q. Values for each of the parameters describing the single-step chemical model are provided in Table 1 [34]. The equation of state is that of an ideal gas.

Figure 1(b) shows the corresponding laminar flame structure produced by this single-step model along a fluid parcel trajectory, including the evolutions of $\dot{w}$ and D from Eq. (1). In this

Table 2
Chemical, turbulent, and physical parameters for each of the H_2–air DNS cases. The laminar flame speed is S_L, δ_L is the laminar flame thermal width based on the maximum temperature gradient, $L \times L \times L_z$ is the physical domain size, Δ is the uniform grid cell size, U is the turbulent velocity at the scale of the domain width L, $\tau_c = \delta_L/S_L$ is the chemical time scale, and $\tau_{ed} = L/U$ is the domain-scale turbulent eddy turnover time. The Damköhler number is defined as $Da = \tau_{ed}/\tau_c$ and the Karlovitz number is $Ka = \tau_c/\tau_K$, where $\tau_K = (\nu_r/\varepsilon_r)^{1/2}$ is the Kolmogorov time scale in the reactants with $\varepsilon_r = U^3/L$. Each simulation has $256 \times 256 \times 2048$ grid cells and 32 grid cells per δ_L.

Case	Chemistry	S_L (cm/s)	δ_L (cm)	L (cm)	L_z (cm)	Δ (cm)	U (cm/s)	τ_c (s)	τ_{ed} (s)	U/S_L	Da	Ka
S1	Single	302	3.24×10^{-2}	0.259	2.072	1.01×10^{-3}	4.83×10^{3}	1.07×10^{-4}	5.36×10^{-5}	16	0.50	162
S2	Single	302	3.24×10^{-2}	0.259	2.072	1.01×10^{-3}	9.67×10^{3}	1.07×10^{-4}	2.68×10^{-5}	32	0.25	460
M1	Multi	250	3.42×10^{-2}	0.272	2.176	1.06×10^{-3}	3.99×10^{3}	1.37×10^{-4}	6.82×10^{-5}	16	0.50	152
M2	Multi	250	3.42×10^{-2}	0.272	2.176	1.06×10^{-3}	7.98×10^{3}	1.37×10^{-4}	3.41×10^{-5}	32	0.25	431

case, the laminar flame speed is $S_L = 302$ cm/s and the laminar flame thermal width based on the maximum temperature gradient is $\delta_L = 0.032$ cm; this value of δ_L is similar to the value for the multi-step case, but S_L is somewhat higher than in the multi-step case. Although a single-step model could be constructed that is more closely tuned to the multi-step kinetics, we have chosen to use the same single-step model that was used in a number of prior studies [2–4,9,10,25] in order to facilitate comparisons between present and prior results. Moreover, as will be seen in the following, there is extensive qualitative agreement between results from the multi- and single-step cases, particularly with respect to the complexity of thermochemical trajectories in highly turbulent premixed flames.

Both multi- and single-step simulations model premixed, stoichiometric H_2–air turbulent flames in unconfined domains at atmospheric conditions (Table 2 provides a summary of parameters used to setup the simulations). Three-dimensional (3D) domains are discretized using a uniform grid of size $256 \times 256 \times 2048$ in all cases, with physical domain widths (in x and y directions) of $L = 0.272$ cm in the multi-step cases and $L = 0.259$ cm in the single-step cases. This gives a domain of width $L \approx 8\delta_L$ and length $L_z = 8L$ for all cases. The resulting grids thus have uniform resolution $\Delta \approx 1 \times 10^{-3}$ cm for both multi- and single-step cases, which gives 32 computational cells per laminar thermal flame width δ_L. The turbulent flow field is similarly well resolved in the burned products for each case, with at least three grid cells per Kolmogorov scale $\eta_K = (\nu^3/\varepsilon)^{1/4}$, where $\nu = \mu/\rho$ is the kinematic viscosity and ε is the mean kinetic energy dissipation rate. However, the resolution within the flame region is somewhat lower due to the decrease in viscosity with decreasing temperature T, and η_K is only resolved with between 0.25–0.5 grid cells in the unburnt reactants. Nevertheless, this resolution is still sufficient to calculate Lagrangian trajectories since the velocity fields that determine the paths of these trajectories are dominated by large and intermediate scale motions at all locations [10]. Further increases in resolution were also limited by the large storage requirements imposed by the Lagrangian analysis, as discussed in the next section.

The simulations are initiated with a uniform cold reactive mixture. Turbulence is allowed to develop for two domain-scale eddy turnover periods, defined as $\tau_{ed} \equiv L/U$ where U is the turbulent velocity at the scale of the domain width L (see Table 2). Turbulence in the simulations is sustained through large-scale isotropic forcing, as described in [2]. The resulting turbulence properties were previously analyzed in detail in [2–4,10]. After the spin-up period, a planar laminar flame is initialized in the domain using a detailed structure obtained using `CHEMKIN` for multi-step cases or a separate high-fidelity solver for single-step flames. Subsequently, a turbulent flame is allowed to develop for another τ_{ed} before data collection for the analysis begins. Periodic boundary conditions are used in the x and y directions, and boundaries in the z direction are periodic prior to ignition and zero-order extrapolations thereafter. This initialization procedure was first employed by Poludnenko and Oran [2] and the open boundary conditions after initialization permit any pressure waves introduced by the initialization to exit the simulation domain. It should be noted that the integral-scale eddy turnover time $\tau_{ed,\ell} = \ell/U_\ell$ is roughly 2–3 times smaller than the domain-scale eddy turnover time τ_{ed} in all simulations, where ℓ is the integral length scale and U_ℓ is the integral velocity. Consequently, there are roughly $2–3\tau_{ed,\ell}$ between flame initialization and the start of the Lagrangian analysis. In prior studies [2,25] using the same flame initialization procedure as that employed here, the turbulent burning rate was found to reach an approximately statistically stationary state roughly one τ_{ed} after flame initialization.

Two different turbulence conditions are examined for both multi- and single-step cases, corresponding to normalized turbulence intensities U/S_L of 16 and 32, giving a total of four DNS cases analyzed in this study. Chemical, turbulent, and physical properties for each of the simulations are outlined in Table 2. In all cases, the high Ka and low Da numbers examined here place the flames in the thin reaction zone regime [1], and all simulations can thus be considered as modeling high-speed turbulence. In the following, the lower speed multi- and single-step cases are denoted M1 and S1, respectively, and the higher speed cases are denoted M2 and S2. Following [10], the Damköhler number is defined as $Da = \tau_{ed}/\tau_c$ and the Karlovitz number is $Ka = \tau_c/\tau_K$, where $\tau_c = \delta_L/S_L$ is the chemical time scale and $\tau_K = (\nu_r/\varepsilon_r)^{1/2}$ is the Kolmogorov time scale in the reactants. It is assumed that the energy cascade in the reactants is conservative such that the mean dissipation rate can be written in terms of the large-scale energy input as $\varepsilon_r = U^3/L$.

Figures 2 and 3 show example fields of temperature, fuel mass fraction, z-direction velocity u_z, and vorticity magnitude $\omega \equiv (\omega_i\omega_i)^{1/2}$ for the multi- and single-step cases, respectively, where $\omega_i = \epsilon_{ijk}\partial u_k/\partial x_j$ is the vorticity vector and ϵ_{ijk} is the alternating tensor. Figure 3 additionally shows the reaction rate $\dot{w}$ for the single-step cases. Consistent with prior studies [3,10], the temperature isosurfaces for all cases are more wrinkled near the reactants and this wrinkling increases at all flame locations with increasing turbulence intensity (i.e., from M1 to M2, or from S1 to S2). For both multi- and single-step cases, the temperature dependence of the viscosity results in substantially greater viscosity and a corresponding decrease in Reynolds number through the flame. Combined with the effects of dilatation due to heat release, this reduction in Reynolds number results in a substantial suppression of small-scale turbulence [10,35], which is manifested in Figs. 2 and 3 as a suppression of vorticity magnitude from reactants to products. Although the fields in Figs. 2 and 3 are qualitatively similar between the multi- and single-step cases, there are differences in the extent of the burned regions of the flames (particularly when comparing the locations of the $T = 2000$ K iso-contours in each panel). We will show in the following, however, that these differences have no impact on comparisons of thermochemical complexity between the multi- and single-step cases, or on conclusions based on these results.

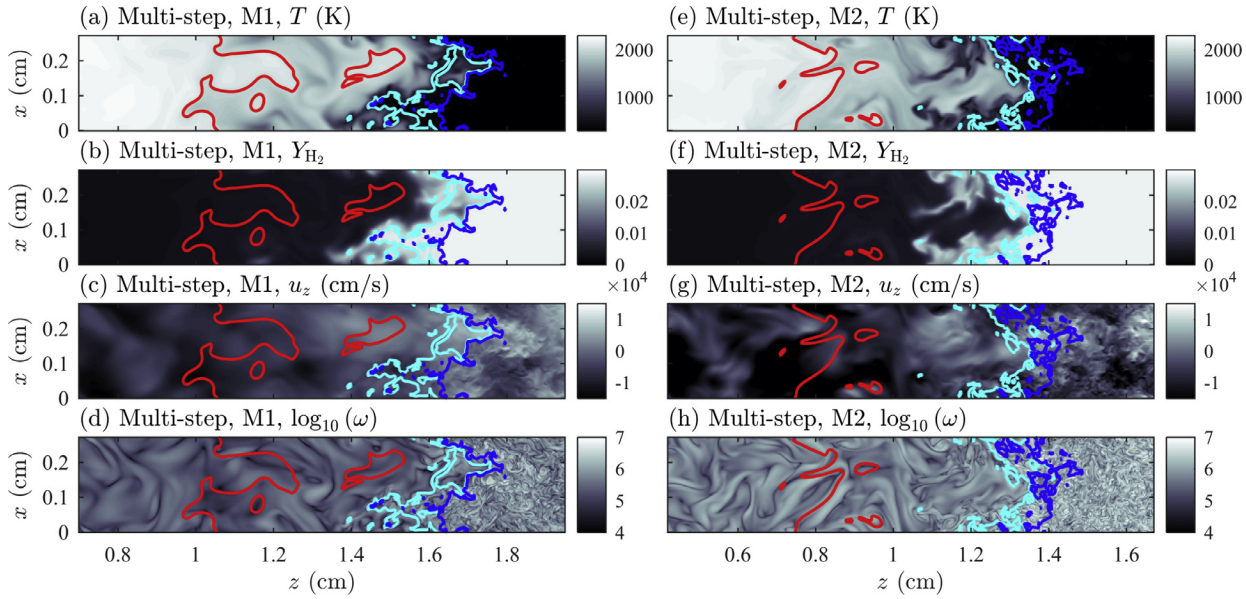


Fig. 2. Fields of temperature T (a,e), fuel mass fraction Y_{H_2} (b,f), z-direction velocity u_z (c,g), and vorticity magnitude ω (d,h) for multi-step H_2–air turbulent premixed flames at moderate (a–d) and high (e–h) turbulence intensities (see Table 2 for properties of the M1 and M2 cases). Shown are domain cross-sections through the midplane, with the initial fluid parcel locations seeded along the $T = 350$ K isosurface (blue lines). Isosurfaces for $T = 500$ K (cyan lines) and $T = 2000$ K (red lines) are also shown. (For interpretation of the references to color in this figure legend, the reader is referred to the web version of this article.)

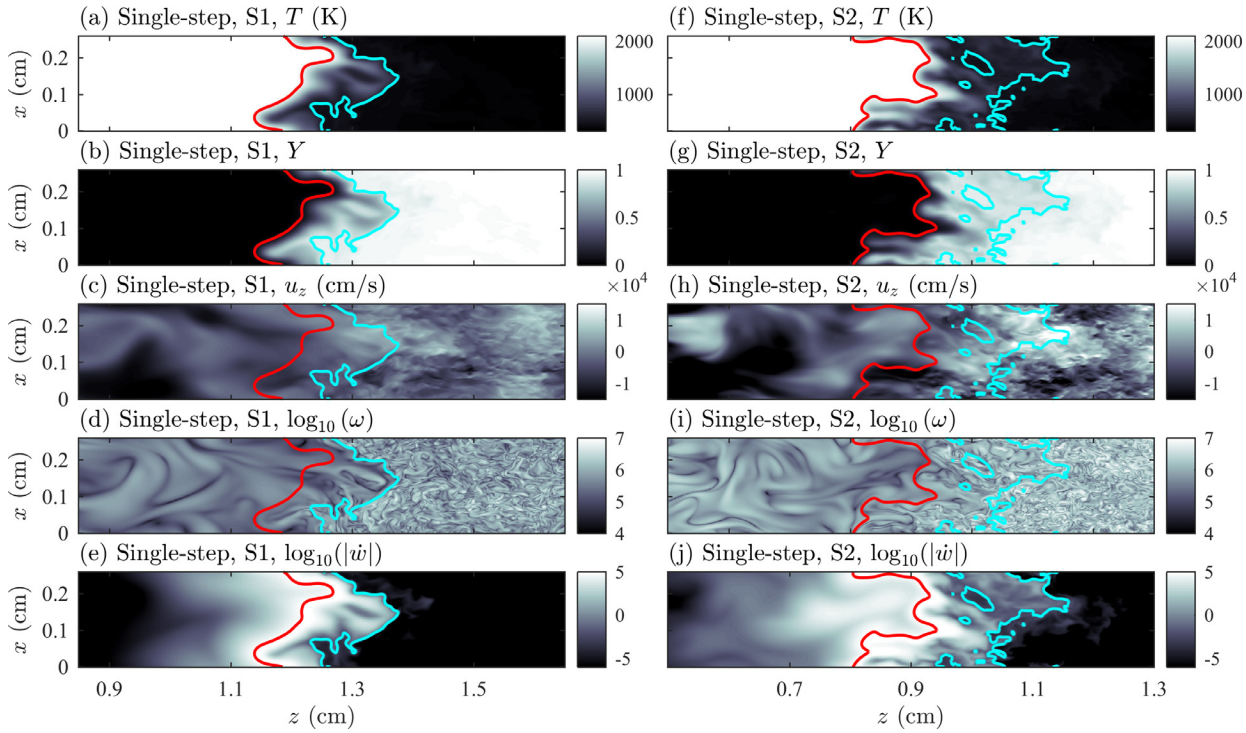


Fig. 3. Fields of temperature T (a,f), reactant mass fraction Y (b,g), z-direction velocity u_z (c,h), vorticity magnitude ω (d,i), and reaction rate $\dot{w}$ (e,j) for single-step H_2–air turbulent premixed flames at moderate (a-e) and high (f-j) turbulence intensities (see Table 2 for properties of the S1 and S2 cases). Shown are domain cross-sections through the midplane, with the initial fluid parcel locations seeded along the $T = 500$ K isosurface (cyan lines). Isosurfaces for $T = 2000$ K (red lines) are also shown. (For interpretation of the references to color in this figure legend, the reader is referred to the web version of this article.)

3. Lagrangian analysis approach

A detailed description of the Lagrangian analysis approach used here, including validation and verification tests, can be found in Darragh et al. [36]. In the following, we outline specific details relevant to the present Lagrangian analysis of premixed reacting flows. Calculation of Lagrangian trajectories in any fluid flow requires the solution of the ordinary differential equation

$$\frac{\mathrm{d}\mathbf{x}}{\mathrm{d}t} = \mathbf{u}(\mathbf{x}, t)\,, \tag{4}$$

where $\mathbf{x}(t)$ is the position of a fluid parcel that moves according to the Eulerian velocity field $\mathbf{u}(\mathbf{x}, t)$. Integration of Eq. (4) is typically performed for many different initial locations $\mathbf{x}(t_0)$, where t_0 is the

initial time in the Lagrangian analysis, resulting in Lagrangian trajectories for a number of fluid parcels in the same flow.

Given sufficiently resolved velocity fields $\mathbf{u}(\mathbf{x}, t)$ obtained from the solution of reactive-flow governing equations, there are two ways in which Eq. (4) can be integrated, referred to as 'online' and 'offline' approaches. In the online approach, Eq. (4) is solved during the course of the simulation used to obtain $\mathbf{u}(\mathbf{x}, t)$. This approach greatly reduces data storage requirements and allows data at every time step in the simulation to be used in the trajectory calculation.

By contrast, in the offline approach, velocity fields are output at a high cadence and Eq. (4) is solved as a post-processing step. The main disadvantage of the offline approach is the enormous disk storage requirements it imposes. On the other hand, it has the advantage of complete flexibility in modifying the analysis strategy and solution algorithms as needed. In particular, it allows high-order temporal interpolation of data using a symmetric stencil, which can substantially improve the overall accuracy of the trajectory integration. In an online approach, only backwards interpolation in time is possible, since higher-order interpolation is generally not practical due to the large amount of memory required to store data from multiple sequential time steps. In the present study, we adopt the offline approach in order to allow the use of higher-order temporal interpolation methods.

For the four DNS cases summarized in Table 2, the offline Lagrangian approach employed here made use of roughly 10,000 individual output data snapshots for the M1 and S1 cases with a time interval of $\Delta t = 1 \times 10^{-8}$ s, and roughly 20,000 snapshots for the M2 and S2 cases with a time interval of $\Delta t = 5 \times 10^{-9}$ s. These time intervals correspond to roughly four numerical integration time steps in the M1 and S1 simulations and roughly two time steps in the higher intensity M2 and S2 simulations. For the lower intensity cases, the integration time step was set by a Courant–Friedrichs–Lewy (CFL) condition based on diffusion, whereas in the higher intensity cases the time step was set by a convective CFL condition. Even in the lower intensity cases, however, the convective time step was quite close to the diffusive time step. As a result, data were output every 2–3 convective time steps in both low and high intensity simulations. The required data output intervals are connected to the dynamics of the turbulent flow field and must be sufficiently short in order to allow accurate reconstruction of Lagrangian trajectories from DNS velocity fields. These output intervals result in roughly 6,000 output snapshots per eddy turnover time τ_{ed} for each simulation. The total number of snapshots output from each simulation (or, alternatively, the total duration of the Lagrangian calculations) is determined by the characteristic chemical time scale $\tau_c = \delta_L / S_L$, which loosely corresponds to the laminar flame crossing time. As will be seen in Section 4.3, high-speed turbulent flame crossing times are typically shorter than for laminar flames, but the Lagrangian analysis was nevertheless carried out over durations similar to τ_c in order to provide sufficient time for most fluid parcels to undergo complete combustion. The data requirements for this analysis were thus extreme, which constrained the computational domain to a relatively modest size compared to previous studies using `Athena-RFX` [9,10,35]. It is possible that larger data output intervals Δt or an online analysis approach with lower-order (or no) temporal interpolation could be used with similar success, but here small Δt and the offline approach have been used to enable the use of higher-order interpolation methods and to ensure the accuracy of the results presented herein.

Given discrete velocity data, there are a number of numerical approaches for solving Eq. (4), but high-order methods are generally required to accurately capture Lagrangian trajectories for long times in turbulent flows, which are inherently nonlinear and chaotic. Integration of Eq. (4) is thus performed here using both fourth and fifth order Runge–Kutta–Fehlberg methods [37], denoted in the following as RKF4 and RKF5, respectively. For these methods, given a fluid parcel location at a prior time step $\mathbf{x}_n \equiv \mathbf{x}(t)$, the parcel position at time step $\mathbf{x}_{n+1} \equiv \mathbf{x}(t+h)$ is given by

$$\mathbf{x}_{n+1} = \mathbf{x}_n + h \sum_{i=1}^{N} b_i \mathbf{k}_i \,, \tag{5}$$

where h denotes the Lagrangian integration time step, which need not be the same as Δt (in fact, it is typically much smaller than Δt, as is the case in the present study). In Eq. (5), N is the number of steps in the RKF method and the $\mathbf{k}_i$ coefficients are obtained from the Eulerian velocity field $\mathbf{u}(\mathbf{x}, t)$ as

$$\mathbf{k}_i = \mathbf{u}\left(\mathbf{x}_n + h \sum_{j=1}^{N} a_{ij} \mathbf{k}_j,\ t_n + c_i h \right), \tag{6}$$

where a_{ij}, b_i, and c_i are constant numerical coefficients given in Refs. [36,37] for the RKF4 and RKF5 methods.

In order to obtain $\mathbf{k}_i$ in Eq. (6), both spatial and temporal interpolations of the velocity field data are required. The accuracy of the computed Lagrangian trajectories depends sensitively on the order of the spatial interpolation method [17], and here second-order Akima splines are used for both spatial and temporal interpolations. Once the parcel positions are computed, thermochemical trajectories are obtained by performing spatial interpolations of species mass fractions, temperature, as well as reaction and diffusion terms (in the single-step cases) to these coordinates. These interpolations are also performed using Akima splines.

The resulting Lagrangian trajectory numerical algorithm has been verified by Darragh et al. [36] through tests on both steady and unsteady idealized flows, for which trajectories can be calculated analytically. In these tests, computed trajectories have been compared with true trajectories for various integration schemes and interpolation methods in order to determine the optimal approach for the analysis of premixed reacting flows and to verify the accuracy of the numerical algorithm. Moreover, in order to ensure the accuracy of the computed trajectories, both RKF4 and RKF5 methods are used to compute trajectory locations. The resulting trajectories are compared in order to determine the accuracy of the method, as described in the next section.

4. Properties of thermochemical trajectories in H_2–air flames

For each of the four simulations performed in this study, 16,384 separate Lagrangian trajectories were calculated over a duration of roughly one flame crossing time τ_c in the laminar case. Thermodynamic and chemical properties, as well as certain dynamical terms, were then interpolated to these trajectories. For the multi-step simulations (i.e., M1 and M2), each of the 16,384 trajectories were initialized on the $T = 350$ K isosurface and for the single-step simulations (i.e., S1 and S2) each trajectory was initialized on the $T = 500$ K isosurface. These initial trajectory locations correspond to the region where temperature begins to vary most rapidly in the multi-step cases and to the beginning of the preheat zone in the single-step cases. Note that while the single-step laminar flame has a well defined preheat and reaction zone, a more realistic H_2–air flame, as modeled in the multi-step simulations, does not exhibit such a clear distinction between these two flame regions.

The trajectories were integrated forward in time using both RKF4 and RKF5 methods with a Lagrangian time step of $h = 0.4\Delta t$ for all cases, where Δt is the data output time from the simulations. Lagrangian trajectories were calculated up to a maximum time of $\tau_{max} \approx \tau_c$, which allowed the parcels sufficient time to undergo combustion. It should be noted, however, that some fluid parcels cooled and returned to pure unburnt reactants after initialization. Of the 16,384 fluid parcels in the analysis, approximately 10% in both the multi- and single-step cases failed to reach a

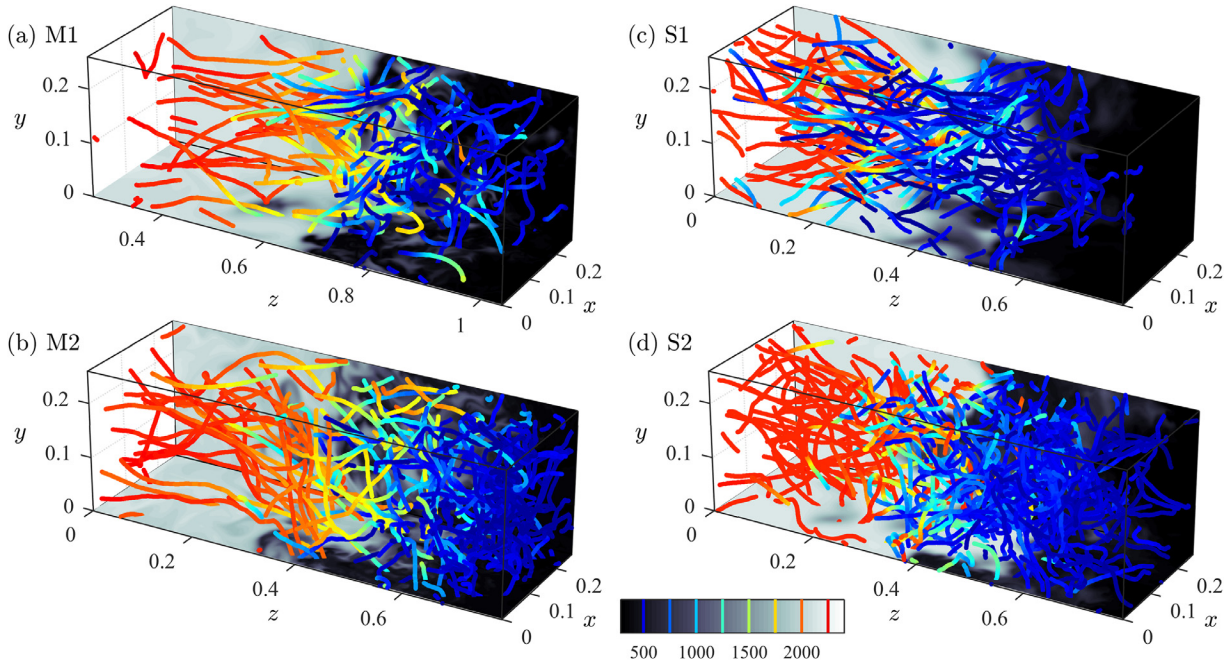


Fig. 4. Selection of 3D trajectories for the multi- (a,b) and single-step (c,d) simulations. Trajectories are colored by the value of the temperature along the trajectory (colors are indicated on the grayscale colorbar at bottom). The bottom and back planes show the temperature field near the initial time in the Lagrangian analysis. The multi-step trajectories (a,b) were initialized on the $T = 350$ K isosurface and the single-step trajectories (c,d) were initialized on the $T = 500$ K isosurface.

temperature of 600 K, indicating that these parcels had reverted to unburnt reactants.

Comparing RKF4 and RKF5 trajectories in order to determine accuracy, 100% of all trajectories that undergo complete combustion were found to have RKF4 and RKF5 differences smaller than one grid cell size Δ for the lower intensity S1 and M1 cases. Roughly 80% of the trajectories met this same criteria for the S2 and M2 cases. However, the accuracy of the trajectories is likely to be greater than 80% in the higher intensity cases, since this is only the percentage of RKF4 trajectories that are in good agreement with RKF5 trajectories. It is likely that greater than 80% of the RKF5 trajectories would match the 'true' trajectories from the data. As a result, all 16,384 of the computed trajectories are included in the analysis presented in the following sections, and RKF5 results are shown in all cases.

Figure 4 shows a selection of trajectories calculated for each of the simulation cases. The trajectories are highly tangled (i.e., not straight for long periods) near the reactants, but after passing through the flame, the trajectories become increasingly more uniform. This is primarily due to the suppression of small-scale turbulent fluctuations after the flame (see also Figs. 2 and 3), as well as due to the large velocities u_z directed away from the flame in the products. As the turbulence intensity increases (i.e., comparing M1 to M2, or S1 to S2), the trajectories become increasingly tangled and non-straight. There is little qualitative difference between the multi- and single-step trajectories shown in Fig. 4 for the same Ka and Da.

4.1. Thermochemical complexity in H_2–air flames

Figure 5 shows joint probability density functions (pdfs) of species mass fractions Y_{H_2}, Y_{OH}, Y_H, and Y_{HO_2} versus temperature T along Lagrangian trajectories for the multi-step cases. Since the pdfs in Fig. 5 represent single-point and single-time statistics, however, they are identical to pdfs that would be obtained from a corresponding Eulerian analysis of the same locations visited by the Lagrangian trajectories. As has been observed in prior studies of high-speed turbulent flames [38], these joint pdfs indicate that there is a substantial likelihood of finding thermochemical states that differ from laminar states. As the turbulence intensity increases (i.e., from M1 to M2), however, the joint pdfs in Fig. 5 are only marginally changed. There are some minor quantitative differences in the values of the joint pdfs, but the 'envelopes' of the pdfs are relatively independent of turbulence intensity for the two multi-step cases examined here.

Despite the similarity of the joint pdfs in Fig. 5, the detailed time-history information provided by the Lagrangian analysis does reveal pronounced differences between the M1 and M2 cases when comparing trajectories in thermochemical phase space. Figure 6 shows a collection of such individual Lagrangian trajectories. Overall, the envelopes of states explored by the trajectories are fully consistent with those shown in Fig. 5. At the same time, however, individual trajectories in phase space are highly complex, including many instances of 'loops' and rapidly changing phase-space states that do not occur in the laminar case. Comparison of results for the two different intensities in Fig. 6 indicates that the complexity of phase-space trajectories increases with increasing turbulence intensity (i.e., from M1 to M2), resulting in more rapid phase-space state variations.

The 'loops' and rapid state changes shown in Fig. 6 suggest that the consumption of H_2 and the rise in temperature are generally non-monotonic as fluid parcels undergo combustion. This is indicated more clearly in Fig. 7, which shows a selection of trajectories that have been centered such that each trajectory reaches $T = 1400$ K at the same time. This temperature approximately corresponds to the peak heat release rate in the case of multi-step kinetics. These plots show that even at temperatures above $T = 1400$ K, the ensuing evolution is highly complex and fluid parcels can either undergo much more rapid increases in temperature than in the laminar case, or the temperature can fall again after reaching $T = 1400$ K. Moreover, large changes in temperature and composition for $T > 1400$ K are generally more prevalent and more rapid for the higher intensity M2 case shown in Figs. 7(e)–(h), as compared to the M1 case in Figs. 7(a)–(d). This is supported

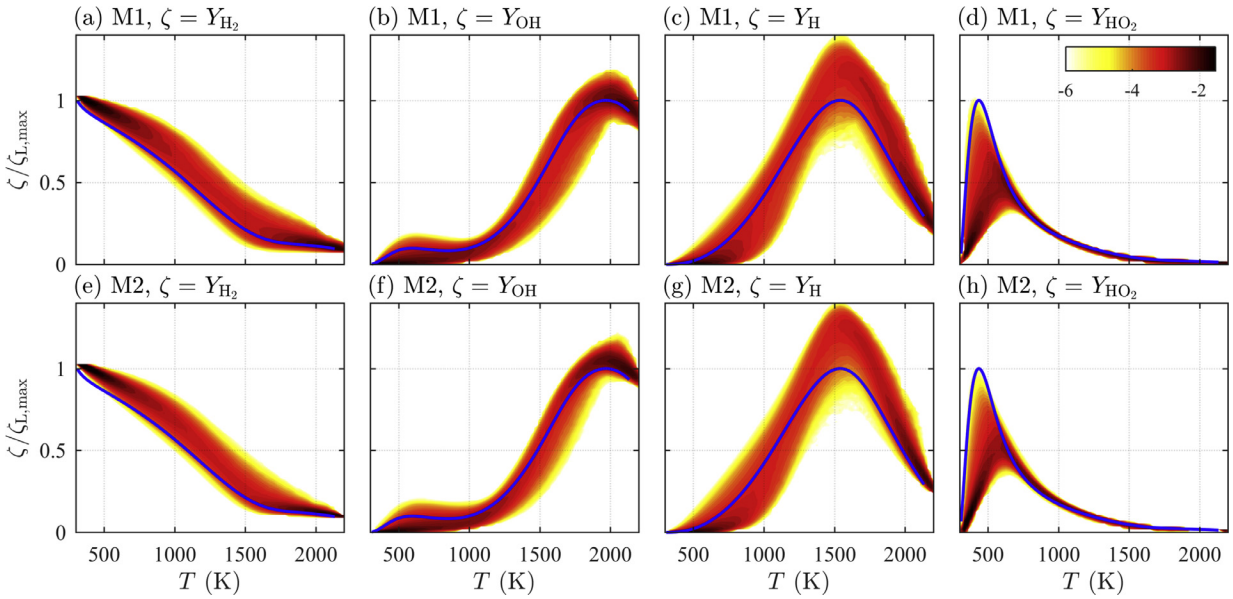


Fig. 5. Joint probability density functions (pdfs) of Y_{H_2} (a,e), Y_{OH} (b,f), Y_H (c,g), and Y_{HO_2} (d,h) versus temperature T for the multi-step cases M1 (a–d) and M2 (e–h). Species mass fractions are normalized by their corresponding maximum values in a laminar flame and the joint pdfs comprise all points and all times on Lagrangian trajectories. Shown are logarithms of the joint pdf $\log_{10}[P(\zeta/\zeta_{L,\,max}, T)]$. Solid blue lines in all panels are the corresponding laminar flame profiles.

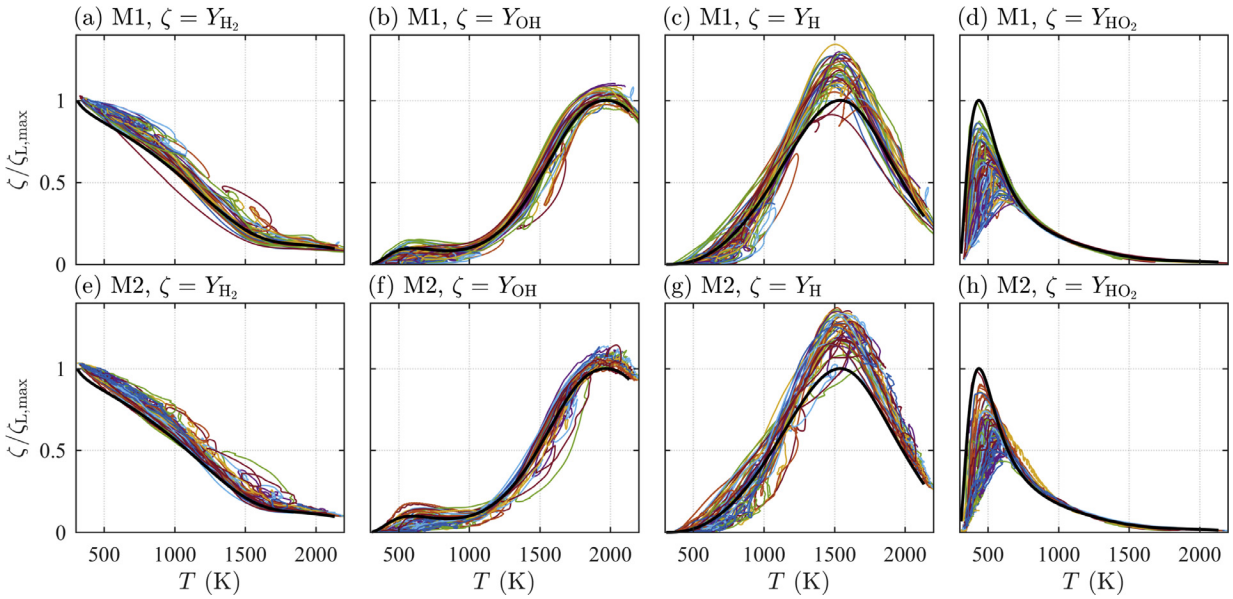


Fig. 6. Thermochemical phase-space diagrams of species mass fractions Y_{H_2} (a,e), Y_{OH} (b,f), Y_H (c,g), and Y_{HO_2} (d,h) versus temperature T for the multi-step cases M1 (a–d) and M2 (e–h). For clarity, only 50 of the 16,384 computed thermochemical trajectories are shown. Species mass fractions are normalized by their corresponding maximum values in a laminar flame. Solid black lines in all panels are the corresponding laminar flame profiles.

quantitatively by the finding that 76% of all trajectories reach a temperature of 1400 K for M1, but only 72% of trajectories reach 1400 K for M2. Only 66% of all trajectories then reach a temperature of 1800 K for M1, while 63% of trajectories reach 1800 K for M2. It is interesting to note, however, that a greater total of the trajectories reach 2100 K in the M2 case than in the M1 case (47% versus 43% of total trajectories, respectively).

The non-monotonicity and complexity along thermochemical trajectories is also indicated in Fig. 8, which shows detailed time series for two sample trajectories in cases M1 and M2 compared to laminar flame results (as shown in Fig. 1). In panels (a) and (c) of Fig. 8, the thermochemical evolutions are similar to the laminar case. However, such similarities are relatively rare and a large proportion of the trajectories, for example those in Fig. 8(b,d), exhibit substantial deviations from laminar trajectories, with non-monotonic fuel consumption and temperature rise during combustion. Comparison of M1 and M2 in Fig. 8 once again indicates that variations in thermochemical quantities are much more rapid in the higher intensity case.

The degree of non-monotonicity in both of the multi-step cases can be quantified using conditional pdfs of time derivatives (i.e., the rate of change) of various quantities along Lagrangian trajectories, as shown in Fig. 9. In particular, this figure indicates that non-monotonicity in T (corresponding to $dT/dt < 0$ along a trajectory) is generally most pronounced for $T < 1000$ K, although non-monotonicity in Y_{H_2} (corresponding to $dY_{H_2}/dt > 0$) is most pronounced for somewhat higher temperatures. In both cases, however, there is a significant probability of non-monotonic

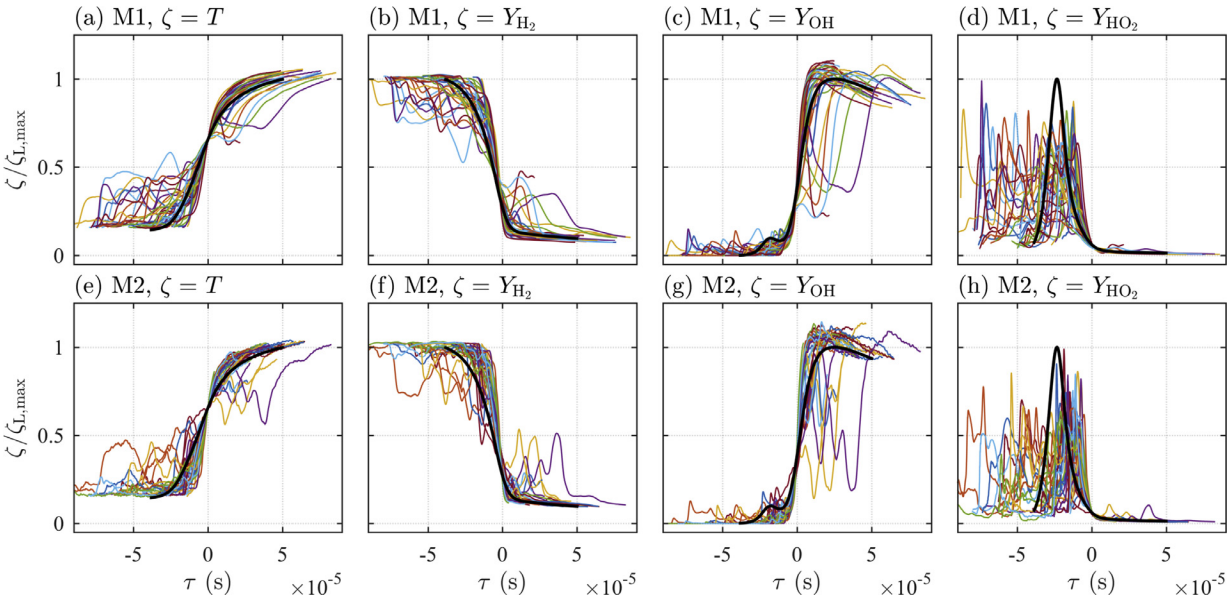


Fig. 7. Time series for the same 50 thermochemical trajectories as in Fig. 6, showing evolutions of T (a,e), Y_{H_2} (b,f), Y_{OH} (c,g), and Y_{HO_2} (d,h) for multi-step cases M1 (a–d) and M2 (e–h). The time series are all shifted such that at $\tau = 0$ s, fluid parcels first reach a temperature of $T = 1400$ K, which approximately corresponds to the temperature of the peak heat release rate. All quantities are normalized by their corresponding maximum values in a laminar flame. Solid black lines in all panels are the corresponding laminar flame profiles.

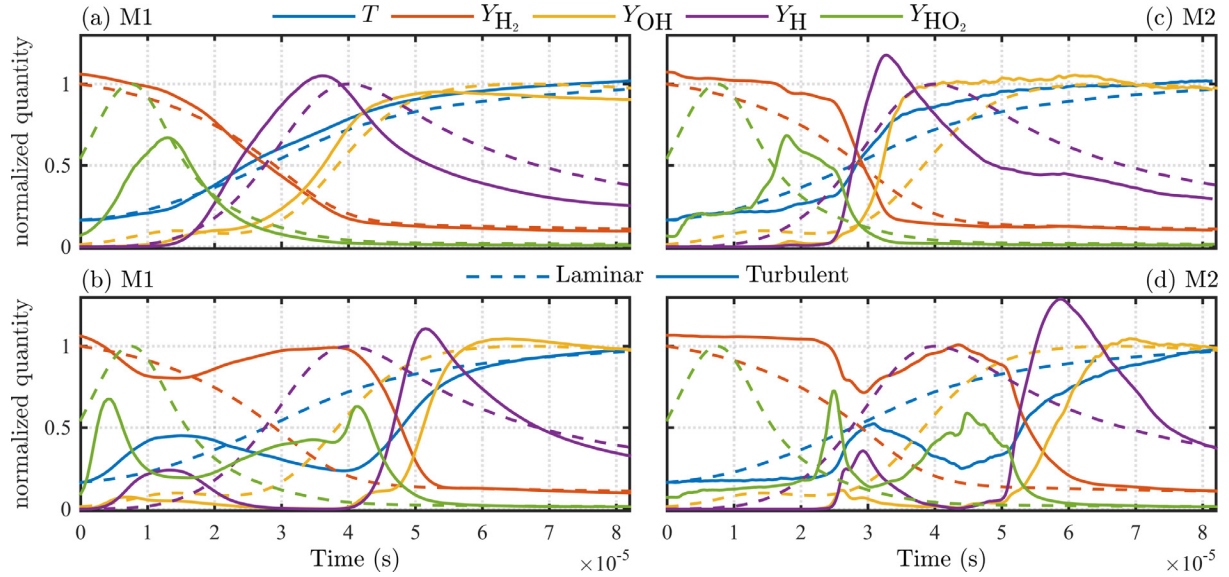


Fig. 8. Thermochemical trajectories for the M1 (a,b) and M2 (c,d) multi-step cases. Panels (a) and (c) show trajectories with evolutions similar to that of a laminar flame, while panels (b) and (d) show examples of non-monotonic fuel consumption and temperature rise. Solid lines are turbulent trajectories and dashed lines are laminar trajectories. All quantities are normalized by the corresponding maximum values in the laminar flame.

behavior at essentially any point during the combustion process. Comparison of M1 and M2 results in Fig. 9 further indicates that the range of values for the time derivative increases substantially with increasing turbulence intensity, corresponding to the more rapid changes in thermochemical states observed for M2 than M1 in Figs. 7 and 8. For high T, Fig. 9 shows that thermochemical trajectories conform more closely to laminar trajectories, although non-monotonicity is still present.

Although non-monotonic thermochemical trajectories are present in both of the multi-step cases, determining the underlying causes of this phenomenon is complicated when using multi-step kinetics. For example, a decrease in temperature along a trajectory could be due to (i) thermal conduction of temperature away from a fluid parcel, (ii) molecular diffusion of species causing enthalpy transport, or (iii) endothermic reverse (or forward, if present in a given mechanism) chemical reactions. Fully separating these various effects would require consideration of the detailed balance of thermal conduction, net heat release, as well as diffusion and net production/consumption of each of the individual species present in the reaction network. Such detailed analysis in a multi-step configuration is deferred to a follow-up paper focused on combustion of hydrocarbon fuels.

In this study, we take the first step on this path. In particular, we turn to single-step simulations in order to determine whether molecular transport effects alone are capable of creating non-monotonic changes in temperature and fuel mass fraction along trajectories in high-speed turbulent reacting flows.

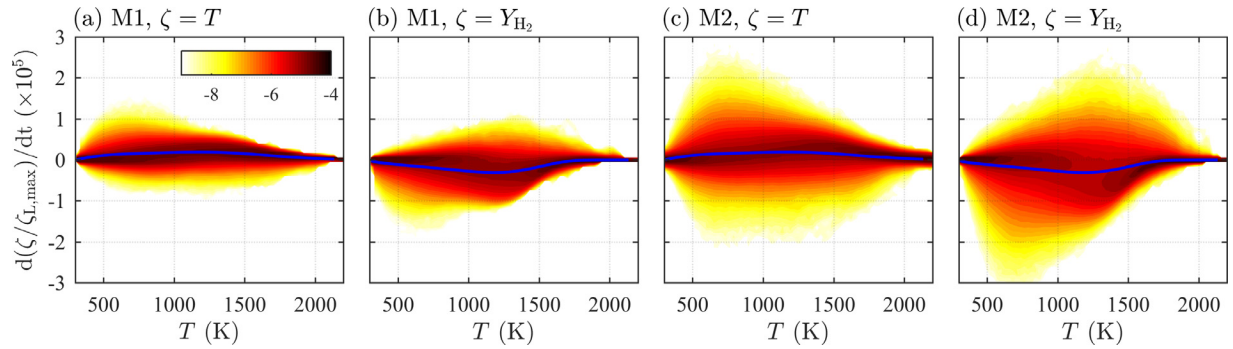


Fig. 9. Conditional probability density functions (pdfs) of the time rates of change of T (a,c) and Y_{H_2} (b,d) along Lagrangian trajectories for the M1 (a,b) and M2 (c,d) multi-step cases. The conditioning is based on the value of T along the trajectory and values of $\log_{10}\{P[\mathrm{d}(\zeta/\zeta_{L,\max})/\mathrm{dt}|T]\}$ are shown, where ζ is the quantity of interest and $\zeta_{L,\max}$ is the corresponding maximum value in a laminar flame. Solid blue lines show corresponding laminar flame values of the time derivatives as functions of T. (For interpretation of the references to color in this figure legend, the reader is referred to the web version of this article.)

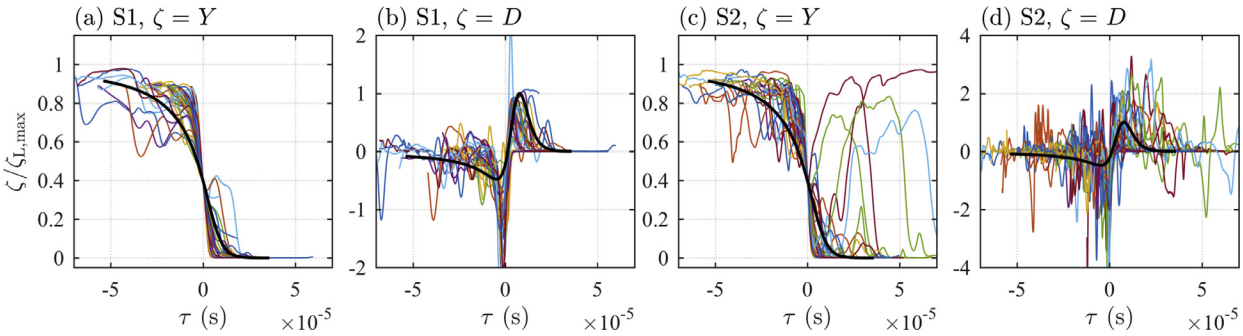


Fig. 10. Thermochemical time series for 50 representative trajectories out of 16,384 total computed trajectories, showing evolutions of the reactant mass fraction Y and the total diffusive transport D from Eq. (1) for the single-step cases S1 (a,b) and S2 (c,d). Time series are shifted such that fluid parcels first reach a temperature of $T = 1400$ K at $\tau = 0$ s, and D is normalized by its maximum value in a laminar flame. Solid black lines are the corresponding laminar flame profiles.

4.2. Origins of thermochemical complexity

Non-monotonic thermochemical trajectories are present not only in the multi-step cases, and Fig. 10 shows that substantial non-monotonicity is also observed in the evolution of the reactant mass fraction Y for the single-step cases. Note that in the case of single-step kinetics with $\mathrm{Le} = 1$, T and Y are uniquely connected as $(T - T_{\min})/(T_{\max} - T_{\min}) = 1 - Y$. Thus, here we consider only Y and its corresponding balance equation given by Eq. (1). Similar to the multi-step results shown in Fig. 7, many of the fluid parcels in the single-step cases undergo an increase in Y after reaching $T = 1400$ K. Figure 10 further shows that there are many more non-monotonic trajectories in the higher intensity case (i.e., S2), and that variations in Y become more rapid as the turbulence intensity increases.

The primary advantage of analyzing single-step cases is that the source of variability in Y along trajectories can be more easily identified than in multi-step cases. In particular, in the case of a general single-step reaction, Y can change along a trajectory either due to reactive, $\dot{w}$, or diffusive, D, effects, as shown in Eq. (1). When the reaction is irreversible, however, as in the single-step cases considered here, $\dot{w} \leq 0$ and thus any non-monotonicity can arise only due to D.

Panels (b) and (d) of Fig. 10 provide the first indications that the diffusion term D is substantially different and often much larger in turbulent flames as compared to laminar flames. Figure 11 demonstrates this point more clearly by showing representative non-monotonic thermochemical trajectories for S1 and S2, along with the corresponding evolutions of $\dot{w}$ and D from Eq. (1). In particular, panels (b) and (d) of this figure show that increases in Y are entirely associated with positive values of D, and that during periods when $\dot{w} \approx 0$, $\mathrm{d}Y/\mathrm{dt}$ virtually coincides with D. These results suggest that molecular transport is responsible for the non-monotonic behavior of Y along trajectories in the single-step cases. Figure 12 shows conditional pdfs of $\mathrm{d}Y/\mathrm{dt}$ and D for the two single-step cases. As with the multi-step cases shown in Fig. 9, more extreme values of $\mathrm{d}Y/\mathrm{dt}$ are observed in the higher intensity case S2, and there is a substantial probability of finding increases in Y for essentially any value of T. Comparison of the conditional pdfs of $\mathrm{d}Y/\mathrm{dt}$ and D in Fig. 12 also indicates that D not only causes decreases in Y, but increases as well. This is particularly evident for $T \lesssim 1000$ K (i.e., in the preheat zone where reactions are negligible), and the conditional pdfs of $\mathrm{d}Y/\mathrm{dt}$ and D are not only essentially identical but they also show non-negligible positive values. It should be noted that conditional pdfs of the reaction rate $\dot{w}$ as a function of T for the two turbulent cases (not shown here) are nearly identical to laminar results, further emphasizing the importance of the role played by D in creating non-monotonicity.

These results suggest that the complexity of thermochemical trajectories in high-speed turbulent flames, and non-monotonicity more specifically, is directly associated with molecular transport effects, either of temperature, chemical species, or (particularly in the multi-step cases) both. These transport effects result in substantial variability of temperature and chemical species mass fractions during all phases of the combustion process, and the non-monotonicity becomes more prevalent, with greater temporal rates of change, as the turbulence intensity increases. This dependence on turbulence intensity arises due to its connection with turbulent advection. That is, despite the fact that advection does not directly appear in the dynamical equations when following fluid parcel trajectories, it does still have an effect by stirring the flow. This stirring increases the magnitude of gradients in temperature, chemical species concentrations, and other quantities. As evidence of this, the joint pdfs of reactant mass fraction gradient magnitude,

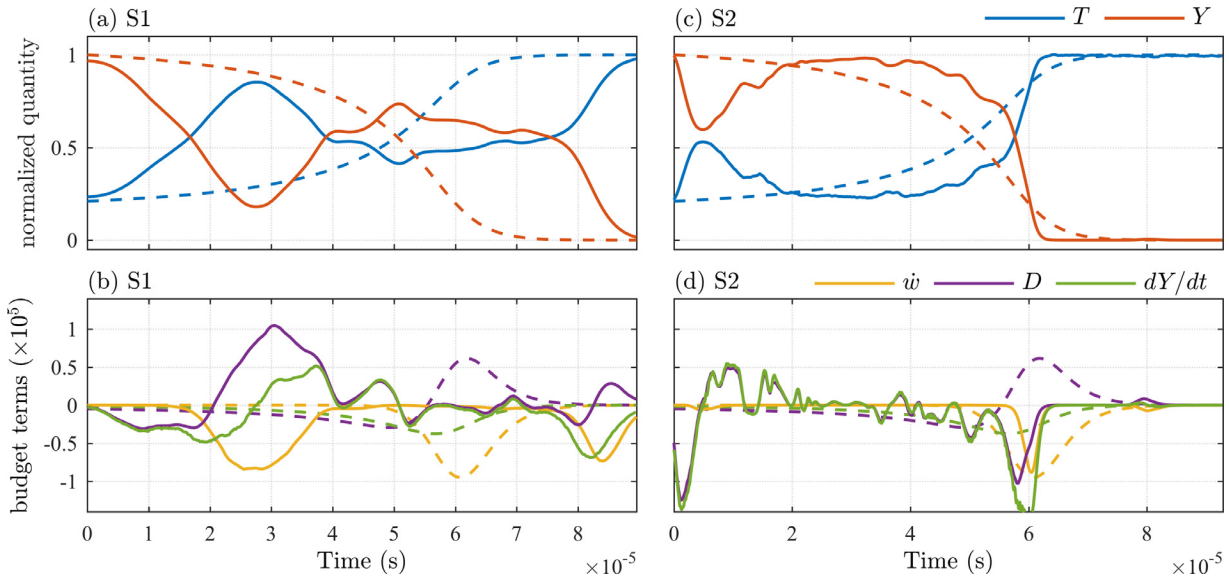


Fig. 11. Thermochemical trajectories for the S1 (a,b) and S2 (c,d) single-step cases. Shown is the evolution of Y as well as Y budget terms (see Eq. (1)). Solid lines are turbulent trajectories and dashed lines are laminar trajectories. Quantities in panels (a,c) are normalized by the corresponding maximum values in the laminar flame.

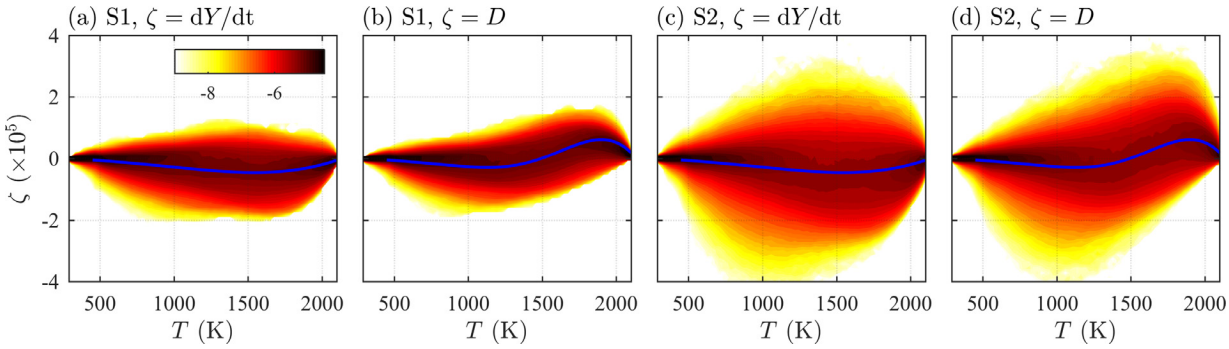


Fig. 12. Conditional probability density functions (pdfs) of the time derivative dY/dt (a,c) as well as its transport term D (b,d) in the budget equation (see Eq. (1)) for the S1 (a,b) and S2 (c,d) single-step cases. The conditioning is based on the value of T along the trajectory and values of $\log_{10}[P(\zeta\,|\,T)]$ are shown, where ζ is the quantity of interest. Solid blue lines show the corresponding laminar flame profiles.

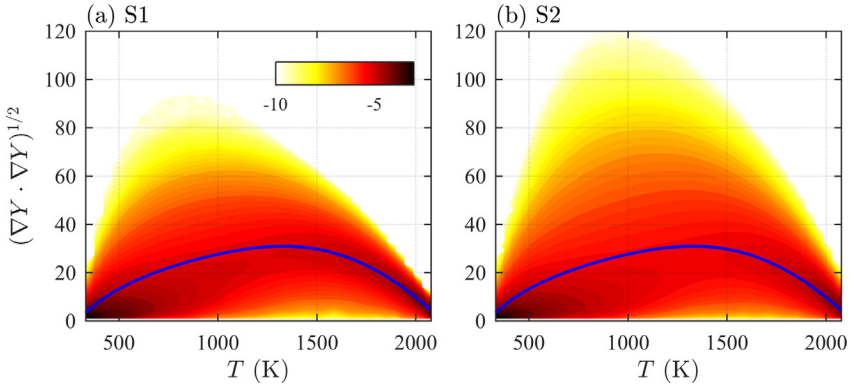


Fig. 13. Joint probability density functions (pdfs) of the reactant mass fraction gradient magnitude $(\nabla Y\cdot\nabla Y)^{1/2}$ versus temperature T for the S1 (a) and S2 (b) single-step cases. Shown is $\log_{10}\{P[(\nabla Y\cdot\nabla Y)^{1/2}, T]\}$. Solid blue lines show the corresponding laminar flame profiles. (For interpretation of the references to color in this figure legend, the reader is referred to the web version of this article.)

$(\nabla Y\cdot\nabla Y)^{1/2}$, in Fig. 13 show that for both S1 and S2, there is a significant probability of finding gradients much larger than laminar gradients at all T. Moreover, the probability of finding very large gradients increases as the turbulence intensity increases (i.e., from S1 to S2). With these increased gradients, molecular transport effects become much larger than in an unstirred laminar flame, resulting in the increased prevalence of thermochemical complexity and non-monotonicity. In short, stirring by turbulent advection creates the conditions for molecular transport effects to become dominant drivers of the flame dynamics.

With respect to the multi-step cases, it is likely that molecular transport is at least one of the factors (and possibly the only factor) responsible for non-monotonic thermochemical trajectories. In particular, Fig. 14 shows that for temperature and a range of

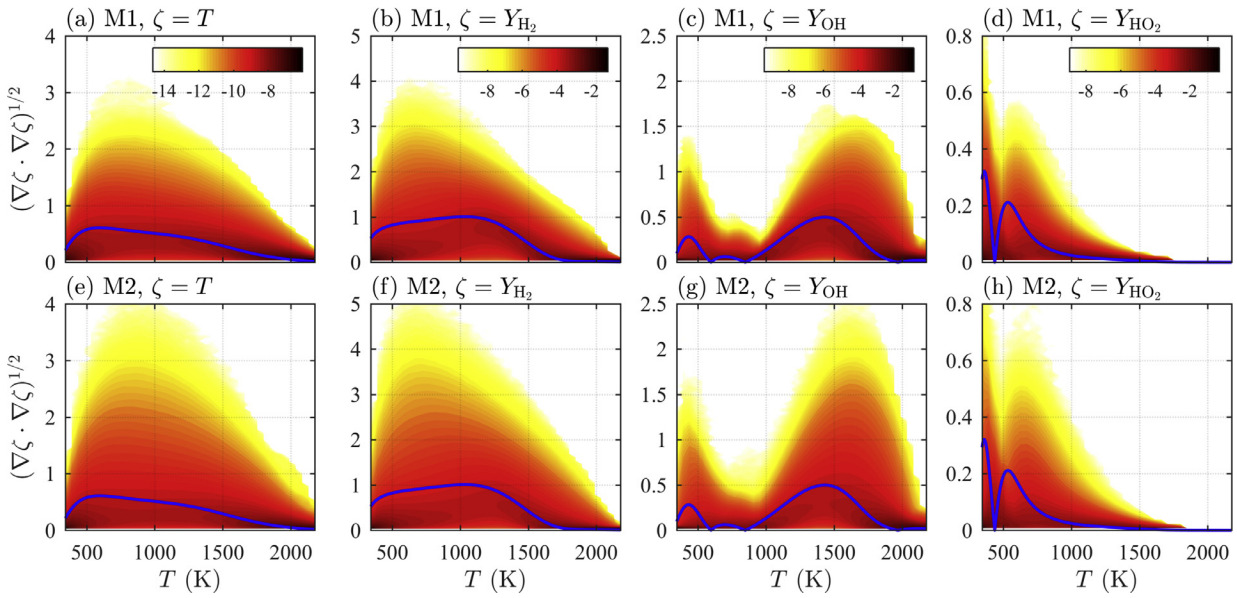


Fig. 14. Joint probability density functions (pdfs) of gradient magnitudes for T (a,e), Y_{H_2} (b,f), Y_{OH} (c,g), and Y_{HO_2} (d,h) versus temperature T for the M1 (a–d) and M2 (e–h) multi-step cases. Shown is $\log_{10}\{P[(\nabla\zeta \cdot \nabla\zeta)^{1/2}, T]\}$, where ζ is the quantity of interest. The gradient magnitudes of T in panels (a,e) are scaled by 10^5 for clarity and consistency with the other gradient magnitudes. Solid blue lines show the corresponding laminar flame profiles. (For interpretation of the references to color in this figure legend, the reader is referred to the web version of this article.)

different chemical species in the multi-step cases, turbulent advection creates substantially different (and often much larger) gradient magnitudes than in a laminar flame. Figure 14 shows that, as with the single-step cases in Fig. 13, gradient magnitudes increase with increasing turbulence intensity. These increased gradients will, in turn, be associated with increased molecular transport of temperature and chemical species. However, further work is required to definitively separate the effects of thermal conduction and diffusion of each species in these cases. Conductive and diffusive effects must also be considered in combination with flame residence times (discussed in more detail in the next section) in order to determine whether there is sufficient time for such effects to have a substantial impact on thermochemical trajectories. Furthermore, the presence of reversible reactions (or endothermic forward reactions) is an additional complicating factor in the multi-step cases.

4.3. Residence times and path lengths in H_2–air flames

Using the Lagrangian analysis, we can quantitatively determine residence times and path lengths of fluid parcels during different phases of the combustion process. In particular, we define the following residence times, τ_i, and path lengths, δ_i, along fluid parcel trajectories as

$$\begin{aligned}
\tau_1 &\equiv t(T=1000\,\mathrm{K}) - t(T=600\,\mathrm{K}), & \delta_1 &\equiv d(T=1000\,\mathrm{K}) - d(T=600\,\mathrm{K}),\\
\tau_2 &\equiv t(T=1400\,\mathrm{K}) - t(T=1000\,\mathrm{K}), & \delta_2 &\equiv d(T=1400\,\mathrm{K}) - d(T=1000\,\mathrm{K}),\\
\tau_3 &\equiv t(T=2000\,\mathrm{K}) - t(T=1400\,\mathrm{K}), & \delta_3 &\equiv d(T=2000\,\mathrm{K}) - d(T=1400\,\mathrm{K}),\\
\tau_{tot} &\equiv t(T=2000\,\mathrm{K}) - t(T=600\,\mathrm{K}), & \delta_{tot} &\equiv d(T=2000\,\mathrm{K}) - d(T=600\,\mathrm{K}),
\end{aligned}$$

where $t(T=\alpha)$ denotes the time taken for the temperature within a fluid parcel to first reach the value $T=\alpha$ and $d(T=\alpha)$ denotes the distance traveled by the parcel up to time $t(T=\alpha)$ (corresponding to the path length along the trajectory).

As defined in Eq. (7), the values of τ_i and δ_i correspond to temperature ranges related to different phases of the combustion process within a fluid parcel. For the multi-step cases considered here (see Fig. 1), temperatures $T \approx 600$ K are characterized by the formation of radicals HO_2 and H_2O_2. In particular, the peak concentration of peroxide in a laminar flame occurs at 575 K. At $T \approx 1000$ K, the net local thermal conduction flux switches from being positive (i.e., causing local heating), which is characteristic of a preheat zone, to negative (i.e., causing local cooling). The peak heat release rate occurs at $T \approx 1400$ K. Finally, temperatures $T \approx 2000$ K are associated with the peak mass fraction of OH, corresponding to the end of OH production and the onset of OH consumption, marking the gradual onset of chemical equilibrium. Both τ_{tot} and δ_{tot} are intended to represent total "flame crossing" times and distances, respectively, between $T = 600$ K and 2000 K.

Note that here, τ_i and δ_i in Eq. (7) correspond to the times and distances at which a fluid parcel *first* reaches a given temperature; as shown in earlier sections of this paper, the temperature of fluid parcels often decreases after this point, particularly for smaller values of T. However, such decreases are accounted for in the present analysis of residence times and path lengths, since a decrease in temperature after reaching a particular value of T will be reflected in subsequently larger values of τ_i and δ_i. Also, the path length measured here is the total distance traveled by a fluid parcel, as opposed to the displacement of a parcel from some reference point. Path lengths measured in this manner are expected to provide a more direct connection to advection, which can result in many changes in direction and complex trajectories.

Figure 15 shows pdfs of flame residence times τ_i for the multi-step cases. For the high turbulence intensities considered here, turbulence creates a wide range of residence times in all sub-regions of the flame with values both significantly larger and smaller than the laminar case. However, for both intensities, the majority of fluid parcel trajectories undergo combustion more quickly than in the laminar case. In particular, as the turbulence intensity increases (i.e., from M1 to M2), peaks in the residence time pdfs occur for smaller values, indicating that fluid parcels undergo increasingly rapid combustion as the turbulence intensity increases. Table 3 provides a comparison of the median residence times relative to the laminar values for each of the pdfs shown in Fig. 15 for both M1 and M2. Note that the median values are used here since the mean is a poor descriptor of the asymmetric and long-tailed pdfs shown in Fig. 15.

By contrast to the shorter residence times in the turbulent cases as compared to the laminar case, Fig. 16 shows that fluid parcels

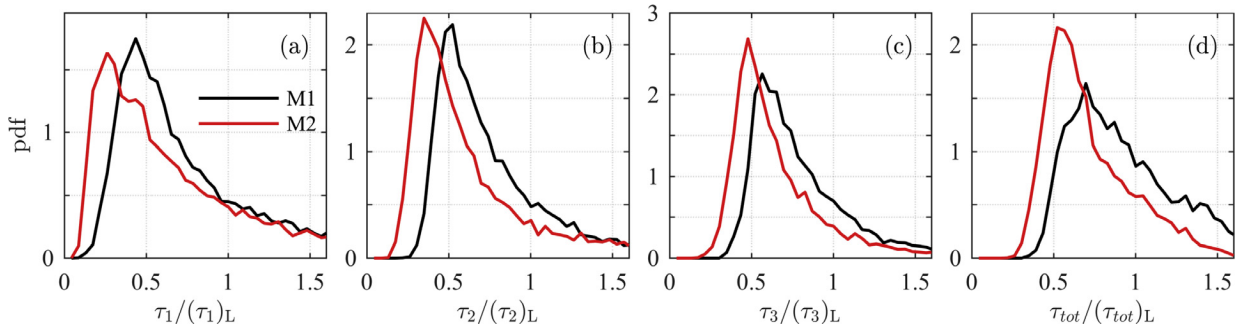


Fig. 15. Probability density functions (pdfs) of normalized fluid parcel residence times $\tau_i/(\tau_i)_L$ between $T = 600 - 1000$ K (a), $T = 1000 - 1400$ K (b), $T = 1400 - 2000$ K (c), and $T = 600 - 2000$ K (d) for multi-step cases M1 (black lines) and M2 (red lines). All times are normalized by the corresponding laminar values, $(\tau_i)_L$, with residence time ratios less than 1 indicating faster than laminar residence times, and ratios greater than 1 indicating slower than laminar times. Median values of $\tau_i/(\tau_i)_L$ for each pdf are shown in Table 3. (For interpretation of the references to color in this figure legend, the reader is referred to the web version of this article.)

Table 3
Medians of normalized residence times $\tau_i/(\tau_i)_L$, path lengths $\delta_i/(\delta_i)_L$, and time-averaged velocities $S_i/(S_i)_L$ for multi-step cases M1 and M2. Residence times τ_i and path lengths δ_i are defined in Eq. (7). The domain width turbulence intensity U_L/S_L and turbulent flame speed S_T/S_L are also shown, where S_L is the laminar flame speed. The turbulent flame speed S_T is defined based on the total reactant consumption rate and is an average over the approximate duration of the Lagrangian analysis.

	Median $\tau_i/(\tau_i)_L$				Median $\delta_i/(\delta_i)_L$				Median $S_i/(S_i)_L$					
Case	τ_1	τ_2	τ_3	τ_{tot}	δ_1	δ_2	δ_3	δ_{tot}	S_1	S_2	S_3	S_{tot}	U_L/S_L	S_T/S_L
M1	0.81	0.70	0.72	0.86	6.4	4.4	3.6	4.6	7.5	5.8	4.9	5.3	16	5.4
M2	0.62	0.54	0.57	0.65	9.7	6.3	5.5	6.9	15	11	9.2	10	32	9.8

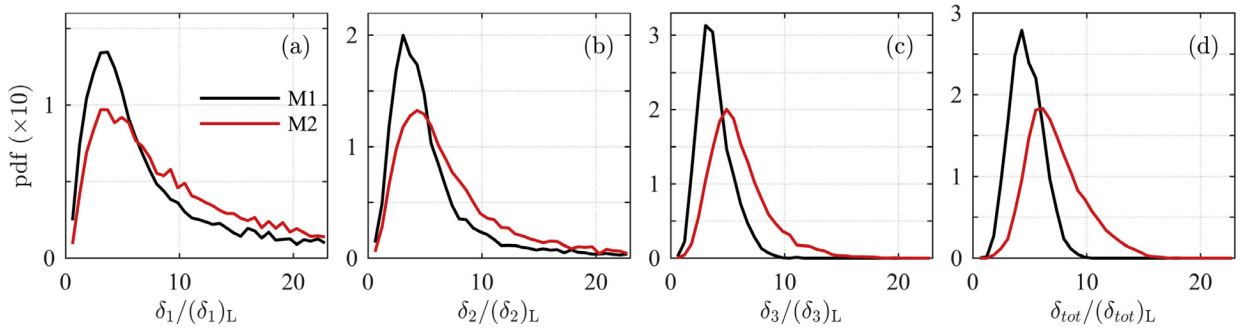


Fig. 16. Probability density functions (pdfs) of normalized fluid parcel path lengths $\delta_i/(\delta_i)_L$ between $T = 600 - 1000$ K (a), $T = 1000 - 1400$ K (b), $T = 1400 - 2000$ K (c), and $T = 600 - 2000$ K (d) for multi-step cases M1 (black lines) and M2 (red lines). All distances are normalized by the corresponding laminar values, $(\delta_i)_L$, with distance ratios less than 1 indicating shorter than laminar path lengths, and ratios greater than 1 indicating longer than laminar path lengths. Median values of $\delta_i/(\delta_i)_L$ for each pdf are shown in Table 3. (For interpretation of the references to color in this figure legend, the reader is referred to the web version of this article.)

typically travel many times further between different values of T for turbulent flames. In particular, Fig. 16 shows that there is a substantial probability of fluid parcels with path lengths more than 10 times greater than in the laminar case. There is also increased probability of large path lengths as the turbulence intensity increases (i.e., from M1 to M2). Once again, Table 3 provides a comparison of the median distances traveled for each interval shown in Fig. 16.

Taken together, these results indicate that fluid parcels have shorter residence times but travel longer distances in the turbulent cases than in the laminar cases, and that the disparity between laminar and turbulent results increases as the turbulence intensity increases (i.e., residence times decrease and path lengths increase as the turbulence intensity increases). Overall, these trends correspond to substantially greater fluid parcel speeds in turbulent flames. This can be seen by noting that the distance traveled by a fluid parcel along a trajectory between two temperatures $T = \alpha$ and $T = \beta$, with $\beta > \alpha$, is given from Eq. (4) as

$$d(T = \beta) - d(T = \alpha) = \int_{t(T=\alpha)}^{t(T=\beta)} u(\tau) d\tau \,, \tag{8}$$

where $u \equiv (u_i u_i)^{1/2}$ is the speed of the fluid parcel as a function of time along the trajectory. From this, we can define a temporally-averaged speed $\langle u \rangle_{\alpha\beta}$ between two temperatures $T = \alpha$ and $T = \beta$ as

$$\langle u \rangle_{\alpha\beta} = \frac{d(T = \beta) - d(T = \alpha)}{t(T = \beta) - t(T = \alpha)} = \frac{\delta_{\alpha\beta}}{\tau_{\alpha\beta}} \,, \tag{9}$$

where $\tau_{\alpha\beta}$ and $\delta_{\alpha\beta}$ correspond to the residence time and path length, respectively, between temperatures $T = \alpha$ and $T = \beta$. Thus, $\delta_{\alpha\beta}/\tau_{\alpha\beta}$ represents the average speed $\langle u \rangle_{\alpha\beta}$ of a fluid parcel along a given trajectory between any two temperatures $T = \alpha$ and $T = \beta$. From this and the definitions in Eq. (7), an average fluid parcel speed can therefore be defined for the temperature ranges in Eq. (7) as $S_i \equiv \delta_i/\tau_i$.

Values for $S_i/(S_i)_L$ in the present simulations [where $(S_i)_L$ denotes the corresponding average parcel speed in a laminar flame] are captured by the joint pdfs of $\delta_i/(\delta_i)_L$ versus $\tau_i/(\tau_i)_L$ shown in Fig. 17. There is a tendency towards increasing slopes of these joint pdfs as the turbulence intensity increases. From the residence time and path length for each fluid parcel, an average speed S_i can be calculated, and Table 3 provides the resulting median

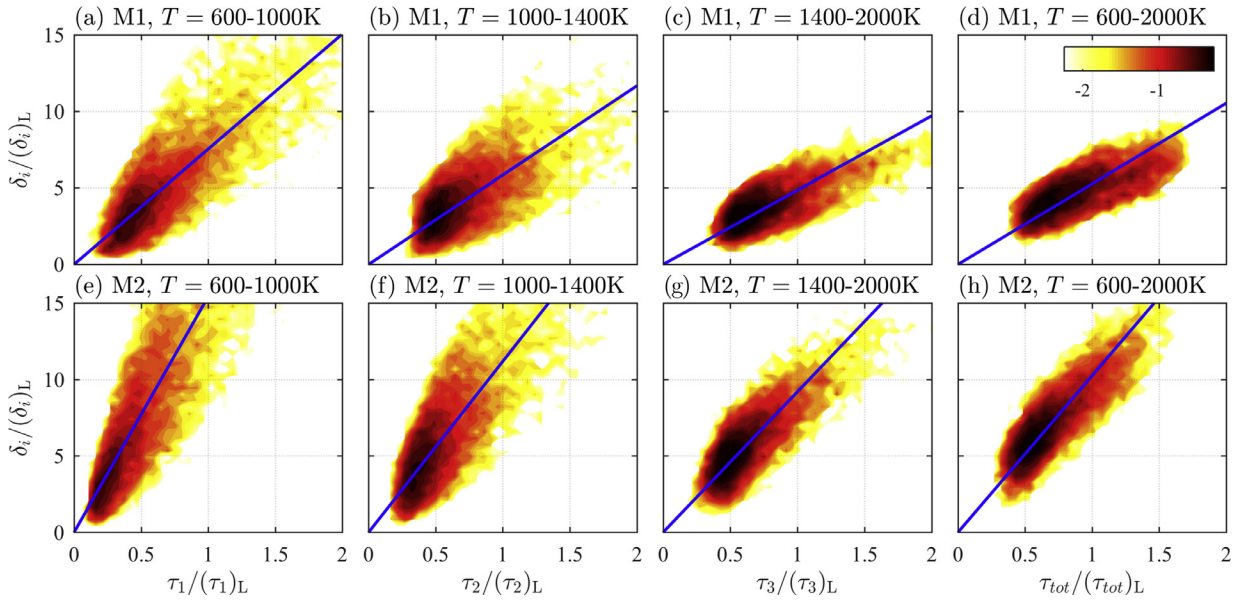


Fig. 17. Joint probability density functions (pdfs) of normalized fluid parcel path length, $\delta_i/(\delta_i)_L$, versus residence time, $\tau_i/(\tau_i)_L$, between $T = 600 - 1000$ K corresponding to τ_1 and δ_1 (a,e), $T = 1000 - 1400$ K corresponding to τ_2 and δ_2 (b,f), $T = 1400 - 2000$ K corresponding to τ_3 and δ_3 (c,g), and $T = 600 - 2000$ K corresponding to τ_{tot} and δ_{tot} (d,h) for the M1 (a–d) and M2 (e–h) multi-step cases. Here $(\delta_i)_L$ and $(\tau_i)_L$ denote laminar flame values and definitions for each interval are also provided in Eq. (7). Solid blues lines in each panel have slopes equal to the median values of $S_i/(S_i)_L$ from Table 3, where $S_i \equiv \delta_i/\tau_i$. The logarithm of the joint pdf, $\log_{10}\{P[\tau_i/(\tau_i)_L, \delta_i/(\delta_i)_L]\}$, is shown in each panel, and a colorbar for all panels is shown in (d).

values of $S_i/(S_i)_L$ for each of the intervals considered here. From M1 to M2, the average parcel speed in each case approximately doubles, corresponding to the factor of two increase in turbulence intensity (i.e., U/S_L) between these two cases. The median speeds are shown as sloped lines in Fig. 17 and there is good agreement between these lines and the angles made by the joint pdfs.

Of additional interest is the connection between average fluid parcel speeds S_i and the turbulent burning velocity S_T. There is reason to think that such a connection may exist, particularly between S_T and S_{tot}, where the latter gives the average speed during essentially the complete combustion process from $T = 600$ K to $T = 2000$ K. Similar to common definitions of S_T/S_L [1], median values of $S_{tot}/(S_{tot})_L$ in Table 3 represent aggregated speeds of all fluid parcels in the flame brush which, when multiplied by appropriate densities along each trajectory, give global mass flow rates. Table 3 shows that the median values of $S_{tot}/(S_{tot})_L$ and the computed turbulent flame speeds S_T/S_L are in good agreement for both intensities (i.e., for M1 and M2). The connection between fluid parcel speeds and the turbulent burning velocity was also noted by Pagnini and Bonomi [39] and Osborne et al. [21], and the present results provide additional support for this observation. However, further examination of the relationship between S_{tot} and S_T requires analysis of additional values of U/S_L, as well as a more rigorous theoretical justification. Exploration of this connection, as well as its implications for turbulent flame speed relations in terms of flame surface area, is left as an important direction for future research.

5. Summary and conclusions

A Lagrangian analysis approach has been used to examine properties of thermochemical trajectories in DNS data of high-speed stoichiometric H_2–air premixed flames at two different turbulence intensities for both multi- and single-step chemical kinetics. Such high-speed turbulence is found to substantially alter the evolutions of chemical composition and temperature within individual fluid parcels as they undergo combustion. In particular, fuel mass fractions and temperature often vary non-monotonically during the combustion process, with frequent decreases in temperature and increases in fuel mass fraction after combustion has begun. Moreover, the prevalence of non-monotonicity, as well as the rate at which temperature and species mass fractions change, both increase with increasing turbulence intensity.

Using single-step simulations, non-monotonic thermochemical trajectories were shown to be caused by enhanced molecular transport resulting from the creation of large gradients in temperature and species mass fractions by turbulent advection. The role of turbulence in creating this complexity casts serious doubt on the applicability of laminar flamelet models in high-speed turbulent premixed flames, since the evolution of temperature and chemical species are markedly different than the laminar case. There are reasons to expect, however, that flamelet models may be more applicable at lower intensities, particularly given the less complex thermochemical trajectories observed by Day et al. [19,22] in low swirl burners. It should be noted that, despite many quantitative differences, there were no significant qualitative differences between multi- and single-step results in the present analysis. In particular, non-monotonic trajectories were observed for all cases.

Fluid parcel residence times and path lengths between different temperature values were found to be substantially altered by the presence of high-speed turbulence. In particular, residence times were up to 40% shorter than laminar residence times for the highest intensity case, consistent with the findings by Osborne et al. [21], and distances traveled were up to 10 times longer. Together, these results imply substantially greater fluid parcel speeds in the turbulent flame cases, and average speeds during the combustion process were empirically determined to closely match the turbulent burning rate S_T/S_L. For more complex hydrocarbon fuels, reduced residence times in highly turbulent flames may result in insufficient time for fuel pyrolysis, thereby impacting the progress of the overall combustion process; examining this possibility is an important direction for future research.

The Lagrangian analysis approach outlined here can be extended in many different directions. Further research is required to examine thermochemical trajectories in hydrocarbon flames and to separate the effects of multi-species diffusion, thermal conduction,

and endothermic reactions in creating non-monotonic trajectories, as well as to examine the effects of non-unity Lewis numbers. The cases examined here all had relatively high Karlovitz numbers, and it would be of value in the future to characterize the prevalence of non-monotonicity and thermochemical complexity for lower intensity cases, particularly with respect to understanding the range of applicability of laminar flamelet models. The Lagrangian analysis also provides a unique way to study turbulent flow structure in premixed reacting flows. For instance, the changing contributions of physical effects such as dilatation, baroclinic torque, and strain-rate production on the vorticity can be examined as fluid parcels pass through the flame. Finally, the present results suggest a connection between the average speed of fluid parcels during different phases of combustion and the turbulent flame speed, and this connection deserves further consideration in the future.

Acknowledgments

PEH, CAB, and CAZT were supported in part by AFOSR awards FA9550-14-1-0273 and FA9550-17-1-0144, and by the Department of Defense (DoD) High Performance Computing Modernization Program (HPCMP) under a Frontier Project award. RD was supported by a National Defense Science and Engineering Graduate (NDSEG) Fellowship. AYP was supported in part by AFOSR award F4FGA06055G001. Computing resources were provided by the DoD HPCMP under the Frontier project award.

References

[1] N. Peters, Turbulent combustion, Cambridge University Press, 2000.
[2] A.Y. Poludnenko, E.S. Oran, The interaction of high-speed turbulence with flames: Global properties and internal flame structure, Combust. Flame 157 (5) (2010) 995–1011.
[3] P.E. Hamlington, A.Y. Poludnenko, E.S. Oran, Interactions between turbulence and flames in premixed reacting flows, Phys. Fluids 23 (12) (2011) 125111.
[4] P.E. Hamlington, A.Y. Poludnenko, E.S. Oran, Intermittency in premixed turbulent reacting flows, Phys. Fluids 24 (7) (2012) 075111.
[5] N. Swaminathan, R.W. Grout, Interaction of turbulence and scalar fields in premixed flames, Phys. Fluids 18 (4) (2006) 045102.
[6] S.-H. Kim, H. Pitsch, Scalar gradient and small-scale structure in turbulent premixed combustion, Phys. Fluids 19 (11) (2007) 115104.
[7] E.R. Hawkes, R. Sankaran, J.C. Sutherland, J.H. Chen, Scalar mixing in direct numerical simulations of temporally evolving plane jet flames with skeletal CO/H2 kinetics, Proc. Comb. Inst. 31 (1) (2007) 1633–1640.
[8] N. Chakraborty, N. Swaminathan, Influence of the Damköhler number on turbulence-scalar interaction in premixed flames. I. Physical insight, Phys. Fluids 19 (4) (2007) 045103.
[9] A.Y. Poludnenko, Pulsating instability and self-acceleration of fast turbulent flames, Phys. Fluids 27 (1) (2015) 014106.
[10] C.A.Z. Towery, A.Y. Poludnenko, J. Urzay, J. O'Brien, M. Ihme, P.E. Hamlington, Spectral kinetic energy transfer in turbulent premixed reacting flows, Phys. Rev. E 93 (5) (2016) 053115.
[11] P.K. Yeung, Lagrangian characteristics of turbulence and scalar transport in direct numerical simulations, J. Fluid Mech 427 (2001) 241–274.
[12] K.D. Squires, J.K. Eaton, Lagrangian and Eulerian statistics obtained from direct numerical simulations of homogeneous turbulence, Phys. Fluids A 3 (1) (1991) 130–143.
[13] Y. Kimura, J.R. Herring, Diffusion in stably stratified turbulence, J. Fluid Mech. 328 (1996) 253–269.
[14] J. Schumacher, M.S. Emran, Lagrangian analysis of turbulent convection, Advances in Turbulence XII, 132 (2009), pp. 15–18.
[15] P.K. Yeung, Lagrangian investigations of turbulence, Ann. Rev. Fluid Mech. 34 (1) (2002) 115–142.
[16] F. Toschi, E. Bodenschatz, Lagrangian properties of particles in turbulence, Ann. Rev. Fluid Mech. 41 (2009) 375–404.
[17] P.K. Yeung, S.B. Pope, An algorithm for tracking fluid particles in numerical simulations of homogeneous turbulence, J. Comput. Phys 79 (2) (1988) 373–416.
[18] H. Yu, K. Kanov, E. Perlman, J. Graham, E. Frederix, R. Burns, A. Szalay, G. Eyink, C. Meneveau, Studying Lagrangian dynamics of turbulence using on-demand fluid particle tracking in a public turbulence database, J. Turb. 13 (2012) N12.
[19] M. Day, S. Tachibana, J.B. Bell, M. Lijewski, V. Beckner, R.K. Cheng, A combined computational and experimental characterization of lean premixed turbulent low swirl laboratory flames: I. Methane flames, Combust. Flame 159 (1) (2012) 275–290.
[20] A.M. Steinberg, B. Coriton, J.H. Frank, Influence of combustion on principal strain-rate transport in turbulent premixed flames, Proc. Combust. Inst. 35 (2) (2015) 1287–1294.
[21] J.R. Osborne, S.A. Ramji, C.D. Carter, A.M. Steinberg, Relationship between local reaction rate and flame structure in turbulent premixed flames from simultaneous 10 khz TPIV, OH PLIF, and CH2O PLIF, Proc. Combust. Inst. 36 (2) (2017) 1835–1841.
[22] M. Day, S. Tachibana, J. Bell, M. Lijewski, V. Beckner, R.K. Cheng, A combined computational and experimental characterization of lean premixed turbulent low swirl laboratory flames: II. Hydrogen flames, Combust. Flame 162 (5) (2015) 2148–2165.
[23] H.A. Uranakara, S. Chaudhuri, H.L. Dave, P.G. Arias, H.G. Im, A flame particle tracking analysis of turbulence-chemistry interaction in hydrogen–air premixed flames, Combust. Flame 163 (2016) 220–240.
[24] J.M. Stone, T.A. Gardiner, P. Teuben, J.F. Hawley, J.B. Simon, Athena: a new code for astrophysical MHD, Astrophys. J. Supp. 178 (1) (2008) 137.
[25] A.Y. Poludnenko, T.A. Gardiner, E.S. Oran, Spontaneous transition of turbulent flames to detonations in unconfined media, Phys. Rev. Lett. 107 (5) (2011) 054501.
[26] T.A. Gardiner, J.M. Stone, An unsplit Godunov method for ideal MHD via constrained transport in three dimensions, J. Comput. Phys. 227 (8) (2008) 4123–4141.
[27] A.L. Sánchez, F.A. Williams, Recent advances in understanding of flammability characteristics of hydrogen, Prog. Energy Combust. Sci. 41 (2014) 1–55.
[28] B.J. McBride, S. Gordon, M.A. Reno, Coefficients for calculating thermodynamic and transport properties of individual species, NASA Technical Memorandum No. 4513, NASA, 1993.
[29] R.J. Kee, G. Dixon-Lewis, J. Warnatz, M.E. Coltrin, J.A. Miller, A Fortran computer code package for the evaluation of gas-phase multicomponent transport properties, Report No. SAND86-8246, 13, Sandia National Laboratories (1986), pp. 80401–81887.
[30] A. Ern, V. Giovangigli, Multicomponent transport algorithms, 24, Springer Science & Business Media, 1994.
[31] J.O. Hirschfelder, C.F. Curtiss, R.B. Bird, Molecular theory of liquids and gases, Wiley-Interscience, 1964.
[32] J. Warnatz, Numerical methods in flame propagation, Vieweg and Sohn, Wiesbaden, 1982.
[33] Z. Chen, M.P. Burke, Y. Ju, Effects of Lewis number and ignition energy on the determination of laminar flame speed using propagating spherical flames, Proc. Combust. Inst. 32 (2009) 1253–1260.
[34] V.N. Gamezo, T. Ogawa, E.S. Oran, Flame acceleration and DDT in channels with obstacles: effect of obstacle spacing, Combust. Flame 155 (1) (2008) 302–315.
[35] J. O'Brien, C.A.Z. Towery, P.E. Hamlington, M. Ihme, A.Y. Poludnenko, J. Urzay, The cross-scale physical-space transfer of kinetic energy in turbulent premixed flames, Proc. Combust. Inst. 36 (2) (2017) 1967–1975.
[36] R. Darragh, C.A.Z. Towery, P.E. Hamlington, A.Y. Poludnenko, Development of a Lagrangian fluid parcel tracking algorithm for reacting flows, AIAA Pap. (2017) 2017–3466.
[37] E. Fehlberg, Low-order classical Runge–Kutta formulas with stepsize control and their application to some heat transfer problems, NASA Technical Report No. r-315, NASA, Washington, DC, 1969.
[38] A.J. Aspden, M.S. Day, J.B. Bell, Turbulence-flame interactions in lean premixed hydrogen: transition to the distributed burning regime, J. Fluid Mech. 680 (2011) 287–320.
[39] G. Pagnini, E. Bonomi, Lagrangian Formulation of Turbulent Premixed Combustion, Phys. Rev. Lett. 107 (2011) 044503.

Combustion and Flame 213 (2020) 172–183

Contents lists available at ScienceDirect

Combustion and Flame

journal homepage: www.elsevier.com/locate/combustflame

Detonation initiation by compressible turbulence thermodynamic fluctuations

Colin A.Z. Towery[a,a,*], Alexei Y. Poludnenko[b], Peter E. Hamlington[a]

[a] Department of Mechanical Engineering, University of Colorado Boulder, UCB 427, 1111 Engineering Drive, Boulder, CO 80309, USA
[b] Department of Aerospace Engineering, Texas A&M University, College Station, TX 77843, USA

ARTICLE INFO

Article history:
Received 19 June 2019
Revised 14 November 2019
Accepted 14 November 2019
Available online 7 December 2019

Keywords:
Compressible turbulence
Premixed autoignition
Detonation initiation

ABSTRACT

Theory and computations have established that thermodynamic gradients created by hot spots in reactive gas mixtures can lead to spontaneous detonation initiation. However, the current laminar theory of the temperature-gradient mechanism for detonation initiation is restricted to idealized physical configurations. Thus, it only predicts conditions for the onset of detonations in quiescent gases, where an isolated hot spot is formed on a timescale shorter than the chemical and acoustic timescales of the gas. In this work, we extend the laminar temperature-gradient mechanism into a statistical model for predicting the detonability of an autoignitive gas experiencing compressible isotropic turbulence fluctuations. Compressible turbulence forms non-monotonic temperature fields with tightly-spaced local minima and maxima that evolve over a range of timescales, including those much larger than chemical and acoustic timescales. We examine the utility of the adapted statistical model through direct numerical simulations of compressible isotropic turbulence in premixed hydrogen-air reactants for a range of conditions. We find strong, but not conclusive, evidence that the model can predict the degree of detonability in an autoignitive gas due to turbulence-induced thermodynamic gradients.

© 2019 The Combustion Institute. Published by Elsevier Inc. All rights reserved.

1. Introduction

Turbulence compressibility, autoignitive combustion, nonlinear interactions between turbulence and chemistry, and transitions to detonation are all fundamental aspects of many different high-speed reacting flows, from human-scale engineered flows such as supersonic combustion ramjet engines (scramjets) [1] to astrophysical flows such as Type 1a supernovae [2]. It is now well-established that thermodynamic gradients within localized *hot spots* (also termed *exothermic centers*) can lead to the direct initiation of detonations in auto-igniting gas mixtures [3–6]. It is also established that nonlinear turbulence-chemistry interactions alone can induce deflagration-to-detonation transition (DDT) in high-speed turbulent flames. This can occur via the same localized mechanism of hot-spot autoignition [7,8], where the necessary thermodynamic gradient is created by the turbulent flame rather than an external source. Alternatively, DDT can be induced through a self-reinforcing amplification of an initial large-scale pressure wave generated during a self-acceleration event of an unsteady turbulent flame propagating with a speed above that of a Chapman-Jouguet (CJ) deflagration [9,10]. All three mechanisms — autoignitive hot-spot initiation, local hot-spot DDT, and turbulence-driven DDT in super-CJ flames — rely, at least in part, on a thermomechanical feedback loop between chemical heat release and pressure in order to amplify an acoustic wave into a detonation wave. This unsteady feedback loop is described in detail for the particular case of sub-detonable shock waves, termed *shock wave amplification by coherent energy release*, or SWACER, in Lee et al. [4]. Qualitatively, the critical difference between the detonation mechanisms is the source that initiates and drives the feedback mechanism: autoignition or turbulent deflagration.

In autoignitive gaseous flows, spatial gradients in temperature, pressure, and species mixture fractions produce spatial gradients in the chemical ignition delay time, denoted t_{ign}. As long as advective and diffusive processes operating on the temperature and species gradients are slow compared to the range of ignition delay times present [7], a monotonic gradient will form a *spontaneous* reaction front that propagates with a speed equal to the inverse of the local ignition delay time gradient magnitude, namely $u_{\mathrm{sp}} = |\nabla t_{\mathrm{ign}}|^{-1}$.

Neglecting any thermomechanical response of the gas to initial conditions or subsequent heat release, an isolated hot spot with a constant u_{sp} as the initial condition will form either a subsonic or supersonic spontaneous ignition wave that will transition to a conventional deflagration or detonation wave within specific regimes of the spontaneous wave-speed. These four propagation

* Corresponding author.
E-mail address: colin.towery@colorado.edu (C.A.Z. Towery).

https://doi.org/10.1016/j.combustflame.2019.11.025
0010-2180/© 2019 The Combustion Institute. Published by Elsevier Inc. All rights reserved.

regimes are delineated by the magnitude of u_{sp} with respect to the local CJ detonation speed, D_{CJ}, the upstream speed of sound, a, and the laminar deflagration speed, S_L [5]. Only in the case where $a < u_{sp} < D_{CJ}$ will the spontaneous ignition wave formed from initial conditions transition to a detonation wave.

When the thermomechanical response of the gas to both the initial conditions and heat release are taken into account, a far larger range of u_{sp} can transition to a detonation wave than would be expected from an analysis of the initial conditions alone [4,7,11]. Most notably, when $S_L < u_{sp} < a$, a spontaneous subsonic ignition wave would be predicted to form and propagate through the hot spot without transitioning to another regime [5]. However, the thermomechanical response of the surrounding gas to the initial creation of the hot spot will form an acoustic wave, independent of the ignition wave [4,11]. Due to the monotonically-decreasing speed of sound, the downstream pressure increase due to heat release from the subsonic ignition wave will propagate upstream faster than the leading acoustic wave, allowing the trailing subsonic ignition wave to amplify the leading acoustic wave. In turn, the ignition-delay-time gradient between the acoustic and ignition waves will be smaller than in the initial conditions, and therefore the ignition wave will accelerate towards the acoustic wave. Consequently, the heat release rate will increase within the reaction zone of the wave. This process is self-reinforcing, in the same manner as the SWACER feedback mechanism [4], and will eventually accelerate the ignition wave to supersonic speeds. At this point, the ignition wave will overtake and coalesce with the leading acoustic wave and transition to a detonation wave. This broader temperature-gradient-based mechanism for the direct initiation of detonation waves has been extensively validated from both an analytical perspective, through asymptotic analysis and reduced order models, and from a numerical perspective, through one- and two-dimensional (1D and 2D, respectively) numerical simulations of simplified hot spot configurations. The reader is directed to Refs. [12,13] for comprehensive reviews of the foundational literature.

Both Khokhlov [7] and Bradley [6] numerically studied the thermomechanical response of 1D hot spots to chemical heat release in order to discern the critical range of hot-spot radii and temperature-gradient magnitudes that lead to detonation initiation. In addition to the ratio a/u_{sp}, these studies determined that detonation initiation also depends on the ratio of the characteristic time scale of exothermic heat release, t_{exo}, within the hot spot to the acoustic residence time of the hot spot, r_0/a, where r_0 is the initial radius prior to thermomechanical relaxation. The importance of this *acoustic-exothermicity coupling* was expanded upon in subsequent studies [14–18], establishing that the detonability of an isolated hot spot can be characterized by two non-dimensional parameters, given as

$$\xi = \frac{a}{u_{sp}} = a|\nabla t_{ign}| \approx a t_{ign} \frac{T_a}{T^2} |\nabla T|_{hs} , \tag{1}$$

$$\zeta = \frac{r_0}{a t_{exo}} , \tag{2}$$

where T is the temperature, $T_a = \mathrm{d}(\ln t_{ign})/\mathrm{d}(1/T)$ is the effective activation temperature of the chemistry, $|\nabla T|_{hs}$ is the average or constant temperature gradient of the hot spot, and t_{ign}, t_{exo}, T, and T_a are each evaluated from the initial conditions at the radial midpoint, $r_0/2$. It should be noted that no assumptions have been made about the explosive or autoignition limits of the reactant mixture in deriving ξ and ζ. The only assumptions are that the two chemical timescales, t_{ign} and t_{exo}, are quantifiable, or alternatively that $|\nabla t_{ign}|$ is well approximated by $t_{ign} T_a |\nabla T|_{hs}/T^2$.

As described by Gu et al. [14], the acoustic-exothermicity coupling, ζ, predicts the detonability of the hot spot according to the following criteria:

- If $\zeta \gg 1$, then the spontaneous ignition wave will form much faster than an acoustic wave can exit the hot spot, and the two waves will coalesce and transition into a fully-developed detonation wave before both waves exit the region of negative speed-of-sound gradient in the hot spot that enables the self-reinforcing thermomechanical coupling between the waves.
- If $\zeta \approx 1$, then the ignition wave will form in the same time that the acoustic wave will have crossed the initial hot spot radius, and whether a detonation wave forms will be strongly dependent on the value of ξ, because the continuous thermomechanical relaxation of the hot spot *may* continue to decelerate the acoustic wave long enough to allow for the self-reinforcing thermomechanical coupling to bring the two waves together.
- If $\zeta \ll 1$, then the ignition wave will not form before the acoustic wave has left the hot spot and ceased to decelerate, and none of the heat release within the ignition wave will be capable of amplifying the acoustic wave in a self-reinforcing manner.

In accordance with these criteria, the *acoustic-induction coupling*, ξ, has upper and lower detonability limits that correspond to a/S_L and a/D_{CJ} in the asymptotic limit $\zeta \gg 1$, whereas at $\zeta \approx 1$, the upper and lower detonability limits contract to a single point, typically in the range $2 < \xi < 7$, forming a "detonation peninsula" within the $\zeta - \xi$ parameter space [18].

The temperature-gradient mechanism of detonation initiation is, however, limited to the prediction of detonations in localized and isolated hot spots that are formed on timescales shorter than, or comparable to, chemical and acoustic timescales. In the case of highly turbulent autoignitive flows, by contrast, turbulence compressibility can generate non-monotonic temperature fields with tightly-spaced minima and maxima that vary over a wide range of length and time scales, including those much larger than chemical and acoustic length and time scales. As such, there is currently no *predictive* model for the initiation of detonations by compressible turbulence fluctuations in an autoignitive flow. Therefore, in this work, we adapt these governing non-dimensional parameters of the laminar temperature-gradient mechanism into a statistical model for the *a priori* prediction of spontaneous detonation initiation by thermodynamic gradients formed from flow-field fluctuations in compressible homogeneous isotropic turbulence (HIT). We then use three-dimensional (3D) direct numerical simulations (DNS) of compressible HIT in premixed hydrogen-air reactants over a small — but critical — range of conditions to examine the utility of the adapted statistical model for predicting compressible turbulence detonability.

The present focus on autoignitive HIT is motivated by prior studies of velocity and thermodynamic fluctuations in both non-reacting and reacting turbulent flows. For non-reacting equilibrium turbulent flows at very high Reynolds numbers, it is widely hypothesized that the smallest scales behave in a universal manner independent of any particular large-scale flow geometry, and, as a consequence, the turbulent fluctuations must be statistically homogeneous and isotropic [19–21]. In this context, the interactions of HIT with chemistry can be viewed as a model problem that approximates, on a statistical basis, the dynamics of high-pass-filtered turbulent fluctuations in a material volume of reacting fluid advecting with the bulk flow of any sufficiently high Reynolds number combustion process that has the same initial reactant and final product states [22–25]. Similarly, the effect of compressible HIT thermodynamic fluctuations on autoignition can be isolated from the effect of turbulent fluctuations in reactant mixture fractions by analyzing fully premixed reactants. In this case, the assumptions of small-scale homogeneity and premixed reactants allow for highly detailed analyses of turbulence-chemistry interactions, including multi-scale and cross-scale interactions [10,26–30].

The present work draws upon previous 2D DNS studies of superimposed temperature and turbulent kinetic energy fluctuations at conditions relevant to homogeneous charge compression ignition engines to study the importance of turbulent mixing and diffusive timescales on the development of reaction fronts [31–35], and the dynamical impact of chain-branching-regulated chemical kinetics, including negative-temperature-coefficient behavior, compared to the thermally-regulated one-step Arrhenius chemistry models [36,37]. Additionally, Yu and Bai [38] compared saddle-shaped and spherically-curved reaction fronts, as well as the effects of 3D turbulence on autoignition, in what may be the only computational study to date that utilizes 3D DNS with detailed chemistry to focus exclusively on premixed autoignition waves. Furthermore, the present work draws upon previous studies of 3D compressible HIT, particularly 3D DNS studies of compressible turbulence thermodynamics [39–41]. However, no previous study has performed DNS of turbulent premixed autoignition where the controlling temperature gradients were a direct result of compressible turbulence fluctuations. This intrinsic, turbulence-induced mechanism of detonation initiation is the primary focus of the present study.

This paper is organized as follows. First, we extend the dimensional analysis for detonation initiation in isolated hot spots to turbulence-induced thermodynamic fluctuations in compressible mixtures. Next, we describe details of the numerical simulation algorithms and procedures. This is followed by a detailed analysis of the results, with conclusions presented at the end.

2. A predictive statistical model for turbulence detonability

In a turbulent autoignitive flow, turbulence compressibility generates spatial and temporal variations in temperature that evolve over timescales both smaller and potentially much larger than chemical and acoustic timescales. This would seem to violate much of the theoretical basis for the temperature-gradient mechanism of detonation initiation in quiescent gases with isolated hot spots, outlined in the previous section. However, due to the statistically-predictable structure and scale of turbulence fluctuations, we can characterize and predict, *a priori*, the global system detonability of the auto-igniting gas using suitable spatial averages of the thermodynamic fluctuations as arguments in a dimensional analysis of the system detonability. This is carried out by replacing the laminar hot-spot temperature, temperature gradient, and radius in Eqs. (1) and (2) with the mass-average temperature, mass-weighted root-mean-square (rms) temperature gradient, and a temperature-field equivalent to the Taylor length scale, respectively. These substitutions yield new turbulence-based expressions for ξ and ζ, denoted ξ_t and ζ_t, given as

$$\xi_t = a_{\rm rms}\tau_{\rm ign}\frac{T_a}{\{T\}^2}|\nabla T|_{\rm rms}\,, \tag{3}$$

$$\zeta_t = \frac{2\lambda_T}{a_{\rm rms}\tau_{\rm exo}} = \frac{2T'}{a_{\rm rms}\tau_{\rm exo}|\nabla T|_{\rm rms}}\,, \tag{4}$$

where $\{\cdot\} = \langle\rho\cdot\rangle/\langle\rho\rangle$ denotes a mass-weighted spatial average, $\langle\,\cdot\,\rangle$ denotes a volume-weighted spatial average, $a^2_{\rm rms} = \{\gamma P/\rho\}$ is the rms speed of sound, $\lambda_T = T'/|\nabla T|_{\rm rms}$ is the temperature-field Taylor scale, ρ is the density, and P is the pressure. The standard deviation of the temperature fluctuations, T', and the rms temperature gradient, $|\nabla T|_{\rm rms}$, are

$$T' = \left\{(T-\{T\})^2\right\}^{1/2}, \tag{5}$$

$$|\nabla T|_{\rm rms} = \left\{\frac{\partial T}{\partial x_j}\frac{\partial T}{\partial x_j}\right\}^{1/2}. \tag{6}$$

In deriving ζ_t, we assumed that a linearized approximation of an effective "rms hot spot" has a radius $r_0 = 2\lambda_T$ and varies from a maximum temperature of $\{T\}+T'$ at its center down to $\{T\}-T'$ in the surrounding cold gas, giving a piecewise-constant temperature gradient magnitude of $|\nabla T|_{\rm rms}$. Similarly, ξ_t represents an effective "rms spontaneous velocity" for the entire simulation domain. Each thermodynamic moment (i.e., mean, and rms or standard deviation) is assumed to be computed for the turbulent flow field at the initiation of reactions in the simulation (see Section 3, below), while the characteristic ignition delay time, $\tau_{\rm ign}$, exothermicity time, $\tau_{\rm exo}$, and effective activation temperature, T_a, are computed for a homogeneous constant volume reaction with initial conditions $\langle P\rangle$ and $\{T\}$.

Although it is possible to compute rms values for ζ and ξ directly from a simulation, *a posteriori*, or even obtain complete probability distribution functions as a function of time within the unreacted regions of the domain, such a diagnostic approach to assessing turbulence detonability cannot provide the basis for an *a priori* predictive model. By formulating the single characteristic values ξ_t and ζ_t as functions solely of the initial thermodynamic conditions, dimensional analysis of inert compressible HIT can be used to compute *a priori* estimates of T' and $|\nabla T|_{\rm rms}$ for any given simulation conditions, as outlined in Section 3.3.

It is also possible to use only volume-weighted statistics to derive ξ_t and ζ_t, which could simplify comparisons to experimental investigations. In fact, at low Ma_t, the mass-weighted and volume-weighted averages deviate only slightly. However, the disagreement between the two averages increases significantly with Ma_t, as reported in Jagannathan and Donzis [41]. More importantly, the use of a mass-average for temperature statistics is the natural result of solving a conservative formulation of the reacting flow equations for an ideal gas, given in Section 3.1. In particular, if one knows the volume-averaged pressure and density in either a computational simulation or experimental apparatus, and the mixture-averaged molecular weight is uniform in space (i.e., the gases are fully premixed but unreacted), then $\{T\} = \langle P\rangle/(\langle\rho\rangle R)$ is easily obtained. Due to this algebraic consistency in both the governing differential equations and the ideal gas law, the mass-average temperature is preferred to the volume-average temperature as an input to a computational model for compressible turbulence where Ma_t is a free parameter.

We hypothesize that the degree of detonability of temperature fluctuations induced by compressible turbulence can be reliably predicted by comparing ζ_t to unity within some empirical upper and lower bounds of ξ_t, as with laminar hot spots (see the criteria outlined in the previous section). In the following sections, we test this hypothesis using five new DNS cases of auto-igniting stoichiometric hydrogen-air mixtures subject to compressible isotropic turbulence in which ζ_t is varied while ξ_t is held nearly constant at an intermediate value likely to favor detonability.

3. Methods

3.1. Physical model of turbulent autoignition

In the present simulations, premixed turbulent combustion is represented using a system of partial differential equations derived from the compressible Navier–Stokes equations (which describe conservation of mass, momentum, and total energy) subject to initial and boundary conditions, as given by

$$\frac{\partial\rho}{\partial t} = -\frac{\partial}{\partial x_j}(\rho u_j)\,, \tag{7}$$

$$\frac{\partial(\rho u_i)}{\partial t} = -\frac{\partial}{\partial x_j}(\rho u_i u_j + P\delta_{ij} - \sigma_{ij}) + F_i\,, \tag{8}$$

$$\frac{\partial(\rho E)}{\partial t} = -\frac{\partial}{\partial x_j}\Big(\rho E u_j + P u_j - q_j - u_i\sigma_{ij}\Big) + \rho\Delta h_{\mathrm{f},k}\dot{\Omega}_k + u_j F_j\,, \tag{9}$$

$$\frac{\partial(\rho Y_k)}{\partial t} = -\frac{\partial}{\partial x_j}\Big(\rho Y_k u_j - \mathcal{D}_{kj}\Big) + \rho\dot{\Omega}_k\,, \tag{10}$$

where twice-repeated indices in a term imply summation, u_i is the velocity vector, Y_k is the mass fraction of the kth chemical species, E is the specific total energy, $\Delta h_{\mathrm{f},k}$ is the specific enthalpy of formation of the kth species, and $\dot{\Omega}_k$ is the production rate of the kth species. The viscous stress tensor, σ_{ij}, diffusive heat flux, q_j, and diffusive species flux, $\mathcal{D}_{kj}$, are

$$\sigma_{ij} = 2\mu\Big(S_{ij} - \frac{1}{3}\theta\delta_{ij}\Big) + \mu_b\theta\delta_{ij}\,, \tag{11}$$

$$q_j = \kappa\frac{\partial T}{\partial x_j} - \rho h_k\mathcal{D}_{kj}\,, \tag{12}$$

$$\mathcal{D}_{kj} = \rho D_k\frac{Y_k}{X_k}\frac{\partial X_k}{\partial x_j} \quad \text{(no summation over } k\text{)}\,, \tag{13}$$

respectively, where the multiply-repeated index k does not imply summation in Eq. (13). Here, $S_{ij} = \frac{1}{2}(\partial u_i/\partial x_j + \partial u_j/\partial x_i)$ is the strain rate tensor, $\theta = S_{ii}$ is the dilatation, μ, μ_b, and κ are the mixture-averaged shear viscosity, bulk viscosity, and thermal conductivity, respectively, and D_k, h_k, and X_k are the mixture-averaged mass diffusivity, specific enthalpy, and mole fraction for the kth species, respectively. The fluid is modeled as a thermally-perfect ideal gas, where thermodynamic variables are related to each other by the ideal gas equation of state, $P = \rho R_{\mathrm{u}}T/W_{\mathrm{mix}}$, where R_{u} is the universal gas constant. Additionally, a time-varying body force, F_i, is applied in order to generate and maintain isotropic turbulence fluctuations within the periodic domain; further details of this forcing are outlined in the next section.

The physical domain of the HIT simulations examined here is triply-periodic and is therefore a closed, adiabatic, and isochoric control volume. As a result, without turbulence fluctuations in the thermodynamic state of the premixed autoignitive ideal gas mixture, the entire system would undergo a homogeneous constant-volume (CV) explosion. With the turbulence fluctuations, the spatially-averaged system remains isochoric, but with a different temporal evolution than a homogeneous CV reaction.

Locally and instantaneously, each infinitesimal parcel of reacting gas may undergo any kind of change in pressure and specific volume during combustion, including constant-pressure (isobaric) auto-ignition and detonation cycles that do not correspond to ideal CJ detonation speeds and Zel'dovich–von Neumann–Döring (ZND) wave structure (see [42–44], e.g., for descriptions of CJ and ZND theory). Despite this, all combustion modes (i.e., autoignition, deflagration, and detonation) can be universally characterized by the evolution of the *total thermicity*, $\dot{\omega}$, which has units of s^{-1} and expresses the total thermodynamic effect of chemical reactions, including both the volume increase at constant pressure due to the change in the number of molecules, and the heat release due to the breaking of chemical bonds [43,44]. For an ideal gas, $\dot{\omega}$ is given as

$$\dot{\omega} = \left(\frac{W_{\mathrm{mix}}}{W_k} - \frac{h_k}{c_P T}\right)\dot{\Omega}_k\,, \tag{14}$$

where the twice-repeated index k implies summation, c_P is the mixture-averaged specific heat capacity at constant pressure, W_{mix} is the mixture-averaged molecular weight, and W_k is the molecular weight of the kth species in the gas mixture.

Within this context, we can define the ignition delay time, t_{ign}, to be the time required to reach the maximum total thermicity from the upstream or initial condition, and the exothermicity time, $t_{\mathrm{exo}} = t_{\mathrm{shm}} - t_{\mathrm{fhm}}$, as the difference between the time that the thermicity first rises to 50% of its maximum [i.e., the first half-max (fhm) state] and the time that the thermicity subsequently drops back below 50% of its maximum [i.e., the second half-max (shm) state] [44]. The reaction-zone width of a propagating combustion wave is equivalently defined as the distance in space between these two states, i.e., $\delta_{\mathrm{exo}} = |\boldsymbol{x}_{\mathrm{shm}} - \boldsymbol{x}_{\mathrm{fhm}}|$.

Chemical reactions in this study are modeled using a multi-species kinetic mechanism for hydrogen combustion based on the 2014 San Diego mechanism [45]. This mechanism includes 21 reactions involving 8 reacting species (i.e., H, H_2, O, O_2, OH, H_2O, HO_2, and H_2O_2) and the inert N_2. Thermodynamic properties are given by polynomial functions of temperature in the NASA seven coefficient format [46]. Pure species viscosity coefficients and binary diffusion coefficients are computed from standard kinetic theory given in Hirschfelder et al. [47], while thermal conduction coefficients of pure species are computed from expressions given in Warnatz [48]. Mixture-averaged conduction, shear viscosity, and bulk viscosity coefficients are computed from averaging formulas of order 1/4, 6, and 1/2, respectively [49], while mixture-averaged species diffusion coefficients are computed using the same method as in the TRANSPORT library [64].

3.2. Details of the direct numerical simulations

Equations (7)–(10) are solved numerically on a uniform grid by operator splitting the reaction and forcing terms from the conservative advection and diffusion terms. Advection and diffusion are advanced forward in time by the fully unsplit corner transport upwind finite-volume scheme with piecewise-parabolic monotone spatial reconstruction and the HLLC Riemann solver [50,51] implemented in the code `Athena-RFX` [10,22,52].

Specialized code for the chemical reaction source terms is generated from a CHEMKIN [53] input file in a preprocessing step that generates the rates of change and analytical Jacobian [54] of the species mass fractions and temperature due to chemical reactions. At run time, `Athena-RFX` reads CHEMKIN and TRANSPORT input files to obtain thermodynamic and transport property data and tabulates pure species transport properties, as well as forward and reverse reaction rate constants and their temperature derivatives, for subsequent evaluation by interpolation [55]. The stiff system of equations for the chemical kinetics is integrated using the non-iterative, single step, semi-implicit ODE integrator YASS [56]. It does not employ any approximations to the Jacobian matrix, it explicitly conserves species mass fractions and total energy, and it provides an excellent balance between accuracy and efficiency, which is critical for large-scale DNS.

Isotropic turbulence is sustained in each DNS case by introducing a body force, F_i, in the governing equations for the momentum and specific total energy [Eqs. (8) and (9), respectively]. This body force is implemented as a large-scale, isotropic perturbation momentum field δf_i that is added discretely after each time-step [57]. Moreover, the effective kinetic energy of δf_i is modulated to provide a constant rate of energy injection, $\varepsilon_{\mathrm{inj}}$. In this context, $F_i = \delta f_i/\Delta t$, where Δt is the current simulation time-step. The forcing method amplifies the large-scale motions of the momentum field, and thus δf_i is formed deterministically from the solution momentum field ρu_i as

$$\delta f_i = \frac{\langle\rho\rangle\varepsilon_{\mathrm{inj}}}{\Big\langle u_i\Big(\sqrt{\rho}\delta w_i^s - \langle\sqrt{\rho}\delta w_i^s\rangle\Big)\Big\rangle}\Big(\sqrt{\rho}\delta w_i^s - \langle\sqrt{\rho}\delta w_i^s\rangle\Big)\,, \tag{15}$$

where $w_i = \sqrt{\rho}u_i$, and δw_i^s is computed in spectral space as

$$\widehat{\delta w_i^s}(k) = \begin{cases} \left(\delta_{ij} - k_i k_j / k^2\right)\hat{w}_j(k), & \text{if } 2\Delta k \le k < 4\Delta k \\ 0, & \text{otherwise,} \end{cases} \tag{16}$$

where k_i is the wavenumber vector (also denoted $\boldsymbol{k}$), $k = |\boldsymbol{k}|$ is the wavenumber magnitude, $\Delta k = 2\pi/L$ is the spectral grid resolution, L is the domain width, and $\widehat{(\cdot)}$ denotes a Fourier transform. The perturbation momentum, δf_i, is recomputed every $t_{\text{vp}} = \max(\Delta t, \tau_{\text{K}}/4)$, where τ_{K} is the Kolmogorov time scale, and is appropriately normalized to ensure a constant energy injection rate with no mean momentum addition. For well-resolved DNS at weak to moderate compressibility levels, the typical simulation time-step, Δt, will be much less than τ_{K}, and therefore limiting the refresh rate to $t_{\text{vp}} = \tau_{\text{K}}/4$ provides significant computational cost savings by greatly reducing the number of forward and inverse parallel fast Fourier transforms that must be computed on the solution field.

3.3. Physical setup of the simulations

Collectively, the constant rate of kinetic energy injection from turbulence forcing, ε_{inj}, the domain box size, L, and the initial temperature, T_{init}, pressure, P_{init}, and species mole fractions $X_{k,\text{init}}$, fully determine the physical configuration and dimensional scaling of each simulation prior to the start of reactions. Based upon the particular turbulence forcing scheme and solution procedure used, very accurate empirical estimates of the rms velocity, $u_{\text{rms}} = \{u_i u_i\}^{1/2}$, $\{T\}$, and $\langle P\rangle$ at the start of reactions can be made from ε_{inj}, L, T_{init}, and P_{init}.

Neglecting the initial chemical mixture, $X_{k,\text{init}}$, which we hold constant across all simulations, four independent non-dimensional parameters will govern the dynamics of non-reacting compressible HIT: the Taylor-scale Reynolds number, Re_{t}, the turbulence Mach number, Ma_{t}, the characteristic ratio of specific heats, $\gamma_0 = \gamma(\{T\})$, and the Prandtl number, Pr, where

$$Re_{\text{t}} = \frac{u_{\text{rms}}\lambda_u}{\sqrt{3}\{\nu\}} \approx u_{\text{rms}}^2 \left(\frac{5}{3\nu_0\varepsilon_{\text{inj}}}\right)^{1/2}, \tag{17}$$

$$Ma_{\text{t}} = \frac{u_{\text{rms}}}{a_{\text{rms}}} \approx \frac{u_{\text{rms}}\langle\rho\rangle}{\gamma_0\langle P\rangle}, \tag{18}$$

$$Pr = \frac{\nu_0}{\alpha_0}. \tag{19}$$

Here, λ_u is the (velocity-based) Taylor length scale, $\nu_0 = \mu(\{T\})/\langle\rho\rangle$ is the characteristic kinematic viscosity, and $\alpha_0 = \kappa(\{T\})/[\langle\rho\rangle c_p(\{T\})]$ is the characteristic thermal diffusivity.

The standard deviation of the temperature fluctuations, T', and the rms temperature gradient, $|\nabla T|_{\text{rms}}$, can then be predicted from scaling laws of these four parameters, given generically as

$$\frac{T'}{\{T\}} = A Ma_{\text{t}}^a Re_{\text{t}}^c \gamma_0^e Pr^g, \tag{20}$$

$$\frac{|\nabla T|_{\text{rms}} L}{\{T\}} = B Ma_{\text{t}}^b Re_{\text{t}}^d \gamma_0^f Pr^h, \tag{21}$$

if the leading coefficients (i.e., A and B) and power-law exponents (i.e., $a - h$) were known with a high degree of certainty. In fact, previous numerical and theoretical studies of inert and calorically-perfect (i.e., with constant γ and Pr) compressible HIT (see Refs. [20,40,58], and citations therein) have found that a should be exactly 2. However, A and B can be expected to depend on the initial chemical mixture and thermally-perfect equations of state, and no previous studies have sought a scaling law for $|\nabla T|_{\text{rms}}$. Therefore, we made coarse estimates for these scaling laws in order to determine the required simulation input parameters for a given choice of Ma_{t}, Re_{t}, ζ_{t}, and ξ_{t}.

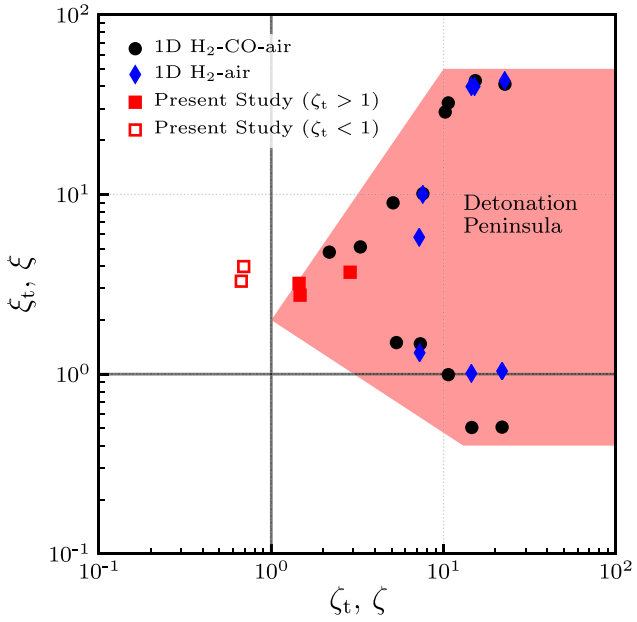


Fig. 1. Hot-spot detonability regime diagram with present 3D turbulent simulation cases shown as red squares, with closed squares indicating $\zeta_{\text{t}} > 1$ and open squares indicating $\zeta_{\text{t}} < 1$. Also shown are select simulations of detonating 1D laminar hot spots of H_2–air (blue diamonds, [14]) and H_2–CO–air (black circles, [18]), which provide an empirical approximation of the upper and lower detonability limits. (For interpretation of the references to color in this figure legend, the reader is referred to the web version of this article.)

Since both γ_0 and Pr depend only on $\{T\}$, and we expected the initial $\{T\}$ to vary only slightly between simulations (i.e., from 900–1200 K), we assumed that $e = f = g = h = 0$ for our present purposes. Furthermore, previous studies [40,58] found that $T'/\{T\}$ is essentially independent of Re_{t}, and so we assumed that $c = d = 0$. The remaining exponents (a and b) and leading coefficients (A and B) were estimated from a series of inert HIT simulations at $Ma_{\text{t}} = [0.1, 0.2, 0.4]$ and $Re_{\text{t}} = 50$. We found from least-squares fits that $a = b = 2.0$, $A = 0.063$, and $B = 11$. These coarse numerical approximations of T' and $|\nabla T|_{\text{rms}}$ as power-law functions of Ma_{t} only, along with the system of differential equations for the chemical kinetics mechanism, were then used inside a root-finding algorithm to determine the necessary values of ε_{inj}, L, T_{init}, and P_{init} for each simulation.

Due to the high cost of simulating the chosen low-Mach conditions, only five simulations were performed, all targeted for $\xi_{\text{t}} = 4$, with one simulation at $\zeta_{\text{t}} = 2$ and two simulations each at $\zeta_{\text{t}} = 1$ and 0.5, but with different Ma_{t} at the same ζ_{t}. Additionally, each simulation was initialized with a stoichiometric H_2-air mixture (i.e., H_2:O_2:N_2 = 2:1:3.76), and targeted a fixed value of $Re_{\text{t}} = 230$. Since we set four non-dimensional parameters for each simulation (ξ_{t}, ζ_{t}, Ma_{t}, and Re_{t}), there is no remaining relational freedom to hold fixed any dimensional parameters between simulations, and, therefore, each simulation must have a different T_{init}, P_{init}, L, and ε_{inj}. The input physical model parameters for each simulation and the resulting properties of the fully-developed turbulence are outlined in Table 1. It can be seen that the actual values of ξ_{t} and ζ_{t}, computed *a posteriori* at $t = 0$ in each case, maintain the trend of sweeping through unity ζ_{t} at roughly constant ξ_{t}, despite deviating from their precise target values.

Figure 1 shows a detonability regime diagram of the present simulations, along with a selection of detonating conditions from

Table 1
Input physical model parameters of the direct numerical simulations and resulting actual turbulence properties, computed *a posteriori*, at $t = 0$ s.

Simulation	Z1	Z2a	Z2b	Z3a	Z3b
$\langle\rho\rangle\varepsilon_{\text{inj}}$ (J/m^{3}s)	5.556×10^5	4.001×10^4	1.524×10^6	9.579×10^4	2.066×10^7
L (m)	3.278×10^{-2}	1.116×10^{-1}	3.087×10^{-2}	1.113×10^{-1}	1.729×10^{-1}
T_{init} (K)	1118	998.1	1096	966.7	1119
P_{init} (atm)	6.987	1.796	4.585	1.096	4.160
Ma_{t}	0.03	0.03	0.05	0.05	0.1
$\{T\}_0$ (K)	1119	998.8	1098	968.5	1128
$\langle P\rangle_0$ (atm)	6.993	1.798	4.593	1.098	4.192
T_0' (K)	0.1213	0.1068	0.2931	0.2648	1.183
$\lvert\nabla T\rvert_{\text{rms},0}$ (K/m)	4.257	1.151	11.53	2.905	85.59
$\lambda_{T,0}/\Delta x$	8.9	8.5	8.5	8.4	8.2
ζ_{t}	2.87	1.47	1.45	0.69	0.67
ξ_{t}	3.69	2.75	3.20	3.97	3.29

two previously published studies of 1D laminar hot spots containing H_2–air [14] and H_2–CO–air [18] fuel mixtures. Together, these prior studies sketch out the approximate upper and lower bounds of the hot-spot detonation peninsula. The 3D turbulent simulations presented here cut across the critical limit of $\zeta_{\text{t}} = 1$, between the empirical upper and lower ξ detonability limits. These simulation conditions therefore provide an adequate test of our hypothesis that the detonability of compressible turbulence should abruptly increase as ζ_{t} increases from below to above unity. It is cautioned, however, that these simulations do not provide adequate information to draw firm conclusions about how the detonability may vary with either ξ_{t} or Ma_{t}.

Each simulation was solved on a uniform computational mesh of size 1024^3. The resulting Kolmogorov scale resolution at the time of reaction initiation was $\eta_{\text{K},0}/\Delta x = 0.5$, where Δx is the grid cell size. This relatively coarse resolution was a necessary compromise between computational cost and physical fidelity, with the first four statistical moments of the temperature fluctuations being fully converged and the second moment of the temperature gradient field (i.e., $\lvert\nabla T\rvert_{\text{rms}}$) being approximately converged, and with at least one grid cell per ZND detonation exothermic width for all simulations. Although the ZND detonation resolution is marginal, all characteristic gas-dynamic wave speeds, including reaction waves, are correctly captured by the Godunov finite-volume scheme, regardless of the grid size and wave orientation, and depend only on the Rankine–Hugoniot jump conditions across the wave.

We performed each simulation as follows. We randomly initialized each simulation with the chemical reactions turned off, uniform temperature and pressure, and a random velocity field with a prescribed isotropic energy spectrum and turbulence Mach number, Ma_{t}, significantly lower than the target turbulence Mach number. This initialization procedure was intended to ensure that any dynamical inconsistencies in the initial conditions did not impact the simulations at later times [59,60]. The turbulent flow field was allowed to develop from these random initial conditions for $10.5\tau_\ell$, where τ_ℓ is the predicted integral-scale eddy turnover time, until $Ma_{\text{t}} = Ma_{\text{t},0}$, and reactions were turned on. We define the time at which reactions are initialized as $t = 0$. We then ran the five simulations for an additional $1.0\tau_\ell$ each, at which point the entire domain of each simulation was essentially finished reacting. Full three-dimensional fields of the solution variables were output at a rate of $0.5\tau_{\text{exo}}$. The turbulence forcing mechanism remains active throughout the entire duration of each simulation, and, due to the low values of Ma_{t} in all five cases, the thermodynamic turbulence statistics, $\{T\}$, T', and $\lvert\nabla T\rvert_{\text{rms}}$ would have been essentially stationary over a single τ_ℓ, were reactions not active.

A 2D section of the temperature field at $t = 0$ is shown for case Z1 in Fig. 2; this slice is qualitatively representative of the multi-scale structure of the temperature fluctuations for all five

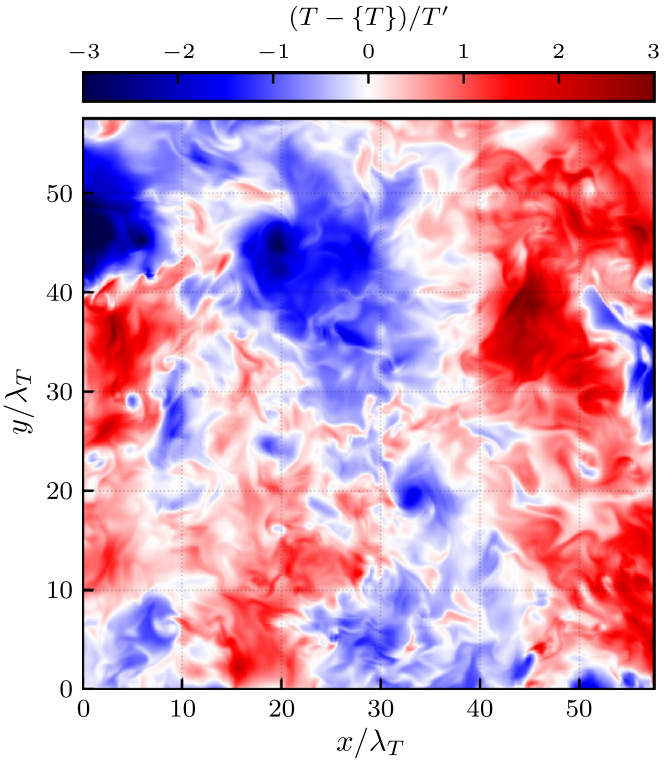


Fig. 2. A pseudocolor image of a 512×512 cell slice of the normalized temperature fluctuations, $(T - \{T\})/T'$, at $t = 0$ from case Z1.

cases. Given the wide range of temperature values and associated temperature gradients found in Fig. 2, the isotropic compressible turbulent flow fields generated in the present simulations are likely to form many isolated ignition kernels of various shapes and sizes. Therefore, the *degree* to which a simulation forms detonation waves versus shockless auto-ignition waves can be quantified, rather than simply assessing a binary state of positive or negative detonability, as in the 1D laminar case. Even in cases Z3a and Z3b, where we do not predict that detonation waves will form since $\zeta_{\text{t}} < 1$ (see Fig. 1), we still expect to find qualitative differences between combustion in an idealized homogeneous CV reactor and the spontaneous ignition waves that form along temperature gradients in these cases.

3.4. Reaction wave profiling

In Section 4, we analyze the spontaneous ignition wave fronts within a single volumetric data output from each simulation. A 2D

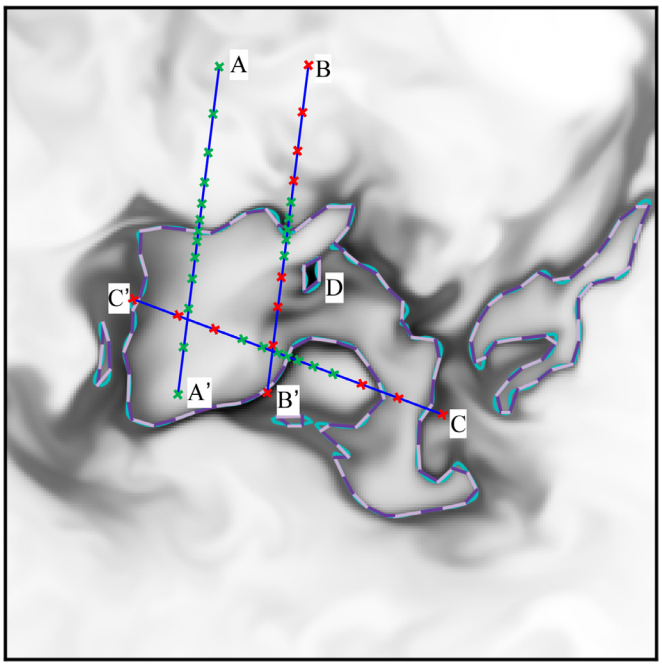


Fig. 3. A two-dimensional representation of the reaction wave profiling procedure. See text in Section 3.4.

schematic representation of the reaction wave profiling is shown in Fig. 3 to aid explanation.

First, using Lewiner's marching cubes algorithm [61], as implemented in the python package scikit-image [62], we find the isosurface of Y_{H_2} corresponding to the peak thermicity of a homogeneous CV reactor with the same initial conditions as the mean thermodynamic state of each simulation at $t = 0$ s. The marching cubes algorithm builds a polygonal mesh made entirely of triangular elements whose vertices are the linearly-interpolated locations where the chosen value of a scalar field intersects each finite-volume cell edge. In Fig. 3, the 3D piecewise-triangular isosurface is represented as a 2D piecewise-linear isocontour, shown as alternating light and dark purple lines, that approximates the "true" underlying ignition-delay isocontour, shown in cyan.

Second, for each triangular face of the isosurface, we compute the surface area, barycenter, and normal vector to the surface. From each face barycenter, we extract a reaction-front profile along the normal vector of the surface by interpolating all quantities of interest, computed at the finite-volume cell centers, to 29 geometrically-spaced points along each direction of the normal vector, such that each successive point is $2^{1/4}$ times farther from the face barycenter than the previous point. These points are located between $\pm\, 0.5\Delta x$ and $\pm\, 64\Delta x$, for a total of 59 interpolation points, including the face barycenter point, and quantities of interest are interpolated to these points using tri-cubic Akima spline interpolation [63]. Three sample reaction-front profiles are represented in Fig. 3 as the blue lines marked $\overrightarrow{AA'}$, $\overrightarrow{BB'}$, and $\overrightarrow{CC'}$, with interpolation stencil points marked as green and red crosses.

Third, we immediately truncate the interpolated profiles wherever they intersect another face of the isosurface, such as in the case of line $\overrightarrow{CC'}$ in Fig. 3, which overlaps the 2D isocontour in three places other than the line segment from which it was interpolated. We also compute a smoothed thermicity profile using a five-point convolution filter and find the local maximum thermicity nearest the profile center-point. We then truncate the profiles to the nearest local minimum on either side of this center-most maximum. This step is demonstrated by displaying a smooth thermicity field as a gray-scale image underneath the 2D hydrogen mass-fraction isocontours in Fig. 3. Any points which clearly cross over either another segment of the isocontour or a local minima in the thermicity field are colored red, indicating they have been discarded, and only the green points are retained. Any profile which has retained a complete reaction zone, defined as the region of exothermicity between the first and second half-max states, is considered to be a freely-propagating reaction wave profile, equivalent to a turbulent deflagration flamelet profile.

It should be noted that interpolated profiles that lack a complete reaction zone may correspond to one of three scenarios: (i) *Quasi-homogeneous autoignition*, wherein the underlying spontaneous autoignition wave would be longer than the periodic domain of the simulation (i.e., $\delta_{exo} > L$); (ii) *End-gas reactant pockets* bounded by colliding reaction waves, such that the thermicity has risen above 50% of the profile peak everywhere along the profile within the pocket and therefore no first half-max point (x_{fhm}) exists for the profile; or (iii) *Emerging ignition kernels* bounded by cold reactants, such that the thermicity has not yet dropped below 50% of the profile peak within the kernel and therefore no second half-max point (x_{shm}) exists for the profile. An isolated end-gas reactant pocket marked as region *D* in Fig. 3 is representative of sections of isosurface whose reaction-front profiles would not be retained due to the lack of a complete reaction zone structure.

4. Results

4.1. Global system evolution

Figure 4 shows time series of the mass-average H_2 mass fraction, $\{Y_{H_2}\}$, and thermicity, $\{\dot{\omega}\}$, for each turbulent simulation case. The corresponding time histories for a homogeneous CV reactor are also shown for the same spatially-averaged thermodynamic conditions found in each of the simulation cases at $t = 0$ s (i.e., $\langle P\rangle_0$ and $\{T\}_0$). As ζ_t decreases from case Z1 to Z3b, Fig. 4 shows that the rate at which $\{Y_{H_2}\}$ changes in the simulations increasingly conforms to the rate of change in a homogeneous CV reactor. In particular, for case Z1, which has the largest value of ζ_t of all simulations examined here, the rate of change of $\{Y_{H_2}\}$ is substantially smaller than for the homogeneous CV reactor. Similarly, $\{\dot{\omega}\}$ is substantially smaller in the turbulent cases, as compared to the homogeneous CV reactor, for large ζ_t (i.e., case Z1). There is thus a close correspondence between the turbulent and homogeneous CV cases when ζ_t is small and, as ζ_t increases from case Z3b to Z1, the turbulent time histories increasingly diverge from those of the corresponding homogeneous CV reactors.

Figure 4 further shows that the global ignition delay time measured with respect to the $\{\dot{\omega}\}$ profiles, which we call the domain-average ignition delay time, $\widetilde{t}_{\mathrm{ign}}$, where $\tilde{t}$ denotes a global time scale computed from $\{\dot{\omega}\}$, decreases relative to the homogeneous CV ignition delay time, τ_{ign}, as ζ_t increases. Figure 4 also shows that there are substantial changes in the corresponding domain-average exothermicity time, $\widetilde{t}_{\mathrm{exo}} = \widetilde{t}_{\mathrm{shm}} - \widetilde{t}_{\mathrm{fhm}}$, relative to the homogeneous CV exothermicity time, τ_{exo}, as ζ_t increases. In particular, $\widetilde{t}_{\mathrm{exo}}$ is more than five times the corresponding τ_{exo} in case Z1, and still nearly double τ_{exo} in case Z3b.

The spatial structure of the simulations during the domain-averaged exothermic pulse is indicated by the partial 2D slices of pressure at three times shown in Fig. 5 for case Z1. The initial emergence of isolated ignition kernels just before the first domain-average half-max point, $\widetilde{t}_{\mathrm{fhm}}$, is shown in Fig. 5(a), while Fig. 5(b) shows that reaction waves from the ignition kernels have rapidly strengthened and are interacting with secondary ignition kernels just after the domain-average ignition-delay time, $\widetilde{t}_{\mathrm{ign}}$. By the second domain-average half-max point, $\widetilde{t}_{\mathrm{shm}}$, the flow field is dominated by colliding reaction waves and merging ignition kernels, as

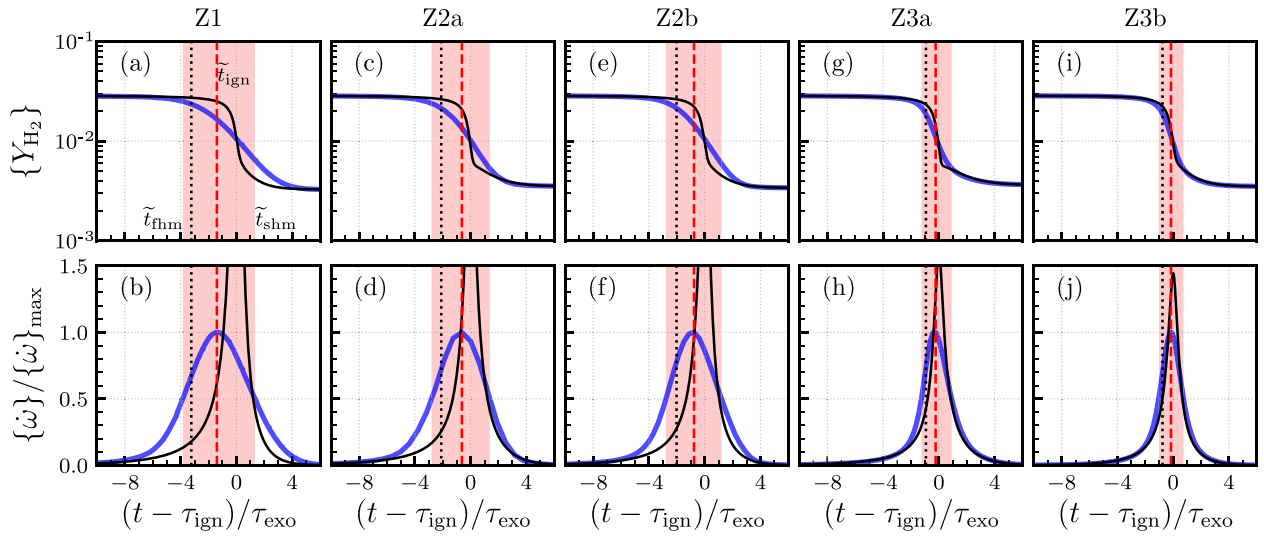


Fig. 4. Time series of (a, c, e, g, i) mass-average H_2 mass-fraction, $\{Y_{H_2}\}$, and (b, d, f, h, j) mass-average thermicity $\{\dot{\omega}\}$, shown as thick blue lines. Corresponding homogeneous autoignition profiles are shown as black lines, the domain-average ignition delay times, $\tilde{t}_{ign}$, are shown as vertical red lines, and the domain-average exothermicity times, $\tilde{t}_{exo}$, are shown as red shaded regions starting at $\tilde{t}_{fhm}$ and ending at $\tilde{t}_{shm}$. Vertical black dotted lines mark the time of the data output analyzed in each case. (For interpretation of the references to color in this figure legend, the reader is referred to the web version of this article.)

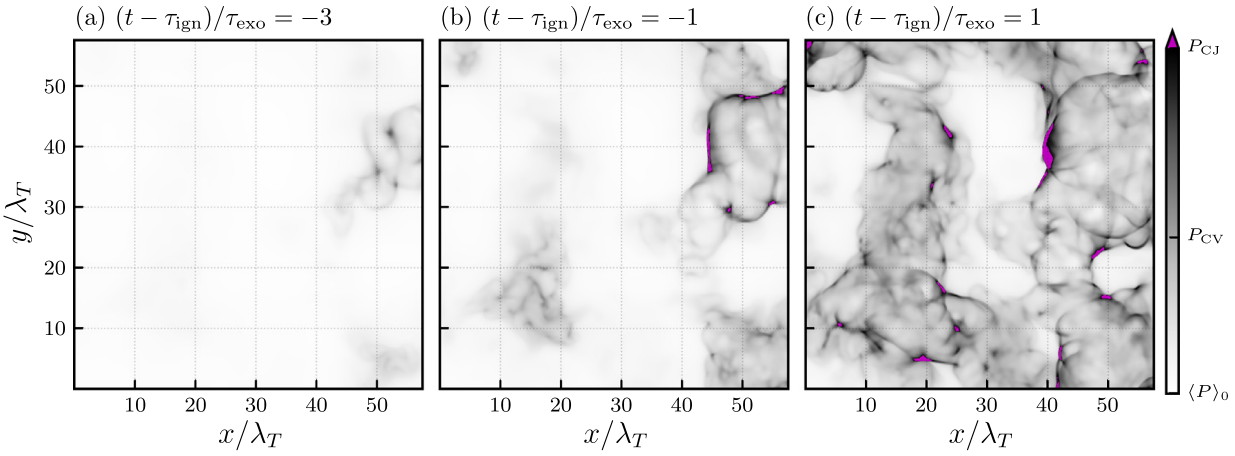


Fig. 5. Pseudocolor images of 512 × 512 cell slices of the pressure field, P, taken from case Z1 at (a) $(t-\tau_{ign})/\tau_{exo}=-3$, (b) $(t-\tau_{ign})/\tau_{exo}=-1$, and (c) $(t-\tau_{ign})/\tau_{exo}=1$, approximately corresponding to $\tilde{t}_{fhm}$, $\tilde{t}_{ign}$, and $\tilde{t}_{shm}$. Pressures greater than P_{CJ} are highlighted as magenta. (For interpretation of the references to color in this figure legend, the reader is referred to the web version of this article.)

shown in Fig. 5(c). Therefore, to specifically examine hot-spot autoignition and detonation formation, in the following we analyze the single volumetric data output from each simulation that most closely corresponds to $\tilde{t}_{fhm}$, marked by vertical black dotted lines in Fig. 4 and shown for case Z1 in Fig. 5(a). It should be noted that while the analysis of the ignition front isosurfaces and their associated reaction-front profiles is performed at $t=\tilde{t}_{fhm}$, each simulation continues to be characterized by the values of ξ_t and ζ_t computed at $t=0$.

4.2. Reaction wave classification

The simple configuration of an isolated laminar hot-spot ensures that there can only be self-reinforcing acoustic-exothermicity coupling, as both the exothermic ignition wave and acoustic wave formed from initial conditions travel in the same direction along a negative gradient in the speed of sound. Similarly, once the reaction wave has exited the hot spot, it is assumed to travel through a quiescent cold gas at a fixed wave speed. Accordingly, the expected reaction wave speed inside the hot spot is a critical indicator of detonability, and the final steady-state wave speed alone could be used as an indicator of successful detonation.

However, in the case of igniting compressible turbulence, it is possible that, locally and instantaneously, an exothermic reaction wave may either support or oppose an acoustic or shock wave, depending on the degree of misalignment between the waves, as compressible turbulence hot spots are not isolated from one another, do not form in a quiescent acoustic field, and the temperature and speed of sound do not monotonically decrease away from the hot spot. Instead, the local and instantaneous wave speed along a reaction wave profile, which could be computed as the ignition isosurface displacement speed as in Chen et al. [32], can be expected to vary rapidly and significantly in time, because the ignition-delay-time gradient along the direction of the reaction wave profile will tend to oscillate above and below zero, and the spontaneous wave speed will therefore tend to intermittently shoot to infinity along the profile.

For this reason, we do not classify reaction wave profiles based upon their instantaneous isosurface displacement speed. Instead, we classify each reaction wave identified in the five simulations based on both the magnitude of the profile-maximum

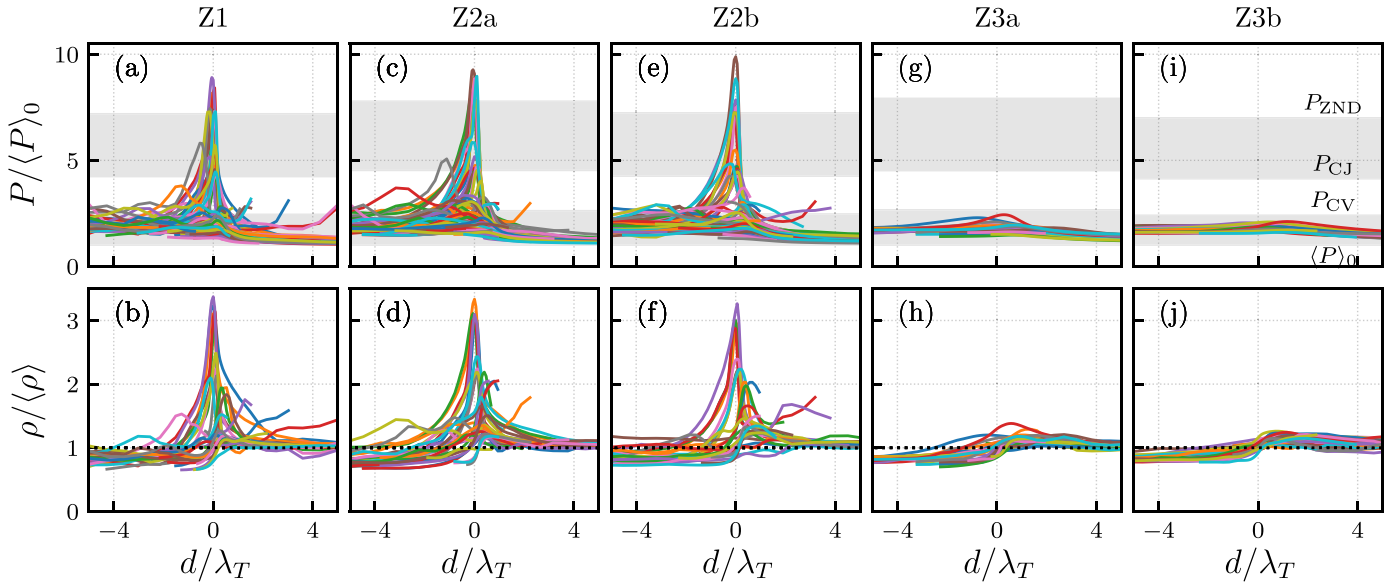


Fig. 6. Forty selected reaction wave profiles of (a, c, e, g, i) pressure, P, and (b, d, f, h, j) density, ρ, shown as solid colored lines. Distance along the profile interpolation stencils is denoted as d, with $d = 0$ corresponding to the isosurface face barycenter, positive d on the upstream (reactant) side of the reaction wave, and negative d on the downstream (product) side of the reaction wave. The various pressure regimes used for wave classification are denoted by alternating bands of gray shading in panels (a)–(i). (For interpretation of the references to color in this figure legend, the reader is referred to the web version of this article.)

pressure, P_{max}, which we take as a measure of the magnitude of the acoustic-exothermicity coupling, and the relative position of the pressure peak with respect to the profile reaction zone, which we take as a measure of the direction of the coupling between the reaction and pressure wave. We delineate detonation waves of various strengths from ignition waves with marginal or weak acoustic coupling by comparing P_{max} to the post-shock pressure for a planar ZND detonation wave propagating through a gas at the mean thermodynamic state of each simulation at $t = 0$ s, denoted P_{ZND}, the corresponding CJ post-detonation sonic-point pressure of that ZND detonation, P_{CJ}, and the final pressure of a homogeneous CV reactor with the same initial conditions, P_{CV}. These criteria are:

- If $P_{\mathrm{max}} \geq P_{\mathrm{ZND}}$, then the reaction wave is a *high-pressure detonation*;
- If $P_{\mathrm{ZND}} > P_{\mathrm{max}} \geq P_{\mathrm{CJ}}$, then the reaction wave is a *low-pressure detonation*;
- If $P_{\mathrm{CJ}} > P_{\mathrm{max}} \geq 1.1P_{\mathrm{CV}}$, then the reaction wave is a *high-pressure ignition*; finally,
- If $P_{\mathrm{max}} < 1.1P_{\mathrm{CV}}$, then the reaction wave is a *low-pressure ignition*.

Reaction front profiling resulted in several million individual profiles in each simulation, and so we show a selected small number of the resulting reaction wave profiles for each case in Fig. 6. Based on the above criteria, we find detonation waves in all three cases where $\zeta_{\mathrm{t}} > 1$ (namely, Z1, Z2a, and Z2b) and no detonations in cases Z3a and Z3b. Figure 6 shows a subset of the reaction wave profiles identified in each of the simulations. Both high-pressure (HP) and low-pressure (LP) detonations are observed in the detonating cases, although only a very small fraction of the total ignition isosurface area is classified as either a detonation wave or HP ignition wave, as shown in Fig. 7. In cases Z3a and Z3b, only a very small fraction of the total isosurface area is categorized as a complete reaction wave at all, with all identified waves being LP ignition waves. It should be noted that the area fraction of the ignition isosurfaces associated with reaction profiles that lack a complete reaction zone are not plotted in Fig. 7 and the sum of the reaction-wave area fractions is less than 100% in all five simulation cases.

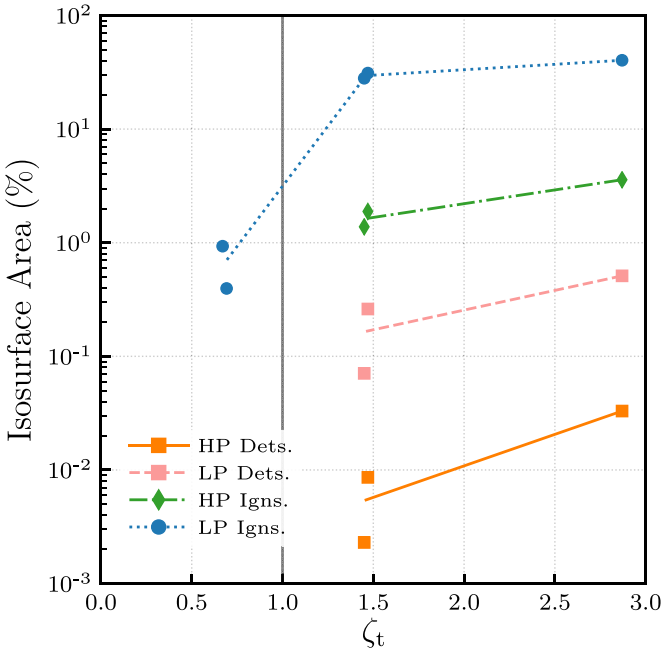


Fig. 7. Percentage of total ignition-isosurface area corresponding to each reaction wave classification as a function of ζ_{t}, directly computed at $t = 0$ for each of the five simulation cases. Colors and symbols correspond to HP detonation waves (orange squares), LP detonation waves (pink squares), HP ignition waves (green diamonds), and LP ignition waves (blue circles). Piecewise-linear trend lines are shown by averaging the area fractions of cases Z2a with Z2b, and Z3a with Z3b. (For interpretation of the references to color in this figure legend, the reader is referred to the web version of this article.)

The position of maximum pressure in each profile relative to its reaction zone allows for a more refined assessment of the acoustic-exothermicity coupling of each detonation wave, and therefore for the system as a whole. In particular, we can sub-classify the stability of HP and LP detonations according to the position of the maximum pressure, $x_{\mathrm{mp}} = x|_{P=P_{\mathrm{max}}}$. Specifically, if $x_{\mathrm{mp}} > x_{\mathrm{fhm}}$, then the reaction zone is behind a leading shock and we consider this

to be a *positively-coupled* detonation. If $x_{\mathrm{fhm}} \geq x_{\mathrm{mp}} \geq x_{\mathrm{shm}}$, then the reaction zone overlaps the shock and we consider this to be a *neutrally-coupled* detonation. Finally, if $x_{\mathrm{shm}} > x_{\mathrm{mp}}$, then the reaction zone is in front of a trailing shock and we consider this to be a *negatively-coupled* detonation.

We found no positively-coupled HP detonations in the three $\zeta_{\mathrm{t}} > 1$ cases and classify less than 0.001% of the isosurface area as a positively-coupled LP detonation in each of those cases. Moreover, we classify just 0.0330%, 0.0086%, and 0.0023% of the total ignition surface as neutrally-coupled HP detonations in cases Z1, Z2a, and Z2b, respectively.

We note that the marginally-interacting HP ignition waves could also be sub-classified in a similar manner, and in fact it is possible that a wave classified as an HP ignition wave is in fact an emerging or very-low-pressure detonation wave. However, due to the nature of the single-time Eulerian analysis we use here, it is impossible to properly assess whether or not a given HP ignition wave will eventually develop into a detonation wave.

4.3. Evolution in thermodynamic state space

In order to directly illustrate the variety of thermodynamic cycles that each reacting fluid parcel may undergo locally and instantaneously throughout the domain, including well-defined, if less than ideal, detonation wave cycles, joint probability distributions (pdfs) of pressure, P, versus specific volume, $v = 1/\rho$, are constructed from the full domain of volumetric data that was analyzed in each case. Figure 8 shows the variation in the joint pdf of the P–v state space for the three cases (Z1, Z2a, and Z2b) that exhibit strong acoustic-exothermic coupling, including detonations, while Fig. 9 shows the two cases (Z3a and Z3b) with very weak acoustic-exothermicity coupling throughout their domains.

In each panel of Figs. 8 and 9, the joint pdf has an envelope corresponding to the chemically-frozen Hugoniot curve for pure reactants (dashed blue lines) and the chemical-equilibrium Hugoniot curve of the reaction products (dashed red lines). Each panel also highlights the average initial thermodynamic state at $t = 0$ s, $(\langle P\rangle_0,\ 1/\langle\rho\rangle)$, the von Neumann post-shock state, $(P_{\mathrm{ZND}},\ v_{\mathrm{ZND}})$, CJ post-detonation sonic state, $(P_{\mathrm{CJ}},\ v_{\mathrm{CJ}})$, and the equilibrium state for a homogeneous constant-volume reactor, $(P_{\mathrm{CV}},\ v_{\mathrm{CV}})$. Of particular note, Fig. 9 reveals that in neither case Z3a nor Z3b has any point within the domain fully reacted, since, in both cases, the joint pdf falls noticeably short of the equilibrium product Hugoniot curve.

For the reaction waves which show only very weak acoustic-exothermicity coupling, namely the LP ignition waves, there is generally no sharp pressure peak [see, for instance, panels (g) and (i) of Fig. 6], and therefore it is easier to sub-classify these LP ignition waves by assessing whether or not they follow an approximately constant pressure or constant volume trajectory through state space. Therefore, we compute the normalized ratio of the change in pressure over the change in specific volume across the reaction zone of a wave as

$$m = \frac{v_{\mathrm{fhm}}|P_{\mathrm{shm}} - P_{\mathrm{fhm}}|}{P_{\mathrm{fhm}}|v_{\mathrm{shm}} - v_{\mathrm{fhm}}|}\,. \tag{22}$$

If $m > 4$, then we consider the LP ignition wave to be a quasi-constant-volume ignition wave, and if $m < 1/4$, then the LP ignition wave is a quasi-constant-pressure (QCP) ignition wave. We chose the threshold slopes of 4 and 1/4 empirically, based upon trial and error, until we found reciprocal slopes that adequately isolated waves with relatively straight (whether horizontal or vertical) state-space trajectories within the reaction zone of each profile. We found that a significant fraction of the LP ignition waves in all five cases undergo QCP heat release and both Figs. 8 and 9 show ten examples of QCP ignition waves, randomly-chosen from among all identified QCP profiles in each case. For comparison, Fig. 8 also

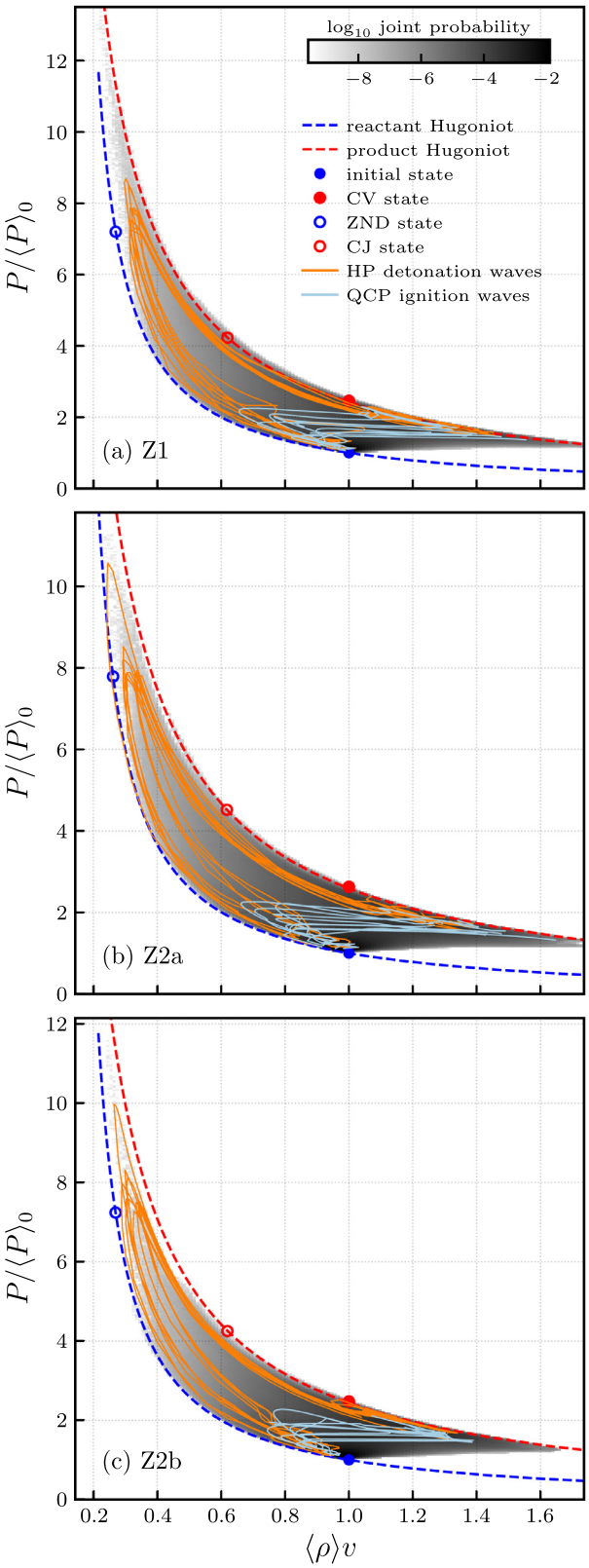


Fig. 8. Joint probability distributions of pressure, P, and specific volume, v, over the full domains of cases (a) Z1, (b) Z2a, and (c) Z2b, along with 10 randomly-chosen examples each of developing HP detonations (thin orange lines) and quasi-constant-pressure ignition waves (thin light blue lines). Lines, symbols, and colors are defined for all cases in panel (a). (For interpretation of the references to color in this figure legend, the reader is referred to the web version of this article.)

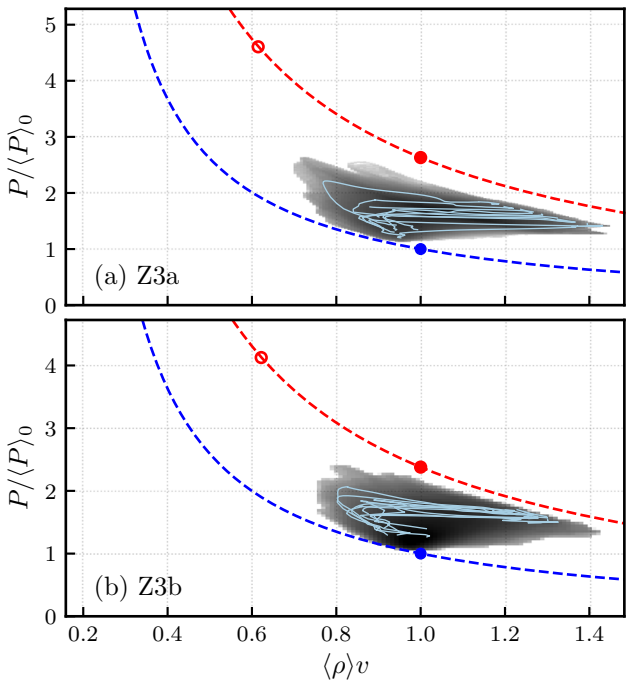


Fig. 9. Joint probability distributions of pressure, P, and specific volume, v, over the full domains of cases (a) Z3a, and (b) Z3b, along with 10 randomly-chosen examples of quasi-constant-pressure ignition waves. Lines and symbols as in Fig. 8(a). (For interpretation of the references to color in this figure legend, the reader is referred to the web version of this article.)

shows ten randomly-chosen HP detonation wave profiles for cases Z1, Z2a, and Z2b.

5. Conclusions

In autoignitive gaseous flows, detonations can be directly initiated by the thermomechanical feedback between spontaneous ignition waves and acoustic waves which emanate from isolated and laminar hot spots with suitable temperature gradients. Two non-dimensional parameters have been found to predict the detonability of such hot spots, namely the acoustic-ignition coupling parameter, ξ, which is an inverse Mach number for the ignition wave, and the acoustic-exothermicity coupling parameter, ζ, which is a ratio of the sound-crossing time to the exothermic time of the hot spot. In this work, we have adapted the definitions of ξ and ζ into a statistical model for spontaneous detonation initiation by thermodynamic gradients formed from compressible homogeneous isotropic turbulence (HIT) fluctuations. We then examined the utility of the adapted statistical model, denoted ξ_t and ζ_t, for predicting turbulence detonability in five new direct numerical simulations (DNS) of compressible HIT in premixed hydrogen-air that sweep a small, but critical, range of the turbulence detonability parameters, namely at values of ζ_t both above and below unity.

We found strong evidence that ζ_t is a sensitive measure of the degree of acoustic-exothermicity coupling between the turbulence thermodynamics and the combustion chemistry, as all three simulation cases where $\zeta_t > 1$ contained developing detonation waves, and the two simulation cases where $\zeta_t < 1$ showed no evidence of strong coupling between spontaneous ignition waves and the very weak leading pressure waves formed as isolated ignition kernels emerged. Additionally, while detonation waves accounted for only a very small fraction of the total ignition-front isosurface area in each case where $\zeta_t > 1$, the area fraction of detonation, detonation strength, and detonation stability all increased monotonically with ζ_t. We conclude, therefore, that our formulation of ζ_t is a predictive parameter of compressible turbulence detonability.

There are, however, several limitations of the present study, which constrain its immediate applicability to the engineering design process. Namely, the choice of HIT as the unit flow problem simplifies the required dimensional analysis but greatly limits the ability to extrapolate these findings to the prediction of detonability of geometrically-complex turbulent flows with large-scale variations in autoignitive conditions, as would be found in any real-world application. Similarly, the limited range of turbulence Mach and Reynolds numbers, Ma_t and Re_t, that were computationally accessible for this study precluded testing whether these parameters also have a direct impact on detonability separate from their influence on ζ_t. Additionally, due to the approximate nature of the derived scaling of $|\nabla T|_{\text{rms}}$ with Ma_t, Re_t, Pr, and γ, we are unable to draw any definitive conclusions about how detonability varies with ξ_t from the paired simulations Z2a/Z2b and Z3a/Z3b. However, the high level of consistency of the results observed between the two pairs of cases provides confidence in our ability to predict detonability based on ξ_t and ζ_t alone, independent of Ma_t and the thermodynamic properties of a system. High computational cost also forced us to choose between simulating an interesting set of points in the ξ_t–ζ_t parameter space and performing simulations on highly-refined meshes. As a result, given the diffusive, monotone, and shock-capturing nature of the numerics, it is likely that each case would exhibit a higher degree of detonability were the simulations run with a much higher mesh resolution capable of resolving the internal thermochemical structure of the detonation waves.

For these reasons, future work will focus on empirically determining the non-dimensional scaling of T' and $|\nabla T|_{\text{rms}}$ with Ma_t, Re_t, Pr, and γ, performing detonability simulations at both higher Ma_t and Re_t, and determining how superimposed compressible turbulence fluctuations alter the detonability of large-scale and coherent temperature gradients. Future work could also test alternative statistical formulations of the turbulence detonability model that use a model for the isotropic temperature autocorrelation function, or other forms of higher-order statistical information, to better capture the contribution of the highest temperature regions of the domain and the largest temperature gradients.

Declaration of Competing Interest

None.

Acknowledgments

The authors would like to thank D. R. Kassoy for helpful discussions. CAZT and PEH were supported in part by AFOSR awards FA9550-14-1-0273 and FA9550-17-1-0144, and by the Department of Defense (DoD) High Performance Computing Modernization Program (HPCMP) under a Frontier Project award. Computing resources were provided by the DoD HPCMP under the Frontier project award.

References

[1] J. Urzay, Supersonic combustion in air-breathing propulsion systems for hypersonic flight, Annu. Rev. Fluid Mech. 50 (2018) 593–627.
[2] E.S. Oran, V.N. Gamezo, Origins of the deflagration-to-detonation transition in gas-phase combustion, Combust. Flame 148 (2007) 4–47.
[3] Y.B. Zel'dovich, V.B. Librovich, G.M. Makhviladze, G.I. Sivashinsky, On the development of detonation in a non-uniformly heated gas, Astronaut. Acta 15 (1970) 313–321.
[4] J.H. Lee, R. Knystautas, N. Yoshikawa, Photochemical initiation of gaseous detonations, Acta Astronaut. 5 (11–12) (1978) 971–982.
[5] Y.B. Zel'dovich, Regime classification of an exothermic reaction with nonuniform initial conditions, Combust. Flame 39 (2) (1980) 211–214.

[6] D. Bradley, "Hot spots" and gasoline engine knock, J. Chem. Soc. Faraday Trans. 92 (16) (1996) 2959–2964.
[7] A. Khokhlov, Mechanisms for the initiation of detonations in the degenerate matter of supernovae, Astron. Astrophys. 246 (1991) 383–396.
[8] A.M. Khokhlov, E.S. Oran, J.C. Wheeler, A theory of deflagration-to-detonation transition in unconfined flames, Combust. Flame 108 (4) (1997) 503–517.
[9] A.Y. Poludnenko, T.A. Gardiner, E.S. Oran, Spontaneous transition of turbulent flames to detonations in unconfined media, Phys. Rev. Lett. 107 (5) (2011) 1–4.
[10] A.Y. Poludnenko, Pulsating instability and self-acceleration of fast turbulent flames, Phys. Fluids 27 (1) (2015) 14106.
[11] D.R. Kassoy, The response of a compressible gas to extremely rapid transient, spatially resolved energy addition: an asymptotic formulation, J. Eng. Math. 68 (3–4) (2010) 249–262.
[12] A.M. Bartenev, B.E. Gelfand, Spontaneous initiation of detonations, Prog. Energy Combust. Sci. 26 (1) (2000) 29–55.
[13] A.K. Kapila, D.W. Schwendeman, J.J. Quirk, T. Hawa, Mechanisms of detonation formation due to a temperature gradient, Combust. Theory Model. 6 (4) (2002) 553–594.
[14] X.J. Gu, D.R. Emerson, D. Bradley, Modes of reaction front propagation from hot spots, Combust. Flame 133 (1) (2003) 63–74.
[15] M.I. Radulescu, G.J. Sharpe, D. Bradley, A universal parameter quantifying explosion hazards, detonability and hot spot formation: χ number, 7th International Seminar on Fire and Explosion Hazards (2013).
[16] J.D. Regele, D.R. Kassoy, A. Vezolainen, O.V. Vasilyev, Indirect detonation initiation using acoustic timescale thermal power deposition, Phys. Fluids 25 (9) (2013) 091113.
[17] M.D. Kurtz, J.D. Regele, Acoustic timescale characterisation of a one-dimensional model hot spot, Combust. Theory Model. 18 (4–5) (2014) 532–551.
[18] L. Bates, D. Bradley, G. Paczko, N. Peters, Engine hot spots: modes of auto-ignition and reaction propagation, Combust. Flame 166 (2016) 80–85.
[19] U. Frisch, Turbulence: the legacy of AN Kolmogorov, Cambridge University Press, 1995.
[20] P. Sagaut, C. Cambon, Homogeneous Turbulence Dynamics, 2nd ed., Springer International Publishing, 2018.
[21] J. Schumacher, J.D. Scheel, D. Krasnov, D.A. Donzis, V. Yakhot, K.R. Sreenivasan, Small-scale universality in fluid turbulence, Proc. Natl. Acad. Sci. 111 (30) (2014) 10961–10965.
[22] A.Y. Poludnenko, E.S. Oran, The interaction of high-speed turbulence with flames: global properties and internal flame structure, Combust. Flame 157 (5) (2010) 995–1011.
[23] P.E. Hamlington, A.Y. Poludnenko, E.S. Oran, Interactions between turbulence and flames in premixed reacting flows, Phys. Fluids 23 (12) (2011) 125111.
[24] A.J. Aspden, M.S. Day, J.B. Bell, Turbulence–flame interactions in lean premixed hydrogen: transition to the distributed burning regime, J. Fluid Mech. 680 (2011) 287–320.
[25] E.R. Hawkes, O. Chatakonda, H. Kolla, A.R. Kerstein, J.H. Chen, A petascale direct numerical simulation study of the modelling of flame wrinkling for large-eddy simulations in intense turbulence, Combust. Flame 159 (8) (2012) 2690–2703.
[26] H. Kolla, E.R. Hawkes, A.R. Kerstein, N. Swaminathan, J.H. Chen, On velocity and reactive scalar spectra in turbulent premixed flames, J. Fluid Mech. 754 (2014) 456–487.
[27] C.A.Z. Towery, A.Y. Poludnenko, J. Urzay, J. O'Brien, M. Ihme, P.E. Hamlington, Spectral kinetic energy transfer in turbulent premixed reacting flows, Phys. Rev. E 93 (5) (2016) 053115.
[28] J. O'Brien, C.A.Z. Towery, P.E. Hamlington, M. Ihme, A.Y. Poludnenko, J. Urzay, The cross-scale physical-space transfer of kinetic energy in turbulent premixed flames, Proc. Combust. Inst. 36 (2) (2017) 1967–1975.
[29] J. Kim, M. Bassenne, C.A.Z. Towery, P.E. Hamlington, A.Y. Poludnenko, J. Urzay, Spatially-localized multi-scale energy transfer in turbulent premixed combustion, J. Fluid Mech. 848 (2018) 78–116.
[30] S.H.R. Whitman, P.E. Hamlington, C.A.Z. Towery, A.Y. Poludnenko, Scaling and collapse of conditional velocity structure functions in turbulent premixed flames, Proc. Combust. Inst. 37 (2) (2019) 2527–2535.
[31] R. Sankaran, H.G. Im, E.R. Hawkes, J.H. Chen, The effects of non-uniform temperature distribution on the ignition of a lean homogeneous hydrogen–air mixture, Proc. Combust. Inst. 30 (1) (2005) 875–882.
[32] J.H. Chen, E.R. Hawkes, R. Sankaran, S.D. Mason, H.G. Im, Direct numerical simulation of ignition front propagation in a constant volume with temperature inhomogeneities: I. fundamental analysis and diagnostics, Combust. Flame 145 (1) (2006) 128–144.
[33] E.R. Hawkes, R. Sankaran, P.P. Pébay, J.H. Chen, Direct numerical simulation of ignition front propagation in a constant volume with temperature inhomogeneities: II. Parametric study, Combust. Flame 145 (1) (2006) 145–159.
[34] C.S. Yoo, T. Lu, J.H. Chen, C.K. Law, Direct numerical simulations of ignition of a lean n-heptane/air mixture with temperature inhomogeneities at constant volume: parametric study, Combust. Flame 158 (9) (2011) 1727–1741.
[35] H.G. Im, P. Pal, M.S. Wooldridge, A.B. Mansfield, A regime diagram for autoignition of homogeneous reactant mixtures with turbulent velocity and temperature fluctuations, Combust. Sci. Technol. 187 (8) (2015) 1263–1275.
[36] M.A. Liberman, A.D. Kiverin, M.F. Ivanov, Regimes of chemical reaction waves initiated by nonuniform initial conditions for detailed chemical reaction models, Phys. Rev. E 85 (5) (2012) 056312.
[37] P. Dai, Z. Chen, S. Chen, Y. Ju, Numerical experiments on reaction front propagation in n-heptane/air mixture with temperature gradient, Proc. Combust. Inst. 35 (3) (2015) 3045–3052.
[38] R. Yu, X.S. Bai, Direct numerical simulation of lean hydrogen/air auto-ignition in a constant volume enclosure, Combust. Flame 160 (9) (2013) 1706–1716.
[39] J. Wang, Y. Yang, Y. Shi, Z. Xiao, X. He, S. Chen, Statistics and structures of pressure and density in compressible isotropic turbulence, J. Turbul. 14 (6) (2013) 21–37.
[40] D.A. Donzis, S. Jagannathan, Fluctuations of thermodynamic variables in stationary compressible turbulence, J. Fluid Mech. 733 (2013) 221–244.
[41] S. Jagannathan, D.A. Donzis, Reynolds and mach number scaling in solenoidally-forced compressible turbulence using high-resolution direct numerical simulations, J. Fluid Mech. 789 (2016) 669–707.
[42] K.K. Kuo, Principles of combustion, John Wiley & Sons, 1986.
[43] W. Fickett, W.C. Davis, Detonation: theory and experiment, Courier Corporation, 2000.
[44] S. Kao, J.E. Shepherd, Numerical Solution Methods for Control Volume Explosions and ZND Detonation Structure, Tech. Rep. GALCIT Report FM2006.007, Aeronautics and Mechanical Engineering, California Institute of Technology, Pasadena, CA, 2008.
[45] A.L. Sánchez, F.A. Williams, Recent advances in understanding of flammability characteristics of hydrogen, Prog. Energy Combust. Sci. 41 (2014) 1–55.
[46] B.J. McBride, S. Gordon, M.A. Reno, Coefficients for Calculating Thermodynamic and Transport Properties of Individual Species, NASA Technical Memorandum 4513, National Aeronautics and Space Administration, 1993.
[47] J.O. Hirschfelder, C.F. Curtiss, R.B. Bird, M.G. Mayer, Molecular Theory of Gases and Liquids, 26, John Wiley & Sons, New York, 1954.
[48] J. Warnatz, Influence of transport models and boundary conditions on flame structure, in: N. Peters, J. Warnatz (Eds.), Numerical Methods in Laminar Flame Propagation. Notes on Numerical Fluid Mechanics, 6, Vieweg+Teubner Verlag, Wiesbaden (1982), pp. 87–111.
[49] A. Ern, V. Giovangigli, Multicomponent Transport Algorithms, Lecture Notes in Physics Monographs, 24, Springer-Verlag Berlin, Heidelberg, 1994.
[50] P. Colella, Multidimensional upwind methods for hyperbolic conservation-laws, J. Comput. Phys. 87 (1990) 171–200.
[51] T.A. Gardiner, J.M. Stone, An unsplit Godunov method for ideal MHD via constrained transport in three dimensions, J. Comput. Phys. 227 (2008) 4123–4141.
[52] J.M. Stone, T.A. Gardiner, P. Teuben, J.F. Hawley, J.B. Simon, Athena: a new code for astrophysical MHD, Astrophys. J. Suppl. Ser. 178 (1) (2008) 137.
[53] R.J. Kee, F.M. Rupley, E. Meeks, J.A. Miller, CHEMKIN-III: a FORTRAN chemical kinetics package for the analysis of gas-phase chemical and plasma kinetics, Technical Report SAND-96-8216 (1996). Sandia National Labs, Livermore, CA
[54] F. Perini, E. Galligani, R.D. Reitz, An analytical Jacobian approach to sparse reaction kinetics for computationally efficient combustion modeling with large reaction mechanisms, Energy Fuels 26 (8) (2012) 4804–4822.
[55] P.E. Hamlington, R. Darragh, C.A. Briner, C.A.Z. Towery, A.Y. Poludnenko, Lagrangian analysis of high-speed turbulent premixed reacting flows: thermochemical trajectories in hydrogen-air flames, Combust. Flame 186 (2017) 193–207.
[56] A. Khokhlov, I. Domínguez, C. Bacon, B. Clifford, E. Baron, P. Hoeflich, K. Krisciunas, N. Suntzeff, L. Wang, Three-dimensional simulations of thermonuclear detonation with α-network: numerical method and preliminary results, Advances in Computational Astrophysics: Methods, Tools, and Outcome. Proceedings of a Conference Held at Cefalù, Italy 13 - 17 June 2011., ASP Conference Proceedings, 453, Astronomical Society of the Pacific, San Francisco (2012), p. 107.
[57] M.R. Petersen, D. Livescu, Forcing for statistically stationary compressible isotropic turbulence, Phys. Fluids 22 (11) (2010) 116101.
[58] J. Wang, T. Gotoh, T. Watanabe, Spectra and statistics in compressible isotropic turbulence, Phys. Rev. Fluids 2 (1) (2017) 013403.
[59] J.R. Ristorcelli, G.A. Blaisdell, Consistent initial conditions for the DNS of compressible turbulence, Phys. Fluids 9 (1) (1997) 4–6.
[60] R. Samtaney, D.I. Pullin, B. Kosović, Direct numerical simulation of decaying compressible turbulence and shocklet statistics, Phys. Fluids 13 (5) (2001) 1415–1430.
[61] T. Lewiner, H. Lopes, A.W. Vieira, G. Tavares, Efficient implementation of marching cubes' cases with topological guarantees, J. Graph. Tools 8 (2) (2003) 1–15.
[62] S. van der Walt, J.L. Schönberger, J. Nunez-Iglesias, F. Boulogne, J.D. Warner, N. Yager, E. Gouillart, T. Yu, The scikit-image contributors, Scikit-image: image processing in Python, PeerJ (2014) 2:e453.
[63] H. Akima, A new method of interpolation and smooth curve fitting based on local procedures, J. Assoc. Comput. Mach. 17 (4) (1970) 589–602.
[64] R.J. Kee, G. Dixon-Lewis, J. Warnatz, M.E. Coltrin, J.A. Miller, A Fortran computer code package for the evaluation of gas-phase, multicomponent transport properties, Technical Report SAND-86-8246, 1986. Sandia National Labs, Livermore, CA.

Available online at www.sciencedirect.com

ScienceDirect

Proceedings of the Combustion Institute 38 (2021) 2845–2852

Proceedings of the Combustion Institute

www.elsevier.com/locate/proci

Particle pair dispersion and eddy diffusivity in a high-speed premixed flame

Ryan Darragh [a], Colin A.Z. Towery [b], Alexei Y. Poludnenko [c,d], Peter E. Hamlington [b,*]

[a] Department of Aerospace Engineering Sciences, University of Colorado, Boulder 80309, USA
[b] Department of Mechanical Engineering, University of Colorado, Boulder 80309, USA
[c] Department of Mechanical Engineering, University of Connecticut, Storrs 06269, USA
[d] Department of Aerospace Engineering, Texas A& M University, College Station, TX 77843, USA

Received 8 November 2019; accepted 3 June 2020
Available online 18 August 2020

Abstract

Turbulent mixing is a physical process of fundamental importance in high-speed premixed flames. This mixing results in enhanced transport of temperature and chemical scalars, leading to potentially large changes in flame structure and dynamics. To understand turbulent mixing in non-reacting flows, a number of classical theories have been proposed to describe the scaling and statistics of dispersing fluid particle pairs, including predictions of the effective, or turbulent, eddy diffusivity. Here we examine the validity of these classical theories through the study of fluid particle pair dispersion and eddy diffusivity in a highly turbulent premixed methane-air flame at a Karlovitz number of approximately 140. Using data from a direct numerical simulation and a higher-order Lagrangian tracking algorithm, particle pair centroids are seeded at different initial temperatures and separations, and then integrated forward in time. We show that scaling relations and results developed for pair dispersion in non-reacting flows remain relevant in this high-intensity premixed flame, and we identify the impacts of heat release on dispersion and eddy diffusivity.
© 2020 The Combustion Institute. Published by Elsevier Inc. All rights reserved.

Keywords: Premixed flame; Turbulent combustion; Direct numerical simulation; Lagrangian analysis

1. Introduction

Turbulence leads to substantially enhanced rates of scalar mixing in a wide range of natural and engineering flows. This enhanced mixing is especially important in turbulent premixed combustion, since the properties and evolution of scalar quantities such as temperature and fuel mass fraction have leading-order effects on the rate of fuel consumption and heat release. Moreover, in many high-speed practical applications such as scramjets and detonation engines, the turbulence intensity is high and turbulent mixing can substantially alter the structure of the flame, leading to, for example, flame broadening, distributed burning, and broken reaction zones [1].

* Corresponding author.
E-mail address: peh@colorado.edu (P.E. Hamlington).

https://doi.org/10.1016/j.proci.2020.06.056
1540-7489 © 2020 The Combustion Institute. Published by Elsevier Inc. All rights reserved.

Although turbulent mixing is fundamentally an advective process whereby large turbulence-induced scalar gradients lead to more rapid molecular transport, this overall process is often referred to as simply "turbulent diffusion." Beginning with the foundational work by Richardson [2], and recognizing the fundamental connection to turbulent advection, a common approach to studying turbulent diffusion has been to examine the dispersion, or separation, of pairs of fluid particles. In cases where particles separate more rapidly, turbulent diffusion is stronger, and Richardson [2] predicted that the turbulent diffusivity is related to the 4/3 power of the distance between the two particles. This relation has since been extensively studied and validated in a variety of non-reacting turbulent flows [3–9].

Substantially less focus has been placed on the connection between fluid particle dispersion and turbulent diffusivity in reacting flows. Chaudhuri [10] examined the dispersion of pairs of flame (as opposed to fluid) particles during hydrogen-air premixed combustion, finding that the early-time behavior of the particle pairs is non-universal and varies based on the temperature of the isosurface on which the flame particles reside. For the fluid particles that are the focus of the present study, however, this dependence on flame location may not be as strong, particularly at high turbulence intensities. Indeed, other tests of classical turbulence theories (such as the Kolmogorov hypotheses and corresponding scaling laws) have shown that turbulence properties during high-speed premixed combustion are generally similar to those found in non-reacting flows (e.g., [11–13]).

In the present study, we seek to understand whether heat release affects pair dispersion and turbulent diffusion in highly turbulent premixed flames, and whether classical theories from non-reacting turbulence remain applicable for such conditions. This study will address three questions in particular: (i) Are classical scaling laws and relations derived for non-reacting turbulent dispersion applicable in high-speed premixed combustion? (ii) How does heat release affect particle dispersion and the applicability of classical scaling laws and relations? (iii) How does turbulent diffusion vary at different locations within a premixed flame?

We address these questions by tracking pairs of fluid particles in a direct numerical simulation (DNS) of a premixed methane-air flame with a Karlovitz number (Ka) of roughly 140. In the following, we provide background on the study of particle pair dispersion and describe the DNS and analysis. We then show that theories developed for pair dispersion in non-reacting flows are applicable in this high-intensity premixed flame, with relatively limited impacts of heat release on dispersion and the turbulent effective eddy diffusivity.

2. Background

Fluid particle pairs consist of two infinitesimal parcels of fluid whose motions are determined by the local instantaneous flow velocity. The locations of each particle are denoted $\boldsymbol{x}^{(1)}(t)$ and $\boldsymbol{x}^{(2)}(t)$, where $t = 0$ corresponds to the time at which particle tracking begins (or when the particles are released). The instantaneous displacement between the two particles is $\boldsymbol{D}(t) = \boldsymbol{x}^{(2)}(t) - \boldsymbol{x}^{(1)}(t)$, where the initial displacement is $\boldsymbol{D}_0 = \boldsymbol{D}(0)$ and the initial separation distance is $D_0 = |\boldsymbol{D}_0|$. The relative displacement of a single particle is $\boldsymbol{R} = \boldsymbol{D} - \boldsymbol{D}_0$, and the mean-square relative displacement is $\langle R^2 \rangle = \langle |\boldsymbol{D}(t) - \boldsymbol{D}_0|^2 \rangle$, where $R = |\boldsymbol{R}|$ and $\langle \cdot \rangle$ indicates an average over all tracked pairs in a flow. In the present analysis of premixed flames, this average is taken over all particle pairs released with a centroid at a particular value of the temperature.

The temporal scaling of $\langle R^2 \rangle$ changes as particle pairs evolve and separate. At very small times, particles evolve ballistically and at intermediate times they enter the Richardson range, which is analogous to the inertial range identified by Kolmogorov [14]. At large times, the particles in a pair become decorrelated and independent of their initial separation, thus entering the diffusive range described by Taylor [15]. Each of these ranges are outlined in the following sections.

2.1. Ballistic range

At very small times, particle velocities are roughly constant [16]. If $D_0 \gg \eta$, where $\eta = (\nu^3/\varepsilon)^{1/4}$ is the Kolmogorov length scale given kinematic viscosity ν and the average rate of turbulence kinetic energy dissipation ε, then this will hold for times $0 \leq t \ll t_0$, where $t_0 = D_0^{2/3}/\varepsilon^{1/3}$ is the Batchelor time, defined as the eddy turnover time at the length scale of the initial particle separation. If $D_0 \ll \eta$, then the velocities will be roughly constant in the range $0 \leq t \ll t_\eta$ [14], where $t_\eta = (\nu/\varepsilon)^{1/2}$ is the Kolmogorov time. While a pair of particles is in this range, their displacement can be approximated by a Taylor expansion about $t = 0$ as [17]

$$\boldsymbol{D}(t) = \boldsymbol{D}_0 + \delta \boldsymbol{v}_0 t + \frac{1}{2}\delta \boldsymbol{a}_0 t^2 + \mathcal{O}\left(t^3\right), \tag{1}$$

where $\delta \boldsymbol{v}_0 = \partial \boldsymbol{D}(t)/\partial t|_{t=0}$ and $\delta \boldsymbol{a}_0 = \partial^2 \boldsymbol{D}(t)/\partial t^2|_{t=0}$ are, respectively, the relative velocity and acceleration at $t = 0$. The mean-square relative displacement in the ballistic range is thus given by

$$\left\langle R^2 \right\rangle(t) = \langle \delta \boldsymbol{v}_0 \cdot \delta \boldsymbol{v}_0 \rangle t^2 + \langle \delta \boldsymbol{v}_0 \cdot \delta \boldsymbol{a}_0 \rangle t^3 + \mathcal{O}\left(t^4\right). \tag{2}$$

For very small times, the leading order term is dominant, and the t^2 dependence of $\langle R^2 \rangle$ is a characteristic feature of particles separating in the ballistic range.

2.2. Richardson range

If the initial separation of the particles is much less than the energy injection scale, eddies larger than D_0 will advect the particles together, changing their position in space but not the relative distance between the pair. By the locality hypothesis [2], only eddies of a size similar to the separation distance are expected to be effective at changing the relative distance between particles. If, additionally, $D_0 \gg \eta$ and t is large enough such that initial conditions have been forgotten, or if $D_0 \ll \eta$ and the later time separation distance is in the inertial range, Kolmogorov's second hypothesis of scale similarity applies, assuming a large enough Reynolds number [14]. Consequently, it can be assumed that the statistics will depend only on the length scale and ε. By taking the time-dependent distance between two particles, $D(t) = |\boldsymbol{D}(t)|$, as the length scale and combining it with ε, the turbulent diffusivity is given as [2]

$$K\left(\langle D^2\rangle\right) = k_0 \varepsilon^{1/3} \langle D^2\rangle^{2/3}, \tag{3}$$

where k_0 is a dimensionless constant. This relation is known as the four-thirds law and is attributed to Richardson, who arrived at it experimentally, and to Obhukhov, who derived it using similar arguments to those presented here [2,14,18]. This law is analogous to the Kolmogorov four-fifths law for the scaling of third order structure functions [14] and states that the diffusivity increases with separation distance.

The scaling of $\langle R^2\rangle(t)$ in the Richardson range can be obtained by combining Eq. (3) with Einstein's definition of fluid particle diffusivity, given as [19]

$$K\left(\langle D^2\rangle\right) = \frac{1}{6}\frac{d\langle D^2\rangle}{dt}. \tag{4}$$

Integrating this definition using Eq. (3) yields

$$\langle R^2\rangle(t) = g\varepsilon t^3, \tag{5}$$

where g is the dimensionless Richardson constant. Although g has traditionally been difficult to measure precisely [4], recent estimates have ranged from roughly 0.5 to 0.6 [20–25]. In order to accurately determine g, there must be a large separation of scales, thus requiring a sufficiently high Reynolds number in the flow.

In addition to the predicted t^3 scaling of $\langle R^2\rangle$ in the Richardson range, both Richardson [2] and Batchelor [16] provided analytical predictions for the distribution of relative separation distances R. In particular, Richardson predicted that the probability density function (pdf) of $R' = R/\langle R^2\rangle^{1/2}$, denoted $p(R', t)$, should obey the isotropic diffusion equation [2,14]

$$\frac{\partial p(R',t)}{\partial t} = \frac{1}{R'^2}\frac{\partial}{\partial R'}\left[R'^2 K(R',t)\frac{\partial p(R',t)}{\partial R'}\right], \tag{6}$$

which can be solved [24] as

$$p(R',t) = \alpha R'^2 \exp\left(-\beta R'^{2/3}\right), \tag{7}$$

where $\alpha = 117$ and $\beta = 5.44$. By contrast, Batchelor predicted a Gaussian distribution for $p(R', t)$ by arguing that integration over the velocity amounts to an application of the central limit theorem [16]. In practice, for non-reacting flows, the Richardson solution in Eq. (7) has been observed at intermediate times, and a Gaussian-like distribution has been observed at later times outside the Richardson range [4,26].

2.3. Diffusive range

At very long times, the particles in each pair become decorrelated and spread according to single particle statistics. Practically, Taylor [15] showed that, in this "diffusive" range, the mean-square separation between two particles increases linearly with t, and there is no dependence on the initial separation. Here we track particle pairs over sufficiently long durations to capture the scaling of $\langle R^2\rangle$ in both the ballistic and Richardson ranges, but only begin to approach this diffusive range scaling. However, it will be seen that the Gaussian-like prediction for $p(R', t)$ from Batchelor is approximately recovered at long times in high-intensity turbulent premixed flames, consistent with observations in non-reacting turbulence [26].

3. Direct numerical simulation

A direct numerical simulation (DNS) of premixed methane-air combustion has been performed by solving the compressible reactive-flow Navier-Stokes equations [27] using `Athena-RFX` [28,29]. This code solves the governing equations on a fixed, equispaced, three-dimensional (3D) mesh using the unsplit corner transport upwind scheme [30,31] with a nonlinear HLLC Riemann solver and piecewise-parabolic spatial reconstruction. Periodic forcing at the scale of the domain width, L, is performed throughout the entire domain and has been confirmed to produce statistically stationary turbulent flames [29]. Overall, the simulation has third-order spatial and second-order temporal accuracy. A 19-step reduced chemical mechanism [32] is used to model stoichiometric methane-air combustion at atmospheric conditions. All physical parameters used to initialize and setup the simulations are shown in Table 1.

The computational domain consists of an unconfined prismatic box with an aspect ratio of $1 \times 1 \times 16$, with periodic boundaries in all three directions prior to ignition; this configuration has been described in numerous previous studies (e.g., [11,13,29,33]). Turbulence develops in the domain for one large-scale eddy turnover time τ_L (see

Table 1
Physical model parameters of the premixed methane-air flame DNS examined in the present study.

L	0.70037 cm	Domain width
T_r	300 K	Unburnt temperature
P_r	1.01325×10^6 erg/cm^3	Unburnt pressure
ρ_r	1.12×10^{-3} g/cm^3	Unburnt density
δ_f	4.38×10^{-2} cm	Laminar thermal width
S_f	37.2 cm/s	Laminar flame speed
ℓ	2.05×10^{-1} cm	Unburnt integral scale
U'_ℓ	785 cm/s	Unburnt integral vel.
τ_L	5.922×10^{-4} s	Eddy turnover time
Da	0.19	Damköhler number
Ka	142	Karlovitz number
ε	1.181×10^9 erg/g s	Energy dissipation rate
η_r	1.382×10^{-3} cm	Unburnt Kolm. length
η_p	1.734×10^{-2} cm	Burnt Kolm. length
t_{η_r}	1.174×10^{-5} s	Unburnt Kolm. time
t_{η_p}	6.340×10^{-5} s	Burnt Kolm. time
Re_{T_r}	87	Unburnt Reyn. number
Re_{T_p}	28	Burnt Reyn. number

Table 1) before a planar laminar flame with a normal direction along the z axis is introduced near the center of the domain. After ignition, the z boundary conditions are switched to be zero-order extrapolation, allowing flow into and out of the domain, while the x and y boundaries remain periodic.

The simulation domain is discretized using $256 \times 256 \times 4096$ grid cells, giving a resolution of 2.7×10^{-3} cm. This provides half a grid cell per unburnt Kolmogorov scale, η_r, and six grid cells per burnt Kolmogorov scale, η_p (see Table 1). This also corresponds to 16 grid cells per laminar flame thermal width δ_f, which was found in previous studies [29] to be sufficient for resolving the flame when thin radical regions are largely absent, as is the case in the present methane-air flame. The simulation is run for one τ_L prior to ignition and is then run for another one τ_L prior to starting data collection. At this point, data are output at a high frequency to allow the calculation of Lagrangian trajectories; the data collection occurs over roughly $5\tau_L$.

Using the 3D volumes of velocity output by the DNS, fluid particles are tracked using a Lagrangian algorithm [33,34]. Each particle is evolved in time using 4th and 5th order Runge-Kutta time integration to check accuracy; the 5th-order results are used in the present analysis. Spatial and temporal interpolations are performed using Akima splines, giving at least 2nd order accuracy.

The centroids of particle pairs are seeded uniformly in spanwise (i.e., $x - y$) planes at specific values of the temperature along the z direction. The particle pairs are centered at 300, 600, 1000, 1400, 1800, and 2100 K, giving results that span the unburnt reactants, flame region, and burnt products, as well as within the preheat zone where mixing is strongest. At each centroid, three pairs of particles are seeded in the x, y, and z directions, with initial pair separations of $D_0/\eta_r = 1/8$, 1/4, 1, 4, 16, and 32. In total, we examine 65,536 particle pairs at each temperature for each initial separation, resulting in over 14 million trajectories in the present study.

Each particle pair is tracked for $5\tau_L$, corresponding to roughly three thermal-width flame crossing times $t_f = \delta_f/S_f = 1.2$ ms. The analysis is, however, focused almost entirely on times less than t_f, suggesting that the present results are indicative of particle behavior within the flame. In particular, t_{η_p}, corresponding to the approximate end of the ballistic range, is nearly 20 times smaller than t_f, and the integral time scale t_ℓ, roughly corresponding to the end of the Richardson range, is nearly 1.5 times smaller. As a result, only 0.23% of particles with initial centroids at 300 K reached a temperature of 1800 K (roughly corresponding to the end of the region of peak heat release) by t_{η_p} and 28% of these particles reached this temperature by t_ℓ. For the higher centroid temperature of 1400 K, only 37% of particles reached 1800 K by t_{η_p}, with 81% by t_ℓ. Thus, many of the particles remain within the flame for the duration of the ballistic and Richardson ranges, both of which end before the characteristic flame crossing time t_f.

4. Results and discussion

4.1. Particle dispersion scaling and statistics

The time evolution of $\langle R^2 \rangle$ for particle pairs released with an initial separation in the z direction is shown in Fig. 1. Results for initial separations in the x and y directions are similar and are not shown here. In Fig. 1(a), $\langle R^2 \rangle$ is normalized by η_p, and time is normalized by t_{η_p}, both taken in the products (see Table 1). At small times, $\langle R^2 \rangle$ for each initial separation exhibits a t^2 scaling, as expected in the ballistic range, with relatively small differences in the time evolution based on the temperature. There is, however, an offset in $\langle R^2 \rangle$ that depends on temperature, with smaller values of $\langle R^2 \rangle$ occurring for higher temperatures. This is most likely due to differences in the temperature-dependent local viscosity at the particle centroids, while the subsequent evolution of $\langle R^2 \rangle$ is largely independent of temperature.

At intermediate times, the displacement speed begins to increase, as indicated by an increasing slope of $\langle R^2 \rangle$ in Fig. 1(a). Of the initial separations shown, only those with the largest D_0 appear to approach the t^3 scaling predicted in the Richardson range. Pairs with a smaller D_0 achieve a greater than t^3 scaling due to the relatively low Reynolds number of the present case and the resulting influences from the ballistic (i.e., short time) and diffusive (i.e., long time) ranges. Within this range, however, there is relatively little observed temperature

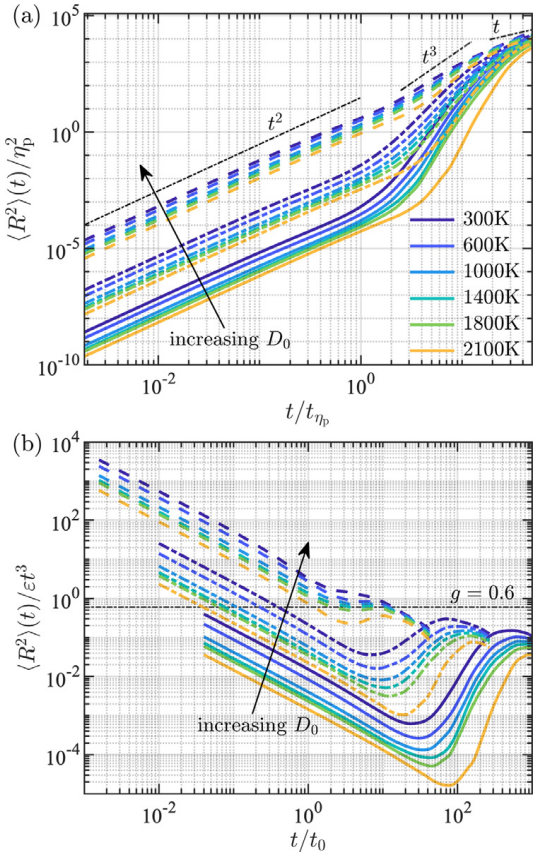


Fig. 1. Uncompensated (a) and compensated (b) time series of the mean-square relative separation $\langle R^2\rangle(t)$ for particle pairs initially separated in the z direction with centroids at six different temperatures. Results are shown for initial displacements $D_0/\eta_r = 1/8$ (solid lines), 1 (dash-dot lines) and 16 (dashed lines). The horizontal dash-dot line in (b) indicates the estimated value of the Richardson constant reported by Sawford et al. [25], $g = 0.6$.

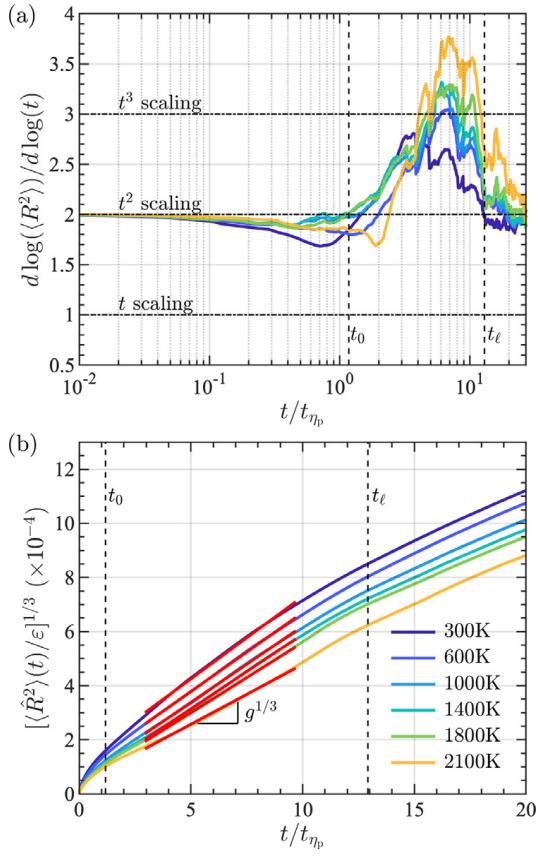


Fig. 2. Local scaling exponent of $\langle R^2\rangle(t)$ from $d\log(\langle R^2\rangle)/d\log(t)$ for $D_0/\eta_r = 16$ (a). Panel (b) shows local linear fits of $\left[\langle \hat{R}^2\rangle(t)/\varepsilon\right]^{1/3}$ (red lines), giving the Richardson constant as $g^{1/3}$.

dependence beyond that which may be attributed to variations in the temperature-dependent viscosity. At large times, displacements approach linear scaling with t as particle pairs become decorrelated in the diffusive range and lose their dependence on the initial separation.

The compensated mean-square relative displacements, $\langle R^2\rangle/\varepsilon t^3$, shown as a function of t/t_0 in Fig. 1(b), indicate the time period over which the Richardson range scaling is present. Here we use a constant value of ε for all separations and temperatures, since it has been shown that ε is only weakly dependent on temperature in high-Karlovitz number flames [13]. The theory from Richardson [2] states that, if D_0 for a pair of particles is in the inertial range, then the corresponding compensated displacement will decrease linearly until leveling off at a plateau. This linear decrease is expected from the ballistic scaling [16], and the plateau corresponds to the scaling from Eq. (5) in the Richardson range.

Both the linear decrease and the plateau are evident in Fig. 1(b) for $D_0/\eta_r = 16$. By contrast, $\langle R^2\rangle/\varepsilon t^3$ for particle pairs with smaller D_0 falls below the plateau before approaching it from below. This is because the separation distance must be in the inertial range to be on the plateau, and since the separation is increasing it will eventually be in the inertial range. In order to hit the plateau, however, the separation distance must be in the inertial range after the particles have forgotten their initial conditions; i.e., after the max of t_η and t_0, but before they become affected by large-scale effects. Thus, if the particles do not separate fast enough, they may never approach the plateau, as shown in Fig. 1(b) for the pairs with smaller initial separations.

The range over which the t^3 scaling of $\langle R^2\rangle$ applies is further indicated by the derivatives of $\log(\langle R^2\rangle)$ with respect to $\log(t)$ for $D_0/\eta_r = 16$, shown in Fig. 2(a). For $t < t_{\eta_p}$, $\langle R^2\rangle$ at all temperatures scales as t^2. Between t_0 and t_ℓ, by contrast, $\langle R^2\rangle$ for all temperatures approaches the Richardson range scaling of t^3. Due to the relatively low Reynolds number of the present case, the range over which this t^3 scaling applies is relatively small,

and there does seem to be a temperature dependence of the scaling exponent. In particular, the intermediate temperature results more completely reach the t^3 scaling, while the lowest and highest temperatures have scaling exponents below and above three, respectively. For $t > t_\ell$, the scaling exponents decrease as the particle pairs enter the diffusive range.

The Richardson constant g can be estimated from the curves of $\left[\langle \hat{R}^2 \rangle(t)/\varepsilon\right]^{1/3}$ shown in Fig. 2(b), where $\hat{R} = |\boldsymbol{D}(t) - \boldsymbol{D}_0 - \delta \boldsymbol{v}_0 t|$, as a function of t within the Richardson range [21,24,25] for $D_0/\eta_r = 16$. The subtraction of the relative velocity $\delta \boldsymbol{v}_0 t$ is required to reduce the impact of the ballistic range scaling on the estimate of g (for further details, see [25]). Given the relation in Eq. (5), the slopes of these curves, shown in Fig. 2(b), give $g^{1/3}$. Estimates of g for initial centroid temperatures within the flame (i.e., for 1000 K, 1400 K, and 1800 K) are between 0.55 and 0.70, bracketing the classical non-reacting value $g = 0.6$ estimated by Sawford et al. [25]. There is some temperature dependence of this constant, however, with g decreasing from a maximum value of 0.88 at 300 K to 0.34 at 2100 K. This indicates that, within the Richardson range for large D_0, the scaling relation in Eq. (5) is valid in high-intensity turbulent premixed flames, but that the Richardson constant is temperature-dependent, generally decreasing with increasing temperature.

The pdfs of R' in Fig. 3 provide a test of the Richardson prediction in Eq. (7) and the Gaussian-like prediction from Batchelor. At intermediate times in Fig. 3(a), the pdfs for each temperature are in good agreement with the Richardson prediction. The pdfs at time $t/t_0 = 4$ shown in Fig. 3(a) correspond to the t^3 scaling range indicated in Fig. 2, further suggesting that we do capture a relatively short Richardson range in these simulations, despite the low Reynolds number.

By contrast, the pdfs at $t/t_0 = 25$ in Fig. 3(b) are in much closer agreement with the Gaussian-like pdf. This corresponds to times greater than t_ℓ where we would expect diffusive range behavior, and the recovery of the Gaussian-like pdf in Fig. 3(b) is consistent with prior results at long times in non-reacting turbulence [24,25]. It should be noted that there is no apparent temperature dependence of the pdfs in Fig. 3 at either time, and the results from Richardson and Batchelor thus appear to be independent of the location in the flame.

Finally, we note that these results are specific to the particular type of conditioning used in this analysis. That is, we examine the dispersion and subsequent evolution of fluid particles beginning at the same location within the premixed flame. However, after initialization, the particles are free to then separate such that either particle may re-enter the unburnt reactants, proceed to the burnt products, or remain within the flame. Fig. 4 shows

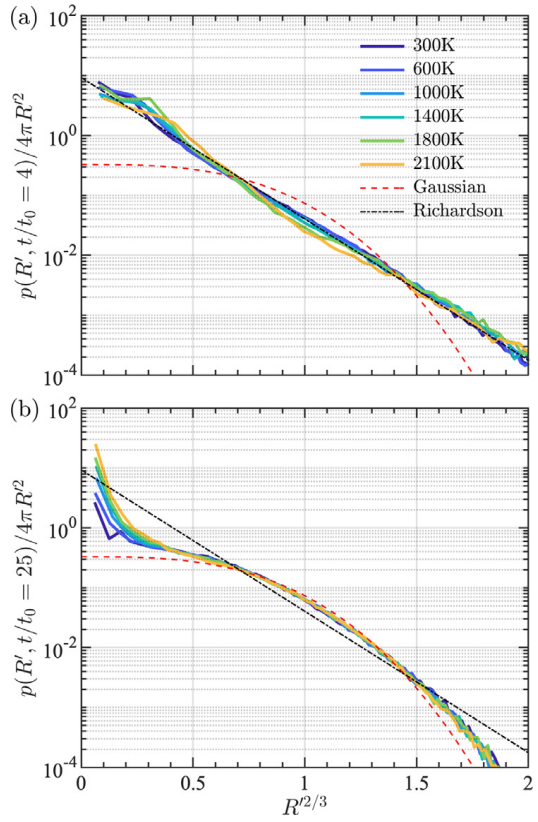


Fig. 3. Probability density functions (pdfs) of $R' = R/\langle R^2 \rangle^{1/2}$ for $D_0/\eta_r = 16$ at (a) $t/t_0 = 4$ and (b) $t/t_0 = 25$. Gaussian distributions and the Richardson prediction from Eq. (7) are also shown.

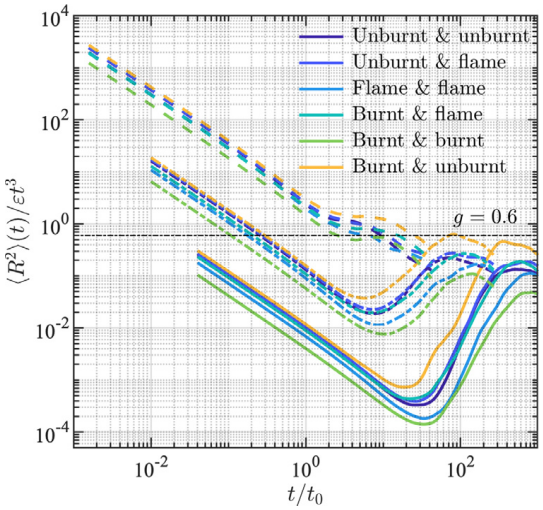


Fig. 4. Compensated time series of $\langle R^2 \rangle(t)$ conditioned on the location of each particle at $t = t_f$ in either the unburnt reactants ($T < 500$ K), flame region ($500\,\text{K} \le T \le 1800\,\text{K}$), or burnt products ($T > 1800$ K). Results are shown for initial displacements $D_0/\eta_r = 1/8$ (solid lines), 1 (dash-dot lines) and 16 (dashed lines).

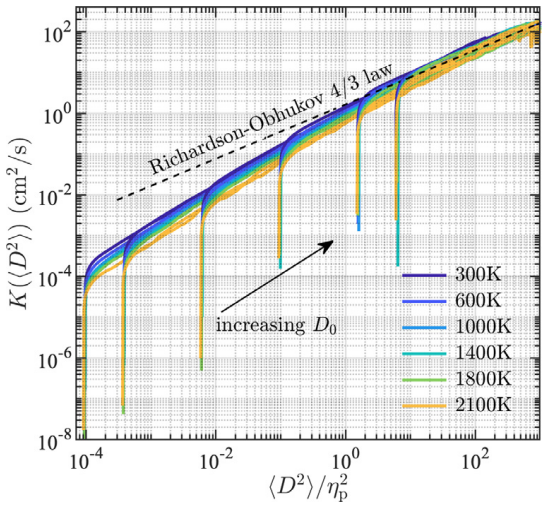


Fig. 5. Turbulent diffusivity $K(\langle D^2\rangle)$ for each initial separation and centroid temperature. Diffusivities for increasing D_0 increase along the direction indicated by the arrow. The dashed black line corresponds to the Richardson-Obhukov 4/3 law in Eq. (3).

results for the compensated mean-square relative displacements, $\langle R^2\rangle/\varepsilon t^3$, depending on whether each particle was in the unburnt reactants (defined as $T < 500$ K), burnt products ($T > 1800$ K), or within the flame ($500\,\text{K} \le T \le 1800\,\text{K}$) at $t = t_f$. In general, these results are largely consistent with the results shown in Fig. 1(b), revealing a dependence on the final locations of the particles, although there is still a general correspondence to classical scaling laws in the ballistic, Richardson, and diffusive ranges. Further conditioning of these results is left as a direction for future research.

4.2. Turbulent diffusivity

The effective eddy, or turbulent, diffusivity is computed from the calculated values of $\langle D^2\rangle(t)$ for each temperature and initial separation using Eq. (4). Fig. 5 shows that $K(\langle D^2\rangle)$ increases with $\langle D^2\rangle$ and approaches the Richardson–Obhukov four-thirds scaling law from Eq. (3) for large $\langle D^2\rangle$. Significantly, results for all temperatures and initial separations approach this scaling law, although there is a persistent difference in the magnitude of K with temperature. In particular, K is largest for small temperatures, corresponding to locations within the preheat zone of the flame where mixing is strongest, and smallest for large temperatures, corresponding to locations in the fully burnt products.

From a modeling perspective, Fig. 5 suggests that the scaling relation between particle pair dispersion and turbulent diffusivity is independent of location in the flame for the highly-turbulent case examined here, but the magnitude of the diffusivity does vary through the flame. This indicates that there may be predictable and potentially universal aspects of turbulent mixing in high-speed combustion. However, further studies spanning a broader range of flow configurations and turbulence conditions must be explored before predictability or universality can be fully established.

5. Conclusions

Using data from a DNS of a highly-turbulent methane-air premixed flame and a Lagrangian analysis, we have examined the dispersion of fluid particle pairs in high-speed premixed combustion. In general, scaling laws and statistical relations in the ballistic, Richardson, and diffusive ranges developed for non-reacting pair dispersion are found to remain largely valid in the highly-turbulent premixed flame examined here. In particular, despite the relatively low Reynolds number of the present case, we observe t^3 scaling of the mean-square relative separation $\langle R^2\rangle$ and a correspondence with the Richardson pdf for particle displacements in Eq. (7); both of these results indicate the recovery of the Richardson range in the simulations.

The Richardson constant was estimated using the cubic local slope approach and found to have a value of $g \approx 0.6$ for intermediate temperatures within the flame, in agreement with previous non-reacting studies at higher Reynolds numbers. For lower and higher temperatures, however, the Richardson constant was found to be larger and smaller, respectively, than the classical value. Finally, turbulence diffusivity was found to approach the Richardson-Obhukov law in Eq. (3) for all initial temperatures and separations, although the magnitude of the diffusivity was temperature dependent.

Overall, this study suggests that many aspects of fluid particle dispersion and turbulent diffusivity are largely similar to non-reacting results for turbulent premixed flames at high turbulence intensities. We do observe a dependence on temperature and, hence, location in the flame, but many of these differences may be due solely to changes in the local viscosity and dissipation rate, both of which are temperature dependent. This suggests that classical non-reacting theories of turbulence and models for turbulent mixing may be relevant at such highly-turbulent conditions. Future research is, however, required to expand the generality of these results for other fuels and flame configurations, including realistic flow configurations where mean shear is present, as well as to examine the applicability of non-reacting results as the turbulence intensity decreases.

Declaration of Competing Interest

None.

Acknowledgments

RD was supported by a National Defense Science and Engineering Graduate Fellowship. CAZT and PEH were supported, in part, by AFOSR award FA9550-17-1-0144 and NSF award 1847111. AYP acknowledges support from AFOSR awards 12RSA-MFD001 and 15RT0942.

References

[1] J.F. Driscoll, J.H. Chen, A.W. Skiba, C.D. Carter, E.R. Hawkes, H. Wang, *Progr. Energy Combust. Sci.* 76 (2020) 100802.
[2] L.F. Richardson, *Proc. R. Soc. Lond. Ser. A Contain. Pap. Math. Phys. Charact.* 110 (1926) 709–737.
[3] G. Falkovich, K. Gawędzki, M. Vergassola, *Rev. Mod. Phys* 73 (2001) 913–975.
[4] B. Sawford, *Annu. Rev. Fluid Mech.* 33 (2001) 289–317.
[5] J.P. Salazar, L.R. Collins, *Annu. Rev. Fluid Mech.* 41 (2008) 405–432.
[6] R. Scatamacchia, L. Biferale, F. Toschi, *Phys. Rev. Lett.* 109 (2012) 144501.
[7] N.A. Malik, *PLOS ONE* 13 (2018) 1–29.
[8] L. Biferale, A. Lanotte, R. Scatamacchia, F. Toschi, *J. Fluid Mech.* 757 (2014) 550–572.
[9] R. Bitane, H. Homann, J. Bec, *Phys. Rev. E* 86 (2012) 045302.
[10] S. Chaudhuri, *Phys. Rev. E* 91 (2015) 021001.
[11] P.E. Hamlington, A.Y. Poludnenko, E.S. Oran, *Phys. Fluids (1994-Present)* 23 (2011) 125111.
[12] B. Bobbitt, S. Lapointe, G. Blanquart, *Phys. Fluids (1994-Present)* 28 (2016) 015101.
[13] S.H. Whitman, C.A. Towery, A.Y. Poludnenko, P.E. Hamlington, *Proc. Combust. Inst.* 37 (2019) 2527–2535.
[14] A. Monin, A.M. Yaglom, Statistical fluid mechanics, v2, 1975,
[15] G.I. Taylor, *Proc. Lond. Math. Soc.* s2-20 (1922) 196–212.
[16] G. Batchelor, *Mathematical Proceedings of the Cambridge Philosophical Society* 48 (1952) 345–362.
[17] J.I. Polanco, I. Vinkovic, N. Stelzenmuller, N. Mordant, M. Bourgoin, *International Journal of Heat and Fluid Flow* 71 (2018) 231–245.
[18] A. Obukhov, *Bull. Acad. Sci. USSR, Geog. Geophys.* 5 (1941) 453–466.
[19] A. Einstein, *Ann. Phys.* 17 (1905) 549–560.
[20] M.-C. Jullien, J. Paret, P. Tabeling, *Phys. Rev. Lett.* 82 (1999) 2872–2875.
[21] S. Ott, J. Mann, *J. Fluid Mech.* 422 (2000) 207–223.
[22] G. Boffetta, I.M. Sokolov, *Phys. Rev. Lett.* 88 (2002) 094501.
[23] L. Biferale, G. Boffetta, A. Celani, B.J. Devenish, A. Lanotte, F. Toschi, *Phys. Fluids* 17 (2005) 111701.
[24] D. Buaria, B.L. Sawford, P.K. Yeung, *Phys. Fluids* 27 (2015) 105101.
[25] B.L. Sawford, P.K. Yeung, J.F. Hackl, *Phys. Fluids* 20 (2008) 065111.
[26] J. Schumacher, *Phys. Rev. Lett.* 100 (2008) 134502.
[27] C.A.Z. Towery, A.Y. Poludnenko, J. Urzay, J. O'Brien, M. Ihme, P.E. Hamlington, *Physi. Rev. E* 93 (2016) 053115.
[28] J.M. Stone, T.A. Gardiner, P. Teuben, J.F. Hawley, J.B. Simon, *Astrophys. J. Suppl. Ser.* 178 (2008) 137–177.
[29] A.Y. Poludnenko, E.S. Oran, *Combust. Flame* 157 (2010) 995–1011.
[30] P. Colella, *J. Comput. Phys.* 87 (1990) 171–200.
[31] J. Saltzman, *J. Comput. Phys.* 115 (1994) 153–168.
[32] A. Vié, B. Franzelli, Y. Gao, T. Lu, H. Wang, M. Ihme, *Proc. Combust. Inst.* 35 (2015) 1675–1683.
[33] P.E. Hamlington, R. Darragh, C.A. Briner, C.A. Towery, B.D. Taylor, A.Y. Poludnenko, *Combust. Flame* 186 (2017) 193–207.
[34] R.A. Darragh, C.A. Towery, P.E. Hamlington, A. Poludnenko, in: Proceedings of the Forty-seventh AIAA Fluid Dynamics Conference, 2017, p. 3466.

Physics of Fluids

Lagrangian analysis of enstrophy dynamics in a highly turbulent premixed flame

Cite as: Phys. Fluids **33**, 055120 (2021); https://doi.org/10.1063/5.0042571
Submitted: 31 December 2020 . Accepted: 12 April 2021 . Published Online: 17 May 2021

Ryan Darragh, Colin A. Z. Towery, Michael A. Meehan, and Peter E. Hamlington

COLLECTIONS

Note: This paper is part of the special topic, In Memory of Edward E. (Ted) O'Brien.

This paper was selected as an Editor's Pick

View Online Export Citation CrossMark

Physics of Fluids
SPECIAL TOPIC: Tribute to
Frank M. White on his 88th Anniversary
SUBMIT TODAY!

AIP Publishing

© 2021 Author(s).

Physics of Fluids ARTICLE scitation.org/journal/phf

Lagrangian analysis of enstrophy dynamics in a highly turbulent premixed flame

Cite as: Phys. Fluids **33**, 055120 (2021); doi: 10.1063/5.0042571
Submitted: 31 December 2020 · Accepted: 12 April 2021 ·
Published Online: 17 May 2021

View Online Export Citation CrossMark

Ryan Darragh,[1] Colin A. Z. Towery,[2] Michael A. Meehan,[2] and Peter E. Hamlington[2,a)]

AFFILIATIONS

[1]Ann and H.J. Smead Department of Aerospace Engineering Sciences, University of Colorado, Boulder, Colorado 80309, USA
[2]Paul M. Rady Department of Mechanical Engineering, University of Colorado, Boulder, Colorado 80309, USA

Note: This paper is part of the special topic, In Memory of Edward E. (Ted) O'Brien.
[a)]**Author to whom correspondence should be addressed:** peter.hamlington@colorado.edu

ABSTRACT

A Lagrangian analysis approach is used to examine the effects of heat release on the dynamics of the enstrophy during highly turbulent premixed combustion. The analysis is performed using data from a direct numerical simulation of a statistically planar premixed methane–air flame at a Karlovitz number of 100. Through cumulative, conditional, and correlation analyses, we show, consistent with prior studies, that vortex stretching and baroclinic torque both increase enstrophy at these highly turbulent conditions, while viscous transport and dilatation both lead to enstrophy destruction. However, although vortex stretching and viscous transport are individually an order of magnitude greater than all other terms in the enstrophy budget, the cumulative and combined effect of these two terms along Lagrangian trajectories is roughly only twice as large as the combined cumulative effect of dilatation and baroclinic torque. Moreover, trajectories that exhibit an increase in enstrophy through the flame are found to frequently have cumulative contributions from budget terms outside a single standard deviation of the mean contribution, indicating that enstrophy production at such highly turbulent conditions is associated with relatively infrequent but large values of dynamical terms. Lagged correlations further reveal a small but measurable contribution of baroclinic torque in enstrophy production, but these increases are overwhelmed, on average, by concurrent decreases in enstrophy due to viscous transport and dilatation. Taken together, these results provide further understanding of enstrophy dynamics in highly turbulent premixed flames.

Published under an exclusive license by AIP Publishing. https://doi.org/10.1063/5.0042571

I. INTRODUCTION

The effects of turbulent premixed flames on the characteristics and dynamics of the enstrophy, $\Omega = \omega_i\omega_i$ (where $\omega_i = \varepsilon_{ijk}\partial u_k/\partial x_j$ is the vorticity vector, ε_{ijk} is the cyclic permutation tensor, and u_k is the velocity vector) have received considerable attention over the past decade. Because it is a gradient-based quantity, the enstrophy provides a measure of turbulence properties at small scales, and the dynamical effects of the flame on the turbulence appear explicitly in the enstrophy transport equation given by

$$\frac{1}{2}\frac{D\Omega}{Dt} = \omega_i\omega_j S_{ij} + \omega_i\varepsilon_{ijk}\frac{\partial}{\partial x_j}\left(\frac{1}{\rho}\frac{\partial \tau_{kl}}{\partial x_l}\right) - \Omega S_{kk} + \omega_i\frac{1}{\rho^2}\varepsilon_{ijk}\frac{\partial \rho}{\partial x_j}\frac{\partial p}{\partial x_k}. \tag{1}$$

Here, $D/Dt = \partial/\partial t + u_j\partial/\partial x_j$ is the material (or Lagrangian) derivative, $S_{ij} = (1/2)(\partial u_i/\partial x_j + \partial u_j/\partial x_i)$ is the strain rate tensor, ρ is the density, p is the pressure, and τ_{kl} is the viscous stress tensor given by

$$\tau_{kl} = 2\mu\left(S_{kl} - \frac{1}{3}S_{mm}\delta_{kl}\right) + \mu_B S_{mm}\delta_{kl}, \tag{2}$$

where μ and μ_B are the dynamic and bulk viscosities, respectively, and δ_{kl} is the Kronecker delta.

The first two terms on the right-hand side of Eq. (1) are generally nonzero in both reacting and non-reacting three-dimensional (3D) turbulent flows and represent vortex stretching and viscous transport processes, respectively. The last two terms, representing dilatation and baroclinic torque, are compressible flow effects that can be significant in the overall dynamics of the enstrophy during premixed combustion due to heat release from chemical reactions.

A number of recent computational and experimental studies have documented the characteristics and dynamics of enstrophy across a range of premixed flame conditions (e.g., spanning different Karlovitz, Ka, and Damköhler, Da, numbers), configurations (e.g., statistically planar[1–6] and jet[7,8] flames, as well as bluff-body stabilized flames[9] and swirl burners[10,11]) and locations within the flame (e.g., in the preheat and reaction zones). These studies have consistently

Published under an exclusive license by AIP Publishing

demonstrated the importance of flame-induced dilatation, baroclinic torque, and enhanced viscous transport (due to the increase in gas phase viscosity with increasing temperature) on the dynamics of the enstrophy during premixed combustion; the reviews by Lipatnikov and Chomiak[12] and Steinberg *et al.*[13] provide comprehensive summaries of these and other studies.

Although much has been learned about vorticity and enstrophy dynamics in turbulent premixed combustion over the past decade, certain questions remain, including: (*i*) What is the *cumulative* effect along fluid pathlines of different physical phenomena on the enstrophy?; (*ii*) When the creation or destruction of enstrophy is observed in a flame, what is the dominant physical cause?; and (*iii*) What is the temporal correspondence between different physical phenomena and changes in the enstrophy? These questions are of particular interest for the highly turbulent conditions (generally corresponding to high Ka) found in many next-generation aerospace propulsion systems.[14,15] Recent results from Geikie and Ahmed[9] and Kazbekov *et al.*[10,11] indicate that, in realistic configurations where mean pressure gradients are present (specifically, bluff-body stabilized flames and high-swirl burners, respectively), baroclinic torque can be a substantial contributor to flame-induced turbulence at highly turbulent conditions. By contrast, baroclinic torque has been found to contribute only weakly on average to the enstrophy dynamics at high Ka in statistically planar flames,[1,4,5] although Poludnenko[16] showed that baroclinic torque can still lead to intermittently large enstrophy production, even in statistically planar configurations.

To address each of the questions noted above, the temporal history of the enstrophy evolution along fluid particle pathlines is required, thereby suggesting a Lagrangian, as opposed to purely Eulerian, analysis approach. There is a considerable historical precedent for the use of a Lagrangian framework in the study of turbulent premixed combustion, including the early application of the Lagrangian direct interaction approximation by O'Brien[17] to model mixing of chemically reactive scalars. More recently, Lagrangian analyses have been used to study the dynamical history of transient combustion phenomena, such as extinction, auto-ignition, pocket formation, and deflagration to detonation transition. Such analyses have included the study of both flame features (described as flame "particle" or "surface" tracking by Uranakara *et al.*,[18] Dave *et al.*,[19,20] and You and Yang[21]) as well as velocity and thermochemical properties within fluid particles, the latter being the more traditional definition of a "Lagrangian" analysis in a turbulent flow context.

With respect to fluid particle tracking, Day *et al.*[22,23] found that thermochemistry along fluid pathlines was complex and non-monotonic (i.e., fuel consumption did not occur monotonically with increasing time, as is the case in laminar flames). Subsequently, Steinberg and collaborators[24,25] performed an analysis of velocity gradient dynamics and fluid particle residence times in premixed jet flames, finding that residence times between reactant and product temperatures decrease in turbulent flames, as compared to laminar flames. Through an analysis of highly turbulent H_2–air premixed combustion in statistically planar configurations, Hamlington *et al.*[26] showed that non-monotonicity and thermochemical complexity are caused by enhanced molecular diffusion due to large turbulence-induced gradients in thermochemical quantities. From the perspective of turbulence characteristics, Geikie and Ahmed[9] and Kazbekov *et al.*[10,11] used Lagrangian approaches to examine enstrophy dynamics in bluff-body stabilized flames and swirl burners, respectively. To date, however, a Lagrangian analysis of enstrophy dynamics in the physically simpler statistically planar configuration has yet to be performed.

In this study, we calculate enstrophy dynamics along Lagrangian fluid particle pathlines using data from a direct numerical simulation (DNS) of a statistically planar turbulent premixed methane–air flame. We first briefly describe the numerical simulation and the Lagrangian analysis approach used to calculate the enstrophy dynamics. We then outline results and conclusions from the Lagrangian analysis, with a particular focus on answering the three questions outlined above. Finally, conclusions and important directions for future research are provided at the end.

II. METHODS

A. Description of numerical simulations

The simulation performed here is identical in its configuration to the simulation described and examined previously by Darragh *et al.*[27] for the analysis of fluid particle dispersion in a turbulent premixed flame. The simulation models a 3D statistically planar stoichiometric methane–air premixed flame in a prismatic unconfined domain, with an aspect ratio of $1 \times 1 \times 16$. Additional details of the simulation are provided by Darragh *et al.*,[27] and here, we give a relatively brief overview of the simulation setup.

The simulation was performed using Athena-RFX,[16,28,29] which is a second-order-in-time, third-order-in-space code that solves the compressible, reactive-flow Navier–Stokes equations[30] using an unsplit corner transport upwind scheme[31,32] on a fixed, equispaced, 3D mesh with a nonlinear HLLC Riemann solver and piecewise parabolic spatial reconstruction. The bulk viscosity, μ_B, was set equal to the dynamic viscosity, μ, and an ideal gas equation of state was used to relate thermodynamic variables. Large-scale periodic forcing was used throughout the domain to sustain turbulence during the simulation, as described and validated by Poludnenko and Oran,[29] resulting in statistically stationary homogeneous isotropic turbulence that interacts with the premixed flame. A 19-step reduced chemical mechanism[33] was used to model the stoichiometric methane–air reaction at atmospheric conditions, and mixture averaging was used to compute molecular transport coefficients. Despite the use of mixture averaging in this study, it should be noted that individual chemical species will each have different Lewis numbers. The effects of these different Lewis numbers are of greater significance in studies of scalar and scalar gradient dynamics, as well as in cases where the analysis is conditioned on specific chemical species compositions. The present analysis of enstrophy dynamics conditioned on temperature is likely to be less dependent on this variability in Lewis number between species, although this topic does warrant further attention in future research, particularly since the Lewis number has been shown by Dopazo *et al.*[34] to affect enstrophy dynamics in premixed combustion, resulting in an increased contribution of baroclinic torque. Further details on the computational setup of Athena-RFX for simulations of multi-species chemically reacting systems are provided by Hamlington *et al.*[26] and Xu *et al.*[35]

A uniform $256 \times 256 \times 4096$ grid with cell size 2.7×10^{-3} cm was used in the simulation, resulting in roughly half a grid cell per Kolmogorov scale in the reactants and six grid cells per Kolmogorov scale in the products. There are 16 grid cells per laminar flame thermal width, $\delta_L = (T_p - T_r)/|\nabla T|_{L,max}$, where T_r and T_p denote the

Published under an exclusive license by AIP Publishing

reactant and product temperatures, and $|\nabla T|_{\mathrm{L,max}}$ is the maximum gradient of temperature, T, in the laminar case. Given the resolution of the turbulent Kolmogorov and flame scales in this simulation, it can reasonably be described as a DNS, and physical characteristics of the present DNS are summarized in Table I.

Periodic boundary conditions were used in the x and y directions for the duration of the DNS. Prior to initialization of the flame, periodic boundaries were used in the z direction, with open zeroth-order extrapolation boundaries used after ignition. The domain was initialized with cold reactants at a temperature of $T_{\mathrm{r}} = 300$ K, and turbulence was allowed to develop over one large-scale eddy turnover time, $\tau_L = L/U_L$, where $L = 0.700\,37$ cm is the width of the domain and U_L is the turbulent velocity at the scale of the domain width L. After the turbulence was fully developed, a planar laminar flame was initialized near the center of the domain with the flame normal in the z direction. The simulation was then allowed to develop for an additional τ_L before 3D Eulerian fields of velocity, density, pressure, and temperature were output at a high rate for the Lagrangian analysis.

Given the relatively high turbulence intensity of $U_\ell/S_{\mathrm{L}} = 21$ in these simulations, the Karlovitz number, $\mathrm{Ka} = \tau_{\mathrm{L}}/\tau_{\eta_{\mathrm{r}}} = 100$, was high and the corresponding Damköhler number, $\mathrm{Da} \equiv \tau_L/\tau_{\mathrm{L}} = 0.50$, was low, where $\tau_{\mathrm{L}} = \delta_{\mathrm{L}}/S_{\mathrm{L}}$ is the laminar flame characteristic timescale given in Table I. As a result, the small-scale turbulent fluctuations occur on short timescales relative to the characteristic timescale of the flame. These flame conditions place the present simulation in the broken reaction zone regime.[36] Although the turbulence is intense, both the bulk flow and turbulent Mach numbers were quite small, and there were subsequently no shocks or shocklets in the domain (recent research[37] has, however, shown that Lagrangian analyses can be accurately performed in flows with such compressible features).

TABLE I. Physical model parameters of the highly turbulent premixed methane–air flame simulated in the present study.

L	0.700 37 cm	Domain width
T_{r}	300 K	Unburnt temperature
p_{r}	$1.013\,25 \times 10^6$ erg/cm^3	Unburnt pressure
ρ_{r}	1.12×10^{-3} g/cm^3	Unburnt density
δ_{L}	4.38×10^{-2} cm	Laminar thermal width
S_{L}	37.2 cm/s	Laminar flame speed
τ_{L}	1.18×10^{-3} s	Laminar flame timescale
ℓ	2.05×10^{-1} cm	Unburnt integral scale
U_ℓ	785 cm/s	Unburnt integral velocity
τ_L	5.922×10^{-4} s	Eddy turnover time
Da	0.50	Damköhler number
Ka	100	Karlovitz number
η_{r}	1.382×10^{-3} cm	Unburnt Kolmogorov length
η_{p}	1.734×10^{-2} cm	Burnt Kolmogorov length
$\tau_{\eta_{\mathrm{r}}}$	1.174×10^{-5} s	Unburnt Kolmogorov time
$\tau_{\eta_{\mathrm{p}}}$	6.340×10^{-5} s	Burnt Kolmogorov time
$\mathrm{Re_r}$	87	Unburnt Reynolds number
$\mathrm{Re_p}$	28	Burnt Reynolds number

B. Description of Lagrangian analysis and trajectory initialization

Fluid particle trajectories were calculated using the Lagrangian algorithm described by Darragh *et al.*[38] and Hamlington *et al.*,[26] with velocities obtained from the 3D Eulerian velocity field output from the DNS. Fluid particles were independently evolved using fifth-order Runge–Kutta time integration to solve the ordinary differential equation $d\mathbf{x}_n/dt = \mathbf{u}(\mathbf{x}_n)$, where $\mathbf{x}_n(t)$ denotes the trajectory of the nth particle and $\mathbf{u}$ is the 3D Eulerian velocity field from the DNS. Akima splines were used for spatial and temporal interpolation during the integration procedure, giving at least second-order interpolation accuracy for all variables. Verification and validation of this algorithm are provided by Darragh *et al.*,[38] and the first demonstration of this algorithm for fluid particle trajectory calculations using Eulerian data from Athena-RFX is outlined by Hamlington *et al.*[26]

In the present study, fluid particles were initialized in 256×256 grids within x–y planes at 15 different z locations near the reactants, roughly at the start of the preheat zone. Each of these 983 040 particles were then evolved forward in time for one τ_L. Because this study is primarily focused on the effects of heat release by the flame on enstrophy dynamics, only particles that underwent complete combustion were considered in the analysis. This was accomplished by restricting the analysis to particles that reach a temperature of 500 K (indicating that reactions have begun to occur), followed at a later time by a temperature of 1800 K. This resulted in a total of 239 068 particles considered in this study.

Through this conditioning procedure, we ensured that all particles examined in the analysis were of a similar type, regardless of their initial spatial location. In particular, each particle analyzed underwent combustion with a corresponding temperature rise from 500 to 1800 K, accomplished via heat release resulting from chemical reactions. There are other particles that do not undergo combustion during the analysis period, but these particles are of lesser interest here since the corresponding enstrophy evolution would be similar to that obtained for particles in homogeneous isotropic turbulence (the type of turbulence in the reactants) in the absence of combustion. Moreover, the requirement that the particles reach a temperature of 500 K in order to be included in the analysis is equivalent, for this statistically stationary flame, to examining only particles initialized at locations where the temperature is at 500 K, that then subsequently undergo combustion.

With the Lagrangian trajectories computed, terms in the enstrophy governing equation in Eq. (1) were calculated from the Eulerian fields output by the DNS and then interpolated to the trajectories. This allowed us to recover the dynamics of the enstrophy along fluid particle pathlines. Gradients were computed by using Akima splines to interpolate quantities of interest to cell edges, followed by the calculation of flux differences to obtain gradients. The time derivative of Ω required to compute $D\Omega/Dt$ was calculated by first smoothing the enstrophy and then using a first-order backward finite difference. Using this approach, we computed each of the four terms on the right-hand side of Eq. (1) along each of the Lagrangian trajectories, and the resulting normalized time-dependent quantities are denoted here by

$$\text{Vortex stretching}: \quad \mathcal{S} = \frac{1}{A}\omega_i\omega_j S_{ij}, \tag{3}$$

Published under an exclusive license by AIP Publishing

$$\text{Viscous transport}: \quad \mathcal{D} = \frac{1}{A}\omega_i \varepsilon_{ijk} \frac{\partial}{\partial x_j}\left(\frac{1}{\rho}\frac{\partial \tau_{kl}}{\partial x_l}\right), \tag{4}$$

$$\text{Dilatation}: \quad \mathcal{L} = -\frac{1}{A}\Omega S_{kk}, \tag{5}$$

$$\text{Baroclinic torque}: \quad \mathcal{B} = \frac{1}{A}\omega_i \frac{1}{\rho^2}\varepsilon_{ijk}\frac{\partial \rho}{\partial x_j}\frac{\partial p}{\partial x_k}, \tag{6}$$

where $A = \langle (\Omega S_{mn} S_{mn})^{1/2} \rangle$ is a normalizing factor that accounts for the intensity of the turbulence prior to its interaction with the flame. A similar normalization was used by Hamlington *et al.*[1] for an Eulerian analysis of enstrophy dynamics in premixed flames, and this factor is computed as an average over the portion of trajectories in the reactants (i.e., for temperatures less than 310 K). Although it is traditional in studies of non-reacting flows to separate the viscous transport term in Eq. (4) into separate diffusive and dissipative parts, an unambiguous separation of this type is difficult in premixed flames where both the density and viscosity are spatially and temporally varying, and the dilatation is non-zero. This results in a number of different terms when expanding $\mathcal{D}$ from Eq. (4), including terms involving gradients of the density and viscosity. Consequently, for simplicity in the present study we examine the viscous transport term in Eq. (4) as a whole.

It should be noted that, as a result of the numerical forcing used to maintain statistical stationarity of the DNS, as well as numerical diffusion introduced by the computational algorithm, the transport equation for Ω in Eq. (1) should also, from a practical standpoint, include an additional residual term. This term is obtained in the present analysis from the Navier–Stokes momentum conservation equation, which is given by

$$\frac{Du_i}{Dt} = -\frac{1}{\rho}\frac{\partial p}{\partial x_i} + \frac{1}{\rho}\frac{\partial \tau_{ij}}{\partial x_j} + N_i, \tag{7}$$

where N_i represents the residual. This term is calculated in the present study by using the 3D Eulerian field output by the DNS to subtract the pressure gradient and viscous transport terms on the right-hand side of Eq. (7) from the material derivative of velocity; this approach has also previously been suggested by Schranner *et al.*[39] as a method to estimate numerical diffusion. The time derivative of velocity is computed using a second-order centered finite difference, while the gradients required in the material derivative are again computed by interpolating quantities to cell interfaces using Akima splines and then computing flux differences.

Given the resulting Eulerian fields of N_i, we then compute the curl of these fields and construct the corresponding normalized residual term in the enstrophy transport equation, given by

$$\text{Residual}: \quad \mathcal{N} = \frac{1}{A}\omega_i \varepsilon_{ijk}\frac{\partial N_k}{\partial x_j}. \tag{8}$$

This time-dependent quantity is combined in the following analysis of enstrophy dynamics along fluid particle pathlines with the other terms in Eqs. (3)–(6).

III. RESULTS

A. Eulerian fields

Instantaneous two-dimensional (2D) Eulerian fields of temperature and enstrophy near the flame are shown in Fig. 1. Consistent with prior studies of statistically planar premixed flames,[1,4,5] there is more spatial variability in the temperature field on the unburnt reactant side of the flame, as compared to the burnt product side. This is also indicated by the greater "wrinkling" of the $T = 400$ K isocontour, corresponding to higher values of the enstrophy, as compared to the $T = 2000$ K isocontour. In general, enstrophy is larger in the reactants and decreases through the flame into the products, again consistent with prior studies of enstrophy magnitude in turbulent premixed flames.[1,4,5] The enstrophy field also shows greater small-scale structure in the reactants, which is destroyed as the temperature increases due to the flame; this is indicative of the suppression of small-scale motions that has been quantified in prior studies of the multi-scale structure of turbulence during premixed combustion.[30,40–42]

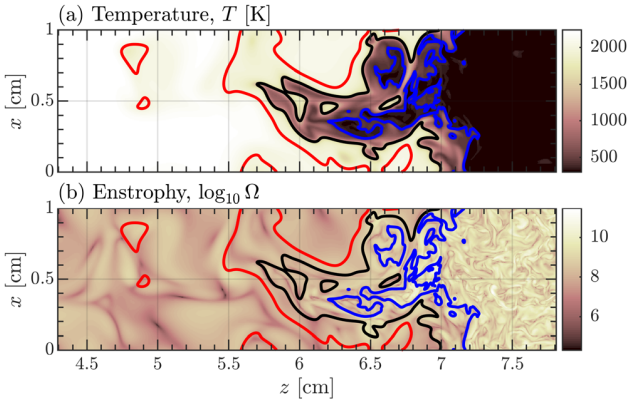


FIG. 1. Instantaneous 2D fields of (a) temperature and (b) enstrophy from the present DNS of a statistically planar methane–air premixed flame. Both panels show isocontours of $T = 400$ (blue lines), 1400 (black lines), and 2000 K (red lines).

Figure 2 shows corresponding 2D Eulerian fields for each of the normalized budget terms from the right-hand side of Eq. (1), where the definitions of each term are given in Eqs. (3)–(6) and (8). The primary balance indicated by the fields in Fig. 2 is between vortex stretching, $\mathcal{S}$, which is generally positive throughout the flow, and viscous transport, $\mathcal{D}$, which is generally negative. This dominant balance is consistent with previous studies of highly turbulent statistically planar premixed flames.[1,4,5]

Dilatation, $\mathcal{L}$, and baroclinic torque, $\mathcal{B}$, shown in Figs. 2(c) and 2(d), are generally smaller than the vortex stretching and viscous transport terms and have their largest magnitudes in the vicinity of the flame. Although both of these fields exhibit both positive and negative contributions to the enstrophy dynamics, the dilatation has more prevalent negative values, indicating enstrophy destruction, while the baroclinic torque is more generally positive, indicating enstrophy generation. Additionally, the baroclinic torque and dilatation appear to have opposite signs at each location; this correlation will be examined in more detail in Sec. III D.

The magnitudes of each of the terms in Fig. 2 are smaller in the products than in the reactants, and the characteristic sizes of the flow features are larger in the products than in the reactants. Both of these results are likely due to the associated changes in enstrophy through the flame shown in Fig. 1(b), particularly given the dependence of each of the budget terms on the vorticity magnitude. The connection between the enstrophy and budget terms will be made more quantitative in Sec. III D, where temporal cross-correlations are used to

Published under an exclusive license by AIP Publishing

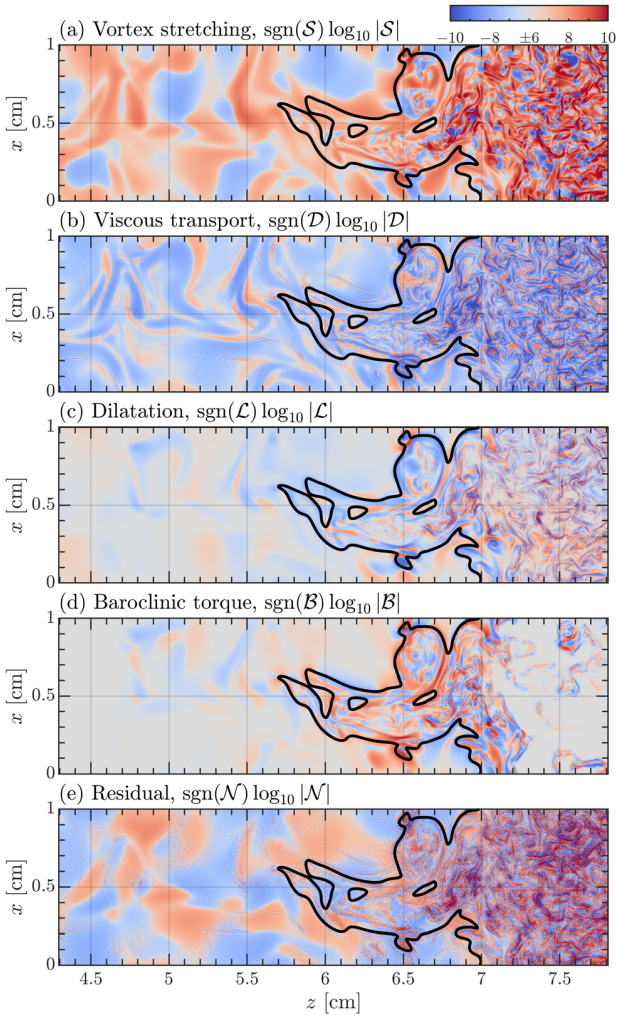


FIG. 2. Instantaneous 2D fields from the present DNS showing the signed logarithm of the normalized enstrophy budget terms $\mathcal{S}$, $\mathcal{D}$, $\mathcal{L}$, $\mathcal{B}$, and $\mathcal{N}$ defined in Eqs. (3)–(6) and (8) (a)–(e). The $T = 1400$ K isocontour is shown by a black line in each panel.

determine the relationship between changes in enstrophy and the budget terms.

The residual field, $\mathcal{N}$, shown in Fig. 2(e) qualitatively resembles fields for the other budget terms, particularly with respect to the change in magnitude and feature size across the flame. However, the residual field also exhibits pixelated noise, which is most apparent in the reactants where the spatial resolution of the DNS is lower relative to the Kolmogorov scale and numerical diffusion is more pronounced. The coherent large-scale structures in the products in Fig. 2(e) are likely associated with the numerical forcing.

B. Lagrangian analysis of enstrophy dynamics

As noted in Sec. II B, in this study we only consider particles that undergo combustion, determined to be particles that experience a temperature of 500 K followed by a temperature of 1800 K. The particles that remain in the reactants or otherwise do not reach a temperature of 1800 K will not be considered in the following analyses. Additionally, all mentions of a particle reaching a specific temperature are assumed to be the first time the particle reaches the given temperature, despite the fact that it is possible for the temperature of the particle to decrease and then increase at a later time. As will be seen in the results, the temperature is frequently non-monotonic along fluid particle trajectories, and so there can be several time instances at which the particle reaches a temperature of $T = 500$ K, for instance. We thus choose the first time at which the particle reaches a specified temperature in the analysis. The duration between 400 and 2000 K will also include trajectories that reach 400 and 1800 K, but may not reach 2000 K before the end of data collection.

Figure 3 shows the temperature, enstrophy, and normalized enstrophy budget terms along a single representative trajectory. At lower temperatures, the particle is still in the reactants where the enstrophy magnitude is larger than in the products, and thus the budget terms are larger in magnitude than at later times and higher temperatures. The rapid variations observed in the budget terms correspond to the small-scale flow features evident in Figs. 1 and 2, which are more prevalent in the reactants. These variations are also characterized by timescales much smaller than the chemical timescale, due primarily to the high Ka and low Da nature of this flame. In particular, Fig. 3(a) shows that the fluid particle undergoes combustion (corresponding to a rapid increase in temperature) over a timescale of roughly 0.1 ms, but the fluctuations in the total budget terms shown in Fig. 3(c) take place over timescales that are over an order of magnitude smaller. Such a

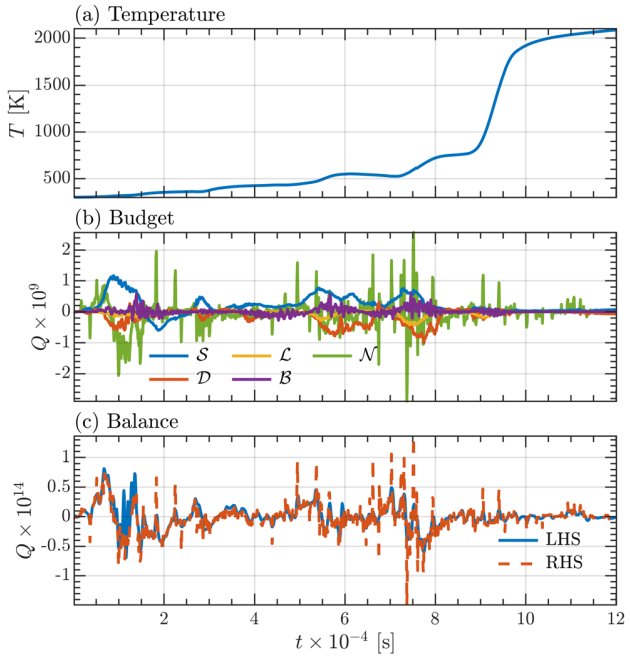


FIG. 3. Lagrangian time histories of (a) temperature, (b) normalized enstrophy budget terms defined in Eqs. (3)–(6) and (8), and (c) the balance between the left- and right-hand sides of Eq. (1) for a single representative fluid particle.

Published under an exclusive license by AIP Publishing

wide disparity in chemical and turbulence timescales is characteristic of highly turbulent flames where Ka is high. In the region of intermediate temperatures (i.e., between roughly $T = 400$ and 1800 K), Fig. 3(b) shows that the baroclinic torque and dilatation become larger in magnitude, with the baroclinic torque tending to have positive values and the dilatation negative values. Additionally, all terms appear to change magnitude together, indicating the presence of correlations between budget terms, which are again examined further in Sec. III D.

The balance between the left- and right-hand sides of Eq. (1) are shown over the entire trajectory in Fig. 3(c), where the right-hand side also includes the residual. There is good agreement between the two resulting time histories, indicating that the enstrophy budgets are accurately calculated using the procedure outlined in Sec. II B.

Temperature, enstrophy, and the normalized enstrophy budget terms are shown for 25 randomly selected trajectories in Fig. 4, where each trajectory is centered on the time at which the fluid particle first reaches a temperature of 500 K in Figs. 4(a)–4(g) and a temperature of 1400 K in Figs. 4(h)–4(n). The centering on 500 K in Figs. 4(a)–4(g) provides an indication of the different particle evolutions from the start of the analysis period, which begins for each trajectory when the corresponding particle first reaches a temperature of 500 K. These figures also indicate the nearly isothermal nature of the particles as they travel through the reactants prior to the onset of combustion. The centering at 1400 K in Figs. 4(h)–4(n) more clearly shows the particle evolutions near the region of peak heat release in the flame, as determined from the laminar flame profile. Although it is difficult from Fig. 4 to discern the specific details of any individual trajectory, this figure does give a sense of the range of values attained along the different trajectories, as well as the abrupt change in the magnitudes of the different normalized budget terms across the flame.

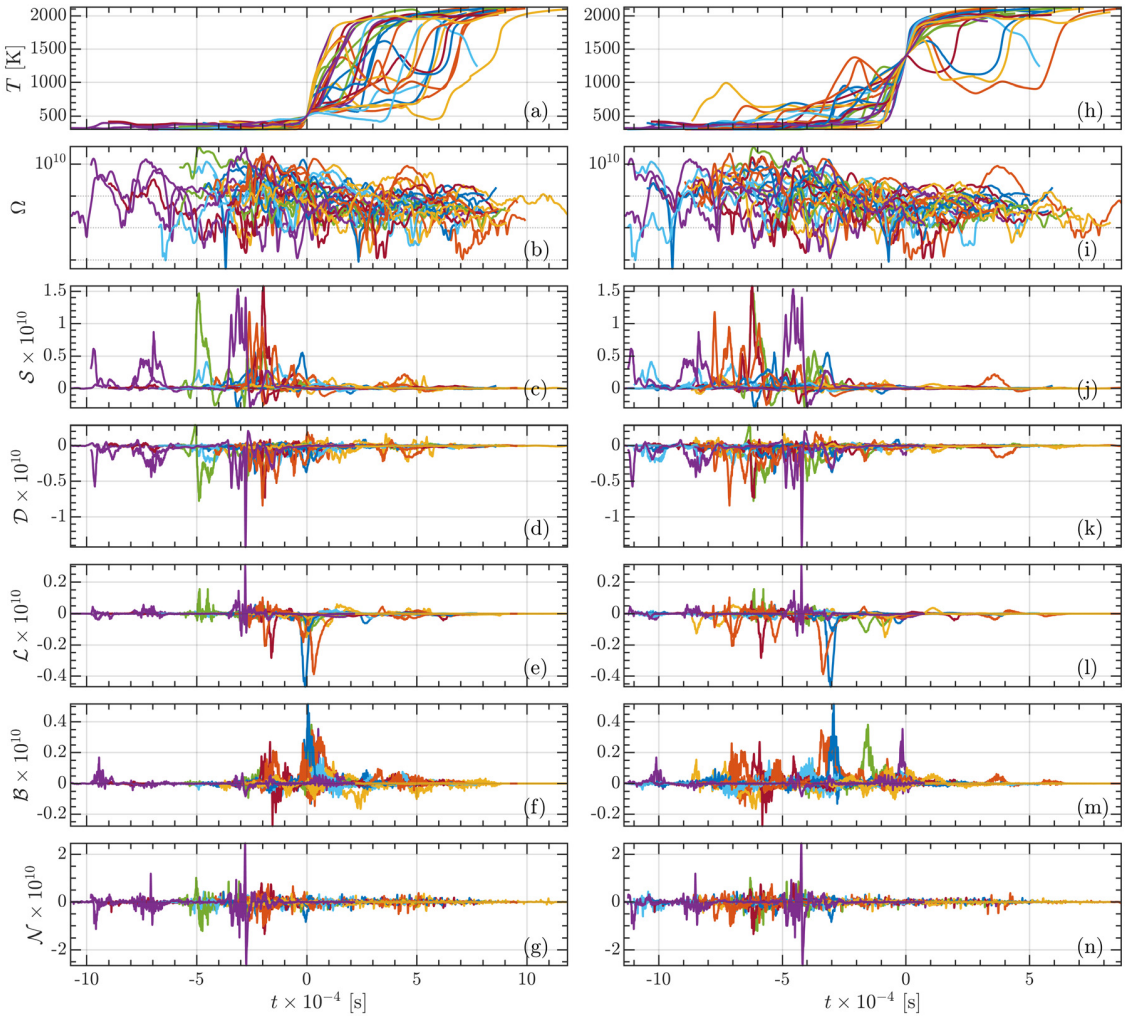


FIG. 4. Twenty-five randomly selected Lagrangian trajectories centered at 500 K (a)–(g) and 1400 K (h)–(n), such that $t = 0$ at the specified temperature. The panels show temperature (a) and (h), enstrophy (b) and (i), vortex stretching (c) and (j), viscous transport (d) and (k), dilatation (e) and (l), baroclinic torque (f) and (m), and residual terms (g) and (n). Each of the enstrophy budget terms is normalized and defined in Eqs. (3)–(6) and (8).

Published under an exclusive license by AIP Publishing

Figures 4(a) and 4(h) show that the temperature time histories along the particle trajectories are frequently non-monotonic, which has also been noted in previous studies of highly turbulent premixed flames.[22,23,26] In general, Figs. 4(b) and 4(i) show that enstrophy tends to decrease through the flame; however, the decrease is once again not monotonic, and some periods of enstrophy increase are observed as different terms compete to increase and decrease the enstrophy through the flame. A conditional analysis of only trajectories that experience an increase in enstrophy while in the flame is presented in Sec. III C.

Figures 4(c)–4(g) and 4(j)–4(n) show the normalized enstrophy budget terms for each of the 25 trajectories. From the trajectories centered at 1400 K, shown in Figs. 4(j)–4(n), the magnitudes of all budget terms tend to be greater prior to peak heat release (which occurs close to 1400 K), with all terms reducing in magnitude at later times, corresponding to higher temperatures. While all terms are capable of both increasing and decreasing the enstrophy, these trajectories more often have enstrophy increased by stretching and baroclinic torque, and decreased by dilatation and viscous dissipation. The residual term tends to be more evenly distributed in positive and negative contributions.

To aggregate these Lagrangian results and develop an overall understanding of the enstrophy characteristics and dynamics, each trajectory is centered at the time when 1400 K is first reached and averages over the temperature, enstrophy, and normalized budget terms are taken over all burnt trajectories, as shown in Fig. 5. This method results in fewer trajectories included in the averages at early or late times because not all trajectories reach 1400 K at the exact same time, although at $t = 0$, all trajectories are included in the average.

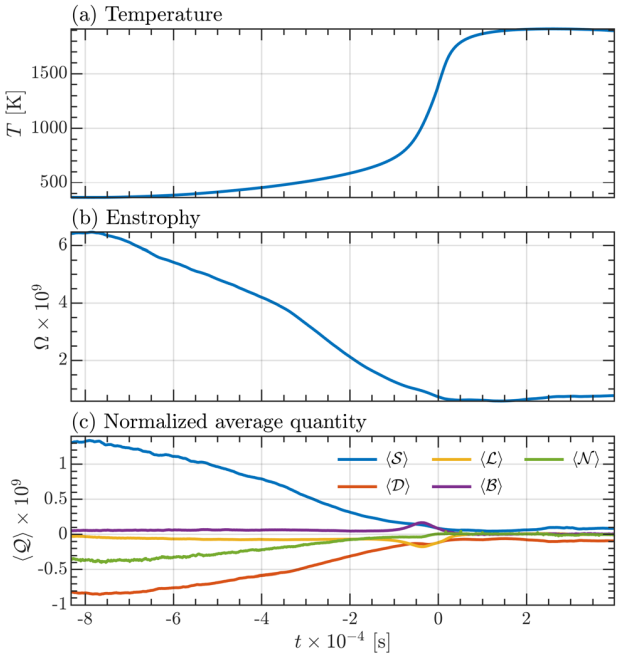


FIG. 5. Average over all burnt trajectories of the (a) temperature, (b) enstrophy, and (c) normalized enstrophy budget terms defined in Eqs. (3)–(6) and (8). Each of the trajectories has been centered such that $T = 1400$ K at $t = 0$ s (see also Fig. 4).

In Fig. 5(a), the average enstrophy is largest at early times when particles are in the reactants and decreases as the particles move through the flame, with almost all of the decrease occurring prior to $t = 0$ (corresponding to $T = 1400$ K). At these early times, the average vortex stretching is positive and the average viscous transport is negative, with both having similar magnitudes that decrease as $t = 0$ is approached. The average baroclinic torque and average dilatation are also mirrors of each other, with opposite values of similar magnitude both peaking immediately prior to $t = 0$. Away from $t = 0$, both of these terms make much smaller contributions to the overall enstrophy dynamics. However, the contribution near $t = 0$ does not result in a large average effect on the enstrophy, suggesting that these terms may be more relevant for individual trajectories, rather than the average evolution.

The range of values attained by each of the normalized enstrophy budget terms is indicated by the probability density functions (pdfs) shown in Fig. 6(a). The pdfs, which are calculated over all trajectories during the period of time that each particle spends between 400 and 2000 K, show that all terms tend to peak near a value of zero, although the pdfs of stretching and baroclinic torque are skewed more toward positive values, while the pdfs of viscous transport and dilatation are skewed more toward negative values. It should be noted that the pdf of the residual term is also skewed to negative values, reflecting its association with numerical diffusion and the destruction of enstrophy.

The enstrophy budget along Lagrangian trajectories can also be examined by considering the cumulative effect of each budget term on the evolution of the enstrophy. This cumulative analysis is motivated by the first of the three questions posed in Sec. I; namely, what is the *cumulative* effect along fluid pathlines of different physical phenomena on the enstrophy? This cumulative effect is determined by integrating each budget term between 400 and 2000 K along a trajectory, and Fig. 6(b) shows pdfs of the resulting cumulative effects aggregated over all trajectories. As compared to the pdfs of the instantaneous budget terms in Fig. 6(a), the cumulative effect pdfs in Fig. 6(b) more clearly show the net positive contributions of vortex stretching and baroclinic torque to enstrophy production, and the net negative contributions of viscous transport and dilatation to enstrophy destruction. The cumulative dilatation effect is the weakest of all effects, and the residual (associated with numerical diffusion) provides the second largest contribution to enstrophy destruction, after the viscous transport effect.

From a more quantitative perspective, the mean of each of the cumulative effects averaged over all trajectories between 400 and 2000 K is shown in Table II. Both dilatation and baroclinic torque are similar in magnitude and opposite in sign, and the same is true for vortex stretching and viscous transport. The magnitude of both baroclinic torque and dilatation is roughly an order of magnitude below the effects of stretching and viscous transport. In a similar type of comparison, Bobbitt *et al.*[5] and Hamlington *et al.*[1] both found around an order of magnitude difference when comparing baroclinic torque and dilatation with stretching and viscous dissipation, consistent with the present observations.

Several combinations of normalized budget terms are also shown in Table II. These combinations (i.e., stretching and viscous dissipation, dilatation and baroclinic torque, and all five budget terms) are

Published under an exclusive license by AIP Publishing

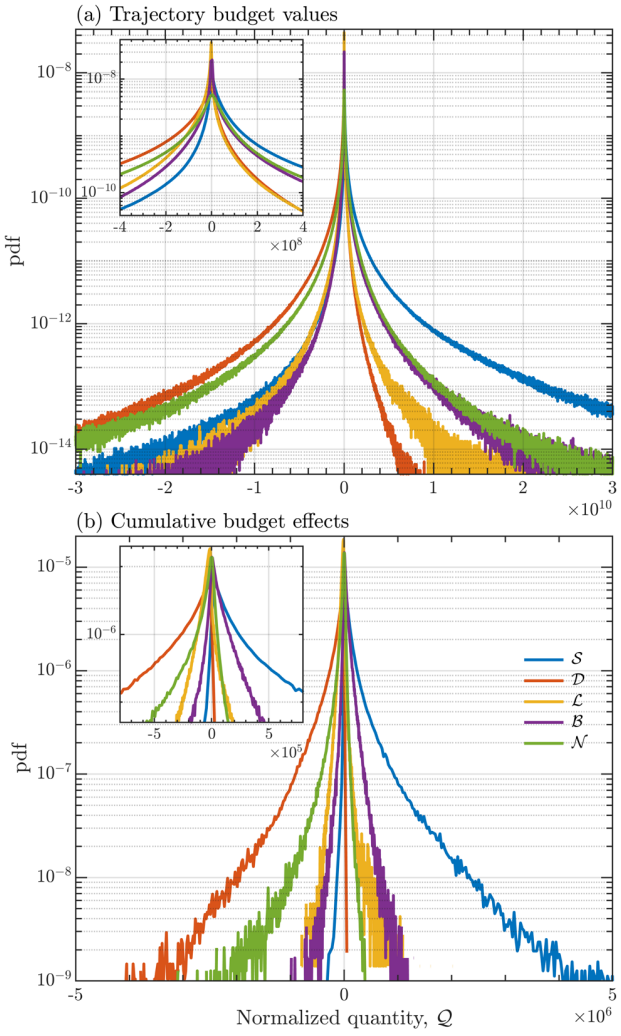


FIG. 6. Panel (a) shows a pdf of the values of normalized budget terms defined in Eqs. (3)–(6) and (8) for all trajectories that pass through the flame for the period of time they are between 400 and 2000 K. Panel (b) shows the cumulative effect of each normalized budget term during this same period. The insets in both panels show the same pdfs for smaller values of the normalized quantity magnitudes.

added together before the integration and averaging are performed. By combining the terms in this way, the combined cumulative effect of stretching and viscous dissipation are found to be similar to the combined cumulative effect of dilatation and baroclinic torque over this range of temperatures, with a difference of slightly less than a factor of two, instead of an order of magnitude when considering each of these terms alone. The combination of baroclinic torque and dilatation represents both terms that are non-zero due to the presence of the flame, and thus their net positive contribution can be considered a manifestation of flame-generated vorticity. That is, the non-negligible, positive, average, cumulative contribution to enstrophy confirms that enstrophy can be enhanced by the flame.

TABLE II. Mean cumulative effect of each normalized budget term defined in Eqs. (3)–(6) and (8) and three combinations of budget terms, where the averaging is computed over all trajectories.

Mean integrated quantity	Effect
$\langle \int_{T=400}^{T=2000} \mathcal{S} \rangle$	2.62×10^5
$\langle \int_{T=400}^{T=2000} \mathcal{D} \rangle$	-2.41×10^5
$\langle \int_{T=400}^{T=2000} \mathcal{L} \rangle$	-3.67×10^4
$\langle \int_{T=400}^{T=2000} \mathcal{B} \rangle$	4.92×10^4
$-\langle \int_{T=400}^{T=2000} \mathcal{N} \rangle$	-5.63×10^4
$\langle \int_{T=400}^{T=2000} (\mathcal{S}+\mathcal{D}) \rangle$	2.07×10^4
$\langle \int_{T=400}^{T=2000} (\mathcal{L}+\mathcal{B}) \rangle$	1.26×10^4
$\langle \int_{T=400}^{T=2000} (\mathcal{S}+\mathcal{L}+\mathcal{B}+\mathcal{D}-\mathcal{N}) \rangle$	-2.30×10^4

C. Conditional analysis

In order to address the second question posed in Sec. I and determine the dominant physical cause when the creation or destruction of enstrophy is observed in a flame, we perform a conditional analysis of the trajectories based on whether the enstrophy increases or decreases during combustion. While most trajectories decrease in enstrophy through the flame due to the increasing temperature and corresponding increase in viscosity, it is also possible for the enstrophy to increase along a fluid particle pathline that passes through the flame. In particular, 28% of the trajectories that underwent combustion and had a temperature range of 400 to 2000 K experienced an enstrophy increase, while 72% decreased in enstrophy. Consequently, despite the overall average decrease in enstrophy indicated in Fig. 5, over a quarter of the trajectories undergo an increase in enstrophy during the combustion process, potentially suggesting the presence of flame generated enstrophy. Figure 7 shows the distribution of ratios between the enstrophy at the end of the analysis period to the enstrophy at the start. Trajectories that decrease in enstrophy are more likely than those that increase, and the decrease is more likely to be large. Conversely, increases in enstrophy are more likely to be small (i.e., the ratio is more likely to be close to unity, with large increases being less probable).

Table III separates the full set of trajectories into two cases: trajectories that increase in enstrophy between 400 and 2000 K, and trajectories that decrease in enstrophy over the same temperature range. The fraction of trajectories with a positive cumulative effect from each budget term for both cases is then given, along with the fraction of trajectories outside a single standard deviation (std) of the mean of the given budget term. These fractions are based on the total number of trajectories that increase or decrease in enstrophy, not the total number of trajectories in the study; however, the mean and standard deviation are computed using the set of all trajectories. Additionally, Table III also shows the fraction of trajectories with at least one budget term outside one standard deviation.

Table III indicates that, among the trajectories that increase in enstrophy, all show a greater fraction of positive cumulative budget effects except for the viscous transport term, which is roughly

Published under an exclusive license by AIP Publishing

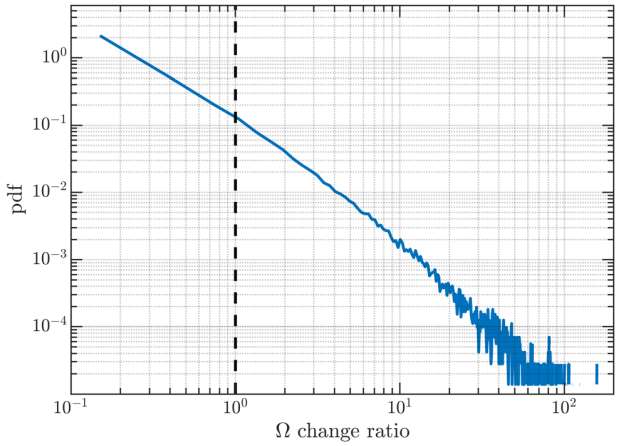


FIG. 7. Ratio of enstrophy at the end of the analysis duration (corresponding to particle temperatures of 2000 K), compared to the start of analysis (corresponding to temperature of 400 K).

equivalent to the set of trajectories that decreased in enstrophy. Additionally, for all budget terms, a greater fraction of cumulative effects lie outside one standard deviation of the mean for trajectories that increase in enstrophy when compared to those that decrease. Furthermore, the fraction of trajectories with at least one term outside a single standard deviation of the mean is roughly 1.6 times greater than the fraction amongst trajectories with decreasing enstrophy. This suggests that these less common but large contributions are associated with increases in enstrophy along a trajectory during the combustion process. The importance of these extreme values suggests a connection between enstrophy production during combustion and turbulence intermittency, whereby large values of velocity gradient quantities are observed with increasing probability (as compared to Gaussian probabilities) for increasing Reynolds number.[43] Thus, although enstrophy production is not observed on average, there are locally large instances of enstrophy production during the combustion process, leading to an overall increase in enstrophy in more than a quarter of the trajectories.

TABLE III. Fraction of trajectories in each case of the trajectories that either increased or decreased in enstrophy.

	Enstrophy increase	Enstrophy decrease
Fraction of trajectories	0.28	0.72
Positive cumulative $\mathcal{S}$	0.99	0.98
Positive cumulative $\mathcal{L}$	0.17	0.05
Positive cumulative $\mathcal{B}$	0.82	0.79
Positive cumulative $\mathcal{D}$	0.01	0.01
Positive cumulative $\mathcal{N}$	0.44	0.27
Outside one std of $\mathcal{S}$ mean	0.17	0.05
Outside one std of $\mathcal{L}$ mean	0.16	0.10
Outside one std of $\mathcal{B}$ mean	0.19	0.13
Outside one std of $\mathcal{D}$ mean	0.17	0.06
Outside one std of $\mathcal{N}$ mean	0.11	0.05
At least one term outside one std of mean	0.32	0.20

With respect to the probabilistic distributions of the different normalized budget terms, Fig. 8 shows pdfs of both the raw value and cumulative effect of each term for trajectories between 400 and 2000 K. Trajectories that increased in enstrophy are separated from those that decreased in enstrophy. Figure 8 shows that pdfs for both the raw values and the cumulative effects have similar peaks, both in height and location, for both sets of trajectories. The largest difference between the two sets of trajectories is found in the tails of the pdfs, again consistent with a connection between enstrophy production and turbulence intermittency. In particular, pdfs for all budget terms show that larger-in-magnitude values are more probable for trajectories that increase in enstrophy than those that decrease in enstrophy. This, along with the results shown in Table III, suggests that, in the highly turbulent statistically planar premixed flame examined here, the greatest increases in enstrophy are associated with relatively infrequent, large magnitude enstrophy budget effects.

D. Cross-correlation analysis

Finally, to determine the temporal correspondence between different physical phenomena and changes in the enstrophy (thereby addressing the third question posed in Sec. I), we examine here the temporal cross-correlations between temperature, enstrophy, and the normalized budget terms. For two generic time-dependent quantities $a(t_n)$ and $b(t_n)$ defined along a Lagrangian trajectory, where t_n denotes the nth discretized time along the trajectory, the cross correlation for a temporal separation of $k\Delta t$, where k is the discrete number of lagged time steps and $\Delta t = 1 \times 10^{-6}$ s is the time step between successive values along the Lagrangian trajectories, is defined as[44,45]

$$c_{ab}(k\Delta t) = \frac{1}{||a||\,||b||}\sum_{n=0}^{N-k} a(t_n + k\Delta t)b(t_n), \tag{9}$$

where N is the total number of time steps in each series and $||\cdot||$ denotes the L2 norm. Using Eq. (9), we compute a temporal cross correlation for each trajectory individually, spanning over all possible values of the number of lagged time steps k along the trajectory. Figure 9 shows the resulting average correlation, denoted $\langle c_{ab}(k\Delta t)\rangle$, which is determined by averaging the cross-correlations $c_{ab}(k\Delta t)$ from Eq. (9) over all trajectories, giving an average that is itself a function of the number of lagged time steps, k. This is done for several selected correlations between pairs of normalized budget terms, temperature, and enstrophy. The notation is such that a negative time shift implies that the first subscript (e.g., a in c_{ab}) is large before the second subscript (e.g., b), while a positive time shift implies the opposite. Correlations between raw values are shown in Fig. 9(a), while Fig. 9(b) shows correlations between the absolute value of quantities that are not strictly positive.

The trajectory-averaged correlation between temperature and dilatation, $\langle c_{T\mathcal{L}}\rangle$, is found to be large with a positive time lag, indicating that large temperatures follow large dilatation (i.e., dilatation is larger on the reactant side of the flame). This matches the results for the time evolutions of the temperature and enstrophy budget terms along trajectories shown in Figs. 3–5, where dilatation is large in magnitude before the temperature becomes large. A similar result is found for $\langle c_{T|\mathcal{L}|}\rangle$ in Fig. 9(b).

Published under an exclusive license by AIP Publishing

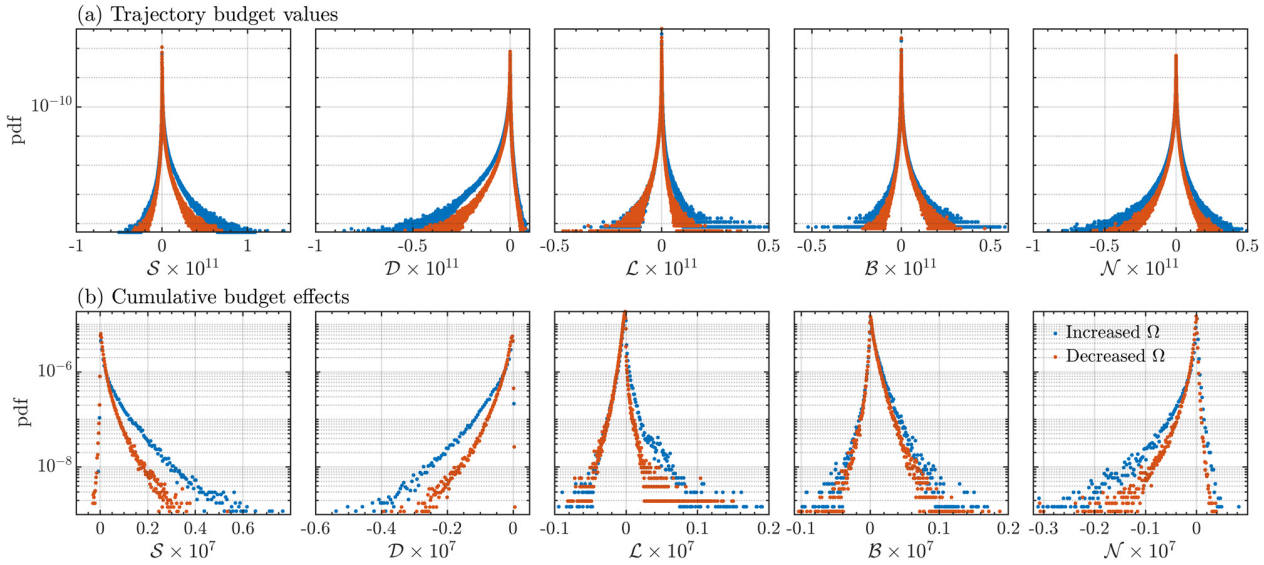


FIG. 8. Row (a) shows the tails of the pdfs of normalized enstrophy budget term values exhibited by each trajectory between 400 and 2000 K. Row (b) shows the tails of the pdfs of the cumulative effects of each normalized budget term. In blue are those trajectories that increased in enstrophy, and in red those that decreased in enstrophy over the same period of time.

For the correlation between the enstrophy and dilatation, $\langle c_{\Omega\mathcal{L}} \rangle$ in Fig. 9(a) is larger in magnitude and more negative at negative time shifts, indicating that enstrophy tends to be larger in the reactants, as expected, and that when it is destroyed, dilatation tends to be large. A stronger correlation with zero time shift is found between enstrophy and the absolute value of dilatation, $\langle c_{\Omega|\mathcal{L}|} \rangle$, in Fig. 9(b).

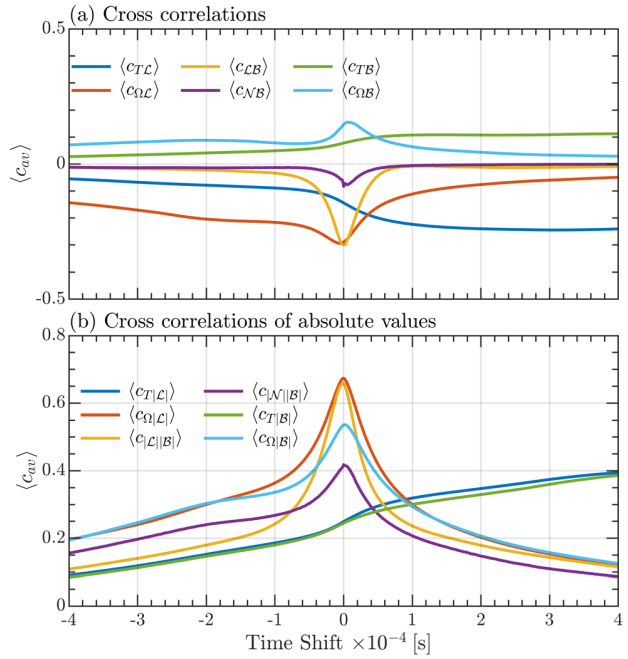


FIG. 9. Panel (a) shows trajectory-averaged cross correlations between the given normalized enstrophy budget terms, where the cross correlation is defined in Eq. (9). Panel (b) shows trajectory-averaged cross correlation between the absolute value of terms that can be negative.

The correlation between dilatation and baroclinic torque, $\langle c_{\mathcal{LB}} \rangle$ in Fig. 9(a), is negative with little to no time shift, thus supporting the findings in Fig. 5, where both terms peak at a similar time and work in opposition, with baroclinic torque enhancing enstrophy while the dilatation diminishes it. With respect to the magnitudes of dilatation and baroclinic torque, Fig. 9(b) further shows that $\langle c_{|\mathcal{L}||\mathcal{B}|} \rangle$ is even greater than $\langle c_{\mathcal{LB}} \rangle$. These results indicate that enstrophy destruction by dilatation and production by baroclinic torque are typically concurrently large along trajectories, such that even when these two effects are large individually, they oppose each other and result in little overall change in the enstrophy. This corresponds to an overall reduction in the effect of the flame on enstrophy, despite the fact that the dilatation and baroclinic torque may each be individually large in magnitude.

Figure 9(a) shows that there is a small negative peak with no time shift in the correlation between the residual term and baroclinic torque, $\langle c_{\mathcal{NB}} \rangle$, indicating little to no correlation between the two terms. However, when $\langle c_{|\mathcal{N}||\mathcal{B}|} \rangle$ is considered in Fig. 9(b), the correlation strengthens. This is explained by the fact that baroclinic torque is typically large where the pressure and density gradients are large. The residual term also tends to be largest where large gradients are located, since part of the residual term is due to numerical diffusion acting to smooth out gradients. Density is one of the solution variables in Athena-RFX, and thus gradients of density are attenuated such that $\mathcal{N}$ should be large wherever gradients of density are large (i.e., where baroclinic torque is also large).

The correlation between temperature and baroclinic torque, $\langle c_{\mathcal{TB}} \rangle$ in Fig. 9(a), is similar to the correlation between temperature and dilatation, with a stronger correlation at positive time lags, indicating that baroclinic torque is large before increases in temperature occur. Consequently, we find that baroclinic torque is most prominent immediately prior to heat release from chemical reactions,

Published under an exclusive license by AIP Publishing

corresponding to flame locations roughly at the transition between the preheat and reaction zones (close to $T = 1400$ K in the present case). The same conclusion is obtained from $\langle c_{T|\mathcal{B}|}\rangle$ in Fig. 9(b), and is also consistent with the observation in Hamlington *et al.*[1] that the conditional average of the baroclinic torque (where the conditioning is based on the reactant mass fraction) is largest near the transition between the preheat and reaction zones.

Finally, the correlation between enstrophy and baroclinic torque, $\langle c_{\Omega\mathcal{B}}\rangle$ in Fig. 9(a), is relatively weak, with a small peak at zero time lag. When $\langle c_{\Omega|\mathcal{B}|}\rangle$ in Fig. 9(b) is instead considered, a stronger correlation is found between enstrophy and the magnitude of baroclinic torque at negative time lags, indicating that enstrophy is smaller after baroclinic torque acts. However, despite the fact Fig. 9 shows that enstrophy decreases after baroclinic torque acts, we cannot conclude that baroclinic torque is responsible for the decrease in enstrophy. Instead, the observed decrease in enstrophy is more likely due to concurrently large dilatation and enhanced viscous transport, both of which have large negative magnitudes when the baroclinic torque has a large positive magnitude; this conclusion is supported, for example, by the strongly negative correlation between $\mathcal{L}$ and $\mathcal{B}$ shown in Fig. 9(a). Once more, despite the fact that baroclinic torque does act to enhance enstrophy through the flame, it is typically large and positive where other effects (e.g., dilatation and viscous transport) are also large but negative, thereby mitigating the overall enhancement of enstrophy by combustion processes.

IV. CONCLUSIONS

Enstrophy dynamics in a highly turbulent statistically planar premixed methane–air flame have been examined using a Lagrangian analysis approach. In addition to vortex stretching, viscous transport, dilatation, and baroclinic torque terms in the enstrophy governing equation, a residual term from the DNS was included in the analysis, allowing for improved agreement between the left- and right-hand sides of the governing equation and ensuring the accuracy of the results. Through the resulting analysis, progress has been made in addressing each of the three questions identified in Sec. I.

For the first question, related to the cumulative effects of different dynamical terms on the enstrophy along trajectories, we found, as in previous studies of highly turbulent statistically planar premixed flames, that the dominant terms in the enstrophy dynamics were vortex stretching and viscous transport. In particular, the cumulative effects of each of these terms along Lagrangian trajectories were roughly an order of magnitude greater than dilatation and baroclinic torque. Consistent with previous studies, the average cumulative effect of stretching and baroclinic torque was found to increase enstrophy, whereas viscous transport and dilatation tended to decrease enstrophy along fluid pathlines. However, although vortex stretching and viscous transport were found to be the dominant individual terms in the enstrophy dynamics, when considered together, the combined cumulative effects of these terms were slightly less than a factor of two larger than the combined effects of dilatation and baroclinic torque, which are both nonzero primarily due to heat release from the flame. These results are consistent with those found in previous studies of statistically planar premixed flames,[1,4,5] although they differ from results for statistically planar flames with smaller Lewis numbers[34] and for more practical configurations with persistent mean pressure gradients,[9–11] both of which reveal a greater importance of baroclinic torque in the overall enstrophy dynamics. There is, however, no inconsistency in any of these results, and the primary conclusion gained is that care should be taken when generalizing results for statistically planar flames with near-unity Lewis numbers to other conditions and configurations.

To address the second question in Sec. I, we performed a conditional analysis of the trajectories, where the conditioning was based on whether each trajectory exhibited an increase or decrease in enstrophy through the flame. This analysis showed that over a quarter of all trajectories had an increase in enstrophy through the flame and that these increases were due primarily to relatively infrequent, but quite large, values of the enstrophy budget terms. Thus, while it is true that, on average, enstrophy decreases through the present highly turbulent, statistically planar premixed flame, we have also shown that individual trajectories are capable of increasing in enstrophy and that these increases are not especially rare events, even in highly turbulent statistically planar premixed flames. Moreover, the importance of extreme events in the overall enstrophy budget suggests a connection to turbulence intermittency, which is more pronounced at the high Reynolds numbers characteristic of many highly turbulent combustion problems. By contrast, decreases in enstrophy were found to be less likely the result of extreme values of enstrophy budget terms.

The observation that the baroclinic torque is large immediately prior to increases in temperature suggest that this term is largest near the preheat zone immediately prior to the transition to the reaction zone. This observation is most likely due to the fact that large values of the baroclinic torque require both large gradients in thermodynamic properties, as well as substantial misalignment between these gradients. These two conditions are approximately satisfied at the transition to the reaction zone where the turbulence, which leads to the misaligned gradients, has not yet weakened appreciably due to viscous transport and dilatation, but the thermodynamic gradients are beginning to increase due to heat release by reactions.

Finally, to address the third question in Sec. I related to the temporal correspondence between different physical phenomena, we performed a temporal cross correlation analysis of temperature, enstrophy, and normalized enstrophy budget terms along particle trajectories. This analysis showed that baroclinic torque and dilatation are strongly negatively correlated, and that smaller vorticity magnitudes are associated with large magnitudes of both the baroclinic torque and dilatation. Correlations between baroclinic torque and enstrophy show that baroclinic torque has a small but measurable effect in increasing enstrophy, although the simultaneously occurring reductions in enstrophy due to viscous transport and dilatation tend to overwhelm the increases due to baroclinic torque, resulting in an average net decrease in enstrophy through the flame.

This study suggests a number of directions for future research. The importance of pressure and density gradients in setting the baroclinic torque, and the observation that the residual tends to be large when the baroclinic torque is large, suggests the need for further increases in spatial resolution to further reduce the residual and obtain an even more accurate analysis of different dynamical effects on the enstrophy. It is not expected, however, that the calculations of the baroclinic torque have been substantially impacted in the present analysis, but rather that further increases in resolution will reduce the contribution of numerical dissipation to the residual.

Published under an exclusive license by AIP Publishing

With respect to other future directions, although we have included viscous transport from Eq. (4) in the analysis, this term can be further separated into contributions from viscous dissipation and viscous diffusion, with and without viscosity and density gradients, for both solenoidal and dilatational modes. This analysis would serve to further elucidate the precise viscous effects on enstrophy through the flame. The present Lagrangian enstrophy analysis should also be extended to other statistically planar premixed flames occurring at lower turbulence intensities and Karlovitz numbers, where effects due to the flame are expected to be more pronounced.

The effects of different Lewis numbers, including flames where species Lewis numbers vary considerably, as well as different fuels, should also be considered, particularly given the dependence of vorticity dynamics on Lewis number[34] and of the turbulence kinetic energy on fuel type[46] noted in previous studies. It would also be beneficial to repeat the cumulative, conditional, and correlation analyses outlined here in more realistic configurations where mean pressure-gradients are present and baroclinic torque is expected to be much stronger, particularly at high turbulence intensities. Recent research by Geikie and Ahmed[9] and Kazbekov and Steinberg,[10,11] in particular, has shown that baroclinic torque becomes an increasingly dominant contributor to enstrophy production at highly turbulent conditions, potentially resulting in a net increase in enstrophy through the flame, by contrast to the reduction in enstrophy observed in statistically planar configurations. The extension of the present analysis to these and other flows would also enable more general statements to be made regarding the importance of baroclinic torque and flame generated vorticity at highly turbulent conditions, as well as provide insights for the development of subgrid-scale models for large eddy simulations of practical combustion problems involving high turbulence intensities.

ACKNOWLEDGMENTS

R.D. was supported by a National Defense Science and Engineering Graduate Fellowship. M.A.M. was supported by a NSF Graduate Research Fellowship. C.A.Z.T. and P.E.H. were supported, in part, by AFOSR Award No. FA9550–17-1–0144 and NSF Award No. 1847111. Helpful discussions with Dr. Alexei Poludnenko are gratefully acknowledged.

DATA AVAILABILITY

The data that support the findings of this study are available from the corresponding author upon reasonable request.

REFERENCES

[1]P. E. Hamlington, A. Y. Poludnenko, and E. S. Oran, "Interactions between turbulence and flames in premixed reacting flows," Phys. Fluids **23**, 125111 (2011).
[2]N. Chakraborty, "Statistics of vorticity alignment with local strain rates in turbulent premixed flames," Eur. J. Mech. B **46**, 201–220 (2014).
[3]A. N. Lipatnikov, S. Nishiki, and T. Hasegawa, "A direct numerical simulation study of vorticity transformation in weakly turbulent premixed flames," Phys. Fluids **26**, 105104 (2014).
[4]B. Bobbitt and G. Blanquart, "Vorticity isotropy in high Karlovitz number premixed flames," Phys. Fluids **28**, 105101 (2016).
[5]B. Bobbitt, S. Lapointe, and G. Blanquart, "Vorticity transformation in high Karlovitz number premixed flames," Phys. Fluids **28**, 015101 (2016).
[6]V. Papapostolou, D. H. Wacks, N. Chakraborty, M. Klein, and H. G. Im, "Enstrophy transport conditional on local flow topologies in different regimes of premixed turbulent combustion," Sci. Rep. **7**, 11545 (2017).
[7]B. Coriton and J. H. Frank, "Experimental study of vorticity-strain rate interaction in turbulent partially premixed jet flames using tomographic particle image velocimetry," Phys. Fluids **28**, 025109 (2016).
[8]H. Wang, E. R. Hawkes, and J. H. Chen, "Turbulence-flame interactions in DNS of a laboratory high Karlovitz premixed turbulent jet flame," Phys. Fluids **28**, 095107 (2016).
[9]M. K. Geikie and K. A. Ahmed, "Pressure-gradient tailoring effects on the turbulent flame-vortex dynamics of bluff-body premixed flames," Combust. Flame **197**, 227– 242 (2018).
[10]A. Kazbekov, K. Kumashiro, and A. M. Steinberg, "Enstrophy transport in swirl combustion," J. Fluid Mech. **876**, 715–732 (2019).
[11]A. Kazbekov and A. M. Steinberg, "Flame- and flow-conditioned vorticity transport in premixed swirl combustion," Proc. Combust. Inst. **38**, 2949 (2021).
[12]A. Lipatnikov and J. Chomiak, "Effects of premixed flames on turbulence and turbulent scalar transport," Prog. Energy Combust. Sci. **36**, 1–102 (2010).
[13]A. M. Steinberg, P. E. Hamlington, and X. Zhao, "Structure and dynamics of highly turbulent premixed combustion," Prog. Energy Combust. Sci. **85**, 100900 (2021).
[14]J. Urzay, "Supersonic combustion in air-breathing propulsion systems for hypersonic flight," Annu. Rev. Fluid Mech. **50**, 593–627 (2018).
[15]J. F. Driscoll, J. H. Chen, A. W. Skiba, C. D. Carter, E. R. Hawkes, and H. Wang, "Premixed flames subjected to extreme turbulence: Some questions and recent answers," Prog. Energy Combust. Sci. **76**, 100802 (2020).
[16]A. Y. Poludnenko, "Pulsating instability and self-acceleration of fast turbulent flames," Phys. Fluids **27**, 014106 (2015).
[17]E. E. O'Brien, "Lagrangian history direct interaction equations for isotropic turbulent mixing under a second–order chemical reaction," Phys. Fluids **11**, 2328 (1968).
[18]H. A. Uranakara, S. Chaudhuri, H. L. Dave, P. G. Arias, and H. G. Im, "A flame particle tracking analysis of turbulence–chemistry interaction in hydrogen–air premixed flames," Combust. Flame **163**, 220 (2016).
[19]H. L. Dave, A. Mohan, and S. Chaudhuri, "Genesis and evolution of premixed flames in turbulence," Combust. Flame **196**, 386–399 (2018).
[20]H. L. Dave and S. Chaudhuri, "Evolution of local flame displacement speeds in turbulence," J. Fluid Mech. **884**, A46 (2020).
[21]J. You and Y. Yang, "Modelling of the turbulent burning velocity based on Lagrangian statistics of propagating surfaces," J. Fluid Mech. **887**, A11 (2020).
[22]M. Day, S. Tachibana, J. Bell, M. Lijewski, V. Beckner, and R. K. Cheng, "A combined computational and experimental characterization of lean premixed turbulent low swirl laboratory flames: I. Methane flames," Combust. Flame **159**, 275–290 (2012).
[23]M. Day, S. Tachibana, J. Bell, M. Lijewski, V. Beckner, and R. K. Cheng, "A combined computational and experimental characterization of lean premixed turbulent low swirl laboratory flames: II. Hydrogen flames," Combust. Flame **162**, 2148–2165 (2015).
[24]A. Steinberg, B. Coriton, and J. Frank, "Influence of combustion on principal strain-rate transport in turbulent premixed flames," Proc. Combust. Inst. **35**, 1287–1294 (2015).
[25]J. R. Osborne, S. A. Ramji, C. D. Carter, and A. M. Steinberg, "Relationship between local reaction rate and flame structure in turbulent premixed flames from simultaneous 10 kHz TPIV, OH PLIF, and CH_2O PLIF," Proc. Combust. Inst. **36**, 1835–1841 (2017).
[26]P. E. Hamlington, R. Darragh, C. A. Briner, C. A. Towery, B. D. Taylor, and A. Y. Poludnenko, "Lagrangian analysis of high-speed turbulent premixed reacting flows: Thermochemical trajectories in hydrogen–air flames," Combust. Flame **186**, 193–207 (2017).
[27]R. Darragh, C. A. Towery, A. Y. Poludnenko, and P. E. Hamlington, "Particle pair dispersion and eddy diffusivity in a high-speed premixed flame," Proc. Combust. Inst. **38**, 2845 (2021).
[28]J. M. Stone, T. A. Gardiner, P. Teuben, J. F. Hawley, and J. B. Simon, "Athena: A new code for astrophysical MHD," Astrophys. J. Suppl. Ser. **178**, 137–177 (2008).
[29]A. Poludnenko and E. Oran, "The interaction of high-speed turbulence with flames: Global properties and internal flame structure," Combust. Flame **157**, 995–1011 (2010).
[30]C. A. Z. Towery, A. Y. Poludnenko, J. Urzay, J. O'Brien, M. Ihme, and P. E. Hamlington, "Spectral kinetic energy transfer in turbulent premixed reacting flows," Phys. Rev. E **93**, 053115 (2016).

Published under an exclusive license by AIP Publishing

[31]P. Colella, "Multidimensional upwind methods for hyperbolic conservation laws," J. Comput. Phys. **87**, 171–200 (1990).
[32]J. Saltzman, "An unsplit 3D upwind method for hyperbolic conservation laws," J. Comput. Phys. **115**, 153–168 (1994).
[33]A. Vié, B. Franzelli, Y. Gao, T. Lu, H. Wang, and M. Ihme, "Analysis of segregation and bifurcation in turbulent spray flames: A 3D counterflow configuration," Proc. Combust. Inst. **35**, 1675–1683 (2015).
[34]C. Dopazo, L. Cifuentes, and N. Chakraborty, "Vorticity budgets in premixed combusting turbulent flows at different Lewis numbers," Phys. Fluids **29**, 045106 (2017).
[35]C. Xu, A. Y. Poludnenko, X. Zhao, H. Wang, and T. Lu, "Structure of strongly turbulent premixed n-dodecane–air flames: Direct numerical simulations and chemical explosive mode analysis," Combust. Flame **209**, 27–40 (2019).
[36]N. Peters, *Turbulent Combustion* (Cambridge University Press, Hochschule, Aachen, Germany, 2000).
[37]Y. Kozak, S. Dammati, L. Bravo, P. Hamlington, and A. Poludnenko, "Weno interpolation for Lagrangian particles in highly compressible flow regimes," J. Comput. Phys. **402**, 109054 (2020).
[38]R. A. Darragh, C. A. Towery, P. E. Hamlington, and A. Poludnenko, "Lagrangian analysis of vorticity dynamics in turbulent premixed flames," AIAA Paper No. 2017-3466, 2017.
[39]F. S. Schranner, J. A. Domaradzki, S. Hickel, and N. A. Adams, "Assessing the numerical dissipation rate and viscosity in numerical simulations of fluid flows," Comput. Fluids **114**, 84–97 (2015).
[40]J. O'Brien, C. A. Towery, P. E. Hamlington, M. Ihme, A. Y. Poludnenko, and J. Urzay, "The cross-scale physical-space transfer of kinetic energy in turbulent premixed flames," Proc. Combust. Inst. **36**, 1967–1975 (2017).
[41]J. Kim, M. Bassenne, C. A. Z. Towery, P. E. Hamlington, A. Y. Poludnenko, and J. Urzay, "Spatially localized multi-scale energy transfer in turbulent premixed combustion," J. Fluid Mech. **848**, 78–116 (2018).
[42]S. H. Whitman, C. A. Towery, A. Y. Poludnenko, and P. E. Hamlington, "Scaling and collapse of conditional velocity structure functions in turbulent premixed flames," Proc. Combust. Inst. **37**, 2527–2535 (2019).
[43]P. E. Hamlington, A. Y. Poludnenko, and E. S. Oran, "Intermittency in premixed turbulent reacting flows," Phys. Fluids **24**, 075111 (2012).
[44]J. R. Buck, M. M. Daniel, and A. C. Singer, *Computer Explorations in Signals and Systems Using MATLAB*, 2nd ed. (Prentice-Hall, Upper Saddle River, NJ, 2002).
[45]P. Stoica and R. Moses, *Spectral Analysis of Signals* (Prentice-Hall, Upper Saddle River, NJ, 2005).
[46]L. Paxton, J. Smolke, and F. N. Egolfopoulos, "Effects of heat release and fuel type on highly turbulent premixed jet flames," Proc. Combust. Inst. **37**, 2565–2572 (2019).

Published under an exclusive license by AIP Publishing

Journal of Computational Physics 402 (2020) 109054

Contents lists available at ScienceDirect

Journal of Computational Physics

www.elsevier.com/locate/jcp

WENO interpolation for Lagrangian particles in highly compressible flow regimes

Y. Kozak [a,*], S.S. Dammati [a], L.G. Bravo [b], P.E. Hamlington [c], A.Y. Poludnenko [a,d]

[a] Department of Aerospace Engineering, Texas A&M University, College Station, TX 77843, USA
[b] Propulsion Division, Vehicle Technology Directorate U.S. Army Research Laboratory, Aberdeen Proving Ground, MD 21005, USA
[c] Department of Mechanical Engineering, University of Colorado, Boulder, CO 80309, USA
[d] Department of Mechanical Engineering, University of Connecticut, Storrs, CT 06269, USA

ARTICLE INFO

Article history:
Received 21 May 2019
Received in revised form 24 September 2019
Accepted 22 October 2019
Available online 28 October 2019

Keywords:
WENO
Lagrangian-particle tracking analysis
Compressible flows

ABSTRACT

Lagrangian particles can be used either to analyze different complex flows, as massless tracers, or to model multiphase flows, as particles with mass. As particles can have arbitrary positions within the computational domain, interpolation of different flow quantities from the Eulerian grid is essential. Low-order centered interpolation schemes generally do not provide a sufficient level of accuracy for many flow configurations of interest. Thus, typically, high-order centered interpolation schemes are utilized. The current study demonstrates that for highly compressible non-reacting and reacting flow regimes, in which discontinuities in the flow field, e.g., shock waves arise, centered interpolation schemes tend to smear the shock and high order schemes also produce numerical oscillations. It is shown that this problem can be remedied by using Weighted-Essentially-Non-Oscillatory (WENO) interpolation schemes. Extensive numerical tests are performed in order to demonstrate this, comparing the performance of WENO-3 and WENO-5 interpolation schemes with a variety of centered interpolation schemes. The first test case involves specially designed steady state two-dimensional vortex flows. For a smooth flow, WENO schemes provide comparable accuracy to other high-order centered schemes. For flow fields with discontinuities, WENO-3 and WENO-5 interpolation schemes can decrease the interpolation error by more than two and three orders of magnitude, respectively, in comparison with centered schemes. Solution accuracy is further studied with a normal shock wave test. It is demonstrated that centered schemes tend to smear the shock, whereas, WENO schemes capture it in a much sharper manner. Moreover, high-order centered schemes tend to oscillate in the vicinity of the discontinuity leading to non-physical results, such as negative absolute pressure values. The same trends are retained for an unsteady three-dimensional spherical blast wave, where the shock is smeared across several grid cells, which is typical for shock-capturing flow solvers. Finally, the benefits of WENO schemes for the Lagrangian-particle tracking analysis of highly compressible reactive flows are explored by comparing various Lagrangian particle trajectories and joint probability density functions (PDFs) for a two-dimensional cellular detonation. The results indicate that high-order centered schemes lead to unphysical results, whereas WENO schemes can provide high-order interpolation that is free of severe numerical oscillations and non-physical artifacts, which is critical for the proper analysis of the flow.

© 2019 Elsevier Inc. All rights reserved.

* Corresponding author.
E-mail address: kozaky@tamu.edu (Y. Kozak).

https://doi.org/10.1016/j.jcp.2019.109054
0021-9991/© 2019 Elsevier Inc. All rights reserved.

1. Introduction

A wide range of flows involve high speeds and compressibility. These include supersonic and hypersonic boundary layers [1], atmospheric flow around the reentry vehicles [2], as well as various propulsion and energy conversion systems, such as scramjet engines, where the combustion process is supersonic [3], and pulsating and rotating detonation engines [4,5]. Other examples include industrial explosions such as in coal mines [6] or storage silos [7]. High-speed regimes can also arise through the complex interaction between exothermic reactions and turbulence that entails significant up-scale transfer of kinetic energy known as backscatter [8–10]. For instance, interaction between flames and high-speed turbulence can lead to a deflagration-to-detonation transition (DDT) [11].

Numerical simulations of these complex flows often involve Lagrangian particles that can be either massless or with a finite mass. Massless particle trajectories can be used to investigate the flow field, in a procedure known as Lagrangian-particle tracking analysis. On the other hand, particles with mass can be used to model multiphase flows, for instance, droplets in spray combustion [12]. Numerical solution of the coupled set of flow and Lagrangian particle equations requires at least two key steps. First, as particle position rarely coincides with the Eulerian flow field cell centers, interpolation is necessary in order to reconstruct different flow quantities at a particle position. Second, a numerical time integration scheme is utilized in order to advect the particles across the grid. For particles with mass, a third step is necessary, as two-way coupling between the particles and the fluid requires feedback of momentum and energy from particles position to the cell centers. For highly compressible flow regimes that involve discontinuities in the flow, such as shock waves, special treatment may be necessary for each of these three steps, in order to attain an accurate and physically sound numerical solution. The current work focuses on the first step in order to tackle this complicated problem. Thus, here we consider solely the operation of interpolation for grid quantities.

As mentioned above, one possible method to investigate complex flows is via the Lagrangian-particle tracking analysis, where a large number of point massless particles (fluid parcels) are seeded in the flow and subsequently their trajectories are followed. The only difference of this representation of the flow field from the classical Eulerian point of view, which is typically used to model flows, is the frame of reference. Lagrangian analysis, however, has several advantages, especially for complex multi-physics flows, e.g., with reactions [13]. First, different quantities of interest such as pressure, temperature, mass fraction of species, etc., can be tracked directly through the flow. This is contrary to the Eulerian frame of reference, where these quantities are defined only at discrete points. Second, as a Lagrangian particle exactly follows the flow trajectory, there is no advection into or out of the particle. This allows one to separate the effect of complex multi-physics processes, e.g., chemical reaction or molecular transport, from the convective transport. Third, particle residence times and path lengths during different stages of interest of the flow evolution can be calculated. All of these attributes of the Lagrangian analysis can provide significant insights into the flow dynamics, not achievable in the Eulerian frame of reference. One should note that proper analysis is only possible once the temporal and spatial numerical errors associated with time integration and interpolation, respectively, are sufficiently small.

Lagrangian analysis of flows based on the direct numerical simulations (DNS) was pioneered more than 40 years ago by Riley and Patterson [14]. They analyzed a non-reacting incompressible turbulent flow, where a low-order linear interpolation was utilized to reconstruct the velocity at the Lagrangian particle positions. Yeung and Pope [15] conducted a comprehensive analysis in order to determine the required level of accuracy for both time integration and spatial interpolation methods. They found that time integration errors are negligible as typically the time-step size used for DNS simulations is rather small. This stems from the fact that for many flow solvers the Courant–Friedrichs–Lewy (CFL) number must be lower than 1 to achieve a stable solution. Spatial interpolation errors, on the other hand, were found to be more significant, and the use of higher-order interpolation methods was recommended, as low-order linear interpolation was found not sufficiently accurate. Since then, many studies have tested the accuracy of different interpolation schemes for non-reacting incompressible turbulent flows [16–18], and today it is agreed that low-order linear interpolation cannot provide a sufficient level of accuracy [19]. For a detailed discussion of the Lagrangian analysis of non-reacting incompressible turbulent flows we refer the readers to the extensive review papers by Yeung [19] or Toschi and Bodenschatz [20].

For more complex, multi-physics flows, in particular with chemical reactions, Lagrangian-particle tracking analysis has started to emerge only in recent years. Day et al. [21] used Lagrangian analysis to investigate premixed turbulent methane flames in a low-swirl combustor. Linear interpolation was used in order to reconstruct different Eulerian field quantities at a particle position [22]. In a follow-up paper, the same configuration was studied with premixed turbulent hydrogen flames [23]. Darragh et al. [24] developed a Lagrangian-tracking particle method for reacting flows. They tested the accuracy of the method using different time integration and interpolation schemes. It was also concluded that linear interpolation does not provide sufficient accuracy, and the chosen methods were high-order Akima splines for spatial interpolation in conjunction with the 4th- and 5th-order explicit Runge–Kutta methods for time integration. Hamlington et al. [13] utilized this framework to study high-speed premixed turbulent hydrogen-air flame with single- and multi-step reaction kinetics. Fukushima et al. [25] used DNS with Lagrangian analysis in order to classify combustion regimes for the homogeneous charge compression ignition (HCCI) and premixed charge compression ignition (PCCI) engines. They interpolated values at a particle position via the 4th-order Lagrange polynomial interpolation and utilized the 3rd order Runge–Kutta method for time integration. Another application that was recently pursued involved the use of the Lagrangian analysis in order to gain a better understanding of premixed autoignition [26]. It is also worth mentioning recent works that consider Lagrangian tracking of flame elements [27,28] and Lagrangian analysis using experimental data sets [29–31]. One should note that

reacting flows typically have variable density, as they involve large density changes due to the expansion of gas in flame. At the same time, for all studies mentioned above, the compressibility levels of the flow are rather low. For instance, Day et al. [21] are using the low-Mach approximation in order to solve the flow equations. Yet, even when fully compressible flow solvers are utilized, as in Ref. [13], the flows themselves are relatively weakly compressible with a turbulent Mach number not exceeding the value of 0.3 in any of the studied cases. Moreover, none of these works deal with highly shocked flows or detonations, and thus it is not surprising that the same methods used for non-reacting incompressible turbulent flows are applicable.

For the Lagrangian analysis of non-reacting compressible turbulent flows, the approaches used are different. Most studies use linear interpolation [32–39], and some of them describe difficulties that arise once high-order interpolation schemes are utilized. For instance, Beetz et al. [32] report difficulties with the interpolation of density, which must always be positive. Yet, they describe negative density values near strong shocks [33]. Yang et al. [34] note that a linear interpolation is used in order to avoid unphysical oscillations near shocklets, which suggests that higher-order interpolation methods tend to oscillate. It should be noted that Federrath et al. [36] and Konstandin et al. [37] report that higher-order schemes do not improve the accuracy of their results, but do not describe any specific issues with high-order interpolation. Obviously, as for the case of incompressible turbulence, high-order interpolation can provide higher level accuracy at least for some applications, and allows one to avoid the need for excessive grid refinement to reduce the spatial interpolation error. Works that deal with both reacting and highly compressible flows are scarce. For instance, in Ref. [40], nonpremixed autoignition is investigated for turbulent Mach numbers as high as unity. Yet, no special treatment for interpolation from the Eulerian grid to the Lagrangian particle position is performed.

The issue of numerical oscillations, which are induced by high-order schemes, discussed above is actually well-known in other quite different fields. For instance, in smooth particle hydrodynamics (SPH), kernel interpolation is performed typically with 2nd-order schemes, which has the same order of accuracy as linear interpolation. The reason is that high-order schemes tend to oscillate and undershoot leading to negative density values [41]. A more common example is the problem faced by compressible flow solvers once shocked flows arise. It is known that low-order methods will never oscillate in the presence of shocks [42]. However, low-order methods are extremely diffusive, inaccurate, and tend to smear the shock, which requires excessive grid refinement that is not always practical. High-order methods are much more accurate, but without any special treatment they will always oscillate near the shock in a rather unphysical manner [42]. Different solutions to this problem have been suggested over the years, e.g., total variation diminishing (TVD) methods [43].

To the best of the authors' knowledge, a solution for this issue for massless Lagrangian point particles has not been demonstrated. For particles with mass, however, Jacobs and Don [44] suggested to use an Essentially-Non-Oscillatory (ENO) interpolation scheme. The idea behind ENO is that the interpolation stencil is divided into several sub-stencils and one stencil is chosen according to its local smoothness [45]. They showed that ENO interpolation can provide a more accurate and stable solution than high-order centered interpolation schemes. In the current work, we suggest to solve the issue of numerical oscillations induced by high-order centered interpolation schemes by utilizing a Weighted-Essentially-Non-Oscillatory (WENO) interpolation scheme. WENO schemes were first developed by Liu et al. [46] and then improved by Jiang and Shu [47]. WENO interpolation is similar to ENO interpolation, and the interpolation procedure is based on a convex combination of all candidate sub-stencils instead of a single sub-stencil like in the case of ENO. This approach has several advantages. First, the approach adopted by Jacobs and Don [44] requires switching between a centered interpolation scheme, once the flow is smooth, and an ENO scheme, once the flow is discontinuous. This means that some threshold criterion for switching has to be chosen, and its specific value can affect the solution. For WENO schemes, no threshold condition is necessary, and the scheme automatically reduces to a centered scheme once the flow is smooth. Second, it is difficult to vectorize ENO schemes as they are based on multiple conditional statements. WENO schemes are based mostly on arithmetic operations, and thus can be vectorized in an efficient manner. Third, the ENO implementation presented by Jacobs and Don [44] cannot handle multiple shocks that cross the stencil. The proposed WENO formulation can handle multiple shocks with some limitations, as will be described below. One should note that both ENO and WENO schemes do not eliminate oscillations completely. However, the magnitude of the oscillations decays as $O(\Delta x^k)$, where Δx is the grid spacing and k is the order of accuracy [45]. Thus, oscillations are greatly reduced as the grid is refined, and for any practical purpose become negligible. This is actually the reason these schemes are referred to as essentially non-oscillatory schemes.

Kozak et al. [48] presented a WENO-3 interpolation scheme for Lagrangian point particles and tested its performance against different centered interpolation schemes. The main focus of that work was on the coupling of different interpolation schemes with symplectic or trajectory-preserving time integration methods. As such, the trajectory errors of particles were analyzed showing that once discontinuities are introduced to the flow, the proposed WENO scheme reduces the trajectory errors by more than an order of magnitude in comparison with different centered schemes. Present work introduces a high-order WENO-5 interpolation scheme. As discussed above, the focus here is solely on the interpolation methods, thus we consider only the interpolated quantities of interest such as velocity, pressure, temperature, etc., which are independent of the time-integrator temporal numerical errors. Hence, the results presented in this paper are applicable to essentially any time-integration method. The numerical tests in this paper focus on massless particles, yet the proposed methods and the results are applicable to particles with mass as well. Various extensive numerical tests are performed, including two-dimensional vortex flows, and realistic flows of interest such a normal shock wave, a three-dimensional spherical blast wave and a two-dimensional cellular detonation, which represents a typical highly-compressible reactive flow case. These

test cases will demonstrate the advantages of WENO schemes over centered schemes and will shed some light on the source of the numerical oscillations for the high-order centered interpolation schemes.

2. Lagrangian tracking method

The equation of motion for a massless Lagrangian point particle is based on the following simple kinematic relation:

$$\frac{d\mathbf{x}}{dt} = \mathbf{v} = \mathbf{u}\big(\mathbf{x}(t), t\big), \tag{1}$$

where $\mathbf{x}$ is the particle position, $\mathbf{v}$ is the particle velocity, and $\mathbf{u}$ is the flow velocity in the Eulerian frame of reference. Equation (1) can be integrated via the following initial condition for the particle position:

$$\mathbf{x}\left(t_0\right) = \mathbf{x}_0, \tag{2}$$

where t_0 is the initial time, and $\mathbf{x}_0$ is the initial particle position. Numerical integration of Eq. (1) requires the Eulerian velocity at the particle position. The Eulerian flow field, however, is typically known only at discrete points. As such, interpolation must be carried out in order to reconstruct the velocity at the particle position. In fact, this is required for any flow quantity of interest, such as pressure, temperature, density, etc. Also, the time derivative needs to be discretized by an integration method. Thus, solution of Eq. (1) involves both spatial and temporal numerical errors. In order to guarantee that the particle will follow the flow trajectory, these errors should be minimized as much as possible. It should be stressed that for massless particles, only the particle position depends both on the temporal discretization and spatial interpolation errors. All other flow quantities of interest, such as velocity, pressure, temperature, density, mass fraction of species, etc., depend solely on the spatial interpolation error. Note that the framework used in this paper is often referred to as an *online* approach. Hence, Eq. (1) is solved at each time step concurrently with the hydrodynamic integration after the flow field is evolved. This is in contrast with an *offline* approach, in which Eq. (1) is solved only after the flow simulation has ended. Yet, all the methods described in the current work are applicable to both approaches.

For the time integration, we use the Crank-Nicolson scheme:

$$\mathbf{x}^{n+1} = \mathbf{x}^n + \frac{1}{2}\Delta t\left(\mathbf{v}^n + \mathbf{v}^{n+1}\right) \tag{3}$$

The full integration procedure is described in [48]. We emphasize, though, that the focus of this current work is not time integration. All tests presented here focus on the interpolation of the flow quantities independently of the temporal discretization error. Thus, results presented in this paper are applicable to essentially any time integration method.

Different interpolation schemes are used for the spatial reconstruction of various quantities from a Eulerian grid to the particle position. These interpolation schemes can be represented by the weight functions [49]. The weight function, W, depends on the following single parameter that represents a dimensionless distance:

$$\tilde{x}_i = \frac{\left|x - x_{c_i}\right|}{\Delta x}, \tag{4}$$

where x is the particle x-position, x_{c_i} is the cell center x-position, and Δx is the grid spacing. Similar dimensionless parameters can be derived for the y- and z-directions. A quantity F can be interpolated from the cell centers to a particle position via the following formula:

$$F\left(x\right) = \sum_i W\left(\tilde{x}_i\right) F\left(x_{c_i}\right), \tag{5}$$

where the sum is taken over all adjacent cell centers, and the maximum value of i depends on the interpolation stencil size. The role of the weight function W in Eq. (5) is to prescribe the interpolation weights for each cell center according to its dimensionless distance from the particle position. All weight functions satisfy the following constraint:

$$\sum_i W\left(\tilde{x}_i\right) = 1. \tag{6}$$

This constraint guarantees that the weight function conserves the interpolated property [50]. Although the weight function is inherently one-dimensional (1D), it allows multidimensional interpolation [50], for instance, for the three-dimensional (3D) interpolation:

$$F\left(\mathbf{x}\right) = \sum_k \sum_j \sum_i W\left(\tilde{\mathbf{x}}_{i,j,k}\right) F\left(\mathbf{x}_{c_{i,j,k}}\right), \tag{7}$$

where

$$W\left(\tilde{\mathbf{x}}_{i,j,k}\right) = W\left(\frac{|x - x_{c_i}|}{\Delta x}\right) W\left(\frac{|y - y_{c_j}|}{\Delta y}\right) W\left(\frac{|z - z_{c_k}|}{\Delta z}\right), \tag{8}$$

and j and k are indices of adjacent cells in the y- and z-direction, respectively. One should note that an equally-spaced grid in each direction is assumed. It is important to mention that even for a multidimensional interpolation, the sum of weights still equals unity in a similar manner to Eq. (6), hence:

$$\sum_k \sum_j \sum_i W\left(\tilde{\mathbf{x}}_{i,j,k}\right) = 1 \tag{9}$$

Although this interpolation method is not multidimensional, as it is based on the product of one-dimensional weight functions, it has been successfully used for different applications [50–53]. A fully multidimensional interpolation can provide a higher level of accuracy. At the same time, the current approach is more computationally efficient [50], easier for implementation, and can provide the same order of accuracy as a fully multidimensional interpolation scheme with the same stencil size.

The following weight functions were implemented and investigated in the current work:

CIC (*Cloud-In-Cell*) [50]:

$$W\left(\tilde{x}\right) = \begin{cases} 1 - \tilde{x}, & \tilde{x} \le 1; \\ 0, & \tilde{x} > 1. \end{cases} \tag{10}$$

This scheme is a linear interpolation, and as such it has a 2-point stencil and it is 2nd-order accurate. It should be noted that its weights are continuous and positive.

TSC (*Triangular-Shaped-Cloud*) [50]:

$$W\left(\tilde{x}\right) = \begin{cases} \frac{3}{4} - \tilde{x}^2, & \tilde{x} < 0.5; \\ \frac{1}{2}\left(\frac{3}{2} - \tilde{x}\right)^2, & 0.5 \le \tilde{x} \le 1.5; \\ 0, & \tilde{x} > 1.5. \end{cases} \tag{11}$$

This scheme can be derived with a quadratic polynomial B-spline, and it has a 3-point stencil. As CIC, its order of accuracy is 2nd, and its weights are also strictly positive. However, it has several advantages over CIC. First of all, both weight values and the 1st derivative are continuous. Second, the locality errors associated with the interpolation position are greatly reduced in comparison with CIC [50]. These properties made this scheme useful for different applications, such as plasma physics and astrophysical flows [51–53].

QP (*Quadratic Polynomial*) [52]:

$$W\left(\tilde{x}\right) = \begin{cases} 1 - \tilde{x}^2, & \tilde{x} < 0.5; \\ \frac{1}{2}\left(1 - \tilde{x}\right)\left(2 - \tilde{x}\right), & 0.5 \le \tilde{x} \le 1.5; \\ 0, & \tilde{x} > 1.5. \end{cases} \tag{12}$$

This scheme is derived using quadratic Lagrange polynomials, and as such it provides 3rd order of accuracy with a 3-point stencil. Although its order of accuracy is greater than that of TSC with the same stencil size, its weight values are discontinuous, which means it is more oscillatory [52].

W_4 [54]:

$$W\left(\tilde{x}\right) = \begin{cases} 1 - \frac{5}{2}\tilde{x}^2 + \frac{3}{2}\tilde{x}^3, & \tilde{x} < 1; \\ \frac{1}{2}\left(2 - \tilde{x}\right)^2\left(1 - \tilde{x}\right), & 1 \le \tilde{x} \le 2; \\ 0, & \tilde{x} > 2. \end{cases} \tag{13}$$

This scheme is based on a cubic B-spline, and as such it has a 4-point stencil. Similar to QP, it is 3rd-order accurate, however, similarly to TSC, its weight values and the 1st derivative are continuous.

Everett's interpolation formula [54]:

$$W\left(\tilde{x}\right) = \begin{cases} \frac{1}{2}\left(2 - \tilde{x}\right)\left(1 - \tilde{x}^2\right), & \tilde{x} < 1; \\ \frac{1}{6}\left(2 - \tilde{x}\right)\left(3 - \tilde{x}\right)\left(1 - \tilde{x}\right), & 1 \le \tilde{x} \le 2; \\ 0, & \tilde{x} > 2. \end{cases} \tag{14}$$

This scheme can be derived with a cubic polynomial, and similarly to W_4, it has a 4-point stencil. It is, however, 4th-order accurate and only its weight values are continuous.

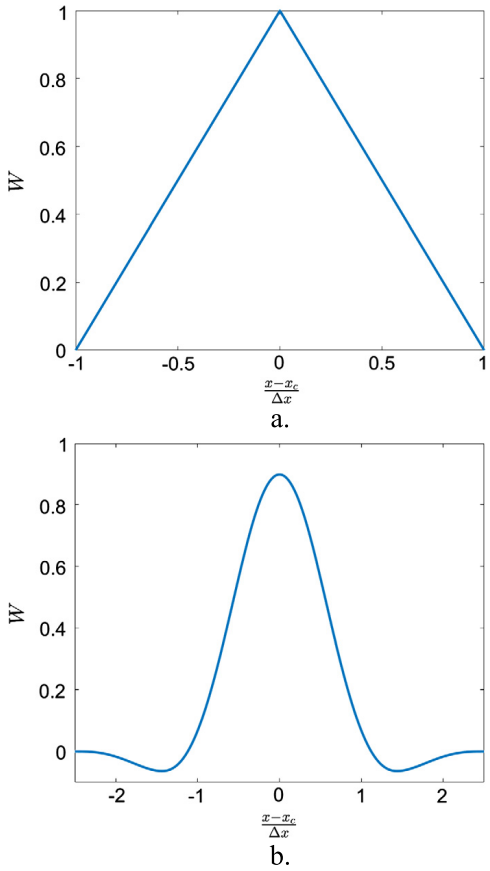


Fig. 1. Two weight functions, showing weight against the dimensionless distance: (a) CIC. (b) W_5.

W_5 [54]:

$$W\left(\tilde{x}\right)=\begin{cases}\frac{1}{48}\left(\frac{345}{8}-75\tilde{x}^2+42\tilde{x}^4\right), & \tilde{x}<\frac{1}{2};\\ \frac{1}{48}\left(\frac{165}{4}+20\tilde{x}-150\tilde{x}^2+120\tilde{x}^3-28\tilde{x}^4\right), & \frac{1}{2}\leq\tilde{x}\leq\frac{3}{2};\\ \frac{1}{48}\left(\tilde{x}-\frac{5}{2}\right)^3\left(7\tilde{x}-\frac{15}{2}\right), & \frac{3}{2}<\tilde{x}\leq\frac{5}{2};\\ 0, & \tilde{x}>\frac{5}{2}.\end{cases} \tag{15}$$

This scheme is an improved version of W_4 with a 5-point stencil. It can be derived with a quartic B-spline. It is 4th-order accurate, as Everett's interpolation formula, yet the weight values and their first two derivatives are continuous.

Note that for all weight functions with the order of accuracy greater than 2nd weights become negative [49]. Fig. 1 illustrates this point by showing two weight functions, CIC and W_5. The weights of CIC as a function of the dimensionless distance, see Eq. (4), can be seen in Fig. 1a. The weight function has a triangular shape, and all the weight values vary between zero and unity. As CIC is only 2nd order accurate, its weights can be strictly positive. In contrast, Fig. 1b shows the weights of W_5 as a function of the dimensionless distance. As the order of accuracy for W_5 is 4th, weights attain negative values. As will be shown later, the negative weights induce numerical oscillations once discontinuous values are being interpolated.

We present two interpolation schemes WENO-3 and WENO-5 [55] that remedy this issue. As these interpolation schemes are not centered, the weight function depends on the following, slightly altered, dimensionless parameter:

$$\tilde{x}=\frac{x-x_{c_i}}{\Delta x}. \tag{16}$$

WENO-3:

This interpolation scheme is derived using 2nd-order Lagrange polynomials, which results in a 3-point stencil. Once the quantities being interpolated are sufficiently smooth, it becomes identical to the QP centered scheme described above. Thus, as long as the flow gradients are low, the scheme is 3rd-order accurate. At the same time, once discontinuities, like shocks, are introduced into the flow, the scheme is reduced to a 2nd-order linear interpolation or extrapolation. The scheme is comprised of two sub-stencils, with each sub-stencil being associated with a linear weight for the left and right directions [55]:

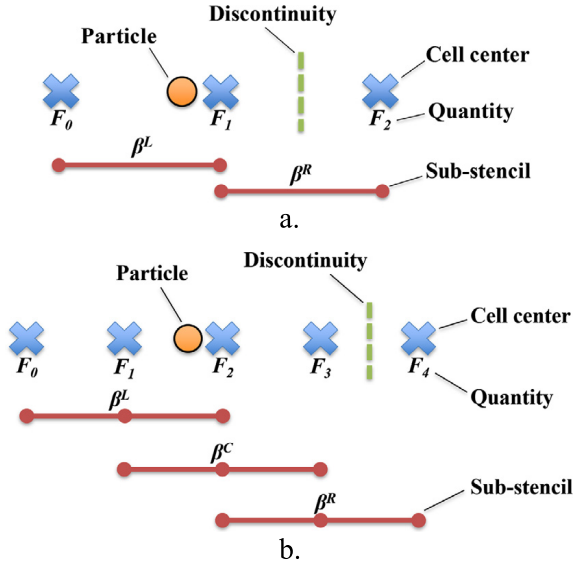


Fig. 2. Schematic description of the WENO interpolation procedure: (a) WENO-3. (b) WENO-5.

$$C^L = \frac{1}{2}\left(1-\tilde{x}\right), \qquad C^R = \frac{1}{2}\left(1+\tilde{x}\right). \tag{17}$$

Each sub-stencil has its own smoothness indicator, which provides an estimate for the gradients of the interpolated quantity in the sub-stencil:

$$\beta^L_{j,k} = \left(F_{1,j,k} - F_{0,j,k}\right)^2, \qquad \beta^R_{j,k} = \left(F_{2,j,k} - F_{1,j,k}\right)^2, \tag{18}$$

where j and k are indices for the y- and z-directions, and their values vary based on the stencil size. In this case, for a 3-point stencil, their range is 0–2. F can be any cell-centered flow quantity, e.g., velocity, pressure, temperature, etc. The non-linear weights are calculated via the following auxiliary variables:

$$\alpha^L_{j,k} = \frac{C^L}{\left(\beta^L_{j,k}+\varepsilon\right)^2}, \qquad \alpha^R_{j,k} = \frac{C^R}{\left(\beta^R_{j,k}+\varepsilon\right)^2}, \tag{19}$$

where ε is a small value in order to avoid division by zero, which is chosen as 10^{-14}. One may note that the values of ε suggested in the literature vary significantly from 10^{-6} to as low as 10^{-40} [55–57]. The value chosen proved to be sufficiently small for all the tests performed in the current work.

The resulting non-linear weights for the two sub-stencils are given by the following relations:

$$\omega^L_{j,k} = \frac{\alpha^L_{j,k}}{\alpha^R_{j,k}+\alpha^L_{j,k}}, \qquad \omega^R_{j,k} = \frac{\alpha^R_{j,k}}{\alpha^R_{j,k}+\alpha^L_{j,k}}. \tag{20}$$

Finally, the interpolation scheme can be presented in the form of the following weight function:

$$W_{j,k}\left(\tilde{x}\right) = \begin{cases} 0, & \tilde{x} < -\frac{3}{2}; \\ -\omega^L_{j,k}\tilde{x}, & -\frac{3}{2} \le \tilde{x} \le -\frac{1}{2}; \\ \omega^L_{j,k}\left(1+\tilde{x}\right) + \omega^R_{j,k}\left(1-\tilde{x}\right), & -\frac{1}{2} < \tilde{x} \le \frac{1}{2}; \\ \omega^R_{j,k}\tilde{x}, & \frac{1}{2} < \tilde{x} \le \frac{3}{2}; \\ 0, & \tilde{x} > \frac{3}{2}. \end{cases} \tag{21}$$

The typical representation of the interpolation scheme can be found in [55], though it should be noted that the weight function representation derived here is exactly equivalent. This new form is useful for the implementation in the code, as it has the same structure as the classical centered weight functions.

Note that in contrast to the centered schemes described above, the weight function (21) is asymmetric. Furthermore, its weights are non-linear, as they depend not only on the particle position but also on the cell-centered quantity gradients. Thus, the weights of the weight function (21) adapt themselves in order to avoid interpolation across a discontinuity. A schematic that depicts the procedure for the WENO-3 interpolation scheme is shown in Fig. 2a. For the presented case, the discontinuity passes through the right sub-stencil, thus, the value of β^R will be large. As such, the non-linear weight

for the right sub-stencil will be close to zero. Thus, interpolation will be performed almost solely with the left sub-stencil, where the flow is continuous, and interpolation through the discontinuity will be avoided.

Multidimensional interpolation can be carried out in a way similar to Eq. (7) for the centered schemes. For WENO schemes, however, even for an equally spaced grid, the one-dimensional weights at different positions are not identical because the flow gradients can be different. Thus, for a 3D interpolation, the following formula is used:

$$F(\mathbf{x}) = \sum_k \sum_j \sum_i W_{i,j,k}(\tilde{\mathbf{x}})\, F\left(\mathbf{x}_{c_{i,j,k}}\right), \tag{22}$$

where

$$W_{i,j,k}(\tilde{\mathbf{x}}) = W_{j,k}\left(\frac{x - x_{c_i}}{\Delta x}\right) W_k\left(\frac{y - y_{c_j}}{\Delta y}\right) W\left(\frac{z - z_{c_k}}{\Delta z}\right). \tag{23}$$

This formulation is based on a dimension-by-dimension approach. Note that the x-direction weights are now two-dimensional and depend also on the y- and z-coordinates, and the y-direction weights are now one-dimensional and depend also on the z-coordinate. The choice of the order of the dimensional sweeps is arbitrary, and although a different choice can change the results, they should not be significantly different [58]. The terms W_k and W in Eq. (23) are weights along the centerline of the stencil. They can be calculated via Eq. (21) by setting $j = 1$ for W_k, and $j = 1, k = 1$ for W.

WENO-5:

This scheme is derived using 4th-order Lagrange polynomials. It is based on a 5-point stencil and it is 5th-order accurate for smooth flows with the accuracy dropping to a minimum of 3rd-order in the vicinity of shocks [55]. The interpolation scheme is divided into three sub-stencils associated with the following linear weights for the left, center, and right positions [55]:

$$C^L = \frac{1}{12}(\tilde{x}-1)(\tilde{x}-2), \qquad C^C = -\frac{1}{6}(\tilde{x}+2)(\tilde{x}-2), \qquad C^R = \frac{1}{12}(\tilde{x}+2)(\tilde{x}+1). \tag{24}$$

The smoothness indicators are defined as follows:

$$\beta^L_{j,k} = \frac{13}{12}\left(F_{0,j,k} - 2F_{1,j,k} + F_{2,j,k}\right)^2 + \frac{1}{4}\left(F_{0,j,k} - 4F_{1,j,k} + 3F_{2,j,k}\right)^2, \tag{25}$$

$$\beta^C_{j,k} = \frac{13}{12}\left(F_{1,j,k} - 2F_{2,j,k} + F_{3,j,k}\right)^2 + \frac{1}{4}\left(F_{1,j,k} - F_{3,j,k}\right)^2, \tag{26}$$

$$\beta^R_{j,k} = \frac{13}{12}\left(F_{2,j,k} - 2F_{3,j,k} + F_{4,j,k}\right)^2 + \frac{1}{4}\left(3F_{2,j,k} - 4F_{3,j,k} + F_{4,j,k}\right)^2, \tag{27}$$

where j and k are indices for the y- and z-directions varying according to the stencil size, in this case in the range of 0–4. The same auxiliary variables described in Eq. (19) for the left and right positions are used here. Also, the following auxiliary variable is calculated for the center position

$$\alpha^C_{j,k} = \frac{C^C}{\left(\beta^C_{j,k} + \varepsilon\right)^2}. \tag{28}$$

Accordingly, the non-linear weights for the three sub-stencils are calculated as follows:

$$\omega^L_{j,k} = \frac{\alpha^L_{j,k}}{\alpha^L_{j,k} + \alpha^C_{j,k} + \alpha^R_{j,k}}, \qquad \omega^C_{j,k} = \frac{\alpha^C_{j,k}}{\alpha^L_{j,k} + \alpha^C_{j,k} + \alpha^R_{j,k}}, \qquad \omega^R_{j,k} = \frac{\alpha^R_{j,k}}{\alpha^L_{j,k} + \alpha^C_{j,k} + \alpha^R_{j,k}}. \tag{29}$$

Finally, the weight function for the WENO-5 interpolation scheme is defined as follows:

$$W_{j,k}(\tilde{x}) = \begin{cases} 0, & \tilde{x} < -\frac{5}{2}; \\ \frac{1}{2}(\tilde{x}+1)\tilde{x}\omega^L_{j,k}, & -\frac{5}{2} \le \tilde{x} < -\frac{3}{2}; \\ -(\tilde{x}+2)\tilde{x}\omega^L_{j,k} + \frac{1}{2}\tilde{x}(\tilde{x}-1)\omega^C_{j,k}, & -\frac{3}{2} \le \tilde{x} < -\frac{1}{2}; \\ \frac{1}{2}(\tilde{x}+2)(\tilde{x}+1)\omega^L_{j,k} - (\tilde{x}+1)(\tilde{x}-1)\omega^C_{j,k} + \frac{1}{2}(\tilde{x}-1)(\tilde{x}-2)\omega^R_{j,k}, & -\frac{1}{2} \le \tilde{x} \le \frac{1}{2}; \\ \frac{1}{2}(\tilde{x}+1)\tilde{x}\omega^C_{j,k} - \tilde{x}(\tilde{x}-2)\omega^R_{j,k}, & \frac{1}{2} < \tilde{x} \le \frac{3}{2}; \\ \frac{1}{2}\tilde{x}(\tilde{x}-1)\omega^R_{j,k}, & \frac{3}{2} < \tilde{x} \le \frac{5}{2}; \\ 0, & \tilde{x} > \frac{5}{2}. \end{cases} \tag{30}$$

Again, we refer the reader to [55] for the traditional form of this interpolation scheme.

Fig. 2b shows a schematic that depicts the procedure for the WENO-5 interpolation scheme. For the presented case, the discontinuity passes through the right sub-stencil, hence, its weight will be essentially zero. Thus, interpolation will be performed using the left and center sub-stencils, dropping the interpolation order of accuracy to 4th.

As mentioned above, multidimensional interpolation is possible as described by Eqs. (22)–(23), and the terms W_k and W in Eq. (23) are weights along the centerline of the stencil. They can be calculated via Eq. (21), in this case, by setting $j = 2$ for W_k, and $j = 2$, $k = 2$ for W. Note that similarly to the centered schemes, Eqs. (6), (9) hold for both WENO-3 and WENO-5. Thus, the sum of weights for WENO schemes always equals unity and the interpolated quantity is fully conserved. Also, for the multidimensional interpolation, WENO schemes can handle accurately multiple discontinuities in the stencil, as long as they do not cross all sub-stencils of any 1D weight function. Note that, similarly to the treatment for centered schemes discussed above, the multidimensional interpolation for WENO schemes is based on the product of the one-dimensional weight functions. Thus, it is not fully multidimensional, and it is performed in a dimension-by-dimension fashion. This approach has been commonly used for both interpolation and reconstruction [59], and it is considered highly efficient for Cartesian structured grids [45], which are utilized in the current work. Note that fully multidimensional WENO reconstruction is also possible [58,60,61], and it can provide a higher level of accuracy, however, the order of accuracy remains the same [60], and the implementation is much more involved [59] with an additional computational cost. For unstructured grids the dimension-by-dimension approach cannot be used, and different fully multidimensional formulations have been developed, including for 2D triangular [62,63] and 3D tetrahedral meshes [64], as well as for adaptive mesh refinement [65] and moving meshes [66].

3. Results and discussion

3.1. Steady-state non-reactive flows

The first two test cases involve steady-state conditions, in which the flow field is stationary, and thus the flow equations are not solved.

3.1.1. Two-dimensional vortex

The first test case is a 2D steady-state vortex flow. Two different cases are compared, a vortex with a uniform and continuous flow (Fig. 3a), and a shocked vortex with an abrupt velocity magnitude jump in the middle of the domain (Fig. 3b). The flow field for both cases can be described by the following relations:

$$u = \frac{dx}{dt} = -u_\infty \sin(\theta), \qquad v = \frac{dy}{dt} = u_\infty \cos(\theta), \tag{31}$$

where u and v are the x- and y-velocity components, and u_∞ is the velocity magnitude. The corresponding cylindrical radial and tangential components, r and θ, can be defined as follows:

$$r = \sqrt{(x - x_c)^2 + (y - y_c)^2}, \qquad \theta = \operatorname{atan2}(y - y_c, x - x_c), \tag{32}$$

where x_c and y_c are the vortex center coordinates, and $\operatorname{atan2}(y, x)$ is defined as follows:

$$\operatorname{atan2}(y,x) = \begin{cases} \arctan(y/x), & x > 0; \\ \arctan(y/x) + \pi, & x < 0;\ y \geq 0; \\ \arctan(y/x) - \pi, & x < 0;\ y < 0; \\ \pi/2, & x = 0;\ y > 0; \\ -\pi/2, & x = 0;\ y < 0; \\ \text{undefined}, & x = 0;\ y = 0. \end{cases} \tag{33}$$

For a uniform flow vortex, u_∞ is constant, whereas for the shocked case, it depends on the x-coordinate according to the following equation:

$$u_\infty(x) = \begin{cases} u_h, & x \leq x_c; \\ u_l, & x > x_c, \end{cases} \tag{34}$$

where u_h and u_l are high and low velocity magnitudes. Note that the shocked vortex test case does not represent a realistic flow configuration. It does allow us, however, to demonstrate the numerical errors that arise once discontinuities in the flow are introduced in comparison with the uniform case. More realistic shocked flow configurations will be discussed in the following test cases.

The problem is solved on a 1×1 m square domain with the periodic boundary conditions. The vortex center is located at $x_c = y_c = 0.5$ m. For the continuous case, the value of u_∞ is set to 100π m/s. For the shocked case, the following values

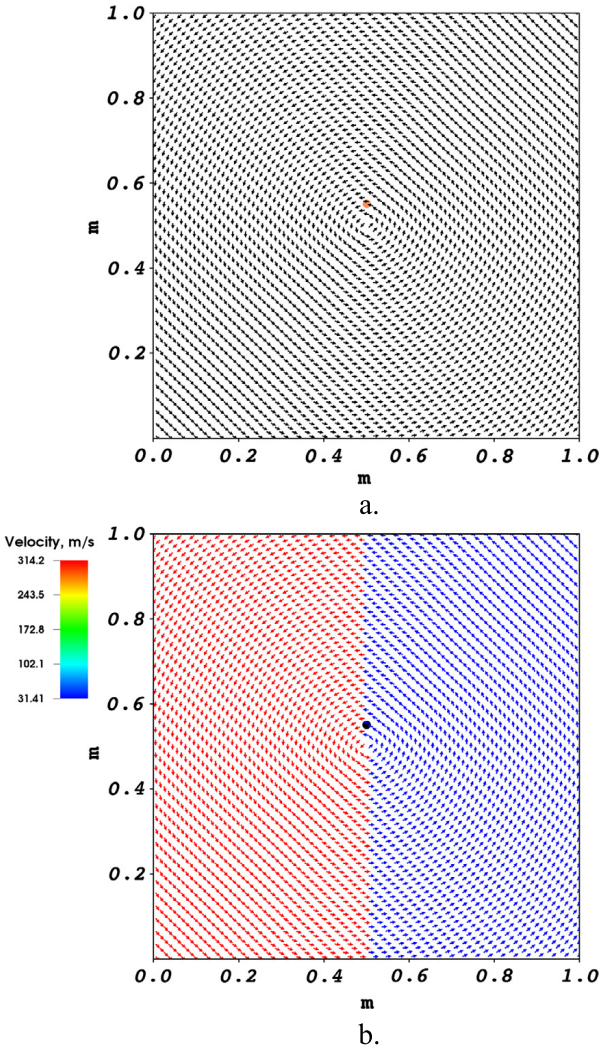


Fig. 3. Velocity vector flow field for the two-dimensional vortex problem. The colored dot marks the initial position of the Lagrangian particle: (a) Uniform flow. (b) Shocked flow. (For interpretation of the colors in the figure(s), the reader is referred to the web version of this article.)

are set: $u_h = 100\pi$ m/s and $u_l = 10\pi$ m/s. These values correspond to the typical order of magnitude in the velocity jump across strong shocks or flame fronts. The time-step is governed by the particle CFL number that can be defined as follows:

$$\mathrm{CFL} = \frac{u_{\max}\Delta t}{\Delta x}, \tag{35}$$

where $u_{\max}$ is the particle maximum possible velocity, Δt is the time-step size, and Δx is the grid spacing. For the two cases above, $u_{\max} = u_\infty = u_h$, hence, the definition for the CFL number is identical for both of them.

First, we can use the uniform flow vortex configuration to verify the order of accuracy for different interpolation schemes. The accuracy is tested by seeding a single particle at a radius of 0.05 m from the vortex center (see Fig. 3a), and propagating the particle through the flow for 1 ms. Velocity magnitude is interpolated to the particle position, and the L_∞ norm of the error is calculated for each of the interpolation schemes that were presented above. Four different grid sizes are used: 100 $\times$ 100, 200 $\times$ 200, 400 $\times$ 400, 800 $\times$ 800 with a small CFL number of about 5×10^{-4}. Note that for massless particles, the velocity error depends only on the accuracy of spatial interpolation as only the particle position propagates in time, see Eq. (1). Thus, this test can be performed with any CFL number or time integration method as long as the particle retains its circular trajectory. As Crank-Nicolson is trajectory preserving, the radial position error is bounded in time and thus negligible [48]. Fig. 4 shows the L_∞ error of the velocity magnitude as a function of grid spacing, Δx, for different interpolation schemes. The velocity errors for all schemes show the expected order of spatial accuracy as described above. One may note that QP and WENO-3 give the same results, as for smooth flows WENO-3 reduces to QP. Also, for the current test case, the interpolation errors for several interpolation methods are identical to within several digits after the decimal point. Thus, the corresponding curves overlap. In the current figure, CIC is hidden by TSC, QP is hidden by WENO-3, and Everett's interpolation formula is hidden by W_5.

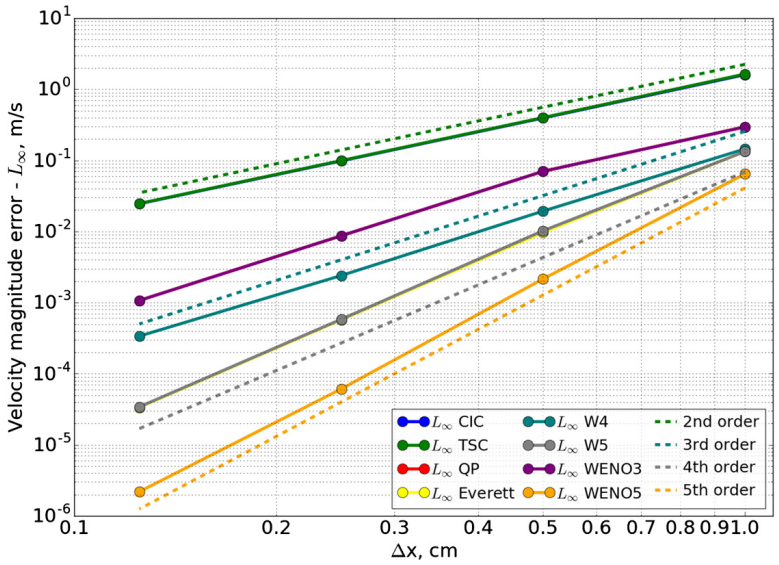


Fig. 4. Spatial accuracy test. L_∞ velocity magnitude errors as a function of the grid spacing Δx. CIC is hidden by TSC, QP is hidden by WENO-3, and Everett's interpolation formula is hidden by W_5.

Table 1
Comparison of the interpolation schemes for the uniform and shocked flow vortices. L_∞ normalized velocity magnitude errors.

Weight function	2-D vortex Normalized velocity error – L_∞	2-D vortex – shock Normalized velocity error – L_∞
CIC	5.112×10^{-3}	4.490
TSC	5.213×10^{-3}	4.491
QP	9.462×10^{-4}	4.465
Everett	4.249×10^{-4}	4.509
W_4	4.614×10^{-4}	4.509
W_5	4.249×10^{-4}	4.509
WENO-3	9.462×10^{-4}	1.374×10^{-2}
WENO-5	2.057×10^{-4}	3.900×10^{-3}

The second test involves a comparison of the relative errors for the two flow configurations and all interpolation schemes. The relative error, E_u, is given by the following relation:

$$E_u = \frac{|U - u_{exact}|}{u_{exact}}, \tag{36}$$

where U and u_{exact} are the interpolated and exact velocity magnitudes, respectively, with the velocity magnitude defined as follows:

$$U = \sqrt{u^2 + v^2}. \tag{37}$$

The test is performed on a coarse grid of 100×100 cells, CFL number of about 5×10^{-4}, and the entire simulation proceeds until the particle completes 5 orbits. Table 1 shows the L_∞ relative velocity magnitude error for all interpolation schemes, and the two flow configurations. One can see that for the uniform flow vortex, the errors for all schemes are lower than 1%. Yet, the errors for CIC and TSC are the largest, whereas the errors for QP and WENO-3 are much smaller, and for other schemes, the errors are about an order of magnitude smaller. For the shocked vortex case, the errors are significant for all centered schemes with values well above 100%. On the other hand, WENO schemes show significantly smaller errors: WENO-3 has an error of about 1% and WENO-5 of about 0.4%.

Tests presented above confirm quantitatively that the accuracy of WENO schemes is comparable to centered schemes for smooth flows. Once sharp discontinuities are introduced to the flow, centered schemes fail and WENO schemes are proven much more accurate. The next test case will demonstrate the advantage of WENO schemes over centered schemes for a more realistic flow configuration, including interpolation of different flow quantities of interest. Also, this test will shed light on the nature of the interpolation errors in centered schemes.

3.1.2. Normal shock wave

For this test case, the classical steady state normal shock solution is being investigated. The domain size is 1×0.25 m with a grid of 320×80 cells. The flow is 1D in the horizontal direction and the shock is located at 0.5 m. The particle is

seeded before the shock and is advected by the flow until it passes the shock. Upstream conditions correspond to pressure, temperature and Mach number of 5×10^4 Pa, 250 K, and 10, respectively. The gas is assumed to be air with a calorically perfect equation of state. The heat capacity ratio and specific gas constant are 1.4 and 287 J/(kg K), respectively. Accordingly, downstream conditions are calculated using normal shock relations [67]. The particle is integrated with the flow CFL number, which is 0.45, and defined as follows:

$$\mathrm{CFL} = \frac{(|V_{\max}| + a)\,\Delta t}{\Delta x} \tag{38}$$

where $V_{\max}$ is the maximum flow velocity and a is the local speed of sound. Three flow quantities of interest are interpolated to the particle position: pressure, temperature, and density. These interpolated quantities are typically of primary interest for the Lagrangian analysis of different flows. Yet, the possible applications can be much broader than that. For example, in simulations of multi-phase reacting flows, these quantities would determine the heat, and mass transfer rates for a fuel spray droplet represented as a point Lagrangian particle [68,69]. For the current test case, it is possible to compare the interpolated values at each position with the exact solution, as the flow field is stationary and known through simple analytic relations.

Fig. 5a shows pressure as a function of position in the vicinity of the shock wave. The exact solution is compared with values interpolated using centered schemes, CIC and W_5, and the two WENO schemes. One can see that for the exact solution, pressure increases sharply at 0.5 m. However, for CIC, the pressure rise is not sharp and the shock is smeared. For W_5, not only is the shock not sharp, but the interpolated values undershoot and overshoot, before and after the shock, respectively. Note that the undershoot is so large that the absolute pressure attains nonphysical negative values. Thus, for calculations with various physical processes dependent on pressure or temperature, e.g., mass transfer or reaction rates, these negative values can lead to a complete breakdown of the calculation. For both WENO schemes, which are effectively indistinguishable for the current case, the pressure rise is much sharper than for the centered schemes, and there are no visible oscillations.

As mentioned above, since CIC has strictly positive weights, it does not oscillate. In contrast, W_5 has an order of accuracy greater than 2nd, hence some of its weights must be negative, and oscillations can occur. The numerical oscillations can be explained through the current test case. As the particle approaches the shock, both high- and low-pressure values are interpolated to the particle position. The high-pressure values receive negative weights. Although these weight values are low, the multiplication with the high-pressure values makes them dominant in comparison with the interpolated low-pressure values. The result is a nonphysical negative pressure. Once the particle passes the shock, low-pressure values receive negative weights. In this case, the contribution of these negative weights to the final result is negligible in comparison with the high-pressure values. However, as the sum of all weights always equals unity, the sum of the high-pressure weights must be greater than one. As a result, the interpolated high pressure is augmented above its correct value and an overshoot occurs. Note that grid refinement can reduce the smearing of the shock, although it may require excessively high resolution that may not be practical. Yet, the oscillations cannot be avoided in this way. In fact, their magnitude is independent of the grid spacing, and they will just shift closer to the discontinuity. On the other hand, for WENO schemes, the oscillation magnitude decreases with the grid size [45]. It is important to stress that these trends are completely general for any centered weight function with no special treatment. For instance, TSC, which is 2nd order accurate and has only positive weights, will smear the shock in a manner similar to CIC. As its stencil is even wider than CIC, the smearing will occur over 3 cells rather than 2. Finally, for any other high order interpolation scheme besides W_5, oscillations will also occur, as the negative weights are unavoidable as mentioned above. Only their magnitude and exact position relative to the discontinuity will vary.

Fig. 5b shows a comparison between the exact and interpolated temperatures as a function of position. The trends are very similar to Fig. 5a, as both CIC and W_5 smear the temperature profile and WENO schemes capture it in a sharper manner. For W_5, oscillations also occur, though, temperature values at the undershoot are not negative, but they reach extremely low values ($\sim$10 K). This is a numerical artifact of the interpolation as values lower than the initial temperature are not possible for this problem according to the second law of thermodynamics [67].

Fig. 5c shows the same plot for density. Again, the same trends can be observed. For W_5, the magnitude of the oscillations is much lower than for pressure and temperature described above. This is related to the fact that the density jump across a shock is bounded in the limit of high Mach numbers, unlike pressure and temperature. This makes the oscillations less severe, yet even so, for the undershoot, the maximum relative interpolation error is higher than 20% and the interpolated values are inconsistent with the exact solution.

This test demonstrates the advantages of WENO schemes in comparison with centered schemes for a basic flow configuration. However, this test case describes a steady state 1D flow with a sharp discontinuity. Realistic flows are 3D and time-dependent. Also, many flow solvers are based on shock capturing schemes, which cause the shock to get smeared across several grid cells [70]. The next test case will show that the same trends observed for a simple normal shock are retained for a much more complex shocked flow configuration.

3.2. Unsteady non-reactive flow

Three-dimensional spherical blast wave

This test case is similar to a strong blast wave problem presented in [71]. The current test case, however, is 3D and does not involve magnetohydrodynamics. Fig. 6 shows the initial setup of the problem. The domain size is $1 \times 1 \times 1$ m

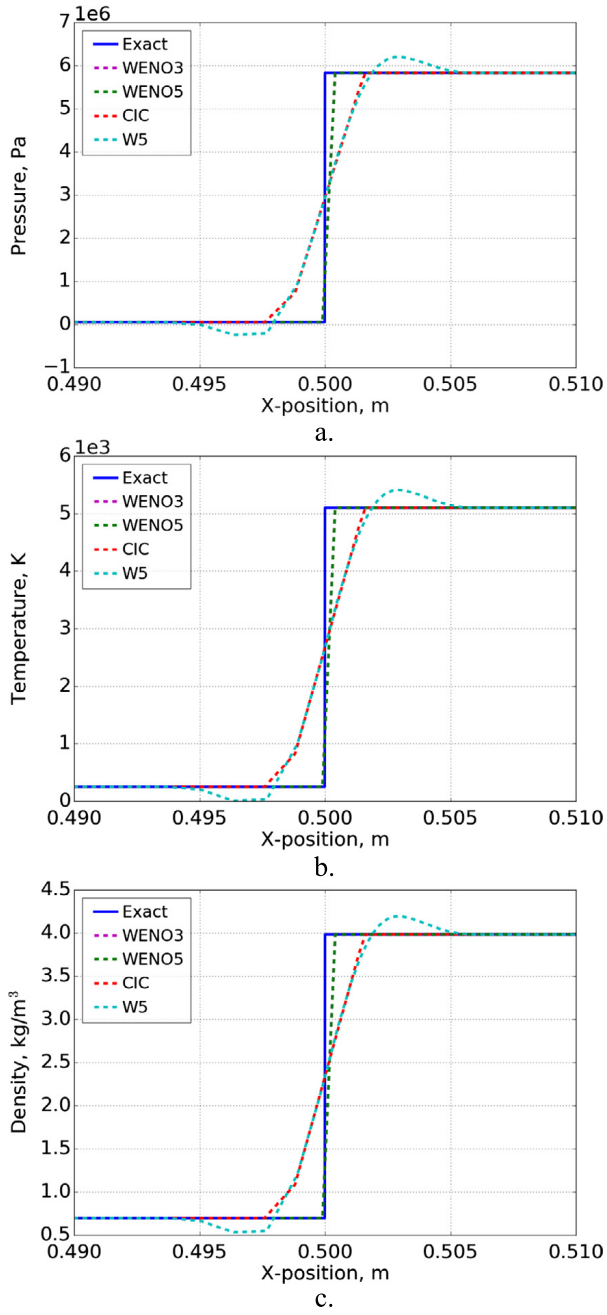


Fig. 5. Normal shock test. Comparison between the exact solution, and the interpolated results for CIC, W_5, WENO-3 and WENO-5: (a) Pressure. (b) Temperature. (c) Density.

with 200 × 200 × 200 grid cells and periodic boundary conditions. As for the normal shock test case, the gas is assumed to be calorically perfect with heat capacity ratio and specific gas constant of 1.4 and 287 J/(kg K), respectively. Initially, the entire domain has pressure of 1 atm, density of 1.2 kg/m^3 and zero velocity, except for a sphere with a radius of 0.1 m from the origin, where the pressure is initially set to 1000 atm. Also, a single particle is seeded at $x = y = z = 0.15$ m. The governing equations are the compressible Euler equations:

$$\frac{\partial \rho}{\partial t} + \nabla \cdot (\rho \mathbf{u}) = 0, \tag{39}$$

$$\frac{\partial \rho \mathbf{u}}{\partial t} + \nabla \cdot (\rho \mathbf{u} \otimes \mathbf{u}) + \nabla P = 0, \tag{40}$$

$$\frac{\partial E}{\partial t} + \nabla \cdot ((E + P)\,\mathbf{u}) = 0, \tag{41}$$

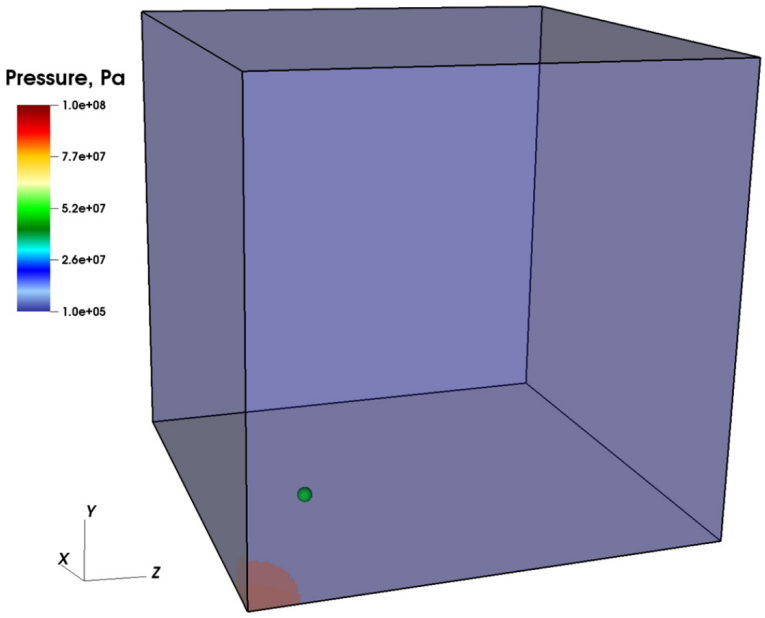


Fig. 6. Pressure distribution for the initial setup of the three-dimensional spherical blast wave test. The green sphere marks the initial position of the Lagrangian particle.

where ρ is density, $\mathbf{u}$ is velocity, P is pressure, and E is the energy density. Equations are solved using the fixed grid massively parallel code Athena-RFX [72], which is a reactive flow extension to the Athena magnetohydrodynamics code [73]. The flow equations integration algorithm is the unsplit corner transport upwind (CTU) [74], which is a fully conservative high-order Godunov-type method. The integration scheme utilizes piecewise parabolic method (PPM) [75] for spatial reconstruction and the HLLC approximate Riemann solver [42] for calculating fluxes at cell faces. The method is 3rd order accurate in space and 2nd order accurate in time. Particle integration is performed at the end of each time-step, as massless particle equations are one-way coupled to the flow equations. All the tests are performed with a flow CFL number of 0.45.

The initial flow field creates a strong spherical blast wave that passes through the point particle. Pressure, temperature, and density are interpolated to a particle position using CIC, W_5, and the two WENO schemes. An exact solution for the interpolated values on the Lagrangian trajectory cannot be derived, thus, comparison between different interpolation schemes is only qualitative. Also, note that even if an exact solution could have been derived, deviations from the analytical solution would arise both from the numerical errors associated with the flow solver and from the solution of the Lagrangian particle evolution equation, and it would be very difficult to determine the individual effect of each error. Fig. 7a shows a comparison of the interpolated pressure as a function of time for different interpolation schemes. In general, trends are very similar to the previous normal shock test case. Both CIC and W_5 smear the shock in comparison with the two WENO schemes that capture its structure in a sharper manner. Also, for W_5, the interpolated pressure undershoots to a nonphysically small value of $\sim$20 kPa. Fig. 7b shows the same plot for the interpolated temperature. Again, the trends are the same. Here for W_5 the temperature drops by about 50 K from its initial value of about 300 K. As discussed above for the normal shock case, this result is a numerical artifact that violates the second law of thermodynamics [67]. Fig. 7c shows results for the interpolated density. The capturing of the discontinuity is similar to the previous graphs, as CIC and W_5 tend to smear it, and WENO schemes reproduce it sharply. For W_5, there is an undershoot before the shock, although its magnitude is rather low. Similar to the previous test, density is bounded according to the conservation laws, and thus oscillations are reduced for this case.

It can be concluded that the trends observed for the normal shock case are present for this 3D time-dependent simulation, where the shocks are broadened over several grid cells. Thus, WENO interpolation schemes are beneficial even at these conditions.

3.3. Unsteady reactive flow

Two-dimensional detonation

An important example of a highly compressible, realistic reactive flow configuration is a multidimensional gas-phase detonation. For sufficiently high activation energies, detonations tend to be unstable with a complex interaction between transverse waves and triple-shock configurations that create cellular structures [76]. This phenomenon has been known for over half a century and has been studied both experimentally [77] and numerically [78,79]. Today, with the increase in computational power, numerical simulations of multidimensional detonations are quite common, including investigations of two- and three-dimensional configurations with single- and even multi-step chemical reaction kinetics [76,80–82]. In

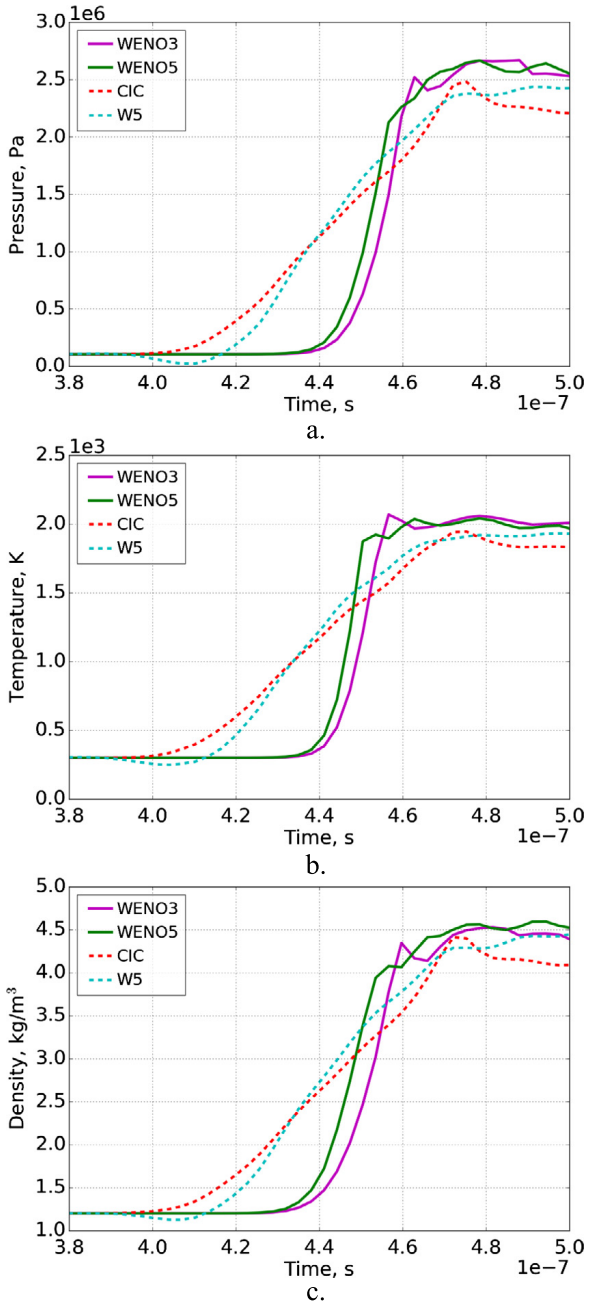


Fig. 7. Three-dimensional spherical blast wave test. Comparison between the interpolated results for CIC, W_5, WENO-3 and WENO-5: (a) Pressure. (b) Temperature. (c) Density.

order to demonstrate the benefits of the proposed Lagrangian-particle approach for this type of flows, a 2D problem with a single-step reaction kinetics is solved.

The governing equations for the problem are the compressible reactive Euler equations with the calorically perfect gas equation of state. The full set of equations includes Eqs. (39)–(40) and the following energy and species equations:

$$\frac{\partial E}{\partial t} + \nabla \cdot ((E + P)\,\mathbf{u}) = -\rho q \dot{w}, \tag{42}$$

$$\frac{\partial \rho Y}{\partial t} + \nabla \cdot (\rho Y \mathbf{u}) = \rho \dot{w}, \tag{43}$$

where q is the chemical energy release, $\dot{w}$ is the reaction source term, and Y is the mass fraction of the reactant. Note that for detonations, molecular transport effects like heat conduction, diffusive mass transfer or viscous shear stresses have typically a negligible effect on the solution. For chemical reactions, a first-order single-step Arrhenius kinetics is assumed:

Table 2
Input parameters and computed properties for the single-step reaction model.

P_0	1.01325×10^5 Pa	Initial pressure
T_0	293 K	Initial temperature
ρ_0	0.87345 kg/m^3	Initial density
γ	1.17	Adiabatic index
M	0.021 kg/mol	Molecular weight
A	3.56×10^7 m^3/(kg s)	Pre-exponential factor
Q	$24.199 \cdot RT_0$	Activation energy
q	$43.28 \cdot RT_0/M$	Chemical energy release
D_{CJ}	1.993×10^3 m/s	CJ detonation velocity
P_{ZND}	$31.47 \cdot P_0$	von Neumann pressure
T_{ZND}	$3.457 \cdot T_0$	von Neumann temperature
ρ_{ZND}	$9.104 \cdot \rho_0$	von Neumann density
x_d	1.927×10^{-4} m	Half-reaction thickness

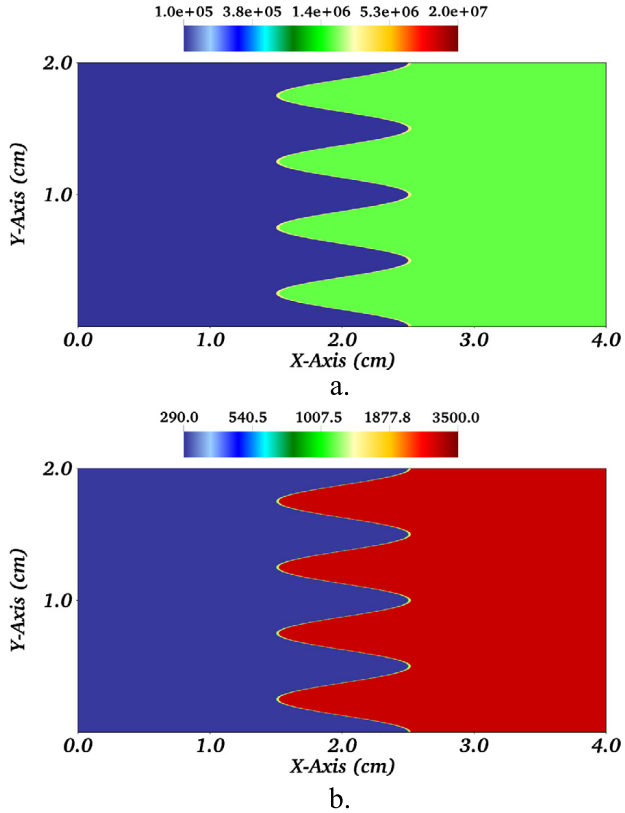


Fig. 8. The initial conditions for a two-dimensional detonation, showing a flow field based on a one-dimensional ZND profile perturbed with a sine function in the direction of propagation. (a) Pressure, Pa. (b) Temperature, K.

$$\frac{dY}{dt} \equiv \dot{w} = -A\rho Y \exp\left(-\frac{Q}{RT}\right), \tag{44}$$

where A is the pre-exponential factor, Q is the activation energy, and R is the universal gas constant. The numerical methods used to solve the equations are the same as those described above, except that piecewise linear method (PLM) [42] is utilized for state reconstruction, instead of PPM that tends to exhibit carbuncle phenomenon for strong shocks such as the ones present in a detonation. Chemical source terms are coupled to the flow equations via Strang splitting [83].

The different parameters and flow properties for the reaction model are summarized in Table 2. This model is based on the single-step reaction mechanism developed by Gamezo et al. [84]. Originally, the model parameters were calibrated to reproduce both one-dimensional laminar flame and Zel'dovich, von Neumann, Döring (ZND) detonation solutions for a stoichiometric hydrogen-air mixture. Taylor et al. [76], however, have shown that this model cannot successfully predict the cellular structure of a detonation wave. In particular, it leads to an incorrect temperature profile and an extremely irregular cell structure. They suggested to modify the model by lowering the values of both the activation energy, Q, and the pre-exponential factor, A, in order to obtain a more regular cellular structure. The chosen values maintain the correct half-reaction thickness, yet, they cannot reproduce the correct laminar flame solution. As the current problem of interest involves only detonations, this deficiency should not affect the results. It is stressed that the changes of the original

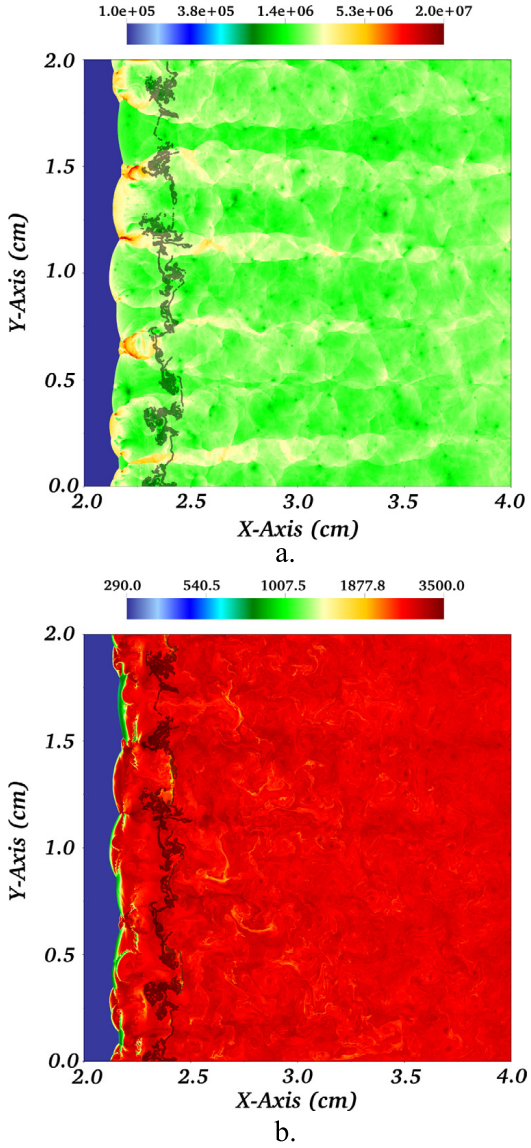


Fig. 9. Fully developed two-dimensional cellular detonation. The flow field is shown after 3.3 flow-through times. Final particle positions are marked as black dots: (a) Pressure, Pa. (b) Temperature, K.

model have no effect on the Chapman-Jouguet (CJ) detonation velocity or the post-shock conditions. Accordingly, one of the suggested modified parameter sets was implemented in our simulations, as shown in Table 2.

The problem is solved in a 4 $\times$ 2 cm rectangular domain with 32768 $\times$ 16384 equally spaced grid cells that comprise in total about half a billion cells. The boundary conditions are no-slip and no-penetration for the upper and lower boundaries and zero-order extrapolation (outflow) for the left and right boundaries. The initial flow field is based on the 1D ZND profile and the entire problem is solved in the shock frame of reference. The post-shock values that represent the first data point in the ZND profile are located at the center of the domain and they have an x-direction displacement according to a sine function (see Fig. 8a and Fig. 8b for the initial pressure (Pa) and temperature (K) contours, respectively). Gas ahead of the shock has the initial thermodynamic property values as shown in Table 2, and it moves with the CJ detonation velocity to the right. All the property values after the end of the reaction zone are constant according to the last value of the ZND profile. As the initial front is curved, it becomes unstable and a multi-cellular detonation arises. It should be noted that the initial ZND profile is calculated according to the original model of Gamezo et al. [84] and not the modified one. As mentioned above, this does not change the post-shock state, but it does change the initial profile. This initial structure is only used to initiate a detonation, which after the initial transient develops a fully multi-dimensional structure. After the initial conditions are set, the flow equations are integrated for about 3.1 flow-through times, where one flow-through time is defined as the domain length, L, divided by the CJ detonation velocity, $\tau_d = L/D_{CJ}$. This time duration allows for the multidimensional detonation structure to become fully developed. Then, a total of 49,152 tracer point-particles are injected at $x = 2$ cm. The particles initially comprise three sequential columns, spanning the entire height of the domain, with each particle seeded at a cell center. Finally, the entire set of flow and particle equations is integrated for 0.2 flow through time.

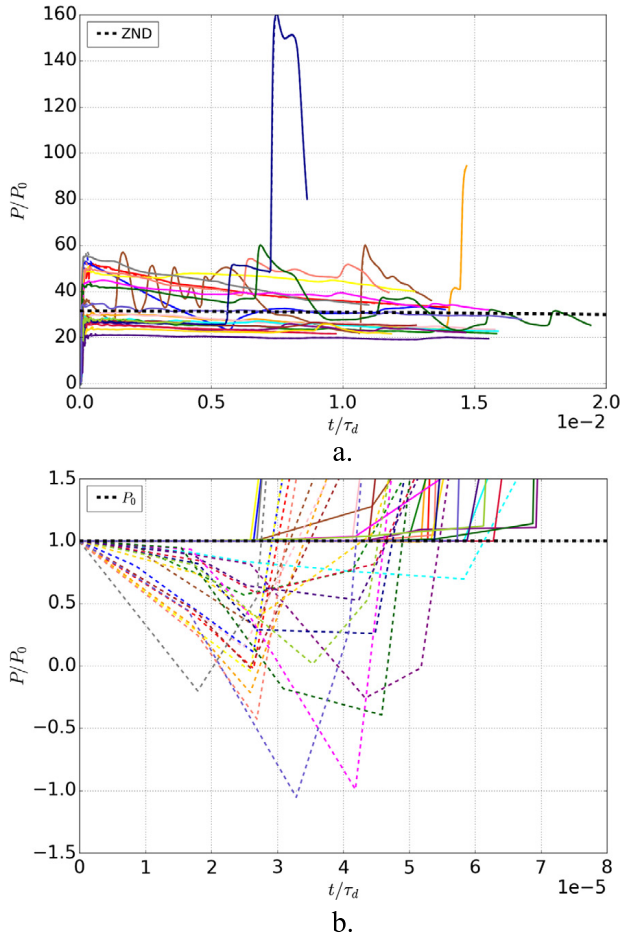


Fig. 10. Twenty sample particle trajectories. Normalized interpolated pressure is shown against the normalized time. Results for WENO-5 (solid lines) and W_5 (dashed lines) interpolation schemes are presented: (a) The entire time duration. (b) A magnified view of the time when particles are crossing the shock.

Figs. 9a and 9b show pressure and temperature field in the domain, respectively, at the end of the simulation with the particle final positions marked as black dots. One can see that the detonation front is corrugated as transverse waves propagate in the y-direction and interact with the leading shock. This creates triple shock points, where the gas is highly compressed, and which divide the front into cells. The results qualitatively agree with those in [76], where the same one-step reaction kinetics mechanism was utilized. Note that the current simulation resolution is much higher, and the grid cell size is 8 times lower than the one used in [76]. We tested the problem with lower resolutions, with the fully developed detonation structure found to be fully converged. The transient process, however, was found to be very different between the high- and low-resolution cases. In particular, at the highest resolution, initially the leading shock decoupled from the reaction front followed by the deflagration-to-detonation transition (DDT). Although this transient process is not relevant for the current study, it deserves further analysis in the future work.

Lagrangian-particle analysis described above is carried out using the high-order interpolation methods, W_5 and WENO-5, in order to compare their performance. As mentioned above, high-order interpolation is preferred due to its superior accuracy. The entire analysis is performed for a data set that includes the particle interpolated pressure and temperature approximately between 3.13 and 3.16 flow-through times since the start of the simulation. This time interval starts slightly before the first column of particles enters the leading shock and ends slightly after the last of column of particles leaves the reaction zone. Fig. 10a shows a sample of 20 particle trajectories, for W_5 (dashed lines) and WENO-5 (solid lines), respectively, where interpolated pressure normalized by the initial pressure, P_0, is shown against time normalized by the flow-through time, τ_d. The time series are all shifted, according to the results of W_5, such that at $t = 0$ s, particles first reach a pressure different than the initial one. Also, the ZND pressure profile is shown with a dashed black line.

For both interpolation schemes, the trajectories are quite irregular and can be very different. For instance, pressure spikes to values over 150 bar for one of the trajectories, which is about 3 times higher than the maximum pressure for most of the presented trajectories, and about 5 times higher than the ZND pressure. Comparison between the trajectories reproduced by the two interpolation schemes shows that the trajectories differ in one important respect. In particular, Fig. 10b shows a magnified view of the time the particle enters the shock region. One can see that in the case of W_5, for all the trajectories,

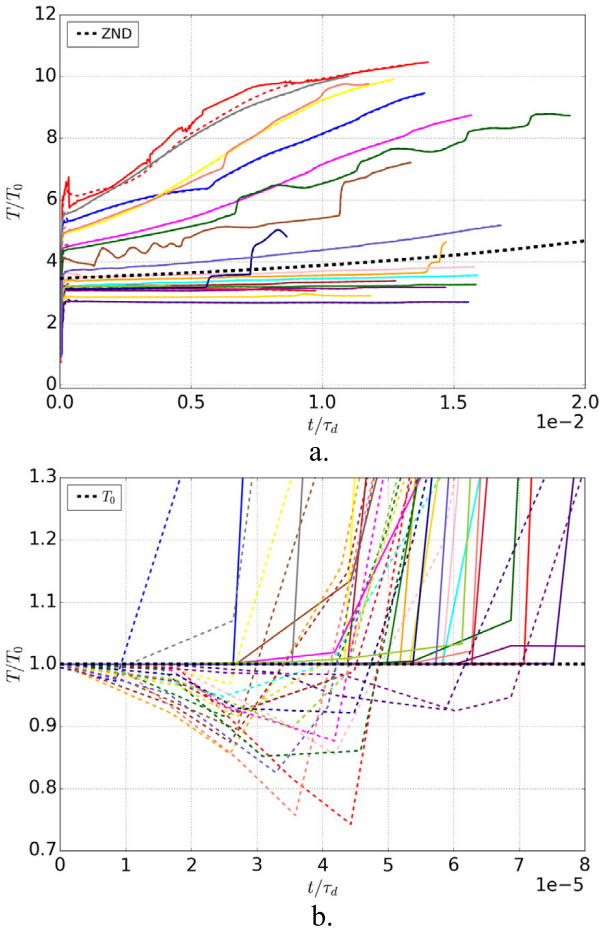


Fig. 11. Twenty sample particle trajectories. Normalized interpolated temperature is shown against the normalized time. Results for WENO-5 (solid lines) and W_5 (dashed lines) interpolation schemes are presented: (a) The entire time duration. (b) A magnified view of the time when particles are crossing the shock.

the normalized pressure values fall below its initial value of unity, which is unphysical. For some of the trajectories, the pressure becomes negative, with a value as low as −1. On the other hand, for WENO-5, the magnified view shows that for all sampled trajectories, the normalized interpolated pressure is always higher than its initial value, and no numerical oscillations are observed. Fig. 11a is similar to Fig. 10a showing temperature normalized by the initial temperature, T_0. The normalized interpolated temperature trajectories are also highly irregular and differ from the ZND temperature with a maximum value higher by almost 3 times. Fig. 11b shows a magnified view of the time the particle enters the shock. Again, the results for W_5 are lower than the initial normalized interpolated temperature of unity, with values almost as low as 0.7, which is unphysical. For WENO-5, all the normalized interpolated temperatures are higher than unity and no visible oscillations are observed.

Fig. 12 shows normalized interpolated pressure vs. temperature for WENO-5 and the same 20 particle trajectories presented in the figures above. The dashed black line corresponds to the ZND profile. This graph illustrates the way a joint probability density function (PDF) shown below is constructed from different particle trajectories. Each data point represents a time that a Lagrangian particle attained a certain value of pressure and temperature. By using all data points from the numerical simulation results, a joint PDF can be constructed. Figs. 13a and 14a show joint PDFs for W_5 and WENO-5, respectively, where the color bar denotes the natural logarithm of the joint PDF, and the black dashed line corresponds to the ZND profile. The two PDFs show very similar trends, although they are not identical. For both PDFs, normalized pressure and temperature can change significantly along the particle trajectory and reach values higher than 200 and 11, respectively, which are very different from the ZND profile. The main difference between the two PDFs is in the low pressure and temperature region corresponding to the initial shock crossing. For W_5 (see Fig. 13a), this region is much broader in comparison to the same region in the WENO-5 PDF (see Fig. 14a). Results again reveal non-physical trends once W_5 is utilized for interpolation. A magnified view of the low pressure and temperature region for W_5 is shown in Fig. 13b. One can see that the normalized pressure becomes negative with values as low as about −2. Normalized temperature also drops below its initial value to values as low as about 0.7. On the other hand, for WENO-5 (see Fig. 14b) the magnified view shows that for all the trajectories, interpolated pressure and temperature values are always higher than their initial value. This result shows that for the Lagrangian-particle tracking analysis of highly compressible reactive flows, high-order centered schemes,

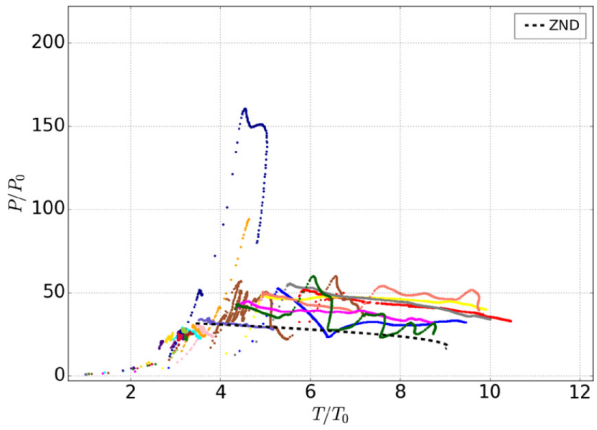


Fig. 12. Twenty sample particle trajectories. Normalized interpolated pressure is shown against the normalized temperature for the WENO-5 interpolation scheme.

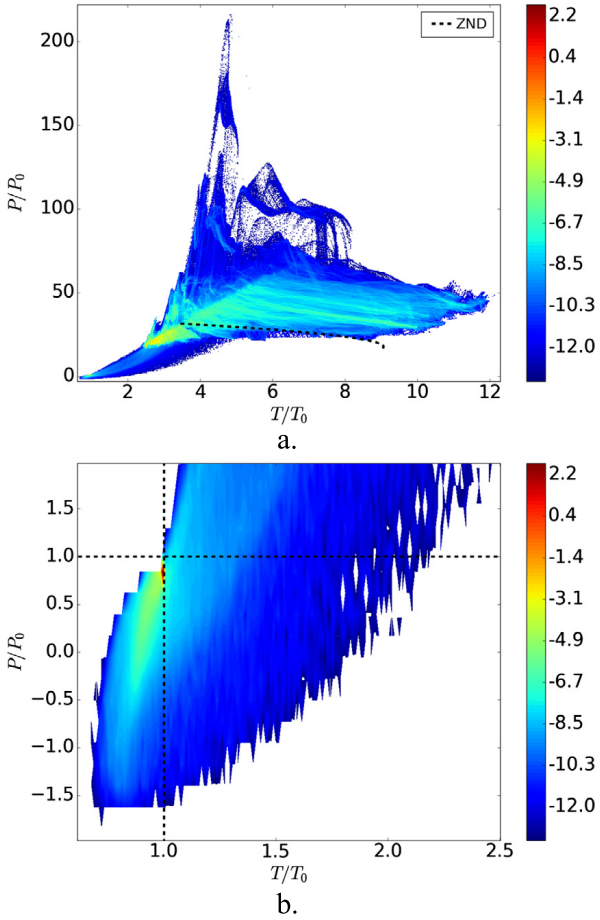


Fig. 13. Joint PDF of the normalized interpolated pressure and temperature for all particle trajectories. The color bar denotes the natural logarithm of the joint PDF. Values are reconstructed with the W_5 interpolation scheme: (a) The full data set. (b) A magnified view for the low pressure and temperature region.

like W_5, can lead to unphysical thermochemical trajectories, whereas WENO schemes provide an alternative with the same order of accuracy, yet free of severe numerical oscillations and unphysical numerical artifacts.

4. Conclusions

In the current work, we present WENO-3 and WENO-5 interpolation schemes for the purpose of Lagrangian-particle advection in highly compressible flows. Extensive set of tests is described, including comparison against various traditional centered interpolation schemes. The interpolation accuracy is first tested for simple two-dimensional vortex flows. Two

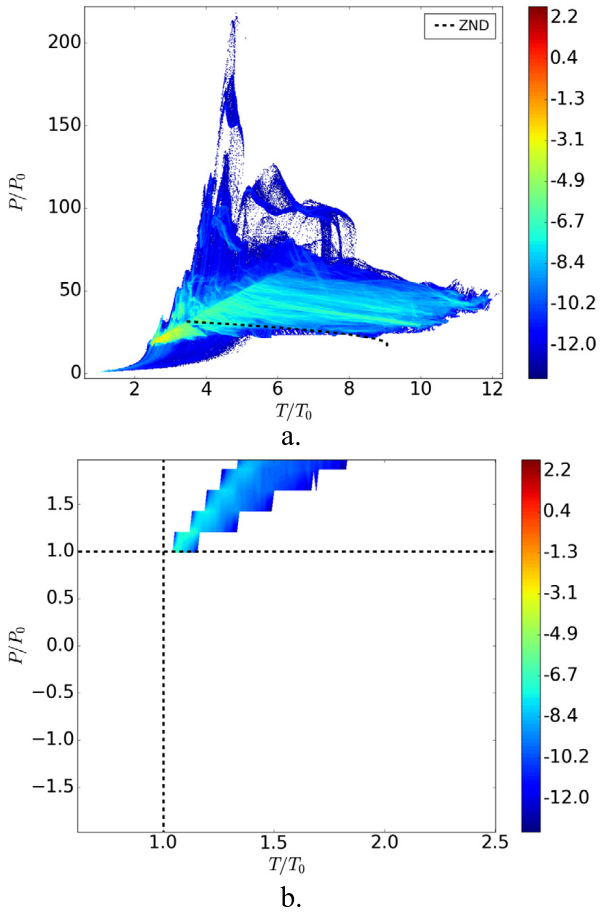


Fig. 14. Joint PDF of the normalized interpolated pressure and temperature for all particle trajectories. The color bar denotes the natural logarithm of the joint PDF. Values are reconstructed with the WENO-5 interpolation scheme: (a) The full data set. (b) A magnified view for the low pressure and temperature region.

cases have been investigated, namely a uniform vortex and a shocked vortex with a velocity discontinuity. For smooth flows, it is demonstrated that WENO schemes provide accuracy comparable to high-order centered schemes with the same order of accuracy. At the same time, once discontinues are introduced into the flow, it is shown that the maximum relative interpolation errors of centered schemes in the vicinity of the discontinuity can be larger than 100%. On the other hand, the maximum relative interpolation errors for WENO-3 and WENO-5 are about 1% and 0.4%, respectively.

The benefits of WENO interpolation over centered schemes were further explored by interpolating pressure, temperature, and density at the particle position for a Mach 10 normal shock wave. It is shown that low-order schemes, like CIC, smear the shock structure. High-order interpolation schemes, like W_5, not only smear the shock, but also produce numerical oscillations that can lead to unphysical results, such as negative absolute pressure values. It is explained that the origin of the oscillations lies in the negative weights that are inherent for any weight function, without special treatment, with an order of accuracy greater than 2nd. For WENO schemes, the shock is captured in a much sharper manner than for centered schemes, and no visible oscillations occur. A similar test is then performed for an unsteady three-dimensional spherical blast wave, where the shock is reconstructed by a shock capturing method, and thus it is broadened over several grid cells. The results show that qualitatively the same trends as for the normal shock test are observed. Thus, WENO schemes are advantageous even for more complex compressible flow fields.

The final test demonstrates Lagrangian-particle tracking analysis of a highly compressible reactive flow, namely, two-dimensional cellular gas-phase detonation. The two high-order interpolation methods, W_5 and WENO-5, are used to reconstruct pressure and temperature at the particle position. Comparison between the two includes several sampled particle trajectories and joint PDFs that are constructed according to each interpolation scheme. The results show that for all sampled trajectories, W_5 leads to interpolated pressure and temperature values that are lower than their initial value, which is physically impossible. For WENO-5, the interpolated values are always equal to or higher than their initial value. Comparison between the two joint PDFs reveals that the low normalized pressure and temperature regions are significantly different. It is shown that for W_5, normalized pressure and temperature values can drop as low as -2 and 0.7, respectively, which is not possible physically. For WENO-5, all the 49,152 particle trajectories do not exhibit any non-physical trends. It is concluded that for the Lagrangian-particle tracking analysis of highly compressible reactive flow regimes, high-order centered interpolation schemes, like W_5, can lead to numerical oscillations and non-physical results that may produce incorrect PDFs.

WENO schemes, like WENO-5, are shown to provide high-order interpolation without any severe numerical oscillations and non-physical artifacts.

WENO interpolation for Lagrangian particle advection is a robust numerical tool for highly compressible flows, where low-order centered interpolation schemes cannot provide a sufficient level of accuracy and high-order centered interpolation schemes tend to oscillate. Although the current work is focused on massless point particles, this interpolation method can be used for particles with mass as well. These might involve more complex physics like two-way coupling with the gas, as well as chemically reacting particles. In general, WENO interpolation can be found advantageous for a variety of practical applications, including high-fidelity direct numerical simulations of multi-physics flows in supersonic and hypersonic aerodynamics, and in advanced airbreathing hypersonic and detonation-based propulsion systems.

Declaration of competing interest

The authors declare that they have no known competing financial interests or personal relationships that could have appeared to influence the work reported in this paper.

Acknowledgements

YK, SSD, and AYP were supported in part by the Department of Defense (DoD) High Performance Computing Modernization Program (HPCMP), Lorton, VA under the User Productivity, Technology Transfer and Training (PETTT) program, contract number GS04T09DBC0017. PEH was supported by the Air Force Office of Scientific Research (AFOSR), Arlington, VA, USA, contract number FA9550-17-1-0144. Computing resources were provided by the DoD HPCMP under the Frontier project award and by the Naval Research Laboratory. LB was supported by the US Army Research Laboratory 6.1 basic research program in propulsion sciences.

References

[1] A. Fedorov, Transition and stability of high-speed boundary layers, Annu. Rev. Fluid Mech. 43 (2011) 79–95.
[2] A. Martin, I.D. Boyd, Modeling of heat transfer attenuation by ablative gases during the stardust reentry, J. Thermophys. Heat Transf. 29 (3) (2015) 450–466.
[3] A. Ben-Yakar, R.K. Hanson, Cavity flame-holders for ignition and flame stabilization in scramjets: an overview, J. Propuls. Power 17 (4) (2001) 869–877.
[4] P. Wolański, Detonative propulsion, Proc. Combust. Inst. 34 (1) (2013) 125–158.
[5] K. Eto, N. Tsuboi, A.K. Hayashi, Numerical study on three-dimensional CJ detonation waves: detailed propagating mechanism and existence of OH radical, Proc. Combust. Inst. 30 (2) (2005) 1907–1913.
[6] R.W. Houim, E.S. Oran, Numerical simulation of dilute and dense layered coal-dust explosions, Proc. Combust. Inst. 35 (2) (2015) 2083–2090.
[7] T. Skjold, Dust explosion modeling: status and prospects, Part. Sci. Technol. 36 (4) (2018) 489–500.
[8] J. O'Brien, C.A. Towery, P.E. Hamlington, M. Ihme, A.Y. Poludnenko, J. Urzay, The cross-scale physical-space transfer of kinetic energy in turbulent premixed flames, Proc. Combust. Inst. 36 (2) (2017) 1967–1975.
[9] C.A.Z. Towery, A.Y. Poludnenko, J. Urzay, J. O'Brien, M. Ihme, P.E. Hamlington, Spectral kinetic energy transfer in turbulent premixed reacting flows, Phys. Rev. E 93 (5) (2016) 053115.
[10] J. Kim, M. Bassenne, C.A.Z. Towery, P.E. Hamlington, A.Y. Poludnenko, J. Urzay, Spatially localized multi-scale energy transfer in turbulent premixed combustion, J. Fluid Mech. 848 (2018) 78–116.
[11] A.Y. Poludnenko, T.A. Gardiner, E.S. Oran, Spontaneous transition of turbulent flames to detonations in unconfined media, Phys. Rev. Lett. 107 (5) (2011) 054501.
[12] W.A. Sirignano, Fluid Dynamics and Transport of Droplets and Sprays, Cambridge University Press, 2010.
[13] P.E. Hamlington, R. Darragh, C.A. Briner, C.A. Towery, B.D. Taylor, A.Y. Poludnenko, Lagrangian analysis of high-speed turbulent premixed reacting flows: thermochemical trajectories in hydrogen–air flames, Combust. Flame 186 (2017) 193–207.
[14] J.J. Riley, G.S. Patterson, Diffusion experiments with numerically integrated isotropic turbulence, Phys. Fluids 17 (2) (1974) 292–297.
[15] P.K. Yeung, S.B. Pope, An algorithm for tracking fluid particles in numerical simulations of homogeneous turbulence, J. Comput. Phys. 79 (2) (1988) 373–416.
[16] S. Balachandar, M.R. Maxey, Methods for evaluating fluid velocities in spectral simulations of turbulence, J. Comput. Phys. 83 (1) (1989) 96–125.
[17] K. Kontomaris, T.J. Hanratty, J.B. McLaughlin, An algorithm for tracking fluid particles in a spectral simulation of turbulent channel flow, J. Comput. Phys. 103 (2) (1992) 231–242.
[18] A.L. Rovelstad, R.A. Handler, P.S. Bernard, The effect of interpolation errors on the Lagrangian analysis of simulated turbulent channel flow, J. Comput. Phys. 110 (1994) 190–195.
[19] P.K. Yeung, Lagrangian investigations of turbulence, Annu. Rev. Fluid Mech. 34 (1) (2002) 115–142.
[20] F. Toschi, E. Bodenschatz, Lagrangian properties of particles in turbulence, Annu. Rev. Fluid Mech. 41 (2009) 375–404.
[21] M. Day, S. Tachibana, J. Bell, M. Lijewski, V. Beckner, R.K. Cheng, A combined computational and experimental characterization of lean premixed turbulent low swirl laboratory flames, I: methane flames, Combust. Flame 159 (1) (2012) 275–290.
[22] J.B. Bell, M.S. Day, J.F. Grcar, M.J. Lijewski, A computational study of equivalence ratio effects in turbulent, premixed methane-air flames, in: Proc. ECCOMAS-CFD, 2006.
[23] M. Day, S. Tachibana, J. Bell, M. Lijewski, V. Beckner, R.K. Cheng, A combined computational and experimental characterization of lean premixed turbulent low swirl laboratory flames, II: hydrogen flames, Combust. Flame 162 (5) (2015) 2148–2165.
[24] R. Darragh, C.A.Z. Towery, P.E. Hamlington, A.Y. Poludnenko, Development of a Lagrangian fluid parcel tracking algorithm for reacting flows, in: 47th AIAA Fluid Dynamics Conference, AIAA AVIATION Forum, Colorado, Denver, 2017.
[25] N. Fukushima, M. Katayama, Y. Naka, T. Oobayashi, M. Shimura, Y. Nada, M. Tanahashi, T. Miyauchi, Combustion regime classification of HCCI/PCCI combustion using Lagrangian fluid particle tracking, Proc. Combust. Inst. 35 (3) (2015) 3009–3017.
[26] C.A. Towery, R.A. Darragh, A. Poludnenko, P.E. Hamlington, Compressible turbulence effects on premixed autoignition, in: 23rd AIAA Computational Fluid Dynamics Conference, 2017 (p. 4286).

[27] H.A. Uranakara, S. Chaudhuri, H.L. Dave, P.G. Arias, H.G. Im, A flame particle tracking analysis of turbulence–chemistry interaction in hydrogen–air premixed flames, Combust. Flame 163 (2016) 220–240.
[28] H.L. Dave, A. Mohan, S. Chaudhuri, Genesis and evolution of premixed flames in turbulence, Combust. Flame 196 (2018) 386–399.
[29] A.M. Steinberg, B. Coriton, J.H. Frank, Influence of combustion on principal strain-rate transport in turbulent premixed flames, Proc. Combust. Inst. 35 (2) (2015) 1287–1294.
[30] J.R. Osborne, S.A. Ramji, C.D. Carter, S. Peltier, S. Hammack, T. Lee, A.M. Steinberg, Simultaneous 10 kHz TPIV, OH PLIF, and CH_2O PLIF measurements of turbulent flame structure and dynamics, Exp. Fluids 57 (5) (2016) 65.
[31] J.R. Osborne, S.A. Ramji, C.D. Carter, A.M. Steinberg, Relationship between local reaction rate and flame structure in turbulent premixed flames from simultaneous 10 kHz TPIV, OH PLIF, and CH_2O PLIF, Proc. Combust. Inst. 36 (2) (2017) 1835–1841.
[32] C. Beetz, C. Schwarz, J. Dreher, R. Grauer, Density-PDFs and Lagrangian statistics of highly compressible turbulence, Phys. Lett. A 372 (17) (2008) 3037–3041.
[33] C. Schwarz, C. Beetz, J. Dreher, R. Grauer, Lyapunov exponents and information dimension of the mass distribution in turbulent compressible flows, Phys. Lett. A 374 (8) (2010) 1039–1042.
[34] Y. Yang, J. Wang, Y. Shi, Z. Xiao, X.T. He, S. Chen, Acceleration of passive tracers in compressible turbulent flow, Phys. Rev. Lett. 110 (6) (2013) 064503.
[35] Y. Yang, J. Wang, Y. Shi, Z. Xiao, X.T. He, S. Chen, Intermittency caused by compressibility: a Lagrangian study, J. Fluid Mech. 786 (2016).
[36] C. Federrath, S.C.O. Glover, R.S. Klessen, W. Schmidt, Turbulent mixing in the interstellar medium: an application for Lagrangian tracer particles, Phys. Scr. 2008 (T132) (2008) 014025.
[37] L. Konstandin, C. Federrath, R.S. Klessen, W. Schmidt, Statistical properties of supersonic turbulence in the Lagrangian and Eulerian frameworks, J. Fluid Mech. 692 (2012) 183–206.
[38] S. Genel, M. Vogelsberger, D. Nelson, D. Sijacki, V. Springel, L. Hernquist, Following the flow: tracer particles in astrophysical fluid simulations, Mon. Not. R. Astron. Soc. 435 (2) (2013) 1426–1442.
[39] F. Vazza, C. Gheller, G. Brunetti, The mixing and transport properties of the intra cluster medium: a numerical study using tracers particles, Astron. Astrophys. 513 (2010) A32.
[40] C.A. Towery, B.E. Schmidt, J.A. Sutton, P.E. Hamlington, Benchmark direct numerical simulations with Lagrangian tracers for evaluating combustion diagnostics algorithms, in: AIAA SciTech 2019 Forum, 2019 (p. 0836).
[41] J.J. Monaghan, Smoothed particle hydrodynamics, Annu. Rev. Astron. Astrophys. 30 (1) (1992) 543–574.
[42] E.F. Toro, Riemann Solvers and Numerical Methods for Fluid Dynamics: A Practical Introduction, Springer Science & Business Media, 2013.
[43] A. Harten, High resolution schemes for hyperbolic conservation laws, J. Comput. Phys. 49 (3) (1983) 357–393.
[44] G.B. Jacobs, W.S. Don, A high-order WENO-Z finite difference based particle-source-in-cell method for computation of particle-laden flows with shocks, J. Comput. Phys. 228 (5) (2009) 1365–1379.
[45] C.W. Shu, Essentially non-oscillatory and weighted essentially non-oscillatory schemes for hyperbolic conservation laws, in: In Advanced Numerical Approximation of Nonlinear Hyperbolic Equations, Springer, Berlin, Heidelberg, pp. 325–432, 1998.
[46] X.D. Liu, S. Osher, T. Chan, Weighted essentially non-oscillatory schemes, J. Comput. Phys. 115 (1) (1994) 200–212.
[47] G.S. Jiang, C.W. Shu, Efficient implementation of weighted ENO schemes, J. Comput. Phys. 126 (1) (1996) 202–228.
[48] Y. Kozak, S.S. Dammati, L.G. Bravo, P.E. Hamlington, A. Poludnenko, Novel Lagrangian-particle tracking method for highly compressible, turbulent, reacting flows, in: AIAA SciTech 2019 Forum, 2019 (p. 1642).
[49] A.K. Chaniotis, D. Poulikakos, High order interpolation and differentiation using B-splines, J. Comput. Phys. 197(1) (2004) 253–274.
[50] R.W. Hockney, J.W. Eastwood, Computer Simulation Using Particles, Adam Hilger, Bristol, New York, 1988.
[51] X.N. Bai, J.M. Stone, Particle-gas dynamics with Athena: method and convergence, Astrophys. J. Suppl. Ser. 190 (2) (2010) 297.
[52] A. Youdin, A. Johansen, Protoplanetary disk turbulence driven by the streaming instability: linear evolution and numerical methods, Astrophys. J. 662 (1) (2007) 613.
[53] C.K. Birdsall, A.B. Langdon, Plasma Physics Via Computer Simulation, CRC Press, 2004.
[54] J.J. Monaghan, Extrapolating B splines for interpolation, J. Comput. Phys. 60 (2) (1985) 253–262.
[55] Y.Y. Liu, C.W. Shu, M.P. Zhang, On the positivity of linear weights in WENO approximations, Acta Math. Appl. Sin., Engl. Ser. 25 (3) (2009) 503–538.
[56] D.S. Balsara, C.W. Shu, Monotonicity preserving weighted essentially non-oscillatory schemes with increasingly high order of accuracy, J. Comput. Phys. 160 (2) (2000) 405–452.
[57] R. Borges, M. Carmona, B. Costa, W.S. Don, An improved weighted essentially non-oscillatory scheme for hyperbolic conservation laws, J. Comput. Phys. 227 (6) (2008) 3191–3211.
[58] S. Bryson, D. Levy, High-order central WENO schemes for multidimensional Hamilton-Jacobi equations, SIAM J. Numer. Anal. 41 (4) (2003) 1339–1369.
[59] C.W. Shu, High order weighted essentially nonoscillatory schemes for convection dominated problems, SIAM Rev. 51 (1) (2009) 82–126.
[60] D. Levy, G. Puppo, G. Russo, A third order central WENO scheme for 2D conservation laws, Appl. Numer. Math. 33 (1–4) (2000) 415–421.
[61] M. Lahooti, A. Pishevar, A new fourth order central WENO method for 3D hyperbolic conservation laws, Appl. Math. Comput. 218 (20) (2012) 10258–10270.
[62] C. Hu, C.W. Shu, Weighted essentially non-oscillatory schemes on triangular meshes, J. Comput. Phys. 150 (1) (1999) 97–127.
[63] J. Zhu, C.W. Shu, A new type of multi-resolution WENO schemes with increasingly higher order of accuracy on triangular meshes, J. Comput. Phys. 392 (2019) 19–33.
[64] Y.T. Zhang, C.W. Shu, Third order WENO scheme on three dimensional tetrahedral meshes, Commun. Comput. Phys. 5 (2–4) (2009) 836–848.
[65] M. Semplice, A. Coco, G. Russo, Adaptive mesh refinement for hyperbolic systems based on third-order compact WENO reconstruction, J. Sci. Comput. 66 (2) (2016) 692–724.
[66] M. Dumbser, W. Boscheri, M. Semplice, G. Russo, Central weighted ENO schemes for hyperbolic conservation laws on fixed and moving unstructured meshes, SIAM J. Sci. Comput. 39 (6) (2017) A2564–A2591.
[67] J.D. Anderson, Modern Compressible Flow: With Historical Perspective, McGraw-Hill, New York, 1990.
[68] G. Borghesi, E. Mastorakos, R.S. Cant, Complex chemistry DNS of n-heptane spray autoignition at high pressure and intermediate temperature conditions, Combust. Flame 160 (7) (2013) 1254–1275.
[69] L.G. Bravo, D. Kim, F. Ham, K.A. Kerner, High fidelity simulations of primary breakup and vaporization of Liquid Jet in Cross Flow (JICF), in: 2018 Joint Propulsion Conference, 2018, p. 4683.
[70] D. Anderson, J.C. Tannehill, R.H. Pletcher, Computational Fluid Mechanics and Heat Transfer, CRC Press, 1997.
[71] P. Londrillo, L. Del Zanna, High-order upwind schemes for multidimensional magnetohydrodynamics, Astrophys. J. 530 (1) (2000) 508.
[72] A.Y. Poludnenko, E.S. Oran, The interaction of high-speed turbulence with flames: global properties and internal flame structure, Combust. Flame 157 (5) (2010) 995–1011.
[73] J.M. Stone, T.A. Gardiner, P. Teuben, J.F. Hawley, J.B. Simon, Athena: a new code for astrophysical MHD, Astrophys. J. Suppl. Ser. 178 (1) (2008) 137.
[74] T.A. Gardiner, J.M. Stone, An unsplit Godunov method for ideal MHD via constrained transport in three dimensions, J. Comput. Phys. 227 (8) (2008) 4123–4141.
[75] P. Colella, P.R. Woodward, The piecewise parabolic method (PPM) for gas-dynamical simulations, J. Comput. Phys. 54 (1) (1984) 174–201.

[76] B. Taylor, D. Kessler, V. Gamezo, E. Oran, The influence of chemical kinetics on the structure of hydrogen-air detonations, in: 50th AIAA Aerospace Sciences Meeting Including the New Horizons Forum and Aerospace Exposition, 2012 (p. 979).
[77] N. Manson, A.K. Oppenheim, H.G. Wagner, Recent progress in detonation research, AIAA J. 1 (10) (1963) 2243–2252.
[78] S. Taki, T. Fujiwara, Numerical analysis of two-dimensional nonsteady detonations, AIAA J. 16 (1) (1978) 73–77.
[79] E.S. Oran, J.P. Boris, T. Young, M. Flanigan, T. Burks, M. Picone, Numerical simulations of detonations in hydrogen-air and methane-air mixtures, Symp., Int., Combust. 18 (1) (1981) 1641–1649, Elsevier.
[80] K. Eto, N. Tsuboi, A.K. Hayashi, Numerical study on three-dimensional CJ detonation waves: detailed propagating mechanism and existence of OH radical, Proc. Combust. Inst. 30 (2) (2005) 1907–1913.
[81] B.D. Taylor, D.A. Kessler, V.N. Gamezo, E.S. Oran, Numerical simulations of hydrogen detonations with detailed chemical kinetics, Proc. Combust. Inst. 34 (2) (2013) 2009–2016.
[82] D.A. Schwer, R.F. Johnson, A. Kercher, D. Kessler, A.T. Corrigan, Progress in efficient, high-fidelity, rotating detonation engine simulations, in: AIAA SciTech 2019 Forum, 2019 (p. 2018).
[83] G. Strang, On the construction and comparison of difference schemes, SIAM J. Numer. Anal. 5 (3) (1968) 506–517.
[84] V.N. Gamezo, T. Ogawa, E.S. Oran, Flame acceleration and DDT in channels with obstacles: effect of obstacle spacing, Combust. Flame 155 (1–2) (2008) 302–315.

Parameter estimation for complex thermal-fluid flows using approximate Bayesian computation

Jason D. Christopher,[1] Nicholas T. Wimer,[1] Caelan Lapointe,[1] Torrey R. S. Hayden,[1] Ian Grooms,[2] Gregory B. Rieker,[1] and Peter E. Hamlington[1,*]

[1]*Department of Mechanical Engineering, University of Colorado, Boulder, Colorado 80309, USA*

[2]*Department of Applied Mathematics, University of Colorado, Boulder, Colorado 80309, USA*

(Received 7 May 2018; published 11 October 2018)

Approximate Bayesian computation (ABC) is a data-driven technique that uses many low-cost numerical simulations to estimate unknown physical or model parameters (e.g., boundary conditions and material properties), as well as their uncertainties, given reference data from real-world experiments or higher-fidelity numerical simulations. In this study, ABC is used to estimate unknown parameters in complex thermal-fluid flows, and the technique is demonstrated on a periodically forced high-temperature jet and a steadily forced helium-air plume. In the first case, computational reference data are used to assess the accuracy of ABC when estimating the frequency, amplitude, and mean of the periodic velocity forcing at the jet inlet. These tests show that ABC provides accurate and reasonably certain estimates of inflow parameters even when the model simulations imperfectly represent the physics underlying the reference data. These tests also show that measurements far from the inlet can be used to perform the estimation, and that temperature measurements can be used to infer velocity inflow parameters. For the second case, ABC is used to estimate the inlet Richardson number and its uncertainty given experimental measurements of the Strouhal number within the plume. Once again, the approach is able to accurately estimate unknown parameters with relatively low uncertainty. As a result, ABC is shown to be a versatile technique for estimating unknown physical parameters when knowledge of a real-world system is limited or incomplete.

DOI: 10.1103/PhysRevFluids.3.104602

I. INTRODUCTION

Computational simulations are widely used to design and analyze systems involving complex thermal-fluid flows, from microscale heat transfer in thermal management devices to liquid propulsion in heavy-lift rockets. Nearly all such simulations are intended to provide three-dimensional (3D) spatially and temporally resolved numerical solutions of physics-based governing equations for realistic geometries, boundary conditions, and material properties. Prior to making simulation-based design and operational decisions, however, computational accuracy must be demonstrated by validating against (typically experimental) reference data for realistic or canonical test cases. As simulation fidelity has improved over the past decade with the development of higher-order and geometry-resolving numerical techniques, as well as with the increasing use of petascale computing resources to achieve very fine spatial resolutions and improved physical realism, a long-standing difficulty in such validation efforts has come into sharper focus.

Namely: *Even if a simulation is able to solve physically realistic governing equations with high accuracy, unavoidable uncertainties in real-world boundary conditions, material properties, and*

*peh@colorado.edu

 ©2018 American Physical Society

other parameters result in ambiguity as to whether the computational and real-world systems are actually equivalent. That is, there are few assurances that discrepancies between computational and experimental results during a validation test are not simply due to limitations in the characterization of the real-world system. Cases where knowledge of a real-world system is limited include experiments that were not originally intended for validation purposes, systems with limited access, or parameters that are difficult to measure directly [1].

In broad terms, this difficulty can be addressed by proposing distributions of likely parameter values, performing simulations with parameters sampled from those distributions to determine the spread of outcomes in a particular quantity of interest within the flow, and then using statistical inference to determine distributions for unknown parameter values [1–4]. This approach can, in principle, be attempted using full Bayesian analyses, which have recently gained popularity for parameter estimation in engineering applications [5–9]. However, in nearly all such analyses, the requisite components of Bayes' theorem (specifically, the likelihood function) may be unknown or enormously costly to compute, and, consequently, non-physics-based reduced-order surrogate models have often been used to sample the unknown parameter space [6,7,10–12]. Optimization techniques have also been used for parameter estimation (e.g., Refs. [13–17]), but these methods seek to provide single values of unknown parameters, with no intrinsic measure of uncertainty when using potentially imperfect computational models and real-world data.

In the present study, approximate Bayesian computation (ABC), a data-driven Bayesian technique adopted from the biological and geophysical sciences, is used to estimate unknown parameters for complex, turbulent thermal-fluid flows. The power of ABC lies in the fact that far fewer simulations are required than in full Bayesian analyses since ABC does not require a likelihood function, thus permitting the use of physics-based models. Rather than attempting to match the reference data at all locations and times, as in full Bayesian analyses, the ABC method develops an approximate posterior distribution for unknown parameters through comparison of summary statistics from the reference data and model simulations. A wide variety of reference data can be used to drive the estimation, including measurements that are only indirectly related to parameters of interest. Because the technique naturally provides posterior distributions for unknown parameters, Bayesian confidence intervals can be obtained along with parameter estimates. Once parameter estimates are obtained, either they can be used in higher-fidelity numerical simulations of the same system, or they can be considered as part of the description of the real-world system itself (with appropriate uncertainty caveats).

This study is one of a growing number of efforts to use data-driven methods with either experimental or higher-fidelity computational reference data to improve accuracy and quantify uncertainty in turbulent flow simulations. For example, ensemble Kalman filtering (EnKF) approaches have been used to assimilate reference data in simulations [18–21] and to infer turbulence model discrepancies [22]. In such approaches, reference data are used to update the state of a simulation or parameters in the simulation as the simulation progresses. Generally, however, EnKF methods require extensive and high-quality reference data to provide reliable state and parameter estimates. The maximum *a posteriori* (MAP) method has also been used to infer both parameter [23] and model [24] uncertainties. This method maximizes the posterior using either an analytical function or a Monte Carlo approach, but the analytical function used to represent the posterior (or the likelihood function) is often known only approximately, and the number of simulations required in even Markov chain Monte Carlo approaches can be enormous. Recently, the ABC method has been used to infer Arrhenius parameters for chemical kinetics rate coefficients in the context of combustion [25].

The present study is specifically targeted at problems for which the reference data are spatially and temporally sparse, statistical in nature, or otherwise lacking in sufficient detail to update the model simulations at all locations and times (precluding the use of EnKF methods) and for which the true posterior is either intractable or prohibitively expensive to compute (precluding the use of MAP methods). As a demonstration of ABC, this paper outlines the estimation of inflow boundary conditions for two compressible turbulent flows: (1) a periodically forced high-temperature jet and

(2) a weakly but steadily forced helium-air plume. Both cases are two-dimensional (2D) but are physically complex due to compressibility and the corresponding coupling between temperature, density, buoyancy, and forced advection. The first case is intended to demonstrate the utility and breadth of ABC by using computational reference data to estimate the frequency, amplitude, and mean of the forced inflow. Since these parameters and the underlying physical model are precisely known for the computational data, the success of the ABC approach can be quantified. The second case is a demonstration of ABC using experimental measurements in an engineering context.

It should be noted that the present study is focused on demonstrating the use of ABC for estimating *physical* parameters that are difficult to obtain for real-world systems, as opposed to calibrating *model* parameters used in reduced-order or engineering models of more complex phenomena. Such model parameter calibrations are also possible using ABC and are the subject of future research [26].

II. APPROXIMATE BAYESIAN COMPUTATION

The ABC framework is a relatively new approach for linking reference data to physical and model parameters [27–33]. It was first conceived by Rubin [34] and then subsequently applied by Pritchard *et al.* [35] to the study of population dynamics. Although the technique has traditionally been applied in biology [35–41], it has recently gained traction in geophysics [42–48], primarily for calibrating parameters in reduced-order models of complex phenomena. It has also been used recently in the context of chemical kinetics modeling for combustion [25].

From a fundamental perspective, the ABC method produces a posterior distribution of unknown parameters given some reference data. This occurs by comparing observations or summary statistics from the reference data to corresponding data or summary statistics from lower-cost physics-based "model" simulations (e.g., simulations with coarse spatial resolutions or lower-order numerical schemes). The model simulations are repeated many times, with each simulation using parameters drawn from a prior distribution. The prior distribution is the best guess at the span of the unknown parameter space; it must be wide enough to contain the true parameter values, but narrow enough to keep the task computationally manageable. Parameter values are retained if the model data or summary statistics are similar to the reference observations. Once many such candidates are obtained, a posterior distribution is formed, providing estimates for the most likely parameter values as well as their uncertainties, given the reference data.

The specific ABC algorithm used in this work is Method D from Marjoram *et al.* [28]. Given the summary statistic $\boldsymbol{\mathcal{S}}$ obtained from reference data $\boldsymbol{D}$, this algorithm involves the following steps (see also the schematic in Fig. 1):

(1) Generate parameters $\boldsymbol{\theta}$ from the prior distribution $P(\boldsymbol{\theta})$.

(2) Simulate approximate data $\hat{\boldsymbol{D}}$ using parameters $\boldsymbol{\theta}$ and compute the approximate statistic $\hat{\boldsymbol{\mathcal{S}}}$.

(3) Calculate the distance $\delta(\boldsymbol{\mathcal{S}}, \hat{\boldsymbol{\mathcal{S}}})$ between the reference, $\boldsymbol{\mathcal{S}}$, and simulated, $\hat{\boldsymbol{\mathcal{S}}}$, statistics.

(4) Accept $\boldsymbol{\theta}$ if $\delta(\boldsymbol{\mathcal{S}}, \hat{\boldsymbol{\mathcal{S}}}) \leqslant \varepsilon$ (where ε is the "rejection distance") and build the posterior distribution of accepted parameters, denoted $P[\boldsymbol{\theta} \mid \delta(\boldsymbol{\mathcal{S}}, \hat{\boldsymbol{\mathcal{S}}}) \leqslant \varepsilon]$.

(5) Return to step 1 and repeat a total of N times until a reasonable estimate is obtained for the posterior distribution.

In general, the parameters $\boldsymbol{\theta}$, data $\boldsymbol{D}$ and $\hat{\boldsymbol{D}}$, and summary statistics $\boldsymbol{\mathcal{S}}$ and $\hat{\boldsymbol{\mathcal{S}}}$ are multidimensional and are correspondingly indicated by boldface notation.

In broad terms, the prior distribution is simply the initial guess for the values of the true parameters. Greater confidence in the values of unknown parameters permits a more concentrated prior distribution (e.g., a Gaussian instead of a uniform distribution). The only requirement on the prior is that its range spans the true values of the unknown parameters. In many practical cases, a wide prior can be used initially to gain an approximate idea of the true parameter values, and then a narrower prior can be used to determine parameter values with greater precision.

The use of summary statistics is intended to reduce the overall computational cost of the parameter estimation. Although it would be ideal to compare all of the available data $\boldsymbol{D}$ to

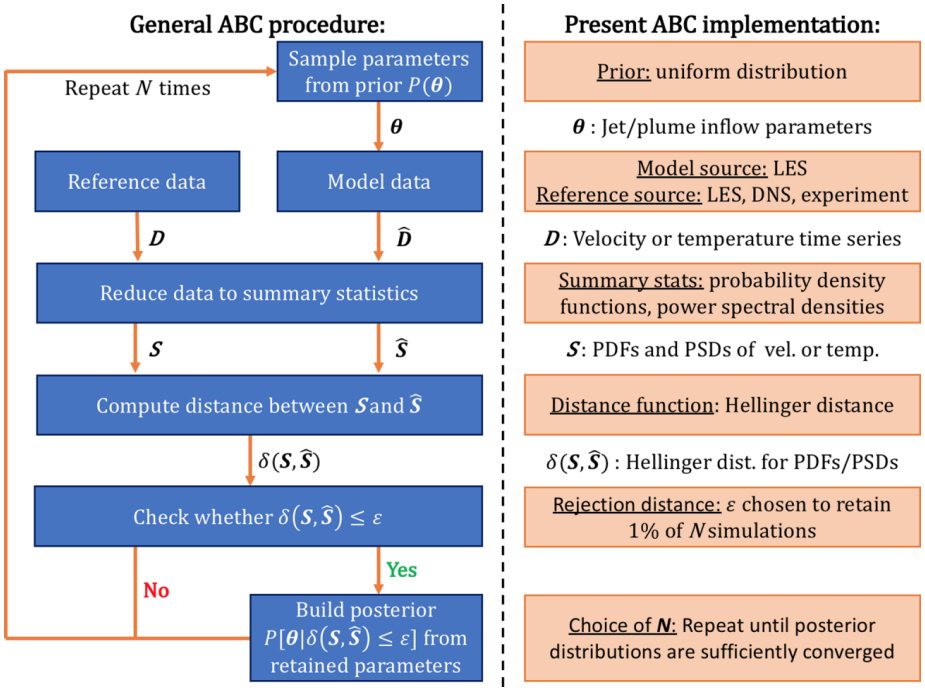


FIG. 1. Schematic of the general ABC approach corresponding to Method D from Marjoram *et al.* [28] and of the specific ABC implementation used in the present study.

all of the simulation data $\hat{\boldsymbol{D}}$, this is typically a very high-dimensional problem and is not computationally feasible in general. Thus, instead, summary statistics are used. A key challenge in successfully implementing ABC is to identify relevant summary statistics that significantly reduce the dimensionality of the data, while still maintaining sufficient identifiability of unknown parameters [49]. Examples of summary statistics include averages, standard deviations, probability distribution functions (PDFs), and power spectral densities (PSDs).

The choice of distance function is typically based on the form of the summary statistic. For example, the root-mean-square error can be used to compare spatial profiles of average quantities, and the Hellinger distance [50] or Kullback-Leibler divergence [51] can be used to compare PDFs. The specific choice of rejection distance, ε, is typically determined by a balance between computational cost and parameter estimate uncertainty. Smaller values of ε lead to higher rejection rates and reduced uncertainty in estimated parameter values [29] but also increase the number of model simulations necessary to generate a sufficiently converged posterior.

With respect to evaluating the success of the ABC parameter estimation, "accuracy" can be assessed either by comparing the approximate posteriors generated using ABC to the true posteriors, or by comparing the estimated parameter values to the true parameter values, along with a measure of certainty in the estimated values. In the present study, the true posteriors are not known analytically, and they are prohibitively expensive to compute numerically. As a result, the accuracy of the ABC approach is quantified here by computing 95% Bayesian confidence intervals (sometimes called credible intervals), denoted C_B, from the approximate parameter posteriors, then determining whether C_B contains the true parameter value. The ultimate measure of accuracy in the present study is indicated by how closely a central tendency of the posterior (such as the mean) matches the true parameter value. The degree of certainty in the estimated parameter value is determined by the width of C_B, where narrower intervals indicate more certain parameter estimates.

Additional details on the specific choices for the prior, summary statistics, distance function, and rejection distances used in the present ABC implementation are outlined in the following sections and are summarized in Fig. 1.

III. DEMONSTRATION OF ABC USING COMPUTATIONAL REFERENCE DATA

As a demonstration of ABC, inflow parameters for a periodically forced high-temperature turbulent buoyant jet [52–56] are estimated using computational reference data. This case is examined due to the simplicity of the geometry combined with the complexity of the high-temperature unsteady compressible flow physics. Large eddy and direct numerical simulations (LES and DNS, respectively) are used as reference data, and model simulations are performed using LES.

The use of computational reference data allows the success of ABC to be assessed when the physics underlying the reference data, as well as all system parameters, are known exactly. Three questions, in particular, are addressed: (1) How accurately can ABC estimate unknown parameters when the reference data physics are exactly reproduced by the model simulations? (2) How accurately can ABC estimate unknown parameters using model simulations that imperfectly represent the physics of the reference case? (3) How accurately can ABC estimate unknown parameters using reference data that are only indirectly connected to the parameters of interest?

The first question represents a "best case scenario" where there is zero model error, and it is examined using both model and reference data from LES. Despite the exact correspondence between the governing equations solved in the model and reference LES, however, the flow fields obtained from each of the simulations differ on a local and instantaneous basis due to the use of different random initial conditions. The second question pertains to a more realistic application of ABC where the physics governing the reference data are not exactly represented by the model simulations. This question is examined here using LES model simulations and DNS reference data and is further addressed in Sec. IV using experimental reference data. The third question addresses the identifiability of unknown parameters using different types of reference data and is examined by performing ABC at different heights above the inlet using either velocity or temperature measurements.

It should be noted that the test where both the model and reference data are obtained from LES most closely resembles an observing system simulation experiment (OSSE), which is a common technique used for the validation of data assimilation methods [57,58]. In the present context, the OSSE represented by this test allows the choices of prior, summary statistic, distance function, and rejection distance to be evaluated in the absence of model error. In this sense, these tests indicate whether the ABC approach can ever be expected to succeed and to what extent. The following analysis illustrates that, even in such a "best case scenario," the ABC parameter estimation does not perfectly recover the true parameter values due to the presence of stochasticity in the model and reference data. That is, the model and reference data are never in perfect local and instantaneous agreement because each of the simulations are initialized with different random temperature fields (even when using identical boundary parameter values). Thus, the true parameter values are only ever recovered approximately, even when the governing equations used to generate the model and reference data are identical.

The test where the model data are obtained from LES and the reference data from DNS is intended to address a common concern when parameter estimation methods are evaluated using OSSEs: namely, that assessments of the method are likely to be overly optimistic due to the exact correspondence between the physics and numerics underlying the model and reference simulations. This issue, sometimes referred to as an "inverse crime" [59,60] or the "identical/fraternal twin problem" [61,62], is typically resolved by using different models, for example with different discretizations, numerics, or physics, for the generation of the reference data and for the parameter estimation. Here the LES-DNS tests are intended to provide a more realistic assessment of the accuracy of the ABC method than the LES-LES tests, since both the grid resolution and underlying governing equations in the LES and DNS are different. The test using experimental reference data and LES model data in Sec. IV is similarly intended to enable a more realistic assessment of the accuracy of the ABC approach.

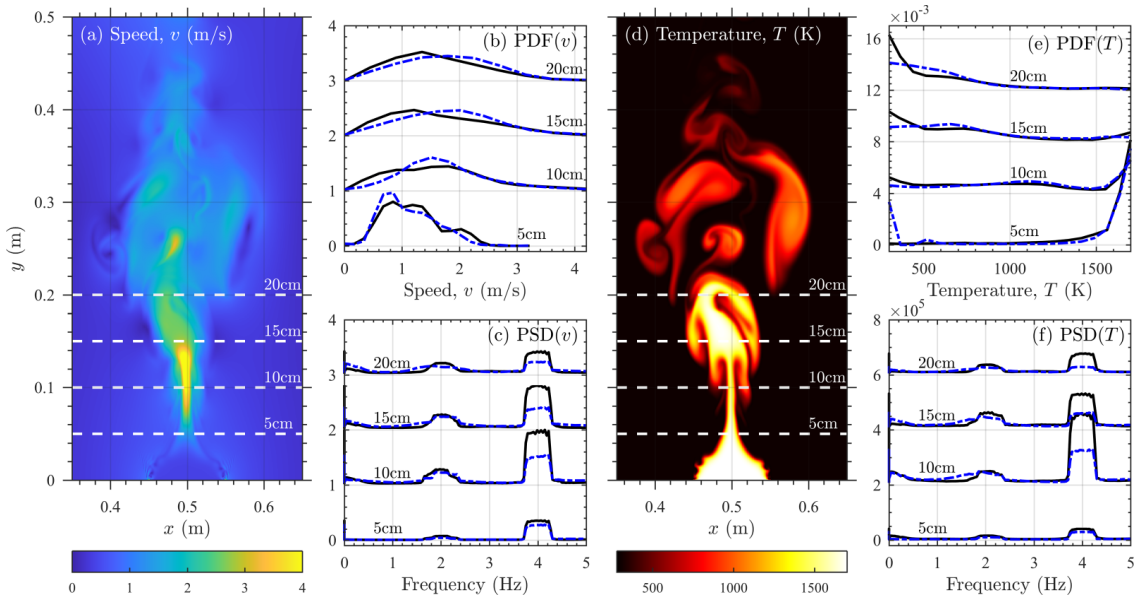


FIG. 2. Representative fields of speed v (a) and temperature T (d) from DNS for the periodically forced turbulent buoyant jet. Panels (b) and (c) show reference probability density functions (PDFs) and power spectral densities (PSDs), respectively, of v at heights of 5, 10, 15, and 20 cm. PDFs and PSDs at different heights are shifted vertically for clarity. Panels (e) and (f) show corresponding PDFs and PSDs of T. Solid black lines in panels (b), (c), (e), and (f) show DNS reference data and dash-dot blue lines show LES reference data. PSDs are computed using Thomson's multitaper estimate [69].

A. Physical and numerical setup

The reference buoyant jet has a sinusoidally varying inlet velocity with a frequency of 4 Hz, an amplitude of 0.2 m/s, and a mean of 0.5 m/s. The inflow velocity is spatially uniform across the inlet. The physical domain is 1×2 m, and the inlet is 0.1 m wide. The ambient and inlet temperatures are 300 K and 1700 K, respectively, resulting in substantial density differences and buoyancy-driven flow. Instantaneous fields of velocity magnitude (i.e., speed) and temperature are shown in Fig. 2.

All of the computations were performed using the FireFoam solver [63] within OpenFOAM [64,65]. The simulations were restricted to two dimensions to minimize computational cost, although the ABC method is equally applicable in three dimensions. For the LES, the compressible filtered Navier-Stokes equations were solved with second-order accuracy in space and time using the one-equation eddy viscosity model [66] for closure of subgrid-scale stresses. The LES domain was discretized using 61 088 cells, with grid stretching in the vertical direction and two levels of refinement near the jet inlet. For the DNS computations, the compressible Navier-Stokes equations were solved in conjunction with the total energy equation at a high spatial resolution, again using a second-order accurate numerical scheme in space and time. The DNS domain was discretized using 745 472 cells with two levels of grid refinement, giving a grid that was more than an order of magnitude larger than the LES grid.

For both the LES and DNS, the ideal gas equation was used to relate state variables, and fluid viscosity and specific heat varied with temperature according to the Sutherland model [67] and JANAF tables [68], respectively. The LES and DNS numerical schemes were also the same, with Crank-Nicolson time stepping and Gauss integration with linear interpolation for spatial derivatives. Pressure-velocity coupling was accomplished using the PIMPLE algorithm, which combines the pressure-implicit split-operator and the semi-implicit method for pressure-linked equations. An adaptive time step was used to limit the maximum CFL condition to 0.5 for the LES and 0.2 for the DNS.

B. ABC implementation

In this demonstration, ABC is used to estimate the frequency, amplitude, and mean of the periodic forcing at the inlet of the buoyant jet given either LES or DNS reference data, with model simulations from LES. The reference data consist of time series of speed or temperature measured at nine heights above the inlet, ranging from roughly 0.5 mm up to 0.2 m. Time series at each height were recorded over approximately 14 s after a 1 s initialization period, and PDFs and PSDs were computed for each time series; these are the ABC summary statistics. The PSDs were calculated using Thomson's multitaper estimate [69,70], which provides a robust estimate of the PSD by reducing energy leakage across frequencies and reducing variance [71].

To ensure statistical convergence of the reference data, ensembles of 100 statistically independent simulations were created using both LES and DNS. Each simulation had the same periodically forced inflow at a frequency of 4 Hz, an amplitude of 0.2 m/s, and a mean of 0.5 m/s, but was initialized using different stochastically generated temperature fields. The final reference data for both the LES and DNS cases were then created by averaging the PDFs and PSDs for each of the 100 simulations in each ensemble, at each of the nine heights, giving the reference data sets shown, for example, in Figs. 2(b) and 2(c) for speed and in Figs. 2(e) and 2(f) for temperature. Moreover, Fig. 2 shows that the LES and DNS reference data are in reasonably good agreement.

Approximately 10^4 additional LES model cases were generated for the parameter estimation. Each simulation was executed with a unique set of inlet parameters randomly sampled from prior distributions for the frequency, amplitude, and mean of the sinusoidal velocity oscillations at the inlet. The priors were uniform with bounds of 3.6–4.4 Hz for the frequency, 0.0–0.4 m/s for the amplitude, and 0.0–1.0 m/s for the mean. Uniform priors were chosen to avoid the creation of anomalous biases in the posterior distributions. The width of the priors for the amplitude and mean were selected to be $\pm 100\%$ the true parameter values, while the width of the frequency prior is $\pm 10\%$ the true value; it will be seen in the following that even with such a narrow frequency prior, the posteriors go to zero at the edges of the prior for all heights. Although wider priors would result in greater recovery of the edges of the posterior distributions, nearly all of the posteriors obtained in this study display a pronounced maximum within the range of values present in the priors. It should also be noted that the current priors are centered on the true values and that off-centered priors could be formed, for example, by using widths that are $[-100\%, +200\%]$ the true values for the amplitude and mean and $[-10\%, +20\%]$ for the frequency. However, once more, the success of the ABC method will not be affected by the use of such off-centered priors provided that the posteriors already display a distinct maximum within the bounds of the current centered priors, as is the case for nearly all of the tests performed here.

The Hellinger distance [50] was used to quantify the agreement between summary statistics from the reference and model data. Values for ε were chosen such that a fixed percentage of the tested parameters were retained in the final posterior [37,40]. Parameter rejection was first performed using the Hellinger distance for the PSD, where ε was selected to reject 80% of all parameters tested. Subsequently, rejection was performed using the Hellinger distance for the PDF, with ε chosen to reject 95% of the remaining parameters. With this sequential approach, only 1% of the parameters tested were included in the final posteriors.

C. Inflow parameter estimation using LES reference data

Figure 3 shows marginal posterior distributions for each inflow parameter using both speed and temperature reference data from LES at different heights. The posteriors are represented by Gaussian kernel estimations with bandwidths from Scott's normal reference rule [72]. As noted previously, these tests represent a best-case scenario for the ABC method where both the model and reference data physics are identical. Correspondingly, Figs. 3(a), 3(c), and 3(e) show that the true parameter values are captured by the ABC posteriors when using speed reference data from LES. In general, the uncertainty is smallest at locations close to the inlet, although reasonable estimates of the true parameters are still obtained at higher locations.

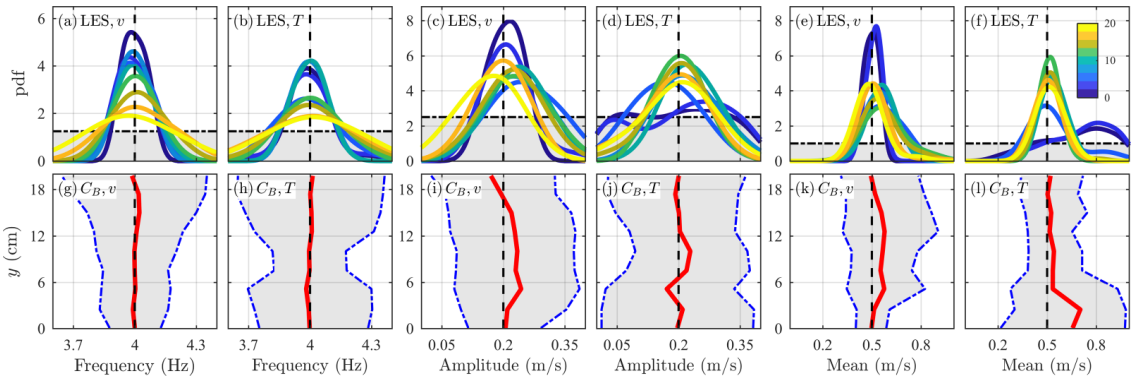


FIG. 3. Top row: Marginal posterior distributions from ABC (visualized using Gaussian kernel estimation) for the frequency (a, b), amplitude (c, d), and mean (e, f) of the periodically forced turbulent buoyant jet using speed (a, c, e) and temperature (b, d, f) reference data from LES. Posteriors are calculated using measurements at heights from 0 to 20 cm (indicated by colors from blue to yellow). True parameter values are shown by vertical black dashed lines. Horizontal dash-dot lines and gray regions show the priors. Bottom row: Vertical profiles of 95% Bayesian confidence intervals, C_B, for the marginal posterior distributions in all panels. Blue dash-dot lines and gray shading indicate the 95% Bayesian confidence regions, and the solid red lines show the mean values of the posteriors. True parameter values are shown by vertical black dashed lines.

For the speed reference data, Figs. 3(g), 3(i), and 3(k) show that C_B is narrowest near the inlet when using LES reference data. This indicates that identifiability of the unknown parameters is greatest near the inlet when using the speed as reference data, although even higher in the domain it is still possible to estimate inflow parameters, albeit with less confidence. Figures 3(g), 3(i), and 3(k) also show that mean values from the posteriors are in good agreement with the true values, particularly near the inlet for the amplitude and mean, and at all heights for the frequency.

The identifiability of unknown parameters using different measured quantities can be assessed by repeating the ABC procedure using PDFs and PSDs computed from temperature time series. Figure 3(b) shows that frequency predictions based on temperature reference data are all roughly centered on the true parameter value, and Fig. 3(h) shows that the posterior means are in good agreement with the true value. The amplitude and mean posteriors in Figs. 3(d) and 3(f) are centered around the true parameter values in the region from approximately 0.5 to 1.5 jet widths above the inlet. Below these heights, however, there is not enough variation in the temperature field to aid in parameter estimation, given the uniform inflow temperature. Because the PDFs were nearly identical at such low heights, the ABC procedure was modified such that 15% of the simulated parameters were accepted based solely on the PSD comparison. Higher than 1.5 jet widths above the inlet, the connection between the temperature field and the inlet velocity becomes weaker, resulting in reduced identifiability of velocity boundary conditions using temperature measurements. Despite these limitations, as shown in Figs. 3(h), 3(j), and 3(l), all parameters are predicted for all heights within the C_B intervals for each posterior.

The amount of information gained about the unknown parameters during the ABC procedure can be quantified using the Kullback-Leibler (KL) divergence [51] between the prior and posterior distributions. Higher values of the KL divergence indicate that the posterior is significantly different than the prior, while values close to zero indicate that the posterior is similar to the prior and that little information about unknown parameters has been gained during the ABC procedure.

Figure 4 shows vertical profiles of the KL divergence for speed and temperature reference data from LES, revealing that, in all cases, at least some information about the unknown parameters is gained at nearly all locations within the domain. For the speed reference data in Fig. 4(a), the greatest information about the unknown parameters is obtained near the jet inlet, and the posteriors for the frequency generally provide more information higher in the domain than the posteriors for the amplitude and mean. By contrast, for the temperature reference data in Fig. 4(b), the greatest

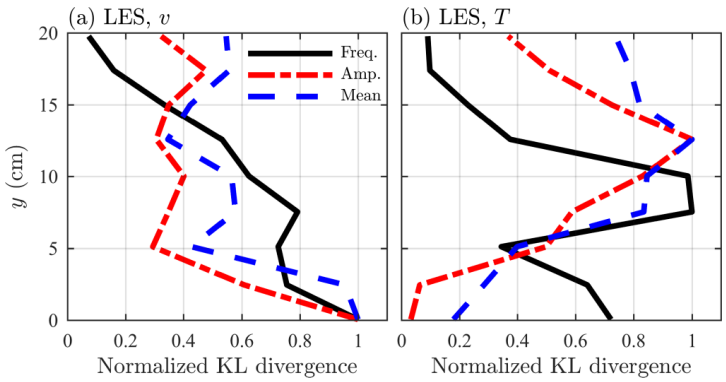


FIG. 4. Vertical profiles of Kullback-Leibler (KL) divergences for the marginal posterior distributions in Fig. 3 obtained using LES reference data. Divergences for the frequency (black solid lines), amplitude (red dash-dot lines), and mean (blue dashed lines) posteriors are shown for speed (a) and temperature (b) reference data. Each KL divergence vertical profile is normalized by its respective maximum value.

information is obtained higher in the domain, close to 10 cm (corresponding to one jet width above the inlet). In general, only the temperature reference data near the jet inlet fail to provide significant information regarding unknown parameter values.

D. Inflow parameter estimation using DNS reference data

As noted previously, evaluations of the ABC method based on tests where the same model is used for the reference data and the parameter estimation (as in the LES-LES tests described in the previous section) are likely to be overly optimistic. To address this issue, tests where the reference data are generated by DNS and the parameter estimation is performed using LES have also been carried out.

Figure 5 shows marginal posterior distributions for each inflow parameter using both speed and temperature reference data from DNS at different heights. As with the LES-LES results shown

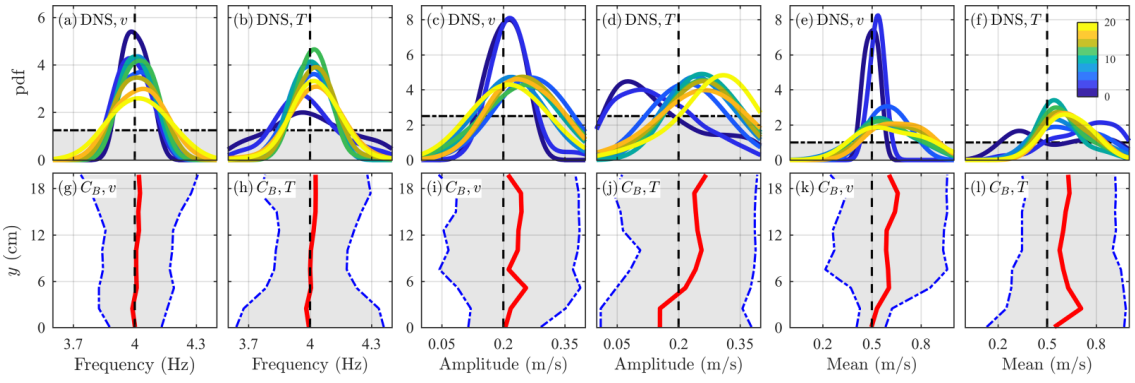


FIG. 5. Top row: Marginal posterior distributions from ABC (visualized using Gaussian kernel estimation) for the frequency (a, b), amplitude (c, d), and mean (e, f) of the periodically forced turbulent buoyant jet using speed (a, c, e) and temperature (b, d, f) reference data from DNS. Posteriors are calculated using measurements at heights from 0 to 20 cm (indicated by colors from blue to yellow). True parameter values are shown by vertical black dashed lines. Horizontal dash-dot lines and gray regions show the priors. Bottom row: Vertical profiles of 95% Bayesian confidence intervals, C_B, for the marginal posterior distributions in all panels. Blue dash-dot lines and gray shading indicate the 95% Bayesian confidence regions, and the solid red lines show the mean values of the posteriors. True parameter values are shown by vertical black dashed lines.

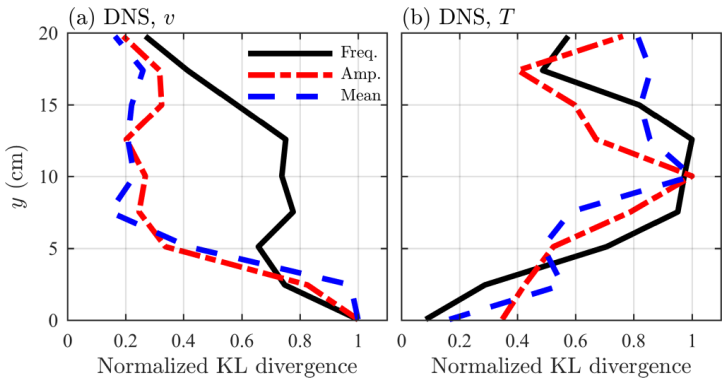


FIG. 6. Vertical profiles of Kullback-Leibler (KL) divergences for the marginal posterior distributions in Fig. 3 obtained using DNS reference data. Divergences for the frequency (black solid lines), amplitude (red dash-dot lines), and mean (blue dashed lines) posteriors are shown for speed (a) and temperature (b) reference data. Each KL divergence vertical profile is normalized by its respective maximum value.

in Fig. 3, Figs. 5(a), 5(c), and 5(e) show that the true parameter values are captured by the ABC posteriors when using speed reference data, with generally narrower posteriors close to the inlet. This is also indicated by the variations of C_B in Figs. 5(g), 5(i), and 5(k), where it can be seen that C_B is narrowest near the inlet when using speed reference data. The width of C_B consistently increases with height as the distance from the inlet increases. For each of the unknown parameters, posterior means are generally close to the true parameter values.

For the temperature reference data from DNS, Figs. 5(b), 5(d), and 5(f) show that the marginal posterior distributions once again capture the true parameter values with reasonable success. There is some bias in the posteriors for the DNS reference data (particularly for the estimates of the amplitude and mean), but the true parameter values are nevertheless contained within reasonably narrow 95% Bayesian confidence intervals. This is also shown in Figs. 5(h), 5(j), and 5(l), where C_B is widest for the temperature-based DNS reference data near the inlet and narrowest roughly one jet width above the inlet.

Vertical profiles of the KL divergence for the DNS reference data are shown in Fig. 6. As with the LES-LES results shown in Fig. 4(a), Fig. 6(a) shows that speed reference data from DNS provides the greatest information about unknown parameters near the jet inlet, with the frequency posteriors providing more information higher in the domain than the posteriors for the amplitude and mean. For the temperature reference data in Fig. 6(b), the greatest information is once again obtained roughly one jet width above the inlet. In general, the trends shown in Figs. 4 and 6 are similar for the LES and DNS reference data, respectively.

Taken together, the results for the DNS reference data in Figs. 5 and 6 indicate that the ABC approach is successful even in non-overly optimistic tests where the reference and model data are significantly different. Overall, the parameter estimation is generally more accurate using LES, as opposed to DNS, reference data, but this is unsurprising given the additional model error introduced when using the DNS reference data. As a result, ABC is able to provide predictions for unknown parameters using either exact or imperfect model simulations (as compared to the reference data), and for locations that are indirectly related to the parameters of interest (i.e., using measurements at locations far from the inlet).

IV. DEMONSTRATION OF ABC USING EXPERIMENTAL REFERENCE DATA

To demonstrate the utility of the ABC approach when the reference data are obtained from an experiment, the ABC technique is next applied to a steadily forced planar plume for which experimental data are available from Cetegen *et al.* [73]. In this experiment, a helium-air mixture is weakly forced into 300 K ambient air, resulting in a natural oscillatory behavior of the plume.

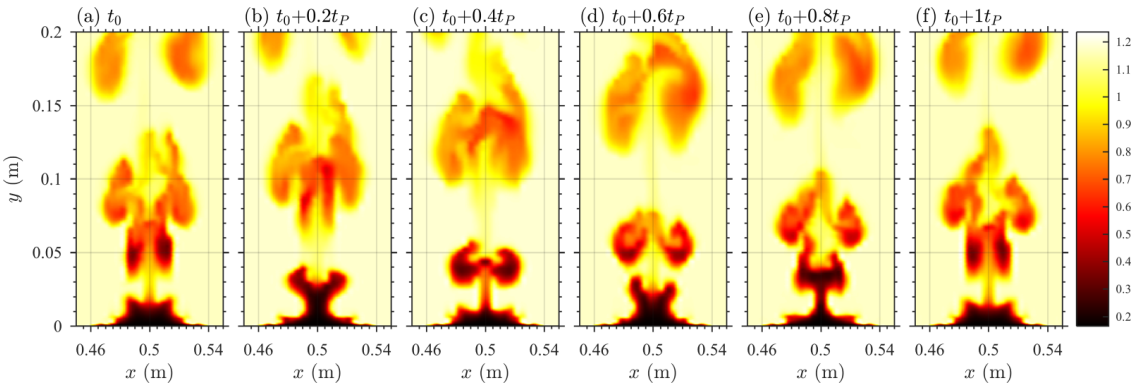


FIG. 7. Representative 2D fields of density (kg/m^3) from LES at six different times (a–f) for the steadily forced plume described in Sec. IV. The fields shown begin at an arbitrary time t_0 late in the LES and are separated by a time interval spanning one complete period, t_P ($t_P = 1/f = 0.22$ s).

By spanning a range of inflow conditions, Cetegen *et al.* [73] determined the empirical relation $\mathrm{St} = 0.55\mathrm{Ri}^{0.45}$ between the Strouhal, $\mathrm{St} = fw/v_i$, and Richardson, $\mathrm{Ri} = (1 - \rho_i/\rho_\infty)gw/v_i^2$, numbers, where ρ_i is inlet density, ρ_∞ is ambient density, g is gravity, w is inlet width, v_i is inlet velocity, and f is the frequency of the natural oscillation.

In this demonstration, ABC is performed assuming that the oscillation frequency above the jet inlet, f, has been measured experimentally and that the density of the inflow mixture, ρ_i/ρ_∞, is unknown (where $\rho_i/\rho_\infty = 0.14$ for pure helium and 1 for pure air). All other properties of the inflow, including v_i and w, are assumed to be known. This case thus serves as the first experimental

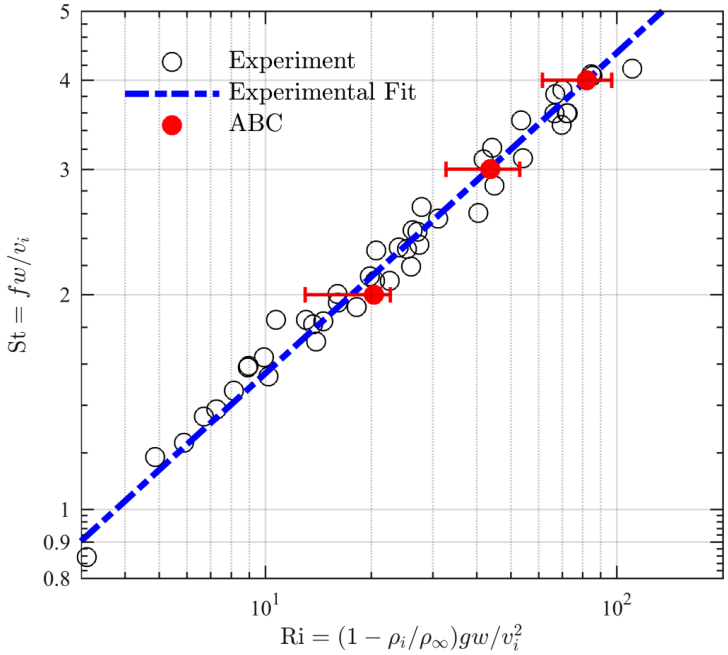


FIG. 8. Relationship between Strouhal number $\mathrm{St} = fw/v_i$ and inlet Richardson number $\mathrm{Ri} = (1 - \rho_i/\rho_\infty)gw/v_i^2$ for the steadily forced helium-air plume. Experimental results from Cetegen *et al.* [73] are indicated by open circles, and the empirical fit $\mathrm{St} = 0.55\mathrm{Ri}^{0.45}$ is shown as a blue dash-dot line. ABC results are indicated by filled red circles located at the mean Ri of the posterior distribution. Uncertainty bars show the minimum and maximum values of Ri in the posteriors.

demonstration that ABC is able to accurately estimate unknown parameters in complex thermal-fluid flows, while also providing measures of uncertainty in the parameter estimates.

The model simulations were once again performed using LES in FireFoam [63]. The plume had a width of $w = 0.07$ m and a steady uniform inflow velocity of $v_i = 0.067$ m/s. The reference Strouhal number was assumed to be $\mathrm{St} = 4$, which is close to several values measured experimentally (see Fig. 8). The inlet width and velocity were held fixed for 100 LES runs while the inlet density ratio varied from 0.14 to 0.6, corresponding to the published range of density ratios from Ref. [73]. The lowest density ratio corresponds to pure helium while the upper value was found in Ref. [73] to be the bounding case beyond which the characteristic natural oscillation was not observed. The Strouhal number was obtained from the peak frequency in a fast Fourier transform of vertical velocity a distance w above the inlet; this was the summary statistic. The distance function consisted of an L1 error norm between reference and model peak frequencies, and ε was chosen to retain 20% of the parameter values from the model simulations. The characteristic oscillation of the plume is captured by the LES, as shown in Fig. 7.

Figure 8 shows that the estimated value of Ri from ABC for $\mathrm{St} = 4$ agrees closely with the experimental data. Additional tests for $\mathrm{St} = 2$ and 3 were also performed using $v_i = 0.1$ m/s and 0.15 m/s, respectively. These different inlet velocities were necessary to span a range of Ri while constraining the physically allowable values of ρ_i/ρ_∞ to between 0.14 and 0.6. Once again, Fig. 8 shows that ABC provides estimates of Ri that are in close agreement with experiments. As a result, ABC correctly identifies the unknown Ri that would provide the desired natural oscillation frequencies for known inlet velocity and width.

V. CONCLUSIONS

Approximate Bayesian computation (ABC) has been used to estimate unknown physical parameters in complex thermal-fluid flows. As a demonstration of the approach, ABC was used to estimate the frequency, amplitude, and mean of the velocity inflow in a periodically forced turbulent buoyant jet, as well as the inlet Richardson number for a steadily forced helium-air plume. In the former case, computational reference data were used to drive the parameter estimation, while in the latter case experimental reference data were used. For both cases, ABC provided accurate estimates of unknown physical parameters even when the model simulations did not exactly match the physics underlying the reference data (e.g., when using LES for the model simulations and reference data from either DNS or experiments), and when the reference data were only indirectly connected to the unknown parameters of interest (e.g., when using measurements distant from the jet and plume inlets, or when using temperature measurements to infer velocity inlet parameters). The primary impacts of using imperfect model simulations or only indirectly connected measurements were observed in the width of the Bayesian confidence intervals. As the physics of the model simulations more closely matched that of the reference data, and as the connection between the measurements and unknown parameters improved, the confidence intervals were found to become narrower.

Although the present demonstration indicates that ABC provides accurate estimates of parameter values with relatively little uncertainty, there are many directions for future research. Different choices for the prior, summary statistic, distance function, and rejection distance can all potentially lead to slightly different parameter estimates. Further work is required to determine the specific effects of each of these choices on the accuracy and uncertainty of ABC. Markov chains can also be used to significantly reduce the cost of ABC by limiting the number of parameter values that are rejected, even for relatively small rejection distances [28]. Such approaches have become more popular in recent years but have yet to be applied in the present context. Finally, the true power of ABC lies in its ability to predict unknown parameters in real-world systems, and future work will more deeply explore the use of experimental reference data to drive parameter estimates, particularly taking into account experimental uncertainty in the context of validation efforts for simulations of complex thermal-fluid problems. An important direction for future research is therefore to apply the ABC method to problems where the true parameter values are unknown.

ACKNOWLEDGMENTS

Helpful discussions with Mark Strobel, Aniruddha Upadhye, Colin Towery, Melvyn Branch, Jeff Anderson, and Daven Henze are gratefully acknowledged. J.D.C., N.T.W., C.L., and T.R.S.H. acknowledge gift support from the 3M Company. J.D.C. and G.B.R. were supported, in part, by NSF Award No.CBET 1454496. P.E.H. was supported, in part, by AFOSR Award Nos.FA9550-14-1-0273 and FA9550-17-1-0144. Computing resources were provided by DoD HPCMP under a Frontier project award and by the Air Force Research Laboratory.

[1] W. L. Oberkampf and C. J. Roy, *Verification and Validation in Scientific Computing* (Cambridge University Press, Cambridge, UK, 2010).

[2] W. L. Oberkampf and T. Trucano, Validation methodology in computational fluid dynamics, AIAA paper AIAA-2000-2549 (2000).

[3] W. L. Oberkampf and T. G. Trucano, Verification and validation in computational fluid dynamics, Progr. Aerospace Sci. **38**, 209 (2002).

[4] W. L. Oberkampf, T. G. Trucano, and C. Hirsch, Verification, validation, and predictive capability in computational engineering and physics, Appl. Mech. Rev. **57**, 345 (2004).

[5] D. C. Estumano, F. C. Hamilton, M. J. Colaço, A. J. K. Leiroz, H. R. B. Orlande, R. N. Carvalho, and G. S. Dulikravich, Bayesian estimate of mass fraction of burned fuel in internal combustion engines using pressure measurements, in *Engineering Optimization IV*, edited by H. Rodrigues, J. Herskovits, C. M. Soares, J. M. Guedes, A. Araujo, J. Folgado, F. Moleiro, and J. A. Madeira (Taylor & Francis Group, London, UK, 2015), pp. 997–1003.

[6] S. Mosbach, A. Braumann, P. L. W. Man, C. A. Kastner, G. P. E. Brownbridge, and M. Kraft, Iterative improvement of Bayesian parameter estimates for an engine model by means of experimental design, Combust. Flame **159**, 1303 (2012).

[7] P. G. Constantine, Q. Wang, A. Doostan, and G. Iaccarino, A surrogate accelerated Bayesian inverse analysis of the HyShot II flight data, AIAA paper AIAA-2011-2037 (2011).

[8] I. Vrbik, R. Deardon, Z. Feng, A. Gardner, and J. Braun, Using individual-level models for infectious disease spread to model spatio-temporal combustion dynamics, Bayesian Anal. **7**, 615 (2012).

[9] S. H. Cheung, T. A. Oliver, E. E. Prudencio, S. Prudhomme, and R. D. Moser, Bayesian uncertainty analysis with applications to turbulence modeling, Reliabil. Eng. Syst. Safety **96**, 1137 (2011).

[10] A. H. Elsheikh, I. Hoteit, and M. F. Wheeler, Efficient Bayesian inference of subsurface flow models using nested sampling and sparse polynomial chaos surrogates, Comput. Methods Appl. Mech. Eng. **269**, 515 (2014).

[11] S. Yeşilyurt and A. Patera, Surrogates for numerical simulations: Optimization of eddy-promoter heat exchangers, Comput. Methods Appl. Mech. Eng. **121**, 231 (1995).

[12] L. Zeng, L. Shi, D. Zhang, and L. Wu, A sparse grid based Bayesian method for contaminant source identification, Adv. Water Resour. **37**, 1 (2012).

[13] A. G. Salinger, R. P. Pawlowski, J. N. Shadid, and B. G. van Bloemen Waanders, Computational analysis and optimization of a chemical vapor deposition reactor with large-scale computing, Ind. Eng. Chem. Res. **43**, 4612 (2004).

[14] W. Jahn, G. Rein, and J. L. Torero, Forecasting fire dynamics using inverse computational fluid dynamics and tangent linearisation, Adv. Eng. Softw. **47**, 114 (2012).

[15] H. Madsen, Parameter estimation in distributed hydrological catchment modeling using automatic calibration with multiple objectives, Adv. Water Resour. **26**, 205 (2003).

[16] S. Wang and X. Xu, Parameter estimation of internal thermal mass of building dynamic models using genetic algorithm, Energy Convers. Manage. **47**, 1927 (2006).

[17] E. Pemha and E. Ngo Nyobe, Genetic algorithm approach and experimental confirmation of a laser-based diagnostic technique for the local thermal turbulence in a hot wind tunnel jet, Prog. Electromagn. Res. **28**, 325 (2011).

[18] H. Kato, A. Yoshizawa, G. Ueno, and S. Obayashi, A data assimilation methodology for reconstructing turbulent flows around aircraft, J. Comput. Phys. **283**, 559 (2015).
[19] X. Gao, Y. Wang, N. Overton, M. Zupanski, and X. Tu, Data-assimilated computational fluid dynamics modeling of convection-diffusion-reaction problems, J. Comput. Sci. **21**, 38 (2018).
[20] J. Sousa, C. García-Sánchez, and C. Gorlé, Improving urban flow predictions through data assimilation, Building Environ. **132**, 282 (2018).
[21] J. R. Stroud, M. Katzfuss, and C. K. Wikle, A Bayesian adaptive ensemble Kalman filter for sequential state and parameter estimation, Mon. Weather Rev. **146**, 373 (2018).
[22] H. Xiao, J.-L. Wu, J.-X. Wang, R. Sun, and C. J. Roy, Quantifying and reducing model-form uncertainties in Reynolds-averaged Navier-Stokes simulations: A data-driven, physics-informed Bayesian approach, J. Comput. Phys. **324**, 115 (2016).
[23] W. N. Edeling, M. Schmelzer, R. P. Dwight, and P. Cinnella, Bayesian predictions of Reynolds-averaged Navier–Stokes uncertainties using maximum a posteriori estimates, AIAA J. **56**, 2018 (2018).
[24] A. P. Singh and K. Duraisamy, Using field inversion to quantify functional errors in turbulence closures, Phys. Fluids **28**, 045110 (2016).
[25] M. Khalil and H. N. Najm, Probabilistic inference of reaction rate parameters from summary statistics, Combust. Theory Model. **22**, 635 (2018).
[26] O. A. Doronina, J. D. Christopher, C. A. Z. Towery, P. E. Hamlington, and W. J. A. Dahm, Autonomic closure for turbulent flows using approximate Bayesian computation, AIAA paper AIAA-2018-0594 (2018).
[27] M. Sunnåker, A. G. Busetto, E. Numminen, J. Corander, M. Foll, and C. Dessimoz, Approximate Bayesian computation, PLoS Comput. Biol. **9**, e1002803 (2013).
[28] P. Marjoram, J. Molitor, V. Plagnol, and S. Tavaré, Markov chain Monte Carlo without likelihoods, Proc. Natl. Acad. Sci. USA **100**, 15324 (2003).
[29] J. M. Marin, P. Pudlo, C. P. Robert, and R. J. Ryder, Approximate Bayesian computational methods, Stat. Comput. **22**, 1167 (2012).
[30] F. Hartig, J. M. Calabrese, B. Reineking, T. Wiegand, and A. Huth, Statistical inference for stochastic simulation models—Theory and application, Ecol. Lett. **14**, 816 (2011).
[31] A. B. Abdessalem, N. Dervilis, D. Wagg, and K. Worden, Model selection and parameter estimation in structural dynamics using approximate Bayesian computation, Mech. Syst. Signal Proc. **99**, 306 (2018).
[32] J. D. Christopher, N. T. Wimer, T. R. S. Hayden, C. Lapointe, I. Grooms, G. B. Rieker, and P. E. Hamlington, Parameter estimation for a turbulent buoyant jet using approximate Bayesian computation, AIAA paper AIAA-2017-0531 (2017).
[33] J. D. Christopher, C. Lapointe, N. T. Wimer, T. R. S. Hayden, I. Grooms, G. B. Rieker, and P. E. Hamlington, Parameter estimation for a turbulent buoyant jet with rotating cylinder using approximate Bayesian computation, AIAA paper AIAA-2017-3629 (2017).
[34] D. B. Rubin, Bayesianly justifiable and relevant frequency calculations for the applied statistician, Ann. Stat. **12**, 1151 (1984).
[35] J. K. Pritchard, M. T. Seielstad, A. Perez-Lezaun, and M. W. Feldman, Population growth of human Y chromosomes: A study of Y chromosome microsatellites, Mol. Biol. Evol. **16**, 1791 (1999).
[36] S. Tavaré, D. J. Balding, R. C. Griffiths, and P. Donnelly, Inferring coalescence times from DNA sequence data, Genetics **145**, 505 (1997).
[37] M. A. Beaumont, W. Zhang, and D. J. Balding, Approximate Bayesian computation in population genetics, Genetics **162**, 2025 (2002).
[38] T. Toni, D. Welch, N. Strelkowa, A. Ipsen, and M. P. H. Stumpf, Approximate Bayesian computation scheme for parameter inference and model selection in dynamical systems, J. R. Soc., Interface **6**, 187 (2009).
[39] K. Csilléry, M. G. B. Blum, O. E. Gaggiotti, and O. François, Approximate Bayesian computation (ABC) in practice, Trends Ecol. Evol. **25**, 410 (2010).

[40] M. A. Beaumont, Approximate Bayesian computation in evolution and ecology, Annu. Rev. Ecol. Evol. System. **41**, 379 (2010).
[41] N. J. R. Fagundes, N. Ray, M. A. Beaumont, S. Neuenschwander, F. M. Salzano, S. L. Bonatto, and L. Excoffier, Statistical evaluation of alternative models of human evolution, Proc. Natl. Acad. Sci. USA **104**, 17614 (2007).
[42] J. A. Vrugt and M. Sadegh, Toward diagnostic model calibration and evaluation: Approximate Bayesian computation, Water Resour. Res. **49**, 4335 (2013).
[43] D. J. Nott, L. Marshall, and J. Brown, Generalized likelihood uncertainty estimation (GLUE) and approximate Bayesian computation: What's the connection?, Water Resour. Res. **48**, W12602 (2012).
[44] M. Sadegh and J. A. Vrugt, Bridging the gap between GLUE and formal statistical approaches: Approximate Bayesian computation, Hydrol. Earth Syst. Sci. **17**, 4831 (2013).
[45] B. Olson, Stochastic weather generation with approximate Bayesian computation, Master's thesis, University of Colorado at Boulder, 2016.
[46] B. Olson and W. Kleiber, Approximate Bayesian computation methods for daily spatiotemporal precipitation occurrence simulation, Water Resour. Res. **53**, 3352 (2017).
[47] D. D. Lucas, A. Gowardhan, P. Cameron-Smith, and R. L. Baskett, Impact of meteorological inflow uncertainty on tracer transport and source estimation in urban atmospheres, Atmos. Environ. **143**, 120 (2016).
[48] J. Rohmer, M. Rousseau, A. Lemoine, R. Pedreros, J. Lambert, and A. Benki, Source characterisation by mixing long-running tsunami wave numerical simulations and historical observations within a metamodel-aided ABC setting, Stochastic Environmental Research and Risk Assessment **32**, 967 (2018).
[49] R. C. Smith, *Uncertainty Quantification: Theory, Implementation, and Applications* (SIAM, Philadelphia, PA, 2014).
[50] L. Le Cam and G. L. Yang, *Asymptotics in Statistics: Some Basic Concepts* (Springer Science & Business Media, CITY, 2012).
[51] D. J. C. MacKay, *Information Theory, Inference, and Learning Algorithms* (Cambridge University Press, Cambridge, UK, 2003).
[52] S. C. Crow and F. H. Champagne, Orderly structure in jet turbulence, J. Fluid Mech. **48**, 547 (1971).
[53] J. A. Lovett and S. R. Turns, Experiments on axisymmetrically pulsed turbulent jet flames, AIAA J. **28**, 38 (1990).
[54] R. B. Farrington and S. D. Claunch, Infrared imaging of large-amplitude, low-frequency disturbances on a planar jet, AIAA J. **32**, 317 (1994).
[55] S. Marzouk, H. Mhiri, S. El Golli, G. Le Palec, and P. Bournot, Numerical study of momentum and heat transfer in a pulsed plane laminar jet, Int. J. Heat Mass Transf. **46**, 4319 (2003).
[56] W. Kriaa, H. B. Cheikh, H. Mhiri, G. Le Palec, and P. Bournot, Numerical study of free pulsed jet flow with variable density, Energy Convers. Manage. **49**, 1141 (2008).
[57] C. P. Arnold Jr. and C. H. Dey, Observing-systems simulation experiments: Past, present, and future, Bull. Am. Meteorol. Soc. **67**, 687 (1986).
[58] M. Xue, M. Tong, and K. K. Droegenmeier, An OSSE framework based on the ensemble square root Kalman filter for evaluating the impact of data from radar networks on thunderstorm analysis and forecasting, J. Atmos. Ocean. Technol. **23**, 46 (2006).
[59] J. Kaipio and E. Somersalo, *Statistical and Computational Inverse Problems*, *Applied Mathematical Series*, Vol. 160 (Springer, Berlin, 2004).
[60] J. Kaipio and E. Somersalo, Statistical inverse problems: Discretization, model reduction and inverse crimes, J. Comput. Appl. Math. **198**, 493 (2007).
[61] A. Stoffelen, G. J. Marseille, F. Bouttier, D. Vasiljevic, S. De Haan, and C. Cardinali, ADM-Aeolus Doppler wind Lidar observing system simulation experiment, Q. J. R. Meteorol. Soc. **132**, 1927 (2006).
[62] W. Lahoz, B. Khattatov, and R. Menard, editors, *Data Assimilation: Making Sense of Observations* (Springer, Berlin, 2010).
[63] Y. Wang, P. Chatterjee, and J. L. de Ris, Large eddy simulation of fire plumes, Proc. Combust. Inst. **33**, 2473 (2011).
[64] C. Greenshields, OpenFOAM, OpenFOAM Foundation, March (2016).

[65] H. G. Weller, G. Tabor, H. Jasak, and C. Fureby, A tensorial approach to computational continuum mechanics using object-oriented techniques, Comput. Phys. **12**, 620 (1998).
[66] A. Yoshizawa, Statistical theory for compressible turbulent shear flows, with the application to subgrid modeling, Phys. Fluids **29**, 2152 (1986).
[67] W. Sutherland, LXXV. A dynamical theory of diffusion for non-electrolytes and the molecular mass of albumin, London Edinburgh Dublin Philos. Mag. J. Sci. **9**, 781 (1905).
[68] D. R. Stull and H. Prophet, JANAF thermochemical tables, Technical report, DTIC document (1971).
[69] D. J. Thomson, Spectrum estimation and harmonic analysis, Proc. IEEE **70**, 1055 (1982).
[70] D. B. Percival and A. T. Walden, *Spectral Analysis for Physical Applications* (Cambridge University Press, Cambridge, UK, 1993).
[71] W. Van Drongelen, *Signal Processing for Neuroscientists: An Introduction to the Analysis of Physiological Signals* (Academic Press, London, UK, 2006).
[72] D. W. Scott, On optimal and data-based histograms, Biometrika **66**, 605 (1979).
[73] B. M. Cetegen, Y. Dong, and M. C. Soteriou, Experiments on stability and oscillatory behavior of planar buoyant plumes, Phys. Fluids **10**, 1658 (1998).

Experiments in Fluids (2021) 62:43
https://doi.org/10.1007/s00348-020-03122-2

RESEARCH ARTICLE

Flow parameter estimation using laser absorption spectroscopy and approximate Bayesian computation

Jason D. Christopher[1] · Olga A. Doronina[1] · Dan Petrykowski[1] · Torrey R. S. Hayden[1] · Caelan Lapointe[1] · Nicholas T. Wimer[1] · Ian Grooms[2] · Gregory B. Rieker[1] · Peter E. Hamlington[1]

Received: 3 June 2020 / Revised: 15 November 2020 / Accepted: 13 December 2020
© The Author(s), under exclusive licence to Springer-Verlag GmbH, DE part of Springer Nature 2021

Abstract

Given spatially sparse or lower dimensional experimental measurements, approximate Bayesian computation (ABC) and numerical simulations can be used to estimate unknown characteristics of complex multi-physics engineering systems. Here, we describe the ABC approach and use it to estimate the speed of high-temperature gases exiting an industrially relevant catalytic burner, as well as to estimate the completeness of combustion within the burner. Using vertical profiles of absorption-weighted average temperature from laser absorption spectroscopy (LAS) at three different burner operating conditions, we combine ABC and large eddy simulations (LES) to generate posterior distributions of inflow speeds and heat addition characteristics above the burner. We show that the ABC method correctly estimates trends in the inflow speed for different conditions, and we find that there is a strong likelihood of incomplete combustion for higher equivalence ratios. We evaluate the predictive capability of the approach using an observing system experiment, indicating that the ABC method, when combined with LES, is able to accurately predict LAS measurements. We thus demonstrate that ABC is an effective tool for obtaining additional insights from available experimental measurements, thereby improving understanding of real-world engineering systems.

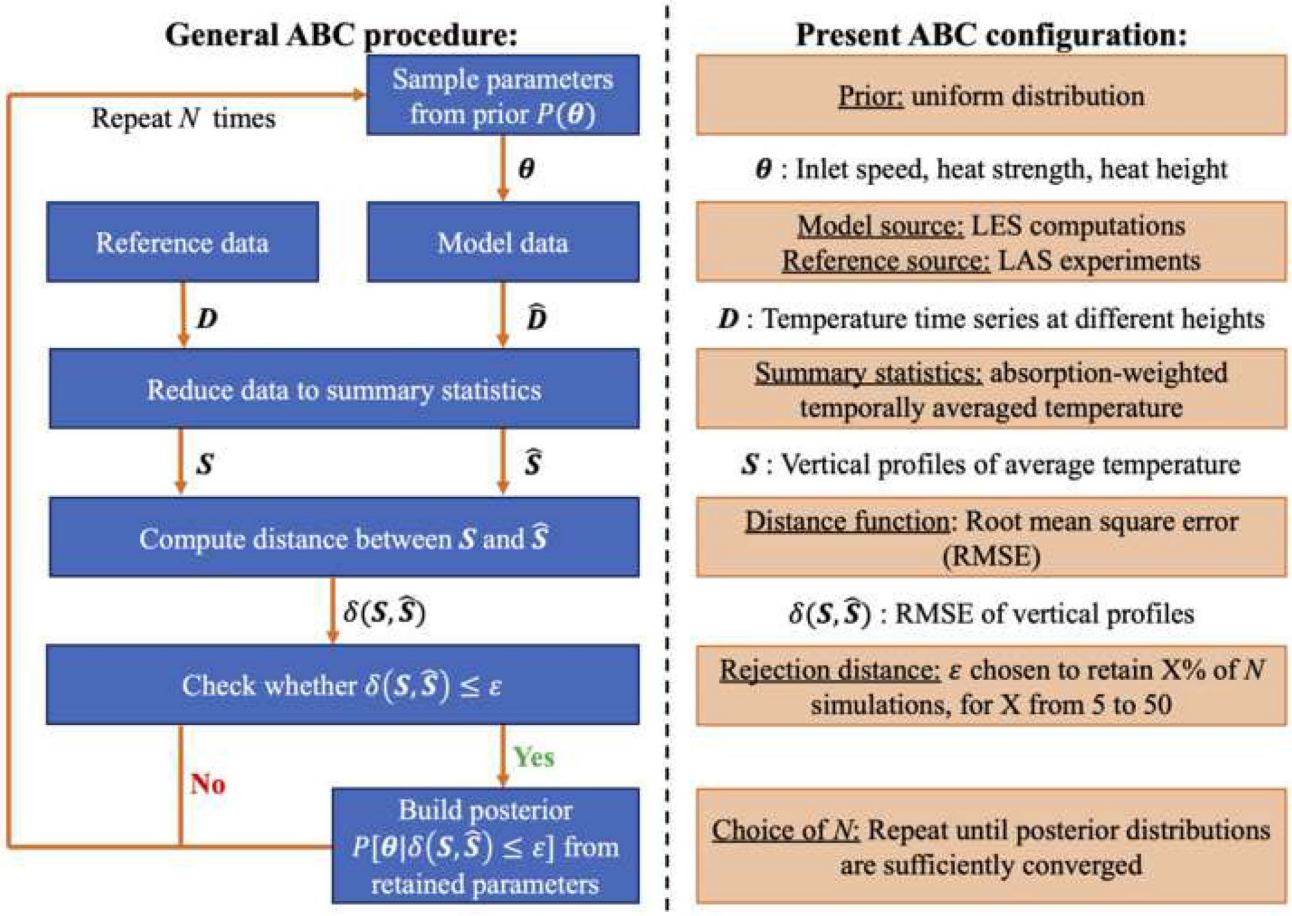
✉ Peter E. Hamlington
peh@colorado.edu

[1] Department of Mechanical Engineering, University of Colorado, Boulder, CO 80309, USA

[2] Department of Applied Mathematics, University of Colorado, Boulder, CO 80309, USA

Published online: 04 February 2021

Graphic abstract



1 Introduction

Despite ongoing advances in the quality and breadth of experimental measurements, the complete characterization of many real-world engineering systems remains a considerable challenge. For example, experimental diagnostics can now provide spatially and temporally resolved measurements of temperature, velocity, chemical composition, and other properties, but few (if any) experiments can provide fully resolved three-dimensional (3D) spatial and temporal fields over the entire system domain simultaneously for all quantities of interest. Although numerical simulations can, in principle, be used to complement experimental measurements and develop a more comprehensive understanding of a system, physically accurate boundary conditions and fluid properties are required to ensure that a truly equivalent configuration is being modeled by the simulations. Once again, however, such information is often difficult to obtain experimentally.

To address this challenge, here we use vertical profiles of absorption-weighted average temperature from laser absorption spectroscopy (LAS) to show how high-frequency—but spatially sparse and line-of-sight averaged—experimental measurements can be used to estimate unknown characteristics (termed 'parameters' herein) of an industrially relevant catalytic burner. Traditionally, the challenge of estimating unknown parameters in real-world engineering systems has been addressed by proposing a priori distributions of parameter values, generating model (e.g., simulation) data using parameters sampled from these distributions, and then calculating likely distributions of true parameters using statistical inversions based on available reference or experimental data (Oberkampf and Roy 2010; Oberkampf and Trucano 2000; Oberkampf and Trucano 2002; Oberkampf et al. 2004). Various optimization methods have been used to perform these inversions (e.g., Madsen 2003; Salinger et al. 2004; Wang and Xu 2006; Pemha and Nyobe 2011; Jahn et al. 2012), but such techniques typically provide single values of unknown

parameters, with limited measures of uncertainty when using imperfect experimental data and computational models.

Bayesian techniques overcome this limitation by providing probability distributions of unknown parameters. For example, several studies have successfully performed parameter estimation for engineering problems using full Bayesian methods (Estumano et al. 2015; Mosbach et al. 2012; Constantine et al. 2011; Vrbik et al. 2012; Sousa et al. 2018). Full Bayesian methods are now also being used in combination with laser diagnostics, for example to infer surface chemistry parameters from LAS measurements (Adowski and Bauman 2018), to estimate characteristics of aqueous films using Fourier transform infrared spectrometry (Pan et al. 2017), to predict the heat of vaporization of iron based on measurements from laser induced incandescence (Sipkens et al. 2018), and to estimate absorbance spectra from LAS-transmitted intensity (Emmert et al. 2019). Bayesian methods have also been extensively used in the development of chemical species tomography for a range of applications (Daun et al. 2016; Grauer et al. 2016; Grauer 2018; Grauer et al. 2017; Grauer et al. 2017; Schmidt et al. 2020; Emmert et al. 2020; van der Kley et al. 2020). Specific methods of Bayesian inference include hierarchical (Grauer et al. 2017) and variational techniques (Fox and Roberts 2012), and Stroud et al. (2018) and sources therein provide additional details on parameter estimation using maximum-likelihood techniques, as well as full Bayesian approaches such as ensemble Kalman filtering.

Despite their advantages, however, full Bayesian approaches require knowledge of the likelihood function; namely, the probability of obtaining the reference data given a particular choice of parameter values. Calculating the likelihood function often requires extensive observations or simplifying assumptions that have varying degrees of accuracy, depending on the source of the reference data and the complexity of the model. In many cases, the likelihood function is assumed to be Gaussian, which may be inaccurate for certain problems.

To address the artificial certainty implied by optimization and to avoid the complexity associated with full Bayesian methods, here we demonstrate the use of approximate Bayesian computation (ABC), which is a robust likelihood-free Bayesian method, for estimating unknown parameters in real-world turbulent thermal-fluid systems. By contrast to prior studies (Mosbach et al. 2012; Constantine et al. 2011; Dwight and Han 2009) where simplified surrogate models have been used for parameter estimation in turbulent flows, we instead use large eddy simulations (LES) during the ABC procedure. To date, ABC has been applied primarily to biological problems (Beaumont et al. 2002; Toni et al. 2009; Csilléry et al. 2010; Beaumont 2010; Fagundes et al. 2007) and is becoming more widely used in other fields, such as geophysical sciences (Vrugt and Sadegh 2013; Nott et al. 2012; Sadegh and Vrugt 2013; Olson et al. 2016; Lucas et al. 2016) and structural mechanics (Abdessalem et al. 2018; Vakilzadeh et al. 2018). This method has recently been explored for thermal-fluid applications by Christopher et al. (2017, 2017, 2018), who performed parameter estimation for a buoyant jet using reference data from direct numerical simulations, and by Khalil and Najm (2018), who used ABC to estimate reaction rate parameters in chemical kinetic mechanisms. Using ABC, it is also possible to improve the accuracy of subgrid scale (SGS) turbulence closure models used in LES (e.g., Doronina et al. 2018, 2019; see also Duraisamy et al. 2019 and Pandey et al. 2020 for reviews of other model improvement approaches), although we focus here on estimating flow parameters in a real-world system, rather than on determining new SGS model parameters.

In this study, we combine line-of-sight, absorption-weighted average temperatures from LAS with ABC and LES to estimate the speed of the high-temperature turbulent flow produced by a catalytic burner, as well as the prevalence of reactive products of incomplete combustion in the exit gases. Although the LAS technique used here (Hayden et al. 2019a, b, 2020) provides accurate, time-resolved temperature measurements above the burner surface, limited information is available regarding the speed of gases exiting the burner. In particular, the tight catalytic burner mesh eliminates the possibility of particle image velocimetry, and the high temperatures challenge hot-wire techniques. We will also show that the available LAS measurements suggest that there is incomplete combustion within the catalytic burner, but specific details of the exit gas chemical composition are not available, because the approach does not probe all of the exit gas species. We will thus use ABC to estimate both the flow speed and the prevalence of additional heat release above the burner due to continued combustion, which is represented in the LES by a half-Gaussian profile of additional heat release extending away from the burner surface. While the focus here is primarily on using ABC to more completely characterize a real-world engineering system, the resulting parameter estimates also increase the correspondence of the LES to the real-world system, improving confidence in the insights and understanding obtained from the simulations.

In the following, we first describe the LAS experiments and the resulting vertical temperature profiles that are used as reference data for the ABC parameter estimation method. We describe the ABC method in Sect. 3, including the configuration used for the present tests and the details of the 3D LES calculations. Parameter estimation results are presented in Sect. 4, including a description of an observing system experiment demonstrating the validity of estimated parameters. Conclusions are outlined at the end.

2 Catalytic burner experiments

The catalytic burner examined here has been studied previously (Hayden et al. 2019a, 2020) and is a scaled-down version of catalytic burners commonly used for industrial heating of food products and polymer films. The catalytic burner is 0.25 m long by 0.075 m wide and combusts a mixture of methane and desiccated air. An iron–chromium alloy catalyst mesh is welded to an open-box metal frame. The catalyst is used to achieve more complete combustion at lower temperatures, thereby reducing the presence of reactive products of incomplete combustion and pollutants (Cottilard 2011) in the burner exit gases. To premix the oxidizer and fuel, the reactants pass through a bed of glass spheres within a cylindrical flame arrestor mounted beneath the combustor. A schematic of the burner experiment is shown in Fig. 1a, and a photograph of the burner in operation, with accompanying laser optics, is shown in Fig. 1b.

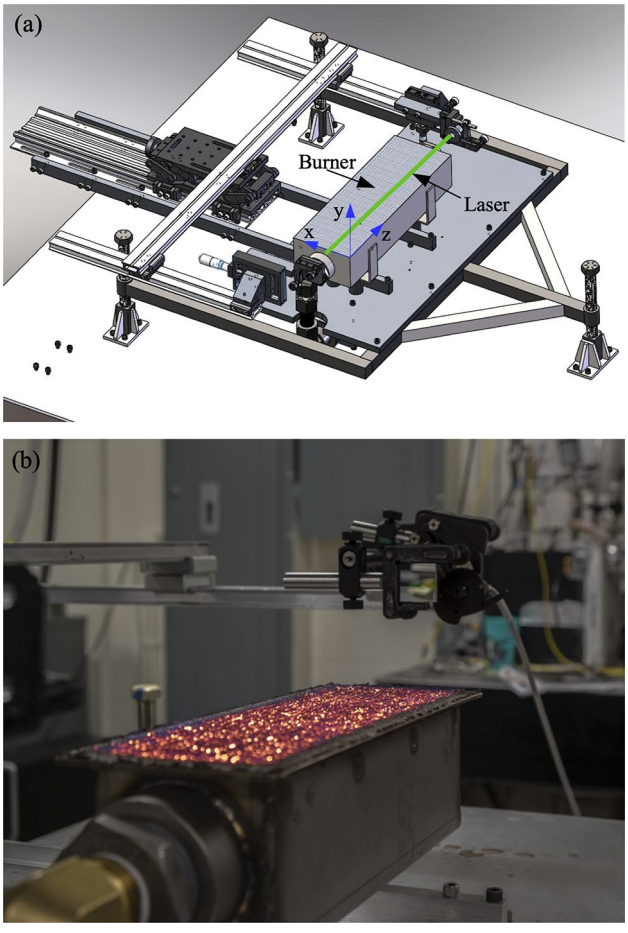


Fig. 1 Schematic of the experimental setup for laser absorption spectroscopy above the catalytic burner (**a**), and an image of the burner in operation, including laser optics (**b**)

Experimental measurements were made using wavelength modulation spectroscopy (WMS), which provides line-of-sight, absorption-weighted average temperature and chemical species concentrations. As shown in Fig. 1, the WMS measurements were made along the longest dimension of the burner (termed the 'length' herein and denoted by the z-axis) at the midpoint of the burner width (i.e., the center of the x-dimension of the burner). Vertical profiles (i.e., as a function of height above the burner along the y-axis) of line-of-sight, absorption-weighted average temperature were measured for three different burner operating powers; these profiles provide reference data for the ABC parameter estimation method described in Sect. 3.

2.1 Laser absorption spectroscopy (LAS)

Tunable diode laser absorption spectroscopy (TDLAS) was used to perform in situ temperature measurements in the flow above the catalytic burner. This method provides a non-intrusive, quantitative, absolute, time-resolved, robust, and portable sensor (Goldenstein et al. 2017) to measure temperature at different locations in the flow. Other laser-based techniques such as Raman or Rayleigh scattering and laser induced fluorescence can also provide quantitative spatial and temporal information (Daily 1997; Mcenally et al. 2000; Schulz and Sick 2005; Frank and Kaiser 2008; Ma et al. 2016; McManus and Sutton 2020). However, such measurements often require large optical setups that are not ideal for industrial applications. The use of TDLAS herein is thus motivated by the practical feasibility of this approach for characterization and control of real-world industrial systems.

In this study, we use WMS, a specialized form of TDLAS, to obtain *in situ* temperature measurements. This method has been used previously to measure temperature and species mole fractions in a variety of combustion environments, from shock tubes to atmospheric flames (Philippe and Hanson 1993; Ebert et al. 2000; Rieker et al. 2009; Cai et al. 2009; Wagner et al. 2009; Huang et al. 2013; Spearrin et al. 2014; Qu et al. 2015; Bolshov et al. 2015; Hayden and Rieker 2016; Goldenstein and Mathews 2020). Compared to traditional TDLAS, where the wavelength of a diode laser is tuned across one or two quantum transitions of the target species, WMS uses additional high-frequency signals and signal isolation to reduce noise for real-world systems.

Although the specific shape of an absorption transition is also dependent on the other non-absorbing gases present in the system (e.g., CO_2, CO, etc., in combustion systems), the integrated absorbance is independent of the collision partner, and is therefore a more useful quantity to measure if all of the species concentrations are not measured. The integrated absorbance is extracted from the measured $2f/1f$ ratio using an approach similar to that described by Hayden and Rieker (2016), Sun et al. (2013), and Goldenstein et al.

(2014). Here, 1*f* and 2*f* denote the first and second harmonics, respectively, and their ratio is sensitive to absorption but insensitive to intensity fluctuations. This ratio makes the sensor robust in harsh environments and enables calibration-free absolute measurements (Rieker et al. 2009). Using the measured WMS 2*f*/1*f* signal as a baseline, the simulated 2*f*/1*f* signal is adjusted until the two signals are in close agreement. In particular, the Voigt line-shape profile parameters (i.e., line-center, integrated area, Doppler width, and Lorentz width) are adjusted in a nonlinear fitting code until the profiles match. The spectral database HITRAN 2012 and the validated line parameters from Goldenstein and Hanson (2015) are used to create initial estimates for the Voigt parameters.

Temperature is calculated using the integrated absorbances from the fitted Voigt profiles for two different measured H_2O transitions. This technique, called two-line thermometry (Hanson and Falcone 1978), calculates temperature using the ratio of integrated absorbances from WMS fits to the two H_2O transitions. Based on a ratio of the signal absorbed at the two different wavelengths (and hence for two different quantum transitions), a temperature can be calculated (Hayden et al. 2020). The resulting temperature is, effectively, an absorption-weighted average temperature over the laser pathlength (or 'line of sight').

2.2 Experimental setup

The present WMS measurements use two NEL Inc. distributed feedback diode lasers centered on H_2O absorption transitions at 1391.7 and 1468.9 nm. These absorption transitions have two primary advantages that make them ideal for temperature measurements in this system. First, they have a large difference in the lower state energy (1045 cm^{-1} and 3319 cm^{-1}, respectively); this optimizes the temperature sensitivity at elevated temperatures. Second, Goldenstein and Hanson (2015) have previously validated these line strength parameters, thus providing ideal conditions for fitting the Voigt profiles.

The lasers are combined and simultaneously passed across the long dimension of the burner (i.e., the lasers initially travel above the burner for 0.25 m parallel to the *z*-axis). To increase the signal-to-noise ratio, the combined laser is reflected twice, causing the laser to pass over the burner three times, creating an effective path length of 0.75 m. The sensor was previously validated in a controlled system for known conditions (Hayden et al. 2020); temperature measurements were found to be accurate within 3% up to approximately 1300 K. Above this temperature, uncertainties were extrapolated using the nonlinear relationship between absorption and temperature. Uncertainty in the measurement of the vertical position above the burner was due to the beam width of 0.9 mm. A fume hood was located several feet above the burner to evacuate exhaust gases, producing a negligible impact on the high-temperature flow close to the burner surface. Calibration data, along with additional setup information and data processing techniques, can be found in Hayden et al. (2020).

To obtain vertical profiles of temperature, a 'y'-shaped optical stage was mounted on a scissor jack, enabling vertical translation of the laser beam along the *y*-axis (see Fig. 1). Measurements were taken at heights of 0.5 mm to 10.5 mm above the burner in 2 mm increments, then 10.5 mm to 150.5 mm above the burner in 10 mm increments. All measurements were performed along the length (i.e., *z*-axis) of the burner centered across the burner width (i.e., 37.5 mm from the edge in the *x*-direction; see Fig. 1). This resulted in temperature measurements at 20 vertical positions. The tighter measurement spacing close to the burner provides additional information in the region most likely to contain sustained combustion after the gases pass through the catalytic mesh. Data are averaged for 10 mins at each height to remove any slow transients in burner conditions or room air fluctuations.

2.3 Burner operating conditions

Mass-flow controllers were used to separately regulate the flow rates of air and methane, allowing independent control of the burner power flux and equivalence ratio, ϕ. The catalytic burner was operated at two power fluxes and three values of ϕ, as summarized in Table 1.

For the first case (denoted 'Case 1' herein), the power flux was 16 W/cm^2 with $\phi = 0.80$. These conditions were thought to result in complete combustion within the catalyst, such that all reactions were finished before hot products exited the burner. This was verified by probing various powers and values of ϕ and determining a condition where OH, a radical that commonly appears during methane–air combustion, was not detected by an additional WMS sensor (Hayden et al. 2020). It will also be seen that temperature consistently decreased away from the burner surface for this case, indicating no significant heat addition.

The line-of-sight, absorption-weighted time-averaged gas temperature immediately above the burner was $T_0 = 1494$ K,

Table 1 Catalytic burner operating conditions studied here, showing the burner power flux, equivalence ratio ϕ, line-of-sight absorption-weighted time-averaged gas temperature immediately above the burner surface T_0, and estimated bulk flow speed V_0 of burner exit gases

Case	Power (W/cm^2)	ϕ	T_0 (K)	V_0 (m/s)
1	16	0.80	1494	0.37
2	27	0.85	1602	0.65
3	27	1.00	1667	0.62

measured 0.5 mm above the surface assuming a laser beam width of 0.9 mm. Based on bulk mass-flow measurements, the measured atmospheric pressure, and the assumed density and composition (i.e., complete combustion was assumed) of gases exiting the burner, the inlet speed was estimated as $V_0 = 0.37$ m/s for this case. Although V_0 is not measured directly in the experiments, this estimate allows us to determine whether the correct trends in V_0 are captured by ABC and whether the predicted values are reasonable.

For 'Case 2', the inlet power was substantially increased as compared to Case 1, but with a similar equivalence ratio; this case had a power flux of 27 W/cm^2 and $\phi = 0.85$. The resulting gas temperature immediately above the burner was $T_0 = 1602$ K and the inlet speed was estimated as $V_0 = 0.65$ m/s. Given the higher power and ϕ of this case, it was thought possible that continued combustion could occur above the burner, although it will be seen in the following that the ABC parameter estimation method predicts that this is unlikely based on the LAS temperature measurements.

Finally, the burner was operated for conditions that suggested the presence of continued heat release above the burner. This case, referred to as 'Case 3', had an inlet power flux of 27 W/cm^2 and $\phi = 1.00$. This power flux was the same as for Case 2, but ϕ was significantly higher than either Cases 1 or 2. Compared to Case 2, this results in a higher temperature immediately above the burner, $T_0 = 1667$ K, and a lower estimated inlet speed, $V_0 = 0.62$ m/s. The additional fuel entering the combustor in Case 3 causes additional chemiluminescence above the burner, indicative of continued combustion, as well as detectable concentrations of OH; it will be seen in Sect. 4 that the ABC method predicts additional heat release above the burner for this case.

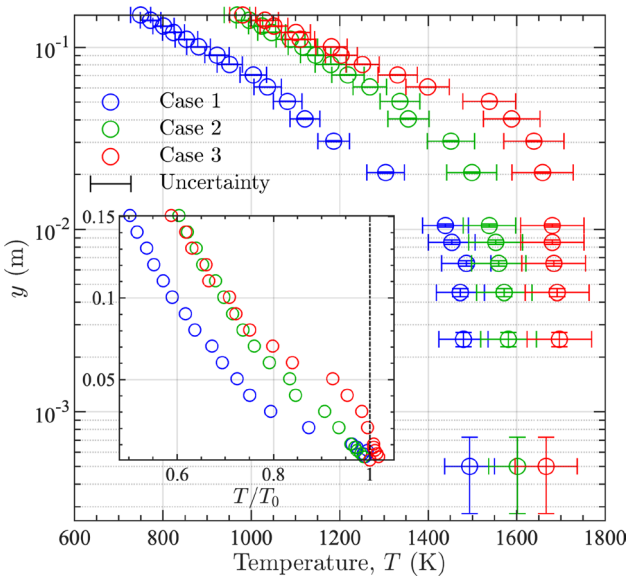


Fig. 2 Vertical profiles of absorption-weighted time-averaged temperature above the catalytic burner. Results are shown for the three experimental cases in Table 1. Experimental uncertainties are based on instrument validation (Hayden et al. 2020) and the beam width of 0.9 mm. The inset shows temperature profiles normalized by T_0 from Table 1

2.4 Vertical temperature profiles

Vertical profiles of line-of-sight, absorption-weighted time-averaged temperature for the three experimental burner operating conditions are shown in Fig. 2. The time averaging spans the entire 10 min time-series obtained using LAS at each measurement height.

The temperature profiles in the main panel of Fig. 2 indicate that, from Cases 1 to 3, the temperature near the burner surface increases from roughly 1500 K to nearly 1700 K. Moreover, the temperature remains high a greater distance above the burner for Case 3, and subsequently decreases rapidly to match the temperatures seen for Case 2 farther from the burner. It should be noted that we decreased the air flow rate to achieve a larger ϕ in Case 3, and thus the estimated inlet speed of Case 2 was actually slightly higher than for Case 3, as indicated in Table 1.

Differences in the profile shapes are more clearly indicated by the profiles of T/T_0 in the inset of Fig. 2, where gas temperatures immediately above the burner surface, T_0, are given in Table 1. To further emphasize the rapid decrease in temperature far from the burner in Case 3, the inset shows that there is an increase in temperature immediately above the burner for this case. This is indicative of additional heat release due to continued combustion, which is assumed to arise from reactive products of incomplete combustion exiting the burner at these conditions.

The temperature profiles in Fig. 2 thus provide valuable information concerning the characteristics of the flow field above the burner for different operating conditions, but these results also lead to new questions about the magnitude and extent of additional heat release for Case 3. Moreover, it is not possible based on the results in Fig. 2 to rule out additional, although more moderate, heat release even for Cases 1 and 2.

In the following, we use ABC and LES to determine inflow speeds and the likelihood of additional heat release. We will show, in particular, that only Case 3 is likely to have additional heat release above the burner. Using LES, we then show that the resulting parameter estimates enable accurate predictions of the vertical temperature profile for each case, including the rapid decrease in temperature far from the burner for Case 3.

3 Parameter estimation method

Based on the LAS measurements, we seek estimates for three characteristics of the catalytic burner system: the speed of gases exiting the burner, the intensity of heat addition above the burner due to continued combustion of reactive chemical species in the exit gases, and the spatial region over which heat addition occurs. The first of these properties is known only approximately based on the measured mass-flow rates and the assumed density of gases exiting the burner, while the other two quantities are implied by the results, as shown in Fig. 2, particularly for Case 3. The additional heat release due to incomplete combustion is modeled in the simulations using a half-Gaussian profile, with the maximum value and vertical extent (or standard deviation) of the profile treated as unknown parameters. Each of these properties are required to obtain a more complete understanding of the catalytic burner, as well as to accurately model the burner using numerical simulations.

In this section, we first describe ABC and then outline the configuration of ABC used herein, including details of the LES and the method by which LAS-equivalent measurements are obtained from the simulations.

3.1 Approximate Bayesian computation (ABC)

The ABC method (Sunnåker et al. 2013; Marjoram et al. 2003; Marin et al. 2012) provides a computationally efficient approach for estimating the 'posterior' probability distribution, $P(\theta|\mathcal{D})$, of unknown system parameters, θ, given reference data, $\mathcal{D}$. The posterior can be obtained exactly using Bayes' theorem, expressed as

$$P(\theta|\mathcal{D}) = P(\mathcal{D}|\theta)P(\theta)/P(\mathcal{D}), \tag{1}$$

where $P(\mathcal{D}|\theta)$ is the 'likelihood' of obtaining the reference data given a particular value of θ, $P(\theta)$ is the 'prior' distribution of parameter values independent of the reference data, and $P(\mathcal{D})$ gives the probability of obtaining the reference data. The prior can be a uniform or Gaussian distribution, for example, and the specific form is based on *a priori* knowledge of anticipated parameter values.

Despite providing an exact expression for the posterior, there are two primary challenges when applying Bayes' theorem to complex real-world thermal-fluid systems: (a) the reference data, $\mathcal{D}$, typically has a very large number of dimensions (e.g., many spatial locations and many measurement times), substantially increasing the computational cost of calculating the posterior, and (b) the likelihood function is typically difficult to obtain exactly for more-complicated models, such as those used in LES, due either to its mathematical intractability or to its computational cost. Both of these challenges provide the fundamental motivation for ABC. In particular, ABC replaces the reference data $\mathcal{D}$ with summary statistics, $\mathcal{S} \equiv \mathcal{S}(\mathcal{D})$, and estimates the posterior by comparing model values of the summary statistic, denoted $\hat{\mathcal{S}} \equiv \mathcal{S}(\hat{\mathcal{D}})$, with the reference statistic $\mathcal{S}$, where $\hat{\mathcal{D}}$ is the model data. The avoidance of an explicitly defined likelihood function makes ABC a 'likelihood-free' Bayesian inference method.

To obtain an estimate of the posterior using ABC given reference data $\mathcal{D}$ and summary statistics $\mathcal{S}$, we first sample values of θ from an anticipated parameter space [i.e., from the prior, $P(\theta)$]. We then use each value of θ to generate model data as $\hat{\mathcal{D}} = \mathcal{F}(\theta)$, where $\mathcal{F}$ denotes the model (e.g., a reduced-order surrogate model, or LES as in the current study). Using $\hat{\mathcal{D}}$, we calculate the summary statistic $\hat{\mathcal{S}}$ for each sampled θ and either 'accept' or 'reject' each parameter using the distance function, $\delta(\mathcal{S}, \hat{\mathcal{S}})$, and 'threshold,' ε. In particular, if the computed δ for a given θ is less than ε, then the parameter is considered viable and is retained in the candidate pool. However, if δ exceeds the threshold, then the parameter is discarded, since it did not produce a realistic model outcome compared to the available observation; for this reason, ε is also often known as the 'rejection distance'. From the accepted parameter values, we then construct the distribution (i.e., the approximate posterior) of parameters that are likely to result in the reference statistics. The resulting approximate posterior, denoted $P[\theta|\delta(\mathcal{S}, \hat{\mathcal{S}}) \leq \varepsilon]$, is assumed to converge to the true posterior $P(\theta|\mathcal{D})$ as $\varepsilon \to 0$, provided that $\mathcal{S}$ is representative of the full data $\mathcal{D}$. This rejection ABC algorithm, known as method D in Marjoram et al. (2003), is summarized in Fig. 3, which also includes details on the specific configuration of ABC used here, as described in the next section.

It should be noted that the specific choices of summary statistic, distance function, and rejection threshold are all important aspects of any successful implementation of ABC. The summary statistic must accurately represent the data, even though such statistics are unlikely to represent all information inherent in the full data for complex flows (Sunnåker et al. 2013). The statistic must also contain information that is correlated with unknown parameters. Specifically, different values of unknown parameters should result in different values of the chosen statistic; this is known as parameter identifiability (Smith 2013). The distance function could, for instance, consist of an L1 or L2 norm, or a root-mean-square error (RMSE), comparing time-averaged reference observations at several locations with corresponding model results. Finally, the rejection threshold, ε, is often based on an initial calibration step or a desired ratio of accepted parameters, although here we will follow previous studies (Sunnåker et al. 2013; Marjoram et al. 2003; Marin et al. 2012; Lintusaari et al. 2017; Rohmer et al. 2020; Christopher et al.

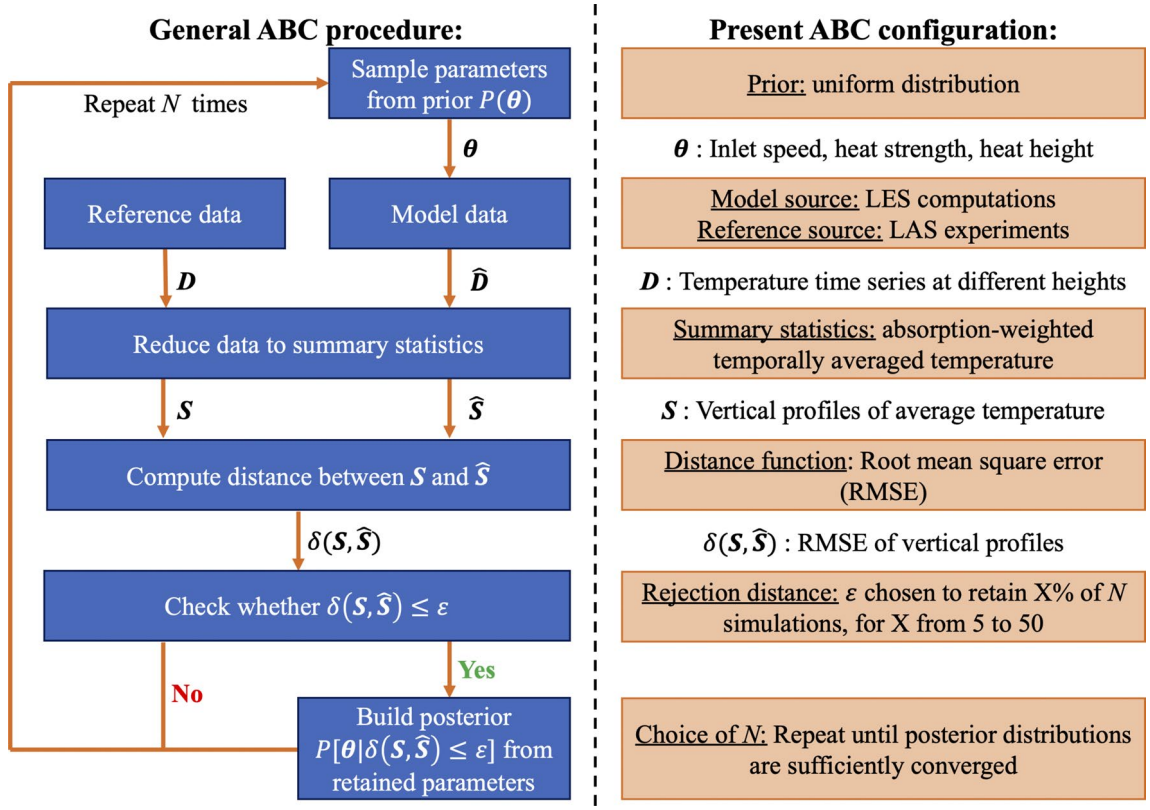


Fig. 3 General ABC procedure from Sect. 3.1 (left) and the present configuration of ABC described in Sect. 3.2 (right)

2018) and provide results for various choices of ε to examine the convergence of the estimated posterior as ε decreases.

3.2 Present configuration of ABC

Here, we use ABC to determine the inlet flow speed and heat addition characteristics near the surface of the catalytic burner. The LAS measurements described in Sect. 2.4 provide line-of-sight absorption-weighted temperature time-series data $\mathcal{D}$, which give the time-averaged vertical profiles of temperature shown in Fig. 2; these profiles are the reference summary statistic $\mathcal{S}$ in the present demonstration of ABC. The model data, $\hat{\mathcal{D}}$, are obtained from 3D LES of the experimental configurations, allowing the calculation of equivalent vertical profiles of time-averaged absorption-weighted temperature, denoted $\hat{\mathcal{S}}$, at the same locations as in the experiments. Details of the numerical model are provided in Sect. 3.3 and the procedure by which LAS-equivalent statistics are calculated from the model data is described in Sect. 3.4. The particular configuration of ABC used here is summarized in Fig. 3.

The present choice of summary statistic is based on prior knowledge of the connection between burner inlet speeds and vertical profiles of temperature in turbulent buoyant jets. In particular, Christopher et al. (2018) used reference data from numerical simulations to show that single-location temperature measurements at heights within approximately 0.5–1.5 burner widths can be used to infer inlet speeds. Here, we further improve our ability to predict the speed using average temperatures at multiple locations simultaneously.

It should be noted that temporally resolved data from the LAS and LES could also have been used during the ABC process. However, we chose not to use this information for several reasons. First, we seek to estimate steady boundary conditions and heat release properties in the LES, for which time-averaged statistics are sufficient to drive the ABC method. Second, as with unresolved small-scale spatial fluctuations, fast temporal fluctuations are influenced by the SGS model in the LES, and it is only longer period resolved motions that can be compared with the LAS measurements. We would thus be restricted to relatively small frequencies in the spectral comparison. Finally, we seek to use a minimal amount of data to estimate simulation parameters, and we will show that line-of-sight average temperature measurements are sufficient for ABC.

For the distance function, $\delta(\mathcal{S},\hat{\mathcal{S}})$, we use the RMSE over all measurement locations. Other metrics are also possible, such as the L1 and L2 norms, or the integrated difference in temperature at all locations. However, we found that the posterior distributions were similar for each of these metrics,

and so here we only show results using RMSE, which is a robust and common metric for computing statistical distances (Chai and Draxler 2014). Each measurement in the RMSE is given equal weighting despite the fact that the measurements near the burner surface are close together; the additional weight given to the near-surface region was intentional, since matching the lower portion of the profile is key to determining whether continued combustion is present above the burner.

The choice of rejection threshold ϵ can have a substantial impact on the approximate posterior distribution. Values of ϵ that are too large will result in the acceptance of too many sampled parameters, giving a biased posterior that is similar to the prior distribution; that is, no additional information is gained from the ABC method (Christopher et al. 2018). Conversely, an ϵ that is too small will result in the rejection of all but a single case, giving a posterior with very low statistical confidence. Although Marin et al. (2012) and Lintusaari et al. (2017) argue that a smaller ϵ is generally preferable, the specific value is often largely determined by the available computational resources. Based on the high computational cost of 3D LES, a relatively limited number [i.e., $\mathcal{O}(10^3)$] of simulations could be performed in the present study. Here, we follow the most common approach used in previous studies (e.g., Sunnåker et al. 2013; Marjoram et al. 2003; Marin et al. 2012; Lintusaari et al. 2017; Rohmer et al. 2018; Christopher et al. 2018) and calculate approximate posteriors corresponding to various values of ϵ to show convergence of the posterior as ϵ decreases. The value of ϵ is characterized by the percentage of sampled parameters retained in the posterior, where smaller values of ϵ give lower acceptance rates.

We do note, however, that a non-zero acceptance threshold, ϵ, and insufficient summary statistics can introduce a bias to the final posterior distribution. The bias related to ϵ is caused by the fact that all parameters with $\delta(\mathcal{S}, \hat{\mathcal{S}}) \leq \epsilon$ are accepted and treated equally, regardless of the actual value of $\delta(\mathcal{S}, \hat{\mathcal{S}})$. Beaumont et al. (2002) suggested improvements to the ABC algorithm to eliminate this bias, including weighting based on $\delta(\mathcal{S}, \hat{\mathcal{S}})$ and adjustment of distance calculations using local-linear regression. Both of these techniques can be applied during post-processing of the ABC results, although for simplicity of the present demonstration, they are left as potential directions for future research. It will be seen that the present approach yields MAP values of unknown parameters that provide reasonable agreement between the LES and LAS measurements.

Uniform distributions were used for the prior, $P(\boldsymbol{\theta})$, where $\boldsymbol{\theta}$ is the vector of unknown parameters corresponding to the burner inlet speed, the intensity (or 'strength') of heat addition, and the extent (or 'height') of heat addition above the burner. The prior must be sufficiently wide to encompass realistic values of $\boldsymbol{\theta}$, but narrow enough to keep the ABC procedure computationally affordable. Grauer (2018) and Grauer et al. (2017) have provided a detailed discussion of the use of Gaussian prior distributions for turbulent quantities, although here the choice of prior distributions is made somewhat simpler, because the unknown parameters consist of non-stochastic boundary and simulation properties. For this purpose, uniform priors that are sufficiently broad to contain the true values are adequate. Based on the experimental estimates of V_0 in Table 1, the range of inlet speeds in the prior was 0.13 m/s to 0.8 m/s for Case 1 and 0.13 m/s to 1.13 m/s for Cases 2 and 3.

Heat addition due to ongoing reactions was modeled in the LES using a half-Gaussian source term that peaks at the burner surface; this source term was parameterized by the total amount of heat added in Watts (W), and by the standard deviation (or height) of the half-Gaussian distribution. The lower limit for heat addition was 0 W, indicating no additional combustion, and the upper limit was determined from an energy balance based on how much power goes into the system from the reactants and how much energy it would take to heat the gases to the measured inlet temperature, giving a maximum value of 2500 W across all cases. The height of heat addition is equivalent to three standard deviations of the half-Gaussian distribution, and corresponds to the height at which the majority of the heat has been added. A lower limit of 0.01 m was chosen to confine the heat addition very close to the burner and, based on previous experimental measurements showing increasing temperature above the catalytic burner, the upper limit was chosen as 0.07 m.

It should be noted that the method by which heat addition is represented in the simulations is both a necessity, since the composition of gases exiting the burner is unknown, but also a likely source of error in the computational model. In particular, it would be ideal to represent the exit gases as composed of, for example, a methane and air mixture that could then undergo additional combustion, but this introduces additional uncertainties in the relative concentrations of different species. As such, the Gaussian representation for heat addition used here is intended simply to indicate whether or not there is additional heat release above the burner; the specific details and causes for this additional heat release require further investigation in the future.

We used a fixed burner surface temperature close to T_0 from Table 1 for all simulations of a given case. This decision was made to reduce the computational cost, since each unknown parameter adds approximately an order of magnitude more simulations to the method; the number of simulations, N, needed to identify n parameters goes as $N \sim 10^n$. More importantly, the temperature measurements at the lowest height are likely to accurately represent the exit temperature of the burner, since the laser skims the burner surface at the lowest measurement height (i.e., at 0.5 mm).

Considerations of computational cost also limited the number of unknown parameters targeted for estimation in this demonstration. In addition to the three parameters considered here, it is also possible, for example, to simultaneously estimate other parameters that are used to post-process the measurements (e.g., spectroscopic quantities) as well as to perform the simulations (e.g., coefficients in the SGS model). However, as noted above, each additional parameter increases the computational cost of ABC by roughly an order of magnitude. Although the cost can be reduced and efficiency increased through the use of Markov Chain Monte Carlo techniques (Doronina et al. 2019), we have chosen for the present demonstration to use the rejection ABC algorithm described in Sect. 3.1, for which the total number of unknown parameters must remain relatively small when using a more complex model such as LES.

During the ABC procedure, parameter values $\boldsymbol{\theta}$ were deterministically chosen to uniformly sample the entire prior $P(\boldsymbol{\theta})$, thereby reducing bias and effectively covering the entire parameter space. This approach was chosen over other viable options (e.g., random draws, Latin hypercube sampling, etc.) due to the cost of the 3D LES for each choice of $\boldsymbol{\theta}$. In total, $N \sim 10^2$–10^3 parameter values $\boldsymbol{\theta}$ were modeled using LES for each of the three experimental configurations.

3.3 Large eddy simulations (LES)

To accurately represent the flow physics above the catalytic burner while maintaining sufficient computational affordability, so that up to $\mathcal{O}(10^3)$ distinct choices of $\boldsymbol{\theta}$ could be sampled, 3D LES was used for the computational model $\mathcal{F}(\boldsymbol{\theta})$, as summarized in Fig. 3. The fireFOAM solver (Wang et al. 2011) in OpenFOAM version 4 (Greenshields 2016; Weller et al. 1998) was used to perform the LES.

The computational configuration consisted of a non-reacting heated, buoyant jet with a rectangular exit matching the size of the catalytic burner described in Sect. 2. The low-pass filtered compressible Navier–Stokes equations were solved with second-order accuracy in space and time, in conjunction with mass, enthalpy, and species conservation equations. The LES equations were closed using a dynamic one-equation eddy SGS model. Coupling between the pressure and velocity was accomplished using the PIMPLE algorithm, which combines the Pressure-Implicit with Splitting of Operators (PISO) and Semi-Implicit Method for Pressure Linked Equations (SIMPLE) algorithms. Heat transfer mechanisms represented in the LES include conduction, transport of temperature by advection of chemical species, and radiative losses approximated using the discrete ordinate method (DOM). For the DOM, we used a gray mean absorption model based on species mass fractions, with mixture-averaged absorption and emission coefficients. The radiation solution occurred every ten flow iterations with a small number of solid angles to maintain computational efficiency.

The LES equations were solved on a 3D grid with approximately 2.4×10^6 hexahedral control volumes stretched vertically to enhance the resolution near the burner, resulting in a

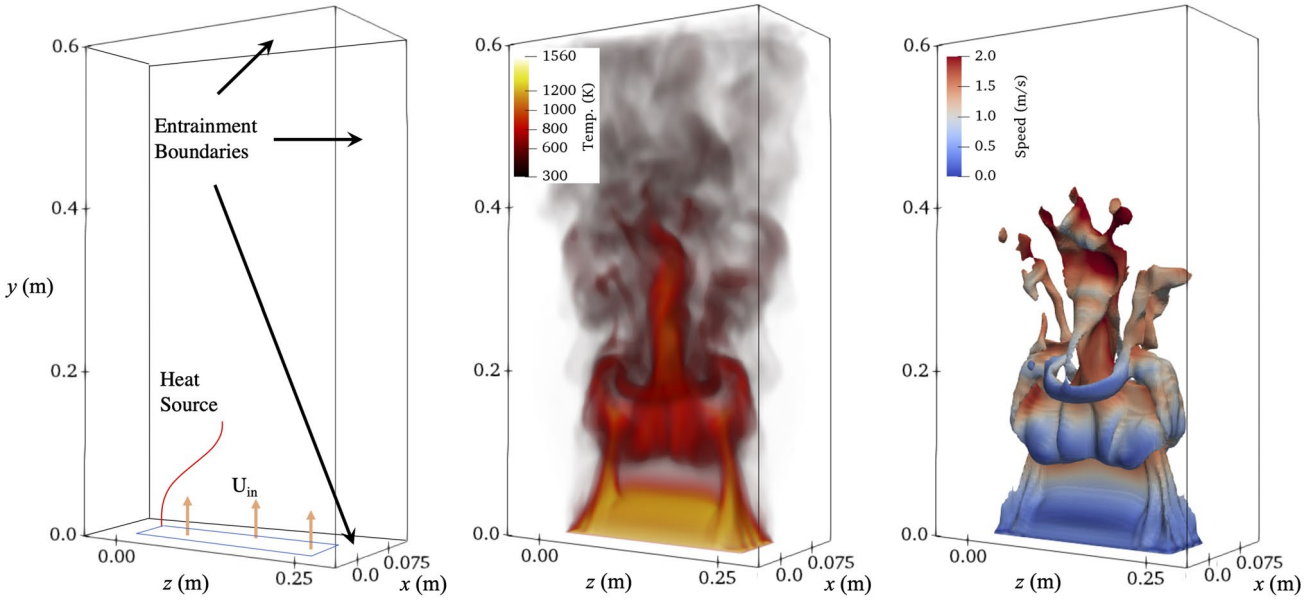


Fig. 4 Schematic showing the setup of the 3D LES domain (left), temperature field (i.e., volume rendering of a 500 K isosurface and additional volume rendering at higher locations) of a single snapshot in time from a simulation with inlet mean temperature of 1515 K and inlet speed of 0.38 m/s with no additional heat added above the burner surface (middle), and speed field on the same temperature isosurface (right)

finest vertical resolution of approximately 0.8 mm. The grid was uniform in horizontal directions. The computational domain is shown in Fig. 4a. The domain dimensions (0.35 m long by 0.175 m wide by 1.2 m tall) were chosen to allow the bottom-driven jet to exit the domain primarily vertically at the top boundary. The burner inflow was centered at the bottom of the domain and was 0.25 m long and 0.075 m wide, corresponding to the dimensions of the catalytic burner, as shown in Fig. 1.

Time stepping was adaptive and controlled by a maximum Courant–Friedrichs–Lewy (CFL) number of 0.4. After a sufficiently long period to allow the flow field to fully develop, mean statistics for temperature were computed over a duration of 1 s. Samples obtained using this time period were found to be within approximately 1% of samples obtained over a 20 s averaging period, while allowing many more simulations to be performed for different parameters $\boldsymbol{\theta}$. Example temperature and speed fields from one such simulation are shown in Figs. 4b and c, respectively.

To account for the possibility of continued combustion within the domain, heat release was modeled above the combustor by adding a source term to the enthalpy equation in fireFOAM. Heat was added using a half-Gaussian distribution with the peak occurring at the burner surface, then trailing off in intensity as height increases above the burner (i.e., in the y-direction), as shown in Fig. 4a. Heat was applied uniformly in the 0.075 m by 0.25 m region directly above the burner; at x- and z-locations beyond the edge of the burner, the heat addition was set to zero.

Inlet conditions were fixed at close to the gas temperatures measured immediately above the burner surface (i.e., close to T_0 in Table 1). The exact values of T_0 from Table 1 were not used in the simulations, because the experimental measurements provide absorption-weighted temperatures, rather than the unweighted temperatures required in the simulations, and because the lowest experimental measurement was still 0.5 mm above the burner surface. We thus increased the temperature boundary condition slightly compared to T_0 in each simulation; we found that surface temperatures of 1515 K, 1610 K, and 1685 K were sufficient to provide reasonable agreement between the experimental and simulation results at the first measurement height of 0.5 mm. The composition of the exit gases was determined by specifying equilibrium products of complete combustion. Mass fractions of N_2, O_2, H_2O, and CO_2 were fixed accordingly, as specified by the NASA software Chemical Equilibrium Analysis (Bonnie and Sanford 1996). The equivalence ratio, ϕ, was set to match the values in Table 1 for each of the three experimental cases.

It should be noted that, although the presence of continued combustion in the burner exit gases is not consistent with equilibrium conditions at the burner surface, the true composition of the exit gases is unknown. However, the assumption of chemical equilibrium is acceptable in the present study, because combustion is not directly modeled in the LES, and the exact composition of the species at the inlet thus has limited impact on the conclusions of the analysis. Additionally, the calculation of absorption-weighted equivalent summary statistics using the LES data, as described in the next section, does not depend on the absolute quantity of H_2O present in the domain, but instead depends on the distribution of H_2O, which is assumed to enter the domain uniformly in space and time.

3.4 LAS-equivalent model summary statistics

To effectively compare the experimental and LES results, as is required for ABC, we constructed summary statistics from the LES that were equivalent to the line-of-sight absorption-weighted average LAS measurements. Although a spatial average over the LES computational cells through which the laser passes would be the simplest option for computing these statistics, this approach neglects the nonlinear relationship between temperature and absorption, as well as the effect of spatial variations in the H_2O mole fraction.

Consequently, we calculated the integrated absorbance that would occur for each of the two lasers passing through the LES domain. To accomplish this conversion, linestrengths (i.e., the amount of laser absorption) were determined for the range of temperatures observed in the LES using the reference temperature linestrengths in Goldenstein and Hanson (2015), with the partition function from Rothman et al. (2013). Based on 3D fields of temperature and H_2O mole fraction from the LES, line strengths were integrated for each laser using spatially resolved temperatures along the laser paths, with each line strength weighted by the normalized H_2O mole fraction. We then used the ratio of integrated line strengths for each laser to determine a line-of-sight absorption-weighted average temperature at a given height.

Temperatures were recorded from the LES at the center of the burner in the x-direction, 3.75 cm from the burner edge, parallel to the z-axis at each of the LAS measurement heights. At each output time, the temperature and H_2O mole fraction at each height were used to calculate a line-of-sight absorption-weighted average temperature. These time-series were averaged to obtain LAS-equivalent temperatures; the resulting vertical profiles of average temperature comprise the modeled summary statistics $\hat{S}$ that are compared with the LAS summary statistics shown in Fig. 2.

The LES data were also adjusted to account for uncertainties inherent in the measurements. For each sampled parameter $\boldsymbol{\theta}$, a uniform random number between $\pm 3\%$ was selected independently 1,000 times, and this amount of uncertainty was added to the entire profile of temperature (assuming that

any bias observed in the experiment was correlated at all heights). This uncertainty corresponds to the experimental uncertainty of ±3% in the temperature measurements estimated under controlled conditions by Hayden et al. (2020). There is also additional model error, particularly due to the SGS modeling inherent to the LES, as well as to the formulation of the half-Gaussian heat addition profiles; these errors are not explicitly addressed in the ABC procedure, although the comparison of the inferred inlet speeds with the experimentally estimated speeds will be used to provide confidence that the underlying physical model is capable of accurately reproducing the experimental measurements. The resulting modeled summary statistics $\hat{\mathcal{S}}$, each with added uncertainty, were then compared with the reference values $\mathcal{S}$ for each of the 1,000 randomly selected uncertainties, for each value of $\boldsymbol{\theta}$. It should be noted, however, that the variation in $\hat{\mathcal{S}}$ was generally larger due to variations in $\boldsymbol{\theta}$, as opposed to variations in the applied uncertainty.

4 Parameter estimation results

Here, we calculate posterior distributions of inlet speed, heat source strength, and heat source height using ABC for each of the three burner cases. The posteriors are calculated for four different values of ϵ, corresponding to sampled parameter acceptance rates between 5% and 20%. A total of $N = 495$ sampled parameters were modeled using LES for Case 1, while $N = 693$ parameters were modeled for each of Cases 2 and 3.

Using parameter estimates from the posterior distributions, we are able to recover trends in the experimentally estimated inflow speed V_0, as well as predict additional heat release above the burner for Case 3, indicating incomplete combustion within the catalyst at these conditions. We then show that LES of the catalytic burner using the estimated parameter values provides modeled vertical profiles of average temperature that agree closely with the LAS measurements for each case. Finally, we present results from an observing system experiment, further demonstrating the predictive power and effectiveness of the ABC method.

4.1 Posterior distributions

The primary outcome from ABC is the multi-dimensional posterior, $P[\boldsymbol{\theta}|\delta(\mathcal{S},\hat{\mathcal{S}}) \leq \epsilon]$, from which we can estimate unknown parameter values and determine the degree of confidence in these values. Here, $\boldsymbol{\theta}$ and the posterior represent three unknown parameters (i.e., inlet speed, heat source strength, and heat source height). As a result, we show one- and two-dimensional (1D and 2D, respectively) marginalized posteriors, computed using Gaussian kernel density estimation (KDE) (Scott 1979). The KDE method does not fit a single Gaussian to the measured posteriors, but rather assumes that each sample is represented by a Gaussian with a bandwidth given by Scott's rule (Scott 1979). Using this approach, the KDE method provides a continuous replacement for the discrete histogram and removes the dependence of the posterior on the choice of bin sizes and locations. We also employ mirroring when the posteriors peak at the bounds of the prior $P(\boldsymbol{\theta})$. This was necessary primarily for the heat strength posteriors which, as will be seen in the following, peak for Cases 1 and 2 at the physically constrained minimum values of 0 W. The maximum a posterior probability (MAP) values from the full 3D posterior with KDE and mirroring provide estimates of the unknown parameters, as summarized in Table 2.

Figure 5 shows the 1D posteriors of the three unknown parameters for each of the three burner cases. For Case 1, the posterior of the inlet speed approaches the bulk flow experimental estimate of $V_0 = 0.37$ m/s as ϵ decreases, as shown in Fig. 5a. Although the mode of the posterior for the smallest value of ϵ occurs at 0.3 m/s, which is lower than the experimental estimate, the rough correspondence nevertheless provides confidence in the accuracy of the ABC method. The inverse relationship between the inlet speed and the heat source strength can be seen in the 2D marginalized posteriors in Fig. 6 for ϵ corresponding to a 5% acceptance rate. The dominant mode in the 2D posterior of heat source strength and inlet speed in Fig. 6a corresponds to 0 W and 0.3 m/s, respectively. However, there is also a non-zero probability of larger heat source strengths as the inlet speed decreases, indicating that additional heat release can compensate for lower inlet speeds. Nevertheless, the peak in the joint posterior at 0.3 m/s, with 0 W heat addition, is the most probable condition corresponding to the experimental measurements for Case 1 (see also Table 2). This is also confirmed by the 1D marginalized posterior of the heat source strength, as shown in Fig. 5b, which peaks at 0 W.

For the heat source height in Fig. 5c, the posteriors generally provide less information gain compared to the prior, and the resulting MAP value of the heat source height is 0.04 m, which is in the exact middle of the prior. As ϵ decreases, however, a modal value of the heat source height does begin to appear in Fig. 5c at the maximum possible value of the height allowed by the prior. This modal value ensures that even if a simulation has some small amount of heat addition, the additional heat is moved as far from the burner surface as possible. This is also shown in Fig. 6c, where smaller heat source heights correspond to very small values of the heat source strength, and it is only for larger values of the height that larger values of the strength have significant probabilities. Taken together, these results strongly suggest that there is no additional heat release above the burner for Case 1, since the MAP values of the heat source strength and height are 0 W and 0.04 m, respectively, and non-zero strengths are

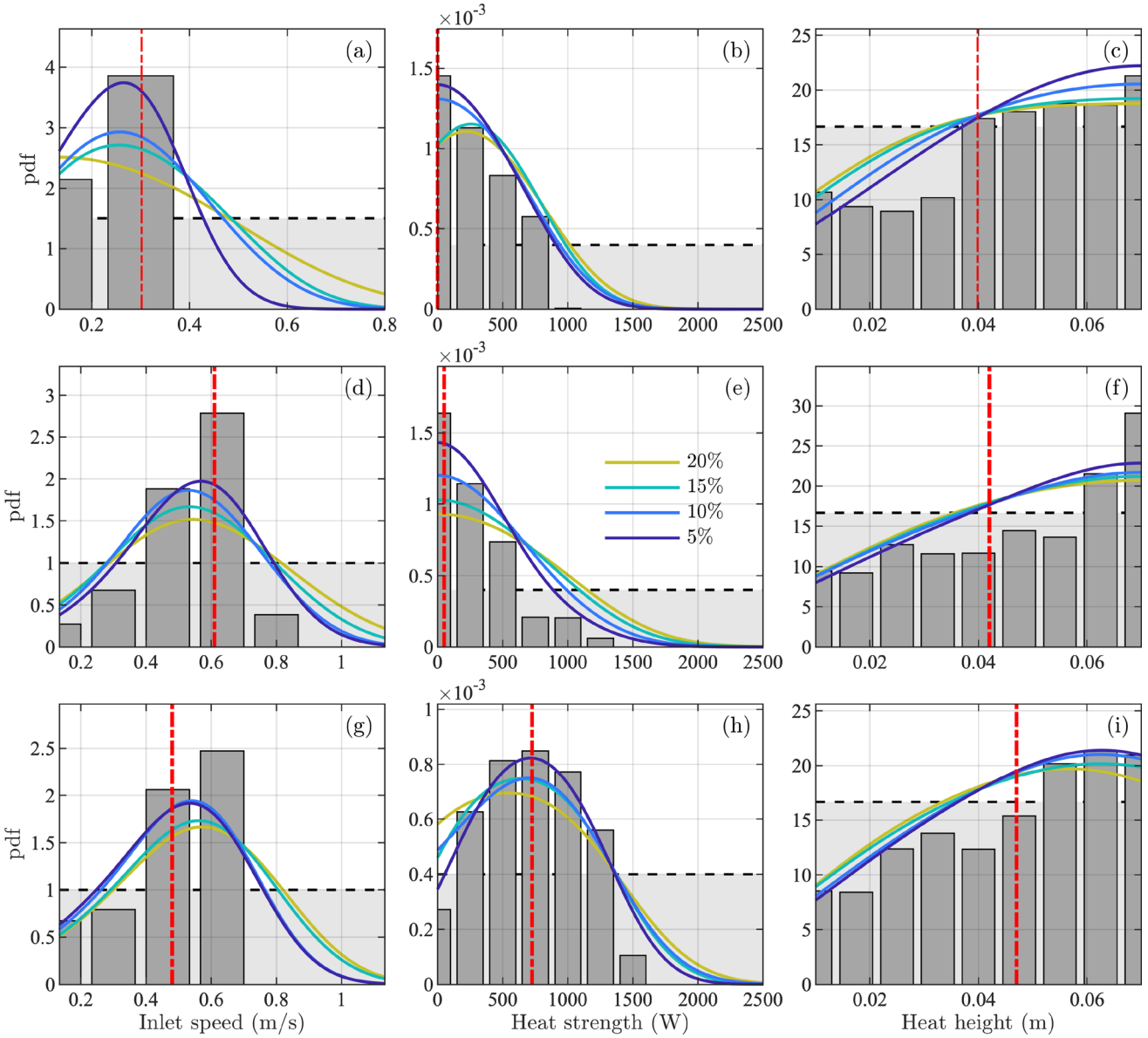


Fig. 5 One-dimensional marginalized posteriors for Cases 1, 2, and 3 (top, middle, and bottom rows, respectively) for inlet speed, heat source strength, and heat source height (left, middle, and right columns, respectively). Line colors correspond to the percentage of accepted simulations, as determined by the rejection threshold ϵ. Raw posteriors (i.e., before Gaussian kernel estimation) are shown by dark gray bars, and prior distributions are shown by the lighter gray regions with black dashed lines. Vertical red dash–dot lines show the MAP values from the full posterior for a 5% acceptance rate, summarized in Table 2

Table 2 MAP estimates from ABC of the burner inlet speed, heat source strength, and heat source height for each case. Estimates are obtained from the 5% acceptance rate full 3D posteriors, and values in parentheses show the nearest simulation values

Case	Inlet speed (m/s)	Heat source properties	
		Strength (W)	Height (m)
1	0.30 (0.30)	0 (0)	0.040 (0.040)
2	0.61 (0.63)	50 (0)	0.042 (0.040)
3	0.48 (0.47)	726 (750)	0.047 (0.048)

only estimated when they occur far from the burner surface, where there is less impact on the temperature profiles.

Figures 5 and 6 show that the posterior distributions for Case 2 are qualitatively similar to those for Case 1. However, the inlet speed estimation for Case 2, corresponding to 0.61 m/s in Fig. 5d, is larger than in Case 1 and is in good agreement with the experimental estimate of $V_0 = 0.65$ m/s for this case. The posteriors for Case 2 in Figs. 5e and 6d, e indicate that the most probable heat source strength is very small, with a MAP value of 50 W. Once again, there is also

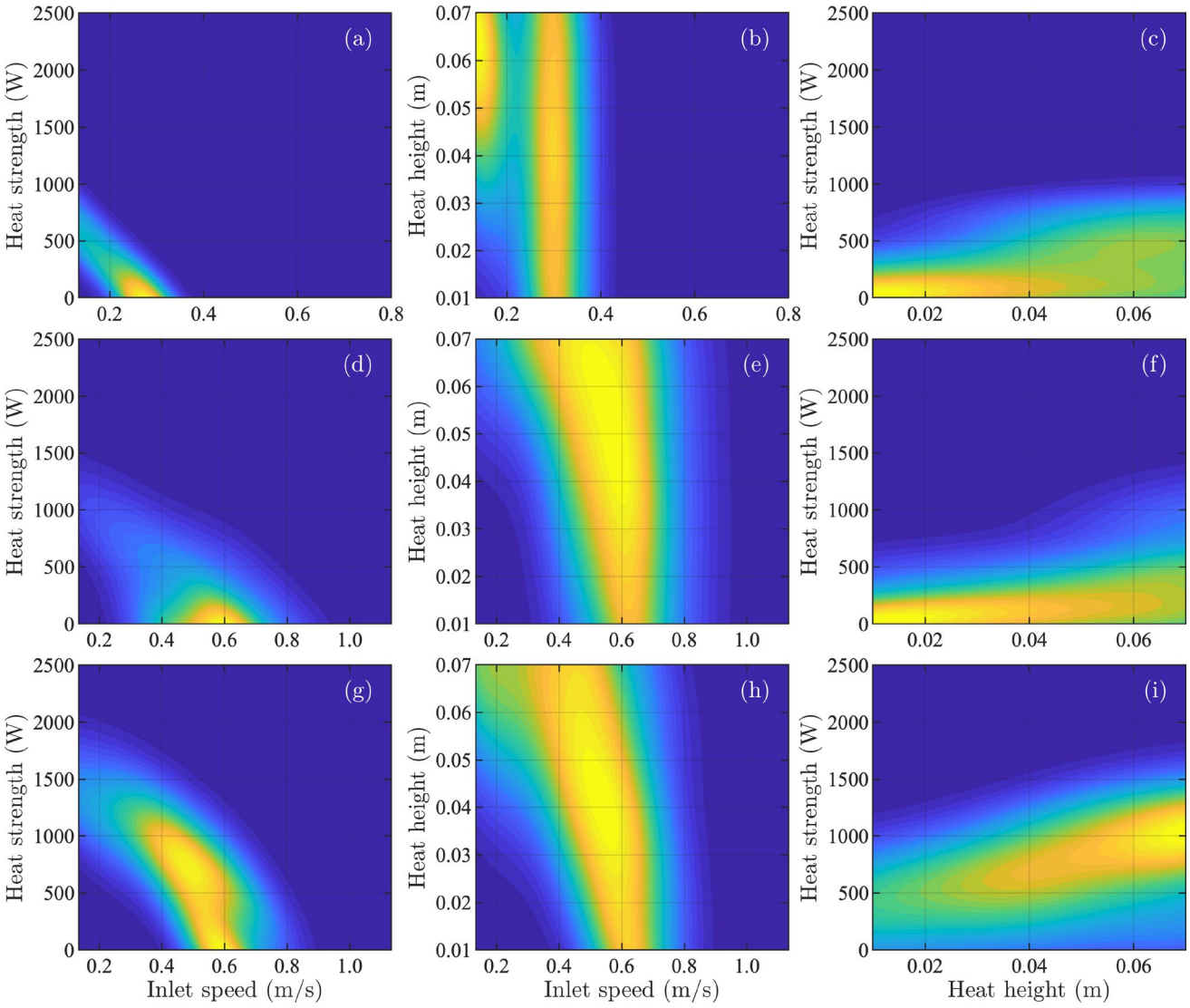


Fig. 6 Two-dimensional marginalized joint posteriors for Cases 1, 2, and 3 (top, middle, and bottom rows, respectively) when ϵ is set to accept 5% of simulations. Columns show joint posteriors for heat source strength and inlet speed (left), heat source height and inlet speed (middle), and heat source strength and heat source height (right). Colors represent the density of the posterior, with yellow and blue corresponding to high and low densities, respectively

relatively little information gained about the most likely heat source height for larger values, with a MAP value of 0.042 m, close to the center of the prior. For smaller values of ϵ in Fig. 5f, where non-zero values of the heat source strength are permissible for sufficiently small inlet speeds (see Fig. 6d), the preferred heat source height is pushed far from the burner surface, as shown in Fig. 6e, f. These results suggest that there is a possibility of heat release above the burner for Case 2, but the heat source strength is so small (only 50 W) that it has a nearly negligible effect on the overall temperature profile for this case.

The lack of substantial additional heat release predicted by ABC for Cases 1 and 2 is consistent with the previous experimental results by Hayden et al. (2019a, 2020) that showed no signs of additional combustion in the flow above the burner (i.e., low quantities of OH and no appreciable increase in temperature above the surface). Posteriors for Case 3 are, however, substantially different. In particular, ABC again provides a most probable inlet speed that is consistent with the trends in the experimental estimates (see Fig. 5g), but the heat source strength now has a modal value between 500 and 1000 W, even for very small values of ϵ, as shown in Fig. 5h. The marginalized posteriors (e.g., Fig. 5i) for the heat source height are qualitatively similar to those for Cases 1 and 2, but the MAP value has shifted to a larger value of 0.047 m, away from the center of the prior. The MAP value of the height is now much more significant, since it corresponds to a non-zero

value of the heat source strength, as shown in Fig. 6i. The non-zero value of the heat source strength indicated by the Case 3 posteriors in Figs. 5 and 6 thus suggests that there is substantial additional heat release due to continued combustion above the surface at these burner conditions.

It should be noted that the MAP inlet speeds predicted by ABC for Cases 1 and 2 are similar to the estimated bulk flow speeds from the experiments. For Case 3, however, the predicted value is lower than the experimental estimate. It is unclear whether this difference occurs due to the modeling used in the LES, to the approximations used to experimentally estimate inlet speeds (specifically, the assumption that combustion was complete when determining the exit gas composition), or to the fact that there is likely additional heat release above the burner for this case. However, it will be seen in the next section that the lower inlet speed for Case 3, when combined with additional heat release, yields excellent agreement between the LES and experimental results, providing confidence in the accuracy of the parameter estimates in Table 2.

4.2 Temperature profile and field comparisons

Using the MAP parameter values in Table 2, LES was performed for each of the three experimental burner configurations. The resulting vertical profiles of temperature are shown in Fig. 7, along with the corresponding experimental measurements from Fig. 2. The LES results generally agree closely with the experimental measurements, including the initial increase, and then rapid decrease, in temperature above the burner for Case 3. It is emphasized that the agreement shown in Fig. 7 for Case 3 requires substantial heat addition to account for continued combustion. For Cases 1 and 2, by contrast, reasonable agreement is obtained with the experimental measurements without including additional heat release above the burner, further indicating that continued combustion is unlikely for these cases.

The agreement between simulation and experimental results in Fig. 7 indicates that the LES, when performed using the MAP values, corresponds closely with the experiments, although the degree of uncertainty is fundamentally dictated by the widths of the posteriors in Figs. 5 and 6. Confidence in the MAP values can be estimated by calculating Bayesian credible intervals from the posteriors, although uncertainty in the posteriors can also be propagated through the LES model by showing the 90% range of values at each measurement location resulting from LES for all accepted parameters. These ranges are shown in Fig. 7, where, in general, the spread of simulation results is close to the ±3% uncertainty in the measurements. The largest LES uncertainties occur near the point at which the temperature begins to decrease, close to 1 cm above the burner in each case. At this height, dilution by cooler ambient gases causes the

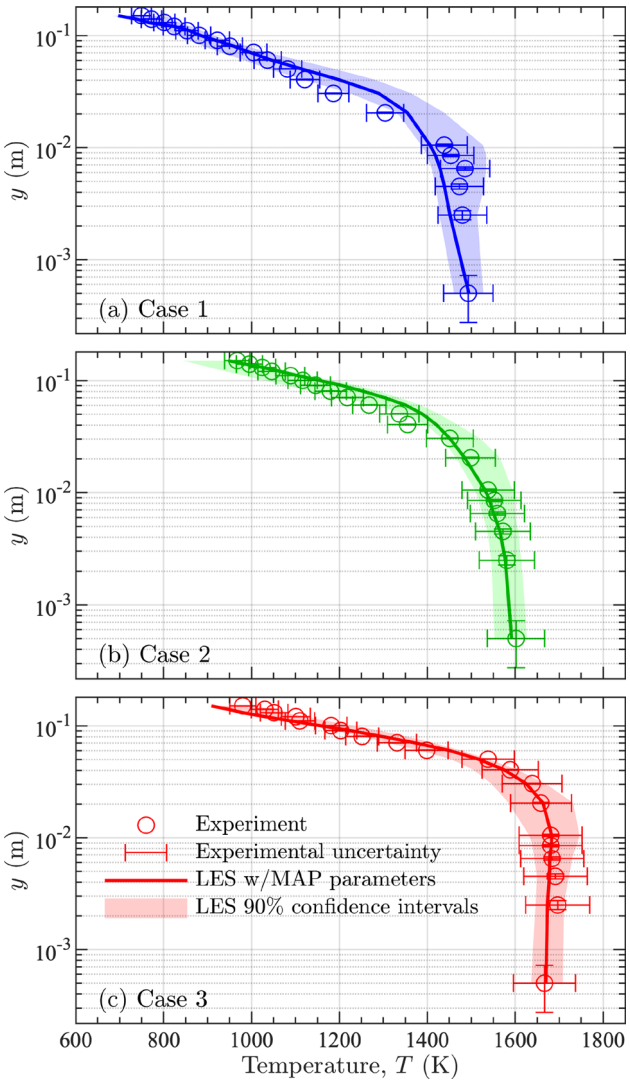


Fig. 7 Vertical profiles of temporally averaged, line-of-sight, absorption-weighted temperature from LES using MAP parameters in Table 2 (solid lines) and from the LAS (empty circles) for each burner case. Shaded regions indicate the 90% confidence intervals in the LES results

temperature to drop at a similar location for each case; this is also evident in the experimental measurements in the inset of Fig. 2.

Using the MAP estimates, the resulting LES fields of velocity, temperature, and chemical species can be used to develop a more complete understanding of the real-world catalytic burner system. For example, Fig. 8 shows 2D fields of temperature along the center plane of the burner for each of the three cases, using the parameter values corresponding to the minimum values of RMSE. This figure illustrates unique aspects of the temperature fields created in each case, including the greater variability of temperature close to the burner for Case 1, as compared to the relatively uniform temperatures close to the burner for Cases 2 and

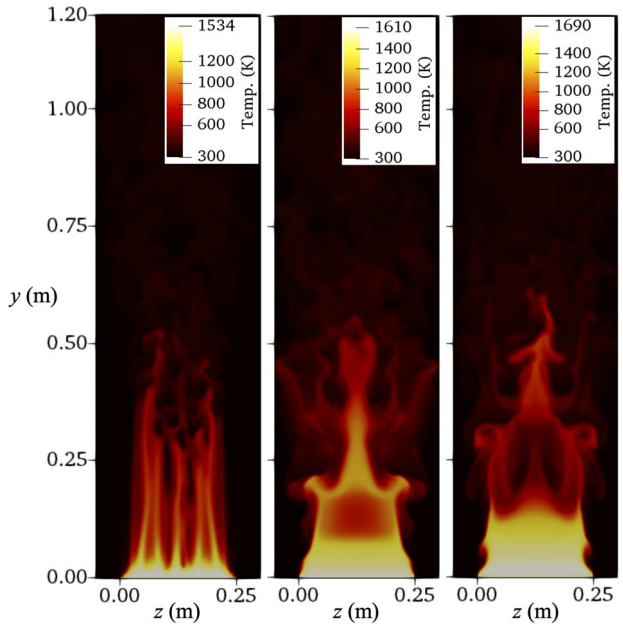


Fig. 8 Two-dimensional LES fields of temperature along the middle of the burner in the x-direction using parameters that give the smallest RMSE values, compared to the LAS measurements, for Cases 1–3 (left to right)

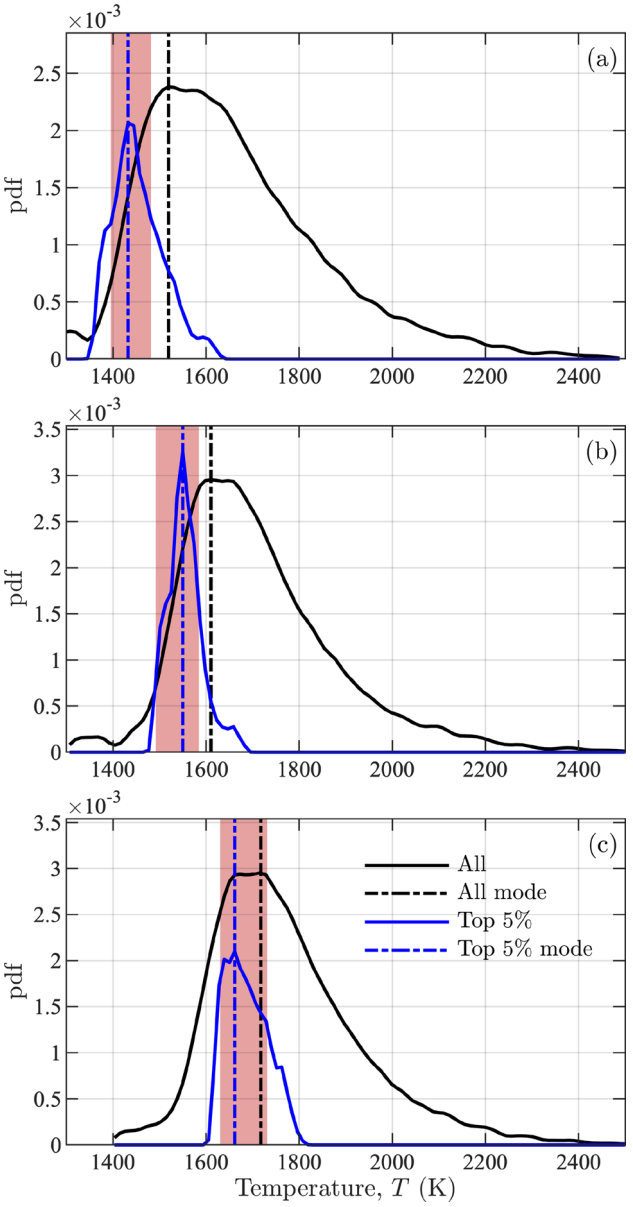


Fig. 9 Probability density functions (pdfs) of temperature 1.05 cm above the burner from LES for Cases 1–3 (a–c), showing results from all tested parameters (black lines) and from the closest 5% of parameters, as determined using ABC (blue lines). The pdf magnitudes for the top 5% results are decreased by a factor of 4 for display purposes. Modes of the pdfs are shown by the vertical dash–dot lines, and the experimental measurements at this height, with uncertainties of ±3%, are indicated by the red shaded regions

3. Additional insights, which are difficult or impossible to obtain experimentally, can also be developed given the increased confidence in the LES enabled by ABC.

4.3 Observing system experiment

As a final test of the predictive power of ABC, an Observing System Experiment (OSE) (Yamaguchi et al. 2009; Bouttier and Kelly 2001) was conducted. In this test, one of the experimental measurement heights was excluded from the reference summary statistics $\mathcal{S}$ prior to performing ABC. During the ABC procedure, parameter values giving the smallest distances $\delta(\mathcal{S}, \hat{\mathcal{S}})$ were identified, where $\hat{\mathcal{S}}$ was again obtained from LES and the RMSE was used for the distance function. The vertical profiles of temperature corresponding to these parameter values were then used to estimate the missing experimental data (which, in this case, was not used to generate the list of 'best' simulations). This approach thus provides insight into how well ABC can predict missing experimental data.

Here, we perform an OSE for each of the three experimental configurations. Because there is a substantial change in the temperature gradient at approximately 1.05 cm above the burner surface, as shown in Fig. 7, this measurement height was deemed difficult to predict and was consequently removed from the reference summary statistics prior to performing ABC; similar tests can also be performed excluding other measurement locations, or excluding multiple locations. Once again, ϵ was set to accept 5% of the sampled parameters.

Figure 9 shows the resulting distributions of predicted temperature 1.05 cm above the surface using all simulations, and using only the best 5% of simulations. For Cases 1 and 2 shown in Fig. 9a, b, respectively, the modes of the full data distributions fall outside the experimental data ranges of 1439 ± 43 K for Case 1 and 1538 ± 46 K for Case 2. For

Case 3 in Fig. 9c, the mode of the full distribution is at the upper end of the experimental range of 1681 ± 50 K.

By contrast, for the best 5% of simulations determined by ABC, the distribution modes are each within the experimental ranges and fall close to the nominal experimental values in each case. The temperatures predicted by ABC are 1433 K, 1550 K, and 1662 K for Cases 1–3, respectively, corresponding to errors of 1% or less compared to the experimental results. It should also be noted that the distributions in Fig. 9 are relatively narrow for the best 5% of simulations, with standard deviations of 55 K, 38 K, and 45 K for Cases 1–3, respectively, indicating high confidence in the values of temperature predicted by ABC.

This OSE indicates that ABC is extremely effective at providing predictive information within the domain where the simulation and reference data match, even when there is no corresponding reference data to inform the inference. In future efforts, this approach could be used to design experiments with the fewest possible measurements, such that the accuracy of the parameter estimation is unaffected.

5 Conclusions

In the present study, we have used ABC to estimate unknown characteristics of a catalytic burner, given spatially sparse measurements from LAS. Vertical profiles of temporally averaged absorption-weighted temperature from LAS were combined with ABC and LES to estimate the speed and heat addition characteristics of the high-temperature flow created by an industrially relevant catalytic burner. The ABC method was performed for the burner operating at three different conditions, corresponding to different power fluxes and equivalence ratios.

We showed that ABC, when given LAS measurements and driven by LES, successfully predicted trends in the inflow speed and also predicted continued combustion above the burner for the case with the highest equivalence ratio. We selected most likely parameter values from the posterior distributions provided by the ABC method and used these values to perform LES of the burner for each of the three burner operating conditions. In each case, the LES results were in close agreement with the experimentally measured vertical profiles of temperature. Additionally, using an OSE, we showed that we were able to successfully predict a missing temperature from the experimental data. We thus demonstrated the utility of the ABC approach for improving knowledge of real-world systems, as well as for improving the physical fidelity of numerical simulations.

This study suggests several directions for future research. In particular, the ABC method should now be tested on more-complicated geometries, as well as extended to directly address the chemical composition and subsequent finite rate combustion of the gases leaving the burner. Furthermore, the present ABC approach can be used to simultaneously adjust boundary conditions, fluid properties, and turbulence model parameters in a simulation to achieve a comprehensive improvement in simulation accuracy. Finally, the OSE performed here suggests that ABC could be used to design more efficient experimental campaigns with reduced measurement locations. Full Bayesian techniques have recently been used for experimental design in the context of chemical species tomography (Grauer et al. 2016), as well as for laser absorption measurements of liquid films (Pan et al. 2017); these and similar design of experiment problems could also be addressed using ABC.

Acknowledgements We acknowledge helpful discussions with Mark Strobel, Melvyn Branch, and Aniruddha Upadhye.

Funding D.P., C.L., N.T.W., and T.R.S.H. acknowledge gift support from the 3M Company. O.A.D. was supported by NASA award NNX15AU24A-03. C.L. was supported by the NSF Graduate Research Fellowship Program under award DGE 1144083. P.E.H. was supported, in part, by AFOSR Award No. FA9550-17-1-0144. J.D.C. and G.B.R. were supported, in part, by NSF Award No. CBET 1454496 and AFOSR Award No. FA9550-17-1-0224. Computing resources were provided by DoD HPCMP under a Frontier project award and by the Air Force Research Laboratory.

Availability of data and material All data and analysis/figure scripts will be placed on Zenodo for permanent archiving.

Compliance with ethical standards

Conflict of interest The authors declare that they have no conflicts of interest or competing interests.

Code availability The code used to perform the simulations is OpenFOAM, which is open-source and publicly available at https://openfoam.org.

References

Abdessalem AB, Dervilis N, Wagg D, Worden K (2018) Model selection and parameter estimation in structural dynamics using approximate Bayesian computation. Mech Syst Signal Process 99:306

Adowski TR, Bauman PT (2018) A numerical study of bayesian inference of surface catalycity in low speed reacting flow using laser absorption spectroscopy. In: 2018 Joint Thermophysics and Heat Transfer Conference (American Institute of Aeronautics and Astronautics, Atlanta, Georgia, 2018). https://doi.org/10.2514/6.2018-4290

Beaumont MA (2010) Approximate Bayesian computation in evolution and ecology. Annu Rev Ecol Evol Syst 41(379–406):1

Beaumont MA, Zhang W, Balding DJ (2002) Approximate Bayesian computation in population genetics. Genetics 162(4):2025

Bolshov MA, Kuritsyn YA, Romanovskii YV (2015) Tunable diode laser spectroscopy as a technique for combustion diagnostics. Spectrochim Acta Part B 106:45

Bonnie JM, Sanford G (1996) Computer program for calculation of complex chemical equilibrium compositions and applications. User's Manual and Program Discription

Bouttier F, Kelly G (2001) Observing-system experiments in the ECMWF 4D-Var data assimilation system. Q J R Meteorol Soc 127(574):1469

Cai T, Tan T, Wang G, Chen W, Gao X (2009) Gas temperature measurements using wavelength modulation spectroscopy at 1.39 μm. Opt Appl 39(1)

Chai T, Draxler RR (2014) Root mean square error (RMSE) or mean absolute error (MAE)? Arguments against avoiding RMSE in the literature. Geosci Model Dev 7(3):1247

Christopher JD, Lapointe C, Wimer NT, Hayden TRS, Grooms I, Rieker GB, Hamlington PE (2017) Parameter Estimation for a Turbulent Buoyant Jet with Rotating Cylinder Using Approximate Bayesian Computation. AIAA Paper, AIAA-2017-3629

Christopher JD, Wimer NT, Hayden TRS, Lapointe C, Grooms I, Rieker GB, Hamlington PE (2017) Parameter estimation for a turbulent buoyant jet using approximate bayesian computation. AIAA Paper, AIAA-2017-0531

Christopher JD, Wimer NT, Lapointe C, Hayden TRS, Grooms I, Rieker GB, Hamlington PE (2018) Parameter estimation for complex thermal-fluid flows using approximate Bayesian computation. Phys Rev Fluids 3:104602

Constantine PG, Wang Q, Doostan A, Iaccarino G (2011) A surrogate accelerated Bayesian inverse analysis of the HyShot II flight data. AIAA Paper, AIAA-2011-2037

Cottilard SA (2011) Catalytic combustion. Nova Science Publ., New York

Csilléry K, Blum MGB, Gaggiotti OE, François O (2010) Approximate Bayesian computation (ABC) in practice. Trends Ecol Evolut 25(7):410

Daily JW (1997) Laser induced fluorescence spectroscopy in flames. Prog Energy Combust Sci 23(2):133

Daun KJ, Grauer SJ, Hadwin PJ (2016) Chemical species tomography of turbulent flows: discrete ill-posed and rank deficient problems and the use of prior information. J Quant Spectrosc Radiat Transf 172:58

Doronina OA, Christopher JD, Towery CAZ, Hamlington PE, Dahm WJA (2018) Autonomic closure for turbulent flows using approximate bayesian computation. AIAA Paper, AIAA-2018-0594

Doronina OA, Towery CAZ, Christopher JD, Grooms I, Hamlington PE (2019) Turbulence model development using Markov chain Monte Carlo approximate Bayesian computation. AIAA Paper, AIAA-2019-1883

Duraisamy K, Iaccarino G, Xiao H (2019) Turbulence Modeling in the Age of Data. Annu Rev Fluid Mech 51(1):357

Dwight RP, Han Z (2009) Efficient uncertainty quantification using gradient-enhanced kriging. AIAA Paper, AIAA-2009-2276

Ebert V, Fernholz T, Giesemann C, Pitz H, Teichert H, Wolfrum J, Jaritz H (2000) Simultaneous diode-laser-based in situ detection of multiple species and temperature in a gas-fired power plant. Proc Combust Inst 28(1):423

Emmert J, Grauer SJ, Wagner S, Daun KJ (2019) Efficient Bayesian inference of absorbance spectra from transmitted intensity spectra. Opt Express 27(19):26893

Emmert J, Wagner S, Daun KJ (2020) Quantifying the spatial resolution of the maximum a posteriori estimate in linear, rank-deficient, Bayesian hard field tomography. Measur Sci Technol. https://doi.org/10.1088/1361-6501/abb550

Estumano DC, Hamilton FC, Colaço MJ, Leiroz AJK, Orlande HRB, Carvalho RN, Dulikravich GS (2015) Bayesian estimate of mass fraction of burned fuel in internal combustion engines using pressure measurements. Eng Optim IV, 997–1003

Fagundes NJR, Ray N, Beaumont MA, Neuenschwander S, Salzano FM, Bonatto SL, Excoffier L (2007) Statistical evaluation of alternative models of human evolution. Proc Natl Acad Sci 104(45):17614

Fox CW, Roberts SJ (2012) A tutorial on variational Bayesian inference. Artif Intell Rev 38(2):85

Frank J, Kaiser S (2008) High-resolution imaging of dissipative structures in a turbulent jet flame with laser Rayleigh scattering. Exp Fluids 44:221

Goldenstein CS, Hanson RK (2015) Diode-laser measurements of linestrength and temperature-dependent lineshape parameters for H2O transitions near 1.4 μ m using Voigt, Rautian, Galatry, and speed-dependent Voigt profiles. J Quant Spectrosc Radiat Transf 152:127

Goldenstein CS, Mathews GC (2020) Simulation technique enabling calibration-free frequency-modulation spectroscopy measurements of gas conditions and lineshapes with modulation frequencies spanning kHz to GHz. Appl Opt 59(5):1491

Goldenstein CS, Strand CL, Schultz IA, Sun K, Jeffries JB, Hanson RK (2014) Fitting of calibration-free scanned-wavelength-modulation spectroscopy spectra for determination of gas properties and absorption lineshapes. Appl Opt 53(3):356

Goldenstein CS, Spearrin RM, Jeffries JB, Hanson RK (2017) Infrared laser-absorption sensing for combustion gases. Prog Energy Combust Sci 60:132

Grauer SJ (2018) Bayesian methods for gas-phase tomography. PhD Thesis

Grauer SJ, Hadwin PJ, Daun KJ (2016) Bayesian approach to the design of chemical species tomography experiments. Appl Opt 55(21):5772

Grauer SJ, Hadwin PJ, Sipkens TA, Daun KJ (2017) Measurement-based meshing, basis selection, and prior assignment in chemical species tomography. Opt Express 25(21):25135

Grauer SJ, Tsang RW, Daun KJ (2017) Broadband chemical species tomography: measurement theory and a proof-of-concept emission detection experiment. J Quant Spectrosc Radiat Transf 198:145

Greenshields C (2016) OpenFOAM | The OpenFOAM Foundation http://openfoam.org/

Hanson RK, Falcone PK (1978) Temperature measurement technique for high-temperature gases using a tunable diode laser. Appl Opt 17(16):2477

Hayden TRS, Rieker GB (2016) Large amplitude wavelength modulation spectroscopy for sensitive measurements of broad absorbers. Opt Express 24(24):27910

Hayden TRS, Malarich N, Petrykowski DJ, Nigam SP, Christopher JD, Lapointe C, Wimer NT, Hamlington P, Rieker GB (2019a) OH radical measurements in combustion environments using wavelength modulation spectroscopy and dual-frequency comb spectroscopy near 1491 nm. Appl Phys B 125

Hayden T, Petrykowski D, Sanchez A, Nigam S, Lapointe C, Christopher J, Wimer N, Upadhye A, Strobel M, Hamlington P, Rieker G (2019b) Characterization of OH, H_2 O, and temperature profiles in industrial flame treatment systems interacting with polymer films. Proc Combust Inst 37(2):1571

Hayden TRS, Wimer NT, Lapointe C, Christopher JD, Nigam SP, Upadhye A, Strobel M, Hamlington PE, Rieker GB (2020) Characterization of the Buoyant Jet above a Catalytic Combustor Using Wavelength Modulation Spectroscopy. Combust Sci Technol 192(6):997

Huang Q, Wang F, Zhang H, Yan J, Ni M, Cen K (2013) In-situ CO measurement of gas and oil combustion flame using near infrared tunable diode laser with direct and modulated absorption signals. Opt Commun 306:99

Jahn W, Rein G, Torero JL (2012) Forecasting fire dynamics using inverse computational fluid dynamics and tangent linearisation. Adv Eng Softw 47(1):114

Khalil M, Najm HN (2018) Probabilistic inference of reaction rate parameters from summary statistics. Combustion Theory and Modelling pp 1–31

Lintusaari J, Gutmann MU, Dutta R, Kaski S, Corander J (2017) Fundamentals and recent developments in approximate Bayesian computation. Syst Biol 66(1):e66

Lucas DD, Gowardhan A, Cameron-Smith P, Baskett RL (2016) Impact of meteorological inflow uncertainty on tracer transport and source estimation in urban atmospheres. Atmos Environ 143:120

Ma L, Wu Y, Xu W, Hammack SD, Lee T, Carter CD (2016) Comparison of 2D and 3D flame topography measured by planar laser-induced fluorescence and tomographic chemiluminescence. Appl Opt 55(20):5310

Madsen H (2003) Parameter estimation in distributed hydrological catchment modelling using automatic calibration with multiple objectives. Adv Water Resour 26(2):205

Marin JM, Pudlo P, Robert CP, Ryder RJ (2012) Approximate Bayesian computational methods. Stat Comput 22(6):1167

Marjoram P, Molitor J, Plagnol V, Tavaré S (2003) Markov chain Monte Carlo without likelihoods. Proc Natl Acad Sci 100(26):15324

Mcenally CS, Pfefferle LD, Schaffer AM, Long MB, Mohammed RK, Smooke MD, Colkei MB (2000) Characterization of a coflowing methane/air non-premixed flame with computer modeling, Rayleigh-Raman imaging, and on-line mass spectrometry. Proc Combust Inst 28(2):2063

McManus T, Sutton J (2020) Simultaneous 2D filtered Rayleigh scattering thermometry and stereoscopic particle image velocimetry measurements in turbulent non-premixed flames. Exp Fluids 61:134

Mosbach S, Braumann A, Man PLW, Kastner CA, Brownbridge GPE, Kraft M (2012) Iterative improvement of Bayesian parameter estimates for an engine model by means of experimental design. Combust Flame 159(3):1303

Nott DJ, Marshall L, Brown J (2012) Generalized likelihood uncertainty estimation (GLUE) and approximate Bayesian computation: What's the connection? Water Resources Research 48(12)

Oberkampf, WL, Trucano T (2000) Validation methodology in computational fluid dynamics. AIAA Paper, AIAA-2000-2549

Oberkampf WL, Roy CJ (2010) Verification and validation in scientific computing. Cambridge University Press, Cambridge

Oberkampf WL, Trucano TG (2002) Verification and validation in computational fluid dynamics. Prog Aerosp Sci 38(3):209

Oberkampf WL, Trucano TG, Hirsch C (2004) Verification, validation, and predictive capability in computational engineering and physics. Appl Mech Rev 57(5):345

Olson B (2016) Stochastic weather generation with approximate bayesian computation. Master's thesis, University of Colorado at Boulder

Pan R, Daun KJ, Dreier T, Schulz C (2017) Uncertainty quantification and design-of-experiment in absorption-based aqueous film parameter measurements using Bayesian inference. Appl Opt 56(11):E1

Pandey S, Schumacher J, Sreenivasan KR (2020) A perspective on machine learning in turbulent flows. J Turbulence **0**(0):1

Pemha E, Nyobe EN (2011) Genetic algorithm approach and experimental confirmation of a laser-based diagnostic technique for the local thermal turbulence in a hot wind tunnel jet. Progress Electromagn Res 28:325

Philippe LC, Hanson RK (1993) Laser diode wavelength-modulation spectroscopy for simultaneous measurement of temperature, pressure, and velocity in shock-heated oxygen flows. Appl Opt 32(30):6090

Qu Z, Ghorbani R, Valiev D, Schmidt FM (2015) Calibration-free scanned wavelength modulation spectroscopy-application to H 2 O and temperature sensing in flames. Opt Express 23(12):16492

Rieker GB, Jeffries JB, Hanson RK (2009) Calibration-free wavelength-modulation spectroscopy for measurements of gas temperature and concentration in harsh environments. Appl Opt 48(29):5546

Rohmer J, Rousseau M, Lemoine A, Pedreros R, Lambert J, Benki A (2018) Source characterisation by mixing long-running tsunami wave numerical simulations and historical observations within a metamodel-aided ABC setting. Stoch Environ Res Risk Assess 32:967–984. https://doi.org/10.1007/s00477-017-1423-y

Rothman LS, Gordon IE, Babikov Y, Barbe A, Benner DC, Bernath PF, Birk M, Bizzocchi L, Boudon V, Brown LR (2013) The HITRAN2012 molecular spectroscopic database. J Quant Spectrosc Radiat Transf 130:4

Sadegh M, Vrugt JA (2013) Bridging the gap between GLUE and formal statistical approaches: approximate Bayesian computation. Hydrol Earth Syst Sci 17(12)

Salinger AG, Pawlowski RP, Shadid JN, van Bloemen Waanders BG (2004) Computational analysis and optimization of a chemical vapor deposition reactor with large-scale computing. Ind Eng Chem Res 43(16):4612

Schmidt A, van der Kley S, Wagner S (2020) Optically accessible generic exhaust gas test bench for the investigation of fundamental SCR-relevant processes. Appl Opt 59(23):6953

Schulz C, Sick V (2005) Tracer-LIF diagnostics: quantitative measurement of fuel concentration, temperature and fuel/air ratio in practical combustion systems. Prog Energy Combust Sci 31(1):75

Scott DW (1979) On optimal and data-based histograms. Biometrika 66(3):605

Sipkens TA, Hadwin PJ, Grauer SJ, Daun KJ (2018) Predicting the heat of vaporization of iron at high temperatures using time-resolved laser-induced incandescence and Bayesian model selection. J Appl Phys 123(9):095103

Smith RC (2013) Uncertainty quantification: theory, implementation, and applications, vol 12. SIAM, New Delhi

Sousa J, García-Sánchez C, Gorlé C (2018) Improving urban flow predictions through data assimilation. Build Environ 132:282

Spearrin RM, Goldenstein CS, Jeffries JB, Hanson RK (2014) Quantum cascade laser absorption sensor for carbon monoxide in high-pressure gases using wavelength modulation spectroscopy. Appl Opt 53(9):1938

Stroud JR, Katzfuss M, Wikle CK (2018) A Bayesian adaptive ensemble Kalman filter for sequential state and parameter estimation. Mon Weather Rev 146(1):373

Sun K, Chao X, Sur R, Goldenstein CS, Jeffries JB, Hanson RK (2013) Analysis of calibration-free wavelength-scanned wavelength modulation spectroscopy for practical gas sensing using tunable diode lasers. Meas Sci Technol 24(12):125203

Sunnåker M, Busetto AG, Numminen E, Corander J, Foll M, Dessimoz C (2013) Approximate Bayesian Computation. PLoS Comput Biol 9(1):e1002803

Toni T, Welch D, Strelkowa N, Ipsen A, Stumpf MPH (2009) Approximate Bayesian computation scheme for parameter inference and model selection in dynamical systems. J R Soc Interface 6(31):187

Vakilzadeh MK, Beck JL, Abrahamsson T (2018) Using approximate Bayesian computation by Subset Simulation for efficient posterior assessment of dynamic state-space model classes. SIAM J Sci Comput 40(1):B168

van der Kley S, Emmert J, Schmidt A, Dreizler A, Wagner S (2020) Tomographic spectrometer for the temporally-resolved 2D reconstruction of gas phase parameters within a generic SCR test rig. Proc Combust Inst. https://doi.org/10.1016/j.proci.2020.09.009

Vrbik I, Deardon R, Feng Z, Gardner A, Braun J (2012) Using individual-level models for infectious disease spread to model spatio-temporal combustion dynamics. Bayesian Anal 7(3):615

Vrugt JA, Sadegh M (2013) Toward diagnostic model calibration and evaluation: approximate Bayesian computation. Water Resour Res 49(7):4335

Wagner S, Fisher BT, Fleming JW, Ebert V (2009) TDLAS-based in situ measurement of absolute acetylene concentrations in laminar 2D diffusion flames. Proc Combust Inst 32(1):839

Wang S, Xu X (2006) Parameter estimation of internal thermal mass of building dynamic models using genetic algorithm. Energy Convers Manag 47(13–14):1927

Wang Y, Chatterjee P, de Ris JL (2011) Large eddy simulation of fire plumes. Proc Combust Inst 33(2):2473

Weller HG, Tabor G, Jasak H, Fureby C (1998) A tensorial approach to computational continuum mechanics using object-oriented techniques. Comput Phys 12(6):620

Yamaguchi M, Iriguchi T, Nakazawa T, Wu CC (2009) An observing system experiment for Typhoon Conson (2004) using a singular vector method and DOTSTAR data. Mon Weather Rev 137(9):2801

Publisher's Note Springer Nature remains neutral with regard to jurisdictional claims in published maps and institutional affiliations.

AIAA JOURNAL
Vol. 59, No. 11, November 2021

Parameter Estimation for Reynolds-Averaged Navier–Stokes Models Using Approximate Bayesian Computation

Olga A. Doronina*
University of Colorado, Boulder, Colorado 80309
Scott M. Murman†
NASA Ames Research Center, Moffett Field, California 94035
and
Peter E. Hamlington‡
University of Colorado, Boulder, Colorado 80309

https://doi.org/10.2514/1.J060308

Downloaded by UNIVERSITY OF COLORADO on January 17, 2022 | http://arc.aiaa.org | DOI: 10.2514/1.J060308

Approximate Bayesian computation (ABC) is used to estimate unknown parameter values, as well as their uncertainties, in Reynolds-averaged Navier–Stokes (RANS) simulations of turbulent flows. The ABC method approximates posterior distributions of model parameters, but does not require the direct computation, or estimation, of a likelihood function. This method thus enables relatively simple and flexible parameter estimation for complex models and a wide range of reference data. This paper describes the ABC approach, including the use of a calibration step, adaptive proposal, and Markov chain Monte Carlo (MCMC) technique to accelerate the parameter estimation, resulting in an ABC approach with improved MCMC, denoted ABC-IMCMC. As a test of the classic ABC rejection algorithm and ABC-IMCMC, parameters are estimated in a nonequilibrium RANS model using reference data from direct numerical simulations of periodically sheared homogeneous turbulence. The use of ABC-IMCMC is then demonstrated to estimate parameters in the Menter shear-stress-transport (SST) model using experimental reference data for an axisymmetric transonic bump. This paper shows that the accuracy of the SST model for this test case can be improved using ABC-IMCMC, indicating that ABC-IMCMC is a promising method for the calibration of RANS models using a wide range of reference data.

Nomenclature

a_{ij}	=	Reynolds stress anisotropy tensor
a_{inf}	=	speed of sound
$\mathcal{C}_i$	=	covariance matrix
C_p	=	pressure coefficient
$C_1, C_2, C_{\varepsilon 1}, C_{\varepsilon 2}$	=	closure parameters in the nonequilibrium turbulence model
$CD_{k\omega}$	=	positive portion of shear-stress-transport cross-diffusion term
$\boldsymbol{c}$	=	vector of unknown parameters
c	=	circular-arc bump length
$\mathcal{D}, \mathcal{D}'$	=	reference/modeled data
D	=	diameter of cylinder
d	=	distance function
$\mathcal{F}$	=	model
F_1, F_2	=	blending functions in shear-stress-transport model
H	=	circular-arc bump height
h	=	probability to accept sampled parameter
k	=	turbulence kinetic energy
L	=	likelihood function
M	=	Mach number
m	=	number of steps without kernel adaptation
N	=	number of sampled parameters
n	=	number of unknown parameters
P	=	probability distribution
P_k	=	kinetic energy production rate
$\bar{p}$	=	mean pressure
p_{inf}	=	freestream pressure
q	=	proposal distribution
Re	=	Reynolds number
$\bar{R}_{ij}$	=	mean rotational tensor
$\mathcal{S}, \mathcal{S}'$	=	reference/modeled summary statistics
$\bar{S}_{ij}$	=	mean strain rate tensor
S	=	amplitude of the mean strain rate tensor
T_{inf}	=	freestream temperature
t	=	time
U_{inf}	=	freestream velocity
$\overline{u}_i$	=	mean velocity
$\overline{u_i' u_j'}$	=	Reynolds stress tensor
x, y	=	distance along/from the wall
α_1, α_2	=	nonequilibrium turbulence model coefficients
δ_{ij}	=	Kronecker delta
ϵ	=	tolerance hyperparameter in approximate Bayesian computation algorithm
ε	=	kinetic energy dissipation rate
μ_t	=	turbulent eddy viscosity
ν_t	=	turbulence kinematic viscosity
π	=	prior distribution
ρ	=	density
$\sigma_{ki}, \sigma_{\omega i}, \beta_i, \beta^*, \kappa, a_1, \gamma_i$	=	shear-stress-transport model closure coefficients ($i = 1, 2$)
τ	=	principal shear-stress
ϕ	=	blended constant in shear-stress-transport model ($\gamma, \beta, \sigma_k, \sigma_\omega$)
Ω	=	vorticity magnitude
ω	=	specific dissipation rate
ϖ	=	shearing frequency

Received 3 November 2020; revision received 31 March 2021; accepted for publication 28 May 2021; published online 7 September 2021. Copyright © 2021 by the American Institute of Aeronautics and Astronautics, Inc. All rights reserved. All requests for copying and permission to reprint should be submitted to CCC at www.copyright.com; employ the eISSN 1533-385X to initiate your request. See also AIAA Rights and Permissions www.aiaa.org/randp.

*Research Assistant, Paul M. Rady Department of Mechanical Engineering, UCB 427. Student Member AIAA.
†Aerospace Engineer. Member AIAA.
‡Associate Professor, Paul M. Rady Department of Mechanical Engineering, UCB 427. Member AIAA.

I. Introduction

DESPITE ongoing advances in the availability of high-performance computing resources, most industrial and engineering fluid

Downloaded by UNIVERSITY OF COLORADO on January 17, 2022 | http://arc.aiaa.org | DOI: 10.2514/1.J060308

flows are still simulated using Reynolds-averaged Navier–Stokes (RANS) approaches. Although progress has been made in recent years on the development of computationally efficient large-eddy simulations (LESs) and hybrid RANS/LES approaches, RANS simulations are likely to remain common in engineering practice for many years to come, primarily because of their substantially lower computational cost compared with LES. Techniques such as optimization and uncertainty quantification are also becoming increasingly important in the engineering design process, but such techniques often require thousands of simulations (or more), and RANS simulations remain the only viable option for such large numbers of calculations.

The primary difficulty with RANS simulations is the requirement that a physically accurate, computationally stable model be provided for the unclosed Reynolds stresses that appear in the ensemble-averaged governing equations. A wide variety of RANS closure models have been suggested over the years (see Speziale and So [1] for a review) but, despite all efforts to create a robust and accurate model, no universal turbulence model exists. Moreover, essentially all RANS models rely on empirical coefficients that must be calibrated for different flows and geometries.

Given this situation, the development of improved methods for inferring model parameters from available experimental, or higher fidelity computational, data is an active area of research [2]. In particular, the inverse statistical problem that is the core of model parameter calibration can be solved using either deterministic or probabilistic approaches. In the deterministic approach, model parameters are determined through an optimization technique by minimizing the error between the model and some reference data. Probabilistic approaches such as Bayesian methods, by contrast, are attractive because they provide not only model parameter values, but also their uncertainties. Oberkampf and Trucano [3,4] have emphasized the importance of such uncertainties in model parameter calibration, particularly when parameter estimation is performed using uncertain reference data and inherently imperfect models.

Cheung et al. [5] were the first to apply a Bayesian inference method to calibrate the Spalart–Allmaras turbulence model using velocity and wall-shear stress experimental data for wall-bounded, incompressible, turbulent flows. Oliver and Moser [6] extended this work by adding more models and stochastic extensions with direct numerical simulation (DNS) channel flow data. Ray and co-authors [7–11] used a similar approach to calibrate RANS model parameters in a jet in crossflow. Zhang and Fu [12] combined a high-dimensional model representation technique and the Gaussian-process machine-learning method to construct a surrogate model, thereby making the Bayesian inference process more affordable. As a demonstration, they calibrated various parameters in the Menter shear-stress-transport (SST) model, using reference data composed of surface drag measurements and velocity profiles for hypersonic turbulent flows over flat plates. Nadiga et al. [13] further showed that hierarchical Bayesian approaches can be used for probabilistic RANS model calibration, avoiding many of the challenges associated with deterministic calibration techniques.

Despite the overall success of these prior approaches, however, solving the full Bayes' problem requires knowledge of the likelihood function, which can be difficult, and/or costly, to compute. In many cases, this likelihood function is approximated by a Gaussian distribution or is obtained using a surrogate model that is trained using available RANS simulations [9,10,14]. Although both of these approaches have proven successful for RANS parameter estimation problems, here we outline an alternative Bayesian approach based on the combination of approximate Bayesian computation (ABC) [15] and Markov chain Monte Carlo (MCMC) sampling [16] to determine unknown model parameters and their uncertainties. The ABC approach allows us to estimate the posterior distribution of model parameters, given some reference data, without knowledge of the likelihood function; as such, ABC is often referred to as a "likelihood-free" Bayesian method.

The ABC method was introduced, and first widely applied, in population genetics [16–18], and it was subsequently implemented in a wide range of other scientific areas [19–24] (detailed reviews are provided by Csilléry et al. [25], Marin et al. [26], Lintusaari et al. [27], Sisson et al. [28], and Beaumont [15]). More recently, ABC has been employed in engineering contexts for the estimation of rate coefficients in chemical kinetic models [29], for the estimation of boundary conditions in complex thermal-fluid flows [30,31], and for determining unknown model parameters in autonomic [32] and nonlinear [33] subgrid-scale closure models for LES. Doronina et al. [34] were the first to take advantage of ABC-MCMC for discovering model parameter values and uncertainties in a multiparameter RANS closure, using relatively simple homogeneous test cases as reference data for calibration of a nonequilibrium turbulence model [35–37] consisting of three coupled ordinary differential equations (ODEs).

In the present study, we verify and validate the ABC algorithm through the estimation of parameters in the same nonequilibrium turbulence model examined in Ref. [34], using reference data from the model itself (i.e., verification) and from DNS of periodically sheared homogeneous turbulence [38] (i.e., validation). We then demonstrate the use of an improved ABC approach with a calibration step, adaptive proposal, and MCMC sampling for the calibration of parameters in the Menter SST model. We show that the efficiency of the resulting ABC approach with improved MCMC, termed "ABC-IMCMC," permits the estimation of parameters using full computational fluid dynamics (CFD) simulations of inhomogeneous flows. In particular, we use ABC-IMCMC to estimate parameters in the Menter SST model given experimental reference data for an axisymmetric transonic bump [39], and using CFD model evaluations in OVERFLOW [40]. Recently, Schaefer et al. [41] and Zhao et al. [42] performed an uncertainty and sensitivity analysis of the Menter SST model for different turbulent flows, and we perform a related calibration study before initiating the Markov chains in order to determine which of the model parameters to include in the estimation procedure. It should be noted that we do not claim herein that ABC, with or without MCMC, is universally better or faster than other likelihood-based Bayesian methods, and we instead focus on demonstrating the flexibility and utility of the method for RANS model parameter estimation.

In the following, we describe the ABC-IMCMC method in Sec. II. In Sec. III, we describe the verification and validation tests for the nonequilibrium RANS model using both the classic ABC rejection algorithm and the ABC-IMCMC algorithm. In Sec. IV, we then present results from the estimation of parameters in the Menter SST RANS model using ABC-IMCMC with experimental reference data for an axisymmetric transonic bump. We provide detailed descriptions, in particular, of the calibration step and summary statistics used during the parameter estimation. Conclusions are provided at the end.

II. Approximate Bayesian Computation with Markov Chain Monte Carlo Sampling

The task of turbulence model parameter estimation can be expressed as an inverse statistical problem where we must determine model parameters $\boldsymbol{c}$ that satisfy $\mathcal{F}(\boldsymbol{c}) = \mathcal{D}$, where $\mathcal{F}$ is the model and $\mathcal{D}$ represents reference data from experiments or higher fidelity simulations. From a statistical perspective, this inverse problem can be solved by calculating the posterior distribution of $\boldsymbol{c}$ given $\mathcal{D}$ according to Bayes' theorem, which is expressed generically as

$$P(\boldsymbol{c}|\mathcal{D}) = \frac{L(\mathcal{D}|\boldsymbol{c})\pi(\boldsymbol{c})}{\int_{\boldsymbol{c}} L(\mathcal{D}|\boldsymbol{c})\pi(\boldsymbol{c})\,\mathrm{d}\boldsymbol{c}} \tag{1}$$

In the above theorem, $P(\boldsymbol{c}|\mathcal{D})$ is the posterior distribution, $L(\mathcal{D}|\boldsymbol{c})$ is the likelihood function, $\pi(\boldsymbol{c})$ is the prior distribution of model parameters, and $\int_{\boldsymbol{c}} L(\mathcal{D}|\boldsymbol{c})\pi(\boldsymbol{c})\,\mathrm{d}\boldsymbol{c}$ is a normalizing factor. A benefit of the Bayesian statistical approach is that $P(\boldsymbol{c}|\mathcal{D})$ naturally provides uncertainties associated with each estimated parameter, in contrast to other inversion techniques that provide only single-point estimates for unknown parameters.

To obtain $P(\boldsymbol{c}|\mathcal{D})$, we must, in general, calculate each of the terms on the right-hand side of Eq. (1). The prior distribution $\pi(\boldsymbol{c})$ in Eq. (1) is typically formed using our knowledge of unknown parameters, and

Downloaded by UNIVERSITY OF COLORADO on January 17, 2022 | http://arc.aiaa.org | DOI: 10.2514/1.J060308

it is often given (as in the current tests) by a uniform distribution with bounds that are sufficiently broad to contain the true parameter values.

The primary challenge in solving Eq. (1) is then the calculation of the likelihood function $L(\mathcal{D}|\boldsymbol{c})$, which gives the probability of obtaining the reference data for different choices of model parameters. Typically, this function is analytically intractable and computationally expensive to compute exactly, and so approximations (e.g., [5,6]) or surrogate modeling (e.g., [9,10,14]) is often used instead. Likelihood-free methods, by contrast, provide an alternative, and potentially highly flexible, method to obtain $P(\boldsymbol{c}|\mathcal{D})$, and here we use one such method—namely, ABC—to directly approximate the posterior without requiring a priori knowledge of the likelihood function.

A. Classic ABC Rejection Algorithm

In general terms, the ABC algorithm samples model parameters $\boldsymbol{c}$ from the prior distribution $\pi(\boldsymbol{c})$ and compares model outcomes, $\mathcal{D}' = \mathcal{F}(\boldsymbol{c})$, with the reference data $\mathcal{D}$. To reduce the computational expense of the approach, ABC makes use of summary statistics, $\mathcal{S}(\mathcal{D})$ and $\mathcal{S}' = \mathcal{S}(\mathcal{D}')$, to compare the model and reference data. Summary statistics can be a mean value, a standard deviation, a probability density function (pdf), or a subsample of the full data. The summary statistic comparison is performed using a statistical distance function, $d(\mathcal{S}, \mathcal{S}')$, such as the Kullback–Leibler divergence, the Hellinger distance, or simply the mean-square error.

If the modeled and reference summary statistics are similar to within some specified tolerance ϵ, where the model results are obtained for a given set of sampled parameter values, then these parameter values are considered to be sampled from the posterior distribution. These values are the outputs of the ABC algorithm [we also refer to them as accepted parameters because they were accepted according to the threshold condition $d(\mathcal{S}', \mathcal{S}) \leq \epsilon$]. Using the postprocessing techniques discussed in Sec. II.C, we can then use these accepted parameters to estimate the posterior distribution $P[\boldsymbol{c}|d(\mathcal{S}', \mathcal{S}) \leq \epsilon]$, where the estimate of the posterior becomes more accurate as the number of accepted parameters increases.

It should be noted that ABC is based on two main assumptions: i) the summary statistic is sufficient, which means that the posterior distribution using the full data and the posterior distribution using summary statistics are the same, such that $P(\boldsymbol{c}|\mathcal{S}) = P(\boldsymbol{c}|\mathcal{D})$; ii) if the threshold ϵ is sufficiently small (i.e., as $\epsilon \to 0$), then ABC produces the exact posterior distribution, $P(\boldsymbol{c}|\mathcal{S}) = \lim_{\epsilon \to 0} P[\boldsymbol{c}|d(\mathcal{S}', \mathcal{S}) \leq \epsilon]$. Although reducing the tolerance ϵ improves the approximation of the posterior, this also significantly increases the number of samples N that must be tested by the algorithm to generate enough accepted parameters for the posterior estimation. There are, however, ways to improve the parameter acceptance rate, including the MCMC method discussed in Sec. II.B.

In terms of the inputs to the ABC algorithm, we must provide: i) the reference data $\mathcal{D}$, ii) the model $\mathcal{F}$, iii) a function to evaluate the summary statistics $\mathcal{S}$ from the full data $\mathcal{D}$, iv) a statistical distance function $d(\mathcal{S}', \mathcal{S})$, v) a tolerance hyperparameter ϵ, vi) the number of parameters to sample N, and vii) the prior distribution $\pi(\boldsymbol{c})$. As output from this algorithm, we obtain a list of accepted parameters $\boldsymbol{c}_i$, which can then be used to estimate an approximate posterior joint pdf. The algorithm described above is called the rejection ABC algorithm (or classic ABC) and is provided in Algorithm 1. With respect to the number of parameters N, larger N leads to better estimates of the posterior. However, in practice, N is limited by the computational cost of the model evaluations and the available computational resources.

Samples from the prior in the classical ABC algorithm are completely independent from each other, which not only makes the ABC algorithm highly parallelizable, but also allows us to calculate the distance function between the modeled and reference summary statistics for each of the sampled parameters before comparing it to the threshold ϵ. Saving all calculated distances, we can then choose the desired acceptance rate $r \in [0, 1]$ by changing ϵ. We discuss the choice of ϵ in more detail in Sec. II.C, where we also provide an example of how the classical ABC algorithm is applied.

Algorithm 1: ABC rejection sampling algorithm

```
Calculate reference summary statistic S from D
Procedure ABC algorithm (N, ε)
    Sample N parameters c_i from prior distribution π(c)
    for each c_i do
        Calculate D' = F(c_i) from model
        Calculate model summary statistic S' from D'
        Calculate statistical distance d(S', S)
        if d(S', S) ≤ ε then
            Accept c_i
    return list of accepted c_i
Using all accepted c_i estimate approximate posterior joint pdf
```

B. ABC Algorithm with Markov Chain Monte Carlo Sampling

The classic ABC rejection algorithm described in the previous section can be computationally expensive, because the number of sampled parameters, N, grows exponentially with the number of unknown parameters, n, in the model. The computational cost of ABC can be significantly improved by using the MCMC method for sampling model parameters, resulting in a higher percentage of sampled parameters accepted for inclusion in the approximation of the posterior. The ABC-MCMC method (or MCMC without likelihood), introduced by Marjoram et al. [16], samples the next parameter $\boldsymbol{c}'$ from the proposal distribution $q(\boldsymbol{c}'|\boldsymbol{c}_i)$. Then, if the statistical distance d is within the tolerance ϵ, the proposed parameters are accepted with probability

$$h = \min\left[1, \frac{\pi(\boldsymbol{c}')q(\boldsymbol{c}_i|\boldsymbol{c}')}{\pi(\boldsymbol{c}_i)q(\boldsymbol{c}'|\boldsymbol{c}_i)}\right] \tag{2}$$

In practice, this is implemented by randomly selecting a number between 0 and 1, which bound h, and then checking whether this random number is less than h. This procedure is necessary to allow the Markov chain to satisfy the detailed balance condition [16].

The choice of proposal distribution q is crucial for enabling a high rate of convergence (with the number of iterations) of the ABC-MCMC algorithm to the approximate posterior distribution. A variable proposal with an adapting size and spatial orientation provides faster convergence, and here we follow the adaptive proposal procedure outlined by Haario et al. [43], where $q_i(\boldsymbol{c}'|\boldsymbol{c}_i) = q(\boldsymbol{c}'|\boldsymbol{c}_i, \mathcal{C}_i)$ is the Gaussian proposal with the current parameter $\boldsymbol{c}_i$ as the mean value and adaptive covariance $\mathcal{C}_i$. The covariance $\mathcal{C}_i$ is calculated as

$$\mathcal{C}_i = \begin{cases} s_n \mathrm{var} I_n, & \text{if } i < m \\ s_n \mathrm{cov}(\boldsymbol{c}_0, \ldots, \boldsymbol{c}_i), & \text{if } i \geq m \end{cases} \tag{3}$$

where $\mathrm{var}I_n$ is the initial estimate of the covariance, var is the variance of the parameters with $d \leq \epsilon$, I_n is the identity matrix, m is the length of the initial period without adaptation, and s_n is a constant that depends on the dimensionality of the parameter space, n, as $s_n = (2.4)^2/n$. This adaptation step does not introduce substantial additional computational cost, because the covariance $\mathrm{cov}(\boldsymbol{c}_0, \ldots, \boldsymbol{c}_i) \equiv \mathrm{cov}_i$ can be calculated recursively as i increases using the formula

$$\mathrm{cov}_i = \left(\frac{i-1}{i}\right)\mathrm{cov}_{i-1} + \left(\frac{1}{i+1}\right)(\boldsymbol{\mu}_{i-1} - \boldsymbol{c}_i)(\boldsymbol{\mu}_{i-1} - \boldsymbol{c}_i)^T \tag{4}$$

where $\boldsymbol{\mu}_i = [1/(i+1)]\sum_{k=0}^{i} \boldsymbol{c}_k$ is the average of all previous accepted parameter values, which also satisfies the recursive formula

$$\boldsymbol{\mu}_i = \boldsymbol{\mu}_{i-1} - \left(\frac{i}{i+1}\right)(\boldsymbol{\mu}_{i-1} - \boldsymbol{c}_i) \tag{5}$$

Although this adaptive Metropolis algorithm is no longer Markovian, Haario et al. [43] have shown that it has the correct ergodic properties, and the accuracy of the algorithm is close to the accuracy of the standard Metropolis–Hastings algorithm given a properly chosen proposal. Ultimately, the adaptation of the size and spatial orientation of the proposal distribution enables faster convergence to the stationary posterior distribution.

For a Gaussian proposal, $q_i(\boldsymbol{c}'|\boldsymbol{c}_i) = q_i(\boldsymbol{c}_i|\boldsymbol{c}')$ and h depends only on the prior. If the prior is uniform, then $\pi(\boldsymbol{c}_i) = \pi(\boldsymbol{c}')$, and the Gaussian proposal leads to $h = 1$ for any $\boldsymbol{c}'$. As a result, the algorithm reduces to a rejection method with correlated outputs [16]. In the more general case, h will not be uniformly equal to 1, and we must compute both $q(\boldsymbol{c}_i|\boldsymbol{c}')$ and $q(\boldsymbol{c}'|\boldsymbol{c}_i)$ to determine h from Eq. (2).

We also adopt a calibration step before performing the ABC-MCMC algorithm, introduced by Wegmann et al. [18]. There are three primary reasons that this calibration step is helpful. First, the bounds of the prior are not known a priori, and it is common to select an initial prior that may be overly broad or overly narrow. During the calibration step, the priors are adjusted to be larger or smaller depending on the variance in the parameters with $d \leq \epsilon$. Second, it is not clear a priori how a given choice of the distance threshold ϵ will correspond to the number of accepted parameters. Finally, the initial covariance used in the adaptive proposal is not known a priori, and it requires an initial estimate to ensure that we do not take overly large or small initial steps in the Markov chains. Specifically, the initial covariance $\mathcal{C}_0$ is calculated using the variance of the parameters with $d \leq \epsilon$ from the calibration step as $\mathcal{C}_0 = s_n \mathrm{var} I_n$, where I_n is the identity matrix. The calibration step is also used to define starting points for the Markov chains, where enough parameters $\boldsymbol{c}_0$ from the calibration step are randomly chosen to initialize each of the Markov chains; N_a is used to denote the number of Markov chains. The final ABC-MCMC algorithm with calibration step and adaptive proposal is termed the ABC algorithm with improved MCMC, or ABC-IMCMC, and is provided in Algorithm 2 and schematically summarized in Fig. 1.

It should be noted that any particular implementation of ABC-IMCMC requires the specification of the model, reference data, summary statistics, statistical distance function, and distance threshold. Specific choices for each of these quantities are outlined in the demonstrations presented in Secs. III and IV, and the generality of the resulting model parameters can be increased through the inclusion of more, and increasingly different, reference data. Eventually, for sufficiently broad reference data sources, the accuracy of the resulting model will be limited by the model form itself, rather than by any limitations intrinsic to the ABC-IMCMC method.

C. Postprocessing of ABC Results and Posterior Estimation

As a result of either the classic ABC or ABC-IMCMC algorithms outlined in Secs. II.A and II.B, we obtain a list of "accepted" parameter values, $\boldsymbol{c}_i$, that are assumed to have been sampled from the approximate posterior distribution. To estimate this approximated joint posterior, we can build an n-dimensional histogram and normalize it to create a discrete joint pdf, but the different choices of bin size and location can lead to distributions that have qualitatively different features, particularly when the number of counts in the histogram is small (as can be the case for small values of the threshold ϵ).

To avoid this dependence on bin size and location in the n-dimensional posteriors, we use Gaussian kernel density estimation (KDE) to represent each parameter sample with a Gaussian, and thereby obtain a continuous replacement for the discrete histogram. The standard deviation of the Gaussian kernel (i.e., the kernel bandwidth) determines the smoothness of the estimated distribution; here we use Scott's rule [44,45] to define the bandwidth in Gaussian KDE. To apply Gaussian KDE to the n-dimensional posteriors, we use the FFTKDE function from the KDEpy Python package (https://github.com/tommyod/KDEpy).

Algorithm 2: ABC-IMCMC algorithm with an initial calibration step and an adaptive proposal

Calculate reference summary statistic $\mathcal{S}$ from $\mathcal{D}$
Procedure Calibration step (N_c, r)
  Sample N_c parameters $\boldsymbol{c}_i$ from prior distribution $\pi(\boldsymbol{c})$
  for each $\boldsymbol{c}_i$ **do**
    Calculate $\mathcal{D}' = \mathcal{F}(\boldsymbol{c}_i)$ from model
    Calculate model summary statistic $\mathcal{S}'$ from $\mathcal{D}'$
    Calculate statistical distance $d_i(\mathcal{S}', \mathcal{S})$
  Using all $d_i(\mathcal{S}', \mathcal{S})$ estimate the distribution $P(d)$
  Define tolerance ϵ such that $P(d \leq \epsilon) = r$
  Randomly choose $\boldsymbol{c}_0$ from $\boldsymbol{c}_i$ parameters with $d \leq \epsilon$
  Adjust prior based on variance of parameters with $d \leq \epsilon$
  Estimate covariance $\mathcal{C}_0$ from parameters with $d \leq \epsilon$
  return $\boldsymbol{c}_0, \mathcal{C}_0, \epsilon$
procedure MCMC without likelihood ($\boldsymbol{c}_0$, ϵ, $\mathcal{C}_0$, m, N_a)
  Start with accepted parameters $\boldsymbol{c}_0$ and covariance $\mathcal{C}_0$
  $i \coloneqq 0$
  while $i < N_a$ **do**
    Sample $\boldsymbol{c}'$ from proposal $q_i(\boldsymbol{c}'|\boldsymbol{c}_i) = q(\boldsymbol{c}'|\boldsymbol{c}_i, \mathcal{C}_i)$
    Calculate $\mathcal{D}' = \mathcal{F}(\boldsymbol{c}')$ from model
    Calculate model summary statistic $\mathcal{S}'$ from $\mathcal{D}'$
    Calculate statistical distance $d(\mathcal{S}', \mathcal{S})$
    if $d(\mathcal{S}', \mathcal{S}) \leq \epsilon$ **then**
      Accept $\boldsymbol{c}'$ with probability

$$h = \min\left[1, \frac{\pi(\boldsymbol{c}')q_i(\boldsymbol{c}'|\boldsymbol{c}_i)}{\pi(\boldsymbol{c}_i)q_i(\boldsymbol{c}_i|\boldsymbol{c}')}\right]$$

      if Accepted **then**
        Increment i
        Set $\boldsymbol{c}_i = \boldsymbol{c}'$
        Update proposal covariance $\mathcal{C}_i$
  return list of accepted $\boldsymbol{c}_i$
Using all accepted $\boldsymbol{c}_i$ estimate posterior joint pdf

To visualize the n-dimensional posterior, we plot one- and two-dimensional (2D) marginalized pdfs produced by Gaussian KDE. Single estimates of unknown parameters are then taken from the n-dimensional posterior as the maximum a posteriori probability (MAP) values. Although MAP values are typically thought of as point estimates, we approximate these values in the present study using the modes of the posterior distributions. Bayesian confidence intervals for the MAP estimates can be directly computed from the n-dimensional posterior, and we can also propagate the posterior distribution to make uncertainty predictions for the quantity of interest.

III. Demonstration of ABC: Nonequilibrium RANS Model

We first demonstrate the use of the classic ABC rejection algorithm (Algorithm 1) and ABC-IMCMC (Algorithm 2) to estimate parameters in a nonequilibrium RANS model for predictions of kinetic energy time series in periodically sheared homogeneous turbulence. Two different reference data sources are considered here. The first source is the nonequilibrium RANS model itself, thereby testing the ability of the ABC algorithms to recover known parameter values (i.e., verification tests). These verification tests demonstrate how well we can recover nominal parameter values when the reference data are free from measurement error and can be exactly recreated by the model; a similar test was performed for the estimation of boundary conditions in LES by Christopher et al. [30]. The second reference data source is provided by the DNS study of Yu and Girimaji [38], showing the ability of ABC to estimate parameters based on higher-fidelity computational reference data (i.e., validation tests). In this case, the model and reference data are independent, and this test

Downloaded by UNIVERSITY OF COLORADO on January 17, 2022 | http://arc.aiaa.org | DOI: 10.2514/1.J060308

Downloaded by UNIVERSITY OF COLORADO on January 17, 2022 | http://arc.aiaa.org | DOI: 10.2514/1.J060308

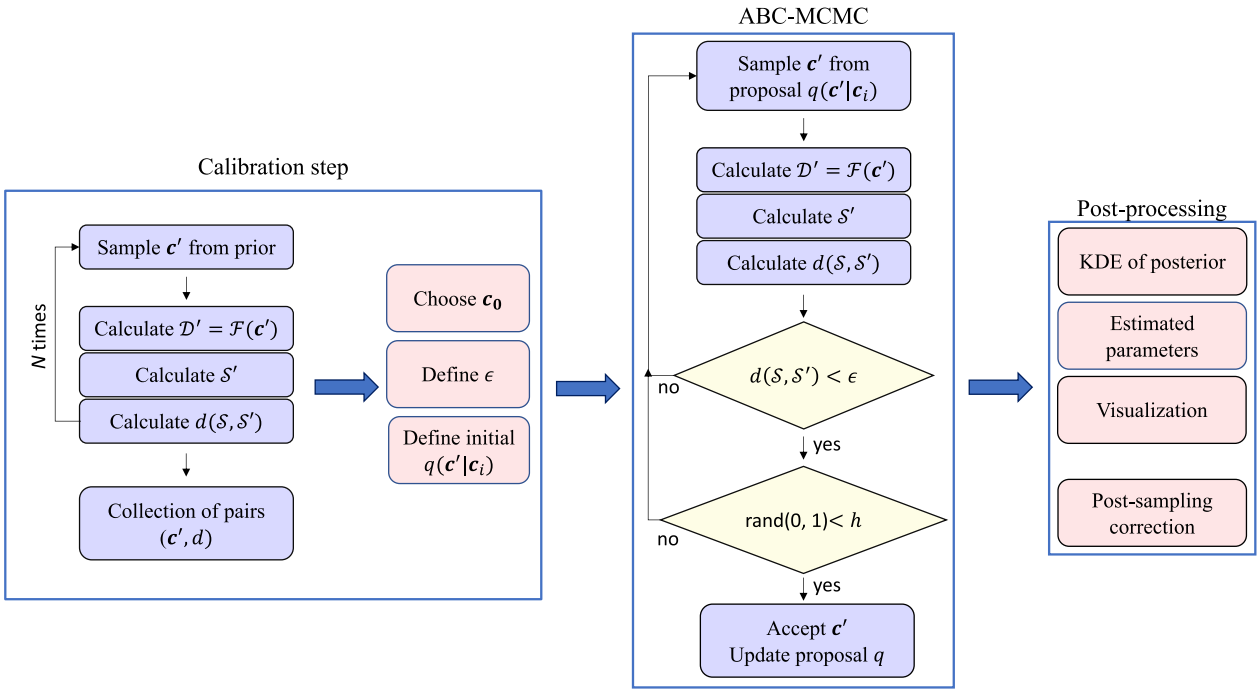


Fig. 1 Schematic representation of the ABC-IMCMC algorithm, showing the calibration step, core MCMC approach, and postprocessing steps.

demonstrates the ability of ABC to recover unknown parameter values when the model is not expected to perfectly match the reference data.

Before continuing, we note that the parameter values estimated here should not be taken as universal for the nonequilibrium RANS model. It is likely that other sources of reference data, and even other choices of summary statistic, will yield different parameter estimates. However, in Sec. IV we show how ABC-IMCMC can be used with multiple summary statistics to increase the generality of the resulting parameter values, and multiple different physical configurations and flows can be incorporated in a single ABC parameter estimation in future work.

A. Nonequilibrium RANS Model

The unclosed Reynolds stress appearing in the ensemble averaged RANS equations can be written in terms of isotropic and anisotropic (or deviatoric) parts as $\overline{u_i' u_j'} = (2/3)k\delta_{ij} + ka_{ij}$ where k is the turbulence kinetic energy and a_{ij} is the Reynolds stress anisotropy tensor. Because the governing equation for k includes relatively few unclosed terms, the primary challenge in RANS modeling is to represent the tensor a_{ij}, which is unclosed. A number of models have been proposed for this tensor, including various nonlinear eddy viscosity models [46–48], but by far the most widely used models continue to be equilibrium models where it is assumed that a_{ij} is proportional to the mean strain rate tensor. Such models include the classical k-ε and k-ω models, as well as their many variants (see Speziale and So [1] for a review).

However, it is now widely understood that equilibrium models become inaccurate in complex flows, and in particular those flows with rapid spatial and temporal variations in mean flow properties [35]. Such "nonequilibrium" turbulent flows arise in many practical applications, including supersonic and hypersonic vehicles where interactions occur between shock waves and turbulent boundary layers, as well as in internal combustion engines where pistons rapidly strain the flow. Nonequilibrium effects introduced in such flows can be significant, requiring new modeling approaches.

The nonequilibrium turbulence model considered in this demonstration of ABC was identified by Hamlington and Ihme [37] as a nearly ideal model, in terms of both accuracy and computational simplicity, for capturing the effects of rapid straining in piston-driven and rapidly compressed flows. This model is expressed for an incompressible flow as

$$\frac{\partial a_{ij}}{\partial t} + \bar{u}_k \frac{\partial a_{ij}}{\partial x_k} = -\alpha_1 \frac{\varepsilon}{k} a_{ij} + \alpha_2 \bar{S}_{ij} \tag{6}$$

where $\bar{u}_i$ is the mean velocity, $\bar{S}_{ij} = (1/2)(\partial \bar{u}_i/\partial x_j + \partial \bar{u}_j/\partial x_i)$ is the mean strain rate tensor, ε is the kinetic energy dissipation rate, and the coefficients α_1 and α_2 are given by

$$\alpha_1 = \frac{P_k}{\varepsilon} - 1 + C_1, \qquad \alpha_2 = C_2 - \frac{4}{3} \tag{7}$$

where $P_k = -ka_{ij}\bar{S}_{ij}$ is the kinetic energy production rate. Parameters C_1 and C_2 in Eq. (7) have traditionally been tied to the choice of pressure-strain rate correlation model [49,50], but here they are treated as unknowns determined by ABC.

It should be noted that the model in Eq. (6) has a rigorous basis in the exact anisotropy transport equation and accounts for both the return to isotropy of unstrained turbulence [i.e., the first term on the right-hand side of Eq. (6)] and the generation of anisotropy in strained turbulence [i.e., the second term on the right-hand side of Eq. (6)]. This model is also the basis for the quasi-analytical nonequilibrium anisotropy model outlined in [35,36].

The test case considered here is homogeneous, which permits substantial simplifications to the RANS and anisotropy equations. In particular, because spatial derivatives of turbulent fluctuating statistics are identically zero in homogeneous turbulence, the Reynolds stresses have no effect on the evolution of $\bar{u}_i$, and the spatial derivative of a_{ij} on the left-hand side of Eq. (6) is identically zero. As a result, for homogeneous flows where $\bar{S}_{ij}$ varies in time only, the evolution of a_{ij} is given by

$$\frac{da_{ij}}{dt} = -\left(\frac{P_k}{\varepsilon} - 1 + C_1\right)\frac{\varepsilon}{k} a_{ij} + \left(C_2 - \frac{4}{3}\right)\bar{S}_{ij} \tag{8}$$

where $a_{ij} = a_{ij}(t)$ is a function of time only and Eq. (7) has been used to replace the α_i coefficients appearing in Eq. (6). Similarly, in homogeneous turbulent flows, $k = k(t)$ and $\varepsilon = \varepsilon(t)$ also depend only on time and their dynamics are represented here using the standard equations employed in classical k-ε models, namely,

$$\frac{dk}{dt} = P_k - \varepsilon \tag{9}$$

$$\frac{d\varepsilon}{dt} = (C_{\varepsilon 1} P_k - C_{\varepsilon 2}\varepsilon)\frac{\varepsilon}{k} \tag{10}$$

where $C_{\varepsilon 1}$ and $C_{\varepsilon 2}$ are additional unknown parameters that will be estimated using the ABC procedure.

The system of nonlinear and coupled ODEs represented by Eqs. (8–10) constitutes the nonequilibrium turbulence anisotropy closure examined in this demonstration of ABC, and depends on the unknown model parameters $\boldsymbol{c} = (C_1, C_2, C_{\varepsilon 1}, C_{\varepsilon 2})$. For a given choice of $\bar{S}_{ij}$ and initial conditions for a_{ij}, k, and ε, Eqs. (8–10) can be straightforwardly integrated as a system of coupled nonlinear ODEs.

B. Periodically Sheared Homogeneous Turbulence

The nonequilibrium anisotropy closure described in Sec. III.A is applied here to predict the evolution of the turbulence kinetic energy in periodically sheared homogeneous turbulence [38]. For this case, the turbulence is assumed to be initially isotropic and unstrained such that $a_{ij} = 0$ and $\bar{S}_{ij} = 0$ for $t < 0$. For $t \geq 0$, the turbulence is then subjected to a periodic mean strain rate tensor $\bar{S}_{ij}$ with a shearing frequency ϖ, given by

$$\bar{S}_{ij} = \frac{S}{2}\begin{bmatrix} 0 & \sin(\varpi t) & 0 \\ \sin(\varpi t) & 0 & 0 \\ 0 & 0 & 0 \end{bmatrix} \tag{11}$$

At time $t = 0$, it is assumed that $k = k_0$ and $\varepsilon = \varepsilon_0$, and the initialization of the case is completed by defining $Sk_0/\varepsilon_0 = 3.3$ and $\varpi/S = 0.5$. The specific case of $\varpi/S = 0.5$ is chosen for the present demonstration because this shearing frequency is close to the frequency at which the system transitions to a fully nonequilibrium state, as described in Hamlington and Dahm [36], and it is thus anticipated to provide a challenging inverse modeling problem for ABC. Using this strain rate time series and initial conditions, the model data, $\mathcal{D}' = \mathcal{F}(\boldsymbol{c})$, for the ABC rejection and ABC-IMCMC algorithms are provided by integrating the system of coupled ODEs in Eqs. (8–10) using the ODEINT function from scipy.integrate [51]. ODEINT uses a variable time step with error checking and solves systems of ODEs using the LSODA algorithm from the FORTRAN library ODEPACK [52]. It automatically selects between nonstiff (Adams) and stiff (BDF) methods. The method was originally detailed in Petzold [53].

C. Setup of Classical ABC and ABC-IMCMC Algorithms

In the following, we verify and validate the classical ABC rejection (Algorithm 1) and ABC-IMCMC (Algorithm 2) algorithms by estimating model parameters for the nonequilibrium anisotropy closure represented by Eqs. (8–10). Reference data for this case are taken from two sources: i) an integration of the nonequilibrium model using the nominal parameter values $\boldsymbol{c} = (1.5, 0.8, 1.44, 1.83)$ [36] for the verification test, and ii) the study by Yu and Girimaji [38] for the validation test, where DNS was performed for a series of different values of ϖ/S.

The reference, $\mathcal{S}$, and modeled, $\mathcal{S}'$, summary statistics for both the verification and validation cases are given by the specific values of the turbulence kinetic energy, $k_i = k(t_i)$, at the times $t = t_i$ when the DNS reference data from Yu and Girimaji [38] are provided. This summary statistic thus represents a subset of all data $\mathcal{D}'$ produced by the model for any choice of $\boldsymbol{c}$.

The distance function is defined simply as the 2-norm of the difference between the reference and modeled summary statistics, namely,

$$d(\mathcal{S}, \mathcal{S}') = \left[\sum_i (k_i' - k_i)^2\right]^{1/2} \tag{12}$$

Here k_i' and k_i indicate the turbulence kinetic energy from the model and reference data, respectively.

To construct the posterior distribution for the classical ABC rejection algorithm, we test $N = 60^4 = 12,960,000$ parameters $\boldsymbol{c}$ obtained by dividing each dimension of the prior into 60 evenly spaced intervals, where the bounds along each dimension are $c_1 = C_1 \in [0.5, 5]$, $c_2 = C_2 \in [0, 2]$, $c_3 = C_{\varepsilon 1} \in [0, 3]$, and $c_4 = C_{\varepsilon 2} \in [1, 2.5]$. For each of the parameters in this "gridded" approach to sampling the prior, we calculate the distance function between the modeled and reference summary statistics. Saving all calculated distances, we choose the desired acceptance rate by changing ϵ. If ϵ is sufficiently small, the approximated posterior resulting from the ABC algorithm recovers the exact posterior distribution. In practice, however, an ϵ that is too small leads to too few sampled parameters

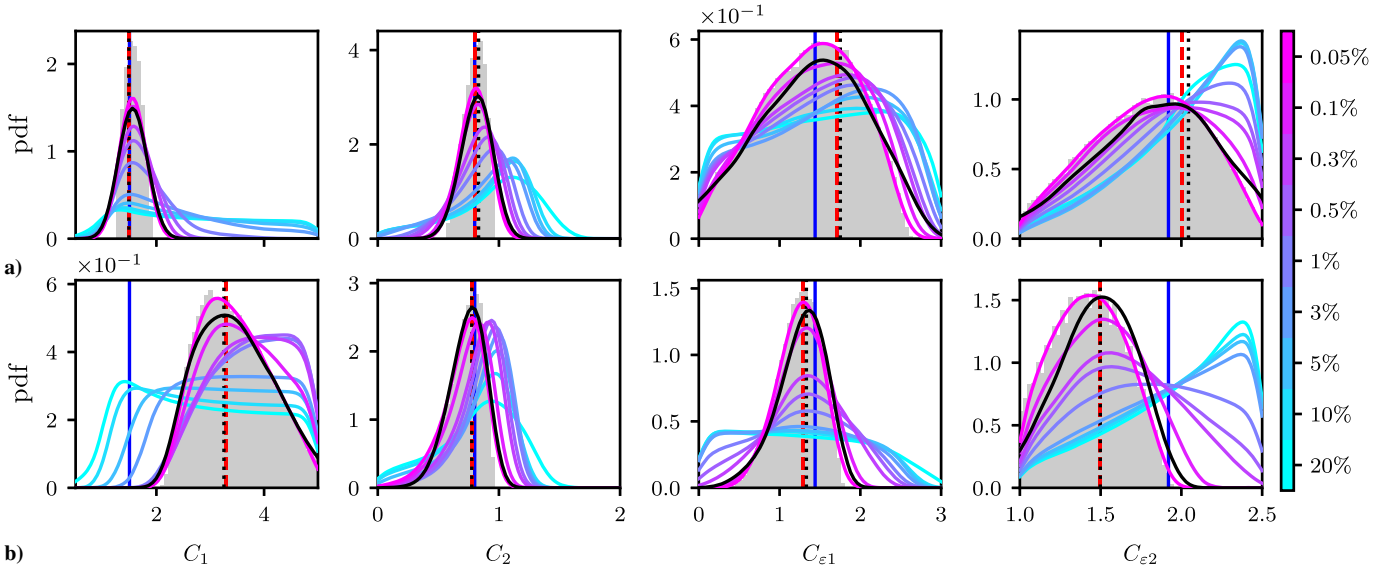


Fig. 2 Marginal posteriors for parameter estimation in the nonequilibrium RANS model for a) the verification case and b) the validation case. Solid colored lines correspond to the percentage of accepted simulations for the classical ABC method. Raw marginals for a 0.05% acceptance rate (i.e., before Gaussian kernel density estimation) are shown by gray bars. Solid black lines indicate the posteriors obtained from ABC-IMCMC. Vertical lines show the nominal parameter values $\boldsymbol{c} = (1.5, 0.8, 1.44, 1.83)$ (blue dashed lines) and the estimated MAP values from classical ABC (red dashed lines) and from ABC-IMCMC (black dotted lines).

Downloaded by UNIVERSITY OF COLORADO on January 17, 2022 | http://arc.aiaa.org | DOI: 10.2514/1.J060308

Downloaded by UNIVERSITY OF COLORADO on January 17, 2022 | http://arc.aiaa.org | DOI: 10.2514/1.J060308

passing the acceptance threshold, $d(\mathcal{S}, \mathcal{S}') \leq \varepsilon$, resulting in a poorly converged posterior. Conversely, relaxing the acceptance criterion too much (i.e., using a larger ϵ) can lead to the final posterior distribution being biased toward the prior. Thus, the hyperparameter ϵ should be reasonably small but should also take into account the computational cost of every model evaluation. For both the verification and validation tests with the classical ABC rejection algorithm presented here, we consider a range of ϵ values to show the convergence of the posterior distribution.

For the verification and validation tests using the ABC-IMCMC algorithm, we performed roughly 130,000 evaluations of the model (for each of the cases) including $N_c = 50,625$ evaluations in the calibration step, resulting in a total of 10,000 parameters accepted. The acceptance rate for the calibration step was set to $r = 0.1\%$, which resulted in an acceptance threshold $\epsilon = 0.44$ for the chains. Four chains ran in parallel and accepted $N_a = 2,500$ parameters each. The accepted parameters from the chains were then combined and the posterior distributions were estimated.

D. Results and Discussion

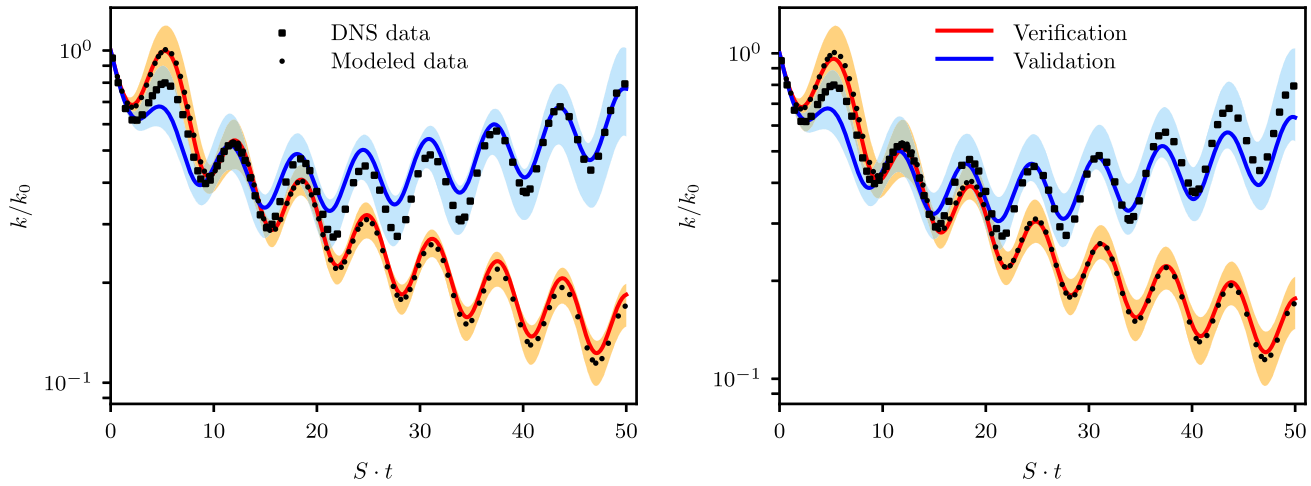
Figure 2 shows marginal posterior distributions for C_1, C_2, $C_{\varepsilon 1}$, and $C_{\varepsilon 2}$ for both the verification and validation cases. All distributions are constructed using Gaussian KDE with bandwidths defined by Scott's rule. Marginal posteriors for different values of ϵ are shown in Fig. 2, with corresponding acceptance rates changing from 20 to 0.05% as ϵ decreases. For the classical ABC test, the resulting MAP values from the posteriors are shown to become increasingly similar as the acceptance rate decreases. For ABC-IMCMC, the resulting posteriors are close to those obtained from classical ABC using acceptance rates of 0.05 and 0.1%.

For classical ABC, estimates of the unknown parameters are obtained as the MAP values of the four-dimensional (4D) posterior distribution with a 0.05% acceptance rate. For the verification test shown in Fig. 2a, the MAP values are $C_1 = 1.49$, $C_2 = 0.8$, $C_{\varepsilon 1} = 1.71$, and $C_{\varepsilon 2} = 2.005$. Parameters C_1 and C_2 agree closely with the nominal values (i.e., the values used to generate the reference data) and have relative errors of 0.66 and 0.0%, respectively. Although the individual MAP values of $C_{\varepsilon 1}$ and $C_{\varepsilon 2}$ differ from the nominal values (corresponding to relative errors of 18.75% and 9.56%, respectively), their ratio is close to the ratio of the nominal values (additional discussion of this point is provided at the end of this section). This demonstrates the ability of the ABC rejection algorithm to recover expected parameter values in the verification test. For ABC-IMCMC, the estimated MAP values for the verification and validation cases are, respectively, $\boldsymbol{c} = (1.49, 0.832, 1.752, 2.044)$. The marginal pdfs and the estimated parameters shown in Fig. 2 for ABC-IMCMC are thus very close to those obtained from classical ABC, using 100 times fewer model evaluations.

Results for the validation test using classical ABC in Fig. 2b, where the reference data are from the DNS, again show a convergence of the MAP estimates from the posteriors as ϵ decreases. The MAP values for classical ABC are $C_1 = 3.29$, $C_2 = 0.78$, $C_{\varepsilon 1} = 1.29$, and $C_{\varepsilon 2} = 1.495$. The MAP estimates of this case for C_1 and $C_{\varepsilon 2}$ are larger and smaller, respectively, than the nominal values $\boldsymbol{c} = (1.5, 0.8, 1.44, 1.83)$ [36], whereas Fig. 2b shows that C_2 and $C_{\varepsilon 1}$ remain close to the nominal values. For the ABC-IMCMC algorithm, we again obtain MAP parameter estimates similar to those for classical ABC [where $\boldsymbol{c} = (3.25, 0.776, 1.332, 1.498)$], but at a computational cost that is two orders of magnitude smaller. We note that the nominal value of C_2 has a fundamental physical justification based on consideration of rapidly strained turbulence [54,55], and so the similarity of the estimated value to the nominal value when using ABC and ABC-IMCMC with DNS reference data is not unexpected (although it is also not guaranteed).

The accuracy of the parameters estimated using classical ABC is indicated in Fig. 3a, which shows the evolution of the turbulence kinetic energy $k(t)/k_0$ for the verification and validation cases. Results for the verification case are in very good agreement with the reference data, again indicating that ABC can accurately recover parameter values used to generate the reference data. The results for the validation case do not match quite as closely with the DNS reference data, but the overall agreement is reasonable and the initial decrease, followed by a subsequent increase, of k is captured by the model. This behavior is due, in part, to the larger value of C_1 and smaller value of $C_{\varepsilon 2}$ estimated by ABC, as compared with the nominal values. Most importantly, the predictions of the model using parameter values estimated from ABC compare better with the DNS data than the prediction of the model obtained with the nominal values (shown as dots in Fig. 3 and used as reference data for the verification case). We can propagate the uncertainty through the model to estimate uncertainty intervals on the output quantity of interest. Figure 3 shows the 99% confidence interval for the modeled kinetic energy, and this confidence interval encompasses the DNS reference data used in the validation case. As expected given the similarity of the MAP parameter values obtained from ABC and ABC-IMCMC, the kinetic energy results in Fig. 3b using ABC-IMCMC show similarly good agreement with the verification and validation data.

To facilitate visualization of the 4D posteriors resulting from the classical ABC procedure for the nonequilibrium model, marginal pdfs for the validation case are shown on the diagonal subplots in



a) Results for classical ABC **b) Results for classical ABC-IMCMC**

Fig. 3 Turbulence kinetic energy $k(t)/k_0$ for the nonequilibrium model computed using estimated parameters (solid lines) and reference data (points) for the periodically sheared turbulence case. The shaded areas indicate the 99% confidence intervals.

Downloaded by UNIVERSITY OF COLORADO on January 17, 2022 | http://arc.aiaa.org | DOI: 10.2514/1.J060308

Fig. 4 for each of C_1, C_2, $C_{\varepsilon 1}$, and $C_{\varepsilon 2}$. Two-dimensional marginalized joint pdfs are shown on the upper-diagonal subplots, and conditional pdfs taken at the MAP values are shown on the lower-diagonal subplots of Fig. 4. These 2D marginalized joint pdfs allow us to identify parameter correlations that may not be obvious from the marginalized posteriors in Fig. 2. It should be noted that posteriors for the verification case are similar to those from the validation case, and posteriors for ABC-IMCMC are similar to those from classical ABC, and we consequently only show posteriors for the validation case with classical ABC herein.

Figure 4 shows that $C_{\varepsilon 1}$ and $C_{\varepsilon 2}$ are closely correlated for the validation case, and the same is also true for the verification case. This explains the shift in the MAP values of these two parameters indicated for the verification case in Fig. 2a. That is, even though both $C_{\varepsilon 1}$ and $C_{\varepsilon 2}$ are shown to be larger than their nominal values, their ratio is nearly identical to the ratio of the nominal values. This indicates that only the ratio of these two parameters is important in the present tests. The importance of this ratio is consistent with the analysis of the periodically sheared case by Hamlington and Dahm [36], where it was shown that $(C_{\varepsilon 2} - 1)/(C_{\varepsilon 1} - 1)$ was a parameter of fundamental importance in determining the evolution of the production to dissipation rate P_k/ε and the transition to the saturated nonequilibrium state for sufficiently large shearing frequencies.

IV. Demonstration of ABC-IMCMC: Menter SST RANS Model

The demonstration in Sec. III shows the effectiveness of classical ABC and ABC-IMCMC for model parameter estimation in a relatively simple homogeneous flow. In the vast majority of cases, however, we would instead like to use reference data from more complex inhomogeneous flows, for which each model evaluation during the ABC procedure is more expensive. This additional computational cost motivates the use of the more efficient ABC-IMCMC algorithm, summarized in Fig. 1.

In the following, we use ABC-IMCMC to estimate parameters in the Menter SST RANS model, given experimental reference data for an axisymmetric transonic bump. We simultaneously use summary statistics based on the mean velocity, shear stress, pressure, and separation and reattachment points, demonstrating the flexibility of the ABC-IMCMC approach. Because of the computational cost of this test case, we perform an initial calibration step to determine which of the unknown SST model parameters to include in the estimation process, in addition to initializing the Markov chains. It will be seen that this initial step allows us to reduce the number of unknown parameters estimated in the model, thereby substantially reducing the computational cost. Final parameter estimates from ABC-IMCMC and comparisons with experimental data are provided at the end of this section.

Before continuing, we once again emphasize that the demonstration in this section is intended to be illustrative of the full ABC-IMCMC approach for an inhomogeneous flow where the model data are provided by forward runs using a CFD code. The resulting estimated parameters should, therefore, not be taken as universal, although the generality of the model can be improved in the future through the simultaneous use of reference data from many different flows; the ABC-IMCMC procedure is sufficiently flexible to accommodate a range of data types and sources.

A. Menter SST RANS Model

The classical Menter SST model is a two-equation eddy-viscosity RANS model introduced by Menter [56] in 1994. It is based on the baseline model [56], which combines the Wilcox $k - \omega$ model [57] in the near-wall region and a standard $k - \varepsilon$ model in the wake region of the boundary layer. This model blending was introduced to take advantage of the freestream independence of the $k - \varepsilon$ model in the outer part of the boundary layer, combined with the superior behavior of the $k - \omega$ model in the logarithmic part of the boundary layer in compressible flows and equilibrium flows with adverse pressure gradients. For convenience, the $k - \varepsilon$ model is transformed into the $k - \omega$ formulation, which differs from the original $k - \omega$ model by a cross-diffusion term in the ω equation and also has different coefficients. Using the same transport equations, the Menter SST model incorporates Bradshaw's hypothesis that the principal turbulent shear stress is proportional to the turbulent kinetic energy k.

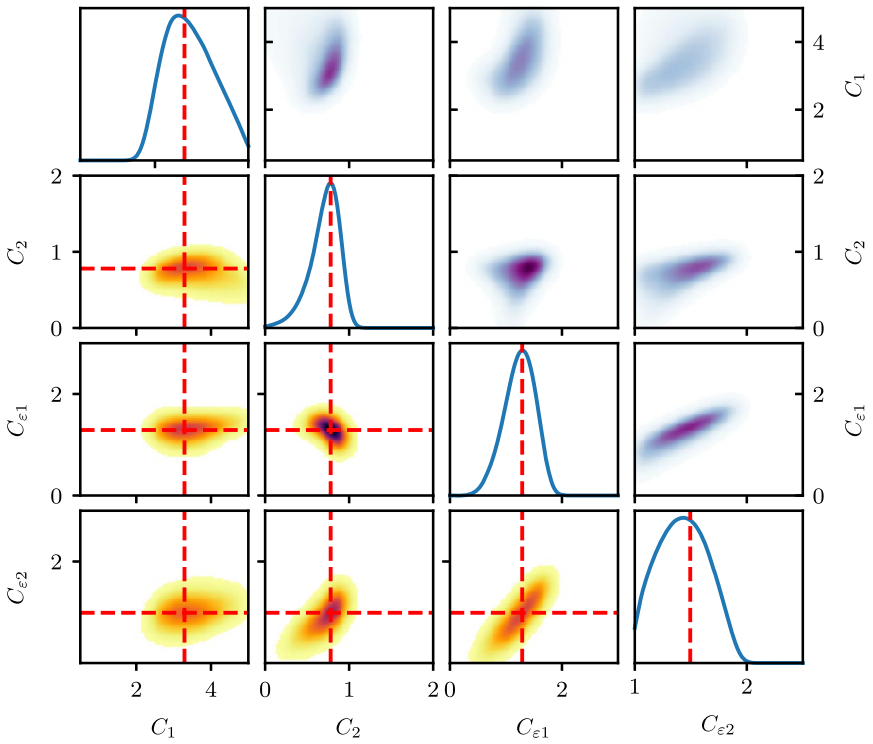


Fig. 4 Posterior distributions of accepted parameters from classical ABC for the nonequilibrium RANS model for the validation case. Diagonal subplots show one-dimensional marginal pdfs, upper-diagonal subplots show 2D marginalized pdfs, and lower-diagonal subplots show conditional pdfs taken at the MAP values. The red dashed lines represent estimated parameters taken from the MAP values of the joint posterior.

Downloaded by UNIVERSITY OF COLORADO on January 17, 2022 | http://arc.aiaa.org | DOI: 10.2514/1.J060308

In this study, we follow the nomenclature of the NASA Langley Turbulence Modeling Resource (TMR; https://turbmodels.larc.nasa.gov/sst.html), and the complete formulation and explanation of the Menter SST model can be found in Menter [56]. Here we repeat the key components of the model in order to identify the parameters that will be estimated in the present ABC-IMCMC approach. The transport equations for k and ω are

$$\frac{\partial(\rho k)}{\partial t}+\frac{\partial(\rho\bar{u}_j k)}{\partial x_j}=P_k-\beta^*\rho\omega k+\frac{\partial}{\partial x_j}\left[(\mu+\sigma_k\mu_t)\frac{\partial k}{\partial x_j}\right] \tag{13}$$

$$\frac{\partial(\rho\omega)}{\partial t}+\frac{\partial(\rho\bar{u}_j\omega)}{\partial x_j}=\frac{\gamma}{\nu_t}P_k-\beta\rho\omega^2+\frac{\partial}{\partial x_j}\left[(\mu+\sigma_\omega\mu_t)\frac{\partial\omega}{\partial x_j}\right]+2(1-F_1)\rho\sigma_{\omega2}\frac{1}{\omega}\frac{\partial k}{\partial x_j}\frac{\partial\omega}{\partial x_j} \tag{14}$$

where ρ is the density, $\nu_t=\mu_t/\rho$ is the turbulent kinematic viscosity, and F_1 is the blending function, such that $F_1=1$ in the near-wall region, activating the original $k-\omega$ model, and $F_1=0$ away from the surface, activating the transformed $k-\varepsilon$ model. The F_1 function is defined as

$$F_1=\tanh(\arg_1^4),\quad \arg_1=\min\left[\max\left(\frac{\sqrt{k}}{\beta^*\omega y},\frac{500\nu}{y^2\omega}\right),\frac{4\rho\sigma_{\omega2}k}{CD_{k\omega}y^2}\right],$$
$$CD_{k\omega}=\max\left(\frac{2\rho\sigma_{\omega2}}{\omega}\frac{\partial k}{\partial x_j}\frac{\partial\omega}{\partial x_j},10^{-20}\right) \tag{15}$$

where y is the distance from the wall and $\arg_1$ goes to zero far from walls because of the y and y^2 factors in the denominators of all three terms. Thus, the cross-diffusion term with $(1-F_1)$ in Eq. (14) disappears near the wall. The coefficients $\phi=(\gamma,\beta,\sigma_k,\sigma_\omega)$ are different for each part of the blended model, with ϕ_1 denoting values for the $k-\omega$ model and ϕ_2 for the $k-\varepsilon$ model. The combined model in Eqs. (13) and (14) thus uses a single ϕ defined as

$$\phi=F_1\phi_1+(1-F_1)\phi_2 \tag{16}$$

Closure coefficients and their nominal values are provided in Table 1. Other closure coefficients are defined using the values in Table 1 as

$$\gamma_1=\frac{\beta_1}{\beta^*}-\sigma_{\omega1}\frac{\kappa^2}{\sqrt{\beta^*}},\qquad \gamma_2=\frac{\beta_2}{\beta^*}-\sigma_{\omega2}\frac{\kappa^2}{\sqrt{\beta^*}} \tag{17}$$

The turbulence kinetic energy production P_k in Eqs. (13) and (14) is defined as

Table 1 Nominal values of Menter SST model coefficients

Coefficient	Nominal value
σ_{k1}	0.85
σ_{k1}	1
$\sigma_{\omega1}$	0.5
$\sigma_{\omega2}$	0.856
β_1	0.075
β_2	0.828
β^*	0.09
κ	0.41
a_1	0.31

$$P_k=-\rho\overline{u_i'u_j'}\frac{\partial\bar{u}_i}{\partial x_j},$$
$$\rho\overline{u_i'u_j'}=\frac{2}{3}\rho k\delta_{ij}-\mu_t\left(\frac{\partial\bar{u}_i}{\partial x_j}+\frac{\partial\bar{u}_j}{\partial x_i}-\frac{2}{3}\frac{\partial\bar{u}_k}{\partial x_k}\delta_{ij}\right) \tag{18}$$

where μ_t is the turbulent (dynamic) eddy viscosity.

In the $k-\varepsilon$ and $k-\omega$ two-equation models, the principal shear-stress $\tau\equiv-\rho\overline{u'v'}$ is usually computed as $\tau=\mu_t(\partial\bar{u}/\partial y)$. However, based on Bradshaw's assumption, the shear stress in the boundary layer is proportional to the turbulent kinetic energy k as $\tau=\rho a_1 k$, with a_1 being constant. Taking this into account, Menter [56] defined the turbulent eddy viscosity as

$$\mu_t=\frac{\rho a_1 k}{\max(a_1\omega,\Omega F_2)} \tag{19}$$

where $\Omega=\sqrt{2\bar{R}_{ij}\bar{R}_{ij}}$ with $\bar{R}_{ij}=1/2(\partial\bar{u}_i/\partial x_j-\partial\bar{u}_j/\partial x_i)$. The second blending function F_2 appearing in this definition for μ_t is given by

$$F_2=\tanh(\arg_2^2),\qquad \arg_2=\max\left(\frac{\sqrt{k}}{\beta^*\omega y},\frac{500\nu}{y^2\omega}\right) \tag{20}$$

In an adverse-pressure-gradient boundary layer, production of k is larger than its dissipation (i.e., $\Omega>a_1\omega$) and the second term in the parenthesis of Eq. (19) becomes dominant over the first term, which is the conventional eddy-viscosity formulation, $\mu_t=\rho k/\omega$, in the $k-\omega$ model.

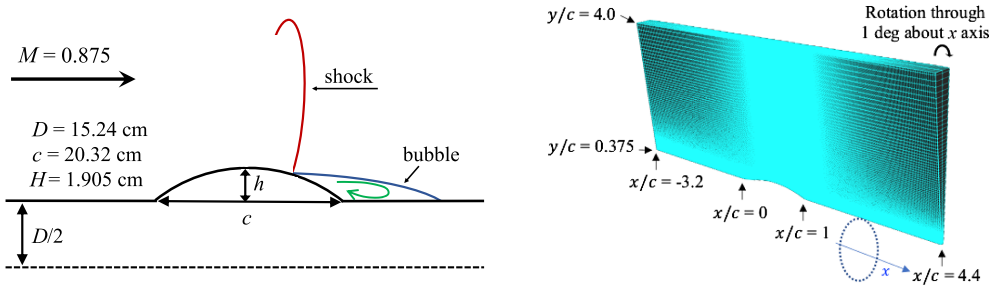
The set of nine parameters given in Table 1 comprises the unknown coefficients $\boldsymbol{c}$ that must be specified in the Menter SST model. Based on the results from the calibration step described in Sec. II.C, we will ultimately reduce the number of unknown parameters to only four: β^*, β_1/β^*, β_2/β^*, and a_1. These are the parameters that will be estimated in the present demonstration of ABC-IMCMC.

B. Axisymmetric Transonic Bump

To estimate parameters in the Menter SST model, we use experimental reference data for an axisymmetric transonic bump from Bachalo and Johnson [39]. This is a widely used test case for shock-induced separated flow, followed by reattachment. The axisymmetric bump in this experiment is a circular-arc bump with a height of $H=1.905$ cm and a length of $c=20.32$ cm attached to a cylinder that is $D=15.24$ cm in diameter. The flow has a freestream Mach number $M=U_{\text{inf}}/a_{\text{inf}}=0.875$, where U_{inf} is the freestream velocity and a_{inf} is the speed of sound corresponding to a temperature of $T_{\text{inf}}=540$°R. The combination of the shock and trailing-edge adverse-pressure-gradient causes flow separation with reattachment downstream of the bump (thereby creating a separation bubble). The Reynolds number $Re=2.763\times10^6$ is calculated based on U_{inf} and the bump length c. All of the computational case parameters are provided on the TMR website (https://turbmodels.larc.nasa.gov/axibump_val.html) and Fig. 5a shows a schematic of the experimental setup that is modeled in the simulations.

Solutions of the Menter SST model for different parameters $\boldsymbol{c}$ were obtained here using the NASA OVERFLOW code version 2.2n (https://overflow.larc.nasa.gov/). OVERFLOW is a three-dimensional (3D) compressible flow code that solves the time-dependent RANS equations using multiple overset structured grids. The code can also operate in 2D or axisymmetric mode. It has been broadly verified and validated [58,59] and is widely used across the aerospace industry.

The axisymmetric transonic bump case has been used previously for Menter SST model validation in OVERFLOW [59] and is thus ideally suited for the calibration of SST model parameters in the present work. Uncertainty quantification for the Menter SST model coefficients [41] has also been performed for this case using the same computational grid as that used here. Minor modifications were made to OVERFLOW to allow the code to read turbulence model



a) Axisymmetric transonic bump experiment **b) Axisymmetric transonic bump simulation**

Fig. 5 Schematics showing a) the experimental setup of the axisymmetric transonic bump geometry, including dimensions and operating conditions [39], and b) the computational mesh used in the axisymmetric RANS simulations with the Menter SST model in OVERFLOW.

Downloaded by UNIVERSITY OF COLORADO on January 17, 2022 | http://arc.aiaa.org | DOI: 10.2514/1.J060308

coefficients from the parameters file in order to perform the ABC-IMCMC algorithm.

For axisymmetric problems, OVERFLOW can be configured in an axisymmetric mode with a three-plane grid. The center plane lies on the x, z plane, and the other two planes lie at $\pm 1°$ rotations from this plane. All computational solutions were obtained using a computational grid with 721×321 cells on the center plane provided by the TMR website. The geometry and grid configuration are shown in Fig. 5b. Each simulation ran for 5000 time steps, requiring ~7 minutes on a single node with two eight-core Intel Xeon E5-2670 2.6 GHz processors.

C. Calibration and Setup of ABC-IMCMC

Before performing ABC-IMCMC, we complete a series of calibration steps that are intended to reduce the computational cost of the parameter estimation procedure, as well as provide the threshold ϵ and the initial values of $\boldsymbol{c}$ and the covariance of the proposal, q, for the Markov chains. During the calibration process, we also select appropriate summary statistics for use with ABC-IMCMC. It is anticipated that this initial calibration will be used with any implementation of ABC that requires computationally expensive CFD simulations. To a large extent, this process also removes the need for substantial user input before initiating the Markov chains, because the selection of initial parameter values, covariances, and thresholds can be automated during the calibration.

To begin, we immediately reduce the number of targeted unknown parameters in the Menter SST model from nine (i.e., those listed in Table 1) to five. In particular, in their sensitivity study of the parameters in the Menter SST model, Schaefer et al. [41] showed that β^*, $\sigma_{\omega 1}$, β^*/β_1, β^*/β_2, and a_1 are the most sensitive parameters in simulations of the same axisymmetric transonic bump case examined here. Based on this analysis, we thus restrict the parameter estimation procedure to, at most, these five parameters, and the nominal values from Table 1 are used for the other four parameters.

The first calibration step is then subsequently used to determine appropriate summary statistics for the ABC-IMCMC procedure. For this step, we sampled $N = 6^5 = 7776$ parameter values, $\boldsymbol{c}$, from a five-dimensional (5D) uniform grid with 6 samples per dimension. Given the relatively small number of samples, we use the less computationally efficient classic ABC rejection algorithm (i.e., Algorithm 1) for this calibration. The advantage of this algorithm during the calibration process is that the samples chosen do not depend on the acceptance criteria (as opposed to Markov chains, where samples are chosen based on knowledge of the previously accepted sample), allowing us to store the model output and measure the distance between reference and modeled summary statistics after all simulations have been performed. This allows us to build posterior distributions for various summary statistics and threshold values, and to choose the best statistics and thresholds for the parameter estimation using Markov chains.

We use experimental data for the axisymmetric transonic bump from Bachalo and Johnson [39] as reference summary statistics. The experiment provides the pressure coefficient $C_p = (\bar{p} - p_{\text{inf}})/\frac{1}{2}\rho U_{\text{inf}}^2$ along the bump wall, as well as eight mean velocity and turbulent shear stress transverse (i.e., wall normal) profiles at $x/c = -0.25$, 0.688, 0.813, 0.938, 1.0, 1.125, 1.25, and 1.375. Thus, the available reference summary statistics, which we denote here as $\mathcal{S}_k(x_i, y_j)$ for different streamwise, x_i, and wall normal, y_j, experimental measurement locations, are the pressure coefficient $\mathcal{S}_1(x_i, y_j) = C_p(x_i, y_j)$, the mean velocity $\mathcal{S}_2(x_i, y_j) = \bar{u}(x_i, y_j)/U_{\text{inf}}$, the turbulent shear stress $\mathcal{S}_3(x_i, y_j) = \overline{u'v'}(x_i, y_j)/U_{\text{inf}}^2$, and the separation and reattachment points for the separation bubble created after the leading shock, denoted x_{sep} and x_{reattach}, respectively. Corresponding modeled summary statistics, $\mathcal{S}'_k(x_i, y_j)$, are then obtained from simulations in OVERFLOW, where the mean pressure and velocity are directly output by the code and the turbulent shear stress was calculated during postprocessing as

$$\overline{u'v'} = -\frac{\mu_t}{\rho}\left(\frac{\partial \bar{u}}{\partial y} + \frac{\partial \bar{v}}{\partial x}\right) \tag{21}$$

where the turbulent eddy viscosity μ_t was taken from SST model calculation.

Given a particular summary statistic $\mathcal{S}_k(x_i, y_j)$, we define the distance function as the 2-norm of the difference between the reference and modeled statistics, namely,

$$d_k(\mathcal{S}_k, \mathcal{S}'_k) = \left\{\sum_j \sum_i [\mathcal{S}'_k(x_i, y_j) - \mathcal{S}_k(x_i, y_j)]^2\right\}^{1/2} \tag{22}$$

where summation over repeated indices is not implied, and i and j span the data points where the reference summary statistics are provided. To combine multiple types of reference data into a single distance function, we normalize each individual summary statistic distance, d_k from Eq. (22), by the maximum over all x_i and y_j, denoted $\max \mathcal{S}_k$, and by number of points N_k in each summary statistic, yielding

$$d(\mathcal{S}, \mathcal{S}') = \left\{\sum_k \frac{1}{N_k}\left[\frac{d_k(\mathcal{S}_k, \mathcal{S}_{k'})}{\max \mathcal{S}_k}\right]^2\right\}^{1/2} \tag{23}$$

For distance functions including error in the separation and reattachment points, we add as a condition that the corresponding statistical distance d_{sep} must be less than a given threshold, where the distance is defined as

$$d_{\text{sep}} = [(x'_{\text{sep}} - x_{\text{sep}})^2 + (x'_{\text{reattach}} - x_{\text{reattach}})^2]^{1/2} \tag{24}$$

Here, x_{sep} and x'_{sep} indicate the reference and modeled separation points, respectively, and x_{reattach} and x'_{reattach} are the corresponding reattachment points.

Figure 6 shows marginal posteriors from the ABC rejection algorithm for the five parameters β^*, $\sigma_{\omega 1}$, β_1, β_2, and a_1 using the three different summary statistics individually (i.e., pressure coefficient, mean velocity, and turbulent shear stress profiles). This figure shows that the marginal posteriors for β_2 and a_1 have completely different MAP values when the shear stresses are used for the summary

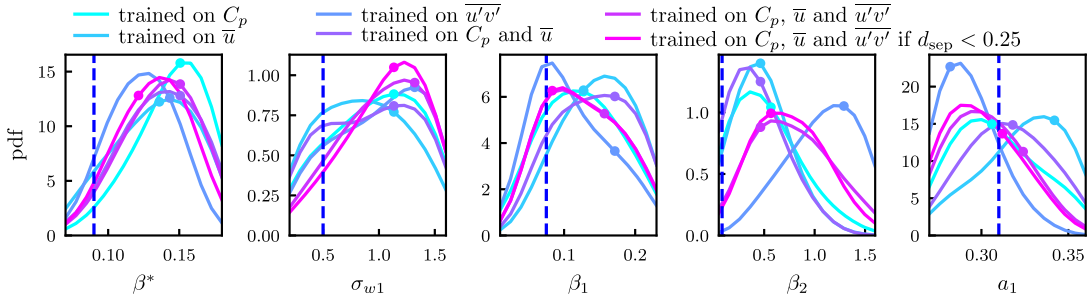


Fig. 6 Marginal posteriors from the calibration of ABC-IMCMC for the Menter SST model and the axisymmetric transonic bump. Line colors correspond to the different summary statistics. Colored dots show the MAP parameter values from the full five-dimensional posterior, and the vertical blue dashed lines show the nominal parameter values listed in Table 1.

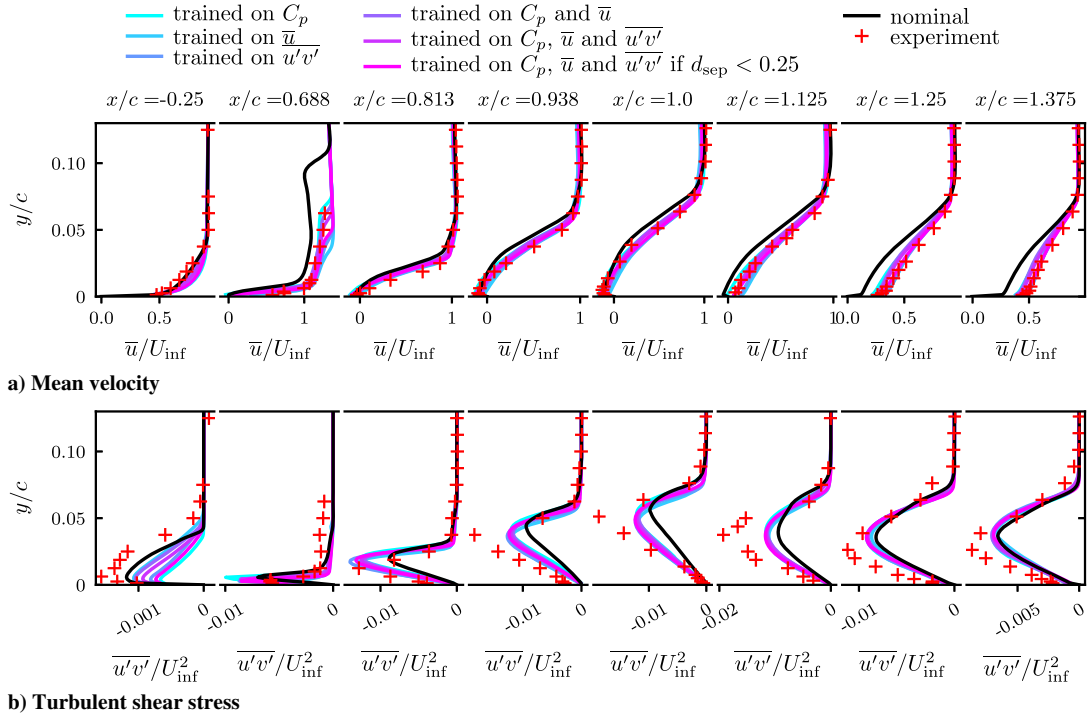
statistic in the ABC approach. This indicates that the SST model may not be able to simultaneously predict C_p, $\bar{u}$, and $\overline{u'v'}$ with a high degree of precision using the same parameter values.

Figure 6 also shows marginal posterior distributions after combining the summary statistics in various ways. In particular, we consider the following combinations: i) pressure coefficient $\mathcal{S}_1$ and mean velocity $\mathcal{S}_2$; ii) pressure coefficient, mean velocity, and turbulent shear stress, $\mathcal{S}_1$–$\mathcal{S}_3$; and iii) the same as ii, but with the condition that the separation and reattachment distance d_{sep} be less than 0.25. Figure 6 shows that the marginals for the combined summary statistics exhibit some features of the marginals for each statistic separately, resulting in posteriors that appear similar to a blend of the individual marginals.

To compare results for different summary statistics, we estimated MAP values of the joint probability distributions with 3% accepted parameters for all six summary statistics presented in Fig. 6, and we performed forward simulations with these parameters in OVERFLOW. Figure 7 shows the resulting mean velocity and turbulent shear stress profiles, and Fig. 8 shows the corresponding pressure coefficient profile. In general, as compared with model results using the nominal parameter values from Table 1, the model results with estimated parameters from ABC agree more closely with the experimental results for mean velocity and shear stress at nearly all locations. The nominal results are only better than the ABC results for these two summary statistics at the first measurement location, $x/c = -0.25$. Figure 8 shows that results for the pressure coefficient are generally similar for each of the models using the estimated parameter values from ABC. However, the nominal values from Table 1 do give reasonable agreement with the experimental measurements for this statistic, despite the more noticeable disagreement for $\bar{u}$ and $\overline{u'v'}$ shown in Fig. 7.

Taken together, Figs. 7 and 8 indicate that any choice of summary statistics in the ABC procedure will generally yield parameter estimates that provide better overall agreement with the experiments than the nominal values given in Table 1. As such, we thus choose to use all available reference statistics in the remaining tests, resulting in a combined distance function based on the pressure coefficient, mean velocity, and turbulent shear stress, with the condition that the error in the separation and reattachment points must be less than 0.25.

During the course of the first calibration step described above, we noticed a strong linear correlation between β^* and β_1 (with a correlation coefficient of 0.79) in the posterior of accepted parameters. Correspondingly, we performed a second calibration step, again with the ABC rejection algorithm, with $N = 28,804$ samples of the five parameters β^*, $\sigma_{\omega 1}$, β_1/β^*, β_2/β^*, and a_1 (i.e., a uniform grid with 6, 13, 6, 7, and 8 samples per dimension, respectively). Figure 9a shows



a) Mean velocity

b) Turbulent shear stress

Fig. 7 Experimental data [39] and simulation results produced using the Menter SST model with nominal coefficients from Table 1 and the estimated MAP values from Fig. 6.

Downloaded by UNIVERSITY OF COLORADO on January 17, 2022 | http://arc.aiaa.org | DOI: 10.2514/1.J060308

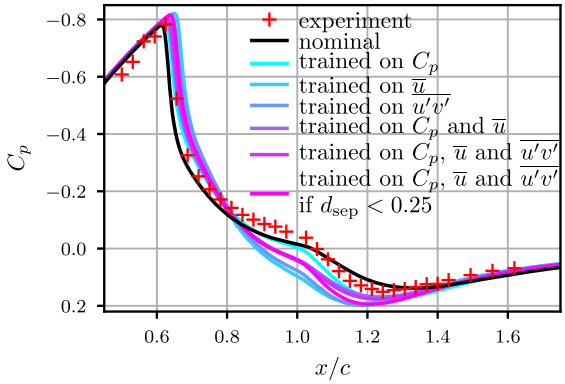


Fig. 8 Experimental data [39] and simulation results for the pressure coefficient C_p produced using the Menter SST model with nominal coefficients from Table 1 and the estimated MAP values from Fig. 6.

the resulting marginal distributions, where the larger number of samples for $\sigma_{\omega 1}$ was chosen to demonstrate that the marginal distribution of this parameter is close to uniform. Thus, to reduce the amount of computation, we removed $\sigma_{\omega 1}$ from the set of unknown parameters and set its value to the nominal value $\sigma_{\omega 1} = 0.5$.

With these four parameters and the combined summary statistic, a final calibration step was performed with $N = 12^4 = 20,736$ samples of the parameters β^*, β_1/β^*, β_2/β^*, and a_1 (i.e., a uniform grid with 12 samples per dimension). Figure 9b shows the resulting marginal distributions for this step, revealing that the MAP values for each parameter are contained within the bounds of the parameter values, and that the posteriors are converging as ϵ decreases.

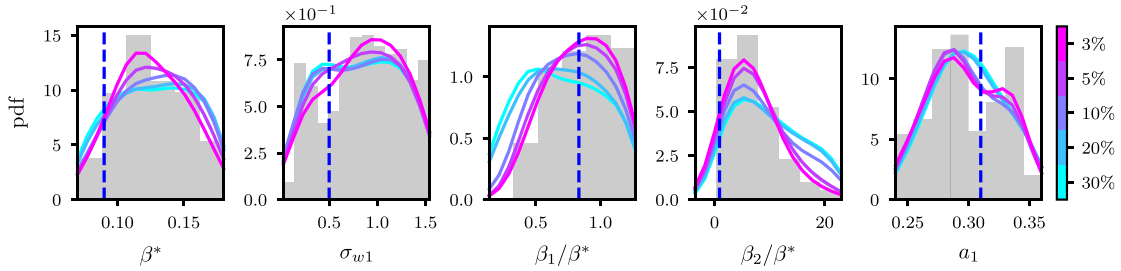
Using the 4D posterior distribution from this final calibration, we defined necessary characteristics for the MCMC component of the ABC-IMCMC algorithm (see the schematic in Fig. 1). In particular, we set the threshold ϵ such that $P[d(\mathcal{S}', \mathcal{S}) \leq \epsilon] = 0.03$ (i.e., the maximum distance value of 3% accepted parameters), and we defined the standard deviation of the initial Gaussian kernel for the Markov chains as 0.25 the standard deviation of the marginal posteriors formed by accepting 3% of the sampled parameters. The starting parameter values for the chains were also randomly chosen from these accepted parameters.

D. Results and Discussion

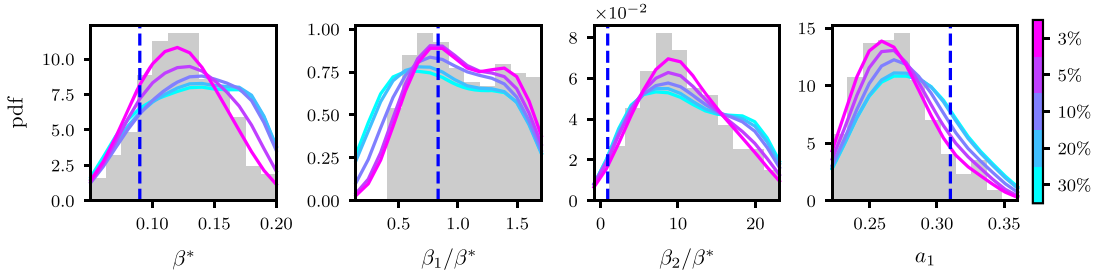
After completion of the calibration described in the previous section, we initiated $N_a = 200$ independent Markov chains for the estimation of β^*, β_1/β^*, β_2/β^*, and a_1 in the Menter SST model, using all available experimental reference summary statistics for the axisymmetric transonic bump. Each of the chains was initialized using parameter values randomly chosen from the accepted parameters (with 3% acceptance rate) in the final calibration step. For an initial period of $m = 100$ steps, the chains were progressed without kernel adaptation.

The Markov chains were then advanced, with kernel adaptation, according to Algorithm 2 (see also Fig. 1). These chains yielded 118,052 accepted parameters that were then used to estimate the 4D posterior distribution of unknown parameter values in the Menter SST model. The total number of sampled parameters (number of OVERFLOW runs) was 801,413 and required roughly 88,000 h on a single node with two eight-core Intel Xeon E5-2670 2.6 GHz processors. The low acceptance rate was caused by the strict condition on the error in the separation and reattachment points, $d_{\text{sep}} \leq 0.25$. However, as compared with the calibration steps using classical ABC where only 3% of the sampled parameters were accepted, using ABC-IMCMC nearly 15% of the parameters were accepted. The resulting posterior is the primary product of the ABC-IMCMC procedure, and Fig. 10 shows the resulting one-dimensional (1D) and 2D marginalizations of the posterior, as well as the 2D conditional distributions at the MAP values of each pair of parameters.

The MAP values of the posterior distribution shown in Fig. 10 provide estimates for the four unknown parameters; a summary of these values, along with the corresponding nominal values, is shown in Table 2. Although the MAP estimates for β^*, β_1/β^*, and a_1 are different from the nominal values, they nevertheless remain the same order of magnitude. By contrast, the MAP estimate for β_2/β^* is over 10 times larger than the nominal value. This parameter is responsible for setting the balance of the production and dissipation of ω, particularly further from the wall where the $k-\varepsilon$ model is active. This, in turn, corresponds to the location at which the shear stress in Fig. 10 is largest, and ABC-IMCMC effectively increases β_2/β^* to the greatest extent possible (i.e., without affecting the accuracy of other summary statistics) in order to drive the shear stress to larger magnitudes. This is also indicated by the calibration result shown in Fig. 6, where the posterior based on stress summary statistic



a) Five parameters and 28,804 samples.



b) Four parameters and 20,736 samples.

Fig. 9 Marginal posteriors from the calibration of ABC-IMCMC for the Menter SST model and the axisymmetric transonic bump. Line colors correspond to the percentage of accepted simulations. Raw marginals for a 3% acceptance rate (i.e., before Gaussian kernel density estimation) are shown by gray bars. Vertical blue dashed lines show the nominal parameter values listed in Table 1.

Downloaded by UNIVERSITY OF COLORADO on January 17, 2022 | http://arc.aiaa.org | DOI: 10.2514/1.J060308

Downloaded by UNIVERSITY OF COLORADO on January 17, 2022 | http://arc.aiaa.org | DOI: 10.2514/1.J060308

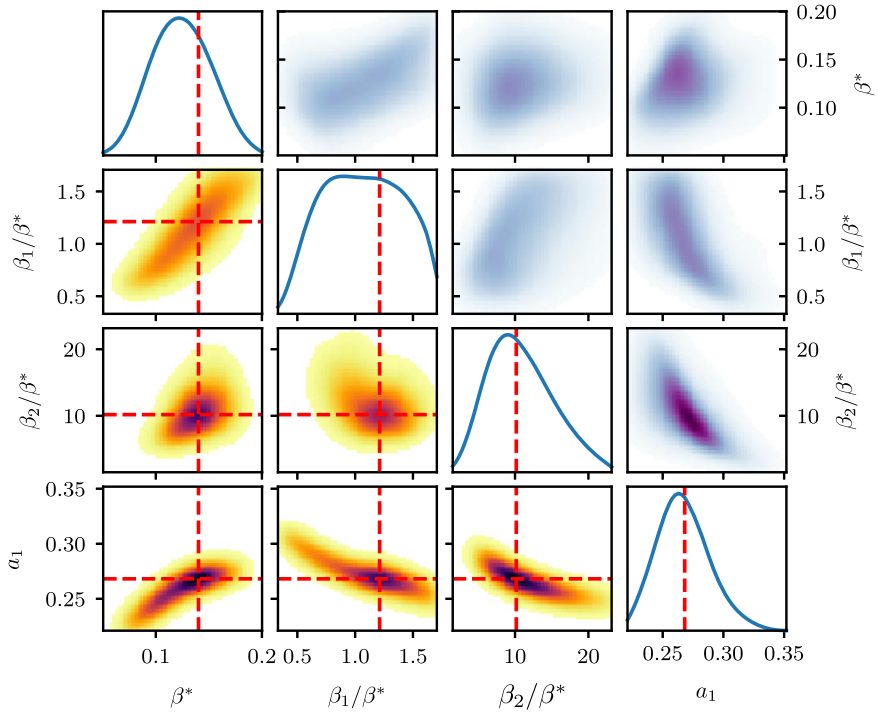


Fig. 10 Posterior distributions of accepted parameters for the Menter SST model using experimental reference data for an axisymmetric transonic bump [39]. Diagonal subplots show one-dimensional marginal pdfs, upper-diagonal subplots show 2D marginalized pdfs, and lower-diagonal subplots show conditional pdfs taken at the MAP values. The red dashed lines represent estimated parameters from the MAP values of the joint posterior.

Table 2 Estimated parameters from ABC-IMCMC for the Menter SST model using experimental reference data for an axisymmetric transonic bump [39]

Coefficient	Nominal value	Estimated value
β^*	0.09	0.14
β_1/β^*	0.833	1.212
β_2/β^*	0.92	10.17
a_1	0.31	0.268

corresponds to a substantially larger MAP value of β_2, as compared with the other cases.

Mean velocity and turbulent shear stress profiles resulting from OVERFLOW simulations with the estimated and nominal parameter values are shown in Fig. 11, and Fig. 12 shows the corresponding results for C_p and the mean velocity along the wall (indicative of the separation and reattachment points). Figures 11 and 12 show that there is a substantial overall improvement in the ability of the SST model to predict the experimental mean velocity and shear stress profiles, at the expense of slightly reduced agreement with the experimental measurements of C_p. However, the flexibility of the ABC-IMCMC method allows a user to easily adjust the weighting of different terms in the combined distance function such that improved agreement for C_p, or improvements in only a certain region of the flow (e.g., before flow separation), can be prioritized. The prediction of the separation point shown in Fig. 12b is also relatively similar for the estimated and nominal values, although the reattachment point is better predicted using the estimated parameters.

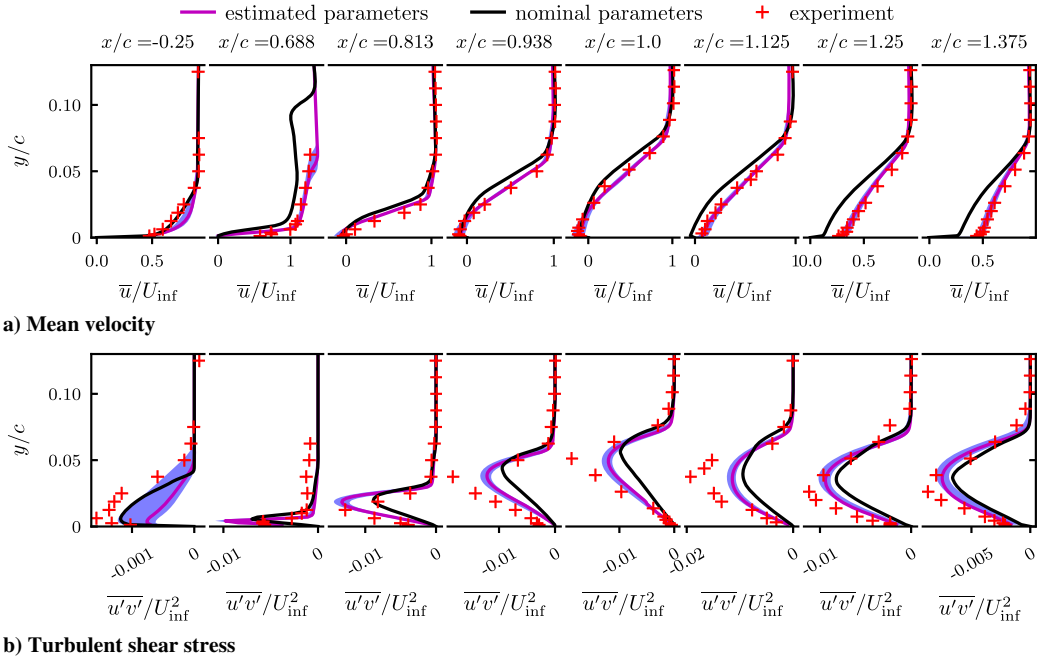
Beyond indicating the MAP values of the parameters, the posteriors in Fig. 10 also indicate that a_1 is positively correlated with β^*, and the widths of the posteriors indicate the degree of confidence in the MAP values as the best parameter estimates. Confidence in the MAP value of β_1/β^* is relatively weak, for example, as indicated by the broader posteriors for this parameter.

The effect of uncertainty in the MAP estimates can be propagated through the models to estimate uncertainty intervals on the output quantities of interest. To this end, we use all of the samples accepted in the ABC-IMCMC algorithm and estimate the distribution of the modeled profiles. The shaded areas in Figs. 11 and 12 indicate the 95% confidence interval for each distribution based on this sampling approach. In general, there is relatively little variability in the results for different choices of accepted parameters, and the greatest variability is observed in the mean velocity along the surface shown in Fig. 12b. This variability along the surface is most likely connected to the broad posteriors for β_1/β^* shown in Fig. 10, because this parameter affects the balance of production and dissipation of ω in the near-wall region, where the results in Fig. 12b are computed.

It should be noted that, for the present axisymmetric bump case, the calibration steps described in Sec. IV.C provide reasonable estimates for the posteriors and the MAP values. Indeed, this will commonly be the case, because the classical ABC used for the calibration steps is intended to be fully consistent with the ABC-IMCMC approach. The critical question, however, is the following: How do we most efficiently sample parameters in order to grow the number of retained parameters used to calculate the posterior distributions? The posteriors become increasingly converged as the number of sampled parameters increases, and we obtain an increasingly precise estimate of the MAP value. Continuing to add parameters using the calibration approach is relatively inefficient, with only 3% of all parameters sampled accepted for the posterior. Using ABC-IMCMC, however, we retained nearly 15% of all sampled parameters, corresponding to a fivefold improvement in the use of computational resources to construct the posterior. It is precisely this efficiency gain that IMCMC enables, and it will be even more pronounced as the number of unknown parameters n increases.

V. Conclusions

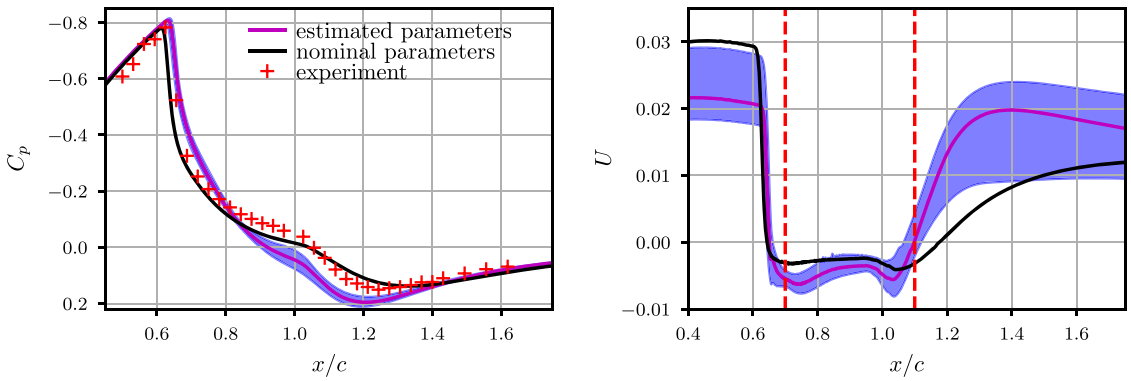
In this study, the estimation of RANS turbulence model parameters using ABC has been demonstrated. Many recent studies of model parameter estimation and uncertainty quantification have focused on statistical approaches. For example, Bayesian inference can be used to provide posterior distributions of unknown parameters, but knowledge of the likelihood function is required, which can be expensive to compute. By contrast, ABC uses a series of approximations to estimate the posterior without knowledge of the likelihood function.



a) Mean velocity

b) Turbulent shear stress

Fig. 11 Experimental data [39] and simulation results produced using the Menter SST model with nominal coefficients from Table 1 and the estimated MAP values from Table 2. The shaded areas indicate the 95% confidence interval.



a) Pressure coefficient C_p

b) Mean velocity along the surface

Fig. 12 Experimental data [39] and simulation results produced using the Menter SST model with nominal coefficients from Table 1 and the estimated MAP values from Table 2. The shaded area indicates the 95% confidence interval.

Applying ABC to turbulence model parameter estimation reduces the computational burden of Bayesian inference and provides a flexible tool for model calibration. Ultimately, the primary motivation for a Bayesian approach in RANS model calibration is that a posterior distribution of unknown parameters is desired that includes both point estimates of these parameters, as well as credible intervals for these estimates. This paper has shown ABC to be a viable alternative probabilistic parameter estimation method to approaches that estimate the likelihood function, either using a presumed form or a surrogate model.

Here a detailed description of the ABC methodology has been provided, including the baseline algorithm, acceleration using MCMC sampling, a calibration step, and an adaptive proposal. To demonstrate the use of ABC for turbulence model calibration, model parameters are estimated in a nonequilibrium RANS model applied to periodically sheared homogeneous turbulence, and in the Menter SST model applied to an axisymmetric transonic bump. Through these demonstrations, this paper showed the ABC-IMCMC approach to be an effective and efficient method for estimating unknown model parameters, as well as their uncertainties.

Although the MCMC procedure and adaptive proposal accelerate the ABC process and reduce the requirement for computational resources during the parameter estimation, the choice of summary statistics is a crucial component of ABC. These statistics must be sufficiently sensitive to changes in model parameters and must represent the dependence of the underlying reference data on these parameters. From this perspective, the classical ABC rejection algorithm, despite its high computational cost, has a noticeable advantage. Because parameter samples in this algorithm are independent of each other, the output from the simulations with each sampled parameter can be stored and one can experiment with different choices of the summary statistic, distance function metric, and tolerance, to see how this affects the results. Thus, as shown here, the calibration step in the ABC-IMCMC algorithm can provide not only hyperparameters for initiating the Markov chains, but can also be used to design the best summary statistics and distance function.

The estimation of turbulence model parameters in this study shows that models are often unable to simultaneously match all reference data fields, and ABC provides different estimated parameters for different summary statistics constructed from available reference data. As such, ABC provides an additional understanding of the model behavior and its ability to reconstruct real turbulent flows. Once the posterior distribution of model parameters has been estimated, it is further shown that parameter uncertainties can be

Downloaded by UNIVERSITY OF COLORADO on January 17, 2022 | http://arc.aiaa.org | DOI: 10.2514/1.J060308

propagated through the model to estimate uncertainty intervals on the output quantity of interest.

Finally, it should be noted that the present study provides a demonstration of ABC for two types of RANS models and two different sets of reference data. However, the approach is completely general and can also easily be applied to other models and other flows. As such, the present demonstration should be taken as illustrative of the power of the ABC-IMCMC approach, and the framework has been uploaded to GitHub (https://github.com/tesla-cu/turbABC) for use by other researchers on other model development tasks in the future. The model parameters estimated here are also not intended to be taken as universally accurate; instead, the parameters are specific to the choice of model, choice of reference data, and particular setup of each ABC test. However, this does not preclude the development of more widely accurate models in the future; the flexibility of ABC easily allows a multitude of reference data sources and types to be used in the parameter estimation process, thereby increasing the generality of the models developed.

Downloaded by UNIVERSITY OF COLORADO on January 17, 2022 | http://arc.aiaa.org | DOI: 10.2514/1.J060308

Acknowledgments

Olga A. Doronina and Peter E. Hamlington acknowledge financial support from NASA award NNX15 AU24A-03. Peter E. Hamlington was also supported, in part, by Air Force Office of Scientific Research award FA9550-17-1-0144. Helpful discussions with Werner J. A. Dahm, Ian Grooms, Will Kleiber, Greg Rieker, and Jason Christopher are gratefully acknowledged.

References

[1] Speziale, C. G., and So, R. M. C., "Turbulence Modeling and Simulation," *The Handbook of Fluid Dynamics*, edited by R. W. Johnson, Springer, Berlin, 1998, pp. 14.1–14.111, Chap. 14. https://doi.org/10.1115/1.4037557

[2] Xiao, H., and Cinnella, P., "Quantification of Model Uncertainty in RANS Simulations: A Review," *Progress in Aerospace Sciences*, Vol. 108, July 2019, pp. 1–31. https://doi.org/10.1016/j.paerosci.2018.10.001

[3] Oberkampf, W. L., and Trucano, T., "Validation Methodology in Computational Fluid Dynamics," *Fluids 2000 Conference and Exhibit*, AIAA Paper 2000-2549, 2000. https://doi.org/10.2514/6.2000-2549

[4] Oberkampf, W. L., and Trucano, T. G., "Verification and Validation in Computational Fluid Dynamics," *Progress in Aerospace Sciences*, Vol. 38, No. 3, 2002, pp. 209–272. https://doi.org/10.1016/S0376-0421(02)00005-2

[5] Cheung, S. H., Oliver, T. A., Prudencio, E. E., Prudhomme, S., and Moser, R. D., "Bayesian Uncertainty Analysis with Applications to Turbulence Modeling," *Reliability Engineering and System Safety*, Vol. 96, No. 9, 2011, pp. 1137–1149. https://doi.org/10.1016/j.ress.2010.09.013

[6] Oliver, T. A., and Moser, R. D., "Bayesian Uncertainty Quantification Applied to RANS Turbulence Models," *Journal of Physics: Conference Series*, Vol. 318, No. 4, 2011, Paper 042032. https://doi.org/10.1088/1742-6596/318/4/042032

[7] Ray, J., Lefantzi, S., Arunajatesan, S., and Dechant, L., "Bayesian Calibration of a $k-\epsilon$ Turbulence Model for Predictive Jet-in-Crossflow Simulations," *44th AIAA Fluid Dynamics Conference*, AIAA Paper 2014-2085, 2014. https://doi.org/10.2514/6.2014-2085

[8] Lefantzi, S., Ray, J., Arunajatesan, S., and Dechant, L., "Estimation of $k-\epsilon$ Parameters Using Surrogate Models and Jet-in-Crossflow Data," Sandia National Lab. TR SAND2015-0707, Livermore, CA, 2015. https://doi.org/10.2172/1170402

[9] Ray, J., Lefantzi, S., Arunajatesan, S., and Dechant, L., "Bayesian Parameter Estimation of a $k-\epsilon$ Model for Accurate Jet-in-Crossflow Simulations," *AIAA Journal*, Vol. 54, No. 8, Aug. 2016, pp. 2432–2448. https://doi.org/10.2514/1.J054758

[10] Ray, J., Lefantzi, S., Arunajatesan, S., and Dechant, L., "Learning an Eddy Viscosity Model Using Shrinkage and Bayesian Calibration: A Jet-in-Crossflow Case Study," *ASCE-ASME J Risk and Uncertainty in Engineering Systems, Part B: Mechanical Engineering*, Vol. 4, No. 1, 2018, Paper 011001. https://doi.org/10.1115/1.4037557

[11] Ray, J., Dechant, L., Lefantzi, S., Ling, J., and Arunajatesan, S., "Robust Bayesian Calibration of a $k-\epsilon$ Model for Compressible Jet-in-Crossflow Simulations," *AIAA Journal*, Vol. 56, No. 12, 2018, pp. 4893–4909. https://doi.org/10.2514/1.J057204

[12] Zhang, J., and Fu, S., "An Efficient Approach for Quantifying Parameter Uncertainty in the SST Turbulence Model," *Computers and Fluids*, Vol. 181, 2019, pp. 173–187. https://doi.org/10.1016/j.compfluid.2019.01.017

[13] Nadiga, B., Jiang, C., and Livescu, D., "Leveraging Bayesian Analysis to Improve Accuracy of Approximate Models," *Journal of Computational Physics*, Vol. 394, Oct. 2019, pp. 280–297. https://doi.org/10.1016/j.jcp.2019.05.015

[14] Edeling, W., Cinnella, P., Dwight, R., and Bijl, H., "Bayesian Estimates of Parameter Variability in the $k-\epsilon$ Turbulence Model," *Journal of Computational Physics*, Vol. 258, Feb. 2014, pp. 73–94. https://doi.org/10.1016/j.jcp.2013.10.027

[15] Beaumont, M. A., "Approximate Bayesian Computation," *Annual Review of Statistics and Its Application*, Vol. 6, March 2019, pp. 379–403. https://doi.org/10.1146/annurev-statistics-030718-105212

[16] Marjoram, P., Molitor, J., Plagnol, V., and Tavaré, S., "Markov Chain Monte Carlo Without Likelihoods," *Proceedings of the National Academy of Sciences*, Vol. 100, No. 26, 2003, pp. 15,324–15,328. https://doi.org/10.1073/pnas.0306899100

[17] Beaumont, M. A., Zhang, W., and Balding, D. J., "Approximate Bayesian Computation in Population Genetics," *Genetics*, Vol. 162, No. 4, 2002, pp. 2025–2035. https://doi.org/10.1093/genetics/162.4.2025

[18] Wegmann, D., Leuenberger, C., and Excoffier, L., "Efficient Approximate Bayesian Computation Coupled with Markov Chain Monte Carlo Without Likelihood," *Genetics*, Vol. 182, No. 4, 2009, pp. 1207–1218. https://doi.org/10.1534/genetics.109.102509

[19] Wawrzynczak, A., and Kopka, P., "Approximate Bayesian Computation for Estimating Parameters of Data-Consistent Forbush Decrease Model," *Entropy*, Vol. 20, No. 8, 2018, p. 622. https://doi.org/10.3390/e20080622

[20] Cameron, E., and Pettitt, A. N., "Approximate Bayesian Computation for Astronomical Model Analysis: A Case Study in Galaxy Demographics and Morphological Transformation at High Redshift," *Monthly Notices of the Royal Astronomical Society*, Vol. 425, No. 1, 2012, pp. 44–65. https://doi.org/10.1111/j.1365-2966.2012.21371.x

[21] Picchini, U., "Inference for SDE Models via Approximate Bayesian Computation," *Journal of Computational and Graphical Statistics*, Vol. 23, No. 4, 2014, pp. 1080–1100. https://doi.org/10.1080/10618600.2013.866048

[22] Luciani, F., Sisson, S. A., Jiang, H., Francis, A. R., and Tanaka, M. M., "The Epidemiological Fitness Cost of Drug Resistance in Mycobacterium Tuberculosis," *Proceedings of the National Academy of Sciences*, Vol. 106, No. 34, 2009, pp. 14,711–14,715. https://doi.org/10.1073/pnas.0902437106

[23] Zheng, Y., and Aris-Brosou, S., "Approximate Bayesian Computation Algorithms for Estimating Network Model Parameters," bioRxiv, 2017, Paper 106450. https://doi.org/10.1101/106450

[24] Beaumont, M. A., "Approximate Bayesian Computation in Evolution and Ecology," *Annual Review of Ecology, Evolution, and Systematics*, Vol. 41, Dec. 2010, pp. 379–406. https://doi.org/10.1146/annurev-ecolsys-102209-144621

[25] Csilléry, K., Blum, M. G. B., Gaggiotti, O. E., and François, O., "Approximate Bayesian Computation (ABC) in Practice," *Trends in Ecology and Evolution*, Vol. 25, No. 7, 2010, pp. 410–418. https://doi.org/10.1016/j.tree.2010.04.001

[26] Marin, J.-M., Pudlo, P., Robert, C. P., and Ryder, R. J., "Approximate Bayesian Computational Methods," *Statistics and Computing*, Vol. 22, No. 6, 2012, pp. 1167–1180. https://doi.org/10.1007/s11222-011-9288-2

[27] Lintusaari, J., Gutmann, M. U., Dutta, R., Kaski, S., and Corander, J., "Fundamentals and Recent Developments in Approximate Bayesian Computation," *Systematic Biology*, Vol. 66, No. 1, 2017, pp. e66–e82. https://doi.org/10.1093/sysbio/syw077

[28] Sisson, S. A., Fan, Y., and Beaumont, M., *Handbook of Approximate Bayesian Computation*, Chapman and Hall/CRC, Boca Raton, FL, 2018, Chap. 1. https://doi.org/10.1201/9781315117195

[29] Khalil, M., and Najm, H. N., "Probabilistic Inference of Reaction Rate Parameters from Summary Statistics," *Combustion Theory and Modelling*, Vol. 22, No. 4, 2018, pp. 635–665. https://doi.org/10.1080/13647830.2017.1370557

[30] Christopher, J. D., Wimer, N. T., Lapointe, C., Hayden, T. R. S., Grooms, I., Rieker, G. B., and Hamlington, P. E., "Parameter Estimation

for Complex Thermal-Fluid Flows Using Approximate Bayesian Computation," *Physical Review Fluids*, Vol. 3, No. 10, 2018, Paper 104602. https://doi.org/10.1103/PhysRevFluids.3.104602

[31] Christopher, J. D., Doronina, O. A., Petrykowski, D., Hayden, T. R. S., Lapointe, C., Wimer, N. T., Grooms, I., Rieker, G. B., and Hamlington, P. E., "Flow Parameter Estimation Using Laser Absorption Spectroscopy and Approximate Bayesian Computation," *Experiments in Fluids*, Vol. 62, No. 2, 2021, p. 43. https://doi.org/10.1007/s00348-020-03122-2

[32] Doronina, O. A., Christopher, J. D., Towery, C. A. Z., Hamlington, P. E., and Dahm, W. J. A., "Autonomic Closure for Turbulent Flows Using Approximate Bayesian Computation," *2018 AIAA Aerospace Sciences Meeting*, AIAA Paper 2018-0594, 2018. https://doi.org/10.2514/6.2018-0594

[33] Doronina, O. A., Towery, C. A. Z., and Hamlington, P. E., "Parameter Estimation for Subgrid-Scale Models Using Markov Chain Monte Carlo Approximate Bayesian Computation," arXiv: 2005.13993, 2020.

[34] Doronina, O. A., Towery, C. A. Z., Christopher, J. D., Grooms, I., and Hamlington, P. E., "Turbulence Model Development Using Markov Chain Monte Carlo Approximate Bayesian Computation," *AIAA Scitech 2019 Forum*, AIAA Paper 2019-1883, 2019. https://doi.org/10.2514/6.2019-1883

[35] Hamlington, P. E., and Dahm, W. J. A., "Reynolds Stress Closure for Nonequilibrium Effects in Turbulent Flows," *Physics of Fluids*, Vol. 20, No. 11, 2008, Paper 115101. https://doi.org/10.1063/1.3006023

[36] Hamlington, P. E., and Dahm, W. J. A., "Frequency Response of Periodically Sheared Homogeneous Turbulence," *Physics of Fluids*, Vol. 21, No. 5, 2009, Paper 055107. https://doi.org/10.1063/1.3140003

[37] Hamlington, P. E., and Ihme, M., "Modeling of Non-Equilibrium Homogeneous Turbulence in Rapidly Compressed Flows," *Flow, Turbulence and Combustion*, Vol. 93, No. 1, 2014, pp. 93–124. https://doi.org/10.1007/s10494-014-9535-7

[38] Yu, D., and Girimaji, S. S., "Direct Numerical Simulations of Homogeneous Turbulence Subject to Periodic Shear," *Journal of Fluid Mechanics*, Vol. 566, Nov. 2006, p. 117. https://doi.org/10.1017/S0022112006001832

[39] Bachalo, W. D., and Johnson, D. A., "Transonic, Turbulent Boundary-Layer Separation Generated on an Axisymmetric Flow Model," *AIAA Journal*, Vol. 24, No. 3, 1986, pp. 437–443. https://doi.org/10.2514/3.9286

[40] Nichols, R., Tramel, R., and Buning, P., "Solver and Turbulence Model Upgrades to OVERFLOW 2 for Unsteady and High-Speed Applications," *24th AIAA Applied Aerodynamics Conference*, AIAA Paper 2006-2824, 2006. https://doi.org/10.2514/6.2006-2824

[41] Schaefer, J., Hosder, S., West, T., Rumsey, C., Carlson, J.-R., and Kleb, W., "Uncertainty Quantification of Turbulence Model Closure Coefficients for Transonic Wall-Bounded Flows," *AIAA Journal*, Vol. 55, No. 1, 2017, pp. 195–213. https://doi.org/10.2514/1.J054902

[42] Zhao, Y., Yan, C., Wang, X., Liu, H., and Zhang, W., "Uncertainty and Sensitivity Analysis of SST Turbulence Model on Hypersonic Flow Heat Transfer," *International Journal of Heat and Mass Transfer*, Vol. 136, June 2019, pp. 808–820. https://doi.org/10.1016/j.ijheatmasstransfer.2019.03.012

[43] Haario, H., Saksman, E., and Tamminen, J., "An Adaptive Metropolis Algorithm," *Bernoulli*, Vol. 7, No. 2, 2001, pp. 223–242. https://doi.org/10.2307/3318737

[44] Scott, D. W., *Multivariate Density Estimation: Theory, Practice, and Visualization*, Wiley, Hoboken, NJ, 2015, Chap. 6. https://doi.org/10.1080/00401706.1993.10485361

[45] Silverman, B. W., "Density Estimator for Statistics and Data Analysis," *Statistics and Applied Probability*, 1st ed., Routledge, Boca Raton, FL, 1986, Chap. 2. https://doi.org/10.1201/9781315140919

[46] Girimaji, S. S., "Fully Explicit and Self-Consistent Algebraic Reynolds Stress Model," *Theoretical and Computational Fluid Dynamics*, Vol. 8, No. 6, 1996, pp. 387–402. https://doi.org/10.1007/BF00455991

[47] Wallin, S., and Johansson, A. V., "An Explicit Algebraic Reynolds Stress Model for Incompressible and Compressible Turbulent Flows," *Journal of Fluid Mechanics*, Vol. 403, Jan. 2000, pp. 89–132. https://doi.org/10.1017/S0022112099007004

[48] Gatski, T. B., and Jongen, T., "Nonlinear Eddy Viscosity and Algebraic Stress Models for Solving Complex Turbulent Flows," *Progress in Aerospace Sciences*, Vol. 36, 2000, pp. 655–682. https://doi.org/10.1016/S0376-0421(00)00012-9

[49] Launder, B. E., Reece, G., and Rodi, W., "Progress in the Development of a Reynolds Stress Turbulence Closure," *Journal of Fluid Mechanics*, Vol. 68, No. 3, 1975, pp. 537–566. https://doi.org/10.1017/S0022112075001814

[50] Speziale, C. G., Sarkar, S., and Gatski, T. B., "Modeling the Pressure Strain Correlation of Turbulence: An Invariant Dynamical Systems Approach," *Journal of Fluid Mechanics*, Vol. 227, June 1991, pp. 245–272. https://doi.org/10.1017/S0022112091000101

[51] Virtanen, P., Gommers, R., Oliphant, T. E., Haberland, M., Reddy, T., Cournapeau, D., Burovski, E., Peterson, P., Weckesser, W., Bright, J., van der Walt, S. J., Brett, M., Wilson, J., Millman, K. J., Mayorov, N., Nelson, A. R. J., Jones, E., Kern, R., Larson, E., Carey, C. J., Polat, I., Feng, Y., Moore, E. W., VanderPlas, J., Laxalde, D., Perktold, J., Cimrman, R., Henriksen, I., Quintero, E. A., Harris, C. R., Archibald, A. M., Ribeiro, A. H., Pedregosa, F., and van Mulbregt, P., and SciPy 1.0 Contributors, "SciPy 1.0: Fundamental Algorithms for Scientific Computing in Python," *Nature Methods*, Vol. 17, No. 3, 2020, pp. 261–272. https://doi.org/10.1038/s41592-019-0686-2

[52] Hindmarsh, A. C., "ODEPACK, A Systematized Collection of ODE Solvers," *Scientific Computing*, edited by R. S. Stepleman, et al., Vol. 1, IMACS Transactions of Scientific Computation, North-Holland, Amsterdam, 1983, pp. 55–64.

[53] Petzold, L., "Automatic Selection of Methods for Solving Stiff and Nonstiff Systems of Ordinary Differential Equations," *SIAM Journal on Scientific and Statistical Computing*, Vol. 4, No. 1, 1983, pp. 136–148. https://doi.org/10.1137/0904010

[54] Crow, S. C., "Viscoelastic Properties of Fine-Grained Incompressible Turbulence," *Journal of Fluid Mechanics*, Vol. 33, No. 1, 1968, p. 1–20. https://doi.org/10.1017/S0022112068002314

[55] Hamlington, P. E., and Dahm, W. J. A., "Nonlocal Form of the Rapid Pressure-Strain Correlation in Turbulent Flows," *Physical Review E*, Vol. 80, No. 4, 2009, Paper 046311. https://doi.org/10.1103/PhysRevE.80.046311

[56] Menter, F. R., "Two-Equation Eddy-Viscosity Turbulence Models for Engineering Applications," *AIAA Journal*, Vol. 32, No. 8, 1994, pp. 1598–1605. https://doi.org/10.2514/3.12149

[57] Wilcox, D. C., "Reassessment of the Scale-Determining Equation for Advanced Turbulence Models," *AIAA Journal*, Vol. 26, No. 11, 1988, pp. 1299–1310. https://doi.org/10.2514/3.10041

[58] Childs, M. L., Pulliam, T. H., and Jespersen, D. C., "OVERFLOW Turbulence Model Resource Verification Results," NASA Ames Research Center TR NAS-2014-03, 2014.

[59] Jespersen, D. C., Pulliam, T. H., and Childs, M. L., "Overflow Turbulence Modeling Resource Validation Results," NASA Ames Research Center TR NAS-2016-01, 2016.

D. Livescu
Associate Editor

Downloaded by UNIVERSITY OF COLORADO on January 17, 2022 | http://arc.aiaa.org | DOI: 10.2514/1.J060308